Tracing the Cenozoic Southern Patagonian Andes growth (51°15” S-53°39” S) from the integrated study of the orogen-foreland basin pair

Huber Alberto Rivera Rosado

UNIVERSIDAD DE CHILE

Université Grenoble Alpes

THÈSE

Pour obtenir le grade de

DOCTEUR DE L'UNIVERSITE GRENOBLE ALPES

préparée dans le cadre d'une cotutelle entre l'*Université Grenoble Alpes* et *l'Université du Chili*

Spécialité : **Sciences de la Terre et de l'Univers et de l'Environnement**

Arrêté ministériel : le 6 janvier 2005 – 25 mai 2016

Présentée par

Huber Alberto RIVERA ROSADO

Thèse dirigée par **Joseph MARTINOD** et codirigée par **Marcelo FARIAS THIERS**

préparée au sein de **l'Institute des Sciences de la Terre (ISTerre) et le Département de Géologie (UChile)**

dans **l'École Doctorale Sciences de la Terre, de l'Environnement et des Planètes (STEP-UGA) et la Faculté des Sciences Physiques et Mathématiques (FCFM-UChile)**

Traçage de la croissance Cénozoïque des Andes de Patagonie méridionale (51°15''-53°39'' S) à partir de l'étude couplée orogène/bassin d'avant-pays

Thèse soutenue publiquement le **11 mars 2022**,
devant le jury composé de :

Dr Brian HORTON
Professeur à l'Université du Texas à Austin, USA (Rapporteur)
Dr Jean-Nöel PROUST
Directeur de Recherche CNRS à l'Université de Rennes 1 (Rapporteur)
Dr Reynaldo CHARRIER
Professeur à l'Université Andres Bello à Santiago du Chili (Examinateur, Président du jury)
Dr Matthias BERNET
Maître de conférence à l'Université Grenoble Alpes (Examinateur)
Dr Joseph MARTINOD
Professeur des Universités à l'Université Savoie Mont Blanc (Directeur de thèse)
Dr Marcelo FARIAS
Professeur Assistant à l'Université du Chili à Santiago du Chili (Co-Directeur de thèse)

UNIVERSIDAD DE CHILE

Université Grenoble Alpes

THESIS

In order to obtain the grade of

DOCTEUR DE L'UNIVERSITE GRENOBLE ALPES

prepared as part of a cotutelle between the *Université Grenoble Alpes* and *the University of Chile*

Specialty : **Sciences de la Terre et de l'Univers et de l'Environnement**

Ministerial order: January 6th, 2005 – May 25th, 2016

Presented by

Huber Alberto RIVERA ROSADO

Thesis directed by **Joseph MARTINOD** and co-directed by **Marcelo FARIAS THIERS**

Prepared in the **Institute des Sciences de la Terre (ISTerre) and Department of Geology (UChile)**

In the **École Doctorale Sciences de la Terre, de l'Environnement et des Planètes (STEP-UGA) and the Faculty of Physical and Mathematical Sciences (FCFM-UChile)**

Tracing the Cenozoic Southern Patagonian Andes growth (51°15''-53°39" S) from the integrated study of orogen-foreland basin pair

Thesis publicly defended on **11 March 2022**

In front of the jury composed by:

Dr Brian HORTON
Professor at the University of Texas at Austin, USA (Referee)

Dr Jean-Nöel PROUST
Research Director CNRS at the University of Rennes 1 (Referee)

Dr Reynaldo CHARRIER
Professor at the University Andres Bello at Santiago of Chile (Examiner, President of the jury)

Dr Matthias BERNET
Associate Professor at the University Grenoble Alpes (Examiner)

Dr Joseph MARTINOD
Professor at the University Savoie Mont Blanc (Thesis supervisor)

Dr Marcelo FARIAS
Assistant Professor at the University of Chile at Santiago of Chile (Thesis co-supervisor)

UNIVERSIDAD DE CHILE
FACULTAD DE CIENCIAS FÍSICAS Y MATEMÁTICAS
DEPARTAMENTO DE GEOLOGÍA

TRACING THE CENOZOIC SOUTHERN PATAGONIAN ANDES GROWTH (51°15''-53°39"S) FROM THE INTEGRATED STUDY OF OROGEN-FORELAND BASIN PAIR

TESIS PARA OPTAR AL GRADO DE DOCTOR EN CIENCIAS MENCIÓN GEOLOGÍA
EN COTUTELA CON LA UNIVERSIDAD GRENOBLE ALPES

HUBER ALBERTO RIVERA ROSADO

PROFESOR GUÍA :
Dr. MARCELO FARÍAS THIERS

PROFESOR CO-GUÍA :
Dr. JOSEPH MARTINOD

MIEMBROS DE LA COMISIÓN:

Dr. REYNALDO CHARRIER
Dr. BRIAN HORTON
Dr. JEAN-NOËL PROUST
Dr. MATTHIAS BERNET

Este trabajo ha sido parcialmente financiado por los proyectos Fondecyt 1161806 y 1130006, ANID Becas/Doctorado Nacional 21170419 y Bourse d'excellence Eiffel 2019/n°P745330B

SANTIAGO DE CHILE
2022

RÉSUMÉ

La compréhension de la dynamique des processus tectoniques qui ont conduit à la formation de la cordillère des Andes s'appuie sur l'étude de l'enregistrement sédimentaire des bassins d'avant-pays, d'avant-arc et intra-arc situés au pied de la chaîne. Ces travaux ont conduit à proposer différents modèles d'évolution du système orogénique andin. Cependant, l'histoire de l'évolution du segment le plus méridional des Andes, celui des Andes du sud de la Patagonie, reste mal connue et mal comprise. Cette thèse constitue une étude du bassin d'avant-pays Magellan-Austral (situé entre 51°15' S et 53°39' S). Son objectif est de mieux caractériser l'évolution tectonique des Andes de Patagonie méridionale. Pour cela, il a été nécessaire d'utiliser une approche pluridisciplinaire intégrant différents types de données, afin d'obtenir des informations qualitatives et quantitatives permettant de mieux connaitre l'histoire tectonique du prisme orogénique.

Cette thèse s'appuie sur des observations de terrain (directions de paléocourants, épaisseurs et descriptions pétrographiques des unités sédimentaires), sur des données de subsurface (épaisseurs inter-horizons, diagraphies, géométrie et continuité des réflecteurs sismiques) et sur des analyses de laboratoire (concentrations en éléments chimiques et en isotopes, traces de fission). Ces observations et ces mesures ont permis :

- d'estimer les âges maximums de dépôt des sédiments et d'analyser l'évolution temporelle de l'arc magmatique.
- d'analyser les faciès sédimentaires en termes de sismostratigraphie et de stratigraphie séquentielle.
- de faire une analyse qualitative et quantitative des provenances sédimentaires (comptes modaux des conglomérats et des grès, géochimie sédimentaire, âges U-Pb des zircons détritiques).
- de cartographier les épaisseurs stratigraphiques dans le bassin (isopaques) et la subsidence associée.
- de caractériser la structuration de la chaîne plissée et faillée et son exhumation, à l'aide d'analyses thermochronologiques (traces de fission et mesures des concentrations U-Th/He dans les apatites détritiques).

Les résultats obtenus permettent d'affiner le cadre chronostratigraphique du bassin Magellan-Austral (à l'exclusion de sa partie située en Terre de Feu). Ce cadre constitue une base permettant d'intégrer les connaissances géologiques acquises dans les différentes

parties du bassin et d'identifier des hiatus dans l'enregistrement stratigraphique. Sept séquences tectono-stratigraphiques de troisième ordre ont été identifiées. Elles marquent la réponse sédimentaire aux différents stades d'évolution du prisme orogénique andin. Au cours du stade le plus précoce de formation du bassin d'avant-pays, qui débute vers 114 Ma dans la région du détroit de Skyring et de la péninsule du Nouveau-Brunswick (entre 52°20'S et 53°40'S), un large espace d'accommodation apparait en réponse à la subsidence flexurale de la plaque. Il conduit à l'établissement d'environnements marins profonds (bassin sous-alimenté). Le remplissage progressif de la fosse d'avant-pays et le passage à des environnements de dépôt moins profonds se produit progressivement à partir du Campanien. A cette époque, l'érosion du socle s'accentue dans la partie la plus interne du prisme orogénique en réponse à la réactivation de failles normales préexistantes (prisme sous-critique) alors que simultanément, de façon surprenante, la subsidence liée à la flexure de la plaque diminue. Cet épisode de remplissage de la fosse d'avant pays, associé à la réduction de la subsidence et à l'érosion accrue de la chaîne naissante, est attribuée à un phénomène de rebond isostatique résultant du détachement de la croûte océanique dense du bassin de Rocas Verdes qui s'était formée pendant la phase extensive jurassique. La première et la plus vaste transgression marine atlantique se produit au cours du Maastrichtien-Danien. Elle résulte d'une subsidence flexurale accélérée, amplifiée par l'effet combiné de la subsidence dynamique, et conduit au rétablissement d'environnements marins profonds dans l'avant-pays. Cette phase de charge tectonique importante, qui dure jusqu'au début de l'Éocène, entraîne un élargissement du prisme orogénique (prisme supercritique) et une migration rapide de l'avant-pays vers l'est, à mesure que se développe un système de plis et chevauchements associés à un niveau de décollement situé dans les lutites du Crétacé inférieur. L'Eocène moyen enregistre le passage progressif à des dépôts plus superficiels et se caractérise par une tendance à la surrection (diminution de la flexure), une érosion accrue du prisme orogénique et une accalmie de l'arc magmatique qui était resté actif jusqu'au Paléocène. Cette période de quiescence tectonique résulte de la subduction de la dorsale Farallón-Aluk (Phoenix), qui interrompt la compression et l'activité de l'arc magmatique, déclenche un rebond isostatique généralisé et le basculement vers l'est du système de chevauchement développé précédemment. La dernière phase tectonique de contraction (et de flexure) se produit entre la fin de l'Éocène et la fin de l'Oligocène. Elle coïncide avec le début de l'ouverture du passage de Drake et l'expansion océanique de la plaque Ouest-Scotia, dans un contexte de convergence fortement oblique. Elle est marquée par des épisodes ponctuels de subsidence, créant un espace d'accommodation accru qui permet le dépôt de sédiments marins de plateforme, dans un contexte qui est sinon dominé le dépôt de séries

encore moins profondes, marines et continentales. Ces séries recouvrent un domaine bien plus vaste que l'avant-pays et vont jusqu'à enterrer la zone de rebond flexural (passage à un bassin sur-alimenté). La déformation se caractérise à la fois par l'inversion de failles de socle extensives, et par le développement d'un niveau de décollement plus superficiel situé dans les couches de l'Éocène inférieur qui conduit à l'apparition de plis par propagation de faille et de rétro-chevauchements. De plus, une exhumation régionale généralisée affectant à la fois le prisme orogénique et le bassin d'avant-pays se produit à la fin de l'Oligocène. Cette exhumation se poursuit jusqu'au début du Miocène. Elle marque la phase finale du stade de bassin d'avant-pays et l'arrêt de la déformation compressive. L'arc magmatique transitionnel calco-alcalin à alcalin migre vers l'est à cette époque et interfère avec la sédimentation de dépôts continentaux grossiers post-orogéniques qui progradent rapidement bien au-delà de l'ancien forebulge, où la subsidence dynamique se concentre. La subsidence dynamique et les changements eustatiques jouent un rôle important sur les transgressions marines du Miocène. L'arrêt du régime compressif et le léger basculement régional vers l'est, ainsi que l'exhumation généralisée et la migration vers l'est de l'arc magmatique transitionnel, permettent de relier l'évolution géologique du Miocène inférieur à la subduction de la dorsale du Chili. Enfin, à la fin du Néogène, on observe une autre phase d'exhumation due aux processus d'érosion glaciaire ou fluvioglaciaire.

Mots clés : Andes ; Patagonie ; Bassin Magellan-Austral ; Bassin d'avant-pays ; Provenance sédimentaire ; Subsidence ; Sédimentologie ; Tectonique ; Subduction de dorsale ; Thermochronologie ; Exhumation.

ABSTRACT

The understanding of the dynamics of the tectonic processes that have given rise to the orogenic build of the Andean mountain range has been improved by the study of the sedimentary record of the linked foreland, fore-arc and intra-arc basins. The latter has given rise to different hypotheses that attempt to explain the evolution of the Andean orogenic system. However, the complex southernmost Andean segment, the Southern Patagonian Andes, still lacks a comprehensive understanding of its evolution history. Therefore, this thesis focuses on the study of the Magallanes-Austral foreland basin (51°15" S to 53°39" S), to offer greater clarity on the tectonic evolution of the Southern Patagonian Andes. To this purpose, it is required to use an integrative approach that involves multidisciplinary methods and different types of data sources to obtain both qualitative and quantitative information on the tectonic history of the orogenic wedge. This thesis takes advantage of data measured in outcrops (paleocurrent directions, thicknesses, petrographic descriptions), in the subsurface (thicknesses between horizons, well logs response, geometry and continuity of seismic reflectors), and in the laboratory (concentration of chemical elements and isotopes, and fission tracks counts), which constitute the basis for:

- Estimation of maximum deposition ages and analysis of the magmatic arc tempo.
- Facies, seismo-stratigraphic and sequential stratigraphic analysis.
- Qualitative and quantitative analysis of sedimentary provenance (including modal counting of conglomerates and sandstones, sedimentary geochemistry, detrital zircons U-Pb ages).
- Analysis of subsidence and distribution of stratigraphic thicknesses in the basin (isopachs).
- Structural geological analysis and exhumation timing (through detrital apatites fission tracks and U-Th/He thermochronology) of the folded and extended belt.

The results obtained allow the refinement of the chronostratigraphic framework of the Magallanes-Austral basin (excluding Tierra del Fuego), which forms the basis for the integration of geological knowledge of different parts of the basin and a fundamental criterion for the identification and quantification of the hiatus present in the stratigraphic record. Seven 3rd order tectonostratigraphic sequences were identified, which represent the sedimentary response to the orogenic wedge evolution stages of the Southern Patagonian Andes. During the early foreland stage, which is estimated to have started *ca*. 114 Ma in the Skyring Sound-Brunswick Peninsula area (52°20"S to 53°40"S), an ample accommodation

(due to flexural subsidence) develops in the foredeep allowing the establishment of deep marine environments (underfilled basin). A progressive filling and shallower depositional environment occur from the Campanian when erosion is accentuated in an emerging orogenic wedge of basement concentring deformation in its innermost part through the reactivation of pre-existing normal faults (subcritical wedge state). Simultaneously, and anti-intuitively, the flexural subsidence decreases. This increasingly sediment-clogged foredeep, accompanied by decreasing subsidence and enhanced erosion of the incipient fold-and-thrust belt, is attributed to an isostatic rebound process due to detachment of the dense oceanic crust generated during the extensional phase of the predecessor Rocas Verdes Basin. During the Maastrichtian-Danian, took place the first and most extensive Atlantic marine transgression, which was favoured by accelerated flexural subsidence (intensified by the combined effect of dynamic subsidence) that allowed the re-establishment of deep marine environments in the foredeep. This prominent tectonic loading stage, which lasted up to the early Eocene, resulted in a broadening of the orogenic wedge (supercritical wedge state) and rapid eastward foredeep migration as an imbricated thrust and fault propagation fold system developed. The detachment levels by this time were located in Lower Cretaceous shales. The middle Eocene is characterized by the progressive shallowing of the depositional system, a tendency to negative flexural subsidence rates (uplift), increased erosion of the orogenic wedge and a magmatic arc lull (active until the Paleocene). This period of quiescence tectonic is related to the effect of the Farallón-Aluk (Phoenix) ridge subduction, which interrupted the compression and magmatic arc activity, triggering a generalized isostatic rebound and eastwards tilting of the previously developed imbricate thrust system. The last contractional tectonic phase (and flexural loading), occurs between the late Eocene and late Oligocene, coinciding with the beginning of the opening of the Drake Passage and spreading of the West Scotia Sea and highly oblique convergence. It is marked by punctual subsidence pulses, drivers of enhanced accommodation hosting shelf environments in a context that is otherwise dominated by even shallower marine and continental depositional systems, which prograde far beyond of the foredeep until burying the forebulge (transition an overfilled basin). The deformation is characterized by both reactivation of extensional faults in the basement and a jump to more superficial levels of detachment in lower Eocene strata, developing fault propagation folds and backthrusts. Further, a generalized exhumation of the orogenic wedge and the foreland basin is recorded by the end of the Oligocene. This exhumation continues until the early Miocene, portraying the final phase of the foreland basin stage and the cessation of active compressional deformation. A transitional calc-alkaline to alkaline magmatic arc migrated eastward, impacting the concomitant

sedimentation of coarse post-orogenic continental deposits that rapidly prograde far beyond the forebulge, where a dynamic subsidence is concentrated (net overfilled basin). Dynamic subsidence and eustatic changes acquire a more important role on the Miocene marine transgressions. The cessation of the compressive regime and only a slight tilt to the east, generalised exhumation and eastward migration of the transitional magmatic arc, motive to establish a causal relationship with the Chilean ridge subduction. Finally, for the late Miocene, another exhumation phase is recorded, which is related to glacial or fluvioglacial erosion processes.

Keywords*: Southern Patagonian Andes; Magallanes-Austral; Foreland Basin; Sedimentary provenance; Subsidence; Sedimentology; Tectonics; Ridge subduction; Thermochronology; Exhumation.*

RESUMEN

La comprensión de la dinámica de los procesos tectónicos que han dado lugar a la construcción orogénica de la cordillera de los Andes, ha sido favorecida por el estudio del relleno sedimentario de las cuencas de antepaís, ante-arco e intra-arco asociadas. Lo anterior, ha dado lugar a diferentes hipótesis que intentan explicar la evolución del sistema orogénico Andino. No obstante, el complejo segmento andino más austral, los Andes Patagónicos del Sur, adolocen aún de un entendimiento exhaustivo sobre su historia evolutiva. Por lo tanto, esta tesis se enfoca en el estudio de la cuenca de antepaís Magallanes-Austral (51°15”S a 53°39”S), con el propósito de ofrecer mayor claridad sobre la evolución tectónica de los Andes Patagónicos del Sur. A tal efecto, se requiere utilizar un enfoque integrativo que involucre métodos multidisciplinarios y diferentes tipos de fuentes de datos para obtener información tanto cualitativa y cuantitativa sobre la historia tectónica de la cuña orogénica. En esta tesis se toma ventaja de datos medidos en afloramientos (direcciones de paleocorrientes, espesores, descripciones petrográficas), en el subsuelo (espesores entre horizontes, respuesta de registros de pozos, geometría y continuidad de reflectores sísmicos) y en laboratorio (concentración de elementos químicos e isótopos, y conteo de trazas de fisión), los cuales consituyen la base para:

- Estimación de edades máximas de depositación y análisis del tempo del arco magmático.
- Análisis de facies, sismoestratigráfico y estratigráfico secuencial.
- Analisis cualitativo y cuantitativo de proveniencia sedimentaria (incluyendo conteo modal de conglomerados y areniscas, geoquímica sedimentaria, edades U-Pb de circones detríticos).
- Análisis de subsidencia y de distribución de espesores estratigráficos en la cuenca (isópacos).
- Análisis geológico estructural y temporalidad de la exhumación (por medio del análisis termocronologicos de trazas de fisión y U-Th/He en apatitos detríticos) de la faja plegada y corrida.

Los resultados obtenidos permiten el refinamiento del marco cronoestratigráfico de la cuenca de Magallanes-Austral (excluyendo Tierra del Fuego), el cual conforma la base para la integración del conocimiento geológico de diferentes partes de la cuenca y un criterio fundamental para la identificación y cuantificación de los hiatos presentes en el registro estratigráfico. Se identificaron 7 secuencias tectonoestratigáficas de 3er orden, las cuales

constituyen la respuesta sedimentaria a las diferentes etapas evolutivas de la cuña orogénica de los Andes Patagónicos del Sur. Durante la etapa más temprana de antepaís, la cual se estima pudo haber inciado *ca*. 114 Ma en el área de Seno Skyring-Península Brunswick (52°20”S a 53°40”S), se desarrolla una amplia acomodación (por subsidencia flexural) en la antefosa permitiendo el establecimiento de ambientes marinos profundos (etapa de cuenca hambrienta). El relleno de la antefosa y somerización de los ambientes depositacionales sucede de manera progresiva a partir del Campaniano, cuando se acentúa la erosión en una cuña orogénica de basamento emergente que concentra la deformación en su parte más interna mediante la reactivación de fallas normales pre-existentes (estado de cuña subcrítica) pero anti-intuitivamente simultáneamnte disminuye la subsidencia flexural. Esta etapa de colmatación de la antefosa, reducción de la subsidencia y erosión de la prematura faja plegada y corrida, es atribuida a un proceso de rebote isostático por desprendimiento de la densa corteza oceánica generada durante la fase extensional de la predecesora Cuenca de Rocas Verdes. Durante el Maastrichtiano-Daniano, toma lugar la primera y más extendida transgresión marina del Atlántico, la cual fue favorecida por un incremento acelerado de la subsidencia flexural (intensificado por el efecto combinado de subsidencia dinámica) que permitió de nuevo el establecimiento de ambientes marinos profundos en la antefosa. Este estadío de carga tectónica prominente, que se extiendió hasta el Eoceno inferior, se manifestó como un ensanchamiento lateral de la cuña orogénica (estado de cuña supercrítica) que condujo a una migración rápida de la antefosa hacia el este, a medida que se desarrollaba un abanico imbricado de corrimientos y pliegues por propagación de fallas con nivel de despegue situado en estratos lutíticos del Cretácico Inferior. El Eoceno medio se caracteriza por la progresiva somerización del sistema depositacional, tendencia a la inversión de las tasas de subsidencia flexural (alzamiento), aumento de la erosión de la cuña orogénica y un apagado del arco magmático (activo hasta el Paleoceno). Este periodo de quietud tectónica se relaciona con el efecto de la subducción de la dorsal activa de Farallón-Aluk (Phoenix), el cual interrumpió la compresión y actividad del arco magmático, desencadenando una respuesta de rebote isostático generalizado y basculamiento hacia el este del abanico imbricado desarrollado previamente. La última fase tectónica compresiva (carga flexural), se desarrolla entre el Eoceno tardío y Oligoceno tardío, coincidente con el inicio de la apertura del Paso de Drake y del mar de Scotia Oeste. Está marcada por pulsos puntuales de subsidencia, gatillantes de mayor acomodación albergando ambientes marinos de plataforma en un contexto que de otra forma está dominado por sistemas depositacionales marinos cada vez más someros a continentales que progradan más allá de la antefosa hasta sepultar el bulbo periférico (transición a etapa de cuenca sobrellenada). La deformación está

caracterizada tanto por reactivación de fallas extensionales en el basamento y un cambio a un nivel de despegue más superficial en estratos del Eoceno inferior, desarrollando pliegues por propagación de fallas y retrocorrimientos. Adicionalmente, se registra una exhumación generalizada de la cuña orogénica y de la cuenca antepaís para finales del Oligoceno. Esta exhumación continúa hasta el Mioceno temprano, retratando la fase final de la etapa de cuenca antepaís y cese de la deformación activa compresional. Un arco magmático transicional migró hacia el este, impactando la concomitante sedimentación de depósitos continentales gruesos post-orogénicos que progradan rápidamente más allá del bulbo periférico, donde se concentra una subsidencia dinámica (etapa de cuenca sobrellenada neta). La subsidencia dinámica adquiere un rol principal junto con los cambios eustáticos para facilitar las transgresiones marinas del Mioceno. El cese del régimen compresivo y tan sólo un ligero basculamiento hacia el este, generalizada exhumación y migración hacia el este del arco magmatico de naturaleza transicional, incitan a establecer una relación causal con la subducción de la dorsal de Chile. Finalmente, para el Mioceno tardío, se registra otra fase de exhumación la cual se relaciona a procesos de erosion glaciar o fluvio-glaciar.

Palabras claves: *Andes Patagónicos del Sur; Magallanes-Austral; Cuenca de antepaís; Proveniencia sedimentaria; Subsidencia; Sedimentología; Tectónica; Subducción dorsal; Termocronología; Exhumación.*

"Plausible hypotheses often become established as generally accepted facts by the mere passage of time and the lack of a direct challenge"

Richard Dana Russell (1937, p. 1307)

A la memoria de mi amiga Taimis Carrillo

En reconocimiento de la fuerza vital, templanza y perseverancia de Johana Rosado

ACKNOWLEDGMENTS

Mi vida durante estos 4 años (y un poco más!) de tesis se resumen en tres etapas: una incial de motivación y energía, cargada de fuerza mental, creatividad, y alegría; una intermedia con grandes retos, continuos cambios, estrés y desorientación, y fatiga; una última plena de vicisitudes, de pandemia y confinamientos, cambios de planes repentinos, adaptaciones a la separaciones y a las nuevas uniones, extenuación mental y emocional, pero sobretodo cero de motivación. Pero el hecho de que hoy esté escribiendo esto, significa que tengo mucho por agradecer, primero a Dios por darme la fuerza, la paciencia y la convicción que perdí durante una parte de este camino.

Quiero extender mi voz de agradecimiento a mi familia en general, y en especial a mi madre Ada, mi padre Huber, mis hermanas Angélica y Angie, a mi tía Nayibe, mi abuela Magali y a mi tía Faride. Ustedes fueron esenciales en diferentes momentos de este camino sabiendo actuar, hablar o simplemente escuchar.

A mis amigos Leonardo Guerra, William Primera, Andrés Aguilar, Carlos Perea que me apoyaron, me ~~presionaron~~ motivaron y me brindaron su invaluable compañía, alegría y comprensión tanto en presencial como a distancia. Un agradecimiento especial a quien considero mi amigo y maestro, Jacobus Le Roux, por su apoyo y ayuda aún estando lejos de este mundo académico y de Santiago también! A todas las personas que me brindaron su camaradería tanto en Chile como en Francia: Sebastián Herrera; Iván Gómez, quién también fue fundamental en mi último trabajo de terreno en Patagonia; Camila Arróspide (éxitos en tu Doctorado syn-pandémico), a Sandrine Roy, Camila Novoa, María José Hernández. Un grand merci à M. Gérard Frambourg pour son aide et coaching au niveau de la projection professionnelle.

Agradezco a todos los investigadores y personal técnico quienes me ayudaron a alcanzar con éxito los resultados para la tesis y quienes aportaron como co-autores en los artículos. Al personal de ENAP, especialmente a Lisandro Rojas por su amable colaboración en permitir el acceso a valiosa información petrolera. A mis directores de tesis Joseph Martinod y Marcelo Farías por sus constantes comentarios y por ayudarme a ampliar mi visión sobre la Tectónica de los Andes y por su ayuda a nivel personal también; a Stéphanie Brichau y Matthias Bernet por su paciencia, tiempo y dedicación durante la preparación, ejecución y análisis termocronológicos. A los revisores de la tesis Reynaldo Charrier, Jean-Noël Proust, Brian Horton y Matthias Bernet quienes tomaron de su valioso tiempo para

sugerirme mejoras y compartir un poco de su experiencia y conocimiento sobre los Andes y el análisis de cuencas.

Finalmente, un agradecimiento especial a la familia Ouvier quienes me acogieron en su seno familiar de una manera sincera, noble y desinteresada y me han apoyado incansablemente. A mi amada Christelle Dupont quien ha sido un pilar fundamental para mi vida en este último año, quien ha sabido ser comprensiva, amorosa y me ha dado todo su apoyo. Gracias por acompañarme en las noches de trasnocho durante las largas jornadas de escritura, merci beaucoup de *ressentir* avec moi mes frustrations, mes joies, mes souhaits et de m'apporter constamment de l'amour dans ma vie… Je t'aime très fort mi amor.

TABLE OF CONTENTS

LIST OF FIGURES

CHAPTER I-1:

CHAPTER I-2:

CHAPTER II-1:

CHAPTER III-1:

CHAPTER III-2:

CHAPTER IV-1:

CHAPTER V-1:

LIST OF TABLES

CHAPTER II-1:

CHAPTER III-1:

CHAPTER III-2:

CHAPTER IV-1:

FIRST PART

RESEARCH RATIONALE AND METHODOLOGY

CHAPTER I-1 :
GENERAL INTRODUCTION

Chapter I-1 presents an introduction to the subject of study, pointing out the subcontinental-scale geological setting of the research area, objectives, and research questions to be addressed. First, the Andes orogen is approached as one of the most important worldwide Cordilleran systems, followed by a succinct description of the different models that explain its construction. Then, the Magallanes-Austral foreland basin is presented beside the state-of-the-art of its tectonic and sedimentary evolution. Ensuing, the research questions are posed, which constitute the basis of the scientific motivation of this thesis.

I-1.1 Geological context of the Andes

The Andes (Fig. 1) are the most extensive active orogenic system in the world, and its development has long been considered by a simple set of subductions of an oceanic crust beneath a continental margin (Dewey and Bird, 1970; Ramos, 2009), but in fact, the Andean-style orogeny is related to radical changes in plate boundary conditions (Mpodozis and Ramos, 1989; Ramos 2009; Armijo et al., 2015). The latter conditions are expressed as a complex series of subduction of different types of oceanic crust (e.g., oceanic plateaux, aseismic ridges, and microplates), terrane accretions, spreading ridge collisions, tectonic erosion, and flat-slab subduction. A morphostructural segmentation is evident along the Andean orogen (Fig. 1): the northern, central, and southern Andes. Although these discrete segments of the Andes share similar processes during their conformation (i.e., Mesozoic extensional phase, flat-slab subduction, climatic control, etc.), each of them has undergone a complex and unique tectonic evolutionary history that differentiates them from the others (see Ramos, 2009, for a review).

Over the years, many authors have tried to explain the mechanisms that have controlled the Andes' complex evolution and proposed models generalising the complete orogen. Ramos (2009) propose a conceptual model of the Andean orogenic cycle (Fig. 2), which begins after a quiescent period of deformation and magmatism followed by migration and expansion of the magmatic arc, which forces the orogenic front and its associated foreland basin to migrate eastward during the shallowing of the subduction angle. Once the flat subduction is fully established, a broken foreland basin develops while accentuated cortical shortening occurs. Subsequent steepening of the slab led to an extensional collapse of the orogen accompanied by crustal and lithospheric delamination and thermal uplift. The latter facilitates lower crustal ductile contraction and thin-skinned fold and thrust-belt formation in the adjacent foreland.

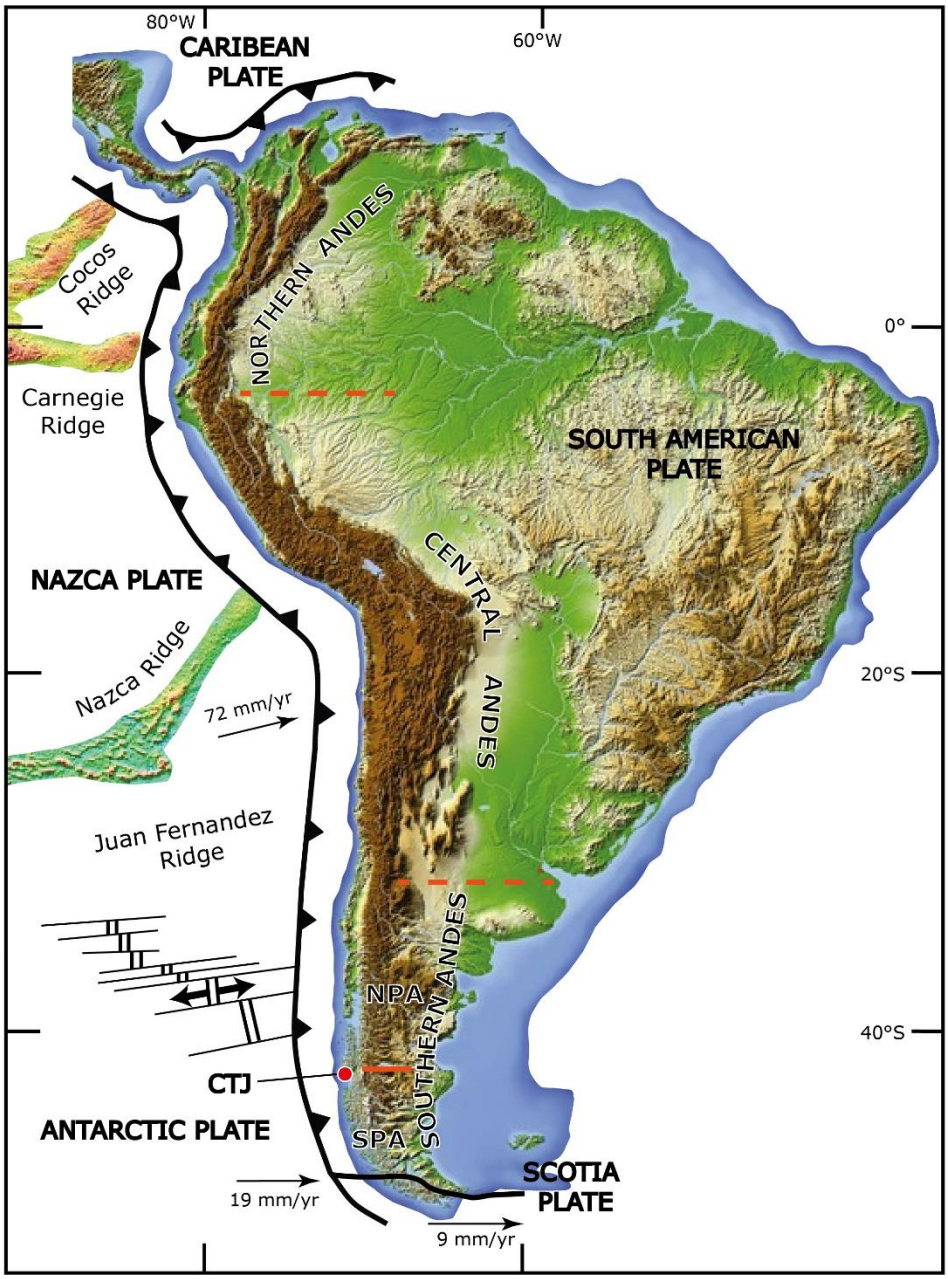

Figure 1. Plate tectonics context and morphotectonic segmentation of the Andes. The Chilean Triple Junction (CTJ) split the Southern Andes into the Northern Patagonian Andes (NPA) and the Southern Patagonian Andes (SPA).

The Cordilleran cyclicity model, proposed by DeCelles et al. (2009, 2015), states that a cyclical removal of thickened orogenic roots (e.g., eclogite bodies under the Altiplano Plateau) in addition to transient periods of shallowing and steepening of the subducting slab acting over a temporal framework of ~25 to 50 Myr exert a strong control in the dynamic of the entire orogen (e.g., flux and composition of arc magmatism, rates of crustal shortening and surface uplift, and foreland basin sedimentation) (Fig. 3).

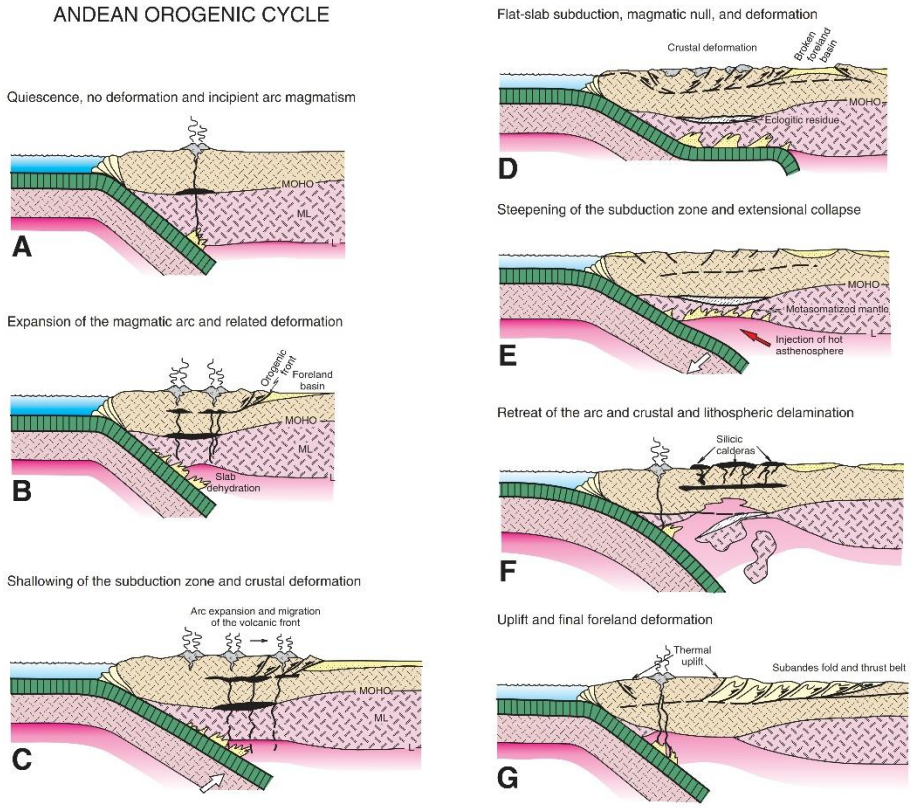

Figure 2. Idealised tectonic evolution of a typical Andean orogenic cycle sensu Ramos (2009), which comprise: A. Quiescence absence of deformation, and incipient arc magmatism; B. Expansion of the magmatic arc and related deformation; C. Shallowing of the subduction zone and crustal thickening; D. Flat-slab subduction, magmatic lull and deformation; E. Steepening of subduction and extensional collapse; F. Retreat of arc magmatism and crustal and lithospheric delamination; G. Uplift and final foreland deformation. ML = lithospheric mantle**.**

On the other hand, Horton and Fuentes (2016) and Horton (2018b) propose that spatial and temporal variability in phases of Andean evolution can be linked to the degree of mechanical coupling or decoupling along the subduction zone, which is related to changes in convergence and variations in slab subduction angle (Fig. 4). The different degrees of mechanical coupling trigger episodic contractional, neutral and extensional tectonic regimes in the Andes orogenic system. More recently, Martinod et al. (2020) proposed a model of growth and widening of the Andes strongly controlled by the geometry of the subducting slab. In this model, horizontal subduction triggers the growth of a second crustal wedge in the continent's hinterland, which widens the Andean and displaces the shortening and foreland basin eastward. This second crustal wedge is distinct from the first crustal wedge developed near the trench during normal-angle slab subduction.

All those previous models are intended to explain the evolution of the Andes mountain in any latitude. However, most of them are based on comprehensive studies on the tempo and style of shortening, magmatism dynamics, exhumation and surface uplift, and basins evolution around the central and southern-central part of the Andes. In contrast, in the

Southern Patagonian Andes (Fig. 1), one of the poorest studied zones in the Andean Cordilleran system, any recent models have never been thoroughly tested. Instead, other hypotheses (described in chapter V-1) have rooted that attempt to reconcile the complex geodynamic evolution of the Patagonian region to explain the evolution of this segment of the Andes.

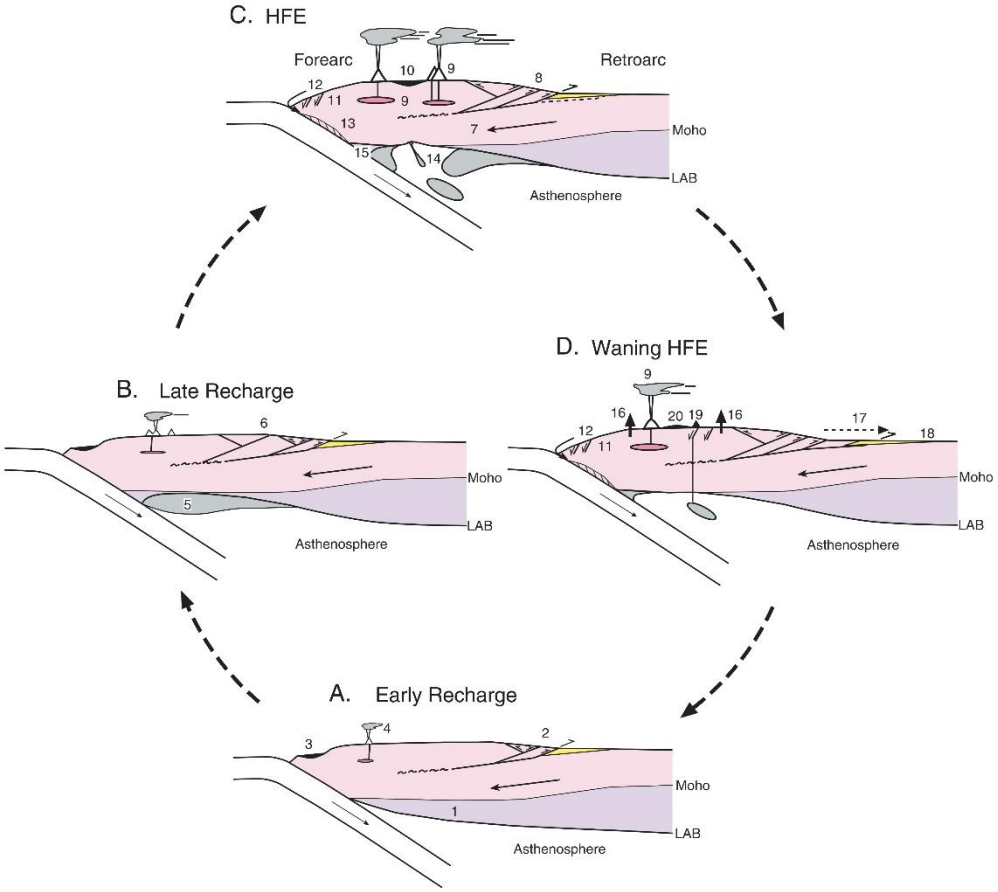

Figure 3. Idealised evolution of an Andean-type orogen (Cordilleran orogenic systems) sensu DeCelles et al. (2009, 2015), which comprises: A. Early-stage of retroarc underthrusting and development of an incipient arc; B. Development of an eclogite root beneath the arc causing a regional isostatic depression of surface elevation, and internal underplating and duplexing in the forearc and retroarc wedges; C. Development of an arc with high-flux episodes (HFE) and eclogite root foundering; D. Regional uplift by upwelling asthenosphere, and outward propagation of the flanking orogenic wedges, upper-crustal extension and ignimbrite flare-up.

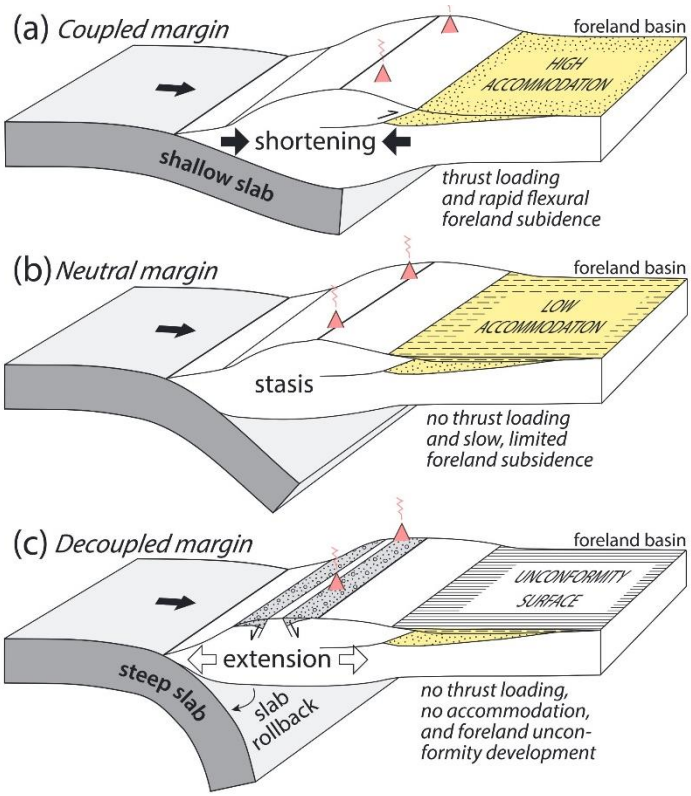

Figure 4. Idealised evolution of Andean-type orogens and tectonic regimes linked to variables modes of mechanical plate coupling sensu Horton (2018b). (a) Coupled margin with shortening and thick, coarse-grained foreland basin fill. (b) Neutral margin with no deformation and thin, fine-grained foreland basin fill. (c) Decoupled margin with extension and no foreland basin accommodation.

I-1.2 The Magallanes-Austral Basin: a key to unravel the Patagonian Andes evolution

Understanding stratigraphic architecture, depositional systems, sediment provenance, sedimentation and subsidence rates in foreland basin systems provides insights into changes in stress regime, patterns of deformation and exhumation within the coupled orogenic wedge (Heller et al., 1988; Jordan, 1995; DeCelles and Giles, 1996; Catuneanu, 2004; Horton, 2018a). Therefore, the study of the Magallanes-Austral foreland basin (Fig. 5a) is key to reconstructing the history of the Southern Patagonian Andes building. In addition, the stratigraphic record of the Magallanes-Austral basin has proved to be very sensitive to changes in the tectonic regimes (Biddle et al., 1986; Wilson, 1991; Olivero et al., 2003; Fildani et al., 2003; Fildani and Hessler, 2005; Barbeau et al., 2009; Klepeis et al., 2010; McAtmney et al., 2011; Aramendía et al., 2019; Rivera et al., 2020; Leonard et al., 2020; Fosdick et al., 2020). For example, many previous studies have suggested the association of first- to second-order prograding shallowing cycles and major intervening transgressions as direct evidence of intensified tectonic activity in the orogen and subsidence in the basin (Ramos, 1982, 1989; Cuitiño and Scasso, 2010, 2012; Ghiglione et al., 2014,

2016; Gutiérrez et al., 2017; Torres Carbonell and Olivero, 2019; Armendía et al., 2019; Rivera et al., 2020; Fosdick et al., 2020). Similarly, the sedimentary evolution of the basin has been critical to providing temporal and kinematics constraints for interpreting the fold and thrust belt evolution (Ghiglione and Ramos, 2005; Torres Carbonell et al., 2008; Fosdick et al., 2011; Ghiglione et al., 2014; Betka et al., 2015; Fosdick et al., 2020).

In the following, I synthesise the tectonic and sedimentary evolution of the Magallanes-Austral foreland basin and highlight how its stratigraphic record in conjunction with previous structural studies allows interpretation of the chronology and kinematic of the deformation in the Southern Patagonian fold and thrust belt.

I-1.2.1 Tectonic and sedimentary evolution of the Magallanes-Austral basin

Before the dominant compressive period that gave rise to the formation of the Magallanes-Austral foreland basin (Fig. 5a), the southern Patagonian Andes region experienced a pre-Andean extensional phase (Fig. 5b). This extensional phase is represented by the Rocas Verdes Basin (RVB; Dalziel et al., 1974; Dalziel, 1981), which was linked to the break-up of Gondwana in the Middle to Late Jurassic (Dalziel, 1981; Calderon et al., 2007), resulting in the formation of an ocean floor, voluminous ignimbrite eruptions, and enlarged extension in the continental lithosphere (Fig. 5b; Pankhurst et al., 2000; Calderón et al., 2013). Opening of the marginal RVB was from south to north (as far as 49°S; Fig. 5b), implicating a south-to-north decreasing magnitude of rifting, age, depth, and stage of evolution of the oceanic crust (Dalziel et al., 1974; de Wit and Stern, 1981; Calderón et al., 2013; Malkowski et al., 2016). The closure of the RVB took place from the end of the Early Cretaceous until the Late Cretaceous in a north-to-south direction, involving underthrusting and obduction of its components (Klepeis et al., 2010; Calderón et al., 2013; Betka et al., 2015), whose remnants now form part of the Southern Patagonian fold and thrust belt, and giving place to the development of the Magallanes-Austral foreland basin (Fig. 5b).

Unlike the archetypal Andean foreland basin systems (Jordan et al., 1983; Jordan, 1995; DeCelles, 2012), the Magallanes-Austral foreland basin evolved superimposed to the extensional Rocas Verdes Basin with a highly attenuated lithosphere (Fosdick et al., 2014). The Magallanes-Austral basin is a depocenter of ca. 230.000 km^2 extension and holds more than 7 km of foreland basin strata (Katz, 1963; Biddle et al., 1986; Ghiglione et al., 2009; Malumián et al., 2013; Sachse et al., 2015), located in the southernmost tip of South America

and comprising the Patagonian and Fuegian region of Chile and Argentina. The basin is bounded by the Southern Patagonian and Fuegian Andes (including the Southern Patagonian and Fuegian Batholiths) to the west and south; the Deseado Massif and the Dungeness-Río Chico Granitic Arc along its northeastern and eastern margin, respectively (Fig. 5a).

As a consequence of the inherited palaeobathymetry and differential closure time of the RVB (Fig. 5b), the onset of the Magallanes-Austral foreland basin history is marked by a north to south diachronism in sedimentation and subsequent evolution (Romans et al., 2010; Fosdick et al., 2014; Malkowski et al., 2018; Rivera et al., 2020). Deep-marine coarse clastic deposition marking the onset of the foreland basin history started as early as ~120 Ma in the northernmost part of the basin, progressing southward by 93 Ma in the middle part and by ~89 Ma in the southernmost part of the basin in Tierra del Fuego (Wilson, 1991; Fildani et al., 2003; McAtamney et al., 2011; Malkowski et al., 2016; Ghiglione et al., 2014; Sickmann et al., 2018). The weakened lithosphere caused an accentuated subsidence and narrowing during the early phases of the basin, promoting great accommodation space and developing a thick, well-developed deep-marine turbidite system (Romans et al., 2010; Fosdick et al., 2014). A southward directed dispersion of sediments was dominant in the northern and middle part of the basin but was more complex farther south (McAtamney et al., 2011). The end of deep-marine sedimentation was reached first in the northernmost part of the basin from the Albian (~113 Ma; see further details in Varela et al., 2012, Malkowski et al., 2016, 2017; Sickmann et al., 2018). This transition in depositional systems does not occur until the latest Cretaceous (~78 – 65 Ma) in the other (southern) parts of the basin, where the deep-marine turbiditic succession is capped by depositional slope and outer shelf, which in turn are followed by deltaic-incised valleys systems and shoreface deposits (Covault et al., 2009; Romans et al., 2011; Schwartz and Graham, 2015; Gutiérrez et al., 2017; Rivera et al., 2020).

The Cenozoic sedimentary history begins with a prolonged hiatus in the Paleocene-Eocene of variable duration (~15-33 Myr) depending upon the position in the basin (Malumián et al., 2000; Fosdick et al., 2015; Gutiérrez et al., 2017; George et al., 2020). This hiatus indicates either an interruption in sedimentation or cannibalisation of the strata. However, in the south of the basin, such a hiatus comprise a time-lapse much more modest of <5 Myr (Rivera, 2017; Torres Carbonell and Olivero, 2019). Above the Paleocene-Eocene hiatus, a generalised shallow marine sedimentation characterises the remaining Eocene depositional systems of the northern and central parts of the Magallanes-Austral basin. These

deposits represent incised valley systems, wave-to-tide-influenced estuaries and tidal-influenced, coastal plain fluvial systems (Santos-García, 1988; Azcuy and Amigo, 1991; Casadío et al., 2009; Le Roux et al., 2010; Pearson et al., 2012; Gutiérrez et al., 2017). By contrast, in the southern reach of the basin, the Paleocene-Eocene is characterised by thick shales, siltstones, and clay-rich, glauconitic sandstones reflecting an initial deep-marine turbidite fan system that progressively is replaced by shelf and fluvial-dominated to tide-influenced deltaic depositional systems (Charrier & Lahsen, 1969; Mella, 2001; Rivera 2017; Rivera et al., 2020). Dominant continental sedimentation was established in the basin during the Oligocene-Miocene (~33–18 Ma). These continental deposits represented by coastal plain and braided to meandering fluvial systems were briefly interrupted by the Patagonian Transgression during the early Burdigalian giving place to deposition of the shelf and shoreface facies (Malumián and Caramés, 1997; Santos-García, 1988; Marenssi et al., 2003, 2005; Cuitiño et al., 2012, 2015; Bostelmann et al., 2013; Gutiérrez et al., 2017; Rivera, 2017). However, at the latitudes of Tierra del Fuego (Fig. 5a), the transition from marine to continental sedimentation never occurred, while turbiditic fan deposits (in the foredeep) and deltaic systems (in the wedge-top) persisted up to the end of the whole evolution of the foreland basin (Ponce et al., 2008; Torres Carbonell and Olivero, 2019). By 14-12 Ma, a regional erosional unconformity, truncates the Magallanes-Austral foreland deposits and separate it from the late Miocene-Quaternary conglomerates called as the Rodados Patagonicos (Lagabrielle et al., 2004; Scalabrino et al., 2009; Armendía et al., 2019). Both the erosional unconformity and the Rodados Patagonicos have been interpreted as the cessation of the compression and foreland basin sedimentation phase in the region and the regional uplift of continental Patagonia (Guillaume et al., 2013; Ghiglione et al., 2016).

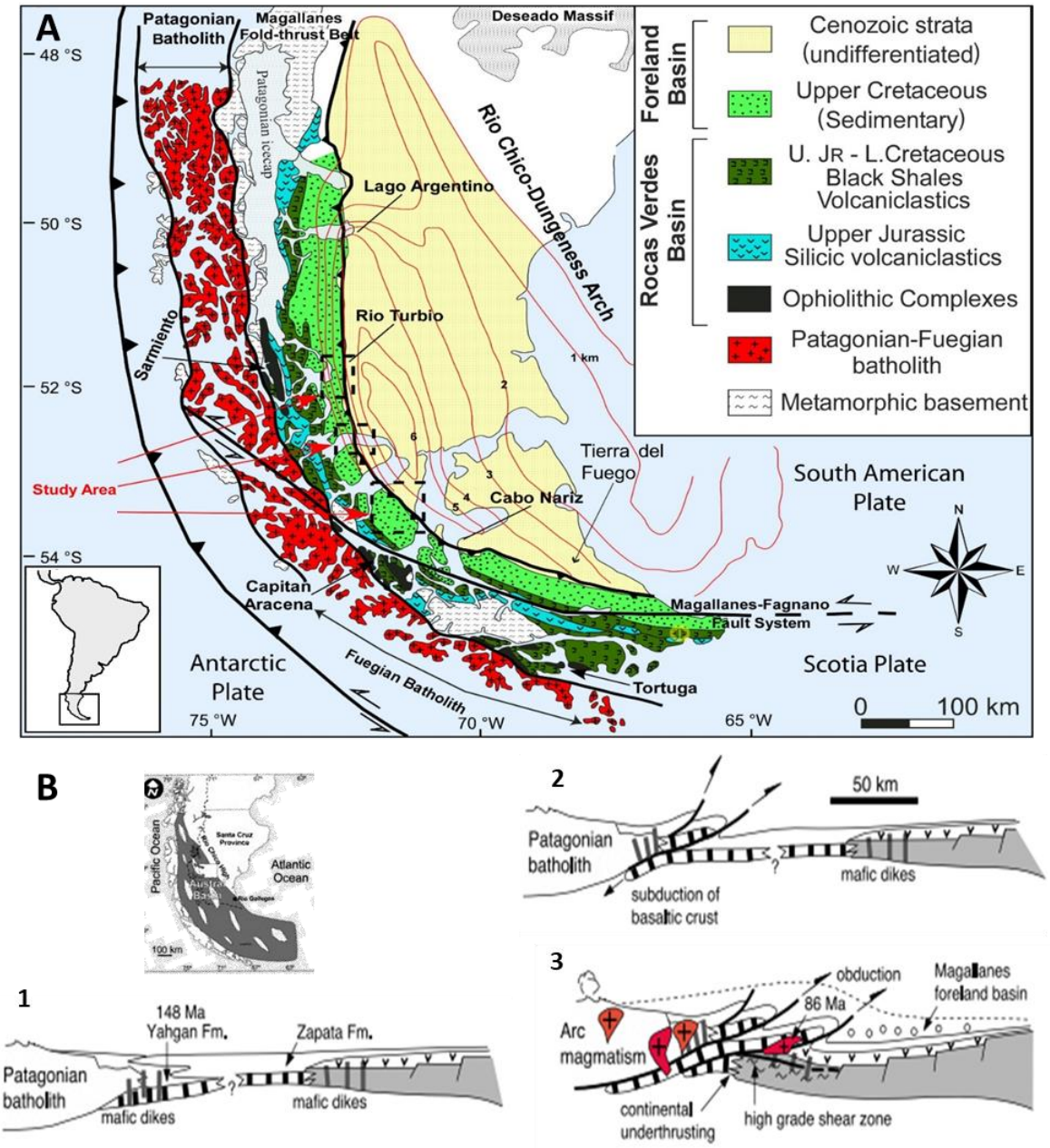

Figure 5. A. Simplified morphotectonic map of the Magallanes-Austral Basin. The black dashed-line box indicates the location of the study areas (see details in Fig. 6). Red isopach lines are the depth to top-Tobífera Formation (Late Jurassic). B. Geographic distribution of the Rocas Verdes Basin and schematic representation of different closure stages (1=final basin stage; 2= westward underthrusting of oceanic crust; 3= obduction and foreland basin formation) during the Late Cretaceous (modified from Klepeis et al., 2010).

I-1.2.2 Chronology of the fold and thrust belt deformation

Early works have highlighted that the progression of the deformation and, in general, the tectonic evolution of the Southern Patagonian Andes is not homogeneous throughout its full extension (e.g., Suarez, 1976; Ramos, 1989; Ramos and Aguirre-Urreta, 1994; Kraemer, 1998; Suarez et al., 2000a; Diraison et al., 2000). These particularities and differences in its evolution are due to the different morphostructural conformation of the fold-and-thrust belt at different latitudes and the structural configuration and basin geometry inherited from the

previous extensional stage (the Rocas Verdes Basin). Nevertheless, three orogenic and deformational episodes have been documented in the Southern Patagonian fold and thrust belt (Coutand et al., 1999; Suárez et al., 2000a; Ghiglione and Ramos, 2005; Fildani et al., 2008; Ghiglione et al., 2016), namely during the Late Cretaceous, Paleogene-Oligocene, and post-Miocene. Some deformational episodes are diachronic along the orogen or with a very loose time constraint. The latter is due to the scarcity of reliable dates for the Cenozoic units and lack of understanding regarding the evolution of the exhumation/unroofing of the terrains comprised in the fold and thrust belt.

The Late Cretaceous contractional deformation is related to the final closure of the RVB and the initiation of Cretaceous foreland basin sedimentation. This event is well documented in the fold and thrust belt by highly strained rocks and peak metamorphism in the Canal de Las Montañas (51°-52°S) and the Cordillera Darwin (54°-55°S) by ~86-85 Ma, as a consequence of obduction of the ophiolite rocks of the RVB in an arc-continent collision stage (Kohn et al., 1993; Klepeis et al., 2010; Maloney et al., 2011; Calderón et al., 2012). However, the onset of this deformation may have started much earlier (by ~115-100 Ma) in some regions of the mountain range, as suggested by the first medium to coarse-grained sandy turbidite units deposited in the northern part of the Magallanes-Austral basin (49°-51° S; Wilson, 1991; Fildani et al., 2003; Fildani and Hessler, 2005; Fosdick et al., 2011; Malkowski et al., 2017).

The second phase of deformation in Paleogene-Oligocene time is by far poorly constrained based only on structural data. Thin-skinned deformation of the Cretaceous depocenter is broadly categorised as sometime between 70-27 Ma (Fosdick et al., 2011) in the Ultima Esperanza Province of the basin (~51°S). Further south (53°S), Betka et al. (2015) suggest that continued shortening resulted in a series of out-of-sequence thick-skinned thrusting ranging from Maastrichtian up to Paleocene-Eocene. A similar situation is exposed in Tierra del Fuego, where basement-involved thrust wedges concomitant with thin-skinned thrust sheets developed in the internal and external part of the fold-and-thrust belt, respectively, from the Maastrichtian-Danian up to the late Oligocene (see synthesis in Torres Carbonell et al., 2020). The Paleocene-Eocene hiatus, which comprise >30 Myr in the northernmost part of the basin (49°15'S) and <5 Myr in the southernmost part (53°-54°S) (Malumián et al., 2000; Rivera, 2017; Gutiérrez et al., 2017; George et al., 2020; Torres Carbonell and Olivero, 2019), have been ascribed as the result of a major deformation event in the region (Malumián et al., 2000; Fildani et al., 2008; Fosdick et al., 2011).

Thermochronological data from the fold-thrust belt in Ultima Esperanza Province (51°S) suggest a phase of 44-42 Ma cooling likely associated with thrust-related unroofing of the external margin of the thrust belt (Fosdick et al., 2013). In the Cordillera Darwin, there are episodes of rapid cooling between 60-40 Ma (Nelson, 1982; Kohn et al., 1995) and between ~48-34 Ma (Gombosi et al., 2009), but their origin concerning whether to compression, extension or transcurrence is not yet clearly defined. On the other hand, provenance data show a significant change in sediment routing and palaeogeography suggesting hinterland-derived sediment structurally dammed during basinward propagation of the fold-and-thrust belt between 60-40 Ma in Ultima Esperanza Province (51°S; Gutiérrez et al., 2017; Fosdick et al., 2020), during at least all the Paleocene in the Magallanes Province (52°-53°S; Rivera et al., 2020). In contrast, in Tierra del Fuego, a major change in provenance occurs from the middle Eocene up to Oligocene, and it is linked to an enhanced contribution of hinterland-derived sediments related to contractional tectonism in the orogen (Barbeau et al., 2009; Torres Carbonell and Olivero, 2019). Finally, it is worth mentioning that independent paleobotanical data indicate the establishment of a rain shadow in the region from the late Eocene-Oligocene, which is interpreted as a reflection of the uplift and growth of the Southern Patagonian Andes (Gutiérrez et al., 2017).

The last deformation phase probably begins at the early Miocene (~22 Ma), but while in most of the Southern Patagonian Andes it manifests itself in a compressive way, in Tierra del Fuego, it acquires a more transtensional character (Winslow, 1982; Diraison et al., 2000; Ghiglione et al., 2014). Structural studies in the north (50°-51°S) have identified a series of thrust faults associated with the deepening of the decollement and faulting of the Patagonian basement that progressively gave place to a forelandward propagation of deformation and wedge thickening through thin-skinned thrusts during the early Miocene (Kraemer, 1998; Fosdick et al., 2011). The deposition of continental deposits of the Santa Cruz Formation and equivalents (~19-15 Ma) after a short period of transgression is exemplified as a result of this contractional event, and a synorogenic nature is assigned (Ramos, 1982, 1989; Malumián and Ramos, 1984; Kraemer, 1998; Suarez et al., 2000a; Ramos and Ghiglione, 2008; Fosdick et al., 2011; Cuitiño et al., 2012, 2015; Gutiérrez et al., 2017). Apatite and zircon thermochronometers show increased denudation in the hinterland part of the orogen by 30-23 Ma, which migrated eastward in the external part of the fold-and-thrust belt until 18-12 Ma (Thomson, 2002; Thomson et al., 2001, 2010; Fosdick et al., 2013). This early Miocene period of compression is interpreted as increased plate coupling during the approach of the Chile Ridge (Folguera and Ramos, 2002). A subsequent late Miocene uplift

is suggested by the eastward tilt of basalts and Santa Cruz Formation deposits in the Ultima Esperanza Province (51°S; Ramos, 1989; Fosdick et al., 2011) and the emplacement of a series of plutons further east in the foreland (Skarmeta and Castelli, 1997; Coutand et al., 1999; Suarez et al., 2000a).

I-1.3 Thesis scientific framework

It can be seen in the synthesis of the previous sections that some conceptual models that apply to the overall Andes could not fully explain the evolution of the Southern Patagonian Andes. Furthermore, the poorly constrained fold and thrust belt deformation history and the still incipient knowledge about the sedimentary evolution of the adjacent foreland basin emphasise the importance of continuous efforts to understand better one of the most crudely studied regions of the Andes.

In this thesis, the Southern Patagonian fold and thrust belt (orogenic wedge) and the Magallanes-Austral foreland basin are conceived as interconnected systems whose joint evolution responds to changing geodynamic configurations and cortical parameters inherited from the precursor Rocas Verdes Basin. Therefore, a detailed and accurate delineation of the temporal and spatial evolution of the sedimentary system's geometry, composition, and filling pattern and the kinematics constraint of the adjacent thrust-and-fold belt will be the key to unveiling the intricate history of the Southern Patagonian Andes orogen.

I-1.3.1 Objectives and research questions

The Ph.D. thesis's general objectives are to determine the different evolution stages of the Magallanes-Austral foreland basin sedimentary infill, and the timing of deformation and exhumation patterns of the orogenic wedge (thrust-and-fold belt), in order to unravel the tectonic evolution of the Southern Patagonian Andes.

Achieving the thesis objectives should lead to answering the following provocative questions:

1) How and to what extent does the inherited crustal architecture of the predecessor Rocas Verdes Basin control the sedimentary system evolution and dispersal of sediments during the Late Cretaceous-early Miocene?

2) How and to what degree does the Cenozoic geodynamic events (subduction of active ridges, opening of Drake Passage) impact the development and evolution of an Andean-type orogen-foreland basin pair?

3) What is the nature of the whole Southern Patagonian Andean growth (including sediment accumulation history) in terms of steady or punctuated episodic behaviour?

I-1.3.2 Study area

This research thesis focus on the central and southern part of the Magallanes-Austral Basin (51°15’ S-54°4’ S) (Fig. 6), comprised of the Chilean XII Magallanes and Chilean Antarctica Region and the Argentinian Santa Cruz and Tierra del Fuego Provinces. The basin is divided into five tectono-stratigraphically well-differentiated localities (sensu Malumián et al., 2013 and attaching one more in this work): 1) the Argentinian Fuegian Atlantic coast, linked with the Fueguian orocline and Malvinas Basin; 2) the Chilean Tierra del Fuego Province, which comprise most of the Fuegian orocline; 3) the Brunswick Peninsula and Riesco Island area, known as the Magallanes Province in chile; 4) the Ultima Esperanza-Rio Turbio area, which group the Chilean Ultima Esperanza Province and the Rio Turbio coals field zone; 5) the Argentinian Calafate-Chaltén area, which represent the northernmost tip of the basin. The research study area comprises from the second to the fourth tectono-stratigraphic localities of the basin. However, it is essential to bear in mind that the study area will be detailed in each chapter (according to the objectives addressed) since not all locations have the same data density.

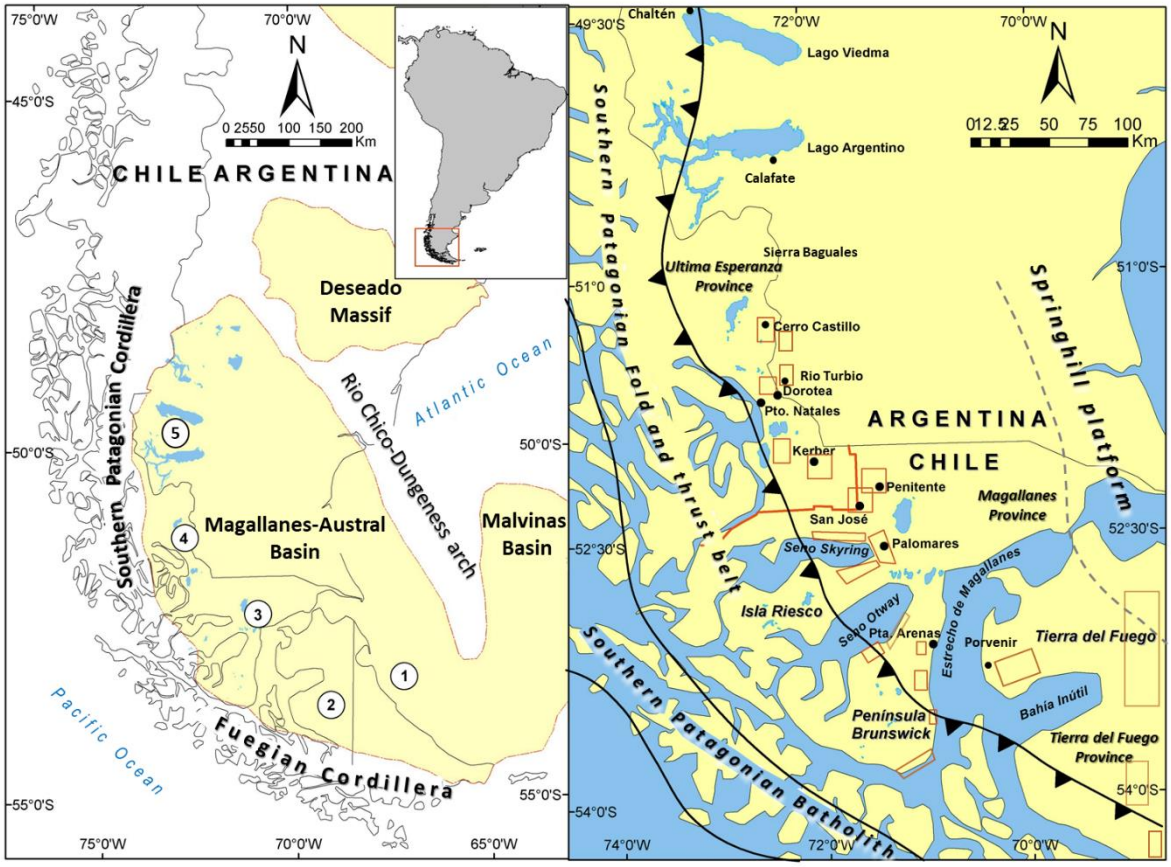

Figure 6. Simplified map of study areas (red boxes) and tectono-stratigraphic localities in the Magallanes-Austral Basin (modified from Rivera, 2017). Red boxes in Tierra del Fuego are localities visited but not fully included in this thesis. (1) Argentinian Fuegian Atlantic Coast; (2) Chilean Tierra del Fuego Province; (3) Brunswick Peninsula and Riesco Island; (4) Última Esperanza-Rio Turbio; (5) Calafate-Chaltén.

I-1.3.3 Thesis organisation and structure

This manuscript is composed of fifth parts. The first part contains two chapters. Chapter I-1 presents succinctly the different models that explain the construction of the Andean orogen in general and the scientific motivation and research objectives of this thesis. Chapter I-2 is aimed to present the methodology and scientific approach that will allow solving the research questions. The following chapters, designed in the form of papers (implying some degree of redundant information e.g., methods, regional geological framework, etc.), constitute the bulk of the results and interpretations, which is the contribution of this thesis to the geological knowledge of this segment of the Andes. In addition, abstracts of oral and poster presentations in scientific meetings can be found in: Annex A-1 "Evolución tectono-estratigráfica de la cuenca de antepaís Magallanes-Austral y su relación a la orogénesis de los Andes Patagónicos" by Rivera et al., 2017 (XVI Congreso Colombiano de Geología); Annex A-2 "Underfilled-to-overfilled cycles in the Magallanes foreland basin, Chilean Patagonia: unravelling the growth of the Southern Patagonian

Andes" by Rivera et al., 2018 (XV Congreso Geológico Chileno); Annex A-3 "Southern Patagonian wedge dynamics inferred by tectono-stratigraphic sequences and evolution of the Magallanes-Austral Foreland Basin (Chile)" by Rivera et al., 2019 (17ème congrès de sédimentologie).

The second part is composed of a single chapter. Chapter II-1 present an updated regional chronostratigraphic framework, revision of the stratigraphic nomenclature and identification of regional unconformities in the basin to assist with deciphering future basin analysis. The refined chronostratigraphic framework incorporates an extensive U-Pb ages database used to report maximum depositional ages from detrital zircons, and it is complemented with relevant biostratigraphic data. A basin lithostratigraphic correlation chart is presented, highlighting the major regional unconformities whose identification is based on geochronological, sedimentological and seismo-stratigraphic criteria. By using the wealth of U-Pb ages data, I also attempt to constraint the episodic nature of the Southern Patagonian Batholith. This chapter is intended to be submitted to the Journal of South American Earth Sciences (JSAMES). Another paper published in JSAMES is related to the arc magmatism addressed in this chapter, Annex B-1: "*Neogene Patagonian magmatism between the rupture of the Farallon plate and the Chile Ridge subduction*" by Ramírez de Arellano, Calderón, **Rivera** et al., 2021.

The third part (composed of two chapters) deals with the sedimentary architecture of the Magallanes-Austral foreland basin and aims to enhance the understanding of the basin-wide siliciclastic sedimentation, marine and continental depositional systems, sediment routing pathways and basin subsidence and foredeep migration. Chapter III-1 is a paper published in Sedimentary Geology (Rivera et al., 2020) which presents a detailed facies and sequential stratigraphy analysis and provenance (sandstone modal composition and U-Pb ages) assessment of the Campanian-Paleocene succession along-strike the Magallanes-Austral basin. These results lead to understanding provenance changes and, in turn, elucidate the origin of one of the most extensive marine transgressions in Patagonia, discerning among tectonic, climatic or eustatic signals. Chapter III-2 focuses on the integration of facies interpretation, multi-approach quantitative sedimentary provenance and subsidence and isopach maps analysis of the Late Cretaceous-Cenozoic foreland strata, which 2 is intended to be submitted to Basin Research or Tectonics. The results of this chapter, allow us to constrain long-term depositional trends, highlight changes in basin accommodation on a

regional scale, investigate sediment transport pathways and propose a tectonic evolution schema of the Southern Patagonian wedge.

The fourth part is composed of a single chapter. Chapter IV-1 presents the structural configuration, timing of the deformation quantification of shortening and exhumation history of the Southern Patagonian fold and thrust belt by integrating a structural analysis and detrital apatite fission-track and (U/Th)-He data.

The fifth part is composed of a single chapter. Chapter V-1 is devoted to examining the different existing hypotheses regarding the evolution of the Southern Patagonian Andes under the light of the new results and to discussing the research question that motivated this PhD thesis. Finally, the main findings of this research are presented as bullet-point conclusions.

CHAPTER I-2 :

METHODS AND DATA SOURCES

Chapter I-2 presents the different methods and techniques used during the thesis. The research methods follow a multidisciplinary approach to face the inherent complexity involved in understanding the evolution of orogenic systems. This multidisciplinary approach is synthesised in 4 methodological pillars: (1) Stratigraphic-sedimentologic and subsurface analysis; (2) Integrated sediment provenance analysis; (3) Low-temperature thermochronological modelling; (4) Structural geological analysis. In an integral view, this approach is called Sedimentary Basin Analysis and constitutes the best way to understand the long-term interactions among the tectonics, climate, erosion, and sedimentation in all type of basins.

I-2.1 Stratigraphic-sedimentologic and subsurface analysis

The analysis of all the aspects related to the sedimentary fill, lithological composition, primary structures, the internal stratigraphic architecture, the spatial and temporal distribution and genetic relationship of the different depositional systems or sequences reveal all the relevant surficial processes occurring in the orogenic wedge as well as the role of climate and sea-level changes in the evolution of the foreland basin system.

Twenty-seven stratigraphic sections were measured along the axis of the Magallanes-Austral basin (between 51°2'S to 54°4'S) using a Jacob staff and tape measure on the best available outcrops on a centimetre to decimetre scale. Each bed measured was subject to a careful examination of grain size, lithology and texture variations (with a hand lens in the field and examining 140 thin sections), bedding thickness, type of contacts, sedimentary structures, palaeocurrent data, fossil content, bioturbation intensity and ichnological suites. Stratigraphic sections were divided into genetically related siliciclastic facies and sub-facies associations representing a distinct depositional environment or sub-environments (architectural elements). Six hundred and eighty-seven palaecurrents measurements, primarily determined from through axes, which comprise 3D through cross-bedding and 3D rib and furrows, 2D planar cross-lamination/stratification, ripples marks, flute and groove casts, clast imbrication, current-oriented wood or tree trunks and tool marks. Palaeoflow direction of bidirectional structures was resolved considering other unidirectional indicators nearby. Before plotting the recorded directions in rose diagrams in the Orient software (Vollmer, 1995, 2015), they were tilt corrected using the standard methodology described in Le Roux (1991) and further analysed by directional and circular statistics (Fisher and Powell, 1989; Davis, 2002) to obtain the vector mean azimuth, consistency ratio, circular variance, Rayleigh's test and p-values of the preferred directions. The ichnological study was based on observations in two-dimensional, vertical to sub-vertical exposures and focused on the identification of ichnofossils, and ichnofaunal assemblages and semi-quantitative estimation of the degree of bioturbation expressed in terms of the bioturbation index (BI, sensu Taylor and Goldring, 1993; Bann and Fielding, 2004). All the body fossil content was documented in the field, recording their type, occurrence, and stratigraphic position. However, some fossils were sampled for a detailed characterisation by specialists.

The subsurface characterisation of the Magallanes and Tierra del Fuego Provinces of the Magallanes-Austral basin were obtained by the correlation of thirty-one (Fig. 1) 2D seismic lines and forty-one (Fig. 1) exploratory wells provided by Enap-Sipetrol (Empresa

Nacional de Petróleos de Chile), in combination with previous interpretations (Biddle et al., 1986; Enap, 1999, 2004, 2006; Mpodozis et al., 2011; Gallardo, 2014). Synthetic seismograms and time-converted logs were produced to conduct the seismic-well tie process to aid the seismostratigraphic delineation and subsequent tectono-stratigraphic analysis. The seismostratigraphic analysis includes identifying sequences boundaries, which were identified based on stratal terminations (onlap, downlap, toplap, erosional truncations), and interpretation of internal reflection patterns (seismic facies) following the procedure explained by Mitchum and Vail (1977) and Mitchum et al. (1977a,b). A subsurface facies analysis was carried out along a ~W-E transect to study the transversal axis of the basin (down-dip) and complement the architectural stratigraphic characterisation previously approached with outcrops-based facies analysis along the basin axis. The electrofacies approach (Selley, 1976, 1985; Cant, 1992) was used to interpret vertical grain size variations, beds contacts/geometry, and depositional systems using the gamma-ray, spontaneous potential, and resistivity log responses. The calibration of the subsurface facies analysis with core logs was only possible in a reduced amount of wells, stressing that this interpretation of depositional systems based on electrofacies must be assumed as an approximation. Formation tops and marker beds in each well were combined with outcrop Formation thickness information to construct isopach maps in certain interesting intervals and tectonic subsidence curves. The procedure utilised to achieve the decompaction of sediments needed for the subsidence analysis is made by the backstripping method assuming Airy isostasy compensation in a 1D stratigraphic column as given by Steckler and Watts (1978),

$$Z_t = W_d + S\left(\frac{\rho_m - \rho_s}{\rho_m - \rho_w}\right) - \Delta_{sl}\left(\frac{\rho_m}{\rho_m - \rho_w}\right)$$

where, Zt is the tectonic subsidence in any geologic time t in the past; Wd is palaeobathymetry; S is the sediment layer after decompaction; ρw, ρm, ρs are the densities of water, mantle, and bulk sediment respectively; Δsl is the global sea-level change (positive for a rise).

The sediment bulk density (ρs) depends on the variation of porosity with depth, and this is taken as a simple exponential decrease with increasing depth as given by Sclater and Christie (1980):

$$\varphi = \varphi_0 e^{-cz}$$

where φ is the porosity at any depth *z*, φ0 is initial porosity when the layer is at the surface, *c* is the compaction coefficient. The palaeobathymetric data (Wd) were extracted from planktonic/benthonic foraminifera estimates of depth (Natland et al., 1974) and according to mean depositional depths assigned to the interpreted facies as described by Ingle (1980) and Le Roux et al. (2016): supratidal flat, 1 m; foreshore, 0 m; estuary, -10 m; upper shoreface, -20 m; middle shoreface, -50 m; lower shoreface, -80 m; inner shelf, -120 m; outer shelf, -170 m; upper continental slope (upper bathyal), -380 m; middle continental slope (mid bathyal), -800 m; lower continental slope (lower bathyal), -1500 m; abyssal plain, -4000 m. The eustatic sea-level correction is not considered because of the complexity of reconstructing reliable global sea-level charts (e.g., Angevine et al., 1990; Miall, 1992; Berra and Carminati, 2010; Allen and Allen, 2013).

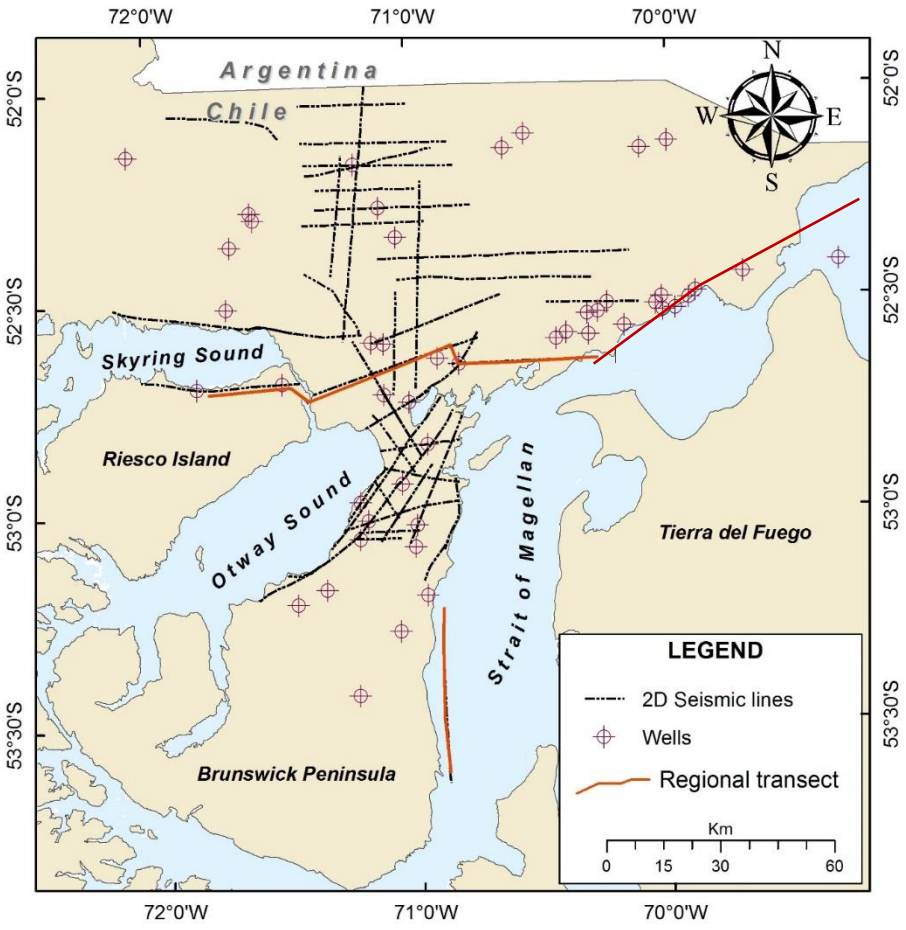

Figure 1. Geographic distribution of 2D seismic lines and exploratory wells (courtesy of ENAP) in the study area.

Sequence stratigraphic units and systems tracts were defined following the model-independent approach (e.g., Catuneanu et al., 2011). Recognition of surfaces of sequence stratigraphic significance, stratal stacking patterns in outcrops, and their correlation among

the different parts of the study area are mainly based on changes in accommodation-sedimentation dynamics and vertical relationships among the sedimentary environments. Sequence stratigraphic units and systems tracts were defined from flooding or transgressive surfaces (TS), subaerial unconformities or sequence boundaries (SB) and maximum flooding surfaces (MFS). As the sequence stratigraphic framework presented in this study is entirely based on outcrop data, where the geometry of stratigraphic sequences cannot be identified with certainty due to the absence of regional correlation plots, some sequence stratigraphic surfaces may have been missed. Moreover, in deeper water, the MFS is, in most cases, ambiguously identified. Despite these limitations, we have defined stratigraphic sequences characterised by the development of two or three systems tracts in the sense of Catuneanu et al. (2011): a lower transgressive tract (TST), and an upper, shallower, highstand systems tract (HST), in deeper water settings. In shallower parts of the sedimentary system, it is also possible to define a third, lowstand systems tract (LST) where a basal subaerial unconformity can usually be recognised. The LST includes deposits accumulated during normal regressions and is bounded by a basal subaerial unconformity (SB) and a flooding or transgressive surface (TS) at the top. The transgressive systems tract begins with a TS characterised by transgressive shell lag or a condensed shell bed that resulted from low net deposition due to sediment bypass, typically accompanied by a deepening-upward trend of facies (Zecchin and Catuneanu, 2013, 2017). Where subaerial unconformities are not present (particularly in deeper water settings), the TS is used as a sequence boundary. The HST is accompanied by a shallowing-upward trend of facies and is separated from the underlying TST by the maximum flooding surface (MFS), that is characterised by the development of nodular horizons (incipient hardground), a high concentration of pyrite and organic matter, phosphate layers and sometimes intense bioturbation.

I-2.2 Integrated sediment provenance analysis

To date, provenance analyses on Late Cretaceous to Cenozoic deposits of the Magallanes-Austral foreland basin are based mainly on the geochronology of detrital zircons and sandstone petrography. However, it has become ambiguous to identify the area of contribution due to the similar or overlapping U-Pb ages and/or uneven zircon fertility of the multiple source terrains, a non-unique lithological signature of source terrains and the sedimentary recycling effects.

An analysis that integrates different techniques will be much more valuable and appropriate to the immature sandstones and the important argillaceous successions present

during the Cenozoic and will also allow a more detailed paleogeographic reconstruction of the basin and a better understanding of the relationship between the activity tectonics and the sedimentary contribution. Therefore, the integrated sediment provenance approach combines sandstone petrography, conglomerate clast analysis, fine-grained geochemistry and detrital zircons U-Pb dating and detrital apatite low-temperature geochronology in order to characterise more accurately the supply of sediments to the basin and to track changes in upland source areas due to tectonic activity during changes in geodynamic settings.

I-2.2.1 Conglomerate clast counting

Conglomeratic units are important sedimentary lithosomes in basin analysis since they provide information regarding the composition of the source terrains which aid in reconstructing the sediment routing systems and unravelling the exhumation of different source rocks in the hinterland areas of a foreland basin (e.g., Gómez et al., 2005; Bascuñan et al., 2016; Horton et al., 2016; Leonard et al., 2020). The conglomerate clast counting allows to quickly determine the petrological composition of deposits in the field and by comparing with lithologic features of the source rocks provide helpful insights into sediment provenance. However, it is necessary to be cautious about provenance interpretation from conglomerates because depositional assemblages of clasts may not faithfully represent all the litho-types and proportions of parent rocks in the source area.

The conglomerate composition was determined by counting around 100 clasts (cobbles and pebbles) within a 1 m^2 grid. Some clasts with dubious macroscopic identification were microscopically examined. The counts are presented as clast percentage, and they were categorised into lithologic groups: (1) metamorphics, which include slates, schists, and minor cataclasites; (2) granitoids, comprising tonalites, monzogranites, granodiorites/diorites; (3) basalts and basaltic scorias; (4) gabbros and dolerites; (5) intermediate volcanics, composed by porphyritic and trachytic andesites; (6) silicic volcanics, comprising rhyolite, pumice, and quartz-porphyry; (7) vein quartz and chert; (8) sedimentary rocks. The criteria for choosing these lithologic groups were based on the primary litho-types on source terranes (e.g., Southern Patagonian Batholith, Tobífera volcaniclastics, Ophiolite suites, and the Eastern Andean metamorphic complexes), which offers us a direct comparison way between the parental rocks sources and depositional assemblages of clasts.

I-2.2.2 Sandstone modal analysis

Sandstone modal analysis has been one of the most widely accepted methods to decipher the sedimentary provenance and tectonic setting of source areas since its consolidation more than five decades ago (Dickinson, 1970, 1985, 1988; Dickinson and Suczek, 1979; Ingersoll et al., 1984). In the last years, sandstone framework composition studies have shed light on the compositional variability of the foreland basin deposits, which is a reflection of different unroofing histories in the fold and thrust belts, complexities in the sediment routing systems, and the inherent dynamic of the depositional processes acting in the basin (e.g., DeCelles et al., 2011; Nie et al., 2012; Bascuñan et al., 2016; Chapman et al., 2019; Rivera et al., 2020; Leonard et al., 2020).

Ninety fine- to medium-grained sandstone samples were selected for modal analysis. The preparation and mounting of the thin sections were conducted in the Sample Preparation Laboratory of the Department of Geology of the University of Chile. About 400-500 points were counted on each thin section, following the Gazzi-Dickinson method (Gazzi, 1966; Dickinson, 1970; Ingersoll et al., 1984). Modal compositions were normalised to traditional quartz-feldspar-lithic (QFL) and monocrystalline quartz-feldspar-total lithic (Q_mFL_t) parameters to be compared with the tectonic fields of Dickinson (1985), even though the Dickinson's model predictive success ratio is 64-78% (Weltje, 2006). In Dickinson's models, it is known that ophiolite-derived detritus cannot be discriminated from the magmatic arc provenance (e.g., Garzanti et al., 2000, 2002). The latter issue can be circumvented by using subcategories of the volcanic lithics fragments (Lv_l, Lv_m, Lv_f, and Lv_v for vitric-neovolcanic) (Dickinson, 1970; Critelli and La Pera, 1994). We assume that lathwork texture is indicative of basaltic lavas commonly found in ophiolite sequences (Dickinson 1970; Garzanti et al., 2000, 2002), microlitic is commonly associated with andesitic magmatic arc detritus (Ingersoll and Cavazza, 1991; Marsaglia, 1993), and felsitic texture with siliceous volcanism (Dickinson 1970; Ingersoll and Cavazza, 1991). However, as ophiolite sequences and volcanogenic shield of magmatic arcs can potentially produce lathwork and microlitic textures in their lithic fragments should these rocks be weathered and eroded (Affolter and Ingersoll, 2019), the relative proportion calculated for the former could be sub-estimated while for the latter over-estimated. In most ternary diagrams used to infer provenance or tectonic fields, we have incorporated multivariate statistically rigorous confidence regions (*sensu* Weltje, 2002) to adequately capture the distribution of data points (i.e., studied modal composition). Each confidence region has a probability associated with

different confidence levels of 90%, 95%, and 99%, which can be used to predict the range of variation of the entire population or mean population studied. This approach provides a quantitative point of view for the sedimentary petrological analyses and supposes an advantage over the traditional non-statistical approach (e.g., the outline of a cluster of data points or eyeball fitting; Fig. 2A). Nevertheless, under some instances, the univariate statistical normal distribution methods (e.g., the arithmetic sample mean and its standard error polygons or hexagonal fields with a confidence interval of variation; Fig. 2B) could produce similar results to multivariate confidence regions (Fig. 2C; Ingersoll and Eastmond, 2007). However, the univariates statistic approach is undoubtedly statistically less robust than multivariate methods (Weltje, 2002; Ingersoll and Eastmond, 2007; Allen and Johnson, 2010; Ingersoll, 2012).

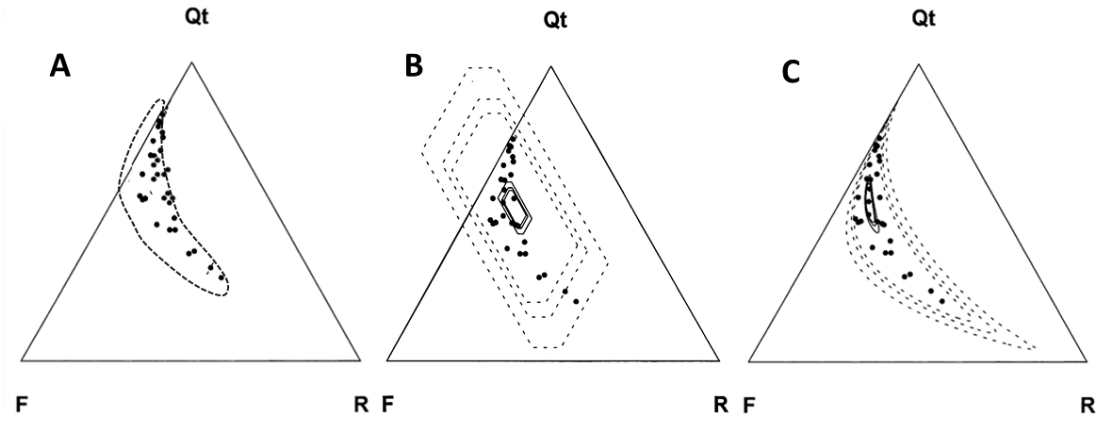

Figure 2. Ternary plots displaying detrital modes and comparison of different ways to predict statistical data variability significance. A. Non-statistically eyeball fitting. B. Univariate arithmetic means and standard deviation and confidence interval hexagons. Note how hexagons limit trespass triangle boundaries, implying negative values for the Feldspar axe. C. Multivariate geometric means and ellipsoids of 90%, 95%, and 99% confidence intervals.

I-2.2.3 Fine-grained bulk-rock geochemistry

The Cenozoic sedimentary record of the Magallanes-Austral basin includes thick successions of fine-grained rocks from which it is possible to extract information on sedimentary provenance using the geochemistry of major, traces, and (REE's). The major, traces, and rare earth elements are insoluble and usually immobile under surface conditions. They are carried mainly in the suspended load during fluvial transport, resulting in uniform distributions in shales (Condie, 1991; Taylor and McLennan, 1985), and have great potential

for preserve the geochemical signature from source rocks in the depositional sink (e.g. Taylor & McLennan, 1985; Bhatia & Crook, 1986; McLennan et al., 1993; Roser et al., 1996). Thus, geochemical provenance information from fine-grained sediments will directly complement the conglomerate clast counting and sandstone modal analysis to resolve exhumation histories in the hinterland sources terrains as have been applied in different previous works (e.g., Basu et al., 1990; Fildani and Hessler, 2005; Roddaz et al., 2005; Romans et al., 2010; Zahid and Barbeau, 2013; Garzanti et al., 2016).

A total of twenty fine-grained samples were selected for major, trace and REE analysis. The samples were pulverised up to obtain a pulp in the Laboratory of Sample Preparation of the Department of Geology of the University of Chile, using an agate mortar. The whole-rock geochemical analyses on all of the samples were conducted at Actlabs (Canada), using a combination of packages as lithium metaborate/tetraborate fusion ICP whole rock (Code 4B) and trace element ICP/MS (Code 4B2). The fused sample was diluted and analysed by Perkin Elmer Sciex ELAN 6000, 6100 or 9000 ICP/MS. One blank and seven controls (four before the sample group and three after) were analysed per group of samples. One duplicate was fused and analysed. The instrument was recalibrated for every 40 samples.

The chemical index of alteration (CIA; Nesbitt & Young, 1982) was employed to evaluate the degree of chemical weathering, which measures the proportion of Al_2O3 vs the mobile oxides in the analysed samples, typically representing the alteration of feldspars to clay minerals. The CIA was calculated using the molar proportions of Al_2O_3, CaO*, Na_2O and K_2O, where CaO* is CaO present in silicates. The REE's were chondrite normalised according to the chondrites values of Boynton (1984), and the Europium anomaly was calculated as follows: $\frac{Eu}{Eu^*} = (2 * Eu)/(Sm + Gd)$. A multivariate statistical analysis (Principal Component Analysis, PCA) was conducted to evaluate the applicability of geochemical proxies to infer parent rocks compositions in terms of mafic, felsic, or mixed signatures (intermediate) and construct a predictive model. Then, some elemental concentrations and key trace-elements ratios values were carefully chosen to qualitatively highlight the geochemical imprint of the assemblage of parent rocks in the studied clastic deposits. The average geochemical composition of the Upper Continental Crust (UCC), North American Composite Shale (NASC), Post-Archean Australian Shale (PAAS), and potential source rocks end-members (Southern Patagonian Batholith, Ophiolite suites, Eastern Andean metamorphic complexes, Barros Arana-La Pera volcanic complex, and

Tobífera volcaniclastic) were included for comparison. Geochemical modelling was employed to quantitatively quantify the proportions of source rock types contributing to the composition of the studied clastic deposits; a linear discriminant analysis (LDA) was performed to most closely match each fine-grained sample with a mix of potential end-members.

As elemental concentration values are by nature compositional data, they are restricted to values between 0 and 1 (or 100%) and are subjected to the constant sum constraint (i.e., all variables sum to a constant 1 or 100%). Consequently, this constant sum property imposes that all variables are not mutually independent (i.e., data is closed) and cannot follow a multivariate normal distribution failing a significant prerequisite of parametric statistical methods, such as standard discriminant analysis (LDA or PCA). The latter long-standing problem is solved by applying a log-ratio transformation (centred log-ratio transformation, clr) of compositional data (for further details about compositional data and sedimentary geology, see Aitchison, 1982; Montero-Serrano et al., 2010; Tolosana-Delgado, 2012; Weltje, 2012 and reference therein). Once the data is clr-transformed, it is possible to represent them in a compositional biplot (Gabriel 1971). The compositional biplot represents multivariate observations (points) and variables (rays) projected into a plane fixed by principal components (Fig. 3).

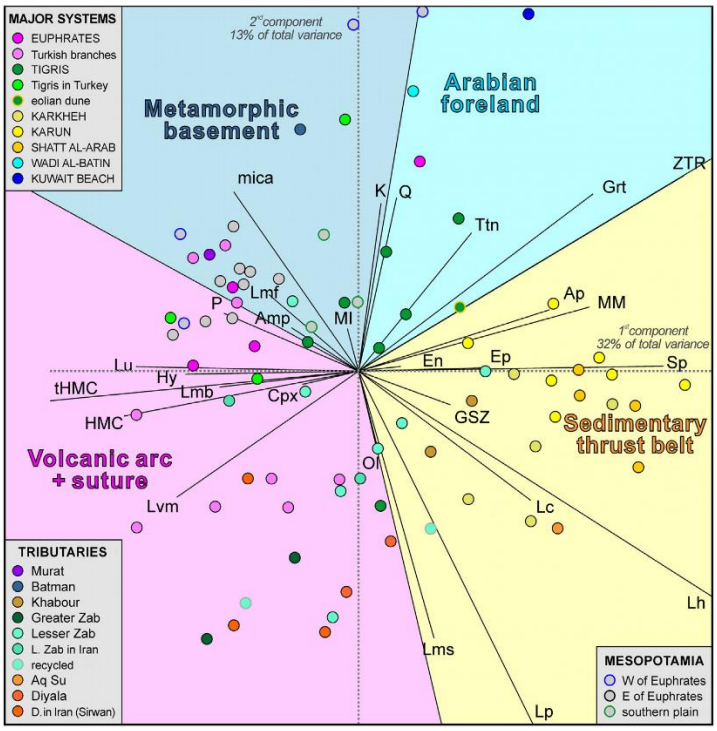

Figure 3. Compositional biplot example (modified Garzanti et al., 2016) where the axes represent the principal components, and the length of each ray is proportional to the variability of the compositional parameter in the

data set. Interpretation: If the angle between the line from a vertex to the origin and an axis is minor, the variable has a strong influence on the corresponding principal component. The larger the vertex's distance to the origin and the smaller the angle, the stronger the influence. If the angle between two rays is close to 0°, 90°, and 180°, then the corresponding compositional parameters are directly correlated, uncorrelated, and inversely correlated, respectively.

I-2.2.4 Detrital zircon geochronology

Due to the advancement in techniques for efficiently determining reliable Uranium-Lead (U-Pb) ages, detrital zircon U-Pb geochronology has rapidly evolved as a required method for investigating sedimentary basins (Cawood, 2005; Thomas, 2011; Gehrels, 2012, 2014). The U-Pb analysis of detrital zircon population ages has three distinct and equally important components that will be addressed in this thesis: 1) reconstruction of provenance and source to sink linkage; 2) calculation of maximum depositional ages of sedimentary units and refinement of chronostratigraphic framework; 3) tracing main pulses of batholith magmatism and their magma production volumes. Numerous works have successfully conducted detrital zircon U-Pb geochronology analysis to resolve questions involved in the latter topics in pursuit of better understanding Andean-type orogenic cycles (Hervé et al., 2004; Gómez et al., 2005; Barth et al., 2013; Paterson and Ducea, 2015; Bascuñan et al., 2016; Horton et al., 2016; Gutiérrez et al., 2017; Daniels et al., 2019; Rivera et al., 2020; Leonard et al., 2020).

A total of thirty-six sandstones samples were prepared for detrital zircon U-Pb dating. However, only twenty-six were dated (which are incorporated in this thesis), and the other ten samples are still waiting to be dated[1]. Detrital zircons were extracted in the Sample Preparation Laboratory of the Geology Department at the University of Chile from medium- to coarse-grained sandstone samples (~5-8 kg) following standard mineral concentration techniques (Fig. 4). The disaggregation process began with a jaw crushing phase, which utilises a chromium-nickel corrugated crushing plate. Through several controlled passes in the crushing step, the hand samples were reduced to gravel (~4–8 mm). We used a roller mill to reduce the sample size from gravel to sand size. The sand-sized material was subsequently sieved in an ASTM E11 Sieve with stainless steel woven wire cloth with 75µm openings. The first gravity separation stage utilised a Gemeni mk2 water table, where the pulverised sample was loaded in a vibratory feeder. This vibratory feeder progressively dropped the

[1] *Inherent equipment problems in 2019 and the following 2020-21 COVID sanitary crisis prevented laser ablation analysis from being performed at the Mass Spectrometry Laboratory (CEGA) of the University of Chile.*

sample to the table, where ribs trapped the material, separating them into three fractions: heavy, light and silt. We selected and dried the heavy fraction under infrared light at 60°C. Before separation with the Frantz magnetic separator, we removed highly susceptible magnetic minerals (e.g., magnetite) from the heavy fraction of the sample by using a hand-magnet. The isodynamic Frantz magnetic separator was set up with a side tilt of 20° (down toward the operator), forward tilt of ~40°, and voltage increments of 0.2 amps, beginning in 0.3, ending at 1.7 amps. The non-magnetic, heavy minerals were treated in the second stage of gravity separation using dense liquid separation in Tribromomethane (2.8 g/cm^3) and Methylene Iodide (3.3 g/cm^3) solutions. Finally, all present detrital zircons[2] (usually ranging from several hundred milligrams to several grams in weight) were then hand-picked from the concentrate using a stainless steel stub with double-sided adhesive and a binocular stereo microscope. Detrital zircon concentrates were plunged manually into epoxy resin mount for subsequent lapping, polishing, imaging and analysis. We obtained Cathodoluminescence (CL) images using an FEI Quanta 250 scanning electron microscope (SEM) with a Centaurus sensor for CL detection. Cathodoluminescence images allow us to examine the internal structure of each detrital zircon and relate it with chemical zoning before conduct isotopic analyses. To clean, eliminate or reduce possible contamination by manipulation, we conducted an ultrasonic washing (with ultrapure water) for all the samples.

[2] *Using the same steps was obtained the detrital apatite concentrate for the low-temperature thermochronological analysis.*

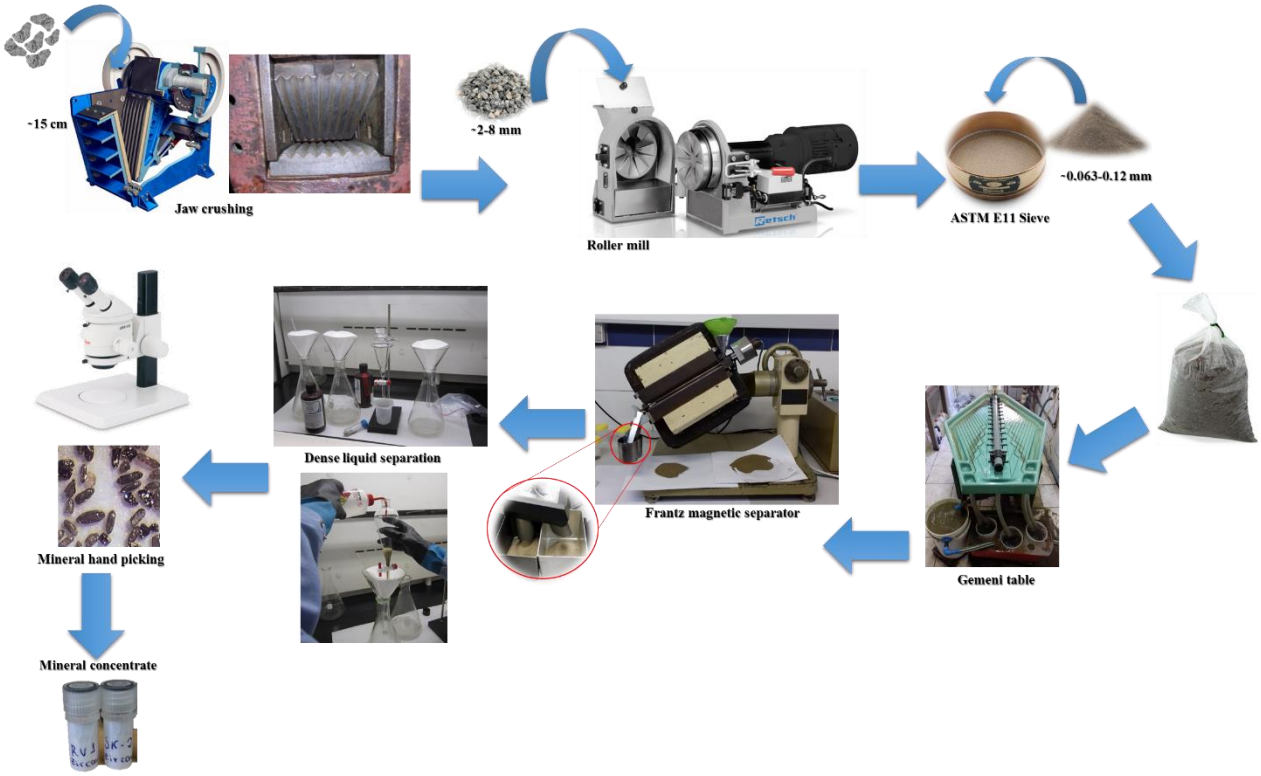

Figure 4. Experimental protocol to extract and concentrate detrital apatites and zircons at the Sample Preparation Laboratory of the Geology Department at the University of Chile.

U-Pb geochronological results were obtained in 3 laboratories (two in Chile and another in Mexico). The Mass Spectrometry Laboratory (CEGA) of the University of Chile uses a laser ablation system-multi-collector-inductively coupled plasma-mass spectrometer (LA-MC-ICP-MS). The laser ablation system is a Photon Machine Analyte G2 193 nm ArF excimer with a double volume HelEx ablation cell that allows for a He atmosphere ablation coupled with a Thermo Fisher Neptune Plus with nine Faraday detectors and eight ion counters. The Geochronology Laboratory of SERNAGEOMIN (Chilean Geology and Mining Service) uses a laser ablation system-inductively coupled plasma-mass spectrometer (LA-ICP-MS). The Thermo Fisher Element XR was equipped with a Photon-Machine Analyte G2 ArF 193 nm wavelength excimer laser. The Laboratory of Isotopic Studies (LEI) of the Geosciences Centre-UNAM, using the LA-ICP-MS technique. The laser ablation system is a Resolution M-50 with a 193 nm ArF excimer laser (LPX 220, lambda Physik) coupled to a Thermo X-Series Quadrupole mass spectrometer (more details in Solari et al., 2010). Analyses on the target zircons were conducted with 30-33 µm diameter spots with output energy of 2.5-3.63 mJ/cm2 and a 5-7 Hz repetition rate. In all three laboratories, at

least 60 grains from each sample were subject to laser ablation analyses, achieving a 95% chance of finding at least one zircon from every population that makes up at least the 5% of the total sample population (Dodson et al., 1988). At least 117 detrital zircons were analysed for each studied formation. This number of analyses helped to ensure that no fraction ≥ of 0.05 was missed with a 95% confidence level (Vermeesch, 2004). The latter implies a good representation of all populations to interpret the provenance and calculate maximum depositional ages. However, to produce a statistically robust maximum depositional age, a number of ≥ 2 grains are required for the calculation (Dickinson and Gehrels, 2009). In this work, there is a 95% chance of finding at least three grains belonging to a population that represents ≥ 7% of the total zircon content (Rossignol et al., 2019). In other words, the relative proportion of the zircon population that remain undetected is low, and the chances to have missing the youngest population are very low.

In both the CEGA and LEI laboratories, the instrumental parameters were optimised by a continual ablation of the reference standard zircon Plešovice (Slama et al., 2008), whereas in the SERNAGEOMIN laboratory with the standard zircon GJ-1 (Jackson et al., 2004). However, both the CEGA and SERNAGEOMIN laboratories measured another standard zircon, TEMORA-2 (Black et al., 2004), to verify the accuracy and the precision of the data obtained. Faraday cups detector and ion counter systems were used simultaneously to measure the following isotopes: ^{202}Hg, ^{204}Hg+^{204}Pb, ^{206}Pb, ^{207}Pb, ^{208}Pb, ^{235}U, ^{232}Th and ^{238}U with an integration time for one cycle of 10 ms. Only in the LEI laboratory, other isotopes were also collected: ^{29}Si, ^{31}P, ^{49}Ti, ^{89}Y, ^{91}Zr, ^{139}La, ^{140}Ce, ^{147}Sm, ^{153}Eu, ^{163}Dy, ^{175}Lu, ^{177}Hf with dwell times of 5 and 10 ms. The acquisition time for each zircon analysis was 90 s, followed by 35 s of a blank signal. A sample bracketing of two primary standards, two secondary standards, and five unknown zircon grains was used to correct for mass bias in the CEGA laboratory. In the CEGA and SERNAGEOMIN laboratories, data reduction was performed with Iolite (Paton et al., 2011) and VisualAge (Petrus et al., 2012). The "UPb.age" code (Solari and Tarner, 2011) was used in the LEI lab to perform the data reduction. In the CEGA and LEI labs, common Pb correction was done following Andersen (2002) for zircons with ^{238}U/^{206}Pb ages >300 Ma. In the SERNAGEOMIN laboratory, common Pb correction followed Williams (1998). The analyses presented were corrected, assuming an evolving isotope composition as given by the second-stage growth curve of Stacey and Kramers (1975). Finally, the preferred reported ages are mainly based on ^{206}Pb/^{238}U ratios for <1000 Ma grains and ^{206}Pb/^{207}Pb for >1000 Ma grains, with uncertainties at the 2σ level (Gehrels,

2000). We plotted probability density and Wetherill Concordia diagrams for each sample using Isoplot (Ludwig, 2003).

To determine each sample's maximum depositional ages (MDA's), $^{206}Pb/^{238}U$ ages were utilised according to the filter of concordance of <80% or >120%. We use four well-known metrics following Dickinson and Gehrels (2009), Schwartz et al. (2017), and Coutts et al. (2019) to obtain the most accurate representation of the MDA's which ranges from the lower to higher statistical robustness using the single youngest grain up to multiple grains, respectively. 1) The youngest single grain (YSG1σ). 2) The weighted mean of the youngest cluster of grains (minimum two) that overlap within 1σ (YC1σ). 3) The weighted mean of the youngest cluster of grains (minimum three) that overlap within 2σ (YC2σ). 4) The weighted average of the youngest statistical population of grains (minimum two) (YSP2σ), which mean square weighted deviation (MSWD) does not exceed 1, indicating that the scatter in ages is explained by analytical uncertainty. Additionally, a range of acceptable MSWD (after Mahon, 1996) was presented for the YC1σ and YC2σ ages considering the sample size involved in the calculation, which is helpful to highlight the meaningfulness of the analyses not exceeding the 95% confidence limit. The criteria employed to select a preferred MDA over another are:

a) The reproducibility of dates (i.e., the higher number of grains included in a youngest-age cluster, the more robustness is reached in results).
b) Proportionality between ages scattering and analytical uncertainty considering the number of grains included in the analysis.
c) Consistency with biostratigraphic ages (for restricted biochrons), stratigraphic position in a stratigraphic column, or similar stratigraphic intervals in different sections.

However, an exception exists when near-depositional age zircons are limited, then we use the YSG metric, which does not provide robust MDA's but is acceptable as it fits well with the last criterion above and because the analyses have a standard error <2%. The calculated YC1σ ages are equal to YC2σ ones for the half of the samples from which both metrics were used. For the other half, the mean difference between both ages is <2%, which magnitude does not overcome its standard error, only in these cases, we preferred the YC1σ because of better stratigraphic consistency and have proven to be useful in chronostratigraphic studies (e.g., Sickmann et al., 2018; Daniels et al., 2019; George et al., 2020).

Analysing each sample's detrital zircons U-Pb age spectra allows identification of a potential provenance by matching detrital-zircon ages with crystallisation ages of potential source terranes (Thomas, 2011). The usefulness of this technique lies in how extensively characterised (by zircons U-Pb geochronology) are the different source terranes and their zircon fertility grade. However, intrinsic complications exist since a sedimentary deposit is the product of detritus derived from multiple parent rocks with non-unique ages, mixing different drainages from multiple localities with variations in zircon fertility, recycling of older sediment and mixing with younger primary sources. The same detrital zircons ages record used for provenance analysis can be utilised as a complementary record (to bedrock ages, see Fig. 5) to complement information about arc duration or temporal pulsing, identification of qualitative high or lull magmatic events during the life of the Southern Patagonian Batholith (Hervé et al., 2007). This complementary information will contribute to overcoming the difficulty of sampling the entire batholith and provide insights related to ancient and eroded plutons of this arc domain.

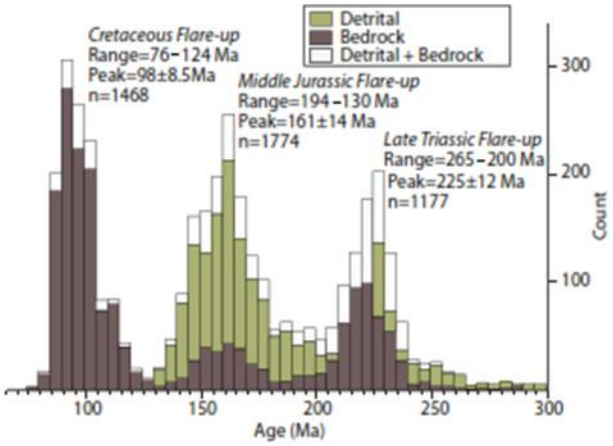

Figure 5. Comparison of bedrock U-Pb zircon ages vs detrital zircon U-Pb ages from the Sierra Nevada Batholith (California, USA) (after Peterson et al., 2015). Note how the integration of both data sets allows characterises episodic magmatism by identifying magmatic flare-ups and lulls.

I-2.3 Low-temperature thermochronology

The characterisation and quantification of exhumation patterns of orogenic wedges have been widely facilitated in light of recent developments in low-temperature thermochronology (Reiners et al., 2005; Reiners and Brandon, 2006; Carrapa, 2010; Painter et al., 2014; Hurford, 2019). The integration of different thermochronometers (e.g., (U-Th)/He on apatite or zircon; apatite or zircon fission-track) open one window to explore denudation histories of mountain belts and provide an efficient way to obtain strong

constraints on the timing and rates of exhumation. Apatite fission-track (AFT) and apatite (U-Th)/He (AHe) ages record the time when the analysed mineral passed through the temperature window of ~120–60°C for AFT (e.g., Gallagher et al., 1998) and of ~80–40°C for AHe (e.g., Farley, 2002).

In the Southern Patagonian Andes, a few previous works on bedrock thermochronology undertaken by Nelson (1982), Gombosi et al. (2009), Thomson et al. (2001, 2010) have shed light on the stages of cooling, erosion, and overall tectonic history of the backbone of this orogen. However, only one study has dealt with the external part of the orogenic wedge (e.g., Fosdick et al., 2013). As the record of erosional exhumation of a mountain belt is preserved in the sedimentary rocks of the adjacent foreland basin, the detrital thermochronology document the long-term history of the orogenic exhumation and its topography evolution (Bernet and Spiegel, 2004; Reiners and Brandon, 2006; Carrapa, 2009; Fosdick et al., 2013; Bernet, 2019). The detrital thermochronological data acquired in the foreland deposits during this thesis and combined with bedrock cooling ages contribute to a better understanding of spatial patterns of time-averaged exhumation rates across the entire orogenic belt.

Twenty-five medium-grained sandstones samples were selected and prepared in the Sample Preparation Laboratory of the Geology Department at the University of Chile for thermochronological analyses. The procedures for extraction of apatites is the same as for zircons, described in the previous section. Detrital apatite grains were carefully selected from the concentrates for (U-Th)/He age dating (n= 12 samples). The selection of apatites grains was conducted at the Geosciences Environnement Toulouse laboratory (GET, France – supervised by Dr Stéphanie Brichau); they were hand-picked under an optical microscope (Nikon SMZ1500), favouring those of euhedral morphology and without inclusions of actinide-rich minerals such as zircons or monazite. For each sample, five aliquots were measured (equivalent radius ranging from 30-90 µm, mean 58 µm) and then placed into a platinum capsule (Fig. 6) for He, U, and Th measurements at Géosciences Montpellier laboratory (France). The aliquots were heated at ~850 °C for 20 min using a 1090 nm diode laser operating at 20 W, allowing total helium (He) degassing. The gas was purified by two SAES AP-10-N getters and trapped on a JANIS cryostat. The released ^{4}He was measured with a Quadrupole PrismaPLus QMG 220 using the peak height method using a ^{3}He spike and are 10–100 times superior to typical blank levels. After helium extraction, aliquots were retrieved for U and Th measurements. Apatite grains were dissolved in 220 ml of doubly

spiked (^{230}U, ^{235}Th) HNO3 13N at 120 °C for two hours, and ^{238}U and ^{232}Th were measured using isotope dilution by a quadrupole ICP-MS (Agilent 7700x). Each calculated apatite age (AHe) was corrected by alpha (α) ejection factor (F_t), determined using the Monte Carlo simulation technique of Ketcham et al. (2011), and equivalent sphere radius (R_s) following Gautheron and Tassan-Got (2010). Durango apatite replicates were analysed for each three analysed aliquots yielding a mean age of 31.2 ± 2.4 Ma (2σ), which agrees with the Durango AHe age of 31.13 ± 1.01 Ma reported by McDowell et al. (2005). The 2σ error on the AHe age calculation is ~8, reflecting both sample heterogeneity and analytical procedure.

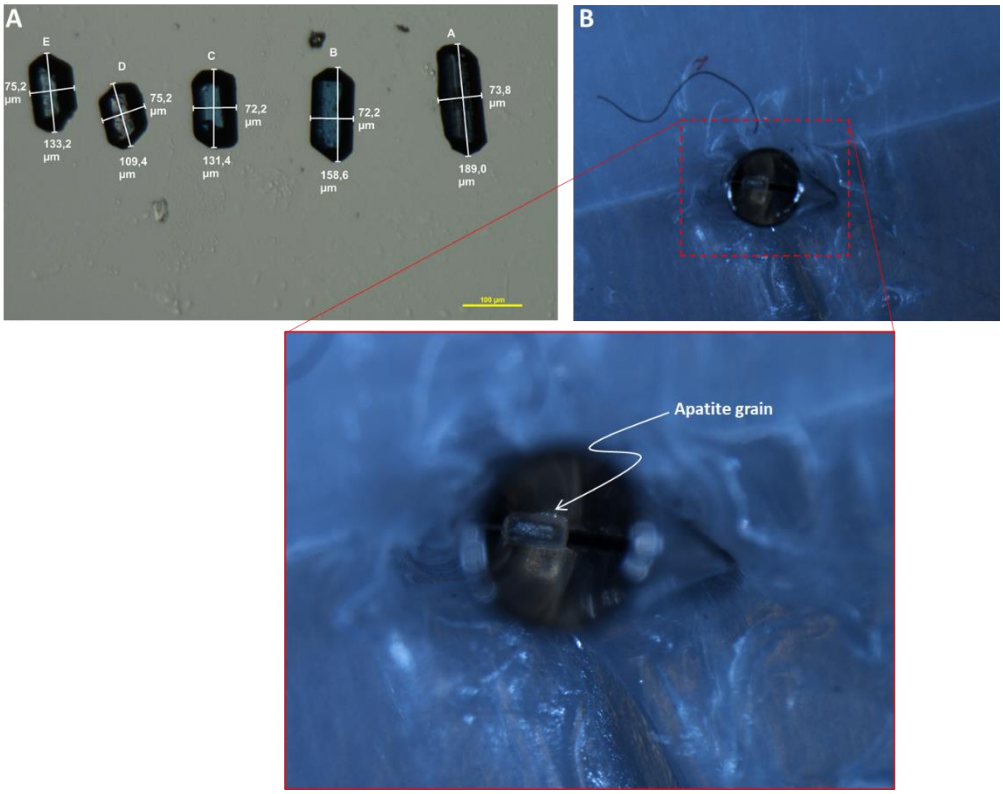

Figure 6. A. Selection and measurement of 5 aliquots of the best apatites crystals. B. Packing into a platinum capsule to posterior degassing phase. Experimental protocol conducted at the GET lab.

For apatite fission-track (AFT) analysis, 18 samples were prepared at the Geosciences Environnement Toulouse laboratory (GET, France – supervised by Dr Stéphanie Brichau), but only 14 were finally analysed (fission-track counting). Over 100 detrital apatites (including all possible morphologies, colour, and sizes) compose a single aliquot of a sample mounted in resin epoxy, then polished to reveal internal surface and finally etched with 5 M HNO_3 for 20 s at 20 ± 0.5 ºC to reveal the spontaneous fission-tracks. Low-U muscovite sheets were attached over apatite sample mounts to be used as external detectors (according to the external detector method, Fig. 7A). The apatite sample mounts

intercalated with CN5 glass dosimeters, and Fish Canyon and Durango standard samples (arranged as in Fig. 7B) were irradiated at the La Reina Nuclear Reactor (Santiago, Chile) with a nominal fluence of 1.10^{16} neutron/cm^2. After irradiation, external detectors of all samples and standards were etched for 40 min in 40% HF at 20 ± 0.5ºC to reveal the induced fission tracks. Fission track densities were measured at the Institut des Sciences de la Terre laboratory (ISTerre, Grenoble-France) under the supervision of Dr Mathias Bernet. Only crystals with polished surfaces parallel to the crystallographic c-axis were counted, using an Olympus BX51 optical microscope with a dry objective at 1250x magnification and a digitising table FTStage 4.04 system (Dumitru, 1993). Fission-track ages were calculated using the zeta-calibration method and the standard fission-track age equation (Hurford and Green, 1983).

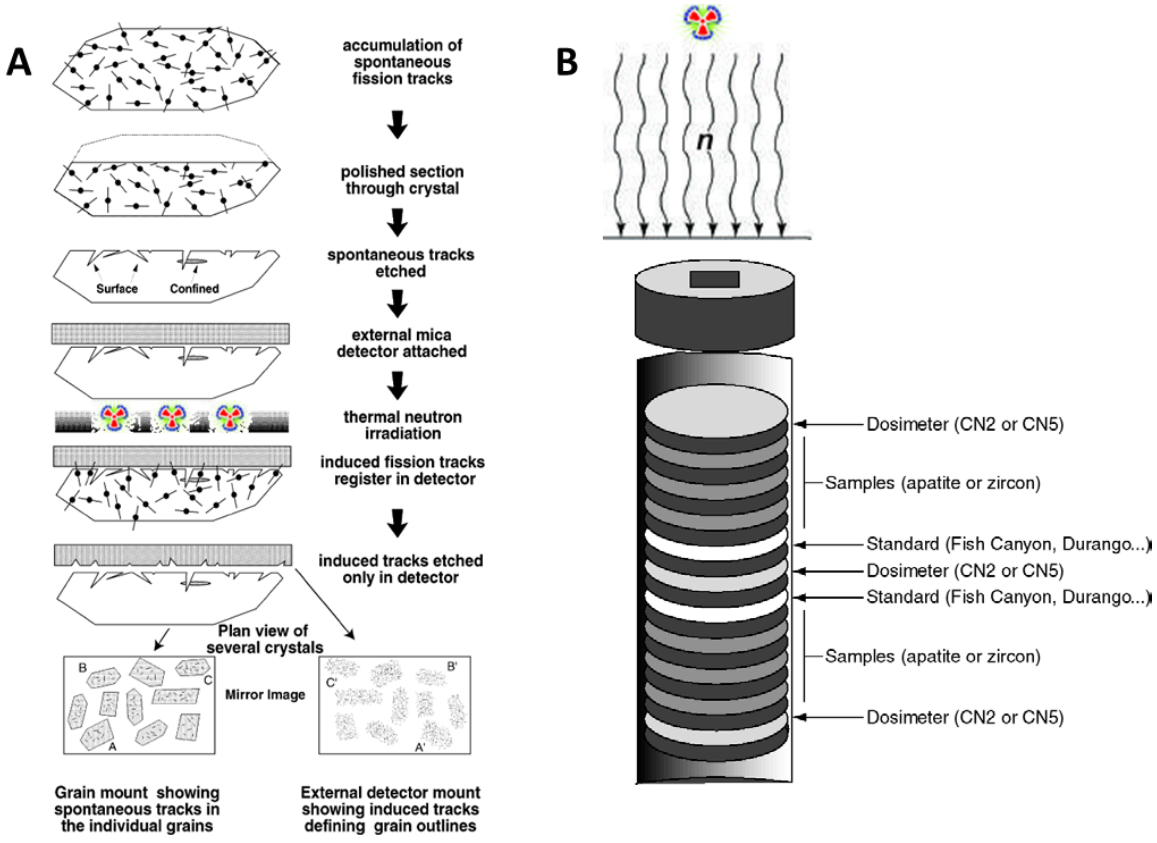

Figure 7. A. Detailed process of the external detector method used for AFT (after Hurford and Carter, 1991). The surface of a given mineral is polished and etched to reveal spontaneous tracks. Then a low-uranium mica sheet is attached to mounting surfaces, and this assembly is submitted to irradiation (B). Some heavy particles cross the interface between the mineral and the mica during the fission process, producing a mirror image of the original grain. After, only the mica is etched to reveal the induced tracks. By counting the number of induced tracks in the mica, it is possible to estimate the mineral's uranium (or parent) concentration, whereas by counting the number of spontaneous tracks in the mineral, it is estimated the concentration of the daughter

product. B. Schematic illustration (modified from Jolivet et al., 2001) of the organisation of the samples in the tube of irradiation which will be bombarded with neutrons to induce fission in ^{235}U.

The calibration parameter Zeta (ζ) is 322.9 ± 7.69, and it was determined using Durango and Fish Canyon Tuff standards at GET and ISTerre laboratories (Fig. 8). The $\chi 2$ test and age dispersion (Galbraith and Green, 1990; Galbraith and Laslett, 1993; Galbraith, 2005) were used to assess the homogeneity of AFT ages. However, due to the high dispersion inherent to sedimentary samples, the central age was chosen as it represents the best measure of the spread in single grain ages. Furthermore, only the youngest peak ages or minimum ages (Brandon et al., 1998) were geologically significant. Due to the low-U content in apatites, horizontal confined track lengths are not abundant, but all those present in each apatite grain were measured to carry out a track length distribution analysis and thermal history reconstruction. Likewise, the D_{par} values (etch pit lengths parallel to the crystallographic c-axis) were measured in all samples and approximated the chemical composition of apatites (crucial parameter for track annealing). The radial plots representation of all AFT ages and computed central ages were conducted with RadialPlotter software (Vermeesch, 2009, 2012). Additionally, to explore plausible t-T trajectories and extract thermal histories consistent with our data, the software HeFTy (Ketcham, 2005) was used to conduct the inverse modelling.

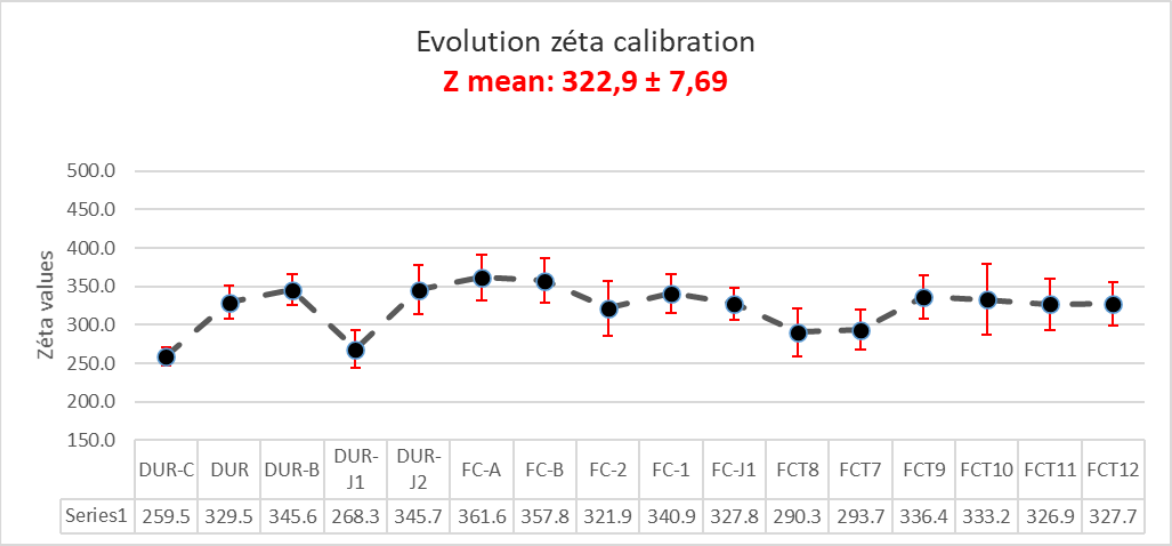

Figure 8. Zeta (ζ) values measurement evolution and weighted mean value (322.9 ± 7.69 for Huber Rivera), determined on Durango and Fish Canyon tuff apatite standards at the GET and ISTerre labs.

I-2.4 Structural geology

The primary purpose of the structural geological analysis is the identification of the main structural domains of the fold and thrust belt (hinterland, internal, external), recognising the different structural styles, and quantifying the amount of deformation. This approach will reconcile the precedent sedimentary infill study with the tectonic history of the orogen to further constrain the geodynamic processes that affected the orogen-basin pair.

One structural section was constructed based on georeferenced field data (contacts, dip measurements, stratigraphic units) and complemented with surface structural data recorded in unpublished reports provided by ENAP (Empresa Nacional de Petróleos de Chile). The structural sections were complemented (merged) with other previous works (Farfán, 1994; Betka et al., 2015) focused on the innermost part of the orogen, where it was not possible to access during the fieldwork campaigns. The projection of the structures in the subsurface and characterisation of the structural geometry of the basin was supported by multiple 2D seismic lines and exploratory wells data, with which two regional seismic profiles were composed. The interpretation of the regional seismic profiles was based on stratigraphic-seismic criteria and their relationship with the structures kinematics. Depth and thickness measurements were derived through velocity-depth conversion models. Shortening was measured by retrodeformation of key stratigraphic intervals. The temporality of the deformation is constrained thanks to the U-Pb dating in detrital zircons, sedimentary provenance, growth strata identified in the seismic and thermochronological results.

SECOND PART

REGIONAL STRATIGRAPHIC FRAMEWORK OF THE MAGALLANES-AUSTRAL BASIN

CHAPTER II-1 :

UPPER CRETACEOUS – MIOCENE CHRONOSTRATIGRAPHIC AND TECTONOSTRATIGRAPHIC FRAMEWORKS

Chapter II-1 present an updated regional chronostratigraphic and tectonostratigraphic framework for the Upper Cretaceous to early Miocene strata fo the Magallanes-Austral Basin (excluding Tierra del Fuego). This chapter is intended to be submitted in 2022 to the Journal of South American Earth Sciences (JSAMES). The refined chronostratigraphic framework incorporates an extensive database of detrital zircon U-Pb analyses to report maximum depositional ages, complemented with relevant biostratigraphic data. The tectonostratigraphic framework is constructed from the analysis of regional 2-D seismic-reflection profiles appropriately tied to boreholes data (markers and formation tops). These new frameworks (and data sources) lead to constraints on the basin correlations, highlight regional unconformities and the episodic nature of the magmatic arc is (identifying main pulses, lulls, and tempos of magmatism). This chapter is complemented by the article published by Ramírez de Arellano, Calderón, **Rivera** et al., 2021 "*Neogene Patagonian magmatism between the rupture of the Farallon plate and the Chile Ridge subduction*" attached as Annex B-1.

HIGHLIGHTS:

- High-precision in maximum depositional ages for numerous Cretaceous to Cenozoic formations.
- Enhanced basin-wide correlations and revision of the stratigraphic nomenclature.
- Five regional unconformities with constraints on age and duration along the basin.
- Identification of two new pulses of magmatism and three magmatic lulls in the arc.
- Farallon-Aluk and Farallon breakup impacted on the unconformity development.

Updated chronostratigraphic and tectonostratigraphic framework for the Upper Cretaceous-Miocene Magallanes-Austral Basin (49.5°-53.6°S): implications in unconformity development and arc magmatic tempos

Huber A. Rivera[1, 2, *], Marcelo Farías[1], Joseph Martinod[2], Jacobus P. Le Roux[1]

[1]Departamento de Geología, FCFM, Universidad de Chile, Plaza Ercilla 803, Santiago, Chile

[2]Univ. Grenoble Alpes, Univ. Savoie Mont Blanc, CNRS, IRD, IFSTTAR, ISTerre, 38000 Grenoble, France

[3]Departamento de Ingeniería en Minas, Universidad de Santiago de Chile, Av. O'Higgins 3363, Estación Central, Santiago, Chile

***Corresponding author:** riverarh@univ-grenoble-alpes.fr; huber.rivera@ug.uchile.cl

II-1.1 Introduction

Andean foreland basins are well known as valuable repositories of information about the temporal shifts in shortening and deformation style of the thrust-belts (Bayona et al., 2008; Ghiglione et al., 2010; Horton et al., 2016), changes in arc magmatism dynamics (Hervé et al., 2004; Butler et al., 2020; Capaldi et al., 2020, 2021), river systems genesis and drainage reorganisation (Hoorn et al., 1995; Horton and DeCelles, 2001), paleoclimate fluctuations and landscape evolution (Fosdick et al., 2017; Gutiérrez et al., 2017; Varela et al., 2018), tectonically and eustatic-driven accommodation harbouring marine transgressions that impact biodiversity (Hernández et al., 2005; Aguirre-Urreta et al., 2011; Jaramillo et al., 2017; Rivera et al., 2020), and also known as essential hosts of important paleontological sites (Hoorn et al., 2010; Antoine et al., 2016; Otero et al., 2015; Otero et al., 2021) and economic resources (Jacques, 2004; Rosello et al., 2008; Macellari, 2021). However, a comprehensive and exhaustive chronostratigraphic framework is required as the key to access those foreland basin records and provide answers to all these scientific and industrial provoking topics.

Even if a chronostratigraphic framework exists in a basin, it must have a level of precision determined by the temporal resolution required from each of the geological processes involved in the different research issues. The timing of backarc to foreland stage transition, stages of basing fill, orogenic-driven cyclicity, clastic wedge progradation, spatial and temporal variation in deformation episodes, palaeodrainage and sediment accumulation rates are processes that operate in foreland basins at the scale of 10^6-10^7 yrs (DeCelles et al., 2009; Miall, 2016; Catuneanu, 2019a). In this regard, a chrono-biostratigraphic basis cannot always accurately bracket the aforementioned geological processes (due to the uncertainty of their biochrons), arising the need for integration with high-resolution methods as detrital zircon U-Pb geochronology (e.g., Dickinson and Gehrels, 2009; Daniels et al., 2018).

The Magallanes-Austral foreland basin, in the southernmost tip of South America (Fig. 1), has long been recognized for its coal and oil/gas resources (Bonarelli, 1917; Feruglio, 1949; Thomas, 1949; Hünicken, 1955; Rosello et al., 2008) and ultimately by its non-conventional hydrocarbons and geothermal potential (Zurita et al., 2013; Schenk et al., 2016). Further, this basin is key to understanding the Andean orogenic evolution in geodynamic complex scenarios (e.g., the interplay of several tectonic plates, active ridge collisions, the opening of Drake Passage), palaeofaunistic and palaeofloristic interchange dynamics between South America and the Antarctic Peninsula (Leppe et al., 2012) and

ecological conditions during the K-Pg transition in southern high-latitudes. The first chronostratigraphic frameworks (e.g., Natland et al., 1974; Cañón and Ernst, 1975; Biddle et al., 1986), very useful in the petroleum industry, were based mainly on the study of foraminiferous fossils and, to a lesser extent on macroinvertebrates. However, the almost exclusive use of benthic foraminifera and low stratigraphic resolution of biochrons prevented precise dating of the formations, limited effectiveness in recognising unconformities and led to problems of correlations of the formations between Chile and Argentina that persist to the present (Fossa Mancini et al., 1938; Hoffstetter et al., 1956; Biddle et al., 1986; Malumián et al., 2013; Sickmann et al., 2018). Nevertheless, with the progress of detrital zircons U-Pb geochronology to estimate maximum depositional ages, the chronostratigraphy of the Magallanes-Austral basin has resumed on a renewed air. The latter has allowed alleviating the confusion in intrabasinal correlations (across political limits), better understanding the evolution of the phases of sedimentary fill and facies transitions, highlighting the presence of unconformities in the stratigraphic record and a better understanding of orogenic uplift in the Southern Patagonian Andes (Fildani et al., 2003; Mpodozis et al., 2007; Barbeau Jr. et al., 2009; Romans et al., 2010; Malkowski et al., 2017; Sickmann et al., 2018; Daniels et al., 2018, 2019; George et al., 2020; Rivera et al., 2020; Fosdick et al., 2020; Ghiglione et al., 2021, among others).

In this work, we present an examination of the chrono- and tectono-stratigraphic relationship for Upper Cretaceous to lower Miocene units along the axis of the Magallanes-Austral foreland basin (49.5°-53.6°S) in the Santa Cruz Province (Argentine) and última Esperanza and Magallanes Provinces (Chile). Our analysis integrates new 25 detrital zircon U-Pb geochronological results and seismostratigraphic characterisation in two regional seismic profiles (~350 km long) with an extensive database of previously-published geochronological results and more than 50 years of active research in regional stratigraphy, sedimentology, and structural geology. The purpose of this work is four-fold: (1) use detrital zircon maximum depositional ages to enhance the chronostratigraphic framework; (2) to identify and constrain the timing and duration of unconformities along-strike the basin; (3) to construct an updated tectono-stratigraphic framework to group different lithostratigraphic units into genetically related packages in terms of orogenic processes that accompany the basin filling; (4) monitor the spatial and temporal behaviour of the magmatic arc. The results have implications to the synergy of stratigraphic-sedimentologic knowledge achieved in different sectors of the basin, to provide a time template for the paleontological research, to

enhance understanding of tempos in subduction-related magmatic arcs, and to decipher the complex tectonic evolution of Southern Patagonian Andes.

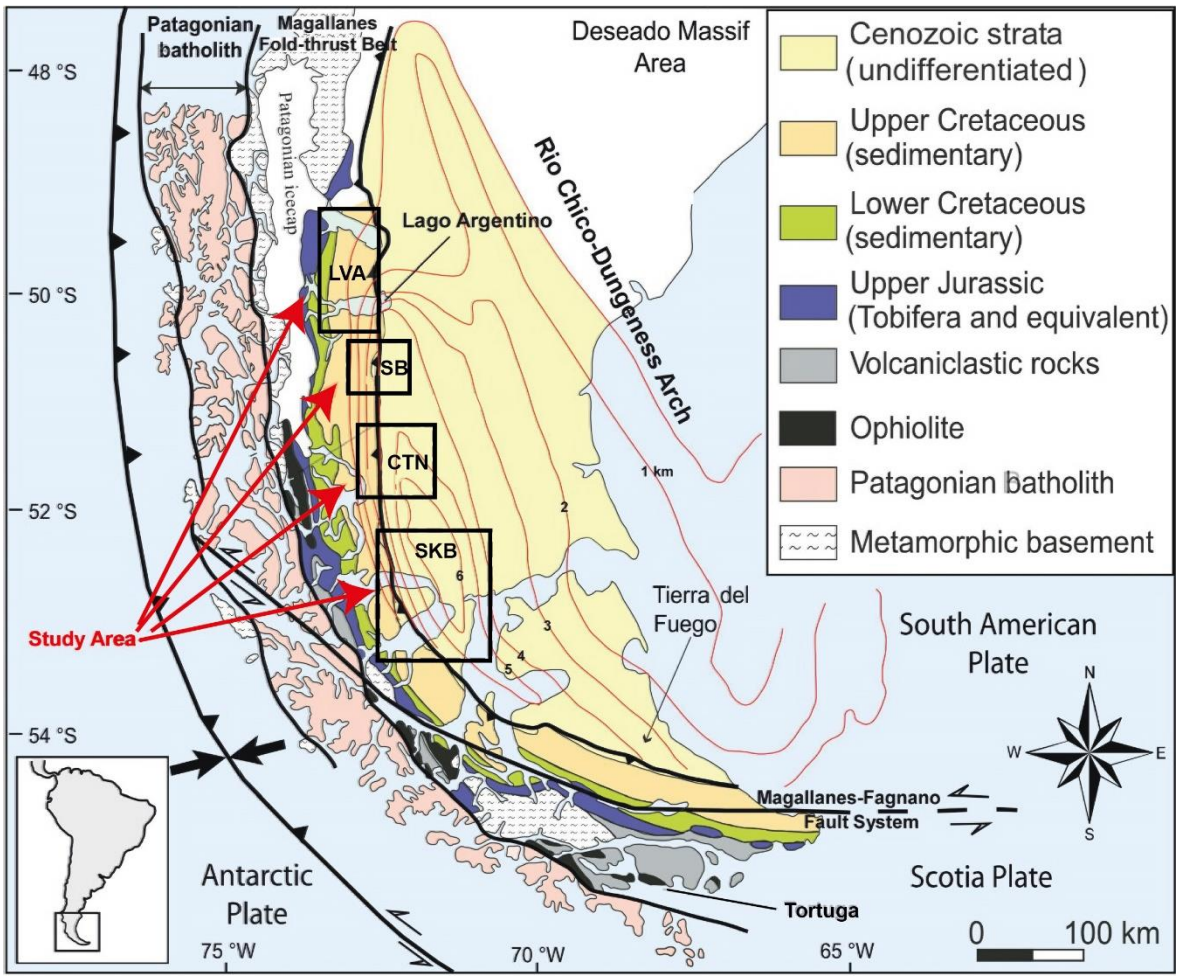

Figure 1. The morphotectonic setting of the Magallanes-Austral foreland basin (modified from Fildani et al., 2008). Contours indicate foreland sediment thickness (after Ghiglione et al., 2009). The black boxes indicate the location of the study areas.

II-1.2 Study areas

The study area encompasses a north to south transect (~420 km; 49.5°-53.6°S) along the axis of the Magallanes-Austral foreland basin (known as Magallanes in Chile and Austral in Argentina) in its continental domain (i.e., excluding Tierra del Fuego) trespassing the international borders of Argentina and Chile, in the Santa Cruz Province (Argentina), and in the Última Esperanza, and Magallanes Provinces (Chile). This study examines numerous stratigraphic units with several nomenclatures and reports new stratigraphic and geochronological data combined with previously published information that constitutes a large database. Therefore, to facilitate the analysis, we subdivided the study area into four stratigraphic areas from north to south (Fig. 2): (1) the Lago Viedma-Argentino area (LVA)

in the Santa Cruz Province; (2) the Sierra Baguales area (SB), in the Última Esperanza Province; (3) the Cerro Castillo-Rio Turbio-Natales (CTN) area, in the Santa Cruz and Última Esperanza Provinces; (4) the Skyring sound-Brunswick Peninsula (SKB) area, in the Magallanes Province.

II-1.3 Geologic and tectonic setting

The tectonic history of the Southern Patagonia onset with the development of the marginal Rocas Verdes Basin (RVB) linked to the breakup of Gondwana in the Middle to Late Jurassic (Dalziel et al., 1974; Dalziel, 1981; Pankhurst et al., 2000; Calderón et al., 2013). This enlarged extension in the continental crust resulted in the formation of a quasi-oceanic floor (the Sarmiento, Capitán Aracena, and Tortuga ophiolite complexes), voluminous ignimbrite eruptions (the El Quemado and Tobífera formations), and a thick fine-grained volcaniclastic and siliciclastic succession (the Springhill Formation and Río Mayer/Zapata/Erezcano/Canal Bertrand formations) (Fig. 1 and 2). The extensional RVB opened from south to north as far as 50°S, being broader, deeper and with a more-evolved seafloor spreading to the south (Dalziel et al., 1974; de Wit and Stern, 1981). The closure of the RVB took place from the end of the Early Cretaceous until the Late Cretaceous, involving underthrusting and obduction of its components (Klepeis et al., 2010; Calderón et al., 2013; Fildani and Hessler, 2005; McAtamney et al., 2011; Malkowski et al., 2017) and whose remnants now form part of the Patagonian fold and thrust belt to the east of the Magallanes-Austral foreland basin and, in turn, to the west of the Southern Patagonian Batholith (Fig. 1).

II-1.3.1 Cordilleran magmatic arc

South of the Chile triple junction is extended the Southern Patagonian Batholith (SPB; 47°S-53°S) formed by the amalgamation of subduction-related calc-alkaline plutons (Bruce et al., 1991; Hervé et al., 2007) which intruded mainly low-grade, metasedimentary components of the Eastern Andean Metamorphic Complexes (late Devonian to Permian; Hervé et al., 2003), and part of the fold-and-thrust belt (Fig. 1). The temporal pulsing of the plutons ranges from Jurassic to Neogene (Bruce et al., 1991; Hervé et al., 2007), where its older plutons (157-145 Ma) are coeval with episodes of voluminous, silicic volcanism of the Tobífera and El Quemado formations in the RVB to the east of the batholith (Pankhurst et al., 2000; Hervé et al., 2007). Although the activity of the SPB reveals a first-order continual record of plutonism (Bruce et al., 1991), over short periods can be highlighted its episodic behaviour. Hervé et al. (2007) have proposed three magmatic pulses during the Cretaceous,

e.g., K1: 144-137 Ma, K2: 136-127 Ma, K3: 126-75 Ma, which are emplaced preferentially in the occidental and axial part of the batholith and characterized isotopically by progressively cortical to mantellic signatures (εNdt from -4 to +2). For the Cenozoic, there are two magmatic pulses, e.g., Pg: 67- 40 Ma, Ng: 25-15 Ma, emplaced spatially in the axial part of the batholith and characterized isotopically by a strong mantellic signature during the Paleogene (εNdt +5) but more variable during the Neogene (εNdt from -1 to +5). Between 48°-51°S, some Miocene calc-alkaline intrusives (younger than ~18 Ma) have been emplaced to the east of the axis of the SPB (Fig. 2), suggesting a possible eastward migration of locus of magmatism (Rámirez de Arellano et al., 2012, 2021). However, farther south (51°-53°S) is not clear the same trending for the Miocene plutons. Nevertheless, it is worth mentioning that the Punta Camden intrusive and the volcanic complex of the Cordillera Vidal-Cordillera Pinto (Fig. 2) represent the most eastward evidence of arc magmatism with calc-alkaline transitional signature around the 19 Ma in the Magallanes Province (Morello et al., 2001; Ramírez de Arellano et al., 2021).

II-1.3.2 Cretaceous foreland basin history

Because of the inherited structural architecture and differential closure time of the RVB, the onset of the Magallanes-Austral foreland basin history is marked by a north to south diachronism in sedimentation and subsequent evolution. Deep-marine, coarse clastic deposition marking the onset of the foreland basin history started as early as 115 Ma in the northernmost part of the basin (LVA; Fig. 2), progressing southward by 93 Ma in the middle part (SB and CTN; Fig. 2), and by ~89 Ma in the southernmost part of the basin (SKB; Fig. 2). The early basin fill is represented by the undifferentiated units of Cerro Toro-Alta Vista formations in the LVA (Malkowski et al., 2017b; Sickmann et al., 2018); the Punta Barrosa Formation in the SB and CTN (Wilson, 1991; Fildani et al., 2003); and Latorre Formation in the SKB (McAtamney et al., 2011).

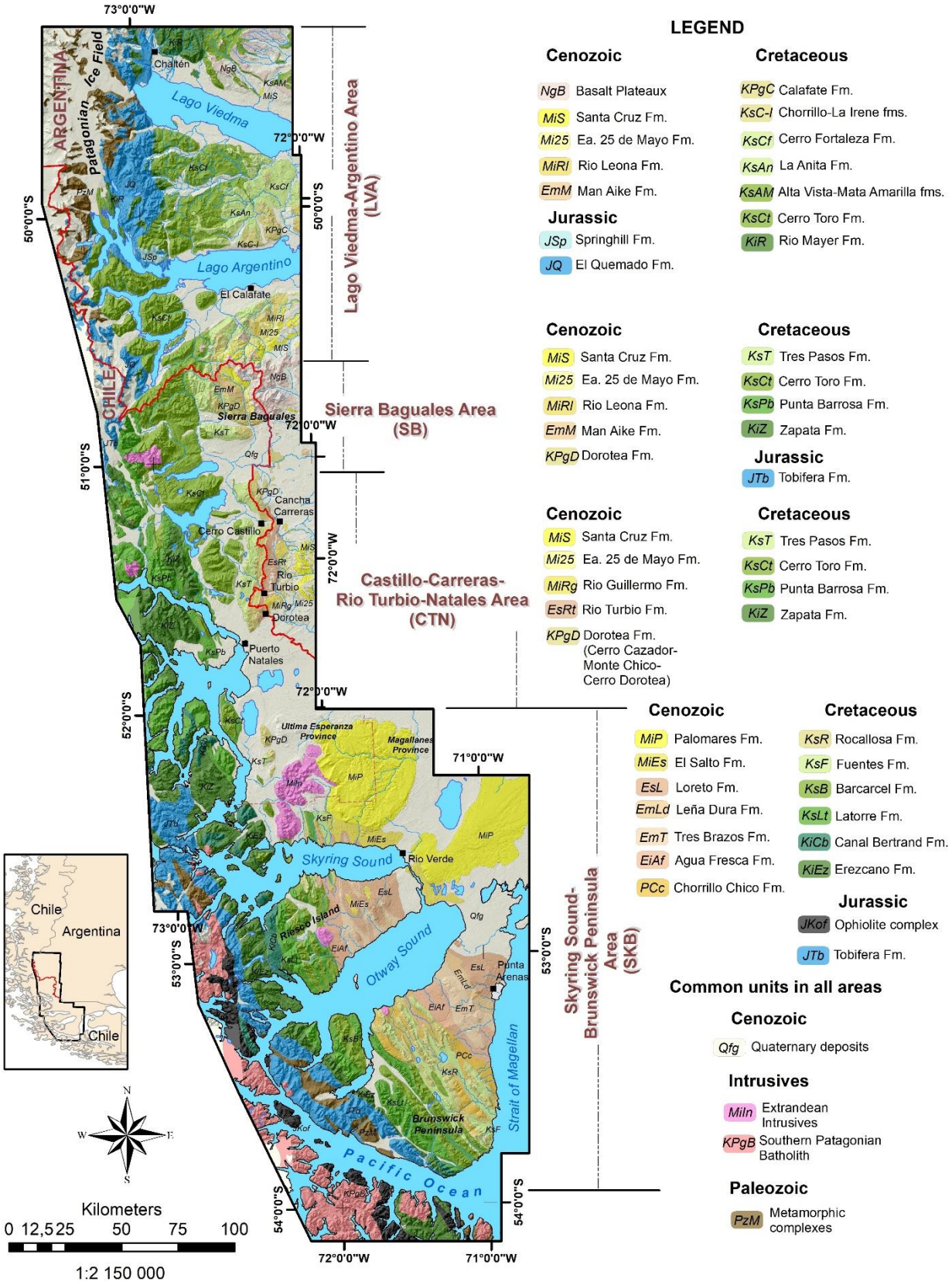

Figure 2. Simplified geological map of the study areas in the Magallanes-Austral foreland basin. For each study area, the stratigraphic nomenclature is indicated on the right. Map-based on first-author fieldwork and modified from Malumián et al. (2000), Sernageomin (2003), Nullo et al. (2006), Fosdick et al. (2011), Giacosa et al. (2013), Gutiérrez et al. (2017), and Daniels et al. (2019).

A southward-directed dispersion of sediments was dominant in the northern and middle part of the basin, but sediment routing systems were more complex farther south (McAtamney et al., 2011; Rivera et al., 2020). The following deep-marine sedimentation stages represent a more confined turbidite system inferred to be coincident with a major phase of thrust-sheet emplacement and are recorded by the Cerro Toro, Alta Vista-Mata Amarilla formations (in LVA), Cerro Toro Formation (in SB and CTN), and Barcárcel Formation (in SKB) (Romans et al., 2011; McAtamney et al., 2011; Malkowski et al., 2017b; Sickmann et al., 2018). The end of the deep-marine sedimentation was reached first in the northernmost part of the basin (LVA), where the assemblage of the Piedra Clavada/La Anita/Mata Amarilla/Cerro Fortaleza formations mark the transition to shallow-to-non marine sedimentation from the Albian up to Campanian depending upon the area investigated (see further details in Varela et al., 2012; Malkowski et al., 2017a,b; Sickmann et al., 2018). This transition does not occur until the latest Cretaceous (~78-65 Ma) in the other parts of the basin, where the deep-marine turbiditic succession is capped by depositional slope and outer shelf facies of the Tres Pasos Formation (in SB and CTN) and Fuentes Formation (in SKB) (Hubbard et al., 2010; Romans et al., 2011; Hubbard et al., 2014; Gutiérrez et al., 2017; Bauer et al., 2020; Rivera et al., 2020). These deposits are, in turn, followed by deltaic-incised valleys systems and shoreface deposits of the Dorotea (in SB and CTN) and Rocallosa Formations (in SKB), respectively (Covault et al., 2009; Romans et al., 2011; Schwartz and Graham, 2015; Gutiérrez et al., 2017; Manríquez et al., 2019; Bauer et al., 2020; Rivera et al., 2020).

II-1.3.3 Cenozoic foreland basin history

The Cenozoic sedimentary fill has been much less studied than its cretaceous counterpart, particularly in the southern reaches of the Magallanes-Austral foreland basin. In the northern (LVA) and middle parts (SB and CTN) of the basin, a prolonged hiatus in the Paleogene of variable duration (~15-33 Myr) depending upon the position in the basin (Fosdick et al., 2015a; Gutiérrez et al., 2017; Sickmann et al., 2018; George et al., 2020) indicates either an interruption in sedimentation or cannibalization of the strata. Towards the south, in the SKB area, the Paleocene-early Eocene is characterized by thick shales, siltstones, and clay-rich, glauconitic sandstones of the Chorrillo Chico and Agua Fresca Formations reflecting a progressive shallowing from deep-marine northwest-ward prograding turbidite fan system to outer shelf deposits, respectively (Charrier and Lahsen, 1969; Mella, 2001; Rivera, 2017; Rivera et al., 2020). Subsequently, during the Eocene

(~45–33.9 Ma), a generalised shallow marine sedimentation occurred in all the studied areas, but with certain particularities from north to south. In the LVA area (Fig. 2), the Man Aike Formation represents the evolution of an incised valley system (Casadío et al., 2009) that southward, in the SB area (Fig. 2), a wave-to-tide-influenced estuary is better represented (Le Roux et al., 2010; Gutiérrez et al., 2017). Further south, in the CTN area (Fig. 2), the first author has recognised tidal-influenced, meandering fluvial channels in the base of Río Turbio Formation (around Cerro Castillo town and at Río Turbio town; Fig. 2). Previous authors have interpreted marginal marine environments for the Río Turbio Formation, which ranges from the foreshore, tidal channels, and tidal flats for its lower member and tide-dominated, outer estuarine and coastal plains for its upper member (Santos-García, 1988; Azcuy and Amigo, 1991; Pearson et al., 2012). On the other hand, in the southernmost part studied in the basin (in SKB), age-equivalent rocks represent a northeast-ward prograding fluvial-dominated and tide-influenced, deltaic facies of the Tres Brazos Formation and the Loreto Formation, respectively, interrupted by shelf mudstones of the Leña Dura Formation (Mella, 2001; Rivera, 2017). In the Oligocene-Miocene (~33–18 Ma), dominant fluvial sedimentation was established, as reflected by the conglomerates and pebbly sandstones of the Río Leona, Río Guillermo, and El Salto Formations (Malumián and Caramés, 1997; Gutiérrez et al., 2017; Rivera, 2017; Leonard et al., 2020). In the LVA and SB areas (Fig. 2), the Río Leona Formation is interpreted as high-energy braided systems to low energy meandering and anastomosed systems in a coastal plain (Marenssi et al., 2005, 2003; Gutiérrez et al., 2017). In the CTN area, particularly near Rio Turbio town (Fig. 2), the first author has recognised facies that can be ascribed to alluvial fans systems in the basal part of the Río Guillermo Formation, which is consistent with a previous work of Santos-García (1988). However, near Cancha Carrera town (Fig. 2), Leonard et al. (2020) interpret a low-energy, tidal-affected coastal plain system and coarse-grained sandy braid plain environments. In the southernmost SKB area (Fig. 2), the El Salto Formation exhibits a proximal, high-energy, braided river system of gravels and sands (its basal member) to a more distal, braided, arenaceous fluvial system close to a coastal plain (its upper member) (Rivera, 2017). However, Mella (2001) interpret fluvial to paralic environments for the El Salto formation. These continental conditions were briefly interrupted by the Patagonian Transgression during the early Miocene, when the shoreface and shelf deposits of the Estancia 25 de Mayo Formation (21-19 Ma) was deposited in most studied areas (LVA, SB, CTN; Fig. 2) (Marenssi et al., 2003; Cuitiño et al., 2012, 2015; Gutiérrez et al., 2017). However, in the southernmost SKB area (Fig. 2), evidence of this marine incursion is absent,

and age-equivalent strata are represented by the arenaceous fluvial system of the upper member of the El Salto Formation (Rivera, 2017). The continental conditions returned soon after that in all the basin by the Burdigalian (~18–15.8 Ma) with the fluvial conglomerates, sandstones and rhyodacitic tuffs of the bearing Santacrucian mammals Santa Cruz (in LVA, SB, and CTN; Fig. 2) and Palomares Formations (SKB; Fig. 2) (Bostelmann et al., 2013; Cuitiño and Scasso, 2013; Cuitiño et al., 2016; Gutiérrez et al., 2017; Rivera, 2017).

II-1.4 Data source and methodology

To refine the Upper Cretaceous-Miocene chronostratigraphic framework and identify regional hiatuses or unconformities, we collected 25 samples of medium-grained sandstones and volcanoclastic deposits to detrital zircon U-Pb dating. These samples correspond to the Latorre (n=1), Dorotea (n=3), Man Aike/Río Turbio (n=4), Tres Brazos (n=2), Río Guillermo (n=1), Loreto (n=7), El Salto (n=4), and Palomares (n=3) formations (Table 1). Detrital zircons were extracted in the Sample Preparation Laboratory of the Geology Department at the University of Chile following standard crushing, density, and magnetic concentration techniques (e.g., Rivera et al., 2020). U-Pb geochronological results were obtained in 3 laboratories: (1) at the Mass Spectrometry Laboratory (CEGA) of the University of Chile, using LA-MC-ICP-MS technique; (2) at the Geochronology Laboratory of SERNAGEOMIN (Chilean Geology and Mining Service) by using LA-ICP-MS practices; (3) at the Laboratory of Isotopic Studies (LEI) of the Geosciences Centre-UNAM, using LA-ICP-MS technique. On average, 91 grains were dated in all samples but 46 in the CC1 sample. Analyses on the target zircons were conducted with a 30-33 μm diameter spots with output energy of 2.5 mJ/cm2, and a repetition rate of 5-7 Hz and the reported ages are based primarily on $^{206}Pb/^{238}U$ ratios for <1000 Ma grains and $^{206}Pb/^{207}Pb$ for >1000 Ma grains both with uncertainties at the 2σ level. Further description of procedures is outlined in Solari et al. (2010) and Rivera et al. (2020). Other previous published geochronological data incorporated in the chronostratigraphic analysis include U-Pb ages determined from detrital zircon (e.g., Hervé et al., 2004; Mpodozis et al., 2006; McAtamney et al., 2011; Otero et al., 2012; Bostelmann et al., 2013; Fosdick et al., 2015, 2020; Gutiérrez et al., 2017; Sickmann et al., 2018; Daniels et al., 2019; George et al., 2020; Rivera et al., 2020) and volcanic ashes (e.g., Fosdick et al., 2011; Cuitiño et al., 2012, 2016), as well as strontium isotope dates (e.g., Cuitiño et al., 2012, 2015). Dates reported in those studies were acquired via SHRIMP-RG (Hervé et al., 2004; Álvarez et al., 2006; Otero et al., 2012; Bostelmann et al., 2013), LA-MC-ICP-MS (Gutiérrez et al., 2017; Rivera et al., 2020; Fosdick et al., 2020), LA-ICP-MS

(McAtamney et al., 2011; Cuitiño et al., 2012, 2016; Fosdick et al., 2015a, b; Sickmann et al., 2018; Daniels et al., 2019; George et al., 2020; Rivera et al., 2020) techniques. Analytical procedures are outlined in the previous references.

To constrain deposition timing in the basin, we determined maximum depositional ages (MDA's) for each sample. The $^{206}Pb/^{238}U$ ages were utilised according to the filter of concordance of <80% or >120%. We use four well-known metrics following Dickinson and Gehrels (2009), Schwartz et al. (2017), and Coutts et al. (2019) to obtain the most accurate representation of the MDA's which ranges from the lower to higher statistical robustness using the single youngest grain up to multiple grains, respectively. 1) The youngest single grain (YSG1σ). 2) The weighted mean of the youngest cluster of grains (minimum two) that overlap within 1σ (YC1σ). 3) The weighted mean of the youngest cluster of grains (minimum three) that overlap within 2σ (YC2σ). 4) The weighted average of the youngest statistical population of grains (minimum two) (YSP2σ), which mean square weighted deviation (MSWD) does not exceed 1, indicating that the scatter in ages is explained by analytical uncertainty. Additionally, a range of acceptable MSWD (after Mahon, 1996) was presented for the YC1σ and YC2σ ages considering the sample size involved in the calculation, which is helpful to highlight the meaningfulness of the analyses not exceeding the 95% confidence limit. The criteria employed to select a preferred MDA over another are:

a) The reproducibility of dates (i.e., the higher number of grains included in a youngest-age cluster, the more robustness is reached in results).
b) Proportionality between ages scattering and analytical uncertainty considering the number of grains included in the analysis.
c) Consistency with biostratigraphic ages (for restricted biochrons), stratigraphic position in a stratigraphic column, or similar stratigraphic intervals in different sections.

However, an exception exists when near-depositional age zircons are limited, then we use the YSG metric, which does not provide robust MDA's but is acceptable as it fits well with the last criterion above and because the analyses have a standard error <2%. The calculated YC1σ ages are equal to YC2σ ones for the half of the samples from which both metrics were used. For the other half, the mean difference between both ages is <2%, which magnitude does not overcome its standard error, only in these cases, we preferred the YC1σ because of better stratigraphic consistency and have proven to be

useful in chronostratigraphic studies (e.g., Sickmann et al., 2018; Daniels et al., 2019; George et al., 2020).

The tectonostratigraphic analysis of the basin was based on the recognising and delimitation of third-order sequences in the subsurface over a ~W-E regional seismic profile (Fig. 1 and 6). The regional seismic profile consists of merging several multichannel 2D seismic lines (recorded up to 5 s TWT) provided by Enap-Sipetrol. To identify the sequence boundaries, we rely on observing seismic reflection terminations (lapouts) such as toplaps, truncations, downlaps, and onlaps; these lapouts allow a boundary can be traced and correlated laterally in the seismic profile. The temporal range of each sequence and the lithostratigraphic units comprised are achieved by concatenating well tops and markers data (from Enap-Sipetrol, e.g., G7 marking K-Pg limit; A1) to the refined chronostratigraphic framework in the surface.

II-1.5 Results and interpretations

II-1.5.1 Detrital zircon U-Pb maximum depositional ages (MDA's)

The geographic distribution of the new 25 samples and their coordinates are shown in Figure 2 and Table 1, respectively. The stratigraphic position of the new 25 detrital zircon samples and their corresponding normalised relatively probability density plots are presented in Figure 3. The weighted mean ages plots used to the MDA's determination from the youngest cluster of age in each sample are presented in Figure 4. The net upward-stratigraphically younging age-population peaks (Fig. 3) suggest a long-term volcanism concomitant to the sedimentation, which implies that MDA's calculated for each lithostratigraphic unit mirror the true depositional age. Furthermore, MDA's calculated reveal an excellent correspondence with previous biostratigraphic constraints.

The synthesis of new and revised detrital zircon MDA's utilised to refine the chronostratigraphic framework for the Campanian to Burdigalian strata of the Magallanes-Austral foreland basin are summarised in Table 1. Recalculated MDA's for samples published by other authors is motivated due to whether lacking an MDA, an MDA previously reported too conservative (i.e., older) according to its stratigraphic position, or because its determination did not follow any of the parameters that we used in this study. These new recalculated MDA's do not underestimate or modify each of the conclusions of their original publications.

II-1.5.1a Revision of published MDA's

Dorotea Formation

In the SB area (Fig. 2), we recalculated the age of two samples (Zr-FB-1; Zr-FB-2; Table 1) previously published by Gutiérrez et al. (2017) in the Tetas de las Chinas locality. Previous MDA's are too conservative and hence older as expected for their stratigraphic position. For the Zr-FB-1 sample, we calculated an MDA of 72.0 ± 0.21 Ma from a subpopulation of 2 grains (YC1σ). For the Zr-FB-2, an MDA of 71.7 ± 1.2 Ma is based on the youngest single grain (YSG1σ). The latter age is not as robust as the former, but it is a good approximation to the depositional age because it is stratigraphically consistent and agree with others reported MDA's in the same locality and stratigraphic layer (e.g., Schwartz et al., 2017).

Man-Aike Formation

In the SB area (Fig. 2), we recalculated the MDA of the Zr-PTO-77 sample (Table 1) previously published by Gutiérrez et al. (2017) from the Chorrillo Jabón locality, which belongs to the top of the unit. The recalculated MDA is 38.74 ± 0.66 Ma from a subpopulation of 11 grains (YC2σ). It is important to mention that the sample collected from the level 7b (~170 m below of the Gutiérrez's sample) in the stratigraphic column measured by Le Roux et al. (2010), which age of 40.48 ± 0.37 first reported by Le Roux (2012a) is slightly older (e.g., conservative), since Otero et al. (2013) have described that this sample has 6 grains ranging from 39 to 40 Ma. In this respect, the recalculated age for the Zr-PTO-77 sample keep a stratigraphic consistency with that of Le Roux (2012a), and in turn, corresponds to the youngest age reported for the Man-Aike Formation in the SB area.

Rio Turbio Formation

In the CTN area (Fig. 2), we recalculated the MDA for the 09-230 sample (Table 1) previously published by Fosdick et al. (2015), which belongs to the base of the upper member of the Rio Turbio Formation. This sample yields an MDA of 38.5 ± 1.2 Ma from a subpopulation of 8 grains (YC2σ), which agrees with our VD1 sample in Chilean territory.

Loreto Formation

In the SKB area (Fig. 2), particularly in the Las Minas River valley (type locality of the Loreto Formation), Otero et al. (2012) have reported two detrital zircons U-Pb ages (MINAS 2008-01; MINAS 2008-02; Table 1) which are too conservative as expected for its stratigraphic position in the uppermost part of the unit. We have merged both samples into a single one since the differences between both ages are within the standard error of both, and they are stratigraphically separated by about 1 m. The final recalculated MDA for this (unified) sample is 34.5 ± 1.1 Ma from a subpopulation of 4 grains (YC1σ). This MDA represents the youngest published radiometric age for the Loreto Formation in its type locality.

Table 1. Summary of sample information and detrital zircon MDA's for new and revised samples from the Upper Cretaceous to lower Miocene in the Magallanes-Austral foreland basin. Acceptable MSWD after Mahon (1996).

Sample	Coordinates (Lat.; Long.)	Biostratigraphic age	YSG (Ma ± 1σ)	YC1σ (+2)			YC2σ (+3)			YSP2σ (+2)			Preferred MDA (Ma ± 1σ)
				Age (Ma)	MSWD (Acceptable MSWD)	n	Age (Ma)	MSWD (Acceptable MSWD)	n	Age (Ma)	MSWD	n	
New samples (this study)													
TFP	-52.274366°; -71.541095°	Santacrucian (Burdigalian)	17.5 ± 0.3	17.82 ± 0.47	1.8 (0.001-5.02)	2	18.07 ± 0.37	1.7 (0.072-3.117)	4	-	-	-	17.82 ±0.47
KER	-52.057444°; -72.006556°		17.8 ± 0.1	17.87 ± 0.16	0.097 (0.072-3.117)	4	17.87 ± 0.16	0.097 (0.072-3.117)	4	18.11 ± 0.07	0.97	16	*17.87 ± 0.16
PT-01	-52.323517°; -71.526515°		18.6 ± 0.7	18.8 ± 1.1	0.14 (0.025-3.69)	3	19.09 ± 0.58	0.2 (0.072-3.117)	4	19.92 ± 0.29	1.00	20	18.8 ± 1.1
RV-1	-52.673056°; -71.445833°	Patagoniense (late Oligocene-early Miocene)	18.8 ± 1.1	19.62 ± 0.90	1.8 (0.072-3.117)	4	19.62 ± 0.43	1.8 (0.072-3.117)	4	-	-	-	*19.62 ± 0.43
CLCG	-52.267922°; -71.653050°		20.6 ± 0.7	20.69 ± 0.93	0.048 (0.001-5.02)	2	20.77 ± 0.79	0.082 (0.025-3.69)	3	20.93 ± 0.70	0.29	4	20.69 ± 0.93
DRT-2	-51.604764°; -72.328008°	latest Eocene-Miocene	25.1 ± 0.4	25.46 ± 0.62	0.96 (0.025-3.69)	3	25.46 ± 0.62	0.96 (0.025-3.69)	3	25.46 ± 0.62	0.96	3	*25.46 ± 0.62
SK-2	-52.551111°; -71.826722°	Patagoniense (late Oligocene-early Miocene)	24.1 ± 0.3	25.51 ± 0.49	0.32 (0.001-5.02)	2	26.18 ± 0.74	3.1 (0.121-2.775)	5	25.51 ± 0.49	0.32	2	25.51 ± 0.49
ES-1	-52.562544°; -71.702528°		29.7 ± 0.9	29.8 ± 1.2	0.007 (0.001-5.02)	2	-	-	-	-	-	-	29.8 ± 1.2
ZIR-1	-52.685233°; -71.625878°	middle Eocene-Priabonian	34.0 ± 0.8	34.1 ± 1.0	0.029 (0.025-3.69)	3	35.26 ± 0.39	0.53 (0.509-1.657)	24	35.42 ± 0.37	0.85	27	34.1 ± 1.0
IR-1	-52.687500°; -71.913944°		34.7 ± 0.5	35.3 ± 1.4	1.5 (0.025-3.69)	3	35.83 ± 0.33	1.3 (0.241-2.286)	8	36.33 ± 0.27	1.00	13	35.3 ± 1.4
SK-1	-52.552861°; -71.851028°		35.3 ± 0.5	35.45 ± 0.67	0.31 (0.001-5.02)	2	35.71 ± 0.48	0.51 (0.072-3.117)	4	35.83 ± 0.43	0.70	5	35.45 ± 0.67
RL-1	-53.160230°; -70.983315°		34.5 ± 0.4	35.44 ± 0.71	2.6 (0.121-2.775)	5	35.52 ± 0.58	2.4 (0.121-2.775)	6	35.91 ± 0.27	0.97	7	*35.52 ± 0.58
RPL-1	-52.702925°; -71.759367°	lower Eocene-late Eocene	36.6 ± 1.2	36.8 ± 1.2	0.023 (0.072-3.117)	4	37.89 ± 0.6	0.46 (0.432-1.800)	17	38.05 ± 0.58	0.68	19	36.8 ± 1.2
VD-1	-51.609861°; -72.338278°		36.6 ± 1.3	37.39 ± 0.73	0.25 (0.072-3.117)	4	37.39 ± 0.73	0.25 (0.072-3.117)	4	38.34 ± 0.38	0.91	15	*37.39 ± 0.73
ÑIRRE-1	-53.137870°; -71.060258°	middle Eocene-Priabonian	37.7 ± 1.0	37.9 ± 1.3	0.089 (0.001-5.02)	2	38.23 ± 0.95	0.20 (0.072-3.117)	4	39.96 ± 0.69	0.94	8	37.9 ± 1.3
RM-1	-53.141239°; -70.992761°		37.9 ± 0.9	38.0 ± 1.2	0.002 (0.001-5.02)	2	38.3 ± 1.0	0.46 (0.025-3.69)	3	38.62 ± 0.87	0.54	5	38.0 ± 1.2
DG-1	-51.242028°; -72.247108°	lower Eocene-late Eocene	42.6 ± 0.6	42.75 ± 0.77	0.12 (0.025-3.69)	3	42.75 ± 0.77	0.12 (0.025-3.69)	3	42.75 ± 0.77	0.12	3	*42.75 ± 0.77
CC2-3	-51.275564°; -72.285456°	Campanian-Maastrichtian	43.7 ± 1.1	-	-	-	-	-	-	-	-	-	43.7 ± 1.1
CC1	-51.256330°; -72.270430°		44.3 ± 0.8	-	-	-	-	-	-	-	-	-	44.3 ± 0.8
TBD-H1	-53.290336°; -71.008133°	Lutetian/Bartonia-late Eocene	48.6 ± 1.6	-	-	-	-	-	-	-	-	-	48.6 ± 1.6
TB2	-53.291715°; -71.014726°		60.18 ± 0.9	60.7 ± 1.3	0.75 (0.001-5.02)	2	61.1 ± 1.1	1.0 (0.025-3.69)	3	61.1 ± 1.1	1.0	3	-
CC2-2	-51.275569°; -72.286314°	Campanian-Maastrichtian	55.8 ± 1.2	60.47 ± 0.8	0.93 (0.025-3.69)	3	59.9 ± 2.9	5.5 (0.072-3.117)	4	60.47 ± 0.8	0.93	3	60.47 ± 0.8
CC2-1	-51.274435°; -72.287449°		61.0 ± 0.7	61.0 ± 1.1	0.0082 (0.001-5.02)	2	61.0 ± 1.1	0.0082 (0.001-5.02)	2	61.0 ± 1.1	0.01	2	61.0 ± 1.1
CCK-1	-51.279137°; -72.313436°		65.3 ± 0.9	66.45 ± 0.83	2.4 (0.025-3.69)	3	66.4 ± 2.8	2.4 (0.025-3.69)	3	-	-	-	66.45 ± 0.83

Chamo-2R	-52.530811°; -72.088392°	Coniacian-Santonian	81.0 ± 1.2	82.1 ± 1.3	0.6 (0.025-3.69)	3	82.8 ± 1.2	2.2 (0.072-3.117)	4	82.1 ± 1.3	0.60	3	82.1 ± 1.3
Revised samples													
SM9[1]	-	Santacrucian (Burdigalian)	17.4 ± 0.7	17.6 ± 0.9	0.114 (0.001-5.02)	2	17.71 ± 0.74	0.16 (0.025-3.69)	3	18.74 ± 0.28	0.98	25	*17.71 ± 0.74
Zr-LF-001[2]	-		16.4 ± 0.5	17.5 ± 0.4	0.36 (0.121-2.775)	6	17.5 ± 0.4	0.36 (0.121-2.775)	6	18.13 ± 0.2	0.99	19	17.5 ± 0.4
09-207[3]	-		15.3 ± 1.3	15.9 ± 1.5	0.3 (0.025-3.69)	3	15.9 ± 1.5	0.3 (0.025-3.69)	3	17.8 ± 0.48	0.94	11	*17.8 ± 0.48
Zr-BAG-25[2]	-	late Eocene-Oligocene	30.9 ± 0.3	31.2 ± 0.3	0.61 (0.072-3.117)	4	31.2 ± 0.3	0.61 (0.072-3.117)	4	31.2 ± 0.3	0.61	4	*31.2 ± 0.3
Zr-PTO-81[2]	-		30.8 ± 1.3	32.3 ± 0.86	0.74 (0.3-2.111)	10	32.3 ± 0.86	0.74 (0.3-2.111)	10	32.5 ± 0.82	0.93	11	*32.3 ± 0.86
MINAS08-1&2[4]	-	middle Eocene-Priabonian	33.8 ± 1.4	34.5 ± 1.1	0.16 (0.072-3.117)	4	35.41 ± 0.44	0.36 (0.402-1.864)	15	36.45 ± 0.25	0.98	48	34.5 ± 1.1
09-230[3]	-	lower Eocene-late Eocene	27.5 ± 2.5	38.5 ± 1.2	0.6 (0.241-2.286)	8	38.5 ± 1.2	0.6 (0.241-2.286)	8	38.5 ± 1.2	0.60	8	*38.5 ± 1.2
Zr-PTO-77[2]	-	middle Eocene	35.0 ± 1.0	38.74 ± 0.66	0.89 (0.3-2.111)	10	38.74 ± 0.66	0.89 (0.325-2.05)	11	39.13 ± 0.56	0.99	15	*38.74 ± 0.66
Zr-FB-2[2]	-	Campanian-Maastrichtian	71.7 ± 1.2	-	-	-	-	-	-	-	-	-	71.7 ± 1.2
Zr-FB-1[2]	-		71.0 ± 1.2	72.0 ± 0.21	2.6 (0.001-5.02)	2	-	-	-	-	-	-	72.0 ± 0.21
865[5]	-	Santonian-Campanian	77.8 ± 3.5	79.18 ± 0.85	0.65 (0.121-2.775)	5	80.29 ± 0.62	1.4 (0.325-2.050)	11	79.18 ± 0.85	0.07	5	79.18 ± 0.85
9116[5]	-		78.5 ± 3.3	81.6 ± 1.2	0.38 (0.072-3.117)	4	82.3 ± 0.91	0.72 (0.207-2.40)	7	82.3 ± 0.91	0.72	7	81.6 ± 1.2
0864A[5]	-	Coniacian-Santonian	91.7 ± 2.1	93.3 ± 2.9	0.67 (0.025-3.69)	3	96.2 ± 1.6	1.4 (0.121-2.775)	5	96.35 ± 0.88	0.98	8	93.3 ± 2.9
993[5]	-		103.8 ± 1.1	104.1 ± 1.6	0.21 (0.001-5.02)	2	106 ± 3.8	3.8 (0.025-3.69)	3	104.1 ± 1.6	0.21	2	104.1 ± 1.6

* MDA's reported at 2σ uncertainty

[1] Sickmann et al. (2018)
[2] Gutiérrez et al. (2017)
[3] Fosdick et al. (2015)
[4] Otero et al. (2012)
[5] McAtamney et al. (2011)

Rio Leona Formation

In the SB area (Fig. 2), we recalculated the MDA's of two samples (Zr-PTO-81; Zr-BAG-25; Table 1) previously published by Gutiérrez et al. (2017) from the Chorrillo Jabón, and Chorrillo Las Flores localities, respectively. Both samples belong to the basal part of the unit. The Zr-PTO-81 sample yields an MDA of 32.3 ± 0.86 Ma from a subpopulation of 10 grains (YC2σ). The Zr-BAG-25 sample yields an MDA of 31.2 ± 0.3 Ma from a subpopulation of 4 grains (YC2σ). These new ages are slightly younger than previously reported but equally consistent stratigraphically.

Santa Cruz Formation

In the LVA area (Fig. 2), Sickmann et al. (2018) reported an MDA of 18.1 ± 0.3 Ma (early Burdigalian) for their SM9 sample (belonging to the informal Cangrejo Sandstone), which may be older (too conservative) than the true depositional age. We recalculated a younger MDA of 17.71 ± 0.74 from a subpopulation of 3 grains (YC2σ). We consider that this age fits better with the stratigraphic context of the surrounding areas (e.g., Bostelmann et al., 2013; Cuitiño et al., 2016; Gutiérrez et al., 2017).

An MDA has not been reported for the 09-207 sample (Fosdick et al., 2015) in the SB area (Fig. 2), placed in the lower to the middle part of the unit. The new MDA calculated for the 09-207 sample (Table 1) is 17.8 ± 0.48 Ma from a subpopulation of 11 grains (YSP2σ). We consider that this age fits well with its stratigraphic position and stratigraphic context from the same unit in surrounding areas (e.g., Bostelmann et al., 2013; Cuitiño et al., 2016; Gutiérrez et al., 2017).

In the same SB area, the MDA of 16.8 ± 0.22 Ma (late Burdigalian) for the Zr-LF-001 sample (Table 1) was calculated by Gutiérrez et al. (2017) sub-estimates the uncertainty, and it may be too younger than the true depositional age. A more conservative age is 17.5 ± 0.4 Ma (mid-Burdigalian) from the subpopulation of 6 grains, excluding the two youngest grains.

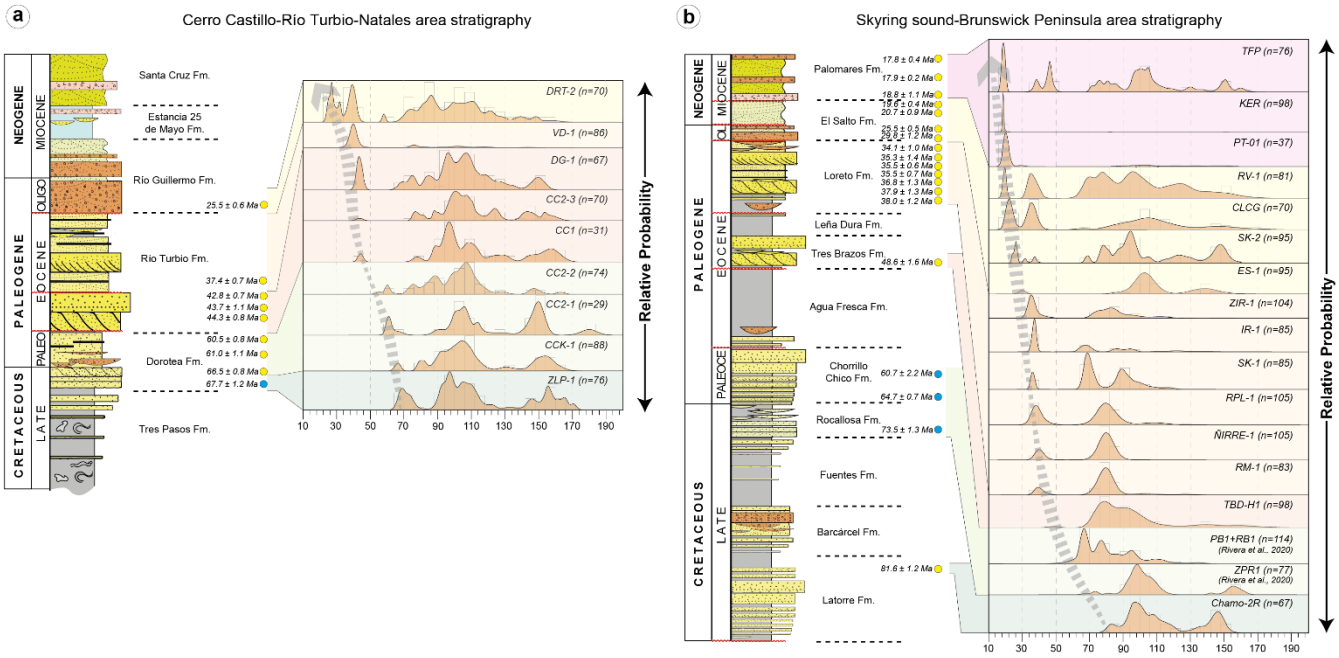

Figure 3. The stratigraphic position of new samples (yellow points) with their composite histograms and normalised probability density plots of detrital zircon U-Pb ages for the Cerro Castillo-Río Turbio-Natales study area (a) and the Skyring sound-Brunswick Peninsula study area (b). Lower case "n" beside the formation name refers to the total number of grains younger than 200 Ma. Bluepoints are samples published by the first author in Rivera et al. (2020).

II-1.5.1b New detrital zircon U-Pb MDA's

Latorre Formation

In the SKB area (Fig. 2), on the north coast of Skyring Sound, the Chamo-2R sample (Fig. 3) was collected from the upper part of the formation (Fig. 3). Detrital zircon ages range between 81.0 to 2909 Ma (Fig. 3; Table 1) and yield an MDA of 82.1 ± 1.3 Ma (Fig. 4; Table 1) from a subpopulation of 3 grains (YC1σ). This MDA matches well with those ages reported by McAtamney et al. (2011) and with unpublished records of Enap (Mpodozis et al. 2006).

Dorotea Formation

In the CTN area (Fig. 2), near the Cerro Castillo village, just <1 km from the international border, three samples were obtained from the middle (CCK1) and upper part (CC2-1; CC2-2) of the formation (Fig. 3). The CC2-1 and CC2-2 samples present ages spectra ranging between 55.8 to 2710 Ma (Fig. 3; Table 1) and yield an MDA of 61.0 ± 1.1 Ma (subpopulation of 2 grains, YC1σ) and 60.5 ± 0.8 Ma (subpopulation of 3 grains, YC1σ) (Fig. 4; Table 1), respectively. For the CCK1 sample, detrital zircons U-Pb ages range from

65.3 to 994 Ma (Fig. 3) and yield an MDA of 66.45 ± 0.83 Ma (Fig. 4; Table 1) from a subpopulation of 2 grains (YC1σ). All our calculated MDA's match those reported by Fosdick et al. (2020) for the same parts of the unit.

Tres Brazos Formation

In the SKB area (Fig. 2), the TBD-H1 and TB2 samples were obtained from the lower part of the unit (Fig. 3) along the valley of the Tres Brazos River in its type locality. Detrital zircons U-Pb ages range from 48.6 to 1456 Ma (Fig. 3). The MDA for the TB2 sample was not possible to calculate because of the lack of near-depositional age zircons, whereas for the TBD-H1 sample, the MDA was based on the youngest single grain (YSG1σ) is 48.6 ± 1.6 Ma (Fig. 4; Table 1), being the first radiometric age for this unit in the basin. We recognise that this age is not statistically robust but could be a fair approximation of the formation's age considering the agreement with the middle Eocene biostratigraphic age previously reported by Malumián et al. (2013).

Río Turbio Formation

All of the samples from this unit are in the CTN area (Fig. 2). Two samples (CC1; CC2-3) were obtained near to the Cerro Castillo village and belong to the lower part of the Río Turbio Formation (Fig. 3), and another sample (DG1) was obtained from the middle part of the unit (Fig. 3) in the Don Guillermo River, just 800 m crossing the international border in Argentina. Detrital zircon U-Pb ages from the CC1 sample range between 44.3 to 2658 Ma (Fig. 3; Table 1) and the MDA of 44.3 ± 0.8 Ma (Fig. 4; Table 1) was calculated based on the youngest single grain (YSG1σ). CC2-3 sample presents detrital zircon U-Pb ages from 43.7 to 2670 Ma (Fig. 3; Table 1), and an MDA of 43.7 ± 1.1 Ma (Fig. 4; Table 1), based on the youngest single grain (YSG1σ). Although these ages are not robust, we consider they represent acceptable MDA's because they have stratigraphic consistency, agree with palaeontological ages and other MDA's for a nearby stratigraphic layer (Fosdick et al., 2015b, 2020). Detrital zircon U-Pb ages from the DG-1 sample span 42.6 to 2211 Ma (Fig. 3; Table 1) and has a robust MDA of 42.75 ± 0.77 Ma (Fig. 4; Table 1) from a subpopulation of 3 grains (YC2σ).

The VD1 sample was obtained near the base of the upper member of the Río Turbio Formation (Fig. 3), between the eastern flank of the Sierra Dorotea and the Dorotea village. Detrital zircons U-Pb ages span from 36.6 to 143.3 Ma (Fig. 3; Table 1), and the MDA calculated is 37.39 ± 0.73 Ma (Fig. 4; Table 1) from a subpopulation of 4 grains (YC2σ).

This age agrees with our recalculated 38.5 ± 1.2 Ma for the 09-230 sample (Fosdick et al., 2015) on the other side of the international boundary between Chile and Argentina.

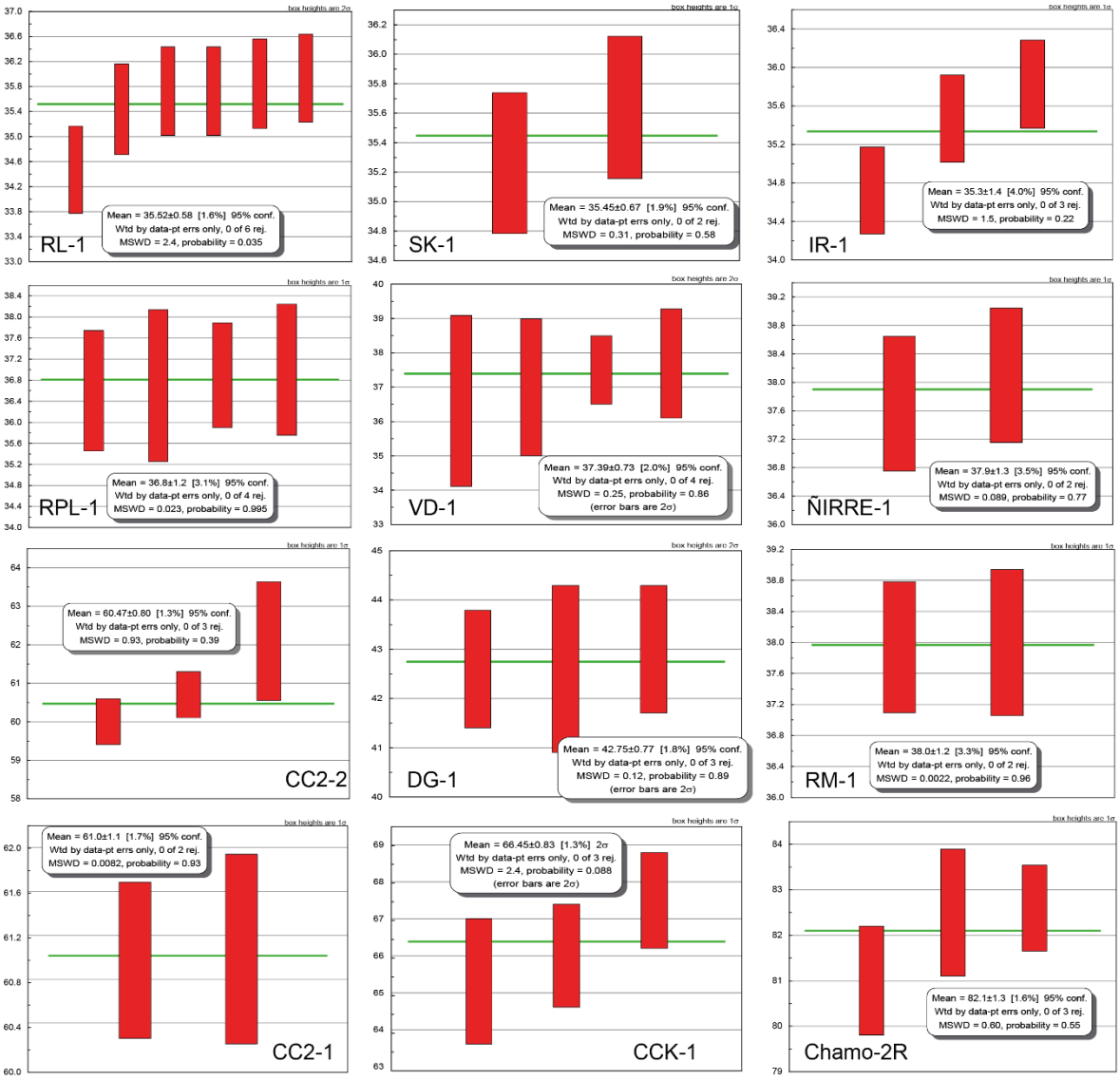

Figure 4. Weighted mean ages plots showing calculated MDA's for the new 21 detrital zircon samples (excluding TBD-H1, CC2-3, and CC1 samples for which was employed YSG1σ metric and TB1 which does not yield near-depositional zircon ages). Individual zircon age uncertainty (error bars at 1σ or 2σ) is indicated on the upper right side of each panel. MSWD = mean squared weighted deviation.

Loreto Formation

A total of seven samples were collected in the SKB area (Fig. 2). Three samples were obtained from the Las Minas River (its type locality) valley and surrounding areas (RM1; ÑIRE1; RL1). The RM1, ÑIRE1, and RL1 samples belong to the upper part of the formation

(Fig. 3). Detrital zircons U-Pb ages range from 37.9 to 2560 Ma (Fig. 3; Table 1) for the RM1 sample, 37.7 to 98.7 Ma (Fig. 3; Table 1) for the ÑIRE1 sample, and 34.47 to 109.9 Ma (Fig. 3; Table 1) for the RL1 sample. The MDA for the RM1 and ÑIRE1 samples are 38.0 ± 1.2 Ma and 37.9 ± 1.3 Ma (Fig. 4; Table 1), respectively, both based on a subpopulation of 2 grains (YC1σ); for the RL1 sample, the MDA determined is 35.74 ± 0.31 Ma (Fig. 4; Table 1) from a subpopulation of 5 grains (YC2σ).

The other four samples were obtained from outcrops on the northern coast of Riesco Island (RPL; IR1; ZIR) and Skyring Sound (SK1) (Fig. 2). Detrital zircons U-Pb ages of the RPL sample span from 36.6 to 129.9 Ma (Fig. 3; Table 1). The estimated MDA is 36.6 ± 1.8 Ma (Fig. 4; Table 1) from a subpopulation of 2 grains (YC1σ). The IR1 sample presents U-Pb ages ranging between 34.7 to 143.7 Ma (Fig. 3; Table 1) with an MDA of 35.8 ± 0.3 Ma (Fig. 4; Table 1) based on a subpopulation of 8 grains (YC2σ). The ZIR sample shows detrital zircon U-Pb ages ranging from 34 to 315.3 Ma (Fig. 3; Table 1) and an MDA of 34.1 ± 1.0 Ma (Fig. 4; Table 1) from a subpopulation of 3 grains (YC1σ). The latter is the youngest radiometric age reported for Loreto Formation in the basin. Finally, the SK1 sample exhibits U-Pb ages from 35.3 to 117.9 Ma (Fig. 3; Table 1) with an estimated MDA of 35.45 ± 0.67 Ma (Fig. 4; Table 1) based on a subpopulation of 2 grains (YC1σ).

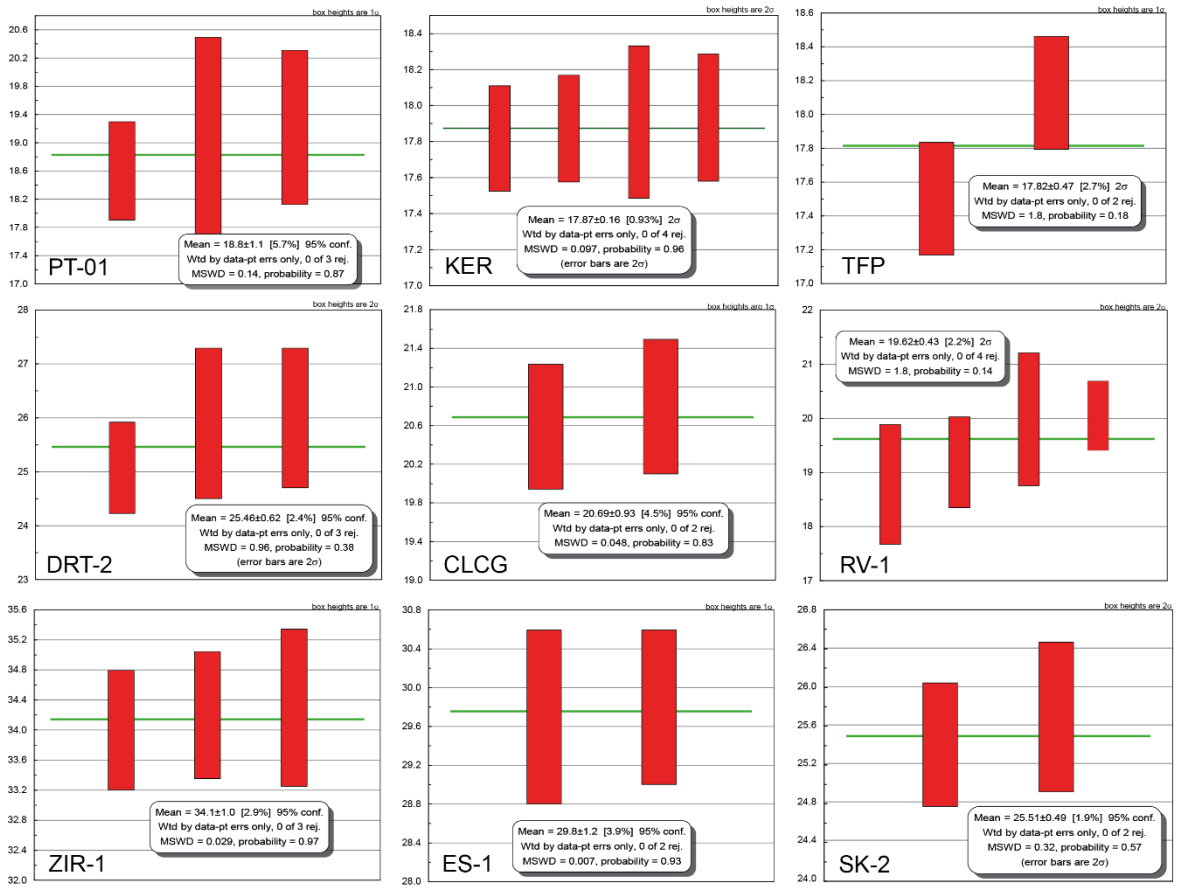

Figure 4. (Continued).

Río Guillermo Formation

The DRT2 sample was obtained near the unit's base (Fig. 3), east of the Dorotea Village, within the CTN area (Fig. 2). Detrital zircons U-Pb ages range from 25.1 to 1033.6 Ma (Fig. 3; Table 1) and yield an MDA of 25.46 ± 0.62 Ma (Fig. 4; Table 1) based on a subpopulation of 3 grains (YC2σ). The latter MDA is the first radiometric age for the Río Guillermo Formation in this locality.

El Salto Formation

Two samples (ES1; SK2) were obtained from the northern coast of Skyring Sound (its type locality), one sample (RV1) to the east of the Fitz Roy channel, and another (CLC) in the Cordillera Chilena locality (Fig. 2). All these samples are within the SKB area (Fig. 2). The ES1 and SK2 samples correspond to the basal Las Coles member of the formation (Fig. 3), and the U-Pb ages spectrum range from 24.1 to 2466 Ma (Fig. 3; Table 1). The MDA for the ES1 is 29.8 ± 1.2 Ma (Fig. 4; Table 1) and 25.51 ± 0.49 Ma (Fig. 4; Table 1) for the SK2 sample, both MDA's based on a subpopulation of 2 grains (YC1σ). The RV1

sample corresponds to the middle Rio Verde member (Fig. 3). Detrital zircons U-Pb ages span from 18.8 to 1696 Ma (Fig. 3; Table 1). The MDA's calculated for the RV1 sample, 19.65 ± 0.9 Ma (Fig. 4; Table 1) based on a subpopulation of 4 grains (YC1σ), is slightly younger than expected for its stratigraphic position; hence, it could not represent the true depositional age. However, in this locality, we do not have an accurate age constraint for the overlying Palomares Formation, and we cannot rule out the possibility of younger ages of the sedimentary system in this position of the study area. Furthermore, the MDA determined is included within the standard error of the overlying CLC sample.

The CLC sample belongs to the upper San Antonio member of the El Salto Formation (Fig. 3). It was collected from an isolated outcrop placed a few meters (stratigraphically) below basaltic breccias belonging to the Conglomerado Vidal member of the overlying Palomares Formation. This CLC sample is composed of cross-bedded, coarse-grained sandstones, and the U-Pb ages spectra range from 20.59 to 649.4 Ma (Fig. 3; Table 1), whereas the MDA calculated is 20.69 ± 0.93 Ma (Fig. 4; Table 1) from a subpopulation of 2 grains (YC1σ). This age could be the youngest for the El Salto Formation in the study area.

Palomares Formation

In the same SKB area (Fig. 2), we dated three samples from different parts of the Cordillera Chilena locality, and they represent the first U-Pb ages for the formation. The KER sample was obtained from medium-grained sandstone from the Conglomerado Vidal member in the Kerber locality. Detrital zircons U-Pb ages span from 17.8 to 529.7 Ma, but 97% of ages are well constrained to 17.8 - 22.4 Ma (Fig. 3; Table 1). The MDA for the KER sample is 17.87 ± 0.16 Ma (Fig. 4; Table 1) based on a subpopulation of 4 grains (YC2σ). The remaining two samples (TFP; PT1) belong to the lateral equivalent San José member, and the detrital zircon U-Pb ages range from 17.5 to 1029 Ma (Fig. 3). The MDA for the TFP sample is 17.82 ±0.47 Ma (Fig. 4; Table 1) and for the PT1 is 18.85 ± 0.97 Ma (Fig. 4; Table 1), both based on a subpopulation of 2 grains (YC1σ). The latter age could be the oldest one for the San José member in the Cordillera Chilena locality.

II-1.5.2 Tectonostratigraphic sequences

We have divided the sedimentary fill in the subsurface of the SKB area into relatively conformable successions accumulated under particular tectonic regimes (tectono-stratigraphic sequences, *sensu lato*) conditioning stratal stacking patterns, which can be

categorised in different hierarchies (first-, second-, or third-order). These sequences are consistent to a certain degree with the previous proposals of Biddle et al. (1986), Macellari et al. (1989), and Mpodozis et al. (2011). It is essential to bear in mind the different foreland depozones (i.e., wedge-top, proximal foredeep, distal foredeep, and forebulge; see DeCelles and Giles, 1996) to avoid confusion in understanding the stratigraphic architecture of the basin filling history.

II-1.5.2a First- and second-order sequences

Three sequences (and bounding unconformities) have been identified, representing first-order tectonic changes leading to the conformation of three different basin types at the first-order scale of observation (Fig. 5). The first sequence groups synrift deposits of the Chon-Aike Province (Pankhurst et al., 1998), manifested in the study area by the Tobífera Formation (Thomas, 1949). This sequence is separated from the Paleozoic basement by the Rift-Onset Unconformity (ROU) and limited in its top by the Breakup Unconformity (BU). The BU marks the onset of a post-rift phase of sedimentation related to thermal subsidence after the extensional climax, and it is characterised by truncation of synrift deposits (under the unconformity surface) and transgressive onlaps (over the surface). This post-rift sequence is represented in the surface of the study area by the Erezcano and Canal Bertrand formations (Fig. 6). Both the synrift and post-rift sequences belong to the RVB. The Basal Foreland Unconformity (BFU) limits the post-rift sequence and registers the change to a compressional regime giving place to the inception of the Magallanes-Austral Foreland Basin.

The Magallanes-Austral Foreland Basin can be divided into two sequences at the second-order scale of observation (Fig. 5). These sequences represent important changes in basin accommodation linked to changes in flexural and dynamic tectonic loads and sedimentation rates (Catuneanu, 2019b; Rivera et al., 2018, 2019). The underfilled sequence is characterised by a wedge geometry and ‘flysch-like’ sedimentation in the proximal foredeep (not shown in Fig. 5), whereas successive depositional onlaps toward the forebulge (Springhill platform) occur. Lithostratigraphic units deposited in the proximal foredeep depozone group from the Latorre to Tres Brazos formations (see Fig. 6); at the same time, in the distal foredeep and forebulge, the subsurface (onshore Chile) stratigraphy is represented by the informal Lutitas Arenosas, Zona Glauconítica, and Bahía Inútil group (Biddle et al., 1986; Mpodozis et al., 2011). The Lutitas Arenosas unit is constituted by marlstones, shaly limestones, and intercalations of shales and limestones deposited in an

open-marine shallow platform or ramp (Mordojovich, 1951; González, 1965; Biddle et al., 1986). The Zona Glauconítica is composed of a time-transgressive succession of silty claystones, siltstones and fine-grained, clayey, glauconitic sandstones with abundant microfauna of foraminifera; some intercalations of pyritic black shales and siltstones, and sandy limestones are present (Hauser, 1964; Mella, 2001; Mpodozis et al., 2011). This unit was deposited under low sedimentation rates and long periods of starvation of sediments above an uplifting shallow platform (Biddle et al., 1986; Mella, 2001). The informal Bahía Inútil group manifested as a succession of shales, siltstones and fine-grained clayey sandstones with abundant macro and microfauna, representing sediments deposited under pelagic conditions and influenced by turbiditic processes in a distal slope environment (Cañon, 1968; Mpodozis et al., 2011). The assemblage of the Lutitas Arenosas-Zona Glauconítica-Bahía Inútil represents the '*underfilled trinity*' (*sensu* Sinclair, 1997) typical of a retreating collisional foreland basin system (c.f. DeCelles, 2012), however, developed in an Andean-type scenario.

The overfilled sequence (Fig. 5) is demarked by the Underfilled to Overfilled Transition Unconformity (UOT = P-2 unconformity), representing about the middle Eocene. The wedge geometry is almost nil and rather resembles a subtabular shape. A prograding to aggrading stacking pattern characterises the overfilled sequence, which group the lithostratigraphic units known in the SKB area as the Leña Dura, Loreto, El Salto and Palomares formations (Fig. 6). The subsurface stratigraphic nomenclature in the forebulge depozone is similar to formal stratigraphic names defined in the Magallanes and Tierra del Fuego Provinces; it includes the Loreto Formation, Areniscas Arcillosas informal unit and the Brush Lake, Filaret and Palomares formations.

II-1.5.2b Third-order sequences

There are five regional unconformities, clearly discernible in the west to east (foredeep to forebulge) seismic profile by terminations in onlap, truncations, toplap and downlaps, limit six stratigraphic sequences at the third-order scale of observation (Fig. 5). These sequences with distinct stacking patterns reflect (1) lateral mobility of the depocenters (or zones of accumulation active) regarding the active orogenic belt and (2) changes in the sedimentation dynamics (e.g., source of sediments, depositional systems) in response to fluctuations in the amount of orogenic loading and eustatic sea-level changes that enlarge or abate accommodation.

The Upper Cretaceous up to the middle Eocene sequences (KS1 to PS2), with characteristic wedge shape geometry and strongly onlaping towards the forebulge (Fig. 5), highlight the flexural tectonism influencing their genesis. In the proximal foredeep, this sedimentary prism represents the filling of a deep-water basin, with shallowing episodes of sedimentation (e.g., KS2, top of PS2). The PS3 sequence from the middle to upper Eocene shows a subtabular to subtle wedge geometry that overflows the flexure and covers the forebulge (Fig. 5). The PS3 sequence can be considered a transient state (filled) between the underfilled and overfilled basin phases. It is characterised by a complex of progradational clinoforms filling the increasingly shallow foredeep, with shallow and continental marine facies in the proximal foredeep passing laterally to deeper water facies in the distal foredeep and above the forebulge. The PS4 sequence exhibit a subtle wedge geometry signalling limited flexural tectonism in its genesis and characterised by continental sedimentation on the wedge-top and proximal foredeep and possibly transitional facies on the forebulge. The NS1 sequence is subtabular to tabular (Fig. 5), reflecting a sediment supply in excess of the available accommodation generated by the marked decreasing flexural and dynamic subsidence. A 'molasse-like' sedimentation characterises the NS1 sequence with dominant continental sedimentation prograding over the forebulge. Further details about the sedimentological characteristics of each sequence (and lithostratigraphic units they include) are beyond the scope of this work and will be presented elsewhere (Chapter III-2).

The correlations with the surface geology of the SKB area allow groups to lithostratigraphic units within each sequence. The KS1 sequence includes the Latorre and Barcárcel formations. The KS2 sequence groups the Fuentes and Rocallosa formations. The first Paleogene sequence, PS1, is represented by the Chorrillo Chico Formation. The PS2 sequence includes the Agua Fresca and Tres Brazos formations. The PS3 sequence groups the Leña Dura and Loreto formations. The PS4 sequence includes the lower part of the El Salto Formation. Finally, the first Neogene sequence, NS1, includes the upper part of the El Salto and Palomares formations. Therefore, the time involved in each sequence is depicted by the age of formations they include (see Fig. 6).

II-1.6 Discussion

II-1.6.1 Refined chronostratigraphic framework

We integrated our U-Pb geochronological results with previously published radiometric ages and foraminifera and dinoflagellate cysts biozones to update the

chronostratigraphic framework of the Upper Cretaceous to lower Miocene strata (Fig. 6) along the axis of the Magallanes-Austral foreland basin (49.5°-53.6°S).

We consider our more robust MDA's to be the best approximation of true depositional ages based on the following arguments. Statistically, the YC1σ and YC2σ rarely are younger than the true depositional ages (Dickinson and Gehrels, 2009; Coutts et al., 2019). Analytically, YC1σ and YC2σ ages are identical, yield standard error <2%, and overlap within the uncertainty of TIMS-acquired ashes in the basin (Daniels et al., 2018; Coutts et al., 2019). Geologically, the Mesozoic-Cenozoic Southern Patagonian Batholith (Hervé et al., 2007) maintained long-term proximity (<200 km) and connectivity with the foredeep (Romans et al., 2010; Rivera et al., 2020), providing syn-depositional zircons to the basin that mirror the ages from constrained biochrons (e.g., Rivera, 2017; Fig. 3).

The maximum age of deposition of the base of the first foreland deposits is well constrained in the north of the basin (LVA, SB, and CTN areas; Figs. 2 and 6) (Daniels et al., 2019). At the same time, in the SKB area, it is necessary to thoroughly investigate the tectonic context of the Canal Bertrand Formation (Figs. 2 and 6) since that may represent the first turbiditic deposits of the foreland basin in this locality. Sedimentological data of the first author, on the northwest coast of the Magellan Strait (between Cabo Froward and Punta Sampaio), allowed to recognise a medium-grained sandy succession, clearly distinguishable from the fine turbidites and slaty shales of the Erezcano Formation, which is interpreted to as amalgamated channels in a deep-sea turbiditic fan lobes complex. Castelli et al. (1993) mapped this succession of medium-grained turbidites as Canal Bertrand Formation and Cecioni (1960) as the Punta Barrosa and Cerro Toro formations. A succession with similar sedimentological characteristics in the Otway Sound was dated by McAtamney et al. (2011) at 104.1 ± 1.6 Ma (Table 1; Fig. 6), interpreted as the Latorre Formation (representative of the oldest foreland deposits), which in fact, corresponds to the Canal Bertrand Formation. Detrital zircon U-Pb age data (Mpodozis et al., 2006; McAtamney et al., 2011) indicate the Canal Bertrand was primarily fed by Metamorphic Basement Complexes (~220-300 Ma and older ages) sources; the Tobífera Formation, and contemporary plutons of the Southern Patagonian Batholith (~156-159 Ma; Pankhurst et al., 2000; Hervé et al., 2007); and predominantly by K1-K3 plutons-sourced detritus (~140-107 Ma; Hervé et al., 2007) of the Southern Patagonian Batholith. These source terranes are very similar to those interpreted from the analysis of the U-Pb age signature for the Punta Barrosa and Cerro Toro formations in Ultima Esperanza Province (Fildani et al., 2003; Romans et al., 2010). These new

constraints allow us to hypothesize that the age of inception of the foreland basin in the SKB area may be as old as 104 Ma (represented by the Canal Bertrand Formation), which has important implications regarding the current conception of southward diachronism of the transition from backarc extension to orogenic shortening (McAtamney et al., 2011; Malkowski et al., 2017).

The maximum age for the top of the foreland basin fill is not rigorously defined in any study area and is estimated at ~15.6 Ma based on inferences of accumulation rates for the Santa Cruz Formation (c.f. Cuitiño et al., 2016). Following, we present chronostratigraphic constraints for different time intervals in the basin, where the implications in correlations, disconformities recognition, and stratigraphic nomenclature will be discussed.

II-1.6.1a Turonian to early Campanian

The chronostratigraphy for this time interval is exhaustively analysed in the Ultima Esperanza Province of Chile (SB, CTN areas; Fig. 2) and adequately synthesized in Daniels et al. (2019). However, the LVA area in the Santa Cruz Province (Argentina) and the SKB area in the Magallanes Province (Chile) have the poorest depositional timing constraints. In the LVA area, previous works by Malkowski et al. (2017), Sickmann et al. (2018), and Ghiglione et al. (2021) allow assigning an age to the base of the La Anita Formation at 86.0 ± 1.0 Ma (Fig. 6) and for the contact between the La Anita and Cerro Fortaleza formations at around 80 Ma (Fig. 6). These units that represent wave- to fluvial-dominated deltaic deposits (La Anita Formation; Macellari et al., 1989; Moyano Paz et al., 2018, 2020) and meandering to braided river systems (Cerro Fortaleza Formation; Macellari et al., 1989; Tettamanti et al., 2018), are age-equivalent to the deep-water turbidite facies and slope deposits of the Cerro Toro and Tres Pasos formations in the Ultima Esperanza Province of Chile (SB and CTN areas; Romans et al., 2011; Daniels et al., 2019).

In the SKB area, the base of the Latorre Formation is defined at 93.3 ± 2.9 Ma (Table 1; Fig. 6; McAtamney et al., 2011), and its upper limit is estimated at 80 Ma, considering the age of 79.2 ± 0.9 Ma for the base of the overlying Barcárcel Formation (Table 1; Fig. 6; same Escarpada Formation in McAtamney et al., 2011). The Latorre Formation is a new lithostratigraphic unit proposed by Mpodozis et al. (2006) on the north shore of the Skyring Sound (Fig. 2) and redefined in Mpodozis et al. (2011) and McAtamney et al. (2011), which designates a 300 to 1100 m-thick, deep water turbiditic succession. We consider that the

adhesion of the Latorre Formation as a new lithostratigraphic unit is well justified since this turbiditic succession was previously correlated with the clearly older Punta Barrosa Formation (e.g., Cecioni, 1957, 1960) of the Ultima Esperanza Province of Chile (Fig. 6; Daniels et al., 2019). Similarly, Mpodozis et al. (2006) proposed the Escarpada Formation, on the north shore of the Skyring Sound and redefined in Mpodozis et al. (2011) and McAtamney et al. (2011), to designate the 800-m-thick succession of cobble-conglomerates and very coarse-grained sandstones interpreted as the filling of submarine canyons and channels that overlies to the new Latorre Formation. We consider that the Escarpada Formation should not be adopted and instead abandoned since said rock succession is isopic facies of the conglomerates of the Rosa Formation (Hollister, 1943-44; Thomas, 1949); also, they are chronostratigraphically correlatives. In turn, in this work, we propose the hierarchical change of the Rosa Formation (Hollister, 1943-44; Thomas, 1949) to the Rosa Member ascribed to the Barcárcel Formation (Hollister, 1943-44; von Goetsche, 1953; Castelli et al., 1993), given that both units are age-equivalents (78-79 Ma; Mpodozis et al., 2006) and because according to sedimentological observations of the first author, both units represent the same deep-water submarine fan system.

II-1.6.1b Middle Campanian to Paleocene

In the LVA area, Campanian-Maastrichtian deposits are represented by the La Irene Formation (Macellari et al., 1989) and the Chorrillo Formation (Feruglio, 1938), which are separated from the underlying La Anita Formation by a 'type II unconformity' (*sensu* Macellari et al., 1989) that likely represent autogenic processes within the depositional system. Macellari et al. (1989) raised the rank of the previously La Irene Member of the La Anita Formation (Arbe and Hechem, 1984). However, the stratigraphic analysis done here encourages the unification of the La Irene Formation with the laterally equivalent Chorrillo Formation, both units representing a braided to meandering fluvial system (Macellari et al., 1989; Tettamanti et al., 2018) lithologically inseparable in outcrops (e.g., Tettamanti et al., 2018). The Chorrillo Formation could include the La Irene Member, representing the proximal fluvial component that feeds the Dorotea Formation's deltaic system in Ultima Esperanza Province (Fig. 2). No depositional ages are available for accurate temporal characterization of the Chorrillo Formation in this sector. The Calafate Formation (Macellari et al., 1989) represents the youngest Cretaceous deposits for this area. Macellari et al. (1989) interpreted a minor angular unconformity at the base of the Calafate Formation of unknown duration; however, its base is defined at 69 ± 2 Ma, according to Ghiglione et al. (2021), which agrees with biostratigraphic ages (Marenssi et al., 2004). The age of the top of the

Calafate Formation is a matter of debate since Malumián and Caramés (1997) suggested that the Paleocene is missing or poorly developed in this area based on a palaeontological examination. However, Marenssi et al. (2004) found dinocyst assemblages that extend into the Paleogene. We suggest a latest to earliest Danian age (64-65 Ma) for the top of the Calafate Formation, considering the trend in which the depositional ages of units placed just below the Eocene unconformity tend to be older northward (Fig. 6).

In the SB and CTN areas (Fig. 2), the latest Campanian to Selandian is represented by the Dorotea Formation (Fig. 6), whose ages of the base have been well synthesised by Daniels et al. (2019), and its top ages by George et al. (2020) and Rivera et al. (2020). In the Argentinian domain of the CTN area (around Río Turbio-Cancha Carrera towns; Fig. 2), the Dorotea Formation is known as to the Cerro Cazador, Monte Chico, and Cerro Dorotea formations (Feruglio, 1938; Malumián et al., 2000). This finely formational subdivision based on paleontological criteria (which characterise much of the Argentinian lithostratigraphy) has complicated the regional integration of the evolutionary knowledge of the basin due to discrepancies in description, thickness, and assignation of boundaries (e.g., Feruglio, 1938; Brandmayr, 1945; Hünicken, 1955; Malumián et al., 2000, pg. 15). A distinction of the three mentioned units is virtually impossible on outcrops based exclusively on lithological differences (essential criteria to define lithostratigraphic units; see Hedberg, 1976; Salvador and Murphy, 1999). This difficulty was recognised a long time ago (see Cecioni comments in Hoffstetter et al., 1957; Katz, 1963), motivating the rejection of such a lithostratigraphic subdivision and adopting the name of the Dorotea Formation to include the Cerro Cazador, Cerro Dorotea and ultimately Monte Chico (Malumián et al., 2000). Since the use of the Cerro Dorotea Formation is being used in contemporary publications (e.g., Leonard et al., 2020; Fosdick et al., 2020; Horton, 2021) to refer to strata that have been proven to be a Paleocene age and, at the same time, the use of the Dorotea Formation for the Campanian to Maastrichtian strata, we advise against this practice. Instead, we recommend referring to a unique Dorotea Formation (with a broader time frame, Campanian-Selandian; Fig. 6) that aligns with the best stratigraphic practices.

In the SKB area (Fig. 2), the Fuentes, Rocallosa and Chorrillo Chico Formation are the unit's representative of the Maastrichtian-Paleocene (Fig. 6). No detrital zircon or paleontological ages are available for an accurate temporal constraint of the Fuentes Formation (facies-equivalent of the Tres Pasos Formation; Rivera et al., 2020). Rivera et al. (2020) reported an MDA of 73.5 ± 1.3 Ma for the base of the Rocallosa Formation in its type

locality and have suggested a minor hiatus in the top. We do not have any age constraint for the top of the Rocallosa Formation, but based on micropalaeontological content (Charrier and Lahsen, 1969; Castelli et al., 1992; Rivera et al., 2020) we suggest a late Maastrichtian age (~67-66 Ma). For the Chorrillo Chico Formation, the oldest age has been reported by Rivera et al. (2020), with an MDA of 65.2 ± 0.5 Ma for the basal part of the formation. The occurrence of *Spiroplectamina beccariiformis* and *S. spectabilis* allows extending the age of the Chorrillo Chico Formation up to the Paleocene/Eocene (Malumián et al., 2013). However, the lack of the *Apectodinum* dynoquist, typical of Paleocene/Eocene limit, and the presence of *Palaeoperidinium pyrophorum* suggest that the uppermost Paleocene is missing and that the Chorrillo Chico Formation cannot be younger than late Selandian (Quattrocchio, 2009). Detrital zircons can support the latter as the grains are not younger than mid-Thanetian (Hervé et al., 2004; Mpodozis et al., 2006; Rivera et al., 2020). We propose a mid-Thanetian (~57 Ma) for the top of the Chorrillo Chico Formation, which agrees with the age of unconformity identified by Biddle et al. (1986) at the top of this unit.

II-1.6.1c Eocene

Most of Eocene is missing in the LVA and SB areas (Fig. 6), being the Man Aike Formation the only unit present. The time involved in the hiatus varies between ~20-18 Myr (Figs. 6 and 7a). In the LVA area, Malumian (1990) constrained its age to P11-P14 zone (39-46 Ma) based on microfossils, later Casadío et al. (2009) reported five $^{87}Sr/^{86}Sr$ reliable ages that span from 38.42-45.3 Ma; recently, Sickmann et al. (2018) have reported an MDA of 43.3 ± 2 Ma. Considering the palaeontological constraints, we suggest an age from 45.3 to 39 Ma for the unit in the LVA area (Fig. 6). The latter age is similar in the nearby SB area, where George et al. (2020) reported an MDA of 45.7±0.6 Ma for the base of the unit, and we recalculated an MDA of 38.74 ± 0.66 Ma (Zr-PTO-77; Gutiérrez et al., 2017) for the top of the Man Aike Formation.

Figure 5. (*following page* →) Interpreted tectono-stratigraphic sequences in the Magallanes-Austral basin. Note enlarged interpretation in the lower scheme at the 3rd-order scale of observation. Uninterpreted seismic lines to the end of this chapter.

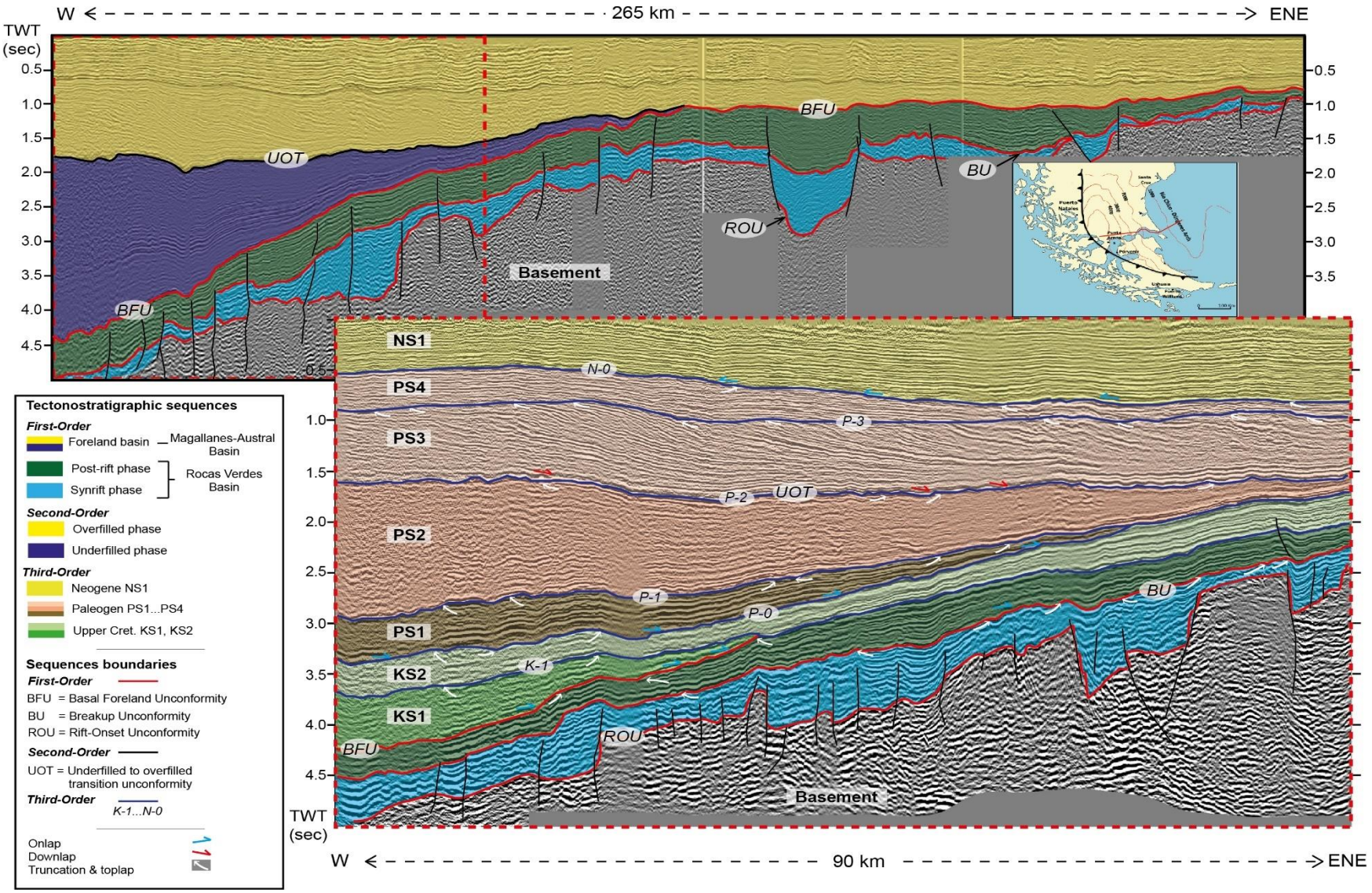
W
265 km
ENE
TWT (sec)
0.5
1.0
1.5
2.0
2.5
3.0
3.5
4.0
4.5
UOT
BFU
BU
ROU
Basement
NS1
PS4
PS3
PS2
PS1
KS2
KS1
N-0
P-3
P-2
P-1
P-0
K-1
Tectonostratigraphic sequences
First-Order
Foreland basin
Magallanes-Austral Basin
Post-rift phase
Synrift phase
Rocas Verdes Basin
Second-Order
Overfilled phase
Underfilled phase
Third-Order
Neogene NS1
Paleogen PS1...PS4
Upper Cret. KS1, KS2
Sequences boundaries
First-Order
BFU = Basal Foreland Unconformity
BU = Breakup Unconformity
ROU = Rift-Onset Unconformity
Second-Order
UOT = Underfilled to overfilled transition unconformity
Third-Order
K-1...N-0
Onlap
Downlap
Truncation & toplap
90 km

In the CTN area ((Fig. 2), the Río Turbio Formation represents the resumed Eocene sedimentation after ~13 Myr of hiatus (Fig. 7b). Between Cerro Castillo town (Chile) and Cancha Carreras town (Argentina) (Fig. 2), Fosdick et al. (2020) have reported MDA's as old as 47.1 ± 2.7 Ma and as young as 41.3 ± 0.3 Ma for the called lower member of the Río Turbio Formation. These ages coincide with our MDA's in the same locality (Table 1; Figs. 3, 4 and 6). For the base of the upper member, we recalculated an MDA of 38.5 ± 1.2 Ma (09-230, Table 1; Fosdick et al., 2015) placed in Argentina, which agree with our MDA of 37.4 ± 0.73 Ma, in Chilean territory (Table 1; Fig. 6); the top of the upper member yield an MDA of 35.4 ± 0.2 Ma (Rupelian; Fosdick et al., 2020) which agrees with E11-O1 biochron (up to 33.5 Ma) indicated by Malumián et al. (2013) and González Estebanet et al. (2015) that demarcates its top limits. However, Fosdick et al. (2020) have reported MDA's as young as 26.6 Ma for the upper member of the Río Turbio Formation, which seems to conflict with the chronostratigraphic and geological context of the unit. In synthesis, the maximum depositional age for the lower member is bracketed from ~47.1 - 41.3 Ma; for the upper member, from ~38.5 - 33.5 Ma, suggesting the presence of a hiatus of ~2.5 Myr. This discordance is not evident on outcrops; however, two lithostratigraphic units can be readily differentiable. In this sense, subdividing the Río Turbio Formation into two independent formations is recommended (Hedberg, 1976; Salvador and Murphy, 1999). The lower member of the unit may be designated as the age- and sedimentary facies-equivalent Man Aike Formation; whereas, the upper member remains as the Río Turbio Formation.

In the SKB area (Fig. 2), the sedimentation was less interrupted, and only ~2.5 Myr is involved in the Paleocene-Eocene unconformity. The Agua Fresca Formation represents the oldest Eocene deposits, we do not have any radiometric ages for this unit, but the well-studied micropalaeontological content allows us to constrain its age. The assemblage of *Acarinina esnaensis*, and *A. interposita* from the lower to medium part of the unit (Malumián et al., 2013) suggests an age of 51-56 Ma (E5-E6 zone; Berggren et al., 2006). The presence of *Elphidium aguafrescaense* and *E. skyringense* allows a correlation with the Punta Torcida Formation of Tierra del Fuego, whose age has been established between 49-52.2 Ma, and with the upper part of the Punta Noguera Formation, whose age is older than 53.9 Ma (Malumián et al., 2013, 2014). Therefore, we constraint the Agua Fresca Formation's age from ~49-53.9 Ma.

The Tres Brazos Formation yield an MDA of 48.6 ± 1.6 Ma for its basal part (Table 1; Fig. 6). However, we do not have any radiometric age restriction for the top rather than

the correlation (based upon the benthic foraminifers) with the Leticia Formation in Tierra del Fuego, which has *Globigerinatheka index* with a first occurrence date not older than 43.7 Ma (Malumián et al., 2013). For the lower-to-middle part of the overlying Leña Dura Formation has been reported *A. bullbrooki* which suggest that at least the lower part of the unit could be older than 41.8 Ma (Malumián et al., 2013). Hence, we extend the basal depositional age tentatively up to 43.0 Ma and up to 41 Ma for the top.

The youngest Eocene unit is the Loreto Formation with a depositional age of 38 ± 1.2 Ma was for the near base, whereas the top is estimated at 34.1 ± 1.0 Ma (at Riesco Island). We suggest a latest Bartonian (~39 Ma) to Rupelian/Priabonien age (33 Ma) for the entire Loreto Formation consistent with paleontological ages (Otero et al., 2012). A likely ~2 Myr hiatus (non-identifiable on outcrops) may be present between this unit and the Leña Dura Formation.

II-1.6.1d Oligocene to Miocene

Spite of the Oligocene-Miocene sedimentation has been much more uniform in all the studied areas of the basin (Fig. 6), another basin-wide significant hiatus, the Eocene-Oligocene unconformity, is unveiled. The time involved in the unconformity varies upon the studied area (Fig. 6).

In the LVA area (Fig. 2), the Eocene-Oligocene unconformity span ~12-11 Myr and separates the Río Leona Formation from the underlying middle Eocene Man Aike Formation. The depositional age for the base of the Rio Leona Formation is 26.2 ± 1.5 Ma (Sickmann et al., 2018). The age for the top of the Río Leona Formation can be constrained through palynomorph assemblages (Barreda et al., 2009) which suggest that the unit is older than the late Chattian (~23.3 Ma). In this way, the Río Leona Formation is bracketed between 26.2 – 23.3 Ma. The base of the overlying Estancia 25 de Mayo Formation was dated by using $^{87}Sr/^{86}Sr$, yielding an age from 21.24-21.34 Ma (Parras et al., 2008). The latter radiometric age agrees with $^{87}Sr/^{86}Sr$ ages of 20.05 Ma of Cuitiño et al. (2012) and with an ash U-Pb age of 19.1 ± 0.5 Ma. Further, Cuitiño et al. (2012) also have dated the uppermost oyster level of the unit yielding an $^{87}Sr/^{86}Sr$ age of 19.15 Ma. Therefore, the Estancia 25 de Mayo Formation span from 21.3 to 19.15 Ma, implying a minor hiatus of ~2 Myr separating it from the Río Leona Formation. For the overlying Santa Cruz Formation, Cuitiño et al. (2012) have dated by U-Pb the tuff (UPL) on the base of the unit yielding an age of 18.9 ± 0.3 Ma and have estimated a depositional age of 15.63 Ma for the top of the unit (Cuitiño et

al., 2016). Similarly, Sickmann et al. (2018) report an MDA of 17.7 ± 0.7 Ma (recalculated SM9 sample; Table 1; Fig. 6), which agree with the chronostratigraphic context for the Santa Cruz Formation.

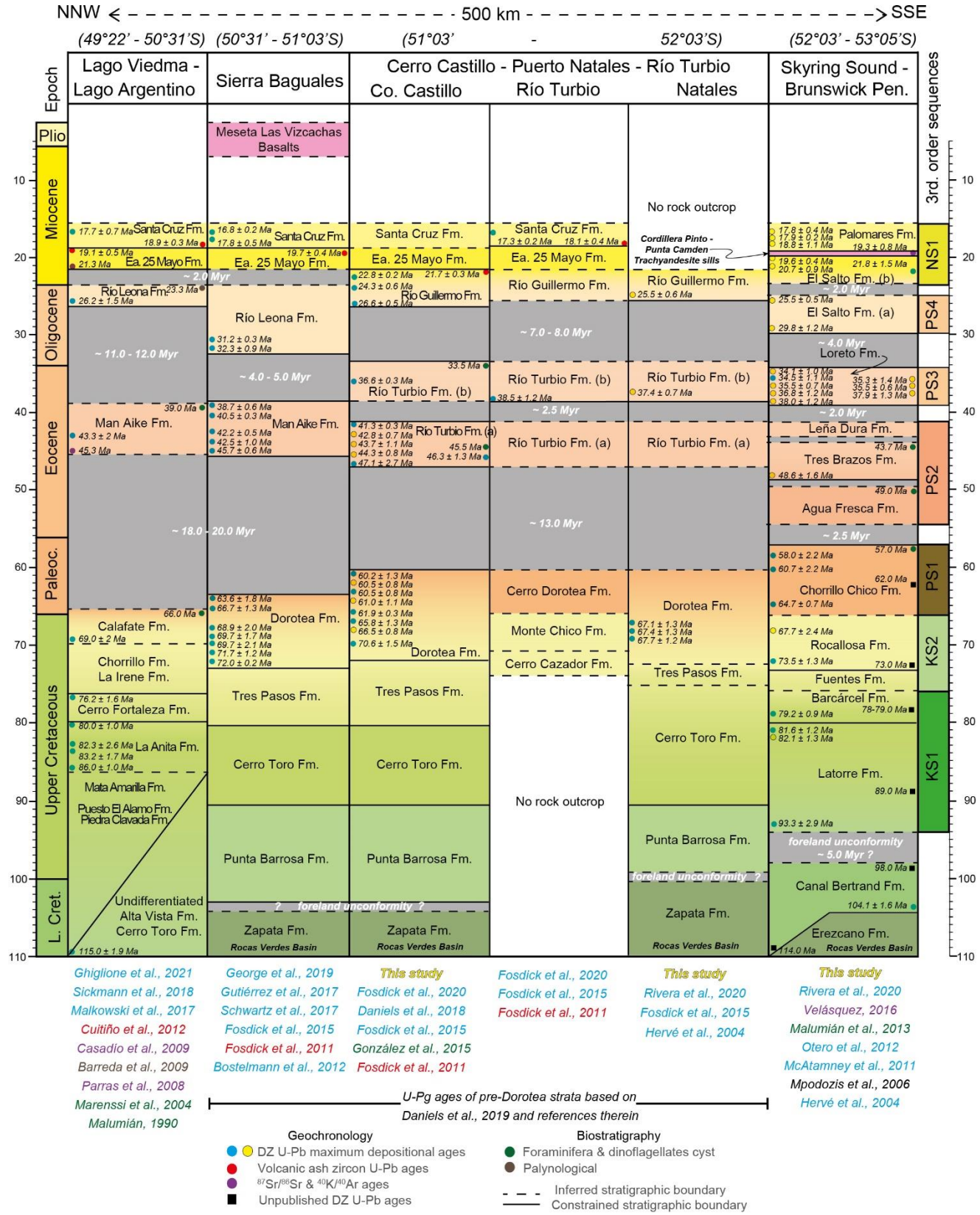

Figure 6. Refined chronostratigraphic framework for the Magallanes-Austral basin (49°22'S-53°5'S). El Salto Formation (a) = Las Coles member; El Salto Formation (b) Río Verde y San Antonio members. See text for a discussion about nomenclature. Tectonostratigraphic sequences as in Fig. 5

In the SB area (Fig. 2), the Eocene-Oligocene unconformity span ~5-4 Myr (Fig. 6) and the oldest depositional calculated for the base of the Río Leona Formation is 32.3 ± 0.86 Ma (recalculated Zr-PTO-81 sample of Gutiérrez et al., 2017; Table 1; Fig. 6). This older age for the onset of the Río Leona Formation sedimentation may be due to the filling of a paleo-valley (paleorelief) product of the erosion and exhumation that accompanied almost the entire basin for this time. Age constraints for the top and base of the Río Leona and Estancia 25 de Mayo formations, respectively, have been extended from the neighbouring LVA area. The only age constraint for the Estancia 25 de Mayo is an ash U-Pb age of 19.7 Ma (Fosdick et al., 2011; Fig. 6) which could correspond to the same LPL level of Cuitiño et al. (2012). For the basal age of the Santa Cruz Formation, we have extended the age constraint from the LVA area, which coincide with our recalculated MDA of 17.8 ± 0.48 Ma (from the 09-207 sample of Fosdick et al., 2015) for the middle to lower part of the formation. Depositional age near the top of the Santa Cruz Formation is indicated at 16.8 ± 0.2 Ma (Gutiérrez et al., 2017), which mirrors the 15.63 Ma calculated by Cuitiño et al. (2016).

In the CTN area (Fig. 2), the Eocene-Oligocene unconformity is represented by a ~7-8 Myr hiatus (Fig. 6). Overlying the unconformity is the Río Guillermo Formation, whose depositional age for the base is estimated in this work as 26.6 ± 0.5 Ma (Fig. 6). The latter MDA was interpreted by Fosdick et al. (2020) as representing the age for the top of the Río Turbio Formation. However, such a young age for the Río Turbio Formation seems inconsistent in light of this new chronostratigraphic framework and based on the foraminifera and dinoflagellates with the most accurate biochrons (Malumián et al., 2000 and references therein; Malumián et al., 2013; González Estebanet et al., 2015). On the other hand, the youngest age for the Río Guillermo Formation is 21.7 ± 0.3 Ma (Fosdick et al., 2011; Fig. 6) on a volcanic ash layer. As far as the stratigraphic nomenclature is concerned, we recommend that the Río Guillermo Formation be included as a member in the Río Leona Formation (recognised and mapped in the CTN area (Fig. 2); Malumián et al., 2000), outcropping between Cancha Carrera and Río Turbio towns. Both units overlap in age, have similar lithological nature and paleoenvironmental significance. There are no age constraints for the Estancia 25 de Mayo Formation in the CTN area, and their limits were extended from the LVA area. Fosdick et al. (2011) reported an ash U-Pb age of 18.1 ± 0.4 Ma (Fig. 6) for the Santa Cruz Formation in the CTN area. This age belongs to a tuff layer supposed placed at the top of the unit (Fig. 5 of Fosdick et al., 2015). However, this age at the top leads to two conundrums: 1) contamination of the tuff layer with older detrital zircons and/or a

problem with the analysis by itself reflecting an analytical artefact; 2) a misunderstanding of the true stratigraphic position of the sample. We favour the latter alternative as an age of 18.1 at the base of the Santa Cruz Formation is consistent with the chronostratigraphic framework proposed for this unit in all the studied sectors (Fig. 6) of the basin and because tuff layers are more frequent in the basal part of the Santa Cruz Formation (e.g., Malumián et al., 2000; Cuitiño et al., 2016; Guitérrez et al., 2017). We think that the age for the top of the unit in the CTN area is equivalent to that reported by Gutiérrez et al. (2017) in the SB area (Fig. 6).

In the SKB area (Fig. 2), the Eocene-Oligocene unconformity is represented by a ~4 Myr hiatus. The El Salto Formation overlies the unconformity (Fig. 7d). The oldest MDA for the basal Las Coles member in its type locality is 29.8 ± 1.2 Ma, whereas the youngest is 25.51 ± 0.5 Ma (Table 1; Figs. 4 and 6). The upper part of the El Salto Formation was dated in the same area by Hervé et al. (2004), yielding an age of 21.8 ± 1.5 Ma, which we think represent the base of the Río Verde member. The latter suggests a possible hiatus between the two members, which would imply that a stratigraphic redefinition is required. We have calculated an MDA of 19.6 ± 0.4 Ma (Table 1; Figs. 4 and 6) for the uppermost exposure of the El Salto Formation, representing the top of the San Antonio member. Therefore, the age for the upper part of the El Salto Formation ranges from 21.8 to 19.6 Ma. Interestingly, we can extend a chronostratigraphic correlation between the upper part of the El Salto Formation and the Estancia 25 de Mayo Formation, which represent the deposits of the Patagonian transgression. However, such a marine incursion does not reach this part of the basin, and the only compelling evidence of this event is related to the increased accommodation space in the fluvial system of the upper reaches of the El Salto Formation (Rivera, 2017). The basal San José member of the overlying Palomares Formation yields an MDA of 18.85 ± 1.1 Ma (Table 1; Figs. 4 and 6), fully consistent with the basal ages for the equivalent Santa Cruz Formation (Fig. 6). In the Cordillera Chilena sector (Fig. 7d), this member changes laterally (westward) to the Conglomerado Vidal member, which is primarily a basaltic breccia (Rivera, 2017) and yields an MDA of 17.9 ± 0.2 Ma (Table 1; Figs. 4 and 6). Recently, Velazquez (2016) have dated by Ar-Ar two of the basaltic blocks of the Conglomerado Vidal member, and those yield an age from 19.3-19.8 Ma, which agrees with our results in that the sedimentation of the Palomares Formation is younger than 19 Ma. We have adopted the age for the equivalent Santa Cruz Formation reported by Gutiérrez et al. (2017) in the SB area for the top of the unit.

II-1.6.2 Monitoring tempo and style of arc magmatism

The sedimentary record through detrital zircon U-Pb analysis provides essential complementary information (to bedrock dating) about the timing and duration of arc magmatism (Hervé et al., 2004; Peterson and Ducea, 2015; Capaldi et al., 2020, 2021).

The direct comparison of the exposed bedrock U-Pb dating with the detrital zircon U-Pb ages (Fig. 7a) shows that the detrital record mimics the main pulses of magmatism already identified employing the direct plutons dating (Hervé et al., 2007), i.e., Late Jurassic (157-145 Ma), Cretaceous 1 to 3 (144-137 Ma; 136-127 Ma; 126-75 Ma), Paleogene (67-40 Ma), and Miocene (25-15 Ma). However, are also apparent two non-widely known phases of magmatism in the batholith. The first is between 75-65 Ma, and the second is between 45-35 Ma (Fig. 7a). Different authors had previously recognised both phases of magmatism in different parts of the basin (Hervé et al., 2004; Gutiérrez et al., 2017; Rivera, 2017; Fosdick et al., 2020), which allows us to affirm that these plutons must have been exposed throughout the entire extension of the batholith. The recognition of these 'new' magmatism phases in the batholith are relevant for a correct interpretation of the sedimentary provenance of the foreland deposits. Malkowski et al. (2016) had also recognised a mismatch at 99 Ma between batholith ages with arc-derived detrital ages populations, for which they propose some explanations to this discrepancy: (1) insufficient age constraint of the batholith due to sampling bias; (2) exhumation and preferential erosion of plutons of this age range. We favoured the first explanation owed to the undeniable difficulty of accessing the batholith outcrops in the Patagonian fjords.

Figure 7b shows the composite bedrock U-Pb ages with detrital zircon U-Pb ages, where an episodic behaviour of the continental magmatic arc is apparent (Hervé et al., 2007) but concentrating the climax of magmatism between 120-70 Ma (Bruce et al., 1991; Malkowski et al., 2016). Four first-order '*flare-ups*' are presented during the Late Jurassic to Early Cretaceous (160-140 Ma), mid to Late Cretaceous (120-70 Ma), late Eocene (45-35 Ma), late Oligocene to early Miocene (25-15 Ma). The mean Th/U ratios (Fig. 7c) from bedrock and detrital zircons for each flare-up event remain almost constant, ranging between 0.5-0.63, suggesting low geochemical variability of the magmas during contractional orogenesis (Kemp et al., 2009; Rubatto, 2017; McKay et al., 2018). However, the middle to Late Cretaceous and Oligocene to early Miocene flare-ups exhibit a tendance to increase Th/U values (up to 1.6; Fig. 7c) by the final of each magmatic pulse, which could suggest that they were produced in hotter (700->1000°C), more primitive magmas with increased

fractionation (Kirkland et al., 2015; McKay et al., 2018). These pulses of magmatism are separated by three first-order '*magmatic lulls*' between 25-33 Ma, 45-65 Ma and 120-140 Ma (Fig. 7b), some of which had been previously recognised (e.g., Rivera, 2017; George et al., 2020). Interestingly, these arc tempos are shorter during the Cenozoic (8-10 Myr) and longer during Cretaceous to Jurassic (20-50 Myr).

The spatial trend in magmatism can be extracted by the age-latitude plotting (Fig. 7d), which allow interpreting relative arc retreat or advance. Interestingly, during periods of magmatic lulls, there is always an arc rearrangement, displacing the relative position of the arc front (Fig. 7d). During the mid to Late Cretaceous (120-70 Ma) flare-up, there is a relative cratonward arc migration followed by an extended arc shut-off period (Fig. 7d). This behaviour has been emphasised by Gianni et al. (2018a) to support their Maastrichtian to Eocene Nale flat slab event (48°-35°S). Likewise, during the late Oligocene to early Miocene (25-15 Ma) flare-up, the arc is broadened, which could be expected due to the subduction erosion and slab flattening episode related to the Chile Ridge collision (e.g., Ramírez de Arellano et al., 2012; Salze et al., 2018). A causal relationship between the collision of the Farallon-Aluk ridge (57-40 Ma) and the Eocene magmatic lull (45-65 Ma) can be envisaged (Ramos, 2005; Aragón et al., 2013; Gianni et al., 2018a, b). The Farallon-Aluk collision may have influenced the isotopic composition of the few coeval plutons (Hervé et al., 2007), leading to a more primitive mantle signature of the magmas (Aragón et al., 2013; Fig. 7d). On the other hand, the magmatic lull between 25-33 Ma could be linked to a plate tectonic reorganisation process during the Farallon breakup (28-23 Ma; Herron and Heirtzler, 1967; Pardo-Casas and Molnar, 1987).

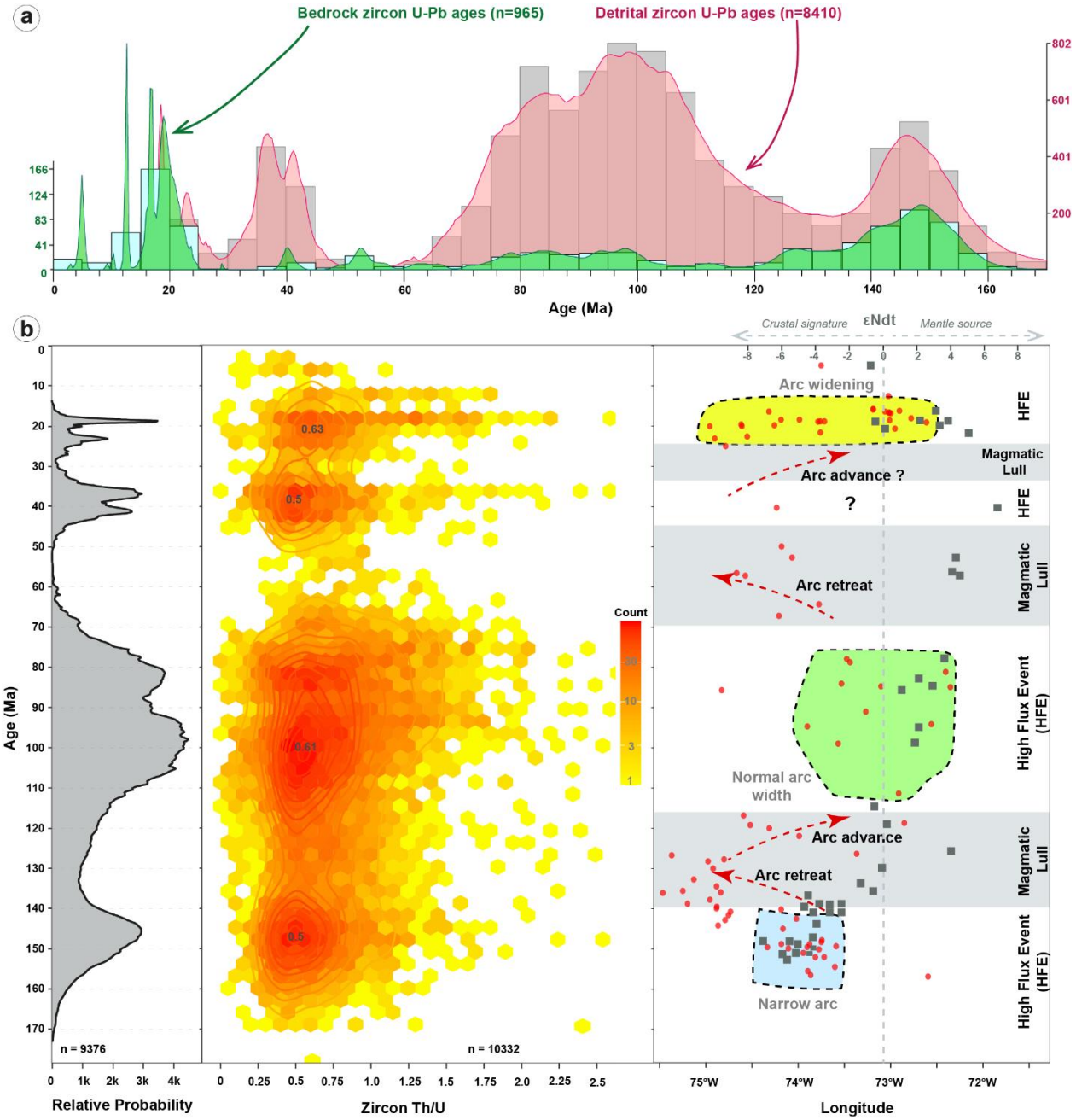

Figure 7. (a) Composite bedrock U-Pb dating (from Hervé et al., 2007; Michael et al., 2008; Leuthold et al., 2012; Müntener et al., 2018; Ramírez de Arellano et al., 2012, 2021) vs detrital zircon U-Pb (references as indicated in Fig. 6). (b) Integrated zircon U-Pb ages highlighting arc flare-ups and magmatic lulls. (c) Compositional variation of arc magmatism based on Th/U ratio (Th/U >1.0, primitive mafic melts; Th/U <0.5, limited geochemical variability); (d) Time-space continental arc migration and variations in isotopic εNdt composition (after Hervé et al., 2007). Arc width constraints after Capaldi et al. (2021).

II-1.6.3 Development of major unconformities

Recognition of unconformities is a vital process in Andean foreland basin analysis, as they allow to extract of the entire evolutionary history of the basin and Andean orogenesis (Horton, 2018a). However, as unconformities occur ubiquitously at different scales (Miall, 2016; Catuneanu, 2019a), only their analysis in a comparable hierarchical order will

facilitate the correct interpretation of the sedimentary and tectonic processes that they represent without combining allogenic and autogenic processes in the same evolutive scenery. Different origins of unconformities have been highlighted in multiple works (Weimer, 1984; Shanmugam, 1988; Heller et al., 1988; Crampton and Allen, 1995; DeCelles, 2012; Miall, 2016; Horton, 2021), which comprise (a) shortening and uplift of the fold-and-thrust belt; (b) cratonward advance of a tectonic-induced flexural wave; (c) basinwide isostatic rebound by episodic tectonic quiescence, slab window development or change in convergence angle; (d) eustatic sea-level drops; (e) basinwide and/or intraforeland basement blocks uplift during slab shallowing. Next, we expose only some of the most significant discordances/unconformities in the basin (in different hierarchical scales) without necessarily addressing an exhaustive analysis of their genesis (since it escapes the objective and data sources of this work) but rather to highlight their temporal and spatial distribution in the Magallanes-Austral Basin.

The basal foreland basin unconformity (BFU) has not been recognised at the surface. However, at the subsurface is characterized by an assembly of different time-transgressive unconformities that, in the most proximal part, are manifested by a series of bright reflectors that may correspond to condensed sedimentation surfaces, separating orogenic-derived deposits from the backarc extensional strata. Over time, this discordance is manifested by onlap terminations of each sequence (KS1-PS2; ~100-40 Ma) that pinch out towards the craton, suggesting a continuous uplift and erosion of the forebulge (Catuneanu, 2019b; Horton, 2018). From the middle to late Eocene, the forebulge is buried, and a thin succession accumulates across. This unconformity represents the cratonward passage of the forebulge in response to the orogenic wedge loading.

For the Cenozoic, two major unconformities are well recognised that can be followed throughout the basin. The Paleocene-Eocene unconformity with the longest ~20 Myr hiatus in the northern part of the basin (LVA area) and the shortest ~2.5 Myr in the southern part (SKB area) (Fig. 6). In the LVA area (Fig. 2), the unconformity becomes erosive (Marenssi et al., 2002), truncating older Maastrichtian-Paleocene shallow marine green glauconitic sandstones and conglomerates (Calafate Formation; Macellari et al., 1989; Marenssi et al., 2004; Odino Barreto et al., 2018). Over the erosive surface, onlaps middle Eocene green conglomerates and sandstones with abundant marine invertebrates representing shallow marine to tidal-embayment deposits filling incised valleys (Man Aike Formation; Macellari et al., 1989; Marenssi et al., 2003; Camacho et al., 2000; Casadío et al., 2009; Pearson et al.,

2013). In the SB and CTN areas (Fig. 2), the unconformity (~13-18 Myr duration; Fig. 6) is manifested by a modest erosive surface (Fig. 8a, b), separating the middle Eocene wave- to tide-dominated estuaries and coastal plains of Man Aike Formation (and ex lower Río Turbio Fm; Santos-García, 1988; Malumián and Caramés, 1997; Malumián et al., 2000; Le Roux et al., 2010; Gutiérrez et al., 2017) from the Campanian-Selandian shallow marine to deltaic Dorotea Formation (Schwartz and Graham, 2015; Gutiérrez et al., 2017; Manríquez et al., 2019; Rivera et al., 2020). In the southern SKB area, the unconformity span ~2.5 Myr (Fig. 6) and becomes correlative conformity or paraconformity, preventing recognising it in outcrops. However, in subsurface (= P-1 unconformity), the Paleocene-Eocene unconformity evidence a nature erosive, truncating conformable strata of the PS1 sequence and acting as a basal surface over which onlaps strata of the PS2 sequence (early to middle Eocene).

Laterally differences in time magnitude of unconformities are very common in foreland basins (Miall, 2016; Horton, 2018a, 2021). For the Magallanes-Austral Basin, lateral variability of hiatus involved in the Paleocene-Eocene unconformity is explained by significant differences in subsidence or accommodation among the different studied areas as the heritage of the predecessor extensional Rocas Verdes Basin (RVB) configuration. There is a consensus that during the development of the extensional RVB, the attenuation of the continental lithosphere increased significantly southward (de Wit and Stern, 1981; Stern and de Wit, 2003; Stern et al., 1992; Calderón et al., 2013; Malkowski et al., 2015), which exerted a strong control on the sedimentation and nature of the discordances in the stratigraphic record of the subsequent foreland basin (Romans et al., 2010; Malkowski et al., 2015, 2017; Sickmann et al., 2018; Rivera et al., 2020). To explain the origin of the Palaeocene-Eocene unconformity, we propose a tripartite mechanism that occurred simultaneously and diachronically southward in the studied region. First, a thrust belt shortening phase that began at the end of the Maastrichtian, evidenced by the angular unconformity, at the base of the Calafate Formation (Macellari et al., 1989), which becomes erosional disconformity affecting the upper part of the Dorotea Formation (around Puerto Natales) and Rocallosa (Rivera et al., 2020) impacting the sediment routing system of the entire basin almost simultaneously. A second, diachronic phase of tectonic quiescence that progressed from north to south, probably related to the collision of the Farallon-Aluk ridge, manifested by basalt volcanism in the backarc (Ramos, 2005; Aragón et al., 2013; Gianni et al., 2018b) and a magmatic arc shutdown between 45-65 Ma (Fig. 7b). While in the northern part of the basin, a generalized isostatic uplift and sediment bypass occurred by early Eocene, in the

southern part (where more subsidence = accommodation is concentrated), the orogen was still active, generating tectonic load evidenced by the uplift of the forebulge (cratonward onlap of PS1; Fig. 5). When the tectonic quiescence reached the southernmost ends of the basin, the northern part was in an enhanced process of isostatic rebound and non-deposition (bypass) for several million years ago. Finally, after the passage of the Farrallón-Aluk ridge, the third phase is a reactivation of thrust belt shortening (and magmatism; Fig. 8a) that occurs throughout the entire extension of the basin, and it is evidenced by the growth strata of the Man Aike Formation (formerly lower Río Turbio Fm) and Loreto Formation seen in seismic-reflection lines.

The Eocene-Oligocene unconformity can be traced across the entire basin on the surface and subsurface. In the LVA and SB areas (Fig. 2), several authors point out an erosive unconformity between the shallow marine to tidal-embayment deposits of Man Aike and the fluvial systems of the Río Leona Formations (Camacho et al., 2000; Marenssi et al., 2002, 2003, 2005; Casadío et al., 2009; Gutiérrez et al., 2017), which encompass ~11-12 Myr (LVA area) and ~4-5 Myr (SB area) (Fig. 6). In the CTN area (Fig. 2), the contact between the outer-estuarine to coastal plain deposits of the Río Turbio Formation and the high-energy fluvial and coastal plain depositional systems of the Río Guillermo Formation (= Río Leona Fm) is interpreted as an erosive unconformity (Hünicken, 1955; Azcuy and Amigo, 1991; Malumián and Caramés, 1997; Malumián et al., 2000; Pearson et al., 2012; Leonard et al., 2020; Fosdick et al., 2020) represented by a ~7-8 Myr hiatus (Fig. 6). In the SKB area (Fig. 2), around the Cordillera Pinto and Cordillera Vidal localities (see Fig. 8d for localitation), García and Cortés (1953) and González (1953) observed a pronounced angular unconformity between the fluvial- to tide-dominated deltaic Loreto Formation and the high-energy fluvial and coastal plain systems of the El Salto Formation (Mella, 2001; Otero et al., 2012; Rivera, 2017). Furthermore, we have identified on the north coast of Skyring Sound (Fig. 2), the base of the El Salto Formation is a surface that truncates the top of the Loreto Formation (Fig. 8d), suggesting an erosive nature for the contact. Additionally, Rivera, 2017 found reworked glauconitic grains from the Loreto Formation present in the basal part of the El Salto Formation, which reinforce the erosive character of their contact. This unconformity represents ~4 Myr hiatus in the SKB area.

To explain the origin of the Eocene-Oligocene unconformity, we appeal to the combination of changes of eustatic sea-level (and climate) and thrust belt uplift. A eustatic sea-level lowstand during the Eocene-Oligocene boundary (Haq et al., 1987), originated by

the first antarctic-continental ice sheet event (Oi1; Miller et al., 1991; Zachos et al., 1996), decline the sediment accommodation significantly across the basin promoting valley incisions (as in SB area, Fig. 6) and unconformity development (Vail et al., 1984; Weimer, 1984; Marenssi et al., 2005). The thrust belt uplift had influence restricted to the wedge-top and proximal foredeep depozones. The latter, established by the strong pinch out of the El Salto Formation westward of the Cordillera Vidal (Fig. 8d) and because the angular unconformity that separates the Loreto and El Salto formations become less prominent eastward, where it can be traced as a conformable contact (based on subsurface data). Furthermore, progressive decreasing in dips (progressive unconformities ?) for the Oligocene-Miocene succession recognised by Malumián et al. (2000) around Cancha Carrera town (Fig. 2) likely attests thrust fault uplift concomitant to sedimentation. Likewise, Fosdick et al., 2020 interpreted a synorogenic origin for the lower Río Leona Formation (ex Río Guillermo Formation), linked to the El Río Rincon thrust fault. Similarly, a tectonic uplift event prior to deposition of the Río Leona Formation (in the LVA area) has been suggested by Marenssi et al. (2005). These pieces of evidence suggest an active and growing Southern Patagonian Andes by the transition Eocene-Oligocene, leading to the rain-shadow effect on the pro-side of the orogen (Gutiérrez et al., 2017). Nonetheless, it seems contradictory that an orogenic event of such magnitude reproduces as little flexural tectonic loading as evidenced by the NS1 sequence (Fig. 5) lacking a typical wedge geometry as could be expected in such a case. Therefore, it is possible that the deformation was concentrated in the innermost parts of the orogenic wedge and/or that there was a period of tectonic quiescence and isostatic rebound probably linked to the Farallon breakup, also manifested by the magmatic lull between 25-33 Ma (Fig. 7b).

Other unconformities of ~2 Myr hiatus as those between the Río Leona and Estancia 25 de Mayo formations, intra-El Salto Formation or between the El Salto and Palomares formations are only appreciable in a wedge-top position (Fig. 6). González and Tapia (1952) and González (1953) described the Palomares Formation as overlying strongly folded and fractured strata of the El Salto Formation. The first author has corroborated such a relationship in the northern foothills of Cordillera Vidal (Fig. 8d), where the Palomares Formation, with dips 18-16° NE, rests discordantly over highly-dipping strata of the El Salto Formation. Similarly, Ramos (1982) recognised an angular unconformity between the Estancia 25 de Mayo and Santa Cruz Formations in the Lago Cardiel area of Argentina. All these unconformities become conformable contacts towards the foredeep.

Figure 8. (→ *next page*). Unconformities expression in outcrops and seismic-reflection data. (a) Moderately pronounced erosive unconformity between the Dorotea and Man Aike formation, in the SB area; photo courtesy of N.M. Gutiérrez. (b) In the CTN area, there is a subtle erosive unconformity between the Dorotea and Man Aike formations (ex lower member of Río Turbio Fm). (c) Progressive unconformities in the Man Aike Formation (ex lower member of Río Turbio Fm) in the CTN area, around Río Turbio town. (d) Wedge-top position setting for unconformities in the SKB area. At the lower panel, erosive truncation of El Salto Formation strata over older units (Loreto Formation); upper panel, structural dips of the El Salto and Palomares formations highlighting a possible unconformity.

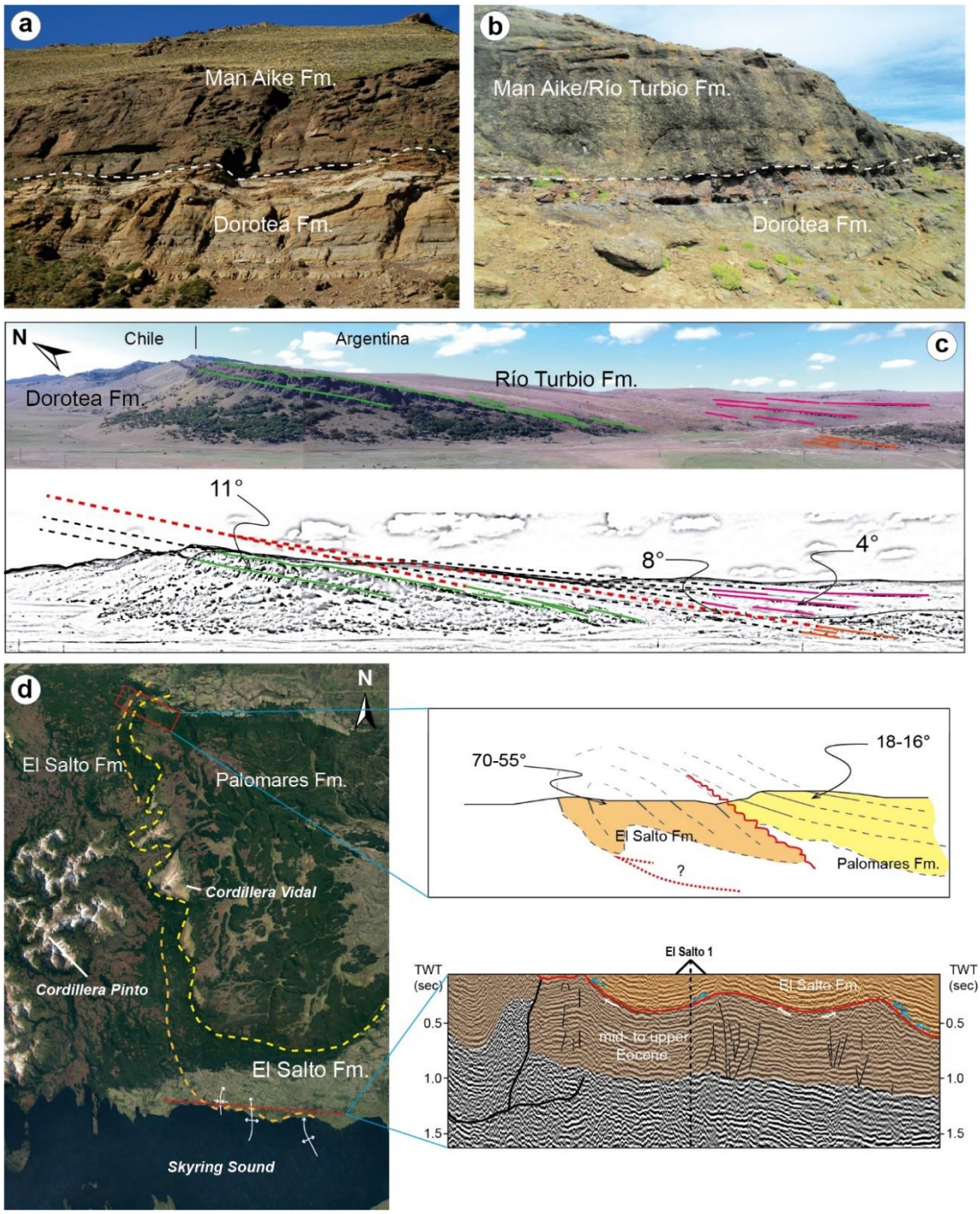

II-1.7 CONCLUSIONS

The integration of previously published chronostratigraphic data with 25 new detrital zircons U-Pb ages facilitates the revision and updating of the Upper Cretaceous to the early Miocene chronostratigraphic framework for the Magallanes-Austral basin, which serves as building blocks for later robust basin analysis and paleontological studies. This new framework provides spatial and temporal constraints in which to:

1. Offer high-precision in maximum depositional ages calculation for numerous Cretaceous to Cenozoic lithostratigraphic formation boundaries along a north-to-south axis-basin transect (49.5°-53.6°S).
2. Evaluate variability in age and duration of at least five unconformities in the basin. The Paleocene-Eocene and Eocene-Oligocene unconformities span ~20 and ~12 Myr around Lago Argentino (Argentina), southward in Brunswick Peninsula (Chile), both diminishes significantly to represent ~2.5 and ~4 Myr, respectively.
3. Establish basin-wide correlations of different lithostratigraphic units and alleviate problems in stratigraphic nomenclature, for instance, suggesting the abandonment of the use of the Escarpada Formation (in the Magallanes Province, Chile). The Cerro Cazador, Monte Chico, and Cerro Dorotea formations unified into a single lithostratigraphic unit called the Dorotea Formation. The lower member of the actual Río Turbio Formation is re-defined as the Man Aike Formation. The actual Río Guillermo Formation becomes a member of the Río Leona Formation.

We portray the invaluable potential of detrital zircon U-Pb geochronology as complementary records of temporal and spatial patterns of arc magmatism. We constrain the episodic behaviour of magmatism of the Southern Patagonian Batholith, with main pulses at Late Jurassic to Early Cretaceous (160-140 Ma), Middle to Late Cretaceous (120-70 Ma), late Eocene (45-35 Ma), late Oligocene to early Miocene (25-15 Ma). Likewise, we highlight two phases of magmatism (75-65 Ma; 45-35 Ma) not recorded in bedrock dating of plutonic rocks (Hervé et al., 2007). Furthermore, we emphasize three first-order magmatic lulls between 25-33 Ma, 45-65 Ma and 120-140 Ma.

The new tectonostratigraphic framework has allowed recognising first-order sequences that demarcate the change from backarc extension to compressive orogenesis in the Southern Patagonian Andes region. Likewise, two second-order sequences allow us to interpret changes in the sedimentation dynamics, evolving from an underfilled basin stage (from Late Cretaceous to middle Eocene) to an overfilled basin (from the Middle Eocene to the early Neogene). Identifying six third-order sequences allows knowing the basin's responses to tectonic changes, sedimentation rates, and variations in accommodation.

Finally, based on regional stratigraphic, structural and seismic-reflection data, we suggest that the combination of thrust belt shortening and tectonic quiescence related to the

Farallon-Aluk collision, acting under certain temporal and spatial conditions, are potential mechanisms to explain the origin of the Paleocene-Eocene unconformity. On the other hand, we postulate changes in eustatic sea-level and orogenic growth as the controlling mechanisms for the Eocene-Oligocene unconformity development.

ACKNOWLEDGEMENTS

This study was financially and logistically supported by FONDECYT projects 1130006 and 1161806 and by the CONICYT-PFCHA-National PhD Scholarship 2017 No. 21170419 and EIFFEL Excellence Scholarship 2019. We gratefully acknowledge L. Rojas (Enap-Sipetrol) for permission to review unpublished reports and to publish industrial 2-D seismic-reflection lines and borehole data, as well as J. Arriagada (Enap-Sipetrol) for his assistance in searching through the Enap technical files database. M. Leisen (CEGA), L. Solari (UNAM), M. Suárez and F. Llona (SERNAGEOMIN) are thanked for detrital zircon age dating. We also thank G. Germain-Ouvier for digitalising some geological units.

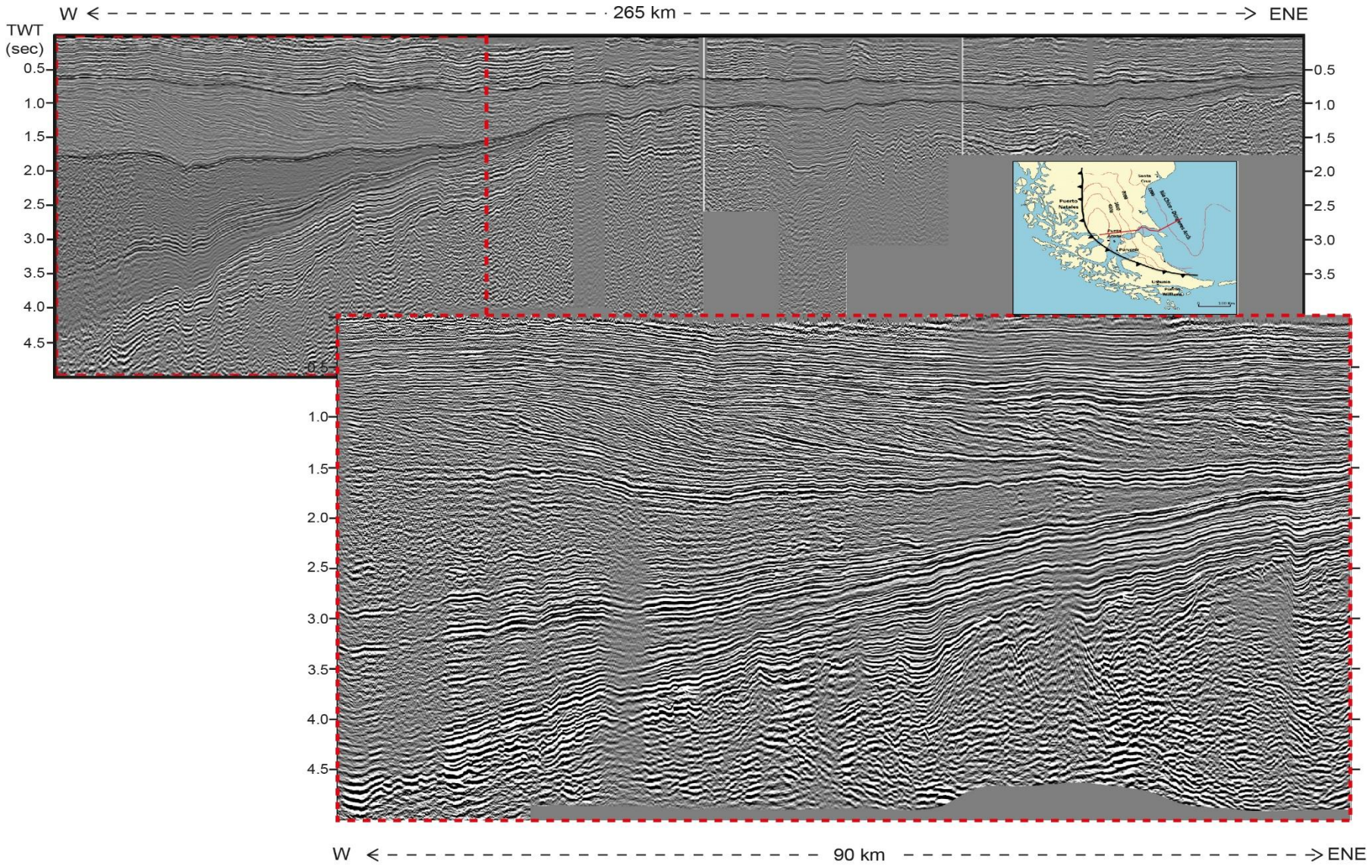
W
265 km
ENE
TWT
(sec)
0.5
1.0
1.5
2.0
2.5
3.0
3.5
4.0
4.5
W
90 km
ENE

THIRD PART

SEDIMENTARY EVOLUTION, SEQUENCE STRATIGRAPHY AND INTEGRATED PROVENANCE

CHAPTER III-1:

TECTONIC CONTROLS ON THE SUBCONTINENTAL MAASTRICHTIAN-DANIAN TRANSGRESSION AND GROWING OF THE PATAGONIAN ANDES

Chapter III-1 addresses deciphering the causative mechanism of the most extensive transgression in Patagonia and most of South America, presenting one of the completest sedimentological studies of this event. A multidisciplinary approach is used, including sedimentology, detrital zircon U-Pb geochronology, provenance analysis, palynology, and sequence stratigraphy. In this way, it was possible to evaluate the relative role of the climate, eustasy and tectonics on this marine ingression. The broader significance of the results can be synthesised in 3 aspects: 1) contributes to the understanding of the variability of transgressive deposits in a basin developed over highly attenuated crust; 2) provides new light on a complex tectonic event around the K-Pg boundary poorly constrained hitherto, and how was the evolution of the routing systems during this time-frame; 3) is the second contribution (after ca. 30 years) that gather into stratigraphic sequences the evolution of the sedimentary fill in a regional context in the Magallanes Basin.

HIGHLIGHTS:

- Flexural and dynamic subsidence originated the Maastrichtian-Danian transgression.
- Estuarine deposits and deep-water turbidites represent the transgression.
- Hinterland exhumation and stalled deformation front during the Maastrichtian.
- Significant forelandward advance of the deformation front by the Paleocene.
- The inherited crustal configuration controls the sedimentation, accommodation, and whether unconformities or correlative conformities may develop.

Sedimentary Geology 403 (2020) 105645

Contents lists available at ScienceDirect

Sedimentary Geology

journal homepage: www.elsevier.com/locate/sedgeo

Tectonic controls on the Maastrichtian-Danian transgression in the Magallanes-Austral foreland basin (Chile): Implications for the growth of the Southern Patagonian Andes

Huber A. Rivera [a,b,*], Jacobus P. Le Roux [a], Marcelo Farías [a], Néstor M. Gutiérrez [a], Alejandro Sánchez [c], Sylvia Palma-Heldt [d]

[a] Departamento de Geología, Facultad de Ciencias Físicas y Matemáticas, Universidad de Chile, Plaza Ercilla 803, Santiago, Chile
[b] Université Grenoble Alpes, Université Savoie Mont Blanc, CNRS, IRD, IFSTTAR, ISTerre, 38000 Grenoble, France
[c] Departamento de Ingeniería en Minas, Universidad de Santiago de Chile, Av. O'Higgins 3363, Santiago, Chile
[d] Departamento de Ciencias de la Tierra, Facultad de Ciencias Químicas, Universidad de Concepción, Victor Lamas 1290, Concepción, Chile

ARTICLE INFO

Article history:
Received 24 January 2020
Received in revised form 12 March 2020
Accepted 14 March 2020
Available online 19 March 2020

Editor: Dr. J. Knight

Keywords:
Cretaceous palaeoclimate
Provenance analysis
Southern Patagonian Andes
Sequence stratigraphy
U-Pb geochronology

ABSTRACT

The Maastrichtian-Danian transgression was one of the most extensive Atlantic-derived marine incursions in Patagonia. This study examines its stratigraphic record and origin in the Magallanes-Austral Basin, revealing an interplay of sedimentation, tectonism, and base-level changes, which contribute to our understanding of foreland basin dynamics. We present a multidisciplinary approach from a relatively poorly documented sector (51°38′-53°50′S) of the basin. This approach includes facies and provenance analysis, palynology, sequence stratigraphy, and U-Pb geochronology. These techniques enable us to evaluate the role of climate, tectonics, and eustasy on the transgression, as well as providing insight into the growth of the Southern Patagonian Andes. A first shallowing-upward cycle (late Campanian to late Maastrichtian) is represented by the transition from outer shelf and upper slope deposits (Fuentes and Tres Pasos formations) to shoreface and deltaic environments (Rocallosa and Dorotea formations), favoured by high erosion rates in the fold-thrust belt and eustatic sea-level drop. A subsequent deepening-upward cycle (late Maastrichtian to Paleocene) records the Atlantic transgression, manifested by estuarine deposits in an incised valley (uppermost Dorotea Formation) and deep-water turbidites (Chorrillo Chico Formation and Cabo Naríz beds). Palynological results suggest a temperate palaeoclimate (~6–17 °C) during the Maastrichtian-Danian, which agrees with significant cooling of the South Atlantic Ocean at this time. Therefore, relative climatic optima are not a driver of marine ingression. The stratigraphic and tectonic evolution of the succession studied suggests that flexural and dynamic subsidence promoted marine incursion into the Magallanes-Austral Basin. Provenance data indicate sediment input to the basin from the Southern Patagonian Batholith, Rocas Verdes Basin remnants, Tobífera Formation, and metamorphic terranes exposed in the hinterland of the Southern Patagonian Andes during the early Maastrichtian. However, by the Paleocene, sediments derived from the hinterland had been structurally dammed during basinward propagation of the fold-thrust belt.

1. Introduction

In foreland basins, transgressive events are considered as an essential tool for understanding tectonic evolution due to their common link with thrusting events (e.g., Kamola and Huntoon, 1995; Hernández et al., 2005; Roddaz et al., 2010; Aguirre-Urreta et al., 2011; Gianni et al., 2018). Furthermore, transgressive deposits have provided valuable insights into the balance among supra-and sub-crustal static loading and unloading phases, sedimentation, and subsidence in the complex and dynamic evolution of foreland basins (Cross and Pilger Jr, 1978; Catuneanu et al., 1997; Catuneanu, 2004; Hernández et al., 2005; Yang and Miall, 2008; Roddaz et al., 2010).

In Patagonia, the Maastrichtian-Danian transgression is considered to have been the most extensive (34°S-54°S) Atlantic-derived marine ingression (i.e., without the influence of Pacific ocean waters) that affected most of Patagonian basins (Náñez and Malumián, 2008; Malumián and Nanez, 2011; del Río and Martínez, 2015) (Fig. 1a). However, the origin of the Maastrichtian-Danian transgression is still controversial. Previous interpretations range from eustatic effects linked with warm-climatic episodes (Náñez and Malumián, 2008; Malumián and Nanez, 2011; Vellekoop et al., 2017) to purely tectonic causes

* Corresponding author at: Departamento de Geología, FCFM, Universidad de Chile, Plaza Ercilla 803, Santiago, Chile.
E-mail addresses: huber.rivera@ug.uchile.cl, riverarh@univ-grenoble-alpes.fr (H.A. Rivera).

https://doi.org/10.1016/j.sedgeo.2020.105645
0037-0738/

Tectonic controls on the Maastrichtian-Danian transgression in the Magallanes-Austral foreland basin (Chile): implications for the growth of the Southern Patagonian Andes

ABSTRACT

The Maastrichtian-Danian transgression was one of the most extensive Atlantic-derived marine incursions in Patagonia. This study examines its stratigraphic record and origin in the Magallanes-Austral Basin, revealing an interplay of sedimentation, tectonism, and base-level changes, which contribute to our understanding of foreland basin dynamics. We present a multidisciplinary approach from a relatively poorly documented sector (51°38'-53°50'S) of the basin. This approach includes facies and provenance analysis, palynology, sequence stratigraphy, and U-Pb geochronology. These techniques enable us to evaluate the role of climate, tectonics, and eustasy on the transgression, as well as provide insight into the growth of the Southern Patagonian Andes. A first shallowing-upward cycle (late Campanian to late Maastrichtian) is represented by the transition from outer shelf and upper slope deposits (Fuentes and Tres Pasos formations) to shoreface and deltaic environments (Rocallosa and Dorotea formations), favoured by high erosion rates in the fold-thrust belt and eustatic sea-level drop. A subsequent deepening-upward cycle (late Maastrichtian to Paleocene) records the Atlantic transgression, manifested by estuarine deposits in an incised valley (uppermost Dorotea Formation) and deep-water turbidites (Chorrillo Chico Formation and Cabo Naríz beds). Palynological results suggest a temperate palaeoclimate (~6-17°C) during the Maastrichtian-Danian, which agrees with the significant cooling of the South Atlantic Ocean at this time. Therefore, relative climatic optima are not a driver of marine ingression. The stratigraphic and tectonic evolution of the succession studied suggests that flexural and dynamic subsidence promoted marine incursion into the Magallanes-Austral Basin. Provenance data indicate sediment input to the basin from the Southern Patagonian Batholith, Rocas Verdes Basin remnants, Tobífera Formation, and metamorphic terranes exposed in the hinterland of the Southern Patagonian Andes during the early Maastrichtian. However, by the Paleocene, sediments derived from the hinterland had been structurally dammed during basinward propagation of the fold-thrust belt.

***Keywords**: Cretaceous palaeoclimate; Provenance analysis; Southern Patagonian Andes; Sequence stratigraphy; U-Pb geochronology*.

III-1.1 Introduction

In foreland basins, transgressive events are considered as an essential tool for understanding tectonic evolution due to their common link with thrusting events (e.g., Kamola and Huntoon, 1995; Hernández et al., 2005; Rodazz et al., 2010; Aguirre-Urreta et al., 2011; Gianni et al., 2018a). Furthermore, transgressive deposits have provided valuable insights into the balance among supra-and sub-crustal static loading and unloading phases, sedimentation, and subsidence in the complex and dynamic evolution of foreland basins (Cross and Pilger, 1978; Catuneanu et al., 1997; Catuneanu, 2004; Hernández et al., 2005; Yang and Miall, 2008; Rodazz et al., 2010).

In Patagonia, the Maastrichtian-Danian transgression is considered to have been the most extensive (34°S-54°S) Atlantic-derived marine ingression (i.e., without the influence of Pacific ocean waters) that affected most of Patagonian basins (Náñez and Malumián, 2008; Malumián and Náñez, 2011; del Río and Martínez, 2015) (Fig. 1a). However, the origin of the Maastrichtian-Danian transgression is still controversial. Previous interpretations range from eustatic effects linked with warm-climatic episodes (Náñez and Malumián, 2008; Malumián and Náñez, 2011; Vallekoop et al., 2017) to purely tectonic causes (Aguirre-Urreta et al., 2011; Giani et al., 2018), or a combination of both (Uliana and Biddle, 1988; Guler et al., 2019). A eustatic cause alone is unlikely, however, because the Maastrichtian-Danian transgression occurred during a period of cooling in the South Atlantic, indicated by □18O records of planktic and benthic foraminifera (Barrera and Savin, 1999; Cramer et al., 2009; Le Roux et al., 2012) (Fig. 1b). Moreover, between the Campanian and Selandian, a gradual eustatic sea-level fall is apparent (Haq, 2014) (Fig. 1b), which may suggest a potential link to tectonically-induced subsidence.

The palaeontological record of the Maastrichtian-Danian transgression has been exhaustively studied over the past 20 years throughout Patagonia (e.g., Malumián and Caramés, 1997; Náñez and Malumián, 2008; Malumián and Náñez, 2011; Aguirre-Urreta et al., 2011; del Río and Martínez, 2015; Vallekoop et al., 2017; Guler et al., 2019). In contrast, few studies deal with the sedimentological record, and most of these were focused on the northernmost basins (Neuquen Basin: Barrio, 1990; Aguirre-Urreta et al., 2011; Cañadón Asfalto Basin: Scasso et al., 2012). In the Magallanes-Austral Basin (MAB; Fig. 1a), Corysphostoma incrassate-bearing sandstones and glauconitic-rich facies have been traditionally related to the transgression (Malumián and Caramés, 1997; Mpodozis et al., 2011). However, these proposals, based on foraminifera or glauconitic content, were not

backed up by systematic facies analysis. In the northern sectors of the MAB, the transition of non-marine to marine deposits facilitated recognition of the flooding event and allowed sedimentological studies in greater detail than previously achieved (e.g., Marenssi et al., 2004; Odino et al., 2018). Nevertheless, the sedimentological record of the transgression remains poorly studied in most of the central and southern parts of the basin.

This study presents a detailed sedimentological and sequence stratigraphic analysis, palynological data, and ~400 new detrital zircon U-Pb geochronological ages from a relatively poorly known sector (51°38'-53°50'S; Fig. 2a) of the MAB. Our work aims to amplify the current knowledge of the stratigraphic and sedimentological record of the Maastrichtian-Danian Atlantic transgression and contribute to the growing body of knowledge regarding the variability of transgressive deposits by characterising both vertical and lateral facies changes, sequence stratigraphic architecture, and sedimentary provenance. This approach also allows us to provide a stratigraphic sequence framework that: (1) facilitates the identification of the transgressive deposits within a context of continuous marine sedimentation, and (2) develops an understanding of the juxtaposition, evolution, and inter-basin correlation of the depositional units (from Campanian-Maastrichtian to Paleocene). Our results enable us to evaluate to what extent climate, eustasy and tectonics controlled the marine incursion into the MAB, and discuss the causative mechanisms on a broad regional scale. Moreover, by combining our provenance results with the conclusions of previous structural studies, we constrain the timing of the latest Cretaceous to early Cenozoic deformation events and shed light on the building phases of the Southern Patagonian Andes.

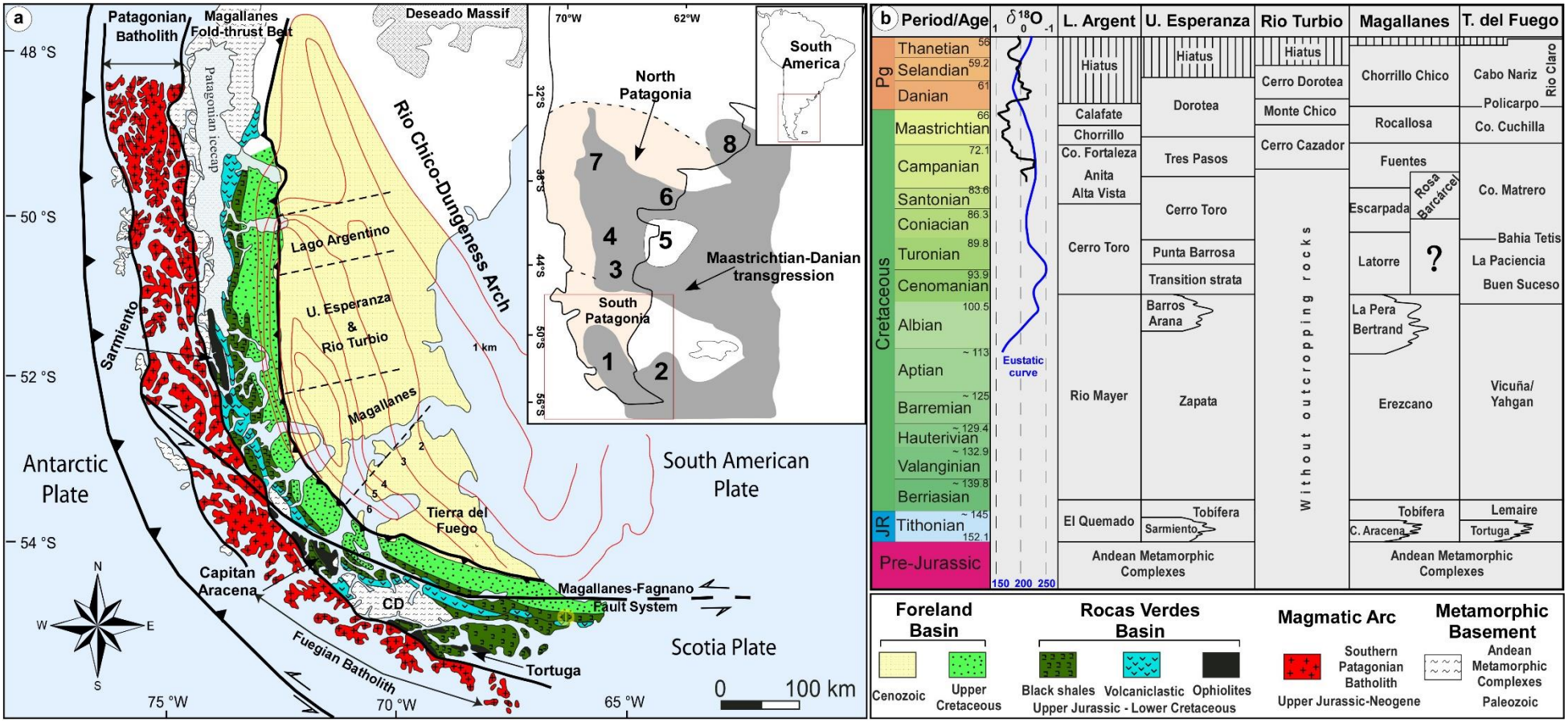

Figure 1. (a) Simplified morphotectonic map of the Magallanes-Austral Basin (modified from Fildani and Hessler, 2005), showing potential source terranes to the basin. Red isopach lines are the depth to top-Tobífera Formation (Late Jurassic). The inset map shows the Maastrichtian-Danian ocean flooding Patagonian basins: (1) Magallanes-Austral, (2) Malvinas, (3) Golfo San Jorge, (4) Cañadón Asfalto, (5) Península Valdes-Rawson, (6) Colorado, (7) Neuquén, (8) Salado. (b) Stratigraphic correlation chart of the studied units, sea-level curve (Haq, 2014), and $\delta^{18}O$ record of South Atlantic foraminifera (Cramer et al., 2009).

III-1.2 Tectonic and stratigraphic setting

The MAB (Fig. 1a) is a retroarc foreland basin (Biddle et al., 1986; Wilson, 1991) resulting from the closure of the extensional Rocas Verdes Basin (RVB) in the mid-to-late Cretaceous (112-86 Ma) (Fildani et al., 2003; Klepeis et al., 2010; Fosdick et al., 2011; McAtamney et al., 2012). The MAB is oriented subparallel to the Jurassic-Neogene Southern Patagonian Batholith (Hervé et al., 2007). These plutonic rocks intruded low- to high-grade metamorphic rocks of the late Devonian-Permian Andean metamorphic complex (Hervé et al., 2003), the Ordovician-Permian Darwin Cordillera (Barbeau et al., 2009; Hervé et al., 2010), and Middle Jurassic-Early Cretaceous volcaniclastic to metavolcanic rocks of the Tobífera-Lemaire-El Quemado formations (Wilson, 1991; Pankhurst et al., 2000; Calderón et al., 2007; Malkowski et al., 2016). The fold-thrust belt that bounds the MAB to the west (Fig. 1a) exposes remnants of the Upper Jurassic-Lower Cretaceous (154-100 Ma) siliceous, argillaceous, volcaniclastic, and ophiolitic rocks of the extensional RVB (Dalziel, 1981; Fildani and Hessler, 2005; Calderón et al., 2007), as well as metamorphic basement and clastic deposits of the exhumed foreland basin strata (Fig. 1a). Together, the terranes described above constitute potential sediment sources for the strata studied here.

III-1.2.1 Stratigraphic overview of the study area

Our study encompasses the uppermost Fuentes, Rocallosa, Dorotea, and Chorrillo Chico formations, representing the late Campanian to Thanetian (Fig. 1b). The Fuentes Formation (Campanian) is a shale-dominated succession with thin sandstone intercalations, overlain by the Rocallosa Formation (Maastrichtian-Danian?) characterised by fine-to-coarse-grained, argillaceous, glauconitic sandstones, which in turn are overlain by the Chorrillo Chico Formation (Paleocene) composed of bathyal shales, siltstones, and clay-rich glauconitic sandstones (Thomas, 1949; Charrier and Lahsen, 1969; McDonnald, 1986; Álvarez et al., 2006; Mpodozis et al., 2011). The latter formations were studied along the northern coast of the Skyring Sound, Riesco Island (Fig. 2a, c), and Brunswick Peninsula (Fig. 2a, d) within the Magallanes Province of Chile (Fig. 2a). The Dorotea Formation (latest Campanian to Selandian) is a sandstone-dominated unit intercalated with conglomerates and mudstones, with southward-directed clinoforms representing a shelf-edge deltaic system (Covault et al., 2009; Schwartz and Graham, 2015; Gutiérrez et al., 2017; Manríquez et al., 2019). The Dorotea Formation was studied at Cerro Pelario, the Demaistre locality, as well as the southern extension of Sierra Dorotea within the Última Esperanza Province of Chile (Fig. 2a, b).

Additionally, we present new petrological data of the turbidite deposits of the Cabo Naríz beds (equivalent to the Chorrillo Chico Formation) studied previously by Sánchez et al. (2010) along the west coast of Tierra del Fuego (Fig. 2a). This strategic distribution of stratigraphic sections (Table 1, Fig. 2a) allows us to study in greater detail the facies changes and depositional evolution along the axis of the basin, particularly in a poorly-known portion of the MAB. In Argentina, the Maastrichtian-Danian deposits are referred to as the Calafate Formation (Fig. 1b) around the Lago Argentino, north of our study area (Fig. 2a), and as the Monte Chico and Cerro Dorotea formations (Fig. 1b) in the Rio Turbio area, to the east of our study area in the Última Esperanza Province (Fig. 2a). South of our study area, in Tierra del Fuego (Fig. 2a), the Maastrichtian-Danian is represented by the Cerro Cuchilla Formation-Cabo Nariz beds (Fig. 1b) (within the Chilean part) and Policarpo Formation (Fig. 1b) (within the Argentinian part) (Olivero et al., 2003; Sánchez et al., 2010).

Table 1. List of measured stratigraphic sections studied and their geographic distribution along the basin strike. For the geographical location, see Fig. 2.

Section Name	Abbreviated Name	Formation studied	Location
Sierra Dorotea	**SD**	Dorotea	Última Esperanza Province
Demaistre	**DM**		
Cerro Pelario	**CP**		
Punta Eulogio	**PE**	Rocallosa	Magallanes Province
Punta Rocallosa	**PR**		
Punta Canelos	**PC**	Chorrillo Chico	
Punta Prat	**PP**	Rocallosa-Chorrillo Chico	
Fuerte Bulnes-Puerto del Hambre	**BH**	Rocallosa	
Río Blanco	**RB**	Chorrillo Chico	

Figure 2.

(a) Geographical distribution of study areas and other locations mentioned in the text. (1) Manzano well, (2) Evans well, (3) Cóndor well.

(b) Geological units, sections, and samples in the Ultima Esperanza Province, (c) Skyring Sound, and (d) Brunswick Peninsula areas within the Magallanes Province. [α]Fosdick et al., 2015; [β]Hervé et al., 2004; [δ]Alvarez et al., 2006.

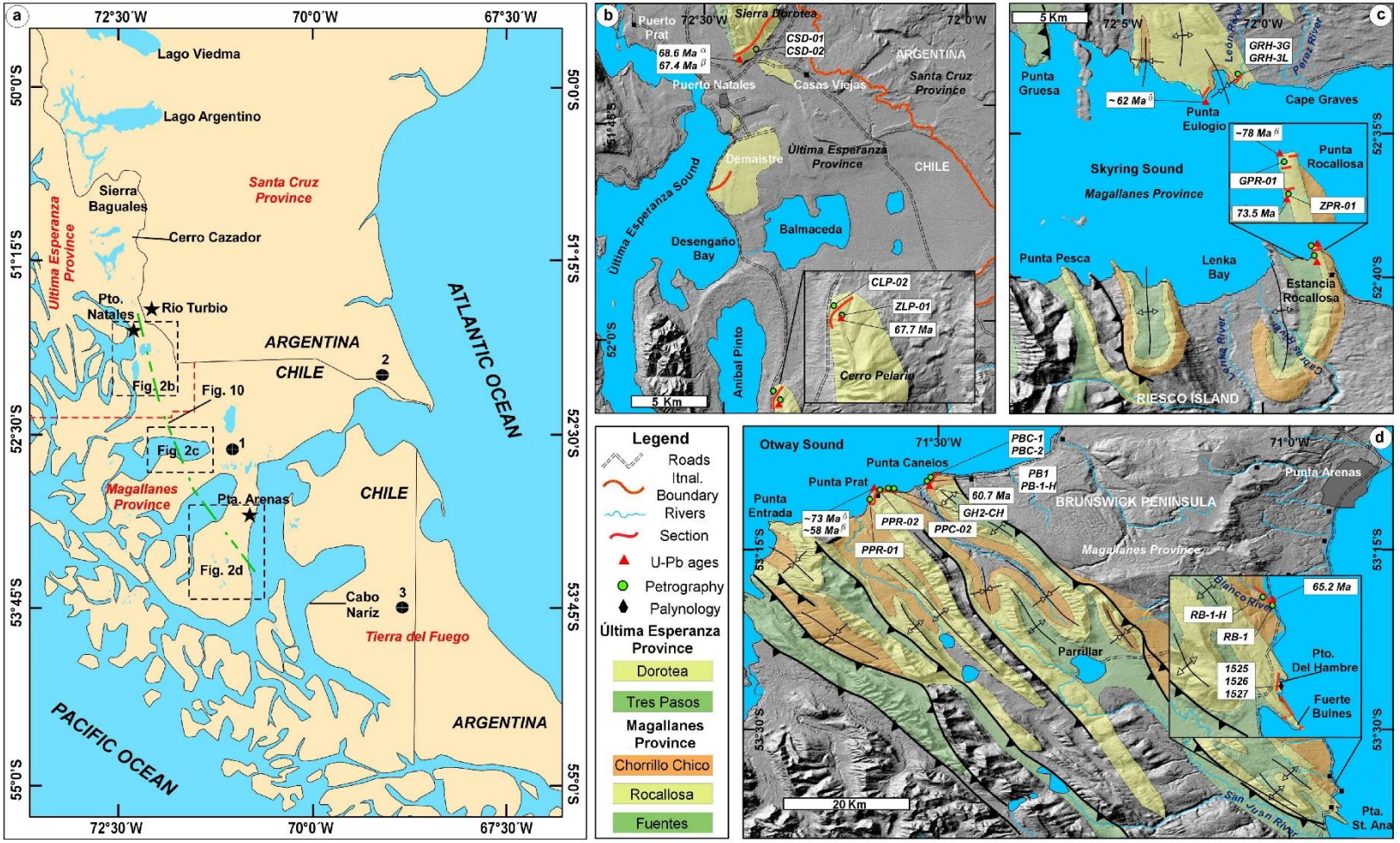

III-1.2.2 Tectonic events in the fold-thrust belt

During the Maastrichtian-Danian transgression, a deformational pulse that took place in the Southern Patagonian Andes may have been one of the primary drivers of transgression in the MAB. In the Ultima Esperanza Province, it is inferred by the Tenerife thrusting (with a basal décollement on the argillaceous Zapata Formation) between 74-27 Ma (Fosdick et al., 2011), which continued exhuming the Tobífera Formation and incorporated Upper Cretaceous foredeep deposits into the fold-thrust belt. In the Magallanes Province, Betka et al. (2015) suggested a phase of out-of-sequence thrusting and basement-involved reverse faulting beginning in the Maastrichtian and extending to the Paleogene. The deformation and cooling ages of ophiolitic blocks in the hinterland around 74-72 Ma (Rapalini et al., 2008) together with progradation and depositional system shoaling (Tres Pasos and Dorotea formations) (Covault et al., 2009; Romans et al., 2009; Schwartz and Graham, 2015; Schwartz et al., 2017; Gutiérrez et al., 2017) may also reflect deformation in the fold-thrust belt. In Tierra del Fuego, brittle-ductile deformation in the internal thrust-belt took place between ~72-64 Ma ("D1" contraction event; see Torres-Carbonell et al., 2013) concomitant with an uplift in the Cordillera Darwin Complex (Kohn et al., 1995).

III-1.3 Methods

We measured nine stratigraphic columns (some composite; Table 1, Fig. 3) totalling ~1500 m, using a Jacob staff and tape measure on the best available exposures, which led us to recognise facies associations comprised by some sub-facies associations. Palaeocurrent measurements were taken mainly from trough axes (i.e., 3D trough cross-lamination/stratification and 3D rib and furrow structures), planar cross-lamination, ripple marks, flute casts, current-oriented wood or tree trunks, and tool marks. The transport direction of the latter two bidirectional structures was usually resolved considering other unidirectional structures nearby. Bioturbation variability was expressed in terms of the Bioturbation Index (BI; after Bann et al., 2004), which is a semi-quantitative estimate of the intensity of biogenic structures based on observations in two-dimensional, vertical to sub-vertical exposures. Additional sedimentological information originally included as an appendix in the published paper is incorporated in this text as Figures A1.

We used a model-independent approach for the sequence stratigraphic analysis (Catuneanu et al., 2011). Our objectives were to (1) highlight changes in basin accommodation on a regional scale; (2) provide a better understanding of the interplay

between the depositional elements in time and space; (3) allow the integration of diverse local stratigraphic architectures among the different sectors of the basin. Recognition of surfaces of sequence stratigraphic significance, stratal stacking patterns in outcrops, and their correlation among the different parts of the study area are mainly based on changes in accommodation-sedimentation dynamics and vertical relationships among the sedimentary environments.

Fine- to medium-grained sandstone samples were used preferentially for petrographic point-counting (n=27), detrital zircon uranium-lead (U-Pb) geochronology (n=4), and palynological analysis (n=3). For sandstone modal analysis, we conducted thin section point counts of 310 to 500 grains by using the Gazzi-Dickinson method (Ingersoll et al., 1984). Modal compositions were then normalised to quartz-feldspar-lithic (QFL) and monocrystalline quartz-feldspar-total lithic (QmFLt) ternary plots to be compared with the tectonic fields of Dickinson (1985). The raw point-counting results are presented in Table A (originally included as an appendix in published paper).

Detrital zircon U-Pb ages were used to assess provenance, as well as to calculate the maximum depositional ages of the studied units. The RB1 and PB1 samples were collected from the lower part of the Chorrillo Chico Formation (Figs. 2d, 3a). In contrast, samples ZPR1 and ZLP1 correspond to the lower and upper parts of the Rocallosa Formation (Figs. 2b, c, 3a, b), respectively. Sample RB1 (n=54) was analysed using LA-MC-ICP-MS at the Mass Spectrometry Laboratory (CEGA) of the University of Chile. Samples ZPR1 (n=79) and ZLP1 (n=83) were analysed using LA-ICP-MS at the Laboratory of Isotopic Studies of the Geosciences Centre, Mexico (UNAM). Sample PB1 (n=63) was analysed at the Geochronology Laboratory of SERNAGEOMIN by using LA-ICP-MS. To determine maximum depositional ages of individual sandstone samples, we calculated the weighted mean age of the youngest peak ($\geq$ 2 grains within a 2σ-level error overlap; after Dickinson and Gehrels, 2009; Schwartz et al., 2017) of the age spectrum. We report each age with its mean square weighted deviation (MSWD) and the associated range of acceptable MSWDs based on the number of analyses contributing to each calculation (after Mahon, 1996). The number of detrital zircons analysed by formation (at least 117) helped to ensure that no fraction ≥ 0.05 was missed with a 95% confidence level (Vermeesch, 2004). Therefore, there is a good representation of all populations to interpret provenance. Likewise, when we considered the number of grains analysed per sample (to calculate a maximum depositional age), there was a 95% chance of finding at least three grains from every population that

makes up ≥ 7% of the total zircon content (Rossignol et al., 2019). A detailed description of the separation, analytical and statistical technique, as well as raw histograms and Concordia plots for detrital zircon analyses, can be found in Annex C-1. The detrital zircon U-Pb geochronological analyses are shown in Annex C-2.

We selected fine-grained sandstone samples from the Rocallosa Formation for palynomorph identification. Approximately 5 g of each sample was crushed and oven-dried (60°C), after which the samples were treated with 10% HCl, HNO3, and 40% HF to dissolve carbonate and silica minerals before the acetolysis process; the residues were mounted in glycerin jelly for observation under an Olympus CH/30 microscope and photographing using an Olympus CX 31 301 camera. All slides are presently housed in the Laboratory of Paleopalynology of the Departamento de Ciencias de la Tierra, Universidad de Concepción, under the codes 1525, 1526, and 1527. We inferred temperature data and the climate type for each identified terrestrial palynomorph identified based on its botanical affinity with the nearest living relatives, assuming little evolutionary change in morphology or habitat preference for each taxon. However, care must be taken with these inferences since a single fossil taxon could be affiliated with one or several modern families with different ecological tolerances, or it could have been affected in the past by allogenic factors that influenced the vegetational composition (for further details about climatic and ecological interpretation cautions see Bowman et al., 2014).

III-1.4 Results and interpretations

III-1.4.1 Sedimentology

We recognised nine facies associations (FA) (see facies synthesis in Table 2) which were described in stratigraphic order, i.e., from the Fuentes to Chorrillo Chico formations. We measured a total of 238 palaeocurrents, of which 86 are from the Cabo Naríz beds. The section location, outcrop photos and additional sedimentary and biogenic structure images are provided in Figures A.1.

III-1.4.1a Fuentes Formation

The upper part of the Fuentes Formation comprises FA1 and FA2 (Fig. 3a) in section BH (Table 1, Fig. 2d). FA1 consists of thin intercalations of laminated shales (Fh), and massive to vaguely laminated siltstones and sandstones (Slm, Sm). Some tabular mudstone (Fm) intervals are also present, which reach up to tens of meters in thickness (Fig. A1a).

Occasionally, units grade internally in cycles typically about 15 cm thick. Slump structures (Fig. 4a), tool marks at the bases of Sm facies, and laterally continuous contorted marlstone beds were also observed. FA2 occurs in the uppermost part of the unit (Fig. 3a), underlying the Rocallosa Formation. FA2 (Fig. A1b) is characterised by tabular Fm and Fh facies that rapidly grade upward into well-stratified siltstones (Slh), massive, fine-grained sandstones (Sm) with tool marks at the base, fine-to-medium-grained sandstones with hummocky cross-stratification (Shcs) and planar, low-angle cross lamination (Spl) commonly showing some wave ripple-lamination (Sw) that is slightly contorted at the tops of units. The glauconite content is ~5% in the mudstone and ~30% in the sandstone facies. In Fh and Fm facies, the bioturbation is low to moderate (BI 0-3). In Fh, bioturbation is characterised by abundant *Stelloglyphus llicoensis* (Fig. A1.1), *Chondrites* isp., *Phycosiphon incertum* ?, *Planolites* isp., and rare *Rhizocorallium* isp., and *Bergaueria* isp. In Fm, bioturbation is characterised by *Phycodes* isp. (Fig. A1.2), *Palaeophycos* isp., *Cladichnus* cf. *fischeri* (Fig. A1.3) and *Phoebichnus bosoensis* (Fig. A.1.4). The Sm and Slm facies are slightly more bioturbated (BI 1-4) with trace fossils confined to the bedding planes, containing *Palaeophycus* isp., *Planolites* isp., *Chondrites* isp., *Zoophycos* isp., *Thalassinoides* isp., *Cylindrichnus* isp., *Teichichnus* isp. (Fig. A1.5) and undetermined trace fossils. Bidirectional palaeocurrent indicators suggest west to east flows.

The fine-grained nature of FA1 and degree of bioturbation related to the Zoophycos ichnofacies suggest a low-energy and open marine environment below the storm-wave base (Bann and Fielding, 2004; Buatois and Mángano, 2011). The thick mudstone facies (Fm) and internally graded units (Fh and Sm) reflect settling of hemipelagic mud and deposition by mud-rich, low-density turbidity currents (Shultz et al., 2005; Romans et al., 2009; Malkowski et al., 2017a) in an outer shelf setting, as supported by the slump and contorted structures, as well as the abundant presence of *Stelloglyphus llicoensis* commonly found in this kind of environments (Le Roux et al., 2008). The relative abundance of silt and sand grain sizes, as well as storm- (Shcs) and wave-generated (Sw) structures in FA2, indicate that the depositional setting was shallower than that of FA1, above storm wave base and close to fair-weather wave base (Rossi and Steel, 2016). However, the trace fossil assemblage still indicates a fully marine environment. These turbidite/tempestite events favoured the colonisation of opportunistic organisms, a mechanism that has proved to be effective to provide higher oxygenation and nutrients to an otherwise poorly oxygenated setting (Rivera et al., 2018). The Shcs and Spl facies suggest the influence of strong oscillatory or combined flows, whereas the associated symmetrical ripples (Sw) indicate the

waning phases of storm-related events (Dott and Bourgeois, 1982). The action of subsequent surge flows can explain the slightly contorted wave ripple tops. Those flows developed high shear stress and liquefied the previously deposited beds. Alternatively, contorted wave ripple tops could also have resulted from gravity-driven instability acting on unconsolidated water-saturated sediments (McDonald, 1986; Myrow et al., 2002). FA2 represents sedimentation in a phase of progradation from an offshore to a lower shoreface environment.

III-1.4.1b Rocallosa Formation

Most of the Rocallosa Formation in sections BH, PR, PE, and PP (Table 1, Fig. 2c, d) is dominated by FA3, while its upper member is mainly composed of FA4. FA2 is locally present (Fig. 3a). FA3 comprises a crudely coarsening- and thickening-upward succession of up to 70 m thick and consists of wispy and planar laminated siltstones (Slh), vaguely stratified, massive siltstones (Slm), well-stratified and massive, bioturbated, fine-grained sandstones (Sm) internally showing crude normally graded beds up to 10 cm thick.

Table 2. Characteristic facies and interpreted sedimentary processes of the studied units in the Magallanes-Austral Basin. BI=bioturbation index.

Code	Lithology	Sedimentary structures	Geometry–contacts–thickness	Fossils – Bioturbation	Sedimentary processes
Fh	Light- to greenish-grey shales and silty shales; carbonaceous or coaly paper shales.	Finely laminated to fissile; normally graded from silt to laminated shales; slump and contorted bedding.	Tabular – Sharp, planar to undulate (wavy) contacts – 15 cm up to 1m.	Rare fossils; (BI=0-2) *Chondrites* isp., *Phycosiphon incertum ?, Planolites* isp., and rarerly *Bergaueria* isp., *Zoophycus* isp.	Deposition by suspension and vertical settling in very low- to moderated-energy and poorly-oxygenated environments, below storm-wave base; or in quiet, low-energy environments with abundant organic material supply and undisturbed by current energy.
Fm	Light-black to greyish mudstones.	Massive to vaguely laminated.	Tabular – sharp and planar contacts – up to 10's m.	Rare fossils; (BI=2-3) *Phycodes* isp., *Stelloglyphus llicoensis, Palaeophycos* isp., *Cladichnus* cf. *fischeri,* and *Phoebichnus bosoensis, Planolites* isp., *Taenidium* isp., *Chondrites* isp.	Deposition by suspension and fast vertical settling in a very low-to-moderated-energy environment, below storm-wave base. In some cases, structureless appearance can be by bioturbation.
Slm	Tan, and greyish siltstones, and very fine-grained sandstone.	Massive to vaguely laminated; normally graded.	Tabular – Sharp-gradual, planar to undulate (wavy) contacts – 15 cm up to 90 cm	Null fossils; (BI=0-1) *Cylindrichnus* isp., horizontal and vertical unidentified trace fossils.	Sedimentation by fast vertical settling in a low-to-moderated-energy environment.
Slh	Beige to pale yellow, buff (weathered) siltstones.	Horizontal laminated, wispy laminated.	Tabular – Sharp, planar to undulate (wavy) contacts – 15 to 50 cm, up to 1 m.	Null fossils; (BI=0-1) horizontal and vertical unidentified trace fossils.	Sedimentation by suspension and vertical settling in a low-to-moderated-energy environment with alternating low and moderate current intensity on the seafloor.
Hlh	Rhythmic intercalations of pale siltstones, very fine-grained sandstones, and reddish mudstones.	Horizontal to low-angle laminated, tidal rythmites; lenticular bedding.	Tabular– sharp contacts—sets of up to 3 m.	Pervasive bioturbation (BI=4-5).	Fluctuations in strength and suspended sediment supply, likely reflecting seasonally or climatic controls, typically associated with a tidal regime.
Sm	Tan, whitish to green, and greyish very fine-to-very coarse-grained (glauconitic or shell-rich) sandstones.	Massive or crudely graded; amalgamated; poorly bedded.	Sub-tabular to tabular, lenticular–sharp and planar contacts, or erosive base–10 cm up to 10's m.	Lenticular bodies with highly fragmented bivalves, gastropods, and oysters. Shell, pebble or mudstone lag deposits on erosional contacts; (BI=0-5) *Thalassinoides* isp., *Cylindrichnus* isp., horizontal unidentified trace fossils.	Rapid accumulation of sand from sediment gravity flows or under conditions of rapid flows carpet shear (fraction-carpet); fast accumulation of sand and shell in channels by high-energy events. Structureless appearance also can be related to bioturbation.
Sw	Beige, buff (weathered) fine-to-medium-grained sandstones.	Symmetrical and asymmetrical wave ripples, undulate lamination; slightly contorted lamination.	Tabular–sharp and planar base, rippled top surface –30 cm up to 50 cm.	Null fossils; (BI=0-2) horizontal and vertical unidentified trace fossils.	Oscillatory and combined flows in shallow waters with bottom friction; alternating traction currents in lower flow regime with vertical accretion processes.
Sr	Pale yellow, light grey very fine-to-fine-grained sandstone.	Current ripples	Tabular– sharp contacts– 30 cm up to 1 m.	Null fossils; in a few cases, mottled texture (BI=4-6).	Deposition of migrating bedforms under unidirectional currents and lower flow regime.

Shcs	Fine-to-medium-grained sandstones; commonly with pebble lag.	Amalgamated or isolated hummocky, and swaley cross-stratification/lamination.	Tabular, amalgamated–sharp or erosive base and gradual top–20 cm up to 60 cm.	Plant or carbonaceous debris; (BI=0-1).	Deposition by combined oscillatory and unidirectional currents well above storm wave-base and near fair-weather wave-base.
Spl	Grey to greenish, fine-to-medium-grained sandstones.	Lower or upper regime planar lamination; low-angle cross-lamination; well-bedded.	Tabular–sharp to gradual base– 20 cm to 1 m.	Plant or carbonaceous debris; (BI=0-2), *Skolithos* isp.	Sedimentation from suspension in calm waters or under supercritical flow conditions; related to sedimentation on the surf or swash zones of beaches.
Spa	Whitish, medium-to-coarse-grained sandstones.	High-angle, planar cross-stratification; crude to well-bedded.	Sub-tabular–sharp and scoured bases–up to 4 m.	Null fossils; (BI=0-1), *Schacylindrichnus* isp.	Related to migration of straight-crested (2D) dunes or sand waves, and scroll bars.
St	Grey to greenish, fine-to-medium-grained sandstones.	Trough cross-lamination; medium-to-large-scale trough cross bedding; tangential-based cross lamination with mud drapes.	Sub-tabular–sharp and planar contacts– 50 cm up to 4 m.	Some *Turritela* sp. and fragmented shells; (BI=1-2), *Macaronichnus* isp., *Planolites* isp., *Diplocraterion* ? isp.	Related to migrating lunate or sinuous (3D) subaqueous dunes, modified by tides forming epsilon cross-bedding. Large-scale migrating dunes are linked to prograding clinoforms.
Shb	Tan, fine- to medium-grained sandstones.	Bidirectional cross-bedding; herringbone cross-lamination; mud-drapes, and mud-partings.	Tabular–sharp contacts–30 cm to 90 cm.	Null fossils and bioturbation absent. Shell hash is common.	Related to migrating 2D-3D dunes products of the high-energy ebb and flood currents, whereas the mud represents irrupting slack water stages.
Gmm	Greyish to pale, (sub-) angular to sub-rounded pebbly to cobble conglomerates.	Sandy matrix-supported, structureless; large clasts up to 1m long.	Lenticular, tabular– sharp, erosive bases– 1 m up to11 m (amalgamated).	Shell hash, carbonaceous fragments, bioturbation absent.	Cohesive debris flow, hyperconcentrated sheet flood, generally high-shear strength preventing turbulence.
Gmg	Greyish to light brown, sub-angular to rounded, coarse to fine pebbly conglomerates.	Sandy clast- to matrix-supported, massive to normally graded, rare inverse grading.	Lenticular to subtabular–sharp, scoured bases; gradational top– up to 5 m.	Null fossils, carbonaceous fragments, bioturbation absent.	Winnowing of finer sediments forming a lag. Bed-load deposition from a diluted turbulent stream flow—inverse grading related to dispersive pressure on density-grain flows.
Gs	Greyish to dark-grey coarse shell-rich conglomerates.	Clast- (shell-) supported, normally graded shells; often massive.	Tabular to subtabular, lenticular– sharp contacts–up to 2m.	Oysters, bivalves, *Turritella* isp., and very fragmented shells; bioturbation absent.	Basal lag or shelly debris product of high-energy erosion and redeposition.

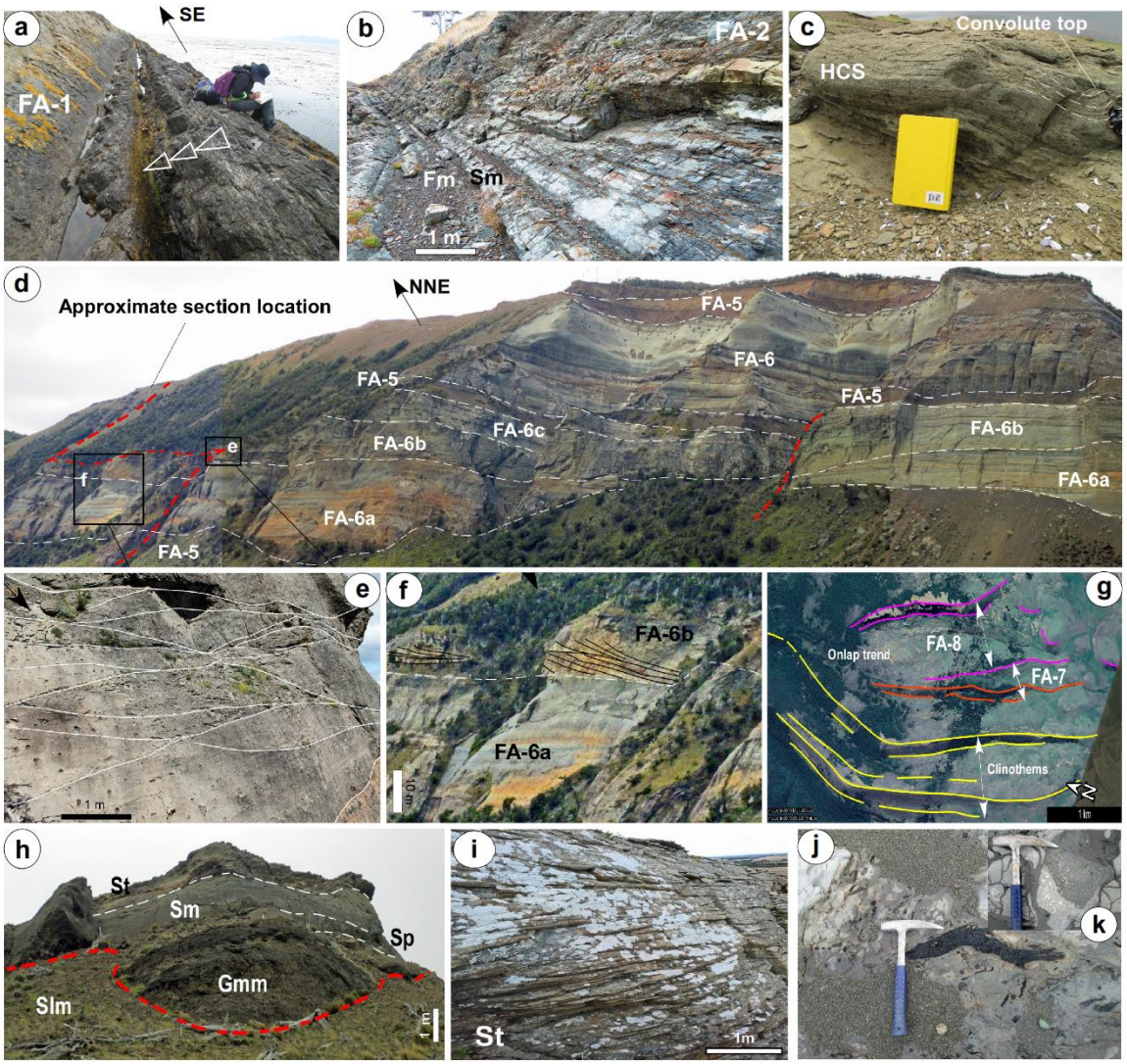

Figure A1. (a) Outcrop expression (view to SE) of FA1, note normally graded beds representing distal turbidity currents in the uppermost Fuentes Formation (section BH). (b) Outcrop expression of tabular mudrocks (Fm and Fh) intercalated with well-stratified siltstones (Slm and Slh) and massive, fine-grained sandstones (Sm). (c) Erosive-based hummocky cross-stratified (HCS) sandstone beds with (slightly contorted) wave rippled beds (Sw) at the top bed. (d) Overview (view to NE) of facies associations interpreted for the Dorotea Formation in the basal part of section SD. (e) Amalgamated channel of FA6b displaying internal planar lamination (Spl) and hummocky, and swaley cross-lamination (Shcs) locally. (f) Example of large-scale foresets of trough cross-stratification of FA6b. (g) Google Earth plane-view of clinothems of the Dorotea Formation and onlap trend of the FA8 over FA7. (h) Distribution of facies within encased channel body (FA7) of the incised valley system in section CP. (i) Washed-out megaripples in estuary mouth complex (FA8a). (j) Angular flakes of coaly wood fragments in FA9. (k) Angular to sub-angular glauconite and pumices pebbles filling scours in FA9.

Locally, hummocky cross-stratified sandstone beds (Shcs) with pebbly sandstones on their erosive bases are associated with wave-rippled beds (Sw). Glauconite is present throughout FA3 (~35-42%), and the bioturbation is variable (BI 1-4), is characterised by

Zoophycos isp., *Chondrites* isp., *Planolites* isp., *Teichichnus* isp. (Fig. A1.6), and *Palaeophycus* isp. FA4 is composed mainly of well-sorted, fine-to-coarse-grained sandstones showing Shcs facies at the base and convolute (Fig. A1c) or wave ripple lamination (Sw) on bed tops together with trough cross-bedding (St; sometimes diffuse), and planar- and low-angle cross-stratification (Spl). Additionally, well-sorted, medium-grained sandstone with low-angle cross-lamination and planar lamination (Spl; up to 1 m thick) and scour-and-fill structures are present. The scours are covered by medium-to-coarse pebbles of quartz, andesite, and reworked glauconite. In some intervals, Sm and Slh facies are intercalated. Locally, angular to sub-angular pebbles and cobbles (up to 7 cm in diameter) composed of glauconite, quartz, and lithic fragments (see Fig. 5a) are dispersed in the sandstone beds. Bioturbation is low to absent (BI 0-1). Palaeocurrent indicators are highly variable, with modes towards the ENW and ESE.

The characteristic well-developed stratification, symmetrical ripples, wispy lamination and abundant trace fossil assemblage of Cruziana ichnofacies in FA3 suggest a wave-dominated open marine environment (Bann and Fielding, 2004; Buatois and Mángano, 2011) where sedimentation mechanisms were similar to FA2. The association of erosive-based HCS beds and wave-rippled sandstones suggest episodic high-energy storm events in which strong unidirectional and oscillatory processes were active (e.g., Malkowski et al., 2016). These scours represent offshore-directed rip currents during storm events. According to its stratigraphic position and the interplay with adjacent facies associations, we interpret FA3 to represent a lower to middle shoreface. The presence of St and Spl facies on well-sorted sediments in FA4 reflects accumulation in longshore runnels and ridges within the high-energy surf and breaker zone above the fair-weather wave base. Hummocky cross-bedding grading upward to wave-rippled beds suggest progressive waning of the large-scale oscillatory flows (storm events) (Dumas and Arnott, 2006; Malkowski et al., 2016). FA4 is interpreted as a mid-to-upper shoreface environment. However, the angular to sub-angular pebbles and cobbles dispersed in scoured, coarse-grained sandstones associated with wave-generated structures and low-angle to planar lamination are interpreted as the transition to a foreshore-beach environment subject to swash processes caused by breaking waves.

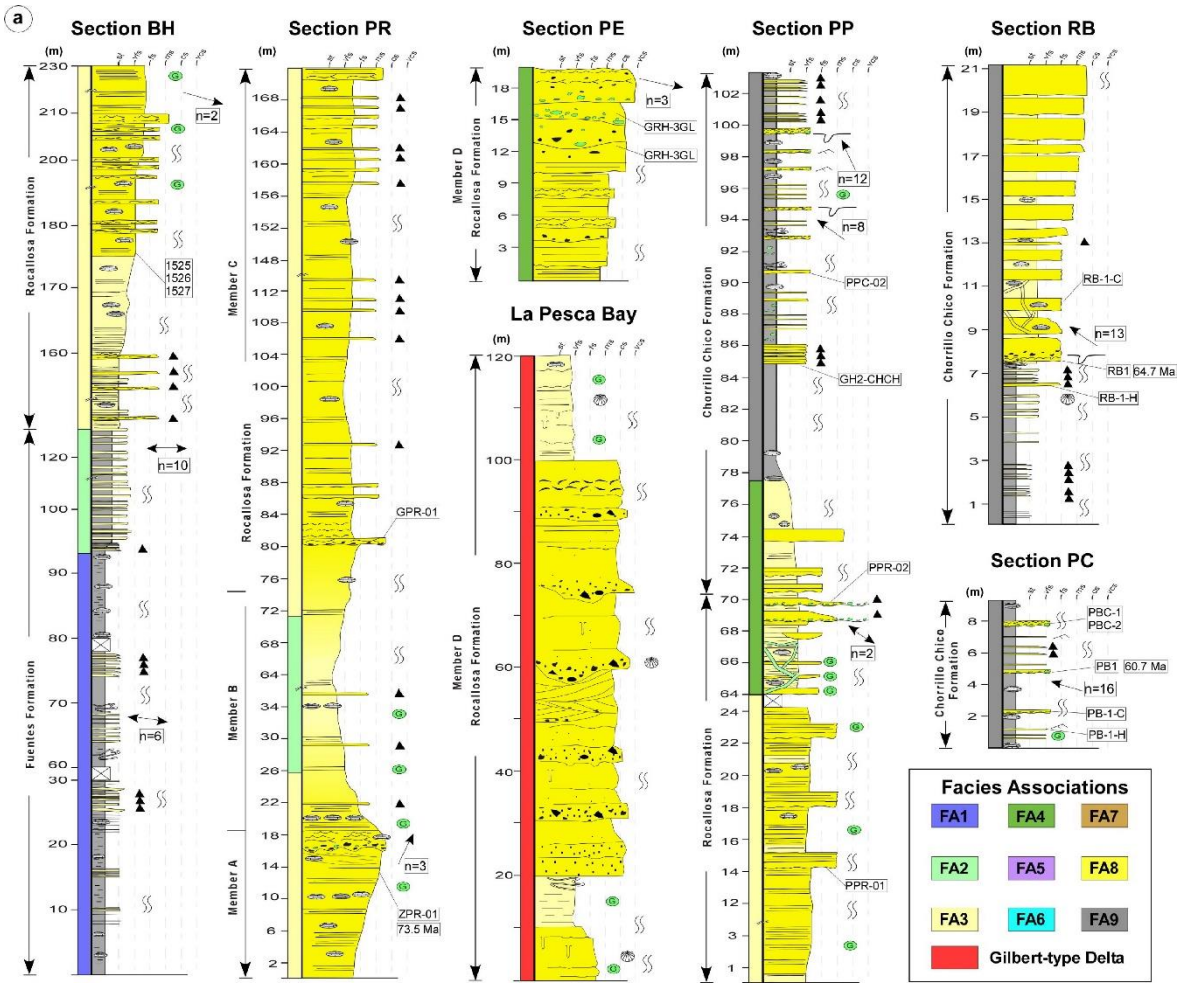

Figure 3. Measured stratigraphic sections with facies associations, palaeocurrents, and sampled intervals. (a) Stratigraphic columns of the Fuentes, Rocallosa, and Chorrillo Chico formations in the Magallanes Province. (b) Stratigraphic columns of the Dorotea Formation in the Ultima Esperanza Province. The column of La Pesca Bay is modified from Elgueta (in Álvarez et al., 2006). For the location, see Fig. 2.

III-1.4.1c Dorotea Formation

The Dorotea Formation includes FA2-8 (Fig. 3b). In sections DM and CP (Table 1, Fig. 2b) The Dorotea Formation presents facies (FA3-4) comparable with the Rocallosa Formation (studied farther south) as described above. However, amalgamated hummocky- and swaley cross-stratification (Shcs; Fig. 4b) is more abundant in FA4 of the Dorotea Formation, where pervasive bioturbation (BI 4-6) is present, as reflected by the massive, fuzzy and reworked textures in some intervals. In section CP, FA7 (Fig. 3b) comprises prominent lenticular to channeliform morphological ridges (Fig. A1h) ranging from 44-140 m long (along strike) and 5-26 m thick, enclosed in interbedded wavy laminated, very fine-grained sandstones and siltstones (Sw) (poorly exposed by vegetation) of FA3-4. FA7 is erosionally based and composed of poorly selected, matrix-supported, massive to normally graded conglomerate (Gmm, Gmg) (rarely showing bedding planes) where large sub-angular

clasts (up to 1 m in diameter; Fig. 4d) are composed entirely of massive sandstones and greenish mudstones. Sub-rounded, coarse pebbles correspond to basalt (70%), andesite (20%), and chert (10%); shell hash and carbonaceous fragments are dispersed throughout the FA7. In addition, there are massive and trough cross-stratified, medium-grained sandstone packages (Sm, St), and fining-upward successions with rip-up clasts (or shell lag mantling a scoured surface; Fig. 4e, f) at the bases, as well as rippled sandstones (Sr), laminated sandstones and siltstones (Spl, Slh) with abundant organic matter and carbonised trunks and pedogenic features in some layers. Bioturbation in FA7 is rare to absent. Overlying FA7, there is a ~90 m thick succession of fine-grained sandstones intercalated with some mafic sills exposed in a vertical cliff, which precludes their detailed study.

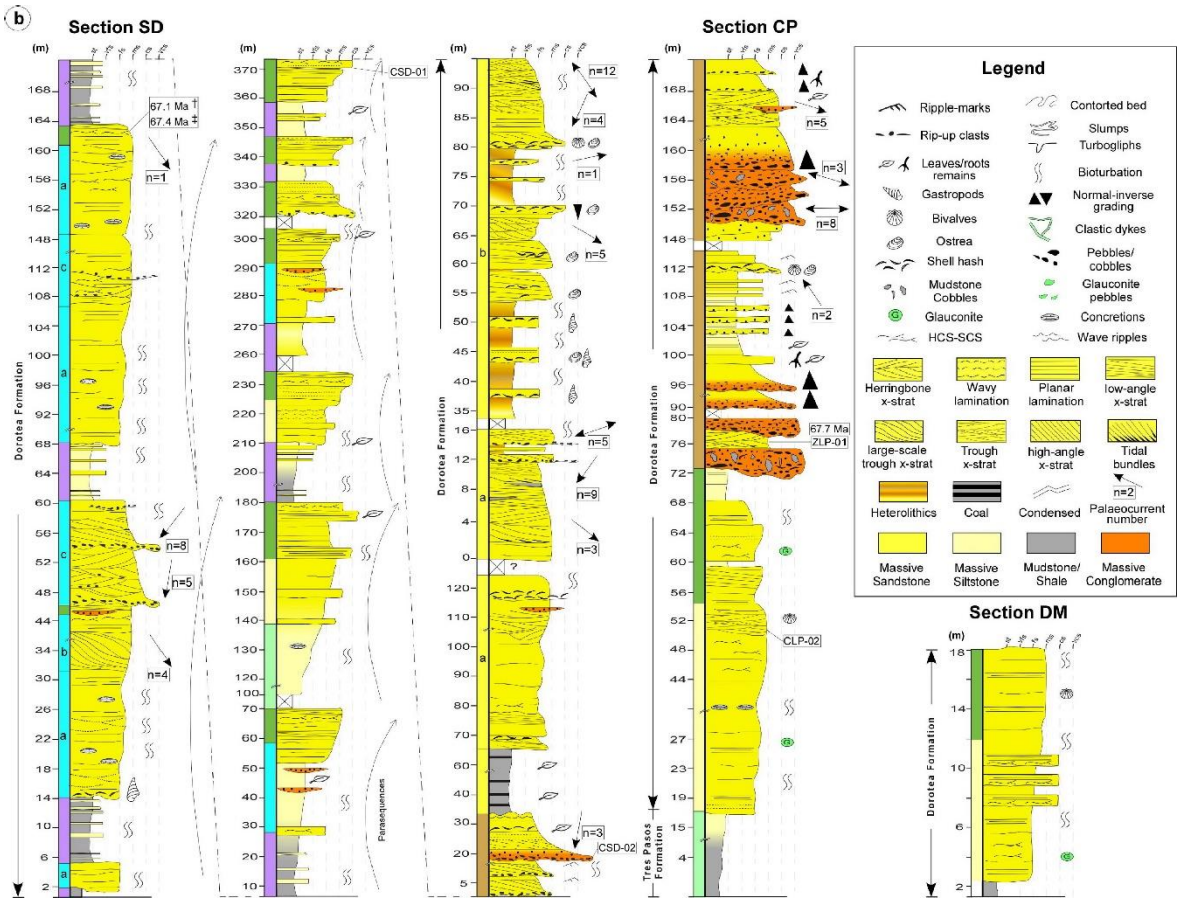

Figure 3. (Continued)

In section SD (Figs. 2b, 3b), the base to the middle part of the formation is arranged in a series of coarsening-upward packages ranging from 15 m to 100 m thick (Fig. 3b). From base to top, the basal packages consist of FA5, FA6 and rarely FA4 on top; those of the middle part of the formation consists of FA5 (or rarely FA2), FA3, and FA4 on top (Fig. 3b). FA4 differs slightly from that previously described in presenting abundant carbonaceous

material and shell hash, and in some intervals, it is possible to observe a transition from hummocky- to swaley cross-stratification (Fig. 4c). FA5 (Fig. A1d) is characterised by 1-6 m thick Fh and Fm facies, intercalated with sharp-based and tabular, Slm and Sm beds up to 50 cm thick. In a few cases, the muddy deposits are separated by 60 cm thick, tabular, very fine-grained sandstones with hummocky cross-stratification (Shcs). The bioturbation is mild (BI 0-2) characterised by *Chondrites* isp., *Zoophycus* isp., *Teichichnus* isp., *Planolites* isp., and *Taenidium* isp. and is distributed in the mudrock intervals. FA6 is divided into three sub-facies associations. FA6a is composed of lower regime planar-laminated, fine-to-medium-grained sandstones (Spl) with St, and Sm facies. Some intercalations consist of massive siltstone beds (Slm), coarse-grained lenses, scour surfaces (filled with hummocky cross-stratification or Spl facies; Fig. A1e) and carbonaceous plant debris. Some Turritela sp. and fragmented shells are present. Bioturbation is moderate (BI 1-4) and restricted to the Sm facies, which consists of *Thalassinoides* isp., *Chondrites* isp., *Taenidium* isp., *Asterosoma* isp., and *Ophiomorpha* isp. FA6b includes 2-4 m thick packages of Sm facies, and medium-grained sandstones with dune-scale (sets of ~10 m wavelength and 1 m high) trough cross-bedding (St) (Fig. A1f) frequently associated with scour-and-fill structures filled with coarse to gritty sandstones. Bioturbation is mild (BI 1-2) and represented by *Macaronichnus* isp. (Fig. A1.7), *Planolites* isp., and *Diplocraterion*? isp. FA6c is arranged in fining-upward successions of up to 8 m thick, which comprise normally graded, very coarse to (upper) medium-grained sandstones (Sm) with scoured bases and rip-up clasts, followed by medium-grained, planar or trough cross-bedded sandstones (Spa, St) with some muddy partings. Bioturbation is low (BI 0-1), being restricted to Schaubcylindrichnus isp. (Fig. A1.8).

The upper part of the Dorotea Formation, in section SD, presents FA7 and FA8 (Fig. 3b). FA7 consists of 1-10 m thick, tabular to lenticular, fining-upward sandstone units. At the base, erosion surfaces covered with pebble and/or shell lag are followed by medium-grained, massive or high-angle planar cross-laminated sandstones (Spa, Sm) that in turn grade upward into mottled, fine- to very fine-grained sandstone with ripple remnants (Sr), Spl facies, and plant remains or carbonised wood at the top. Commonly, bed tops are sharp or wavy. FA8 is divided into three sub-facies associations. FA8a consists of a 15 m thick succession of interbedded greenish, laminated, carbonaceous shales (Fh) with lignite streaks and siltstones (Slm). FA8b comprises a 70 m thick, fining-upward succession of sub-tabular geometry and complex lateral facies relationships, composed from the base upward of massive, pebbly sandstone (Sm) with abundant shelly layers followed by massive, well-stratified, upper-medium-grained sandstones (Sm) grading to lower-medium-grained,

tangential trough cross-bedded (~50 cm height) sandstones (St) with reactivation surfaces and capped by bidirectional-cross stratified beds (Shb) (Fig. 4g) showing mud partings and tidal bundles (Fig. 4h) often intercalated with horizontal-planar laminated sandstones (Spl). The succession continues with fine- to very fine-grained sandstone showing trough cross-stratification (St; ~1 m wavelength and < 0.15 m high; Fig. A1i) and planar lamination (Spl) grading laterally to medium-grained, cross-bedded sandstones (Spa, St, Shb) with scour-and-fill structures, mud drapes and tidal rhythmite (Hlh) intercalations. FA8c consists of a 60 m thick, laterally continuous (km scale) coarsening- to thickening-upward succession comprised by interbedded mudstones/siltstones and very fine-grained sandstones (Hlh) with well-developed horizontal-planar lamination, in some cases with a low angle inclination (< 5° dipping southward; Fig. 4i, j). These are commonly interrupted by scoured, lenticular to sub-tabular, medium- to fine-grained, massive, coarsening-upward, shelly sandstones and conglomerates (Sm, Gs) (Fig. 4i) with upper plane laminated tops (Spl), or by fine- to very fine-grained sandstone beds with herringbone cross-lamination (Shb) (Fig. 4g), as well as epsilon or tangential-based, trough cross-lamination with mud drapes (St). A 15 m thick, crudely fining-upward (medium- to fine-grained) tabular sandstone divides the succession into two segments (Fig. 3b) and is characterised by well-stratified, massive to low-angle planar cross-laminated sandstones (Sm, Spl) with diffuse ripple cross-lamination (Sr) and numerous conglomeratic shelly lenses (Gs). The BI is variable according to each sub-facies association, but in general, the trace fossils are of small size (compared to the previous FAs). FA8b has low bioturbation (BI 0-1), where some Skolithos isp. (Fig. A1.9) are observed. FA8c has high bioturbation (BI 4-5), restricted to the heterolithic facies, where pervasive bioturbation precludes the identification of single trace fossils. However, in some indistinct mottled and crumbly textures, vague *Planolites* isp. and *Palaeophycus* isp. are present. Palaeocurrents directions vary according to each FA, but in general, yield a southward trend with modes to the northwest, east, and west.

We interpret FA2, 3 and 4 to represent an offshore transition, lower to middle shoreface, and middle to upper shoreface (and foreshore), respectively. The amalgamation of hummocky cross-stratified-rich beds and the transition from hummock- to swaley-dominated units in FA4 suggest multiple episodes of erosion triggered by intense storms in areas close to the shoreline (Malkowski et al., 2016). The abundance of organic detritus in FA4 likely denotes fluvial influence or the proximity to plant-rich areas. On the other hand, the dominance of Fh and Fm facies along with open-marine ichnofossils in FA5 suggest a low-energy offshore marine setting below the storm-wave base. The intercalations with Slm,

Sm, and Shcs reflect periods of wave-induced reworking during storm events and/or rapid fallout of sands triggered by hyperpycnal density underflows (Bhattacharya, 2010; Rossi and Steel, 2016). Its relationship with FA6 suggests that FA5 was deposited in a prodelta environment.

The cross-bedded and massive sandstones (St, Sm) in FA6a likely represent deposition under rapidly decelerating unidirectional flows in sandy delta fronts (Bhattacharya, 2010). A fluvial influence is expressed by the abundance of carbonaceous fragments, scours and pebbles, and locally stressed conditions (Schwartz and Graham, 2015). However, the presence of Slm, Spl and Shcs facies suggests shallow-wave reworking processes of these distal delta front deposits. Coarse sandstones overlying scoured surfaces in FA6c indicate bedload deposition by fluvial currents and, considering their association with planar- and trough cross-stratified (subaqueous 2D/3D dunes) beds, we interpreted them as terminal distributary channels (Olariu and Bhattacharya, 2006). Dune-scale trough cross-bedding (FA6b) suggests high-energy currents able to develop 3D dunes migrating seaward. Such a high-energy regime is supported by the paucity of bioturbation and various scour-and-fill structures, which in turn suggest the landward connection of these subaqueous dunes with terminal distributary channels (FA6c). FA6b can be interpreted as short clinoform sets developed in a distal mouth bar, possibly indicating the rollover point of the delta front (Bhattacharya, 2010; Le Roux et al., 2010; Schwartz and Graham, 2015). In general terms, we interpret FA6 to represent a wave-influenced (if not dominated) delta front environment.

In sections CP and SD, the fining-upward succession arranged from the base up by Spa, St, Sr, Spl, and Slh facies represent point-bar deposits of meandering rivers (Miall, 2014), although the presence of carbonaceous material, shell lags, and wavy tops on channels suggest occasional wave reworking. Overbank deposits are represented by units with Sw, Slh, and Sr facies, where organic matter, wood fragments, and pedogenetic nodules are present. The coarse-grained, sediment-rich units represent bed-load deposits of braided rivers with channel-lag and gravel sheets or bars (Gmm, Gmg) and planar to cross-stratification (St, Spl) traction structures indicate lower- to upper-flow regime (Miall, 2014). The sub-angular sandstone and mudstones clasts represent channel lag intraformational conglomerates. In contrast, the sub-rounded basaltic, andesitic, and chert pebbles suggest an extrabasinal input of a nearby fold-thrust belt. We interpret FA7 to represent fluvial deposits.

Figure A1. Selected ichnofossils of the studied succession. (1) *Stelloglyphus llicoensis* in FA1. (2) *Phycodes* isp., in FA1. (3) *Cladichnus* cf. *fischeri* of FA1. (4) *Phoebichnus bosoensis* in FA1. (5) Assemblage of *Chondrites* isp., *Planolites* isp., *Zoophycos* isp., and *Teichichnus* isp. in FA2. (6) *Teichichnus* isp., and *Chondrites* isp., in FA3 (7) *Macaronichnus* isp. of FA6. (8) *Schaubcylindrichnus* isp., of FA6. (9) *Skolithos* isp. suite of FA8. (10) *Neonereites* isp., of FA9. (11) *Scolicia* (Laminites) of FA9. (12) *Rhizocorallium* isp., in the FA9.

Finally, the relatively thick (>70 m) sandstone-dominated succession of FA8a which present Sm, St, Spl, shell-rich and pebbly layers with *Skolithos* isp. suggest deposition under moderate- to high-energy conditions in a nearshore environment. This is interpreted as representing a barrier spit or submerged bar (Dalrymple et al., 1992; Reinson, 1992; Plink-Björklund, 2008; Le Roux et al., 2010). The overlying (0-16 m interval, see Fig. 3b) medium-scale, tangential, trough cross-bedded sandstones (St) associated with Shb and Hlh facies,

and abundant reactivation surfaces, scour-and-fill structures, and mud drapes reflect the existence of reversing currents (e.g., ebb and flood flows) of variable strength and strongly affected by tidal ravinement; their association with barrier deposits suggests that these are tidal-inlet deposits (Dalrymple et al., 1992; Reinson, 1992; Plink-Björklund, 2008). We interpret the overall FA8a as a high-energy estuary mouth complex. In FA8b, the heterolithic units (Hlh) are interpreted as sandy tidal mudflats (sensu Flemming, 2000) near to river mouths where alternation of tractional sand deposition and mud fallout during slack water periods prevailed, while the large-scale, low-angle inclined heterolithic beds can be associated with laterally accreted point bars of meandering tidal channels (Thomas et al., 1987). The horizontal-planar lamination on the tops of the sandstones and shell-rich conglomerates that are intercalated within the sandy tidal mudflats and the Spl facies may indicate wave action on local submerged sandy and/or shell-rich bars, or local beaches developed along the edge of the tidal flats, respectively (Le Roux et al., 2010). The fining-upward sandstones with Shb, and St facies and paired mud drapes are interpreted as point bar deposits of tidal creeks. On the other hand, the thick, tabular, fining-upward sandstone bed dividing the succession is interpreted as distal distributary mouth bars affected by dense underflows and/or seasonal river discharges transporting brackish water fauna (Plink-Björklund, 2008; Le Roux et al., 2010). The latter is supported by laterally coarsening-upward and inversely graded shelly sandstones and conglomerates. The association of Fh and Slm facies with coal streaks suggests deposition by suspension during low-energy conditions but is frequently punctuated by a clastic influx in a marsh plain surrounding the landward side of a lagoon or tidal flat. Overall, FA8b represents the middle to inner estuary sub-environment.

III-1.4.1d Chorrillo Chico Formation

FA9 dominates the Chorrillo Chico Formation in sections RB, PP, PC (Table 1, Fig. 2d) and overlies FA4 of the Rocallosa Formation. In section RB, this formation consists of a coarsening- and thickening-upward succession of mudstones (Fm), massive to normally graded glauconitic siltstones (Slm) and very fine- to medium-grained sandstones (Sm). FA9 is characterised by sharp-based Slm and Sm facies that comprises individual units 10-90 cm thick, interbedded with thick Fm or Slm facies. Amalgamated beds (0.9 m to 1.2 m thick) consist of (from the base upward): medium-grained, massive sandstones (Sm) with slightly erosive to planar bases, overlain by fine-grained, wispy, planar- or ripple-laminated sandstones (Sw, Spl, Sr) grading upward to convolute layers (Fig. 4k) or Slm/Fm intercalations capped by Fm facies. In section PP, the basal part of the formation includes

Fm facies intercalated with bioturbated (clean or glauconitic) sandstones with loaded bases and flames. Angular flakes of coaly wood fragments (aligned preferentially NNW; Fig. A1j) and angular to sub-angular glauconite and pumice pebbles fill scours. Contorted bedding in mudstones and sandstones (Fig. 4l), and flutes are common. Bioturbation is intense (BI 3-6) and characterised by ichnogenera such as Thalassinoides isp., Neonereites isp. (Fig. A1.10), Scolicia (Laminites) (Fig. A1.11), Asterosoma isp., Zoophycos isp., Phycosiphon incertum, Planolites isp., Chondrites isp., Ophiomorpha nodosa, Rhizocorallium isp. (Fig. A1.12), Paradictyodora?, Taenidium barreti, Nereites missourensis, and local occurrences of Skolithos isp. Palaeocurrent indicators yield palaeoflow to the NW. Similarly, palaeocurrents in the Cabo Nariz beds are towards the northwest.

Individual beds are interpreted as a low-density turbidity currents deposits because the basal tool marks, traction structures and normal grading indicate layer-by-layer deposition under turbulent and subsequent waning flow conditions (Shultz et al., 2005; Haughton et al., 2009; Romans et al., 2009; Malkowski et al., 2017a). Massive sandstone beds (Ta), wispy, planar- or ripple-laminated sandstones (Tb, Tc), as well as interbedded siltstones and mudstones (Td) capped by mudstones beds (Te) correspond to internal Bouma divisions (Fig. 4l). However, the presence of angular, coaly wood fragments, glauconite, and pumice pebbles (Fig. A1k) within a fine-grained matrix filling scours is interpreted as debris-flow deposits (H3) and together with the alternating bioturbated (clean or glauconitic) sandstones (H2, H1) within mudstones could represent internal sub-divisions of hybrid beds (Haughton et al., 2009) linked to turbiditic deposits. The trace fossil assemblage shares characteristics of the Zoophycos and Nereites ichnofacies (Buatois and Mángano, 2011) and given the benthic foraminifer content (Charrier and Lahsen, 1969; Rivera, 2017), both suggest deposition in bathyal water depths. Similar facies have been recognised in deep-water turbidites elsewhere in the basin where it is associated with relatively distal or off-axis deposition in lower fan, basin plain, or slope settings (Shultz et al., 2005; Romans et al., 2009; Malkowski et al., 2017a).

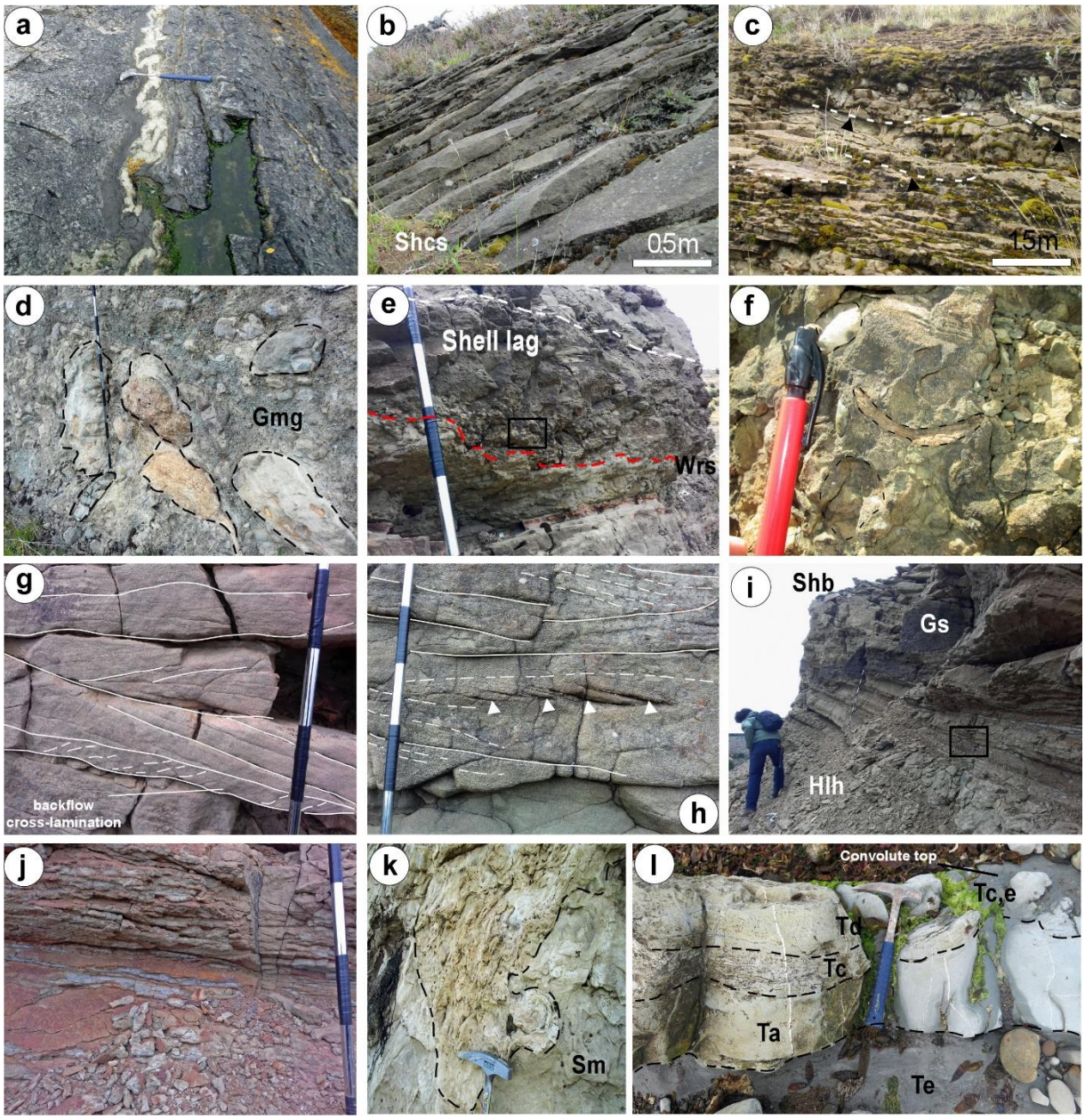

Figure 4. (a) Slump structures in the Fuentes Formation. (b) Amalgamated beds of hummocky and swaley cross-stratification of FA4. (c) Swaley cross-stratification in FA4. (d) Example of mudstone/sandstone blocks in FA7. (e) Shell lag and wave ravinement surface (Wrs) on the fluvial channels marking the start of TST in section Cerro Pelario. (f) Close-up of shells and bivalve moulds. (g) Herringbone and bidirectional cross-stratification in estuary deposits (FA8), section Sierra Dorotea. (h) Tangential, cross-bedding with reactivation surfaces and tidal bundles. (i) Example of low-angle inclined heterolithic units overlain by tidal creek channels in FA8b. (j) Close-up of heterolithic facies. (k) Plan view of contorted bedding in the Chorrillo Chico Formation in section Rio Blanco. (l) Bouma sequence in turbidite deposits of the FA9. Jacob's staff divisions each 10 cm.

III-1.4.2 Sandstone petrography and detrital zircon geochronology

III-1.4.2a Modal composition and detrital zircon U-Pb age distribution

Rocallosa and Dorotea formations. Sandstones are classified as lithic arkose. Monocrystalline quartz constitutes 82% of the total quartz grains in the samples, whereas the feldspar grains are almost in the same proportions between plagioclase (59%) and potassium feldspar (41%). Potassium feldspar (commonly altered; Fig. 5a) is dominated by microcline and orthoclase with perthitic textures (Fig. 5b). The lithic fragments are mainly volcanic (60%; Fig. 5a), followed by metamorphic (21%; Fig. 5c, d), and sedimentary rocks (19%; Fig. 5e). Some well-preserved plutonic fragments are also observed (Fig. 5f). Volcanic lithics are dominated by felsitic (44%; Fig. 5f, g) and microlitic textures (36%; Fig. 5h), whereas the metamorphic lithics are mainly micaceous schist (Fig. 5c), and (meta-) volcanics (Fig. 6g). There are also pelitic fragments (Fig. 5e) accompanied by tremolite-actinolite and chlorite minerals. The detrital zircon age spectrum in sample ZPR1 ranges from 67.7 to 276.5 Ma and shows three significant age peaks at 68-81 Ma, 93-107 Ma, and between 142-160 Ma, with a small peak at 277 Ma (Fig. 6a). The detrital zircon age distribution of sample ZLP1 is similar to that of ZPR1, ranging from 67.1 to 2204 Ma, with main peaks at 69-73 Ma, 92-108 Ma, and 146-171 Ma, but older zircon peaks at 272-315 Ma, 615-640 Ma, and 1930-2200 Ma are better represented (Fig. 6a).

Chorrillo Chico Formation. The sandstones are classified as lithic arkose. Monocrystalline quartz (91%) dominates and increases up-section. Plagioclase (64%) is the main feldspar, but samples closer to the Rocallosa contact are potassium-feldspar-rich and impoverished in lithic fragments. The dominant lithic fragments are of volcanic origin (62%), followed by sedimentary lithics (29%; Fig. 5e) and, to a lesser extent, metamorphic lithics (metapelites; 9%). Volcanic lithics show mainly microlitic (47%; Fig. 5h), lathwork (29%; Fig. 5i), and felsitic textures (12%), but some devitrified volcanic lithics (Fig. 5j) and plutonic fragments (Fig. 5f) are also observed. In general, the sedimentary lithic content increases up-section, as do the abundance of chert and vitric shards (Fig. 5k). The glauconite grains are fragmented and reworked, unlike those of the Rocallosa Formation, which are mainly authigenic. The detrital zircon age distribution of sample PB1 ranges from 54 to 131 Ma and contains a dominant age peak at 65-100 Ma (Fig. 6a). A minor subpopulation that is not discriminated on the probability density curve but differentiated in the raw data ranges from 54-60 Ma (Paleogene), and 110-131 Ma (early Cretaceous). In this sample, the absence of late Jurassic and much older grains is apparent. For sample RB1, detrital zircon U-Pb ages

range from 64 to 655 Ma and are characterised by three significant age peaks at 67, 77, and 95 Ma and a small peak at 108-113 Ma (Fig. 6a). Additionally, a few older grains of early Cretaceous (134 Ma; 1 grain) and Paleozoic-Neoproterozoic (528-655 Ma; 2 grains) ages are present.

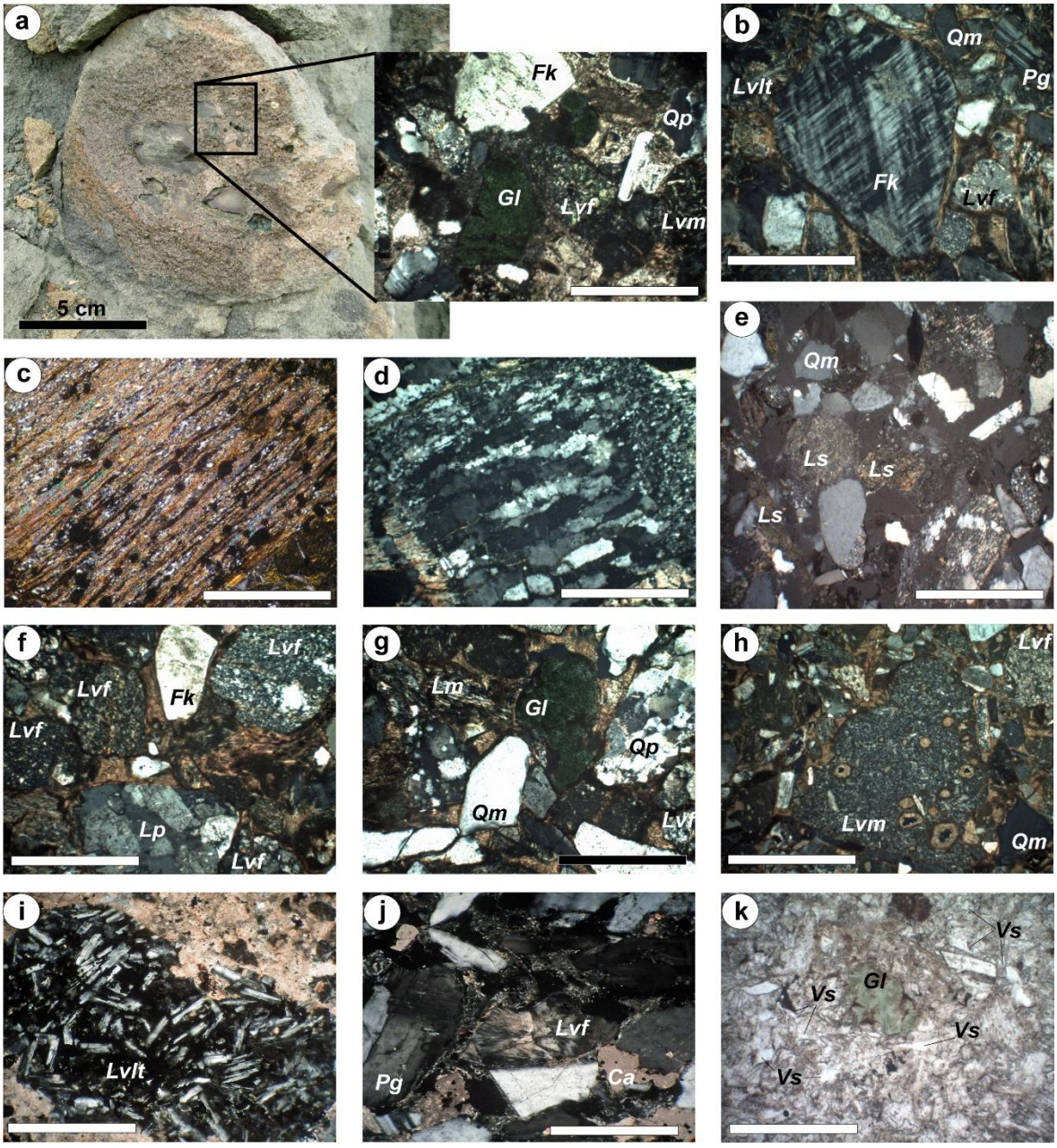

Figure 5. Sandstone framework of the formations studied. (a) Cobble of Member D of the Rocallosa Formation showing (inset) abundant reworked glauconite (Gl) grains, volcanic lithics, and altered K-feldspar (Fk). (b) Microcline grain with exsolution textures. (c) Micaceous schist lithic fragment. (d) Polycrystalline quartz fragment of metamorphic origin. (e) Pelitic sedimentary lithic fragments (Ls). (f) Abundant felsitic (Lvf) volcanic lithic and some plutonic lithic fragments (Lp). (g) Polycrystalline quartz (Qp), felsitic (Lvf) volcanic lithic, metamorphic lithic (Lm) grains. Note siliceous protolith of the metamorphic lithic fragments. (h) Example of microlitic (Lvm) texture with palagonite filling (partly) vesicles of a basalt fragment. (i) Lathwork

texture (Lvlt) of volcanic lithic, suggesting the input of mafic rocks. (j) Devitrified felsitic volcanic lithic in the Chorrillo Chico Formation, suggesting a contribution from the Tobífera Formation. (k) Vitric shards (Vs), glauconite, and angular crystals of quartz. The scale bar is 0.5 mm.

Cabo Naríz beds. The sandstones are classified as feldspathic litharenite. Monocrystalline quartz (80%) dominates in all the studied samples, whereas potassium feldspar (60%) slightly outweighs the plagioclase (40%) content. The lithic fragments are mainly volcanic (74%), followed by metamorphic (17%), and sedimentary rocks (8%; which increase up-section). Lathwork (56%) and felsitic (35%) textures predominate in volcanic lithics (Fig. 5g, i), and micaceous schists in the metamorphic fragments (Fig. 5c). Notably, lower samples from the Cabo Naríz beds are enriched in potassium feldspar, monocrystalline quartz, as well as metamorphic and felsitic volcanic lithic fragments. The detrital zircon age distribution of the Cabo Naríz samples (Sánchez et al., 2010) shows a dominant age peak at 75 Ma, and other significant peaks at 58, 88-94, and 107 Ma, with some minor age peaks at 131 and 161 Ma, and a few Paleozoic-Mesoproterozoic grains also present (Fig. 6a).

III-1.4.2b Provenance record inferred by U-Pb ages and compositional data

The mean modal composition of the Rocallosa-Dorotea Formations (Table B; $Q_{34}F_{44}L_{22}$, $Qm_{25}F_{44}Lt_{30}$) and Chorrillo Chico Formation (Table A; $Q_{34}F_{44}L_{22}$, $Qm_{27}F_{44}Lt_{30}$) reflects a dissected arc tectonic field (Dickinson, 1985) (Fig. 7), which suggests that those units were derived from the unroofing of the Andean magmatic arc (including plutonic roots and volcanogenic material). A similar interpretation applies to the Cabo Naríz beds (Table A; $Q_{19}F_{31}L_{50}$, $Qm_{31}F_{44}Lt_{54}$; misinterpreted as the Cerro Toro Formation in Romans et al. 2010), in which samples plot within the transitional arc field (Dickinson, 1985). Some subtle compositional trends are observed in the Chorrillo Chico Formation (Fig. 7), of which the modal signature of the basal samples is more related to the basement uplift field and for the uppermost samples to the recycled orogen field (Dickinson, 1985). For the Cabo Naríz beds, a compositional trend is unclear despite the richness in K-feldspar and monocrystalline quartz of the lower samples. The Rocallosa-Dorotea formations samples also lack a clear trend.

Based on the presence of Campanian to Paleocene (~80-56 Ma) detrital zircon ages both in the Dorotea-Rocallosa and Chorrillo Chico-Cabo Naríz samples, coincident with the assigned biostratigraphic ages for those formations (Fig. 6a), we interpret a continuous delivery of arc material from the Southern Patagonian Batholith (Hervé et al., 2007). The presence of plutonic fragments and K-feldspar with perthitic exsolution (Fig. 5b, f) in the

Rocallosa-Dorotea and Chorrillo Chico formations support the exhumation of arc roots. The overall abundance of microlitic textures (Fig. 5h) and the relatively high proportion of plagioclase in the studied samples indicate erosion of an andesitic to mafic volcanic carapace in the Andean magmatic arc system. Moreover, microlitic textures with palagonite filling vesicles present in the Rocallosa-Dorotea samples could indicate the input of basaltic lava fragments from the mafic Barros Arana-La Pera complexes (Stern et al., 1991). On the other hand, the abundance of Campanian to Hauterivian (~130-80 Ma.; Fig. 6a) detrital zircon ages suggests either continued input of Cretaceous plutons of the Southern Patagonian Batholith or erosion of Cretaceous foreland deposits hosting significant arc-derived zircons. We cannot rule out the latter possibility given the presence of sedimentary lithics (Fig. 5e) in the samples.

Middle Jurassic to Early Cretaceous detrital zircon ages (~170-135 Ma.; Fig. 6a), mainly in the Rocallosa-Dorotea and (lower) Cabo Naríz samples, indicate that RVB remnants and the Tobífera Formation contributed detritus to the basin. Volcanic lithics with lathwork textures (Fig. 5i) present in all the studied samples corroborate the input of basaltic lava fragments from the ophiolitic suites of the RVB. In contrast, the felsitic and devitrified textures (Fig. 5j, g) support the exhumation of the volcaniclastic Tobífera Formation. On the other hand, Palaeozoic to Paleoproterozoic detrital zircon ages (~270-2200 Ma; Fig. 6a) associated with micaceous schists and other metamorphic fragments (Fig. 5c, d, g) in all samples suggest the incorporation of metamorphic (Andean and Cordillera Darwin Metamorphic complexes) source terranes in the hinterland to the west (Fig. 1a), which is consistent with the heavy mineral suite identified by Charrier and Lahsen (1969). However, we cannot rule out the probable contribution of Palaeozoic zircons from the Río Chico-Dungeness Arch (Fig. 1a) in the Dorotea strata, as previously suggested by Gutiérrez et al. (2017) 100 km north of our study area.

The relative contribution from the Tobífera Formation and coeval Jurassic intrusives (Pankhurst et al., 2000; Calderón et al., 2007; Hervé et al., 2007) together with reworked grains of the Andean Metamorphic Complexes (Hervé et al., 2003, 2010; Barbeau et al., 2009) appears to have been more significant during deposition of the Rocallosa-Dorotea formations (latest Campanian to late Maastrichtian) compared to the Chorrillo Chico Formation (Paleocene) (Fig. 6c). Furthermore, this provenance shift can be distinguished to the north of our study area (at Sierra Baguales), and in the Chilean part of Tierra del Fuego (Fig. 6c), most likely suggesting a regional change in the sediment distribution system.

Table A. Point-count raw data and equations for recalculated Q-F-L, and Qm-F-Lt plots.

Unit	Sample	Qm	Qp	Fk	Plg	Ch	Lsed	Lm	Lvlt	Lvf	Lvm	Lv(u)	Q-F-L	Qm-F-Lt	Total
Dorotea Fm	*CSD-02*	101	38	100	92	27	23	32	3	23	11	1	37,42,21	22,43,35	451
	CSD-01	109	41	89	90	21	20	45	5	32	7	1	37,39,24	24,39,37	460
	*ZLP-01**	93	35	109	94	32	26	20	0	13	15	0	37,46,17	22,46,32	437
	CLP-02	45	17	36	155	21	30	20	2	61	28	2	21,45,34	12,45,43	417
Rocallosa Fm	*GRH-3GL*	61	26	66	115	23	16	16	1	40	19	0	29,47,24	16,47,37	383
	GRH-3BL	106	13	88	96	0	0	20	17	30	15	20	29,46,25	27,47,26	405
	PPR-02	129	28	98	67	14	1	1	12	16	21	0	41,42,17	33,42,25	387
	PPR-01	132	15	50	122	20	20	19	0	0	0	2	44,45,11	35,45,20	380
	GPR-01	141	4	50	134	10	9	1	2	13	7	0	40,50,10	38,50,12	371
	*ZPR-01**	85	31	87	42	18	20	49	25	9	44	0	33,31,36	22,31,47	410
Cabo Nariz beds	*CN05-4*	37	7	57	23	-	23	39	114	76	7	0	11,21,68	10,21,70	383
	CN06-1	52	10	57	58	-	2	25	100	31	2	0	18,34,47	15,34,50	337
	CN06-4	65	18	37	93	-	77	28	64	16	5	0	25,39,36	20,39,41	333
	CN06-5	49	10	74	24	-	10	36	102	29	20	0	17,28,56	14,28,59	354
	CN01-2	44	27	51	50	-	6	16	112	36	1	0	21,29,50	13,29,58	343
	CN03-4	42	8	60	50	-	2	62	67	55	29	0	13,29,57	11,29,60	375
	CN04-1	80	21	108	15	-	6	25	44	76	10	0	26,32,42	21,32,47	385
	CN05-1	70	13	73	49	-	10	28	49	72	17	0	22,32,46	18,32,50	381
	CN12-1	61	9	65	33	-	6	47	83	64	22	0	18,25,57	16,25,59	390
Chorrillo Chico Fm	*PB-1-H**	139	4	65	77	21	38	2	12	19	23	18	39,34,27	33,34,33	418
	PB-1-C	124	4	16	58	2	44	0	65	0	0	0	42,24,34	40,24,37	313
	RB-1-C	148	15	16	38	34	13	11	14	0	0	17	64,18,18	49,18,33	306
	*RB-1-H**	146	20	92	93	26	63	30	5	1	19	9	38,37,25	29,37,34	504
	PBC-1	84	15	38	128	17	21	4	17	10	78	2	28,40,32	20,40,40	414
	PBC-2	81	12	57	92	26	17	11	5	16	75	0	30,38,32	21,38,41	392
	PPC-02	43	4	69	198	7	2	0	5	0	6	2	16,79,4	13,79,8	336
	GH2-CHCH	26	1	117	165	17	6	4	3	7	4	0	13,80,7	7,81,12	350

* samples used for detrital zircon U-Pb geochronology

Codes:

Qm	Monocrystalline quartz (single crystals and within other lithic
Qp	fragments) Polycrystalline quartz
Pg	Plagioclase feldspar (single crystals and within other lithic
Fk	fragments) Potassium feldspar (single crystals and within other
Lv (u)	lithic fragments) Volcanic lithic fragment undifferentiated
Lvf Lvlt	Felsic volcanic lithic fragment
Lvm	Volcanic lithc fragment with lathwork texture
Lsed Lm	Microlitic volcanic lithic fragment
Ch	Sedimentary lithic fragment, generally siltsone Metamorphic lithic fragments, generally schists Chert

Recalculated:

Q	Total quartzose grains
F L	(=Qm+Qp+Ch) Total
Lt	Feldspar (=Pg+Fk) Total lithic fragments (=Lv(u)+Lvlt+Lvf+Lvm+Lsed+Lm) Total lithic fragments (=Qp+Ch+L)

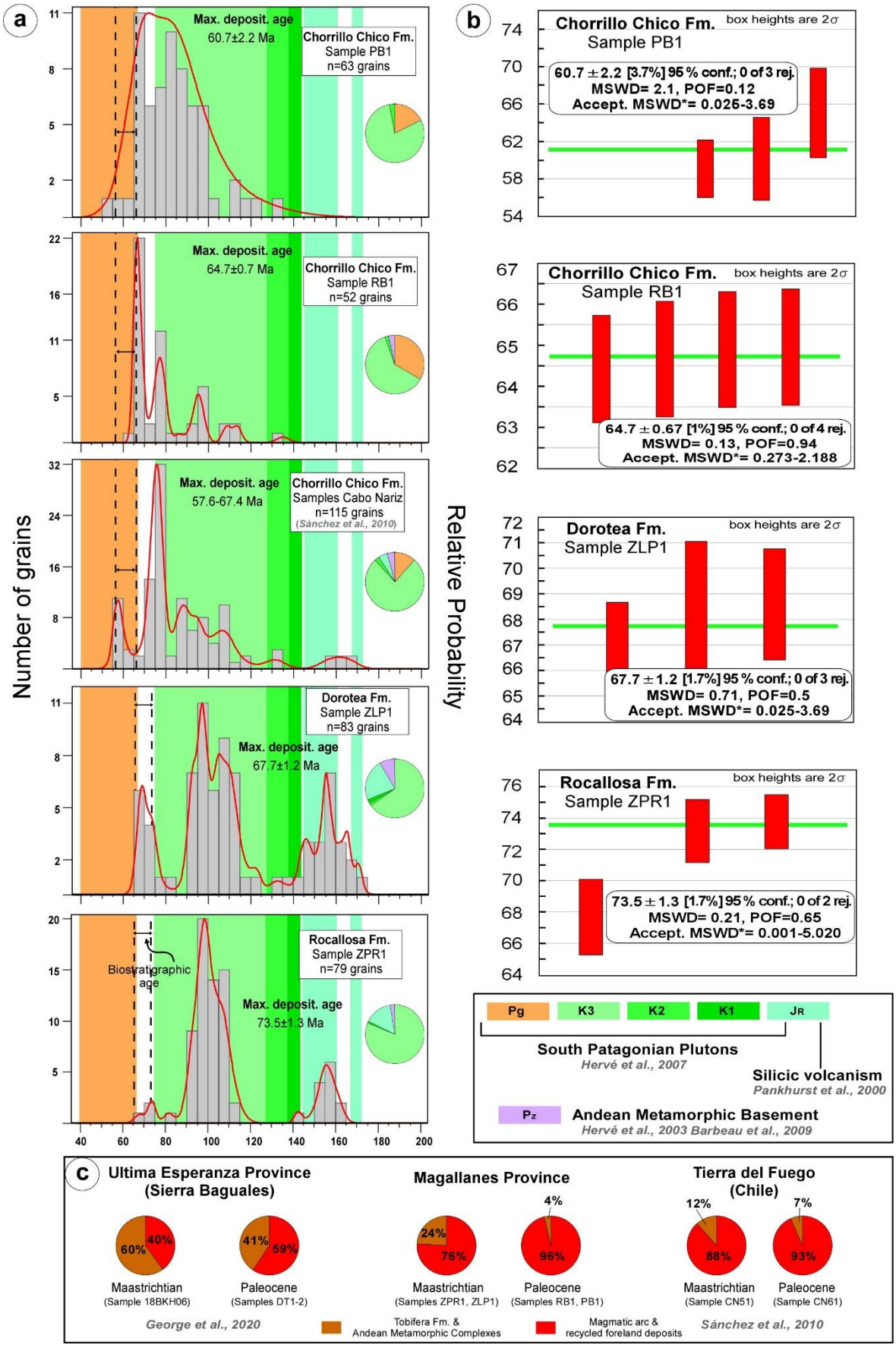

Figure 6. (← *previous page*) Detrital zircon U-Pb geochronology results. (a) Composite histograms and probability plots from the Rocallosa Formation, Cabo Nariz beds (Sánchez et al., 2010), and Chorrillo Chico

Formation. Lower case “n” refers to the total number of grains in each sample; potential source terranes are indicated in the inset box. (b) Maximum depositional age calculations for each sample. Accept. MSWD after Mahon (1996). (c) Comparison of the relative proportions of two age groups in different parts of the Magallanes-Austral Basin: Tobifera Fm and basement versus magmatic arc and recycled deposits. Note how Tobifera Fm and basement proportions decrease systematically in the Paleocene samples indicating a regional shift in the sediment dispersal system.

Components of the Tobífera Formation and metamorphic basement, relatively more abundant in the lower members of both the Chorrillo Chico Formation and the Cabo Naríz beds, decreases up-section (Fig. 6c). At the same time, microlitic volcanic lithics and vitric shard fragments increase up-section, suggesting intermediate to felsic synsedimentary volcanism. This Paleocene volcanic event is recorded in the whole basin (Charrier and Lahsen, 1969; Macellari et al., 1989; Torres-Carbonell and Olivero, 2019).

III-1.4.2c Maximum depositional ages

From the provenance data, it is apparent that the Southern Patagonian Batholith maintained protracted connectivity with the foredeep, providing syndepositionally formed zircons. This connectivity allows estimates of reliable maximum depositional ages very close to the true depositional ages. Sample ZPR1 has a youngest single grain of 67.7±2.4 Ma and a calculated maximum depositional age of 73.5±1.3 Ma from n=2 grains (Fig. 6b). Sample ZLP1 has a youngest single grain of 67.1±1.6 Ma and an estimated maximum depositional age of 67.7±1.2 Ma from n=3 grains (Fig. 6b). Sample RB1 has a youngest single grain of 64.4±1.3 Ma and a calculated maximum depositional age of 64.7±0.67 Ma from n=4 grains (Fig. 6b). Sample PB1 has a youngest single grain of 59.2±3.1 Ma and a calculated MDA of 60.7±2.2 Ma from n=3 grains (Fig. 6b).

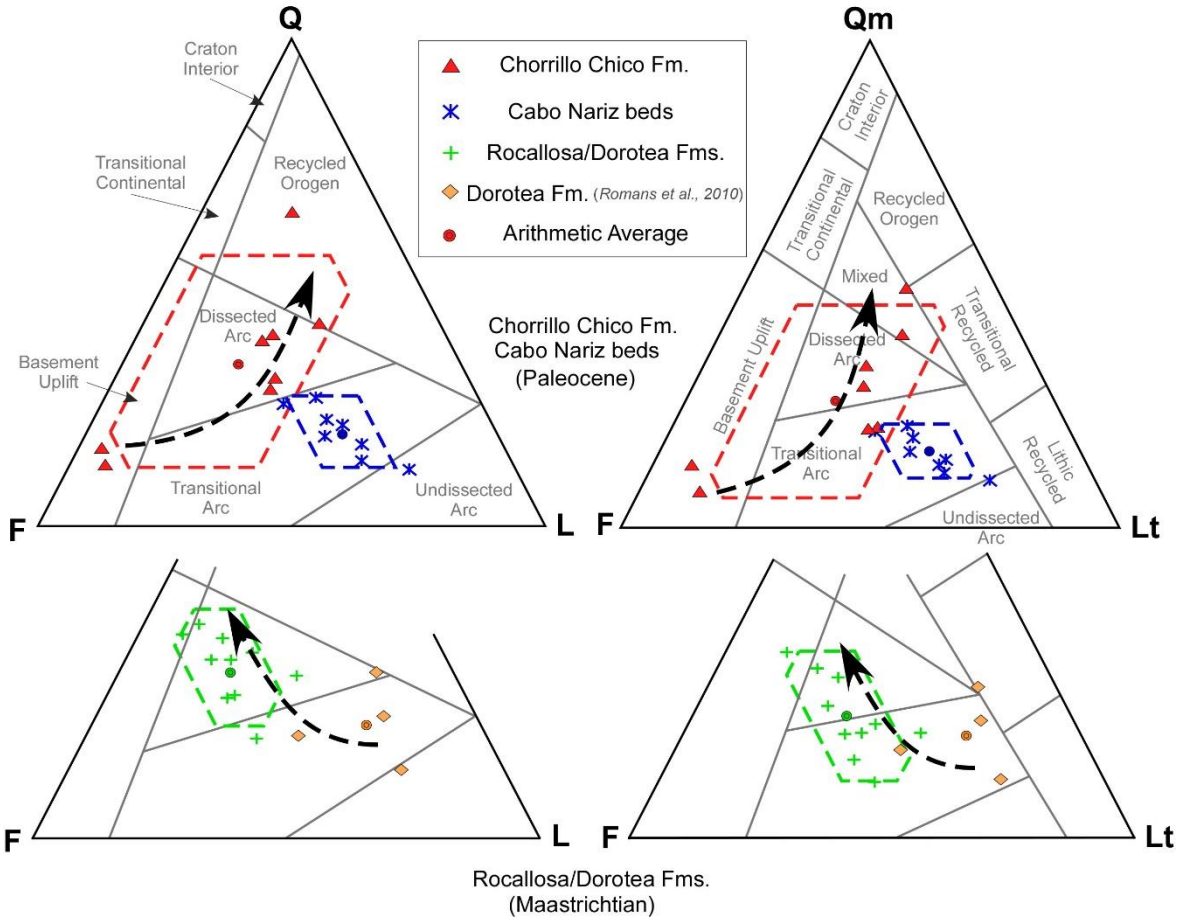

Figure 7. Q-F-L and Qm-F-Lt ternary plots displaying detrital modes for the Rocallosa-Dorotea, Cabo Nariz, and Chorrillo Chico Formations. Tectonic provenance fields from Dickinson (1985); polygons represent univariate confidence intervals. Note the unroofing trend in the Chorrillo Chico Formation and between the Dorotea (northern samples of Romans et al., 2010) and Dorotea-Rocallosa formations (southern samples of this study).

III-1.4.3 Palynology

From the three samples analysed in the Rocallosa Formation (Fig. 2c, 3a), the palynomorph content (Table 3) displays a terrestrial predominance over dinocysts, which are commonly poorly preserved but can tentatively be identified as Spiniferites sp. In order of abundance, epiphytic fungi (40.9%), including *Granatisporites* sp. (Fig. 8a), *Multicellaesporites* sp. (Fig. 8b), and *Monoporisporites* sp.; magnoliophytes (27.7%), including *Nothofagidites brassi* type (Fig. 8c), *N. dorotensis* (Fig. 8d), *N. cincta* (Fig. 8e), *N. diminuta*, *N. flemingii*, *N. spinosus*, *Gaultheria* sp., *Tricolpites* sp., and *Monocoplites* sp.; pteridophytes (21.4%), including *Laevigatosporites vulgaris* (Fig. 8f), *Cyathidites minor*, *Gleicheniidites senonicus*, *Clavifera triplex* (Fig. 8g), *Lycopodium austroclavidites*, *Polypodiisporites* sp., *Gleicheniidites* sp.; Pinophytes (7%), including *Podocarpidites*

otagoensis (Fig. 8h), *P. marwickii*, and *Araucariacites australis*; microalgae colonies (3%), represented by *Botryococcus braunii* (Fig. 8i), are present.

The dominance of terrestrially-derived palynomorphs suggests proximity to the area of continental supply. The association of epiphytic fungi spores, *B. braunii* (Fig. 8i), dinocysts, and pteridophytes (Fig. 8f, g) suggests a marginal estuarine/deltaic brackish environment with a considerable influence of freshwater. It also reflects a highly alkaline and generally oligotrophic environment surrounded by poorly drained areas, probably developing local peat swamps on the damp rainforest floors, where an understorey of shade-tolerant ferns could flourish (Palma-Heldt, 1983; Borel, 2007; Bowman et al., 2014). The association of Podocarpidites, Nothofagidites, and pteridophytes suggests that these dense forests flourished in low coastal areas and humid environments. Typically, Araucariacites and Podocarpidites thrive in elevated areas; however, they have proven to be adaptable and can also be linked to relatively low areas related to coastal and/or marsh environments (Quattrocchio et al., 2006). On the other hand, Araucariacites and Podocarpidites characterise the temperate-cold rainforest of the austral regions (Palma-Heldt, 1983). In contrast, Cyatheaceae currently develops in pantropical regions, and their abundance would also indicate hot and humid palaeoclimatic conditions (Povilauskas, 2017). However, they are more sensitive to variations in humidity than to temperature (Palma-Heldt, 1983). Nothofagidites is the essential genus that inhabits the sub-Antarctic forests of Patagonia and is associated with areas of high humidity (Palma-Heldt, 1983; Herngreen et al., 1996) and temperate climate (Carrillo-Berumen et al., 2013). Particularly the *N. brassii* type (Fig. 8c) is related to temperate-warm climates and low-elevated areas. In synthesis, the palynofloristic association and its relative percentage of abundance allow us to interpret a cool-temperate (6-12°C) to warm-temperate (12-17°C) climate with humid and rainy conditions for the Maastrichtian-Danian.

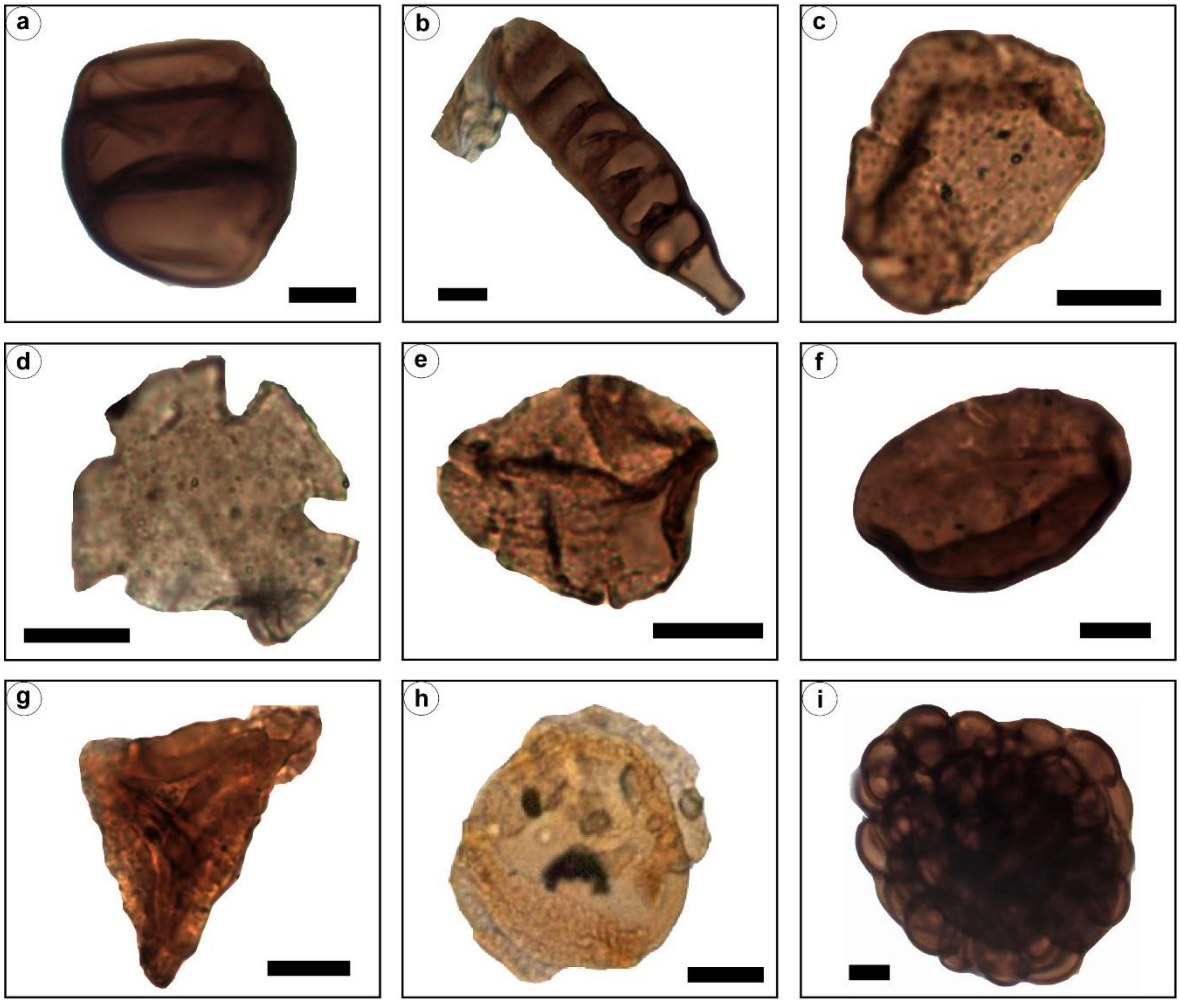

Figure 8. Light transmitted images of selected terrestrial palynomorph specimens from the Rocallosa Formation. (a) *Granatisporites* sp. (b) *Multicellaesporites* sp. (c) *Nothofagidites brassii* type. (d) *Nothofagidites dorotensis*. (e) *Nothofagidites cincta*. (f) *Laevigatosporites vulgaris*. (g) *Clavifera triplex*. (h) *Podocarpidites otagoensis*. (i) *Botryococcus braunii*. Scale is 10 µm.

Table 3. Summary of palynomorph taxa recorded in the Rocallosa Formation with botanical affinities and palaeoclimatic significances. CT= cool temperate (6-12°C), WT= warm temperate (12-17°C).

Palynomorphs	Taxa	Botanical affinity	Climate type
Epiphytic fungus (40.9%)	*Granatisporites* sp. *Multicellaesporites* sp. *Monoporisporites* sp.	Uncertain Meliolaceae	–
Magnoliophytas (27.7%)	*Nothofagidites brassii* type *N. dorotensis* *N. cincta* *N. diminuta* *N. flemingii* *N. spinosus* *Gaultheria* sp. *Tricolpites* sp. *Monocoplites* sp.$^{\Psi}$	Dicotyledonae, Nothofagaceae, *Nothofagus* *Nothofagus betuloides* Dicotyledoneae Monocotyledoneae	CT WT
Pteridophytas (21.4%)	*Laevigatosporites vulgaris* *Cyathidites minor* *Gleicheniidites* sp. *G. senonicus* *Clavifera triplex* *Lycopodium austroclavidites* *Polypodiisporites* sp.	Filicopsida, ?Blechnaceae Filicopsida, Cyatheaceae Filicopsida, Gleicheniaceae *Gleichenia circinata* *Dicranopteris rigida* Lycopodiaceae, *Lycopodium* Uncertain	WT
Pinophytes (7%)	*Podocarpidites otagoensis* *P. marwickii* *Araucariacites australis*	Podocarpaceae, *Podocarpus* *Podocarpus salignus* Araucariaceae (*Araucaria*)	CT
Microalgae colonies (3%)	*Botryococcus braunii*	Chlorophyta, Chlorococcales, Botryococcaceae	–
Minor dinocysts	*Spiniferites* sp.	Dinoflagellata	–

$^{\Psi}$ Representing 10.2% from the overall Magnoliophytas identified; CT=cool temperate; WT=warm temperate

III-1.5 Discussion

III-1.5.1 Evolution of depositional systems

The transition of deep-marine to shallow-marine deposits recorded by the Fuentes and Rocallosa formations (Fig. 3a) in the Magallanes Province, and by the Tres Pasos and Dorotea formations (Fig. 3b) in the Ultima Esperanza Province, signals an upward-shoaling cycle. This cycle 1 began as early as the Cenomanian in the northernmost part of the basin near Lago Argentino (Malkowski et al., 2017b), by the late Campanian to early Maastrichtian in our study area, and as late as the late Paleocene in the southernmost part of the basin in Tierra del Fuego (Olivero et al., 2003; Martinioni et al., 2013; Torres Carbonell and Olivero, 2019) (Fig. 2a). In the Magallanes Province, the uppermost Fuentes Formation is characterised by outer shelf to upper slope environments that grade rapidly to an offshore-

transition environment (Figs. 3a, 9a), where sedimentation was related to turbidity currents. Cycle 1 continued with the establishment of shoreface environments of the Rocallosa Formation (Figs. 3a, 9a), where waves and storms were the main sediment transport mechanisms. Palaeocurrents and provenance data suggest sediment dispersal from the fold-thrust belt in the northwest to the west (Fig. 9c). In the Ultima Esperanza Province, the shift from slope deposits of the Tres Pasos Formation to a deltaic system of the Dorotea Formation (Shultz et al., 2005; Romans et al., 2009; Schwartz and Graham, 2015; Gutiérrez et al., 2017) (Fig. 9a) represents this cycle 1. Palaeocurrent directions of the Dorotea Formation indicate progradation towards the south (Fig. 9c), although the provenance data (Fig. 6a) suggest sediment input from the west. The lower and middle part of the Dorotea Formation (in section SD; 51°40'S) represents a wave-dominated deltaic depositional system (Figs. 3b, 9a), which hindered the clear distinction between shoreface and delta front and inhibited the development of a large number of terminal distributary channels (cf., Olariu and Bhattacharya, 2006; Bhattacharya, 2010). Farther south, in section CP (52°S), the Dorotea Formation represents a storm-dominated shoreface depositional setting. The uppermost Dorotea Formation exhibits both fluvial deposits of different types (meandering in section SD and braided to meandering in section CP), as well as estuarine deposits. The significantly large dimensions of the shoreface-incised (fluvial) channels (in section CP) along with the overlying succession of estuary deposits, lead us to interpret them as incised valley fills.

An incised valley interpretation for the shoreface-incised channels of section CP is supported by the (1) multi-storey channels that record an abrupt basinward facies shift (Fig. 3b); (2) the bounding erosion surface at the base of incised channels correlating with angular unconformities to the north of the basin (at the base of the Calafate Formation) (Fig. 10a); and (3) the estuarine infill onlapping the valley walls in a landward direction (Fig. A1g). These features meet the recognition criteria for incised valleys, as outlined by Zaitlin et al. (1994). The internal vertical evolution of the incised valley fill is reflected by the transition from braided fluvial channels to a meandering fluvial system followed by a protected estuary environment affected by tides (Figs. 3b, 9b), which imply a mixed energy scenario for the incised valley system. Member D of the Rocallosa Formation (sensu Charrier and Lahsen, 1969) in the Magallanes Province, could be the equivalent to the fluvial deposits at the base of the incised valley systems identified in Ultima Esperanza Province as it reflects a change to higher-energy conditions, suggesting the establishment of a Gilbert-type delta in a landward (westerly) position (Fig. 9b). Gilbert-type deltas are dominated by stacked mass flows (boulders and cobbles) and fluvial traction sedimentation (frequently reworked by

waves) in their topsets, while foresets and bottomsets are dominated by subaqueous sediment-gravity flows of coarse to very coarse sand, slumps, and down-slope turbidity currents (Falk and Dorsey, 1998; Rojas and Le Roux, 2005). The facies presented in the stratigraphic column of La Pesca Bay (Fig. 3a) could be interpreted as the topset-foreset transition, dominated by slumps, high-density turbidity current deposits or sediment gravity flows (Lowe, 1982).

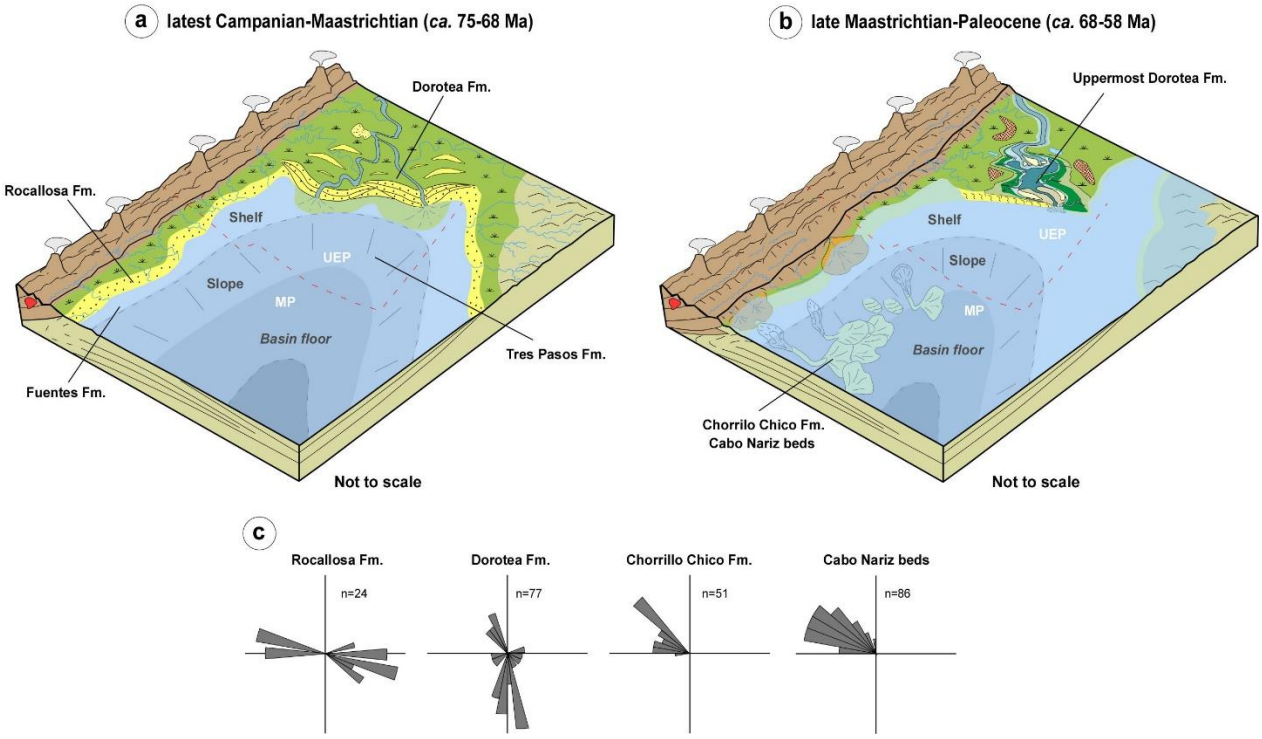

Figure 9. Schematic diagrams of the interpreted sedimentary environments for the Fuentes, Dorotea, Rocallosa and Chorrillo Chico Formations. (a) Before the Maastrichtian-Danian transgression, a wave-influenced delta (Dorotea Formation) existed in the Ultima Esperanza Province, while in the Magallanes Province, shoreface environments dominated (Rocallosa Formation). Note that the Fuentes Formation is represented by outer shelf to slope environments. (b) During the transgression, an estuary system developed as filling of incised valley systems in the Ultima Esperanza Province, while in the Magallanes Province is characterised by prograding deep-water turbidite fans (Chorrillo Chico Formation). (c) Palaeocurrent distribution for each studied formation.

The estuary environment in Ultima Esperanza Province and the deep-marine facies of the Chorrillo Chico Formation and Cabo Naríz beds in Magallanes Province and Chilean Tierra del Fuego (Fig. 9b) represent the change to cycle 2. This cycle 2 is characterised by the deepening of the environments within the basin and represents the sedimentological record of the Maastrichtian-Danian transgression. Cycle 2 is apparent in the northernmost Lago Argentino area (Fig. 2a), where it is depicted by the transition from Campanian to early

Maastrichtian non-marine deposits to estuary systems developed in incised valleys (Marenssi et al., 2004) or shoreface to offshore-transition deposits (Odino et al., 2018) of the Calafate Formation. In the Chorrillo Chico Formation, dilute turbidity currents with episodes of sediment gravity flows were critical components of the middle and distal turbidite fan system. Turbidite currents develop most likely by both erosion of the shoreface, as suggested by the highly fragmented and reworked glauconite grains, and by slope disequilibrium (e.g., Haughton et al., 2009). Such processes could be influenced by tectonic deformation in the nearby fold-thrust belt, as has been previously suggested for time-equivalent strata in Tierra del Fuego (Sánchez et al., 2010; Martinioni et al., 2013; Torres Carbonell and Olivero, 2019). Palaeocurrent directions towards the northwest in the Cabo Nariz beds and Chorrillo Chico Formation (Fig. 9c) suggest a connection between both turbidite deposits. Thus, the observed coarsening- and thickening-upward trend in both formations (Sánchez et al., 2010) depicts a northwest-ward prograding submarine fan system aligned with the foredeep axis, with the channelised upper fan in Tierra del Fuego and the outer fan to fan-fringe in the Brunswick Peninsula.

III-1.5.2 Sequence stratigraphic architecture

Sequence 1. The basal sequence boundary (late Campanian, ~73.5 Ma) is well represented in the northernmost part of the basin (Lago Argentino) by the late Campanian disconformity that separates the La Anita and La Irene formations (Macellari et al., 1989). In our study area, such disconformity is not apparent. However, Mpodozis (in Álvarez et al., 2006) notes a disconformity between the Tres Pasos and Monte Chico-Dorotea formations, ~50 km to the north of our study area, in the Cerro Cazador area (Fig. 2a). The limit between the Tres Pasos-Dorotea formations at Cerro Cazador is approximately late Campanian in age (~73.5 Ma; Daniels et al., 2019). In our study area, the lowstand (LST) and transgressive (TST) systems tracts correspond to segments of the Tres Pasos Formation not studied here. Only the overlying highstand system tract (HST) can be recognised (Fig. 10a), manifested in the Ultima Esperanza Province by the transition from shelf deposits of the Tres Pasos Formation (Gutiérrez et al., 2017) to deltaic deposits of the Dorotea Formation (Fig. 10b). Internally in the Dorotea Formation, the vertically-stacked parasequences (clinothems) passing from prodelta to mid-to-upper shoreface (Fig. 3b) suggest a progressive aggradational to progradational stacking pattern (denoting landward changes in the shoreline trajectory; Fig. 10b) and reduction of basin accommodation. In the Magallanes Province, the HST is represented by the prograding shoreface deposits of the Rocallosa Formation overlying the aggrading outer shelf to upper slope environments (Fig. 10c) of the uppermost

Fuentes Formation. This transition might represent the maximum flooding surface (MFS), giving rise to the beginning of a normal regression (Fig. 10c), where sedimentation tended to balance or outpace the rates of base-level rise.

Sequence 2. The sequence boundary (late Maastrichtian, ~68.9 Ma) is an angular unconformity that separates the Chorrillo Formation of the late Maastrichtian Calafate Formation in the northernmost part of the basin (Lago Argentino area) (Macellari et al., 1989; Marenssi et al., 2004). This angular unconformity correlates with the regional incision surface at the base of the incised valleys in the Ultima Esperanza Province (Fig. 10a), whose early deposits yield a maximum depositional age of 67.7±1.2 Ma (late Maastrichtian). This unconformity is manifested in the Magallanes Province as correlative conformity (Fig. 10a, b). The incised valleys were composed of a low-sinuosity fluvial system which was interpreted as low-accommodation lowstand fluvial deposits (Fig. 3b). At the same time, in the Magallanes Province, the LST is represented by the Gilbert-type delta in Member D of the Rocallosa Formation (Fig. 3a). The vertical change from a braided to high-sinuosity fluvial style with well-developed floodplains (in section CP; Fig. 3b) indicates an increase in basin accommodation; followed by a progressive marine influence on the low-amalgamated, fluvial channels (in section SD; Fig. 3b); which are abruptly overlain by lagoon and mire deposits. The increased accommodation is also reflected by the basal mudstone-dominated interval of the turbidite succession at the base of Chorrillo Chico Formation, as observed in the Magallanes Province (Fig. 10c). In the Lago Argentino area, the shift from fluvial (Chorrillo Formation) to nearshore or shoreface deposits of the Calafate Formation (Marenssi et al., 2004; Odino et al., 2018) attests to the increase in accommodation. The long-term evolution from fully fluvial systems to an estuary or shoreface in the north of the basin, and upper shoreface deposits to deep marine deposits in the south, suggests a backstepping stacking pattern representing a TST (Fig. 10b, c). The development of floodplain deposits indicates the commencement of the TST (section CP; Fig. 3b), whereas the wave-ravinement scouring represents the transgressive surface (TS) (Fig. 4e) of the fluvial channels (in sections SD and CP) in the Ultima Esperanza Province. The location of such a surface in the Magallanes Province is less precise, but it is assumed to be represented by the boundary between the Rocallosa and Chorrillo Chico formations (Fig. 10c). We infer that the development of distal distributary mouth bars (section SD) in the inner to middle estuary sub-environment of the uppermost Dorotea Formation (Fig. 3b), might evidence the onset of an early stage of regression. Therefore, we place an MFS at the base of the distal distributary mouth bars (Fig. 10b) and in the transition to a sandstone-

dominated turbidite system of the Chorrillo Chico Formation (Fig. 10c) that indicates the commencement of an HST.

Figure 10. (*following page* →) (a) Idealised sequence stratigraphic model along-strike the Magallanes-Austral Basin. (b) Sequence stratigraphic framework interpreted for the uppermost Tres Pasos-Dorotea Formations in the Ultima Esperanza Province (b) and the uppermost Fuentes, Rocallosa, and Chorrillo Chico formations in the Magallanes Province (c). LST=lowstand systems tract; HST=highstand systems tract; TST=transgressive systems tract. Location of idealised transect in Fig. 2a.

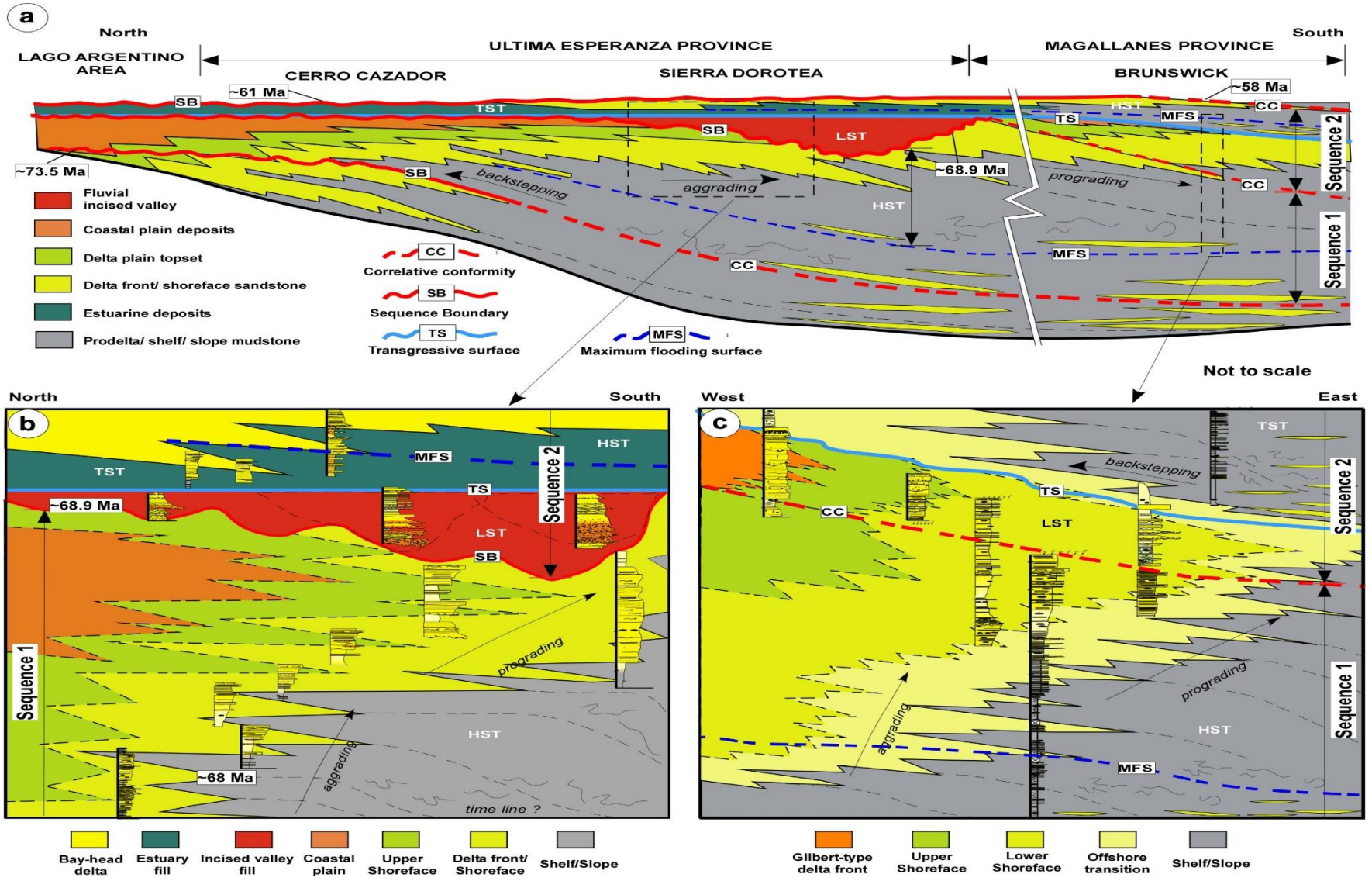
a
North
South
LAGO ARGENTINO AREA
ULTIMA ESPERANZA PROVINCE
MAGALLANES PROVINCE
CERRO CAZADOR
SIERRA DOROTEA
BRUNSWICK
~61 Ma
~58 Ma
~73.5 Ma
~68.9 Ma
SB
TST
LST
HST
TS
MFS
CC
backstepping
aggrading
prograding
Sequence 1
Sequence 2
Fluvial incised valley
Coastal plain deposits
Delta plain topset
Delta front/ shoreface sandstone
Estuarine deposits
Prodelta/ shelf/ slope mudstone
Correlative conformity
Sequence Boundary
Transgressive surface
Maximum flooding surface
Not to scale
b
North
South
~68 Ma
time line ?
c
West
East
Bay-head delta
Estuary fill
Incised valley fill
Coastal plain
Upper Shoreface
Delta front/ Shoreface
Shelf/Slope
Gilbert-type delta front
Lower Shoreface
Offshore transition

The uppermost sequence boundary is represented by the ~18 Myr unconformity between the Dorotea (Maastrichtian-Danian) and Rio Turbio (Eocene) formations in the Ultima Esperanza Province (e.g., Malumián and Caramés, 1997; Gutiérrez et al., 2017; George et al., 2020). Farther south, in the Magallanes Province, the uppermost sequence boundary is represented by the ~3 Myr gap between the Chorrillo Chico and Agua Fresca formations (Rivera, 2017), manifested in outcrops as correlative conformity. It is important to mention the diachroneity of this sequence boundary, marked at ~61 Ma in the Ultima Esperanza Province and by ~58 Ma in the Magallanes Province.

The southward diachroneity of unconformities or sequence boundaries and the recurrence of correlative conformities-bounded sequences are noteworthy (Fig. 10a). These features seem to be coincident with the southward increase in lithospheric attenuation during the precedent extensional phase of the RVB (Malkowski et al., 2016), highlighting a probable interdependency.

III-1.5.3 Forcing signals on the Maastrichtian-Danian transgression

III-1.5.3a Role of climate

Patagonian transgressions are typically linked to warm climatic episodes and are generally associated with abundant large size forams or thermophilic biota (Malumián and Náñez, 2011). However, the Maastrichtian-Danian transgressive deposits lack such faunal assemblages (Malumián and Náñez, 2011), and $\delta^{18}O$ isotopes records in the South Atlantic suggest cold water temperatures during the late Santonian and until the Danian (Barrera and Savin, 1999; Cramer et al., 2009; Le Roux, 2012) (Fig. 1b). Similarly, high-resolution palynological studies in the Antarctic Peninsula (Bowman et al., 2014) indicate a cooling trend between the early Maastrichtian to Paleocene. In the MAB, stable oxygen isotope records at the base of the Chorrillo Chico Formation (ca. 65.2 Ma) suggest a cool palaeoclimate (Sial et al., 2001). This generalised cooling trend rules out any link of the Maastrichtian-Danian transgression with warm climatic events.

While oxygen isotope records favour cold climatic conditions during the Maastrichtian to early Paleocene, our palynological results (Table 3) suggest more temperate conditions (~6-17°C) in the MAB. We envisage a dynamic climatic system with fluctuations between cool and warm conditions. The latter supports the hypothesis of del Río et al. (2015) that the MAB could be placed in a transitional area between warmer and cooler temperate

waters of northern Patagonia and the Antarctica Peninsula, respectively. Our paleoclimatic reconstruction also suggests humid and rainy conditions during the Maastrichtian-Danian. These humid and rainy conditions also prevailed in the Antarctic Peninsula at this time (Bowman et al., 2014).

III-1.5.3b Tectonic versus eustatic triggers

Previous research dealing with sea-level changes or the Maastrichtian-Danian transgression in Patagonia invokes eustatic forcing as the causative mechanism of base-level changes (e.g., Malumián and Nañez, 2011; Vallekoop et al., 2017). However, the progressive decrease of the long-term eustatic sea-level from the late Campanian (Fig. 1b) suggests that eustasy was not the controlling mechanism for the Atlantic transgression in Patagonia. Local or regional tectonism is an alternative, more likely explanation for the origin of the marine ingression, although only a few studies in the region suggested this mechanism (e.g., Aguirre-Urreta et al., 2011; Gianni et al., 2018a).

The late Maastrichtian basal unconformity in sequence 2 (Fig. 10), represented by the erosion surface at the base of the incised valley systems of the upper Dorotea Formation in the Ultima Esperanza Province, and by the angular unconformity at the base of the Calafate Formation in the Lago Argentino area (Macellari et al., 1989) suggests tectonic activity across the MAB by the end of the Cretaceous. The sandy gravel and coarser deposits, typically sub-rounded or sub-angular, in the early fill of the incised valley systems, as well as the abrupt shift to a high-energy Gilbert-type delta setting in member D of the Rocallosa Formation in the Magallanes Province, suggest rivers draining a tectonically active region (Li et al., 2006; Torres Carbonell and Olivero, 2019). Moreover, the turn-over of basement-derived sediments to chert and sedimentary lithics in the Chorrillo Chico Formation and Cabo Nariz beds, as well as their orogen-recycled signature trend (Fig. 7) reflect thrust belt advance during the early Paleocene. This thrust belt activity inferred by the sedimentary record is consistent with the results of structural studies that suggest active deformation and the advancement of the orogenic wedge in both the Ultima Esperanza Province and Tierra del Fuego during the Maastrichtian-Danian (Fosdick et al., 2011; Torres-Carbonell et al., 2013).

Deformation in the orogen generated increased loading, which in turn, caused increased flexural subsidence during the Maastrichtian-Danian. The change from shoreface environments to deep-water sedimentation in the Chorrillo Chico Formation, as well as the

development of estuarine environments during the late filling stages of the incised valleys in the uppermost Dorotea Formation, reflect an increased accommodation as a result of enhanced basin subsidence. Biddle et al. (1986) and Mpodozis et al. (2011) described the wedge geometry of Maastrichtian-Paleocene deposits across the MAB, which thicken westwards, preserving the asymmetric geometry of a subsiding foreland basin. Furthermore, Biddle et al. (1986) and Mella and Sánchez (2000) based on 1D well backstripping showed that the foredeep recorded accelerated subsidence between the Maastrichtian and Paleocene (Fig. 11).

Although our study stresses active regional tectonism in the orogenic wedge as the trigger of subsidence and consequently of the marine ingression during the Maastrichtian-Danian, we recognise that flexural subsidence only accounts for ingressions in areas adjacent to the Andean orogen. Therefore, more distal transgressive deposits cannot be entirely attributed to flexural loading. Accommodation farther from the orogenic load may be created by dynamic sub-crustal loads (Gurnis, 1992; Catuneanu et al., 1997, 2004), which depend on the dynamics of mantle flow related to subduction processes (Mitrovica et al., 1989; Gurnis, 1992) and its effect operates at a long-wavelength (up to ~2000 km) (Burgess and Moresi, 1999).

Some predicted effects of dynamic topography in foreland basin systems are subsidence extending cratonward farther from the orogen (Burgess and Moresi, 1999), suppression or diminution of the erosional characteristics of the forebulge, and sedimentation in the forebulge and backbulge depozones (Catuneanu et al., 1997, 2004). In the MAB, particularly for the Magallanes Province and Tierra del Fuego, Fig. 11 shows that between 70-60 Ma the Manzano and Evans wells (adjacent to the orogenic front) record maximum subsidence while the Condor well (located cratonward) reflects moderate subsidence. Likewise, Náñez and Malumián (2009) and Sachse et al. (2015) highlighted a reduced latest Cretaceous-Paleocene sedimentary thickness (~50 m) over the Rio Chico-Dungeness Arch and Malvinas Basin, which can be interpreted as condensed sections deposited during reduced accommodation conditions. Such a subsidence pattern and distal stratigraphic records match the predicted behaviour for dynamic subsidence acting in a long-wavelength in foreland basins. However, according to Fosdick et al. (2014), the attenuated Patagonian lithosphere of the MAB promoted flexural subsidence that was transmitted great distances cratonward (but was null in the backbulge depozone) and a diminished forebulge uplift. The latter implies that although the moderate subsidence registered cratonward may

be explained by the inherent mechanical parameters of the MAB, the ~50 m thick sedimentary packages that accumulated in the most distal depozones might have been facilitated by dynamic subsidence.

On the other hand, Dávila et al. (2019) based on residual subsidence modelling, suggested that during 130-66 Ma additional subcrustal forces were necessary to explain the amount of subsidence observed in the northernmost part of the MAB. Additionally, Gianni et al. (2018a) proposed the existence of a large flat slab subduction segment during 75-60 Ma in northern Patagonia, which caused enough dynamic subsidence to tilt areas farthest away from the influence of orogenic loading, thus allowing the Maastrichtian-Danian transgression.

Together, these observations suggest that the Maastrichtian-Danian marine ingression in the MAB was influenced by both flexural subsidence and dynamic subsidence.

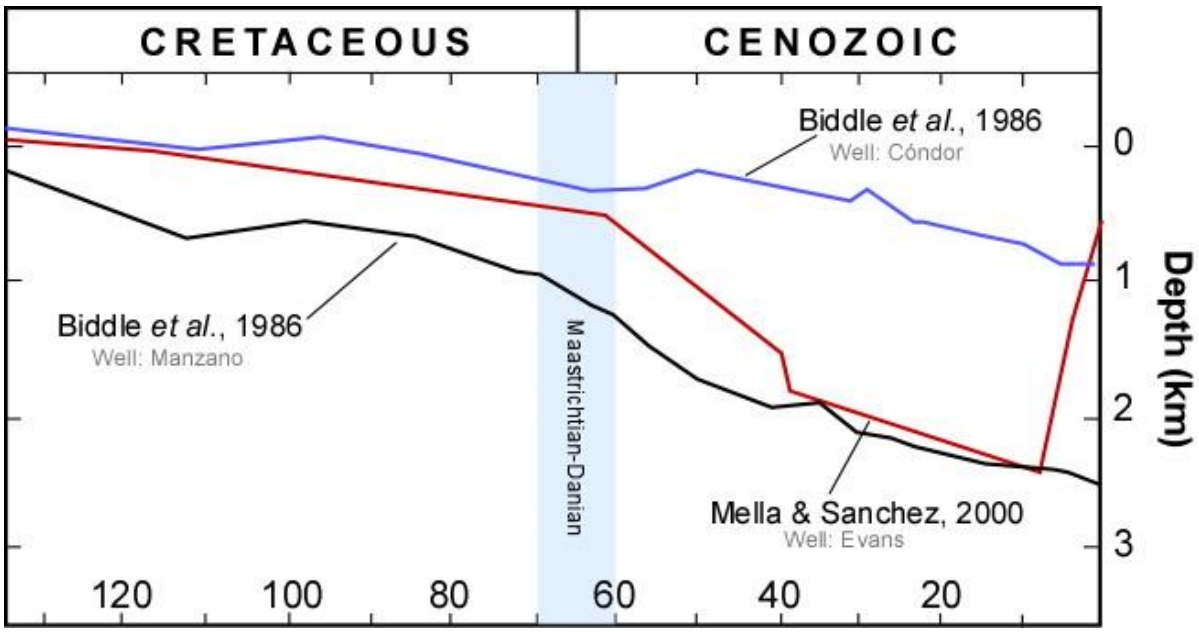

Figure 11. Tectonic subsidence curves for the Manzano, Evans, and Cóndor wells (see Fig. 2a for location). Note accelerated subsidence in the Manzano and Evans wells located adjacent to the orogenic front and minimal subsidence in the well situated near the "forebulge" area during the Maastrichtian-Danian.

III-1.5.4 Constraints on the timing of fold-thrust belt deformation

The integration of our dataset with previous structural and sedimentological data allows us to constrain some phases of active deformation in the Southern Patagonian wedge.

Before the late Campanian (~75 Ma), the fold-thrust-belt underwent protracted exhumation of the hinterland source terranes, involving the Tobífera Formation (and equivalents), remnants of the RVB, Paleozoic basement and rapid exhumation of the Cordillera Darwin core (Nelson, 1982; Kohn et al., 1995; Sánchez, 2006; Mpodozis in Álvarez et al., 2006; Romans et al., 2010; McAtamney et al., 2011). By the Maastrichtian (~72-68 Ma), a continuous exhumation of the hinterland gave rise to moderated to accentuated erosion of the arc (Fig. 8) reflected in the modal signature and detrital zircon ages of the younger deposits of the Dorotea and Rocallosa formations (Figs. 6, 7) and equivalent rocks in Tierra del Fuego (see also Torres-Carbonell and Olivero, 2019). Moderate amounts of sedimentary lithics in the younger Dorotea-Rocallosa strata suggest the incorporation of previous foreland deposits into the thrust-belt. Shoaling during the transition between the Tres Pasos-Fuentes to Dorotea-Rocallosa formations within a normal regressive context can be ascribed to increases in sedimentation rates that outpaced accommodation (by subsidence), the aftermath of accentuated erosion in the hinterland. The results of structural studies suggest an orogen-wide basement-involved faulting event (thick-skinned) manifested by crustal basement shortening and internal deformation (e.g., Fosdick et al., 2011; Betka et al., 2015). Altogether, the fold-thrust-belt evolution and sedimentary records in the basin suggest a phase of mainly internal shortening and thickening of the wedge, with limited forelandward advance of the deformation front (Fig. 12a). The latter may suggest that erosion rates outstripped shortening, promoting stability of the orogenic wedge.

The second phase of shortening, between ~68-58 Ma, is characterised by minor exhumation in the hinterland but significant forelandward advance of the thrust front (Fig. 12b), accompanied by considerable erosion of the wedge at least during the Maastrichtian-Danian transition (Sial et al., 2001). Upper Cretaceous foredeep deposits are incorporated into the fold-thrust belt in the Ultima Esperanza and Magallanes Provinces (e.g., Tenerife Thrust of Fosdick et al., 2011; Betka et al., 2015) while thrusting of Maastrichtian-Danian rocks with brittle-ductile deformation under submarine conditions occurred in Tierra del Fuego (e.g., D1 structures of Torres Carbonell and Olivero, 2019). The forelandward transfer of deformation is evidenced in the sedimentary record by the upward replacement of basement-derived detritus by chert and sedimentary lithics throughout the Maastrichtian-Paleocene strata, portraying a recycled-orogen trend in the Chorrillo Chico Formation (Fig. 7). Moreover, the relative contribution from the RVB, Tobífera Formation and Andean Metamorphic Complexes appear to have decreased by the Paleocene in the Chorrillo Chico

and Cabo Nariz beds, suggesting a structurally dammed hinterland. In Tierra del Fuego, progressively coarser sediments trapped adjacent to the orogenic wedge (Torres Carbonell and Olivero, 2019) indicate either a piggyback mode of thrust propagation or out-of-sequence thrusting. These series of thrust-loads caused an ample accommodation suitable for the establishment of estuarine deposits in the Ultima Esperanza Province and deep-marine turbidite sequences in the Magallanes Province and Tierra del Fuego, which correspond to the sedimentological record of the Maastrichtian-Danian transgression in the MAB. The significant forelandward transfer of deformation evidenced during this stage represents the transition from a thick-skinned to a thin-skinned structural style (Fig. 12b), probably triggered by an increased magnitude of the crustal shortening outpacing erosion rates.

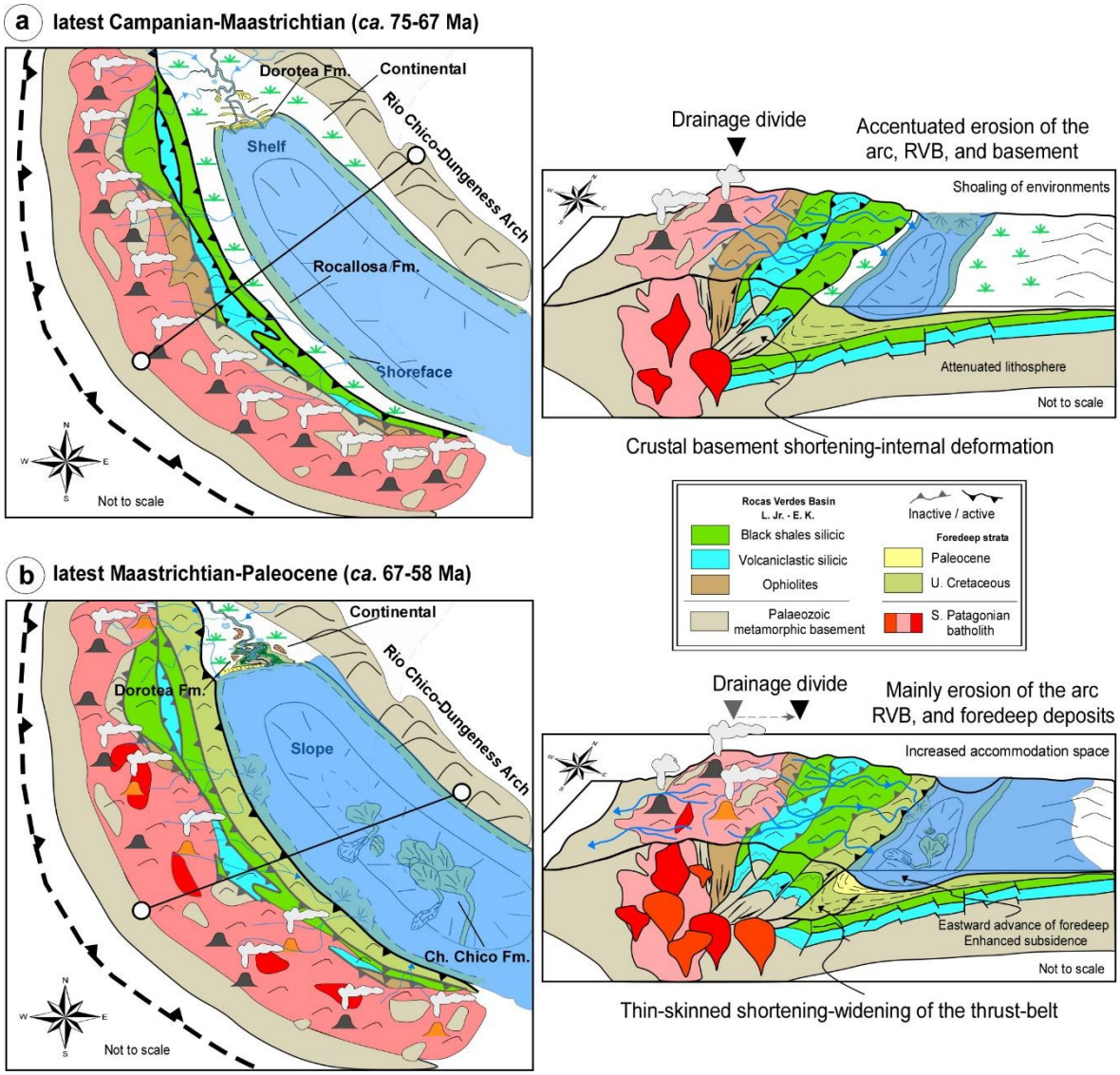

Figure 12. Simplified palaeogeographic/palaeotectonic reconstruction and schematic structural configuration (modified from Fosdick et al., 2015) of the Southern Patagonian wedge. (a) The thick-skinned deformation

phase, characterised by accentuated hinterland exhumation, internal thickening, shoaling of environments and stalling of the deformation front. (b) The thin-skinned deformation phase, characterised by minor hinterland exhumation, recycled foreland deposits, deepening of environments and significant forelandward advance of the deformation front. Note that palaeogeographic maps are not palinspastically restored, and diagrams are not to scale.

III-1.6 Conclusions

An upward-shallowing cycle during the late Campanian to late Maastrichtian of the MAB is recorded from the Fuentes-Tes Pasos to Rocallosa-Dorotea formations, passing from outer shelf-slope deposits to shoreface-deltaic environments, respectively. From the latest Maastrichtian to Paleocene, a deepening cycle took place represented by estuarine deposits in the uppermost Dorotea Formation and by the deep-water fan system of Chorrillo Chico Formation and Cabo Naríz beds. This deepening cycle, which represents the stratigraphic record of the Maastrichtian-Danian transgression, is apparent in the entire basin.

Our palynological results suggest a cool-temperate to warm-temperate (~6-17°C) palaeoclimate during the Maastrichtian-Danian, consistent with cool marine conditions recorded in the South Atlantic, which implies no link between the transgression and relative climatic optima. Progressive sea-level fall during the Maastrichtian-Danian suggests that eustasy was not a driver of the marine ingression. The stratigraphic, tectonic, and subsidence evolution of the basin imply that the orogenic loading of the Southern Patagonian Andes was a primary driver of the transgression in the MAB. Additionally, changes in dynamic topography strongly modulated the extent of the continental flooding event.

Modal composition and ~400 detrital zircons U-Pb ages show a continuous input from the RVB remnants, Paleozoic basement, Tobífera Formation, and magmatic arc during deposition of the Rocallosa-Dorotea and Chorrillo Chico-Cabo Naríz formations. The relative contribution from the RVB, Tobífera Formation and Andean Metamorphic complexes appears to have decreased by the Paleocene, suggesting a structurally dammed hinterland or a regional change in the sediment dispersal system.

We envisage two phases of Southern Patagonian orogenic growth. The first phase (prior to ~68 Ma) would have been characterised by internal deformation, thickening of the orogenic wedge, and accentuated hinterland exhumation, with a low magnitude of crustal shortening and high erosion rates that inhibited forelandward advance of the wedge. The second phase (~68-58 Ma) would have been characterised by minor hinterland exhumation

and significant forelandward advance of the thrust front, probably triggered by an increased magnitude of crustal shortening.

ACKNOWLEDGEMENTS

This study was financially and logistically supported by FONDECYT projects 1130006 and 1161806 and by the CONICYT-PFCHA-National PhD Scholarship 2017 No. 21170419. L.K. Sánchez and I.A. Gómez (Universidad de Chile) are thanked for their invaluable assistance during field campaigns, A.V. Poblete and L. Celle for support in the palynological and petrographic analysis, respectively. We gratefully acknowledge L. Rojas (Enap-Sipetrol) for permission to review unpublished reports. We thank L. Buatois for his very kind and helpful assistance in the identification of some ichnological traces, M. Leisen (CEGA), L. Solari (UNAM), M. Suárez and F. Llona (SERNAGEOMIN) are thanked for detrital zircon age dating. We also thank J. Martinod, Theresa Schwartz, David Barbeau Jr., and Matthew Malkowski for helpful comments on an early version of the manuscript. We are grateful to Sarah W.M George and an anonymous reviewer for their constructive and thoughtful reviews and editor Jasper Knight for his excellent editing work.

CHAPTER III-2:

LONG-TERM SEDIMENTARY EVOLUTION AND PROVENANCE AS RESPONSE TO THE PATAGONIAN ANDES GROWTH

Chapter III-2 deals with the Late Cretaceous to Cenozoic sedimentary architecture and provenance of the Magallanes-Austral foreland basin to enhance the understanding of the basin-wide siliciclastic sedimentation, depositional mechanisms and sediment routing systems. This chapter is approached from the integration of a detailed facies analysis, sedimentary provenance using multiple methods (conglomerate clast counting, sandstone modal composition, fine-grained bulk-rock geochemistry and detrital zircon U-Pb geochronology), accompanied by subsidence rates and isopach maps. The presented results constrain large-scale spatial and temporal depositional trends, highlight changes in basin accommodation on a regional scale, investigate sediment transport pathways and propose a unified stratigraphic architecture schema of the depositional systems. This chapter is intended to be submitted to Basin Research or Tectonics.

HIGHLIGHTS:

- A Late Cretaceous to middle Eocene underfilled phase of sedimentation characterised by deep-water depositional systems but interrupted by punctuated shallowing episodes.
- The overfilled phase reached from the late Eocene and was characterised by the progradation of deltaic and alluvial systems during decreasing flexural subsidence.
- Episodic cratonward migration of the foreland basin in response to fold-and-thrust belt dynamics, mainly during Paleogene.
- Generalised exhumation of the entire orogenic wedge during the middle Eocene and mid-Oligocene.
- Cessation of the compressional regime and abandonment of the foreland basin stage from the latest Oligocene to early Miocene.

The Late Cretaceous to Cenozoic tectonic evolution of the Southern Patagonian Andes is revealed by the sedimentary evolution and quantitative provenance analysis of the Magallanes-Austral Basin (52°0'-53°45'S).

Huber A. Rivera[1,2*], Joseph Martinod[2], Marcelo Farías[1], Jacobus P. Le Roux[1], Alejandro Sánchez[3]

[1]Departamento de Geología, FCFM, Universidad de Chile, Plaza Ercilla 803, Santiago, Chile
[2]Univ. Grenoble Alpes, Univ. Savoie Mont Blanc, CNRS, IRD, IFSTTAR, ISTerre, 38000 Grenoble, France
[3]Departamento de Ingeniería en Minas, Universidad de Santiago de Chile, Av. O'Higgins 3363, Estación Central, Santiago, Chile

Abstract

The Magallanes-Austral Basin records crucial information related to the development of the Southern Patagonian Andes but insufficient integration of multiple methods of study of the stratigraphic record has hampered a complete understanding regarding its evolution and of the orogenic wedge. We present an integrated examination of the evolution of depositional systems, dispersal sediment patterns, provenance data, subsidence rates and isopach data for the Late Cretaceous to early Miocene strata in the Chilean part of the Magallanes-Austral Basin (51°15"-53°39"S). The combined results suggest a new evolution model in which the onset of the foreland sedimentation occurs ~114 Ma. The early foreland stage is characterised by deep-water sedimentation in a continuously subsiding underfilled basin, followed by shallow marine environments during the latest Cretaceous, related to loss of subsidence and enhanced erosion due to isostatic rebound concentred in the narrow fold-and-thrust belt composed of the crystalline basement and Late Jurassic volcaniclastic rocks. The Paleocene-early Eocene is characterised by a phase of deep-water sedimentation in a highly subsiding underfilled basin linked to a rapidly eastward advancing orogenic wedge that incorporates hinterland basement rocks and foreland deposits. The middle Eocene is characterised by generalised isostatic rebound, shallowing of the depositional system and reduced subsidence linked to subduction of the Farallon-Aluk ridge. The late Eocene to late Oligocene is characterised by the transition to an overfilled basin with prograding shallow marine to continental deposits marking the last episode of deformation in the basin and of the flexural subsidence. The Miocene reflect cessation of flexural subsidence and development of a passive depocenter controlled by dynamic subsidence with coarse sediment progradation and continental depositional system.

III-2.1 Introduction

Despite along-strike segmentation of the Andean Cordillera, where each segment exhibits an independent tectonic evolution (see synthesis in Ramos, 2009; Horton, 2018a), the entire cordilleran system seems to experiment a major stage of mountain building during the Cenozoic. Evidence of such orogenic growth is well-documented in the long-lived sedimentary record of their linked retro-arc foreland basins (Kraemer, 1998; McQuarrie et al., 2005; Bayona et al., 2008; Ramos and Ghiglione, 2008; Barbeau Jr. et al., 2009; DeCelles et al., 2011; Fosdick et al., 2013; Horton et al., 2016; Folguera et al., 2018; Horton, 2018a). However, in the Southern Patagonian Andes (the southernmost segment of the Andean Cordillera), the Cenozoic orogenic wedge evolution is blurred due to the lack of exhaustive studies regarding the sedimentary evolution of the adjacent Magallanes-Austral (Fig. 1a) foreland basin. An integrated examination of the evolution of depositional systems, dispersal sediment patterns, provenance data, and subsidence rates for the Cenozoic strata in the Magallanes basin will contribute to tracking the Southern Patagonian Andes building stages. Improved knowledge of the fold-thrust belt tectonic history is essential to evaluate plate-scale geodynamic models of the Andes (Ramos, 2009; Horton, 2018b).

The Cenozoic tectonic evolution of the Southern Patagonian Andes, as inferred from the sedimentary record in different parts of the Magallanes-Austral basin (Fig. 1a), has mostly led to diverging interpretations and minor points in common. There is consensus on a major uplift event in the orogenic wedge during the early Oligocene to early Miocene (Barbeau Jr. et al., 2009; Zahid and Barbeau Jr., 2010, 2013; Gutiérrez et al., 2017; Torres Carbonell and Olivero, 2019; Leonard et al., 2020). On the other hand, for most of Paleogene and post-early Miocene, the debate is framed within whether there were orogenic exhumation and uplift related to an active or inactive retroarc shortening (Barbeau Jr. et al., 2009a; Zahid and Barbeau Jr., 2010, 2013; Torres Carbonell and Olivero, 2019; George et al., 2020; Rivera et al., 2020); or even regarding the position where such an uplift and exhumation event occurred (Gutiérrez et al., 2017).

Conflicting hypotheses possibly owe to the diverse techniques employed to understand the sedimentary record, which often lacks an ultimate integrative analysis and cannot elucidate the contribution of all the source rocks exposed in the orogenic wedge. For instance, the axial backbone of Southern Patagonian Andes exhibits ophiolite, and low- to high-grade metamorphic rocks (Fig. 1a, b), thus the parametric discrimination of their detrital fingerprints in provenance analysis is of paramount importance for interpreting the

dynamic of the orogenic wedge. Furthermore, deriving results have been contrasted with classic tectonic models (e.g., Dickinson and Suczek, 1979; Dickinson, 1985) that although appropriate for the Andean-type orogens and linked foreland basins, turn out not easily extrapolated to the context of the Southern Patagonian Andes and Magallanes Basin. Thus, our approach to understanding the tectonic history of the Southern Patagonian Andes would benefit from the integrated assessment of field-based depositional systems evolution, subsidence rates coupled with quantitative and statistical rigorous provenance analysis, including conglomerate clast counting, sandstone petrography, geochemical analysis, and detrital zircon U-Pb geochronology.

Our study focuses on the Chilean part (the Magallanes Province; Fig. 1a, c) of the Magallanes-Austral foreland basin (51°15”-53°39”S), corresponding to the central part of it, where it is possible to investigate one of most complete Cenozoic stratigraphic records of the basin. Our analysis aims the following: (1) to illustrate the different evolving stages (from Maastrichtian to Burdigalian) of the depositional systems of an atypical retroarc foreland basin (Romans et al., 2010) and their response to the orogenic wedge dynamics; (2) to track the long-term orogenic wedge exhumation to unveil the intricated evolution of the Southern Patagonian Andes; (3) to evaluate whether the contractional orogenesis corresponds to continuous or sporadic events interrupted by neutral or extensional tectonic regimes (Horton, 2018b). Our results allow us to enhance our understanding of Cretaceous to Cenozoic evolution and palaeogeography of the Magallanes-Austral basin and constrain the sedimentary response to the growth of the Patagonian Andes.

III-2.2 Geological background

The Mesozoic history of the southern Patagonia region is characterised by an initial phase of crustal extension, during Late Jurassic to Early Cretaceous, giving rise to the development of the Rocas Verdes Basin (Dalziel, 1981; Calderón et al., 2013); and a subsequent middle to Late Cretaceous basin inversion and contractional phase that promoted the onset of the Magallanes foreland Basin and Southern Patagonian orogenesis (further details in Fildani and Hessler, 2005; Romans et al., 2010; McAtamney et al., 2011; Malkowski et al., 2017a). Unlike the other Andean segments, the enhanced crustal attenuation led to the development of oceanic crust represented by different ophiolitic complexes (Calderón et al., 2013), contemporary with the emplacement of a large rift-related siliceous igneous province (Pankhurst et al., 2000), exposed today in the fold-thrust belt. This particular geological history conditioned this southernmost segment to evolve

differently from the classic model envisaged for the rest of the Andes. Some of these distinguishing features are the (1) long-term input of immature arc- and rift-derived, ophioliticlastic, and metamorphiclastic sands to the foredeep (Barbeau Jr. et al., 2009; Romans et al., 2010; Zahid and Barbeau Jr., 2010; Gutiérrez et al., 2017; Malkowski et al., 2017b; Rivera et al., 2020; Leonard et al., 2020); accompanied by (2) an accentuated mafic signature in shale geochemical composition (Fildani and Hessler, 2005; Romans et al., 2010; McAtamney et al., 2011; Zahid and Barbeau Jr., 2013); (3) protracted, thick, and well-developed deep marine depositional systems as a response to (4) enhanced subsidence and foreland flexure (Fildani and Hessler, 2005; Romans et al., 2010; Fosdick et al., 2014; Torres Carbonell and Olivero, 2019). Furthermore, two ridge-trench collisions and at least one slab window affected the tectonic evolution of this region during the Cenozoic (Cande and Leslie, 1986; Eagles and Scott, 2014).

III-2.2.1 Potential sediment source rocks in the Southern Patagonian wedge

The hinterland domain comprises the Southern Patagonian Batholith, pre-Andean metamorphic basement (e.g., the Duque de York Complex), the Cordillera Darwin Metamorphic Complex, and the Rocas Verdes Basin remnants (Fig. 1b). The Duque de York Complex consists of low-grade (pumpellyite-actinolite facies), quartz-(plagioclase)feldspar-rich mataturbidites and radiolarian metacherts deposited along the palaeo-pacific margin of Gondwana during Permian times (290-270 Ma) (Hervé et al., 2003; Lacassie et al., 2006; Sepúlveda et al., 2010; Castillo et al., 2016). On the other hand, the Cordillera Darwin Metamorphic Complex is a Cambrian-Devonian to Permian (500-400 Ma and 289 Ma) polydeformed, high-grade (amphibolite facies) metamorphic core that decreases in P-T conditions structurally upward and northward (lower greenschist facies) (Kohn et al., 1995; Barbeau et al., 2009; Hervé et al., 2010; Klepeis, 2010). Lithologically, it consists of pelitic schists, quartz-mica schists, metabasites, gneisses, and amphibolites rich in quartz, feldspar, mica, chlorite, staurolite, ilmenite, titanite, garnet, kyanite, and sillimanite. Additionally, underneath the Magallanes Basin, early Cambrian orthogneisses, amphibolites, and foliated granitoids referred to as the Tierra del Fuego Igneous and Metamorphic Complex (Hervé et al., 2010) constitute another potential source of detritus to the basin. The Southern Patagonian Batholith, which intrudes the metamorphic basement and Rocas Verdes Basin remnants indistinctly, is mainly composed of tonalites, granodiorites-diorites, and granites (and scarce olivine-bearing gabbros) of calc-alkaline signature. It experienced two Cenozoic

plutonic episodes (Pg: 67-40 Ma; Ng: 25-15 Ma), three during the Cretaceous (K1-K3: 144-75 Ma), and one during the Late Jurassic (Jr:157-144 Ma) (Hervé et al., 2007).

The Late Jurassic plutonic episode is coeval with widespread silicic volcanism that accompanied the break-up of Gondwana, which is represented in our study area by the Tobífera Formation (Pankhurst et al., 2000). The Tobífera Formation consists of low-grade (prehnite-pumpellyite up to greenschist facies), metatuffs with abundant devitrified glass shards, tuff turbidites with rhyolitic, quartz, and feldspar clasts intercalated with siliceous metasiltstones and mudstones, rhyolitic (peperitic) breccias and intruded by siliceous and mafic dykes (Wilson, 1991; Galaz et al., 2005; Muller et al., 2021). The age of these siliceous volcaniclastic rocks range between 145-190 Ma, peaked at ~170 Ma (Pankhurst et al., 2000; Calderón et al., 2007), contemporary with mafic volcanism of the Rocas Verdes Basin (Calderón et al., 2007). The mafic seafloor rocks of the Rocas Verdes Basin are distributed as incomplete ophiolite sequences (lacking the basal or ultramafic pseudo-stratigraphic components) that from north to south are known as the Sarmiento Complex, the Carlos III-Capitán Aracena Complex, and the Tortuga Complex (Fig 1a), all affected by seafloor-type hydrothermal metamorphism (up to greenschist facies) and of late Jurassic to early Cretaceous age (154-143 Ma) (Calderón et al., 2013). The ophiolite complexes are characterised mainly by massive to pillowed basalts and breccias, mafic dykes/sills of basalts, diabase and gabbros, and intercalations of cherts, siltstones, and black shales (Stern, 1991; Calderón et al., 2013); in the Sarmiento Complex, intercalations and/or dykes of felsic composition (rhyolitic tuffs, dacitic dykes, granophyres, and plagiogranites) are common (Calderón, 2006). These rocks have several primary textures as variolitic, ophitic to sub-ophitic, microgranular to seriate, intersertal to intergranular, amygdaloidal, spherulitic and lathwork, among others (Calderón et al., 2013; Letelier, 2019). The siliciclastic fine-grained cover of the Rocas Verdes Basin referred to as Erezcano/Zapata Formation (Lutitas Gris Verdosas in the subsurface; Mpodozis et al., 2011) is characterised by pyritic hemipelagic black shales and low-density turbidites with penetrative foliation and low-grade metamorphism (lower greenschist facies) (Wilson, 1991; Muller et al., 2021). This muddy cover also outcrops in the internal fold trust belt domain (Fig. 1b).

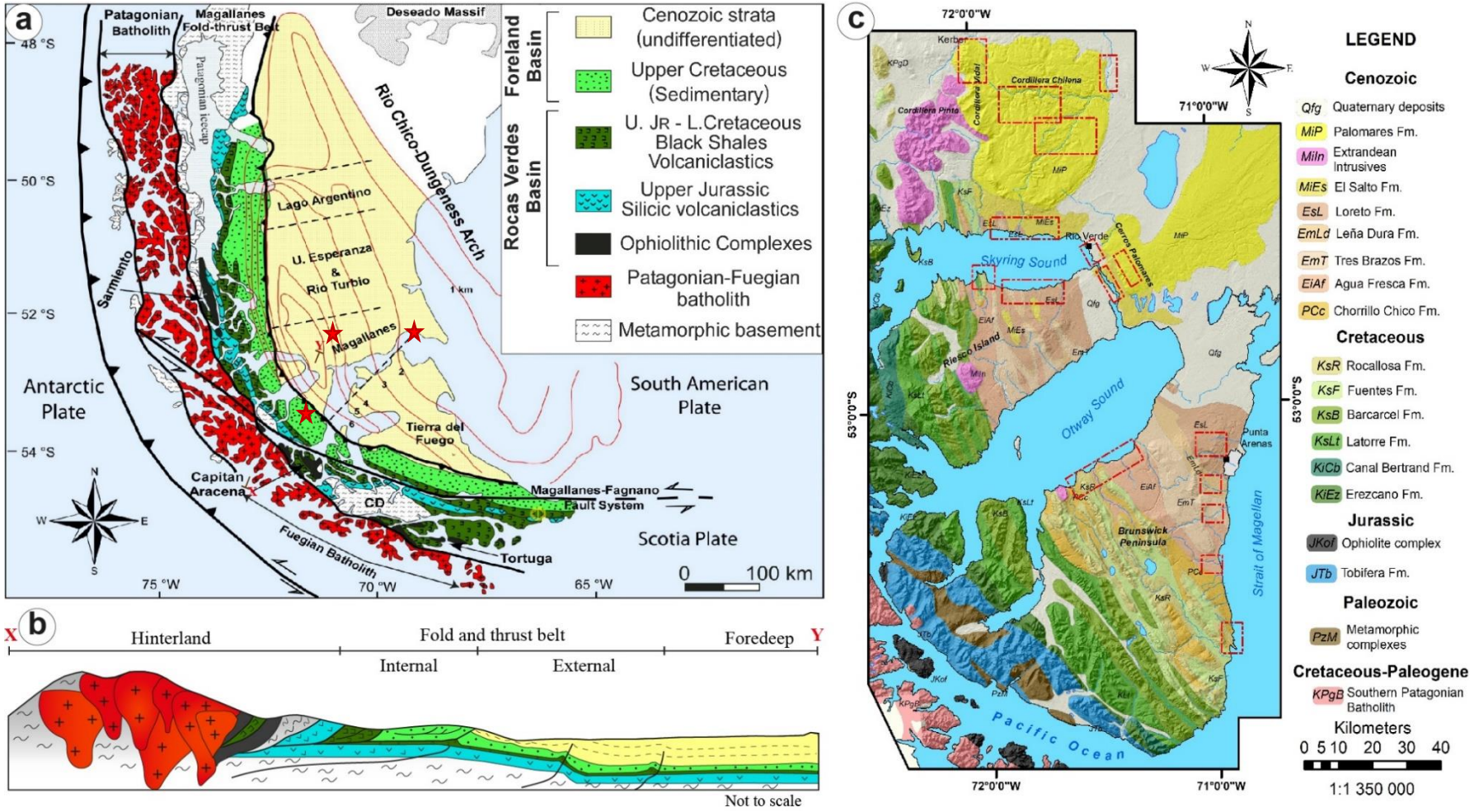

Figure 1. (a) The morphotectonic setting of the Magallanes-Austral foreland basin (modified from Rivera et al., 2020). Red stars for highlight position of subsidence curves in Fig. 9. Red isopach lines are the depth to top-Tobífera Formation (Late Jurassic). (b) A schematic structural transect of the orogenic wedge and foreland showing the location of different potential source terranes. (c) Simplified geologic map of the study area showing the stratigraphic sections (red boxes).

The internal fold thrust-belt domain comprises Lower to Upper Cretaceous siliciclastic rocks with penetrative foliation and tight folds (Fig. 1b). It includes the easternmost exposures of the Erezcano/Zapata Formation and the interfingered clinopyroxene- and amphibole-bearing pillow alkali basalts, andesitic lavas and volcanoclastic breccias of the Barros Arana Formation (in Ultima Esperanza Province) and the La Pera Complex of the Canal Bertrand Formation (in Magallanes Province) (Stern et al., 1991; Stern, 1991; Prades, 2008; Anguita, 2010). The mafic rocks of the Barros Arana Formation underwent low-grade metamorphism (prehnite-pumpellyite facies), which does not obliterate the primary textures (and minerals) similar to those of basalts of the ophiolite complexes (Ramírez de Arellano, 2006). Likewise, the volcanic rocks of the La Pera Complex experienced very low-grade metamorphism (zeolite facies) (Prades, 2008; Anguita, 2010), remaining intact the primary textures (porphyric, glomeroporphyric, intersertal, and amygdaloidal) in the clinopyroxene- and amphibole-bearing andesitic lavas and volcaniclastic rocks (microlitic) (Prades, 2008). The age of both the Barros Arana Formation and La Pera Complex is Albian, 104 ± 3 Ma and 101.4 ± 0.7 Ma (Stern et al., 1991; Mpodozis, en Alvarez et al., 2006), respectively. The internal fold-thrust belt also is composed of shaly, sandy, and some conglomeratic strata, representing protracted deep-marine turbidite sedimentation in the early foreland filling phase. The external fold-thrust belt (Fig. 1b) also includes uppermost Cretaceous and Paleogene foreland deposits and some scattered transitional alkaline to calc-alkaline plutons.

III-2.3 Sedimentology

III-2.3.1 Method

We conducted a detailed sedimentological analysis (at a cm-dm scale) of over ~1500 m thick composite stratigraphic succession at 15 localities across the coast north of Skyring sound, the Riesco Island, and the Brunswick Peninsula (Fig. 1c). The entire Maastrichtian-Burdigamian succession is represented by ten main facies associations (FA1 to FA10; Table 1) that illustrate the big picture of all the existing sedimentary environments in the study area. Composite stratigraphic columns for each studied formation are found in Fig. 2. Each facies association (Table 1) was designated based on lithologies, geometry and contacts, sedimentary structures, fossils, and trace fossils, which altogether represent a particular sedimentary environment. Palaeocurrents directions (n=500; Fig. 2) were determined from trough axes, imbricated clasts, planar cross-lamination, ripple marks, and current-oriented trunks. The paleocurrent data was tilt corrected where necessary following Le Roux (1991);

then, a circular statistical analysis was done to examine the quality and reliability of directions measured and test the existence of a preferential direction (see Table 2) by applying Rayleigh's test following Davis (2002) and Fisher and Powell (1989).

Table 1. Synthesis of facies associations and interpreted sedimentary processes of the studied units in the Magallanes-Austral Basin.

Code	Sedimentary characteristics	Geometry and thickness	Fossils and Bioturbation Index	Sedimentary processes and environment
FA1	Dark grey to black, finely laminated (fissile), siliceous sh. Some intercalations of massive to laminated, calcareous cly slt beds. Contorted beds, slumps, and calcareous concretions.	Sh successions (laterally extensive at 100's m scale) are up to 80 m thick. Tabular cly slt beds are 15-25 cm thick.	Polychaetes (serpulids). (BI=0-1) *Planolites* isp.	**Outer shelf to upper continental slope**: Hemipelagic deposition from suspension and vertical settling, and very dilute, low-density turbidites or distal tempestites, under poorly oxygenated conditions below the storm-wave base (Rivera et al., 2018, 2020).
FA2	Dark grey to light brown, finely laminated (fissile) slty sh, and intercalations of vfg slt beds. Bedding planes are commonly poorly developed. Calcareous concretions and tree trunk burrowed.	Sh successions are up to 50 m thick. Tabular slt beds are 10-25 cm thick.	Bivalves in life position. (BI=0-2) *Teredolites* isp.	**Offshore to nearshore:** Hemipelagic deposition from suspension and vertical settling, below or just above storm-wave base; affected by very dilute, low-density turbidite currents or distal tempestites.
FA3	Light black to grey and brownish, massive to finely laminated (fissile), micaceous sh commonly interbedded with well-stratified, massive to wavy-laminated cly slt, and massive to normally graded vfg ss. Synsedimentary sliding and slumping, and dewatering pipe structures. Calcareous concretions with syneresis cracks and tree trunks burrowed. (2) Small gullies cut some more silty sh intervals.	Laterally extensive sh successions are up to 15 m thick. Tabular slt and ss beds are 10-15 cm thick.	Plant debris. (BI=0-3), *Palaeophycos* isp., *Planolites* isp., *Teredolites longissimus*.	**Prodelta**: High sediment supply on unstable slope substrate with settling of fine mud and silt out of suspension alternating with distal fluvial outflows currents in highly stressed marginal marine environments with occasional wave reworking. (Coates and McEachern, 2007; Bhattacharya, 2010).
FA4	(1) Tan and greyish, sharp-based and well-stratified, massive to laminated ferruginous slt interbedded with massive to normally graded vfg-fg ss beds. Laminae of organic matter and plant debris along stratification planes. Upward, tan-to-whiteish, sharp-based and vaguely stratified, massive vfg ss with soft-sediment deformation structures, mud chips and rarely undulated lamination; the beds commonly display erosive bases. Some lens-shaped, massive mg ss beds are present. (2) Heterolithic, wavy-bedded slt and trough cross-bedded fg-mg ss beds with ubiquitous tidal bundles and mud, and organic matter drapes along foresets. Some gullies filled with cg ss.	Successions are up to 8 m thick. Tabular slt and vfg-fg ss beds are 25–60 cm thick; vfg ss beds are 60-90 cm thick, occasionally with an amalgamated appearance.	Plant debris. (BI=0-2) horizontal and vertical unidentified trace fossils.	**Delta front**: Deposition from rapidly decelerating friction-dominated outflows that pass downdip to a more liquefaction-prone substrate under an overall high sediment supply setting and limited wave reworking (Bhattacharya, 2010; Fielding, 2010). Alternated high and low fluvial discharges promoted river-fed turbidites (or hyperpycnal beds), leading to a high level of environmental stress (Coates and McEachern, 2007; Olariu et al., 2010). (2) Migrating subaqueous dunes produced by fluctuating ebb-flood current speed and direction; alternating traction deposition and mud settling from suspension during slack water (Willis, 2005; Bhattacharya, 2010).
FA5	(1) Beige to pale yellow, erosive-based, massive to trough cross-bedded fg-cg ss beds with poor to moderate sorting and pbl along foresets, intercalated with brown, lenticular clast-supported pbl cgl with poor sorting, shell hash and burrowed. Imbricated clasts and tree trunks are common. Some massive normally graded ss beds are present. (2) Tangential-based and herringbone cross-bedded mg ss beds with moderate to a high degree of bioturbation, mg-cg ss and pbl cgl with trough cross-stratification and mud partings also are present. Abundant tree trunks.	Amalgamated ss units up to 20 m thick. Lenticular bodies are typically 0.4- 2 m thick. Normally graded cycles are 20-30 cm thick.	Plant debris, bivalves, oysters, *Turritella* sp., and Chondrichthyan teeth; (BI=0-4) *Arenicolites* isp., *Skolithos* isp., *Ophiomorpha nodosa*, *Diplocraterion* isp., *Thalassinoides* isp., escape structures (*fugichnia*).	**Subaqueous delta plain:** Deposition by fast unidirectional confined and unconfined flows infilling distributary channels with upstream accretion or migration of subaqueous dunes bedforms (Bhattacharya, 2010); the limited to absent marine bioturbation and plant debris indicate rapid sedimentation rates and strong freshwater input (Rossi and Steel, 2016). (2) The bidirectional crossbedding, mud drapes and more bioturbation further indicates the role of tides at the river mouth (Willis, 2005; Rossi and Steel, 2016).

FA6	A finning-upward succession of pale yellow, slightly scoured laminated slt beds capped by finely laminated carbonaceous sh and coals. Pinstriped slt highly bioturbated interbedded with carbonaceous mdst. Locally, flaser, wavy lamination and rippled fg-ss are present. Accumulations of autochthonous to para-autochthonous shells beds preserved in fg-mg ss. Shell disposition range from in life position, concordant to bedding planes, or chaotic arrangement.	Laterally extensive successions up to 4 m thick. Coal beds are 20-60 cm thick. Shell-rich beds are laterally extensive and up to 5 m thick; rarely wedged.	Plant remains and leaf imprints, broken and articulated bivalves, oysters and gastropods. (BI=3-5) *Ophiomorpha* isp., escape structures (*fugichnia*).	**Interdistributary bay and marsh**: Continuous deposition mainly from suspension in low-energy environments and poorly drained areas with episodic traction sedimentation from decelerating sand-laden currents and overall limited wave action; late filing of abandoned distributary channels (Bhattacharya, 2010; Rossi and Steel, 2016). A buildup of bioherm in interdistributary bay of tidal channels, suggesting brackish conditions (Rodriguez-Raising et al., 2014).
FA7	(1) Grayish to reddish yellow, sharp-based, clast-supported, massive pbl-cbl cgl with poorly to moderately sorted and rounded clasts within a sandy matrix. Sharp- and erosive-based, massive mg-cg ss beds with moderately sorted and sub-rounded grains interbedded with pbl cgl lenses. Imbrication of clasts. (2) Tabular cross-bedded, moderately to well-sorted mg ss beds interbedded with trough cross-laminated, fg-mg ss with pbl along troughs and internally normally graded; tree trunks are present.	Sub-tabular to tabular (laterally extensive) amalgamated ss beds also lenticular mg-cg ss and pbl cgl; lobe-shaped terminations of cgl beds.	Plant remains, vertebrate bones. (BI=0-1) horizontal unidentified trace fossils.	**Braided fluvial system**: (1) proximal gravel-dominated system with the rapid accumulation of high-strength debris and sediment gravity flows, with bedload transported under conditions of rapid laminar to turbulent flows (Miall, 2014). (2) distal sand-dominated system with bed-load deposition from more diluted turbulent unidirectional flows, leading to downstream-accretion bedforms; winnowing of finer sediments forming a lag (Miall, 2014).
FA8	Dark grey to brownish, matrix-supported, massive and disorganised, cbl-bldr monomictic breccia. Matrix is composed of beige mg-cg pyroxene-rich ss, and clast and blocks are mainly basalts with amygdalar and vesicular textures, reaching up to 2 m in diameter. Occasionally, tuffaceous ss constitute the matrix. There are rare intercalations of massive, matrix-to-clast-supported oligomictic pbl-cbl cgl with sub-angular to sub-rounded clasts.	Successions up to 7 m thick. Lenticular cgl beds are up to 1 m thick.	Plant remains. (BI=0).	**Laharic deposits**: Deposition from hyper-concentrated and non-cohesive debris flows rapidly and *en masse* sedimentation without grain separation during transport (Smith and Lowe, 1991; Pierson, 2005). These flows incorporated both pre-and syn-magmatic eruption products and eroded pre-existing epiclastic and bedrock material in the path flow.
FA9	Fining-upward sequences composed of grey, sharp- and erosive-based, intraformational pbl cgl; greyish to blueish, trough to tabular cross-bedded cg-mg ss; whitish, horizontal- and rippled-laminated fg ss and slt. Common intercalations of tuff, tuffaceous mdst lenses and sharp-based, rippled-laminated tuffaceous ss. Mud-cracks in tuffaceous beds and soft-deformation are present.	Fining upward successions are 0.6-1.5 m thick. Tabular tuffaceous beds up to 1.5 m thick.	Null fossils. (BI=0-2) Rhizocretions, *Scoyenia* isp, *Feoichnus* isp.	**Meandering fluvial system**: Migrating 2D-3D bedforms in sinuous channels, developing lateral-accretion deposits and progressive waning in the flow regime (Miall, 2014). Fast channel fill by pyroclastic material leads to subaerial exposure of point bars and avulsion (Cuitiño and Scasso, 2013).
FA10	Tan-to-reddish, massive slt, and tuffaceous mdst interbedded with ripple-laminated fg ss and slt. Some carbonaceous layers are present.	Successions are up to 5 m thick. Tabular fg ss and slt are typically 23-60 cm thick and rare up to 1 m thick.	Plant or carbonaceous debris, leaf imprints. (BI=0-2), *Scoyenia* isp., Rhizocretions.	**Alluvial floodplains:** Deposition of fines from suspension in quiet and poorly drained areas, disrupted by overspilling flows from adjacent major channels; formation of peat locally (Miall, 2014).

BI: bioturbation index; cly: clayish; slty: silty; vfg: very fine-grained; fg: fine-grained; mg: medium-grained; cg: coarse-grained; pbl: pebble; cbl: cobble; bldr: boulder; mdst: mudstone; sh: shale; slt: siltstone; ss: sandstone; cgl: conglomerate.

III-2.3.2 Results and interpretations

III-2.3.2a Rocallosa and Chorrillo Chico Formations (latest Campanian to Thanetian)

The Rocallosa and Chorrillo Chico Formations were studied at the north and south coast of the Skyring Sound and along the east and west coast of the Brunswick Peninsula (Fig. 1b), where a partial thickness of 210 m and 65 m were measured for each formation, respectively (Fig. 2). The Rocallosa Formation spans from the latest Campanian to Maastrichtian (73.5 – 66 Ma; Rivera et al., 2021) and represents a siliciclastic shallow marine depositional system comprising lower to upper (locally foreshore and Gilbert-type deltas) shoreface environments dominated by waves and storms (Fig. 2), as main physical mechanisms, with paleocurrent data indicating a dominantly ESE transport ($\bar{\theta}$ = 106.5 ± 19.4°; L = 66.4%; Table 2). The deposits of the Rocallosa Formation indicate a progradation of the depositional system (Fig. 2), suggesting a progressive increase in sediment supply compared to accommodation available. The Chorrillo Chico Formation spans from the Danian to Thanetian (64.7 – 58 Ma; Rivera et al., 2021) and consists of a succession of deep-water turbidites representing basin plain to distal outer fan environments (Fig. 2) with palaeocurrent data indicating an NNW transport ($\bar{\theta}$ = 307.6 ± 5.09°; L = 94.9%; Table 2). The Chorrillo Chico Formation is a northwestward-prograding deep-marine fan system in a probably narrow foredeep aligned parallel to the Southern Patagonian Cordillera (Fig. 4a) that evidences the abrupt deepening of the basin, where the sediment supply is notoriously insufficient compared to the accommodation. A complete sedimentological characterisation for these formations is found in Sánchez et al. (2010) and Rivera et al. (2020).

III-2.3.2b Agua Fresca Formation (Ypresian)

The contact between the Agua Fresca and Chorrillo Chico formations is gradational (Charrier and Lahsen, 1969) and was interpreted as a paraconformity (Thomas, 1949; Rivera, 2017). In the subsurface, a truncation between these two units is apparent (Biddle et al., 1986; Rivera et al., 2021).

A 210 m-thick shale-dominated composite section of the Agua Fresca Formation was studied in the east and west coast of the Peninsula Brunswick (Fig. 1c), but its fine-grained nature limited its study to isolated outcrops from the middle and upper part. Textural variation in the unit is rather narrow, ranging from shales and silty shales to very fine siltstones, which compose FA1 and FA2 (Table 1). FA1 consists predominantly of non-bioturbated, thick intervals (up to 80 m thick) of finely-laminated (fissile) siliceous shales

intercalated with thin tabular beds of massive to laminated shaly siltstones; contorted beds (Fig. 3a) and concretions with polychaetes (serpulids) are also observed. The FA1 is interpreted to represent hemipelagic deposition interrupted by sporadic low-density turbidite currents in an outer shelf to an upper continental slope environment. FA2 exhibits similar facies (Table 1) that the previous one, however, it is more silty and bioturbated, with tree trunks highly burrowed (Fig. 3b) and marine fauna in life position. Moreover, the interbedded very dilute, low-density turbidites or distal tempestites are slightly coarser than in FA1. Therefore, we interpret a shallower environment, outer to inner shelf, for FA2 compared to the previous FA1. The lower part of the Agua Fresca Formation has been described by other authors (Todd and Kniker, 1952; Katz, 1961) as composed of sandstones, siltstones, and conglomerates that we speculate might represent the proximal (or inner) facies of a submarine fan system, similar to that inferred for the upper part of the Chorrillo Chico Formation. The Agua Fresca Formation represent the progressive silting up of a still underfilled basin (Fig. 4b), displaying a shallowing-upward cycle where sediment supply tends to equal accommodation.

Table 2. Circular statistical analysis results of paleocurrent data of the studied units in the Magallanes-Austral Basin.

Formation	Measures (n)	Vector mean azimuth ($\bar{\theta}$)	Mean resultant length ($\bar{R}$)	Consistency ratio (L)	Circular variance (*V*)	Circular standard error (ν; ± 2σ)	Concentration parameter (κ)*	Rayleigh's test (*p*=0.95) **	*p*-critical ***
Palomares	124	45.6	0.84	83.9%	0.16	5.95°	8.61	0.84	0.16
El Salto	44	47.1	0.94	93.9%	0.06	6.01°	8.61	0.94	0.26
Loreto (mode 1)	118	94.4	0.74	74.3%	0.26	7.90°	2.29	0.74	0.16
Loreto (mode 2)	90	286.2	0.85	84.6%	0.15	6.70°	3.68	0.85	0.18
Loreto (mode 3)	32	185.9	0.99	99.6%	0.004	2.00°	100	1.00	0.31
Tres Brazos	41	66.8	0.87	87.4%	0.13	9.20°	4.17	0.87	0.27
Chorrillo Chico	51	307.6	0.95	94.9%	0.05	5.09°	10.27	0.95	0.24
Rocallosa	28	106.5	0.66	66.4%	0.34	19.39°	1.79	0.84	0.33
Total paleocurrents	**528**								

* from Batschelet (1965) and Gumbel et al. (1953)

** if Rayleigh' test > *p*-critical, H_0 is rejected, and the sample has a preferred mean direction

*** from Mardia (1972)

III-2.3.2c Tres Brazos Formation (Ypresian to Lutetian)

The Tres Brazos Formation spans from the latest Ypresian to Lutetian (48.6 – 43.7 Ma; Rivera et al., 2021) and the contact with the underlying Agua Fresca Formation is poorly exposed on the surface. However, it was interpreted as a paraconformity (Thomas, 1949; Todd and Kniker, 1952; Rivera, 2017; Rivera et al., 2021).

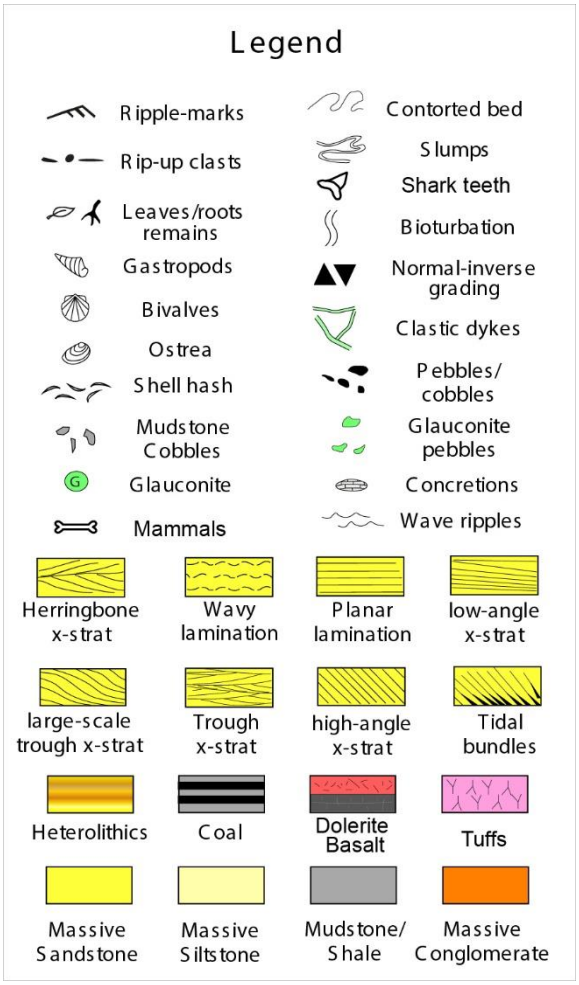

Figure 2. Composite stratigraphic columns with facies associations, palaeocurrents, and sampled intervals for each unit studied. Stratigraphic logs from Rocallosa and Chorrillo Chico formations were modified after Rivera et al. (2020).

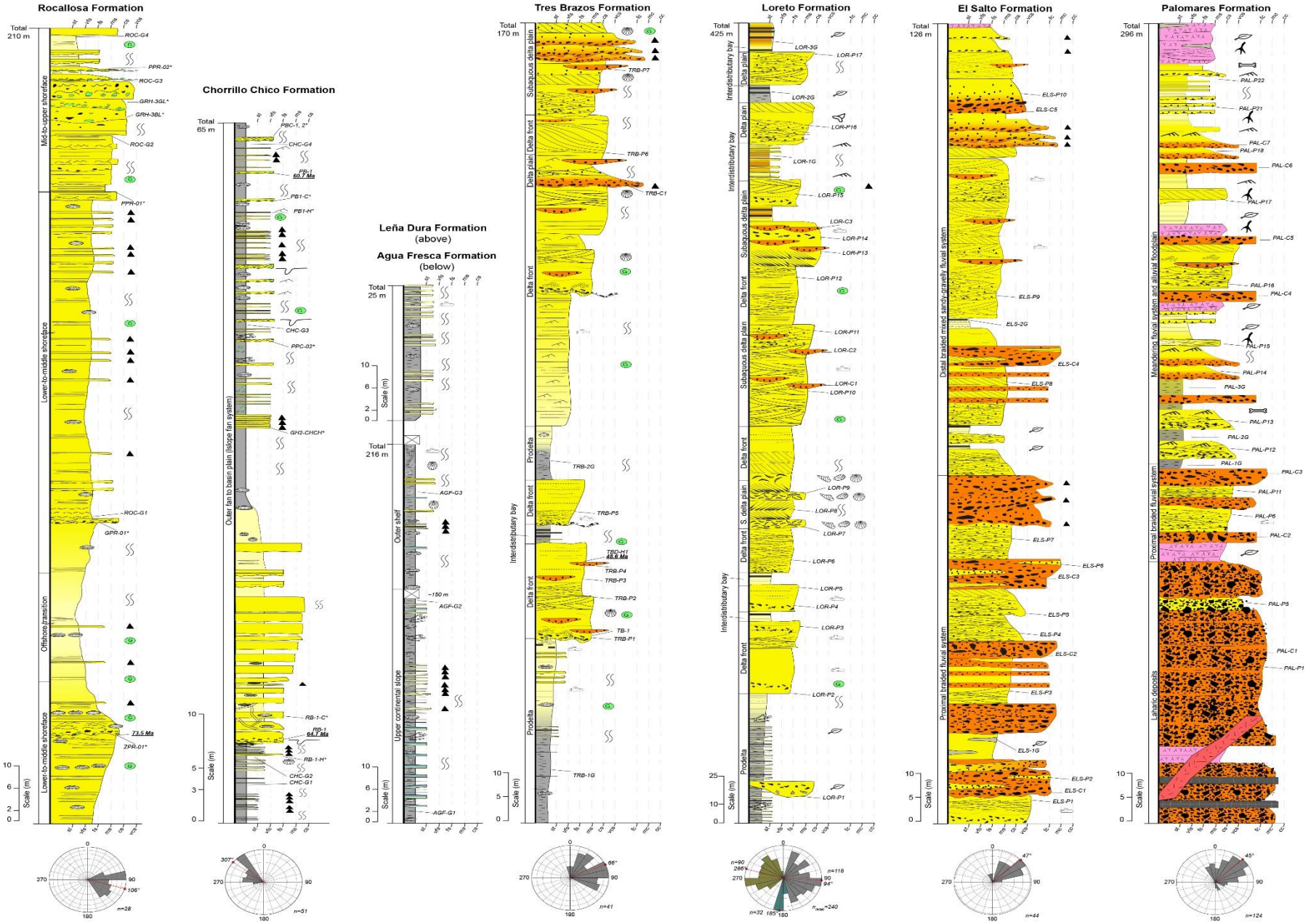
Rocallosa Formation
Total 210 m
Mid-to-upper shoreface
Lower-to-middle shoreface
Offshore-transition
Lower-to-middle shoreface
ROC-G4
PPR-02*
ROC-G3
GRH-3GL*
GRH-3BL*
ROC-G2
PPR-01*
ROC-G1
GPR-01*
73.5 Ma
ZPR-01*
Scale (m)
Chorrillo Chico Formation
Total 65 m
Outer fan to basin plain (slope fan system)
PBC-1, 2*
CHC-G4
PB-1
60.7 Ma
PB1-C*
PB1-H*
CHC-G3
PPC-02*
GH2-CHCH*
RB-1-C*
RB-1
64.7 Ma
RB-1-H*
CHC-G2
CHC-G1
Leña Dura Formation
(above)
Agua Fresca Formation
(below)
Total 25 m
Total 216 m
Outer shelf
Upper continental slope
AGF-G3
~150 m
AGF-G2
AGF-G1
Tres Brazos Formation
Total 170 m
Subaqueous delta plain
Delta plain
Delta front
Prodelta
Interdistributary bay
TRB-P7
TRB-P6
TRB-C1
TRB-2G
TRB-P5
TRG-H1
65.6 Ma
TRB-P4
TRB-P3
TRB-P2
TB-1
TRB-P1
TRB-1G
Loreto Formation
Total 425 m
Interdistributary bay
Delta plain
Subaqueous delta plain
Delta front
S. delta plain
Prodelta
LOR-3G
LOR-P17
LOR-2G
LOR-P16
LOR-1G
LOR-P15
LOR-C3
LOR-P14
LOR-P13
LOR-P12
LOR-P11
LOR-C2
LOR-C1
LOR-P10
LOR-P9
LOR-P8
LOR-P7
LOR-P6
LOR-P5
LOR-P4
LOR-P3
LOR-P2
LOR-P1
El Salto Formation
Total 128 m
Distal braided mixed sandy-gravelly fluvial system
Proximal braided fluvial system
ELS-P10
ELS-C5
ELS-P9
ELS-2G
ELS-C4
ELS-P8
ELS-P7
ELS-P6
ELS-C3
ELS-P5
ELS-P4
ELS-C2
ELS-P3
ELS-1G
ELS-P2
ELS-C1
ELS-P1
Palomares Formation
Total 296 m
Meandering fluvial system and alluvial floodplain
Proximal braided fluvial system
Laharic deposits
PAL-P22
PAL-P21
PAL-C7
PAL-P18
PAL-C6
PAL-P17
PAL-C5
PAL-P16
PAL-C4
PAL-P15
PAL-P14
PAL-3G
PAL-P13
PAL-2G
PAL-P12
PAL-1G
PAL-C3
PAL-P11
PAL-P6
PAL-C2
PAL-P5
PAL-C1
PAL-P1

A 170 m-thick succession of the Tres Brazos Formation was studied at its type locality in the east coast of the Brunswick Peninsula (Fig. 1c), where is characterised by a muddy base and coarsening-upward trend, low degree of bioturbation, high amounts of organic matter, and shallow-water clinoforms typical for progradation of deltaic systems represented by FA3 to FA5 (Table 1). FA3 includes well-stratified laminated shale (Fig. 3c), massive to wavy-laminated muddy siltstone, and sharp-based massive to normally graded sandstone beds. Synsedimentary sliding and thrusting, and dewatering structures are common. FA4 comprises alternations of well-stratified, massive to laminated siltstone and massive to normally graded sandstone beds. Stratigraphically upward, poorly-stratified, lenticular massive very fine- to medium-grained sandstones (Fig. 3e) with soft-sediment deformation structures and rarely undulate lamination. FA5 consists of amalgamated, massive and cross-bedded sandstones, intercalated with lenticular pebble conglomerates and normally graded sandstone beds at the top of the section (Fig. 3f). Palaeocurrent indicators suggest east to northeast flows ($\bar{\theta} = 66.8 \pm 9.2°$; L=87.4%). The Tres Brazos Formation is interpreted as an eastward- to a northeastward-prograded fluvial-dominated delta (Fig. 4c), in a vertical succession FA3 is interpreted as a prodeltaic environment, followed upward by a delta front of FA4 and subaqueous delta plain of FA5. The fluvial-dominated interpretation is based on large amounts of silt, organic matter and a relatively low degree of bioturbation with low ichnodiversity in well-laminated deposits, typical of fluvial flows reflecting fluctuations in river discharge (Coates and McEachern, 2007; Bhattacharya, 2010; Rossi and Steel, 2016). Moreover, the abundance of unidirectional current structures within the sandstones, the presence of channels at the top of the succession with a marked scarcity of tidal or wave reworking, further support the river-dominated delta interpretation (Olariu et al., 2010). The Tres Brazos Formation represents the culmination of the shallowing-upward cycle that began in the Ypresian, evolving from an aggradational to a progradational (sedimentation overcomes accommodation) depositional system.

III-2.3.2d Leña Dura Formation (Lutetian to Bartonian)

The Leña Dura Formation is poorly exposed in our study area, and we studied patchy outcrops (totalling 25 m in thickness; Fig. 2) probably belonging to the middle part of the unit. The contact with the underlying Tres Brazos Formation is poorly exposed (or even not exposed) in the surface. However, Thomas (1949) claim that this contact is discordantly manifested by progressives onlaps of the Leña Dura Formation over the Tres Brazos Formation.

We recognised facies ascribed to FA2 (Table 1), composed of grey to light brown, silty shales with abundant calcareous concretions, some intercalations of thin-bedded siltstones, bivalves in life position and tree trunks whose cores are burrowed by *Teredolites* isp. (Fig. 3b) We interpret an inner to outer shelf environment for the Leña Dura Formation, similar to the upper interval of the Agua Fresca Formation. The Leña Dura Formation represents a short transgressive event with increased accommodation regarding the previous deltaic system of the Tres Brazos Formation.

III-2.3.2e Loreto Formation (latest Bartonian to latest Priabonian)

The Loreto Formation was studied in its type locality, around Punta Arenas, and in several sections along the north and south coast of the Skyring Sound (Fig. 1c). The contact with the underlying Leña Dura Formation is gradational (c.f. Hofstetter et al., 1956).

We have studied a ~430 m-thick succession of the unit, which is characterised by a mainly silty base, several coal seams, and channelised coarse-grained sandstone beds at the top of the succession, exhibiting an overall coarsening-upward trend (Fig. 2) similar to that displayed by the Tres Brazos Formation. The Loreto Formation includes FA3 to FA6 (Table 1), which are consistent with prograding deltas, but with certain particularities that distinguish it from the fluvial-dominated delta of the Tres Brazos Formation. FA3 presents more frequent intercalations of sharp-based glauconitic siltstone beds and is commonly cut by gullies. These gullies are composed of massive, medium- to coarse-grained sandstones with rip-up blocks (Fig. 3m). We interpret FA3 to represent a more proximal prodelta compared to that in the Tres Brazos Formation. A mid-to distal prodelta environment may correspond to the uppermost part of the Leña Dura Formation not studied here. The delta front environment (FA4) includes rhythmic heterolithic siltstones and sandstones beds, wavy-laminated siltstones and trough cross-laminated sandstones and abundant trunks and plant debris (Fig. 3d). Tidal bundles, mud drapes, organic-rich mud partings and several gullies, are also distinctive features of FA4. The subaqueous delta plain (FA5), also include tangential-based and herringbone cross-bedded medium-grained sandstone beds (Fig. 3g) with abundant flow-oriented tree trunks (commonly in cores of concretions), shark teeth, and moderate to high degrees of bioturbation. A low diversity but abundant vertical traces characterises bioturbation, which comprises *Skolithos* isp., *Ophiomorpha nodosa*, *Diplocraterion* isp., mud-lined vertical tubes (cf. *Rosselia* isp.), fugichnia traces, and some *Thalassinoides* isp. FA6 includes finning-upward successions of slightly scoured, horizontal-laminated siltstone beds capped by coaly paper shales interbedded with thin coals

seams (Fig. 3h). Pinstriped siltstones with flaser to wavy lamination (Fig. 3i) and rippled-laminated fine-grained sandstones are interbedded with laterally extensive, autochthonous to para-autochthonous shell-rich (oysters, bivalves, and gastropods) beds. We interpret FA6 to represent relatively low-energy interdistributary bays ending in peat (paralic) marsh areas (Bhattacharya, 2010; Schwartz and Graham, 2015); alternatively, it could be interpreted as abandoned filling of distributary channels (Rossi and Steel, 2016). The vertical stacking of FA's (Fig. 2) indicates that the deltaic system of the Loreto Formation was controlled by the interactions among fluvial, wave, and tidal processes at different scales of magnitude and different stratigraphic (i.e., time) positions. Wave activity, although present, was not determinant as indicated by lack of hummocky- and swaley cross-stratification and combined oscillatory and unidirectional flow structures across the stratigraphic column. On the other hand, fluvial and tidal processes were the dominant controls. Preserved fluvial signals are akin to those of the delta of the Tres Brazos Formation. Moreover, the presence of gullies incised in the prodelta and distal delta front (FA3 and FA4) infilled by coarse-grained sands, further support strong river influence. Tidal indicators (Fig. 3g, i) which are compelling in the proximal delta front and subaqueous delta plain (FA4 and FA5) are represented by tangential-based and bi-directional cross-stratification, abundant mud drapes along foresets of sedimentary structures, rhythmical heterolithic and mud (organic-rich) partings, typically associated with limited ichnodiversity produced by opportunistic marine fauna related to brackish-water settings (Willis, 2005; Bhattacharya, 2010; Schwartz and Graham, 2015; Rossi and Steel, 2016). Deltaic lobes prograded in a dominant east direction ($\bar{\theta}$ = 94.4 ± 7.9°; L = 74.3%), reaching a shelf-edge position as indicated in Fig 4d (see also Gallardo, 2014). However, intense tidal reworking also imprinted a northwest direction ($\bar{\theta}$ = 286.2 ± 6.7°; L = 84.6%) on deposits. Another subordinate southward ($\bar{\theta}$ = 185.9 ± 2°; L = 99.6%) palaeocurrent direction is found locally related to aligned logs in FA4. In synthesis, the Loreto Formation represents a complex eastward-prograding mixed-energy shelf-edge delta, where fluvial and tidal processes prevailed. During deposition of Loreto Formation sediment supply is greater than the available accommodation, leading to progradation of the depositional system, reaching a filled basin stage.

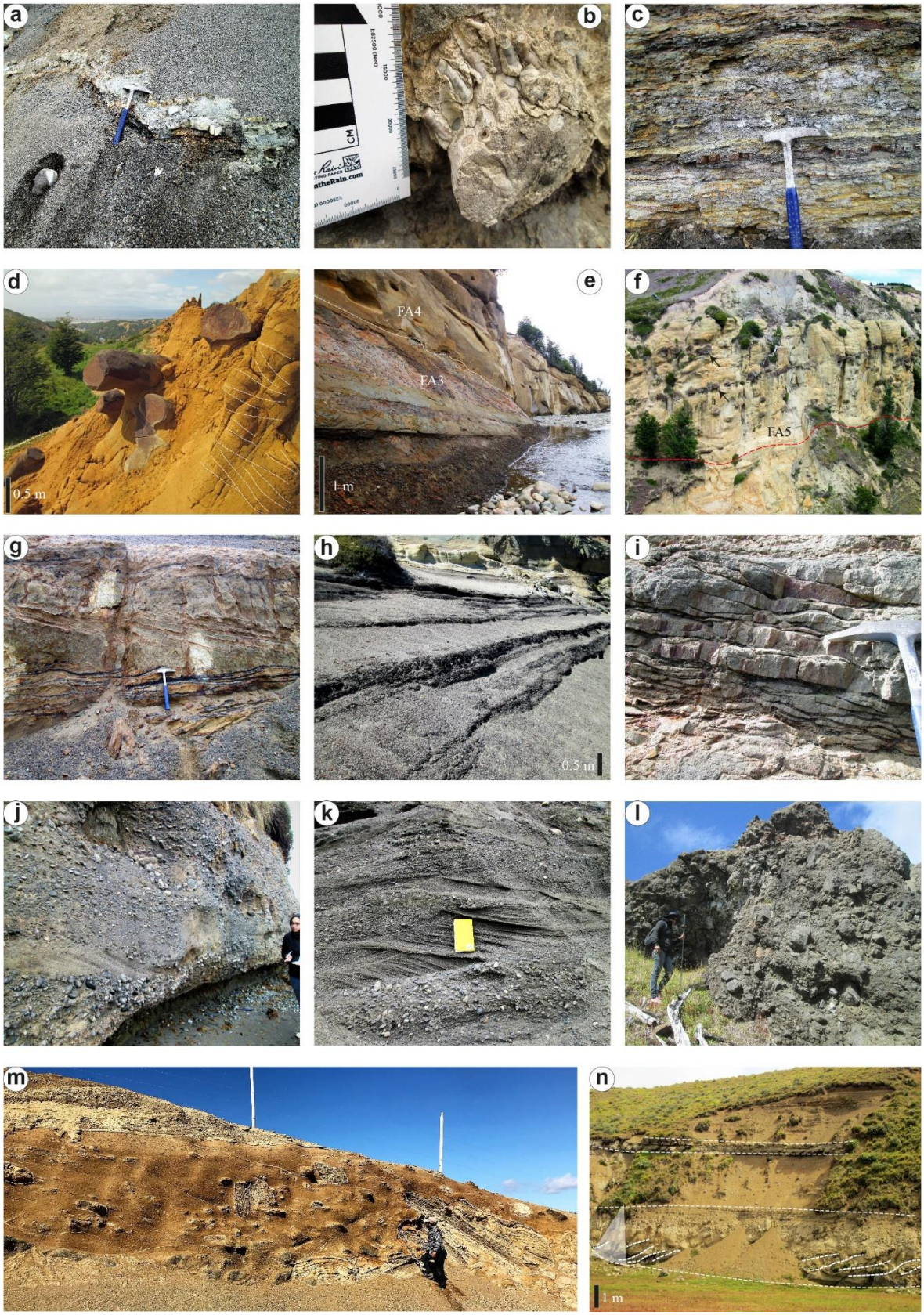

Figure 3. (a) Contorted bedding in FA1, the Agua Fresca Formation. (b) *Teredolites* isp. in fossilised trunks of FA2. (c) Finely-laminated shales intercalated with massive siltstones in FA3. (d) Trough cross-bedding and oriented fossilised trunks in delta front deposits FA4 (e) Sharp contact between prodelta deposits (FA3) and massive sandstones of delta front (FA4). (f) Panoramic view of massive to cross-bedded sandstones and

conglomeratic channels (arrows) of FA5. (g) Bidirectional cross-stratification and carbonaceous/mud drapes in foresets in subaqueous delta plain sandstones (FA5). (h) Fissile coaly paper shales interbedded with thin coals seams (FA6). (i) Pinstriped siltstones with flaser to wavy lamination in FA6. (j) Laterally extensive cobble conglomerate bed with tabular cross-bedded sandstones lenses in gravel-rich subfacies of FA7. (k) Stacked trough cross-bedded sandstones in sand-rich subfacies of FA7. (l) Matrix-supported, boulder monomictic (basaltic) breccia in FA8. (m) Channelised body with rip-up clasts (cobbles and boulders) cutting FA3, note the cobbles and boulders are ripped off from prodelta deposits. (n) Fining-upward cycle displaying laterally accreting sandstones bars at the base (lower third of image; FA9), followed by massive siltstones/mudstones interbedded with tabular, rippled-laminated sandstones (crevasse splay deposit) in FA10.

III-2.3.2f El Salto Formation (latest Rupelian to latest Aquitanian)

We have studied a 126 m-thick succession of the El Salto Formation, along the north and east coast of the Skyring Sound (Fig. 1c). An angular unconformity separates the El Salto Formation from the underlying Loreto Formation (González and Tapia, 1952; González, 1953; Rivera et al., 2021).

The El Salto Formation is dominated by FA7 (Table 1). However, the lower Las Coles member is more gravel-rich than the middle Río Verde member, which is more sand-rich (Fig. 2). The gravel-rich subfacies of FA7 includes clast-supported, coarse pebble (typically 4 cm in diameter) to cobble (up to 24 cm in diameter) conglomerates, with poorly to moderately sorting and a coarse-grained sandy matrix. Conglomerate beds are laterally extensive (at 100's m scale) and reach up to 12 m thick. Conglomerate beds showing tabular geometry rest on basal erosion surfaces and imbricated clasts are observed in some layers. In contrast, those with lobe-shaped geometry have sharp and planar bases and are structureless. Massive to rarely tabular cross-bedded, medium- to coarse-grained sandstone bodies occur as lenses within conglomerate beds (Fig. 3j). More locally, lenses of siltstones and mudstones with lignite streaks were observed. The sand-rich subfacies of FA7 (Fig. 3k) is characterised mainly by stacked, tabular and trough cross-bedded, medium-grained to pebbly sandstones (troughs are lined with small pebbles) intercalated with thin beds of clast-supported, massive, pebble conglomerates. Additionally, well-sorted, massive, very fine- to medium-grained sandstones with ferruginous siltstones and carbonaceous mudstones with small lignite lenses are common, including interbedded small-pebble conglomerate lenses. Sedimentary facies of FA7 are consistent with deposition in a braided fluvial system in a mainly stream-dominated alluvial fan. The gravel-rich facies represent the proximal, high-energy gravel-dominated part of the system composed of gravel bar bedforms but also with frequent accumulations of low-strength, high-density debris and sediment gravity flow during high discharge events (DeCelles et al., 1991; Miall, 2014). On the other hand, the

sand-rich facies of FA7 is interpreted to be a distal braided mixed sandy-gravelly fluvial system with bed-load deposition from more diluted turbulent unidirectional flows, leading to a variety of sandy downstream-accretion bedforms, as indicated by tabular and trough cross-bedding (Miall, 2014). The waning-flood stages and shifting of shallow braided channels or bar-top deposits allowed that fine-grained sediments to fill abandoned channels and develop poorly drained interchannel areas (DeCelles et al., 1991; Miall, 2014). Palaeocurrent data of the El Salto Formation suggest a dominant eastward-northeastward ($\overline{\theta}$ = 47.1 ± 6.01°; L = 93.9%) dispersion of sediments in the alluvial fan system. The El Salto represents the beginning of the net continentalization of depositional systems (Fig. 4e) in an overfilled basin stage, where the sediment supply far exceeds the available accommodation.

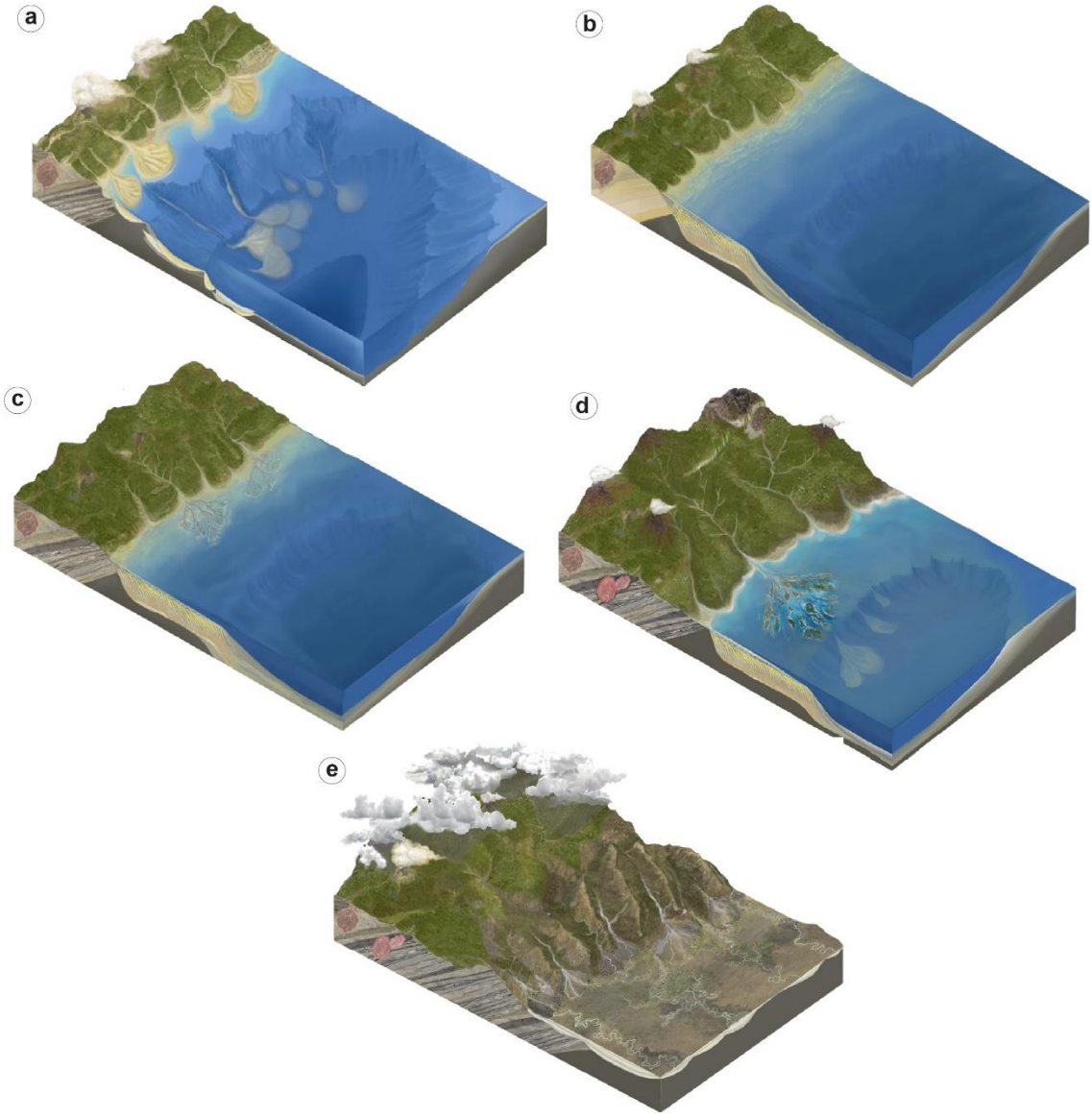

Figure 4. (*previous page* ←) Idealised and schematic depositional systems for the Cenozoic foreland succession. (a) Submarine fan system in Chorrillo Chico Formation. (b) Aggrading (accretionary) shelf margin and slope system in Agua Fresca and Leña Dura formations. (c) Progradding inner shelf ("shoal-water") fluvial-dominated delta system of the Tres Brazos Formation. (d) Progradding mid-shelf to shelf-edge mixed-energy delta system of the Loreto Formation. (e) Braided to meandering fluvial systems of the El Salto and Palomares formations.

III-2.3.2g Palomares Formation (Burdigalian)

In a wedge-top position, the Palomares Formation is separated by an angular unconformity from the El Salto Formation (González, 1953; García et al., 1953; Rivera et al., 2021). However, forelandward a slight erosion surface marks the contact between the Palomares and El Salto formations. In a west-to-east transect, the calibre of sediments decrease from a very coarse breccia (Vidal member) pass laterally and gradually to coarse bluish sandstones (San José member) and then to medium-grained tuffaceous sandstones, and tuffs (Penitente member).

The Vidal member of the Palomares Formation is composed of volcaniclastic rocks formed by fragmentation of lava flows and eroded pre-existing bedrock material. The Vidal member is represented by FA8, which consists of matrix-supported, massive and disorganised, cobble to boulder monomictic breccia (Fig. 3l). The matrix is composed mainly of medium- to coarse-grained pyroxene-rich sandstones, but tuffaceous sandstones are also observed. The cobbles (typically 10-25 cm in diameter) and boulders (reaching up to 2 m in diameter) are composed entirely of basalts, trachybasalts and basaltic trachyandesites. These basalts exhibit amygdalar and vesicular textures. Rare intercalations of matrix- to clast-supported, oligomictic pebble to cobble conglomerates are present. The conglomerate beds are crudely stratified and internally massive, and the clasts are sub-angular to sub-rounded. We interpret FA8 to represent rapid *en masse* non-cohesive debris and hyper-concentrated flows without grain separation during transport and where the interplay of shear stress, buoyancy, and dispersive pressures keep large boulders moving into the flow (Smith and Lowe, 1991; Pierson, 2005). Because basalts and volcanic material is the primary component of debris and hyper-concentrated flows, we interpret FA8 to represent lahar deposits. The remaining succession of the Palomares Formation comprises sedimentary facies already described in FA7 of the underlying El Salto Formation, but also FA9 and FA10 are present. In the Palomares Formation, FA7 mainly represents a distal braided mixed sandy-gravelly fluvial system but with frequent intercalations of thin beds (10-15 cm thick) of clast-supported, sub-angular, pebble-to-small-cobble conglomerates and

matrix-supported, pebble-to-cobble breccias. These conglomerate and breccia beds are poorly-sorted, with sharp and planar bases and basaltic composition. They are interpreted to be the distal reaches of debris and laharic flows (FA8). FA9 is less common, and it consists of erosive-based fining-upward packages (0.6-1.5 m thick) of intraformational clay-pebble conglomerate followed by tabular to trough cross-bedded, coarse- to medium-grained sandstones and horizontal- to rippled-laminated fine-grained sandstone and siltstone beds (Fig. 3n). Some intercalations of structureless and cross-bedded tuff, accretionary lapilli, tuffaceous mudstone with desiccation cracks, and rippled tuffaceous sandstone beds with sharp basal and upper contacts are commonly observed. Bioturbation is characterised by some occurrences of *Scoyenia* isp., and *Feoichnus* isp. FA10 includes massive siltstone and volcaniclastic mudstones beds (up to 5 m thick) rich in plant fragments, leaf imprints (Nothofagaceae plants) and rhizocretions. These mudstone beds are interbedded with tabular, massive to rippled-laminated, fine-grained sandstones (23-60 cm thick) (Fig. 3n). We interpret FA9 to represent filling deposits of sinuous channels (point bars) reflecting waning phases of the unidirectional currents in a coarse meandering fluvial system affected by intermittent strong volcanic activity (surges and ashfall) (Miall, 2014; Cuitiño and Scasso, 2013). On the other hand, sedimentary facies in FA10 are consistent with deposition in quiet and poorly drained areas disrupted by overspills flows from adjacent major channels (crevasse splays), in an alluvial floodplain environment (Miall, 2014). The association of FA9 and FA10 further supports the latter interpretation. Palaeocurrent data in the Palomares Formation, indicate a dominant northeastward ($\bar{\theta}$ = 45.6 ± 5.95°; L = 83.9%) transport direction similar to that of the earlier El Salto Formation. Palomares represents the continuation of a continental depositional system (Fig. 4e) that had begun since the late Oligocene, where the accommodation is insufficient concerning the supply of sediments.

III-2.4 Conglomerate and Sandstone petrology

III-2.4.1 Methods

The conglomerate composition was determined by counting around 100 clasts (cobbles and pebbles) within a 1 m^2 grid in different field stations. Some clasts with dubious macroscopic identification were microscopically examined. The counts are presented as clast percentage (Table 3; Fig. 4), totalling 1860 clasts in the Chorrillo Chico (conglomeratic facies in Cabo Nariz, Tierra del Fuego), Tres Brazos, Loreto, El Salto, and Palomares formations. The clasts were categorised into the following lithologic groups: (1) metamorphics, which include slates, schists, and minor cataclasites; (2) granitoids,

comprising tonalites, monzogranites, granodiorites/diorites; (3) basalts and basaltic scorias; (4) gabbros and dolerites; (5) intermediate volcanics, composed by porphyritic and trachytic andesites; (6) silicic volcanics, comprising rhyolite, pumice, and quartz-porphyry; (7) quartz and chert; (8) sedimentary rocks. It is assumed that primary source terranes are represented by assemblages of specific lithologies as follows: cordilleran magmatic arc, including granitoids and intermediate volcanic rocks; Rocas Verdes Basin remnants, comprising basalts and silicic volcanic and sedimentary rocks; andean metamorphic basement, composed by metamorphic rocks, quartz and chert.

The Gazzi-Dickinson method (Ingersoll et al., 1984) was used in counting about 400-500 points in each thin section of the new forty-seven (47) medium-grained sandstone samples (from Tres Brazos up to Palomares formations) (Fig. 2; Table 4). The modal sandstone analysis also included 25 sandstones samples from the Rocallosa and Chorrillo Chico Formations previously published by Rivera et al. (2020). Framework compositions were normalised to traditional quartz-feldspar-lithics (QFL) and monocrystalline quartz-feldspar-lithic total (Q_mFL_t) to be compared with the tectonic provenance fields of Dickinson (1985). Samples from the Latorre and Barcárcel Formation (McAtamney et al., 2011) were plotted in the ternary tectonic provenance diagrams to gain insights over Cretaceous long-term provenance changes.

In essence, all the framework grains or clasts normalisations are modal (sub)compositions of the sandstones and conglomerates and, in this way, must be analysed as compositional data (see Weltje, 2002, 2012 and Tolosana-Delgado, 2012 for a comprehensive review of this subject). Recognising the compositional nature of this type of data implies that (1) the simple use of traditional ternary diagrams to represent three variables in two-dimensional space can raise predictability and interpretation issues of the fields of provenance (Weltje, 2002, 2006; Ingersoll and Eastmond, 2007). (2) Systematic temporal analysis of increase/decrease in petrographic classes are meaningless, and any classical statistical treatment of this type of dataset could lead to spurious results (Tolosana-Delgado, 2012).

To overcome the latter issues, we applied a centred log-ratio transformation (Aitchison, 1986) to the compositional database. All recorded zeros in the raw data were replaced with 0.5 (maximum round-off error; Weltje, 2002; Ingersoll and Eastmond, 2007) to conduct the logarithmic transformation. To capture reliable compositional variations, we use statistically rigorous confidences and probability (predictive) regions for the sandstone

point-counting data, which are plotted in both the traditional Dickinson Model-based ternary diagram, as well as in the iso-density partitioning of compositional space of the Dickinson Model's provenance fields (Weltje, 2006). Furthermore, we have performed a principal component analysis represented in a triangular space to highlight the affinity of the modal composition for each studied formation with end-members or potential source rocks.

Table 3. Conglomerate clast composition data of the studied units in the Magallanes-Austral Basin.

Formation	Station	Clasts counted	Metamorphic	Granitoid	Basalt / basaltic scoria	Gabbro/ dolerite	Intermediate volcanic	Silicic volcanic	Quartz/ chert	Sedimentary (ss, mdst, slt)
		(n)	(%)	(%)	(%)	(%)	(%)	(%)	(%)	(%)
	PAL-C07	102	4.9	-	26.5	-	29.4	12.7	26.5	-
	PAL-C06	165	-	-	42.4	6.1	9.1	24.2	18.2	-
	PAL-C05	124	12.1	6.5	24.2	-	21.8	29.8	5.6	-
Palomares	PAL-C04	114	-	-	21.9	-	27.2	50.9	-	-
	PAL-C03	90	-	-	83.3	-	-	16.7	-	-
	PAL-C02	115	-	-	26.1	-	-	47.8	26.1	-
	PAL-C01	103	-	22.3	36.9	4.9	-	35.9	-	-
	ELS-C05	122	-	46.7	8.2	-	20.5	-	24.6	-
	ELS-C04	100	31	11	9	8	16	-	25	-
El Salto	ELS-C03	104	28	-	29.8	3.8	16.3	22.1	-	-
	ELS-C02	100	18	7	19	-	29	-	13	14
	ELS-C01	121	20.7	9.9	22.3	-	10.7	-	17.4	19
	LOR-C03	103	8.7	6.8	20.4	-	23.3	10.7	30.1	-
Loreto	LOR-C02	100	5	11	4	-	41	10	29	-
	LOR-C01	103	5.8	4.9	12.6	-	36.9	22.3	17.5	-
Tres Brazos	TRB-C01	106	17	5.7	0	0	10.4	-	39.6	27.3
Chorrillo Chico*	CN08-2	88	5.7	13.6	4.5	2.3	39.8	14.8	5.7	13.6
Total		**1860**								

*Cabo Nariz member

III-2.4.2 Results and interpretations

III-2.4.2a Conglomerate clasts counting

Chorrillo Chico Formation (Cabo Nariz facies): intermediate volcanic (39.8%), silicic volcanic (14.8%), granitoid (13.6%), and sedimentary rock (13.6%) clasts dominate the unit (Table 3). Sedimentary rocks are characterised by shales presenting a considerable amount of epiclastic components (vitric shards, microlites) and evidence of ductile shear suggesting a probable early Cretaceous age; sandstones contain abundant rhyolite rock fragments. In provenance terms, three primary sources terranes contributed detritus to this

Formation: the Cordilleran Magmatic arc (55.7%), Rocas Verdes Basin remnants (32.9%), and metamorphic basement (11.4%) (Fig. 5b).

Tres Brazos Formation: clasts composition in the upper part of the unit are dominated by quartz and chert (39.6%) and sedimentary rocks (27.4%). Slates (17%), intermediate volcanics (10.4%) and minor granitoid (5.7%) clasts are subordinated (Table 3). Siltstones and shales compose the sedimentary rocks present. There is an abrupt decrease of the Cordilleran Magmatic arc (16%) detritus compared to the Paleocene Chorrillo Chico Formation; on the contrary, the metamorphic basement (56.6%) and recycled foreland strata (27.4%) are the primary source of detritus to the Tres Brazos Formation (Fig. 5b).

Loreto Formation: intermediate volcanic, quartz, and chert clasts make up over 50% of all the samples studied. In the upper-mid part of the unit predominates andesites (mean 39.5%), quartz and chert (mean 33.5%), and silicic volcanic (mean 16.5%; mainly pumice and quartz-porphyry) clasts (Table 3). In the uppermost part of the formation, intermediate volcanic (23.3%) clasts decrease as quartz and chert (30.1%), slate (9%) and basaltic (20.4%) clasts slightly increase (Table 3). The primary sources of detritus are the Cordilleran Magmatic arc (41.7%), the metamorphic basement (32.3%), and Rocas Verdes Basin remnants (27%) (Fig. 5b).

El Salto Formation: clasts composition is variable through the three members of the units. The lower two samples belonging to the Las Coles member are dominated by basaltic (mean 20.7%), intermediate volcanic (mean 19.9%), and greenish slate (19.3%; with penetrative foliation likely of Early Cretaceous age) clasts; subordinately, are sedimentary rocks (16.5%; mainly mudstones and siltstones) and chert (15.2%) clasts (Table 3). In the middle Rio Verde member, there is an increase of basaltic (29.8%) and greenish slate (27.9%) clasts, whereas sedimentary rocks, quartz and chert clasts are sparse or null; also appears silicic volcanic (22.1%; entirely pumice) clasts while andesites decrease (16.3%) (Table 3). The upper San Antonio member present an abrupt decrease in basaltic (8.6%) and green slate (15.5%) clasts, whereas granitoid (28.9%), quartz and chert (24.8%), and intermediate volcanic (18.2%) clasts predominate (Table 3). There is an up-section increase in Cordilleran Magmatic arc (from 28.3 to 51.1%) and metamorphic basement (15.2 to 24.8%) detritus. However, the relative contribution of the Rocas Verdes remnants only increases up to the middle Rio Verde member then decrease up-section (Fig. 5b). On the other hand, recycled foreland strata are prevalent only in the lower part of the unit.

Table 4. Point-count raw data and equations for recalculated Q-F-L, and Qm-F-Lt plots of the studied units in the Magallanes-Austral Basin.

Formation	Sample	Qm	Qp	F	P	Ch	Lsed	Lm	Lvlt	Lvf	Lvm	Lv(u)	NLv	Acc_Mafic	Acc_Met	Q-F-L	Qm-F-Lt	Total
Palomares	*PAL-P22*	5	2	13	122	6	2	10	116	5	14	18	0	45	0	4,43,53	2,43,55	358
	PAL-P21	13	2	12	63	8	1	12	118	3	3	10	20	35	0	9,28,63	5,28,67	300
	PAL-P18	4	3	8	210	1	3	1	86	1	16	5	0	48	5	2,64,33	1,64,34	391
	PAL-P17	2	0	8	224	0	0	0	100	0	12	0	0	102	0	1,67,32	1,67,32	448
	PAL-P16	25	3	24	155	22	11	14	157	13	19	39	10	71	2	10,36,53	5,36,59	565
	PAL-P15	14	4	17	189	12	5	7	129	5	16	18	6	76	0	7,49,44	3,49,48	498
	PAL-P14	7	2	14	196	9	6	6	117	5	16	16	0	72	1	5,53,42	2,53,45	467
	PAL-P13	3	0	7	157	5	0	1	136	23	11	1	0	130	1	2,48,50	1,48,51	475
	PAL-P12	0	0	3	148	2	0	6	124	12	9	10	0	138	0	1,48,51	0,48,52	452
	PAL-P11	0	0	4	130	3	0	0	122	0	6	0	0	209	0	1,51,48	0,51,49	474
	PAL-P06	5	10	13	140	11	7	33	97	33	6	6	3	71	5	7,42,51	1,42,57	440
	PAL-P05	37	17	40	126	17	4	44	114	38	19	19	16	82	7	14,34,52	8,34,59	580
	PAL-P01	25	2	24	138	8	4	17	117	9	23	22	5	124	9	9,41,50	6,41,53	527
El Salto	*ELS-P10*	34	22	43	45	6	8	39	40	38	12	9	0	22	5	21,30,49	11,30,59	326
	ELS-P09	114	48	65	114	11	3	27	47	47	1	1	0	30	45	36,37,26	24,37,39	554
	ELS-P08	126	40	15	27	2	73	38	98	1	130	3	0	48	0	21,9,70	13,9,79	544
	ELS-P07	16	13	4	14	4	22	2	273	24	34	0	0	0	0	6,5,89	2,5,93	398
	ELS-P06	34	13	62	71	1	2	25	91	14	26	21	0	17	13	13,37,50	9,37,54	390
	ELS-P05	49	12	46	112	8	23	44	45	31	30	6	0	12	22	17,39,44	12,39,49	440
	ELS-P04	20	20	3	3	2	4	5	152	19	41	28	0	4	2	11,2,87	3,2,94	293
	ELS-P03	86	51	6	22	4	55	22	295	10	25	0	0	18	15	18,5,76	8,5,87	566
	ELS-P02	46	82	10	11	19	34	23	170	4	16	0	0	8	6	32,5,63	6,5,89	406
	ELS-P01	20	45	2	4	7	16	32	165	12	15	0	0	18	5	20,2,78	3,2,95	331
Loreto	*LOR-P17*	352	29	54	62	12	10	48	0	70	1	5	0	13	30	46,25,29	38,25,37	510
	LOR-P16	218	27	47	70	19	2	45	4	76	4	8	0	2	15	51,23,27	42,23,36	537
	LOR-P15	112	42	66	80	9	6	29	45	46	9	3	0	18	40	36,33,31	25,33,42	506
	LOR-P14	72	46	2	89	23	19	24	77	24	73	5	0	32	44	25,22,53	9,22,70	494
	LOR-P13	350	49	18	128	7	24	33	14	0	52	0	0	25	58	46,29,25	35,29,36	610
	LOR-P12	16	18	5	125	0	7	2	56	0	90	0	0	0	0	8,42,50	3,42,56	311
	LOR-P11	74	30	9	61	0	20	17	43	5	65	0	0	0	0	23,24,52	13,24,63	287
	LOR-P10	90	14	18	168	3	14	21	49	11	49	48	0	22	14	14,42,44	10,42,48	483
	LOR-P09	82	43	135	76	18	0	0	3	0	4	0	0	5	5	32,66,2	13,66,21	330
	LOR-P08	68	60	5	59	5	36	4	2	7	23	0	0	5	5	42,27,31	14,27,58	245
	LOR-P07	104	46	15	131	8	20	7	11	22	14	0	0	4	8	33,45,23	16,45,39	341
	LOR-P06	16	19	2	59	6	3	0	92	0	82	0	0	0	0	12,23,65	3,23,75	271
	LOR-P05	104	30	10	169	8	15	16	16	20	29	0	0	10	0	25,49,26	14,49,37	375
	LOR-P04	68	43	8	110	3	47	12	38	12	33	0	0	0	0	25,37,39	10,35,55	340

	LOR-P03	346	90	2	1	32	31	18	1	0	0	16	0	0	0	81,1,18	48,1,52	364
	LOR-P02	78	10	2	105	2	4	3	35	0	127	0	0	3	0	16,33,52	12,33,55	330
	LOR-P01	166	36	62	68	22	13	65	33	21	17	16	0	7	60	32,30,38	19,30,51	510
	TRB-P07	344	54	31	19	1	4	80	2	52	5	9	0	5	14	53,12,35	40,12,48	459
	TRB-P06	346	50	27	22	5	10	60	1	60	4	17	0	0	28	53,11,35	40,11,48	461
	TRB-P05	380	76	30	21	1	3	70	7	45	3	7	0	3	12	59,11,30	42,11,47	470
Tres Brazos	*TRB-P04*	306	84	56	41	30	56	47	0	9	7	6	0	12	8	55,20,26	31,20,49	543
	TRB-P03	308	69	9	9	23	9	8	5	0	0	0	0	0	0	86,6,8	54,6,40	286
	TRB-P02	410	77	28	20	26	33	70	3	62	4	7	0	4	16	58,9,33	38,9,53	596
	TRB-P01	340	56	41	22	16	2	62	0	40	2	3	0	3	20	58,15,26	41,15,44	439

Codes:

Qm	Monocrystalline quartz
Qp	Polycrystalline quartz
P	Plagioclase feldspar
F	Potassium feldspar
NLv	Neo-volcanic fragments
Lv (u)	Volcanic lithic fragment undifferentiated
Lvf	Felsic volcanic lithic fragment
Lvlt	Volcanic lithic fragment with lathwork texture
Lvm	Microlitic volcanic lithic fragment
Lsed	Sedimentary lithic fragment
Lm	Metamorphic lithic fragments
Ch	Chert
Acc. Mafic	(Clino-)pyroxene, Olivine, Opaque
Acc. Meta	Hornblende, Micas, Chlorite, Tourmaline, Epidote

Recalculated:

Q	Total quartzose grains (=Qm+Qp+Ch) Total
F	Feldspar (=P+F)
L	Total lithic fragments (=NLv+Lv(u)+Lvlt+Lvf+Lvm+Lsed+Lm)
Lt	Total lithic fragments (=Qp+Ch+L)

Palomares Formation: the lowermost part of the Vidal member is composed of basaltic (36.9%), silicic volcanic (35.9%; mainly pumice and minor quartz porphyry), and granitoid (22.3%) clasts; a minor proportion of dolerite (4.9%) clasts are also present (Table 3). Basaltic and some pumices clasts dominate the middle and upper part of the Vidal member. On the other hand, the lower part of the San José member is dominated by basaltic (mean 43.8%) and silicic volcanic (mean 38.5%; entirely pumice) clasts; subordinately, intermediate volcanic (13.6%) and quartz and chert (13%) clasts (Table 3). The middle part of the San José member is more variable, mainly composed of silicic volcanic (29.8%; entirely pumice), basaltic (24.2%), intermediate volcanic (21.8%), and slates (12.1%) clasts; granitoid (6.5%) and quartz (5.6%) clasts are also present (Table 3). In the upper part of the San José member dominate basaltic (mean 34.4%), quartz and chert (mean 22.3%), and andesitic (mean 19.3%) clasts; minor dolerite (3%) and slate and micaceous schist (2.5%) clasts are present (Table 3). We did not quantitatively evaluate the upper Penitente member, which is dominated by pumice and minor basaltic scoria clasts. There is an up-section decrease in detritus derived from the Cordilleran Magmatic arc (from 27.2-16.7%) while metamorphic basement sources (up to 15.6%) become more significant in the upper stratigraphic levels (Fig. 5b). A mafic volcanic source is the most persistent and essential throughout the formation (up to 37.4%).

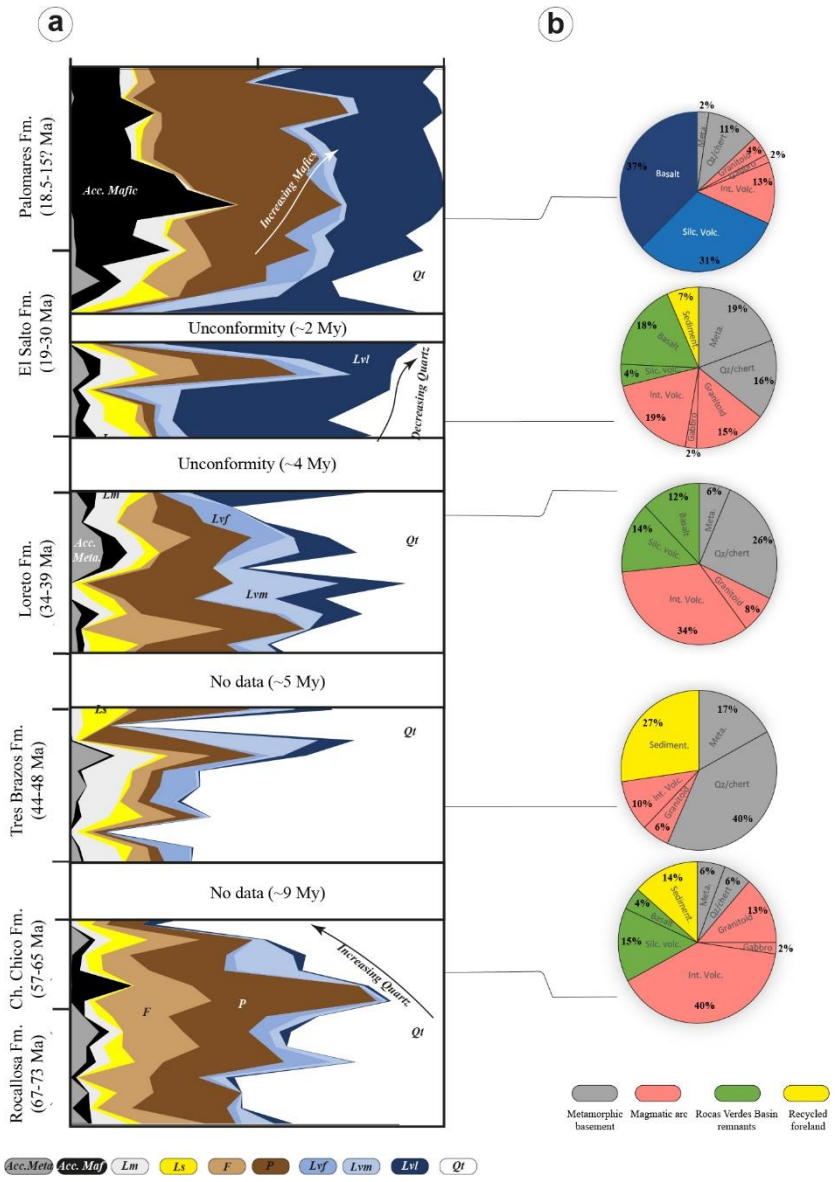

Figure 5. Composite sandstone and conglomerate modal compositions plots. (a) Sandstone framework mineralogy; abbreviation as in Table 4. (b) Proportions of the clast types (abbreviation as in Table 3) in each studied Formation, grouped by colours according to the potential source rock that they represent. For the Palomares Formation basalts and silicic volcaniclastics correspond to a local source, not related to hinterland sources.

To summarize, the modal composition of the conglomerate shows the contribution of the magmatic arch has remained relatively constant from Paleocene to late Oligocene (Fig. 5b), except for the marked decrease during the middle Eocene (Tres Brazos Formation). During the middle to upper Eocene (Tres Brazos and Loreto formations), significant provenance changes occur, since the clasts of metamorphic and sedimentary origin also increase significantly (Fig. 5b). During the mid-Oligocene (El Salto Formation), it is the climax of clast contribution attributed to remnants of the Rocas Verdes Basin (Fig. 5b). The early Miocene is a particular case, where a closer mafic volcanic source in a back-arc

position (given the calibre of the clasts, see the sedimentology section of the Palomares Formation) contributes a large volume of mafic clasts in such a way as to dilute the relative proportions from the other source terranes.

III-2.4.2b Sandstone modal composition

In a long-term perspective, the monocrystalline quartz (grains with straight extinction) dominates (mean = 63%) from the latest Cretaceous (Rocallosa Formation) up to late Eocene (Loreto Formation); whereas, polycrystalline quartz (with more than 3 grains per unit) dominates (mean = 66%) from Oligocene (El Salto Formation) up to early Miocene (Palomares Formation). Plagioclase is the primary feldspar (mean P/F = 0.7), which progressively increases from the latest Cretaceous up to the late Eocene (Loreto Formation) (Fig. 5a). During the middle Eocene (Tres Brazos Formation), the increasing trend in plagioclase content is interrupted; during the Oligocene to the Miocene, the content of plagioclase, although dominant, is relatively lesser (mean P/F = 0.6) than the uppermost Cretaceous and older Paleogene strata (Fig. 5a). Volcanic components (mean = 69%) dominate lithic grains in all studied units except the Tres Brazos Formation (middle Eocene) where metamorphic lithic grains prevail (mean = 45%) (Fig. 5a). The most common textures exhibited in the volcanic lithics are lathwork (mean = 45%) and microlitic (mean = 34%), usually presented in a mixed way in the upper Cretaceous to Paleocene strata (Fig. 5a). However, the proportion of felsitic and microlitic textures tend to be slightly more important in the uppermost Cretaceous strata (Rocallosa Formation; further detail in Rivera et al., 2020) and during the late Eocene (Loreto Formation; Fig. 5a), respectively. Similarly, lathwork texture tends to be more representative in the Chorrillo Chico Formation in Tierra del Fuego (Cabo Nariz facies; further detail in Rivera et al., 2020) and from the mid-Oligocene (El Salto Formation) to the early Miocene (Palomares Formation) (Fig. 5). Accessory minerals of metamorphic origin present a higher proportion during the Maastrichtian, Middle Eocene, and Upper Eocene to Oligocene (Fig. 5a). Likewise, accessory minerals of mafic origin increase significantly from the Upper Oligocene to the early Miocene (Fig. 5a).

In terms of sedimentary provenance, in The Q-F-L diagram (Fig. 6a; Dickinson, 1985) it is observed that a dissected magmatic arc constitutes the main source of sediments during the Maastrichtian-Paleocene. However, during the Chorrillo Chico deposition (Paleocene), there is a tendency to incorporate an increasing amount of recycled debris from pre-existing foreland deposits. This recycling of the orogenic wedge is accentuated during

the middle Eocene during the deposition of the Tres Brazos Formation. From the middle-upper Eocene, there is an apparent tendency to the rejuvenation of the magmatic arc, suggested by the modal evolution from a dissected to intermediate to undissected arc. However, for the Oligocene deposits, represented by the El Salto Formation, both the Qm-F-Lt diagram of Dickinson (1985) and the modified diagrams of Weltje (2006), suggest a mixed provenance between intermediate magmatic arc to non-dissected and recycling of orogenic bed deposits. This pattern of compositional evolution is more consistent with the compositional data of the conglomerates and with the other lines of evidence of sedimentary provenance (e.g., sedimentary geochemistry and detrital zircon geochronology). For the Burdigalian deposits of the Palomares Formation, all ternary diagrams (Fig. 6a) suggest a provenance from an intermediate magmatic arc. Although a magmatic arc is the main source of sediments, the intermediate degree of dissection does not seem to make sense.

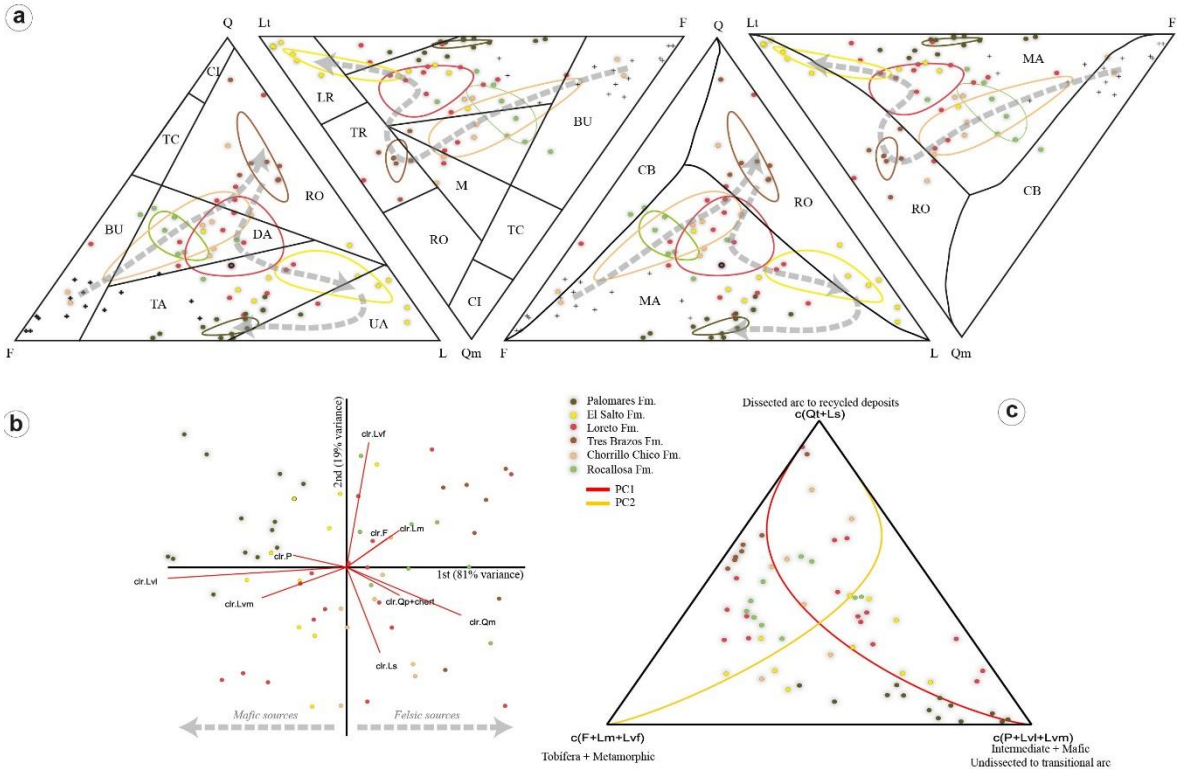

Figure 6. (a) Representation of modal sandstone composition in the Q-F-L and Qm-F-Lt triangular plots with provenance fields according to Dickinson (1985) (two first triangles at left) and isodensity fields of provenance according to Weltje (2006) (two last triangles at right). Black crosses, Upper Cretaceous foreland deposits from McAtmaney et al. (2011). BU= Basement uplifted; TC= Transitional continental block; CI= Craton Interior; UA=Undissected arc; TA=Transitional arc; DA= Dissected arc; RO=Recycled orogen; M= Mixed; TR= Transitional recycled; LR=Lithic recycled; CB= Continental block; MA= Magmatic arc. (b) Compositional biplot of sandstone framework grains. (c) Triangular principal components of studied samples.

The compositional biplot (Fig. 6b) allows discriminating the modal composition of the sandstones responds to two types of well-differentiated sediment sources. One of mafic origin, where the highest proportions of volcanic lithics of lathwork and microlithic textures and plagioclase are presented. The source of felsic origin, groups sediments rich in quartz, orthoclase and lithic fragments of sedimentary, metamorphic or volcanic origin with a felsitic texture. Based on these compositional differences, the principal component analysis (Fig. 6c) allows us to observe in a more rigorous way which are the main source rocks that influence the compositional variations in each studied formation. The samples from Campanian to Lutetian, (the Rocallosa, Chorrillo Chico and Tres Brazos formations) vary along with the second principal component (PC2), which is influenced either by source rocks ascribed to the Tobífera Formation and/or metamorphic basement or to a dissected arch and/or recycled deposits of the orogenic wedge. The Oligocene samples (El Salto Formation) exhibit an additional source rock, of intermediate to mafic composition, interpreted as related to the coeval magmatic arc and reworking of mafic components of the Rocas Verdes Basin remnants. Samples from the upper Eocene (Loreto Formation) represent a mixing of multiple sources. In contrast, the Burdigalian samples (Palomares Formation) are mainly derived from an intermediate to mafic source, related to the early Miocene extra-andean vulcanism (Fig. 6c).

III-2.5 Fine-grained bulk-rock geochemistry

III-2.5.1 Method

Elemental concentrations and key trace-elements ratios values for each studied Formation are reported in Table 5. The average geochemical composition of the upper continental crust (UCC), North American Composite Shale (NASC), post-archean Australian shale (PAAS), and potential source rock end-members are included for comparison. The complete raw data of the geochemical composition of the studied samples are found in Annex C-3. The trace elements, such as Th, Sc, Zr, Hf, Y, Cr, Ni, V, and rare earth elements (REE) are considered to have short residence times in solution and usually immobile behaviour during weathering, transport, diagenesis, and low-grade metamorphism (Bathia, 1985; Taylor and McLennan, 1981; McLennan et al., 1993). Therefore, we assume that these elements behaved as a closed system and preserve source rocks geochemical signatures in the sedimentary record; thus, they are useful to evaluate sediment provenance similar to several previous studies (e.g., Hiscott, 1984; Garver et al., 1996; Cullers, 2000; Asiedu et al., 2004; Roddaz et al., 2005; Zahid and Barbeau Jr., 2013; among others). We

used elemental concentrations and ratios as indicators of the geochemical nature of the assemblage of parent rocks in terms of mafic, felsic, or mixed signatures (intermediate).

Geochemical data are transformed to log-ratios (clr) and displayed in a biplot as a first step to describe quantitatively the compositional variability of samples. In the compositional biplot (Gabriel 1971), both multivariate observations (points) and variables (rays) are indicated. The length of each ray is proportional to the variance of the corresponding element in the dataset. If the angle between the two rays is close to 0°, 90° or 180°, then the corresponding elements are directly correlated, uncorrelated or inversely correlated, respectively. Additionally, we performed a quadratic discriminant analysis to evaluate the probability of correspondence of studied foreland samples to the parental source rocks (SPB, Southern Patagonian Batholith; BAP, Barros Arana-La Pera complex; TOB, Tobífera Formation; MET, metamorphic complexes; OPH, ophiolite complexes). This probability can be expressed as the relative contribution of detritus from each parental source rock to make up each studied formation. For the discriminant analysis, key elements were used (eg, TiO_2, Sc, Ba, Sr, Zr, Cr, Ni, Nb, Th, La_N, Ce_N, Eu_N, Yb_N) that allow differentiating each one of the potential parent rocks (end-members; Table 6). The *a priori* probabilities (basic parameter of the discriminant analysis; for further details see Vermeesch, 2006) were attributed according to the representativeness of each lithological unit within the study area, i.e., rocks with a greater occupied area within the area of study will have higher *a priori* probabilities, while rocks that rarely outcrop within the study area were assigned a lower *a priori* probability.

III-2.5.2 Results and interpretations

Before determining geochemical provenance, it is essential to assess the role of the weathering of the source rocks and sedimentary sorting of sediments on variations in the chemical composition of studied samples. The average chemical index of alteration (CIA; Nesbitt and Young, 1982) for all formations is 60 (average shale is about 65-70; McLennan et al., 1993), with minimum values for the Palomares Formation (49.3 ± 5; Table 5) and maximum for the Loreto Formation (72.6 ± 9.3; Table 5). These values suggest a low to moderate degree of chemical weathering in the source areas and during sediment transport and storage. By plotting the CIA versus the Weathering Index of Parker (WIP; Parker, 1970), we evaluate the incidence of recycling on sediment composition (Garzanti et al., 2014; Garzanti and Resentini, 2016). Fig 7a shows CIA/WIP ratios between 0.6 and 1.8 (ranging from UCC to PAAS typical values), which suggest a negligible effect of recycling on the

Magallanes foreland basin samples. The Th/Sc vs Zr/Sc bivariate plot (McLennan et al., 1993) was applied to evaluate the role of heavy mineral concentration during sorting and sedimentary recycling. Fig. 7b reveals that for all studied formations, the geochemical composition was controlled by igneous differentiation in an active margin (corroborating the evidence of sandstone petrography) rather than sedimentary recycling with zircon enrichment. These results are at odds with typical values for Andean foreland basins (e.g., Basu et al., 1990; Roddaz et al., 2005), where sedimentary recycling is significant. Both the CIA and WIP values and low sedimentary recycling (Figs. 7a, b) allow us to infer that variability in geochemical composition from the foreland samples obey mainly to first-cycle provenance changes.

On the ternary diagram of La-Th-Sc (McLennan and Taylor, 1984; Fig. 7c), the linear array shown by the foreland samples scatters between the Barros Arana-La Pera volcanic complex (Stern et al., 1991; Stern, 1991; Prades, 2008; Anguita, 2010) and Andean metamorphic complexes (typical of UCC geochemical nature) compositions. This behaviour is consistent with a mixing of sourced materials comparable to the Southern Patagonian Batholith (Hervé et al., 2007). Similar trends are evident in the Cr/Th-Th/Sc diagram (Asiedu et al., 2004; Fig. 7d), suggesting a mixture between felsic and intermediate andesitic compositions.

We use a multivariate statistical analysis to evaluate the applicability of geochemical proxies to infer parent rocks compositions. The compositional biplot (which explain 63% of the data variance) cluster the latest Cretaceous-Cenozoic foreland deposits into two main groups (Fig. 7e): (1) characterised by incompatible elements (Th, Zr, Y, La, Ce), generally enriched in felsic rocks; (2) characterised by compatible and ferromagnesian elements (Ni, Cr, Sc, V, Eu, Yb, Lu), generally associated to mafic rocks. Most of the latest Cretaceous-Cenozoic units show a mixture of these two end-member compositions, whereas those from the middle Eocene (Tres Brazos Fm.) and mid-Oligocene to early Miocene (El Salto Fm.) are dominantly felsic and mafic, respectively. Some sedimentary sorting influence is reflected in the coarse-grained (siltstones) fraction of the Chorrillo Chico Formation (Cabo Nariz facies), yielding a high concentration in Hf (Fig. 7e; Table 5). The multivariate statistical analysis demonstrates that source rocks can be well differentiated based on key trace elements and REE's.

Plotting the Th/Sc and Eu/Eu*versus age allows us to examine in more detail significant variations in provenance composition through time. The Th/Sc-age plot (Fig. 7f)

shows that at least 50-75% of analyses of the Maastrichtian to Paleocene deposits (Rocallosa and Chorrillo Chico formations) present a mafic signature (Th/Sc values far lower than UCC, NASC, and PAAS). For the lower to middle Eocene deposits (Agua Fresca and Tres Brazos formations), more than 75% of analyses fall into the mixing domain. The mafic signature is again predominant from the late Eocene to Burdigalian (Loreto, El Salto and Palomares formations). Similarly, the Eu/Eu*-age plot (Fig. 7f) suggests a progressive shift from a mafic to a mixed signature of provenance from the Maastrichtian up to middle Eocene. The lower to middle Eocene deposits present the lowest Eu anomaly values (Agua Fresca Formation = mean 0.76 ± 0.01 and Tres Brazos Formation = 0.73 ± 0.03) closer to typical values of the Andean metamorphic complexes (Table 5). The geochemical signature begins to change again to a more mafic one from the late Eocene, and it is more evident by the Oligocene to Burdigalian (Fig. 7f). Both proxies are exhibiting a clear zig-zag mafic-mixed-mafic trend in provenance signature (Fig. 7f). It is worthy to note that by 35-39 Ma, there is a shift to more felsic source rocks in Argentinean Tierra del Fuego whereas, in the nearby Magellean region (our study area), a more mafic source contribution occurs. We interpret such contradiction by the difference in the type of source rock available in the hinterland by that time.

The Magallanes Province samples (Fig. 7g and Table 5) show low fractionated REE patterns (La_N/Yb_N varying from 5.09 to 7.29) and a slight negative Eu anomaly (mean 0.85). The LREE's are poorly fractioned (mean La_N/Sm_N = 2.8), and the HREE patterns are relatively flat (mean Gd_N/Yb_N = 1.43). These patterns suggest that all studied samples are derived from rocks that have not undergone significative intracrustal differentiation and host a more primitive geochemical signature (e.g., McLennan et al., 1993; Cullers et al., 2000) regarding the typical shales (NASC or PAAS; Table 5) or even to their counterpart in the Argentinian Tierra del Fuego (e.g., Zahid and Barbeau, 2013). The REE patterns are rather comparable to the Southern Patagonian Batholith, the Barros Arana-La Pera volcanic complex and, to a minor degree, to the ophiolitic complexes.

The statistical and quantitative assessment of the contribution of each parental rock source is portrayed by the quadratic discriminant analysis (Table 6). Due to the continuous and voluminous contribution of detritus from the magmatic arc over time, and the consequent dilution effect that this may entail on the relative proportions of the other parental rocks, two case studies were developed including and excluding the batholith end-member. In case 1 (including the batholith; Table 6), from the Campanian to the Thanetian, there is a

higher probability that the Southern Patagonian Batholith (40-74%) and the metamorphic complexes (18-46%) are the main source of sediments to the basin. During the early to middle Eocene, the highest probability corresponds to the metamorphic complexes (> 75%). In contrast, for the Oligocene, the probabilities are almost uniform (~ 30%) for the Southern Patagonian Batholith, the metamorphic complexes and mafic rocks of the Barros Arana-La Pera complex. In case 2 (excluding the batholith; Table 6), the other source rocks take on greater prominence. During the Campanian to the Thanetian, in addition to the metamorphic complexes, the contribution of mafic rocks from the ophiolitic and the Barros Arana-La Pera complexes, and also the volcaniclastic rocks of the Tobiferous Formation stands out. Metamorphic complexes are unquestionably one of the main source rocks during the Eocene. While for the Oligocene, the mafic nature of the sediments that makes up the El Salto Formation is evidenced. For the Miocene, a duality is observed between mafic and more felsic sources.

Table 5. Summary of measured geochemical variables and comparison with potential parental rocks and rock standards.

	Rocallosa Fm. (n=3)		Chorrillo Chico Fm. (n=5)		Chorrillo Chico Fm. - Cabo Nariz Mbr. (n=8)		Agua Fresca Fm. (n=3)		Tres Brazos Fm. (n=2)		Loreto Fm. (n=3)		El Salto Fm. (n=2)		Palomares Fm. (n=3)		TOB	MET	SPB	BAP	OPH	UCC	NASC	PAAS
	mean	SD (1σ)	mean	SD (1σ)	mean	SD (1σ)	mean	SD (1σ)	mean	SD (1σ)	mean	SD (1σ)	mean	SD (1σ)	mean	SD (1σ)								
CIA	52.7	*8.1*	57.6	*2.5*	57.3	*10.4*	69.7	*1.2*	64.5	*0.7*	72.7	*9.3*	56.5	*6.4*	49.3	*5.0*	-	-	-	-	-	-	-	-
WIP	55.0	*13.2*	48.2	*9.9*	52.6	*16.1*	39.3	*1.2*	45.5	*2.1*	40.3	*14.4*	59.0	*9.9*	61.7	*6.5*	-	-	-	-	-	-	-	-
Th	4.7	*0.5*	5.8	*1.3*	5.4	*2.1*	8.1	*0.3*	7.1	*1.0*	6.4	*0.3*	5.0	*3.9*	5.7	*1.3*	14.5	10.0	7.6	4.8	1.4	10.7	12.3	14.6
Sc	13.7	*3.1*	14.2	*3.5*	14.2	*3.1*	17.3	*0.6*	17.0	*1.4*	17.3	*0.6*	24.0	*1.4*	21.7	*2.1*	10.6	10.3	16.7	31.6	37.0	13.6	15.0	16.0
Cr	43.3	*5.8*	44.0	*8.9*	52.1	*16.5*	56.7	*5.8*	51.0	*12.7*	46.7	*5.8*	55.0	*21.2*	38.3	*10.1*	20.2	47.0	22.1	104.6	205.0	83.0	*127.0*	*100.0*
Ni	13.0	-	13.0	-	20.4	*6.5*	26.6	*6.1*	22.5	*3.5*	23.0	*6.1*	49.5	*14.9*	19.5	-	8.1	17.6	7.7	29.8	78.7	44.0	58.0	*60.0*
V	114.3	*21.2*	126.2	*24.4*	109.3	*33.4*	143.0	*5.0*	119.0	*17.0*	139.0	*4.0*	197.5	*13.4*	167.0	*53.7*	40.1	78.2	-	271.6	230.7	107.0	130.0	*140.0*
Y	13.3	*4.7*	15.2	*4.2*	18.0	*4.9*	17.3	*1.2*	22.0	*2.8*	20.0	*1.0*	18.5	*0.7*	20.0	*6.1*	32.1	22.7	21.7	20.7	28.0	22.0	35.0	27.0
Zr	93.7	*17.0*	110.0	*29.5*	117.9	*23.5*	118.7	*19.7*	140.3	*5.3*	148.0	*16.5*	157.0	*82.0*	152.7	*34.7*	130.1	240.3	115.9	89.8	86.8	190.0	200.0	210.0
Hf	1.3	*0.9*	2.6	*0.7*	7.8	*6.7*	3.2	*0.3*	3.2	*0.2*	3.6	*0.4*	3.5	*1.6*	3.4	*0.7*	4.3	6.0	3.3	2.9	2.8	5.8	6.3	5.0
La	12.6	*5.9*	17.4	*9.3*	18.8	*4.5*	20.0	*1.7*	22.4	*5.1*	21.9	*3.0*	17.2	*11.0*	20.6	*2.5*	32.6	31.9	19.1	18.9	7.4	30.0	*32.0*	*38.2*
Ce	28.2	*12.4*	37.1	*17.0*	37.3	*7.8*	49.0	*3.2*	48.5	*9.2*	47.7	*5.4*	40.7	*23.1*	45.3	*5.1*	66.1	70.1	38.3	45.3	17.0	64.0	67.0	80.0
Nd	13.8	*5.8*	16.4	*7.1*	16.7	*3.0*	19.2	*1.9*	20.5	*0.7*	22.2	*2.6*	21.9	*9.3*	24.6	*2.5*	30.3	31.9	18.3	25.8	12.4	26.0	27.4	32.0
Sm	3.1	*1.1*	3.6	*1.4*	3.4	*0.7*	4.1	*0.4*	4.5	*0.0*	4.8	*0.5*	4.8	*1.4*	5.2	*0.4*	6.9	5.8	4.0	5.9	3.5	4.5	5.6	5.6
Eu	0.8	*0.3*	0.9	*0.3*	0.8	*0.2*	1.0	*0.1*	1.0	*0.1*	1.2	*0.0*	1.5	*0.2*	1.5	*0.1*	0.8	1.1	0.9	1.5	1.2	0.9	1.2	1.1
Gd	2.7	*1.1*	3.1	*1.0*	3.2	*0.8*	3.7	*0.4*	4.2	*0.1*	4.3	*0.5*	4.4	*0.6*	4.5	*0.5*	5.4	4.7	3.7	4.7	4.3	3.8	5.2	4.7
Tb	0.4	*0.1*	0.5	*0.1*	-	-	0.6	*0.1*	0.7	*0.0*	0.7	-	0.7	*0.1*	0.7	*0.1*	1.0	0.6	-	0.7	1.0	0.6	0.9	0.8
Yb	1.6	*0.4*	1.7	*0.3*	1.9	*0.3*	2.2	*0.2*	2.3	*0.1*	2.2	*0.2*	2.3	*0.1*	2.1	*0.7*	3.3	2.5	2.2	1.7	2.8	2.2	3.1	2.8
Lu	0.2	*0.1*	0.3	*0.1*	0.3	*0.1*	0.3	*0.0*	0.4	*0.0*	0.3	*0.0*	0.3	*0.0*	0.3	*0.1*	0.6	0.4	0.3	0.2	0.4	0.3	0.5	0.4
Th/Sc	0.4	*0.1*	0.4	*0.0*	0.4	*0.1*	0.5	*0.0*	0.4	*0.1*	0.4	*0.0*	0.2	*0.2*	0.3	*0.1*	1.5	1.0	1.0	0.4	0.0	0.8	0.8	0.9
Zr/Sc	6.9	*0.3*	7.8	*1.7*	8.4	*1.1*	6.8	*1.1*	8.3	*0.4*	8.6	*1.1*	6.7	*3.8*	7.2	*2.0*	13.1	29.5	11.5	3.8	1.9	14.0	13.3	13.1
Cr/Th	9.5	*2.4*	7.7	*1.1*	10.4	*3.9*	7.0	*0.6*	7.4	*2.8*	7.3	*0.7*	13.6	*6.4*	6.8	*1.8*	1.5	4.9	-	8.3	-	7.8	10.3	6.8
Eu/Eu*	0.9	*0.1*	1.0	*0.5*	0.8	*0.2*	0.8	*0.0*	0.7	*0.0*	0.8	*0.1*	0.8	*0.1*	1.0	*0.1*	0.4	0.7	0.8	0.9	1.0	0.7	0.7	0.7
LaN/SmN	2.5	*0.4*	2.9	*0.4*	3.5	*0.6*	3.1	*0.2*	3.2	*0.7*	2.9	*0.2*	2.1	*0.8*	2.5	*0.1*	3.0	3.5	3.0	2.0	1.4	4.2	3.6	4.3

GdN/YbN	1.3	*0.3*	1.5	*0.3*	0.8	*0.7*	1.4	*0.1*	1.5	*0.1*	1.6	*0.2*	1.6	*0.2*	1.9	*0.5*	1.3	1.5	1.3	2.2	1.3	1.4	1.4	1.4
LaN/YbN	5.1	*1.6*	6.7	*2.6*	6.5	*1.3*	6.2	*0.7*	6.6	*1.9*	6.8	*1.1*	5.1	*3.1*	7.3	*2.8*	6.8	8.7	5.7	7.3	1.9	9.2	7.0	9.2

Table 6. Summary of predictive quadratic discriminant analysis.

Formation	Case 1: Including Batholith data					Case 2: Excluding Batholith data			
	SPB (%)	BAP (%)	MET (%)	OPH (%)	TOB (%)	BAP (%)	MET (%)	OPH (%)	TOB (%)
Palomares	30.36	51.77	17.70	0.04	0.13	53.21	39.34	1.04	6.41
El Salto	27.80	36.20	30.15	5.80	0.05	49.20	2.01	46.70	2.10
Loreto	20.34	7.23	72.30	0.10	0.03	0.51	98.74	0.07	0.68
Tres Brazos	17.20	3.13	79.53	0.07	0.07	0.02	98.09	0.03	1.86
Agua Fresca	14.60	9.70	75.19	0.46	0.05	2.33	96.92	0.12	0.62
Chorrillo Chico	40.30	11.32	46.34	2.00	0.04	0.80	60.41	29.06	9.72
Cabo Nariz Mber	59.83	2.30	37.70	0.15	0.02	0.00	47.47	0.35	52.18
Rocallosa	73.97	7.90	17.70	0.40	0.03	21.17	69.7	3.93	5.21

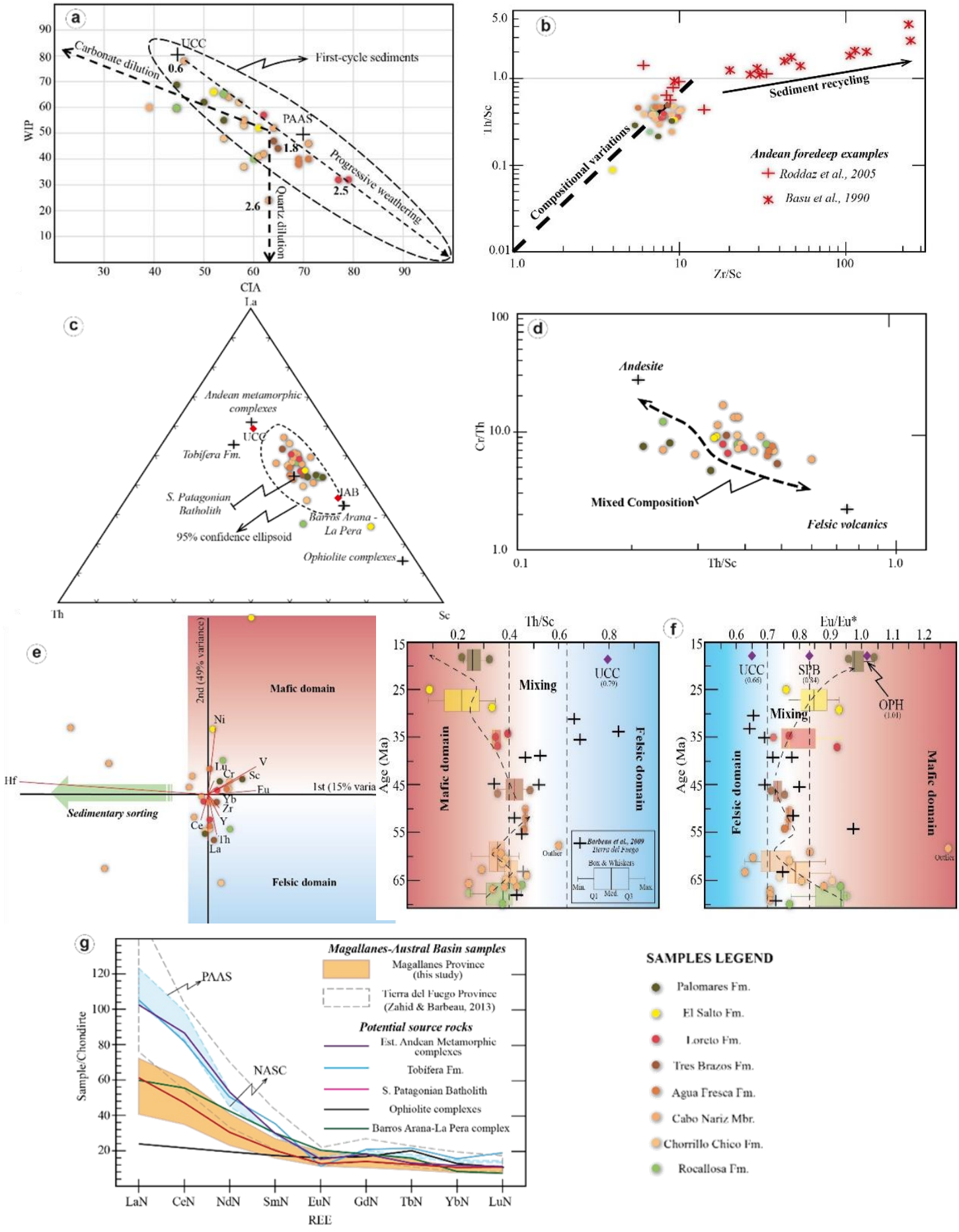
a
WIP
CIA
UCC
0.6
PAAS
1.3
2.5
2.6
Carbonate dilution
First-cycle sediments
Progressive weathering
Quartz dilution
b
Th/Sc
Zr/Sc
Sediment recycling
Compositional variations
Andean foredeep examples
Roddaz et al., 2005
Basu et al., 1990
c
La
Th
Sc
Andean metamorphic complexes
UCC
Tobífera Fm.
S. Patagonian Batholith
JAB
Barros Arana - La Pera
95% confidence ellipsoid
Ophiolite complexes
d
Cr/Th
Th/Sc
Andesite
Mixed Composition
Felsic volcanics
e
2nd (49% variance)
1st (15% varia
Mafic domain
Felsic domain
Sedimentary sorting
Hf
Ni
V
Cr
Sc
Eu
Yb
Zr
Y
Ce
Th
La
Th/Sc
Age (Ma)
Mixing
UCC
(0.79)
Mafic domain
Felsic domain
Outlier
Barbeau et al., 2009
Tierra del Fuego
Box & Whiskers
Min.
Q1
Med.
Q3
Max.
f
Eu/Eu*
UCC
(0.66)
SPB
(0.84)
OPH
(1.01)
Mixing
Felsic domain
Mafic domain
Outlier
g
Sample/Chondrite
REE
LaN
CeN
NdN
SmN
EuN
GdN
TbN
YbN
LuN
PAAS
NASC
Magallanes-Austral Basin samples
Magallanes Province (this study)
Tierra del Fuego Province (Zahid & Barbeau, 2013)
Potential source rocks
Est. Andean Metamorphic complexes
Tobífera Fm.
S. Patagonian Batholith
Ophiolite complexes
Barros Arana-La Pera complex
SAMPLES LEGEND
Palomares Fm.
El Salto Fm.
Loreto Fm.
Tres Brazos Fm.
Agua Fresca Fm.
Cabo Nariz Mbr.
Chorrillo Chico Fm.
Rocallosa Fm.

Figure 7. (*previous page* ←) (a) Weathering Index of Parker (WIP) versus Chemical Index of Alteration (CIA) plot and (b) bivariate Th/Sc vs Zr/Sc plot to assess the degree of recycling. (c) Triangular La-Th-Sc plot of studied samples and comparison with potential parental rocks and standards. (d) Cr/Th vs Th/Sc bivariate highlighting a mixed nature in composition. (e) Compositional biplot of geochemical variables for the studied samples, evidencing the discrimination between mafic and felsic affinities. (f) Th/Sc and Eu/Eu* versus age to evaluate the temporal variability in composition. (g) REE patterns normalised to chondrite (Boynton, 1984) of the foreland samples and comparison with age-equivalent samples of Tierra de Fuego, potential sources rocks, and standard shales. Note the mafic nature of the studied samples.

III-2.6 Detrital zircon U-Pb geochornology

III-2.6.1 Method

Detrital zircons were extracted in the Sample Preparation Laboratory of the Geology Department at the University of Chile following standard crushing, density, and magnetic concentration techniques (e.g., Rivera et al., 2020). Detrital zircon U-Pb ages were used to assess provenance and U-Pb geochronological results were obtained in 3 laboratories: (1) at the Mass Spectrometry Laboratory (CEGA) of the University of Chile, using LA-MC-ICP-MS technique; (2) at the Geochronology Laboratory of SERNAGEOMIN (Chilean Geology and Mining Service) by using LA-ICP-MS practices; (3) at the Laboratory of Isotopic Studies (LEI) of the Geosciences Centre-UNAM, using LA-ICP-MS technique. On average, 91 grains were dated in all samples but 46 in the CC1 sample. Analyses on the target zircons were conducted with a 30-33 µm diameter spots with output energy of 2.5 mJ/cm2, and a repetition rate of 5-7 Hz and the reported ages are based primarily on $^{206}Pb/^{238}U$ ratios for <1000 Ma grains and $^{206}Pb/^{207}Pb$ for >1000 Ma grains both with uncertainties at the 2σ level. Further description of procedures is outlined in Solari et al. (2010) and Rivera et al. (2020).

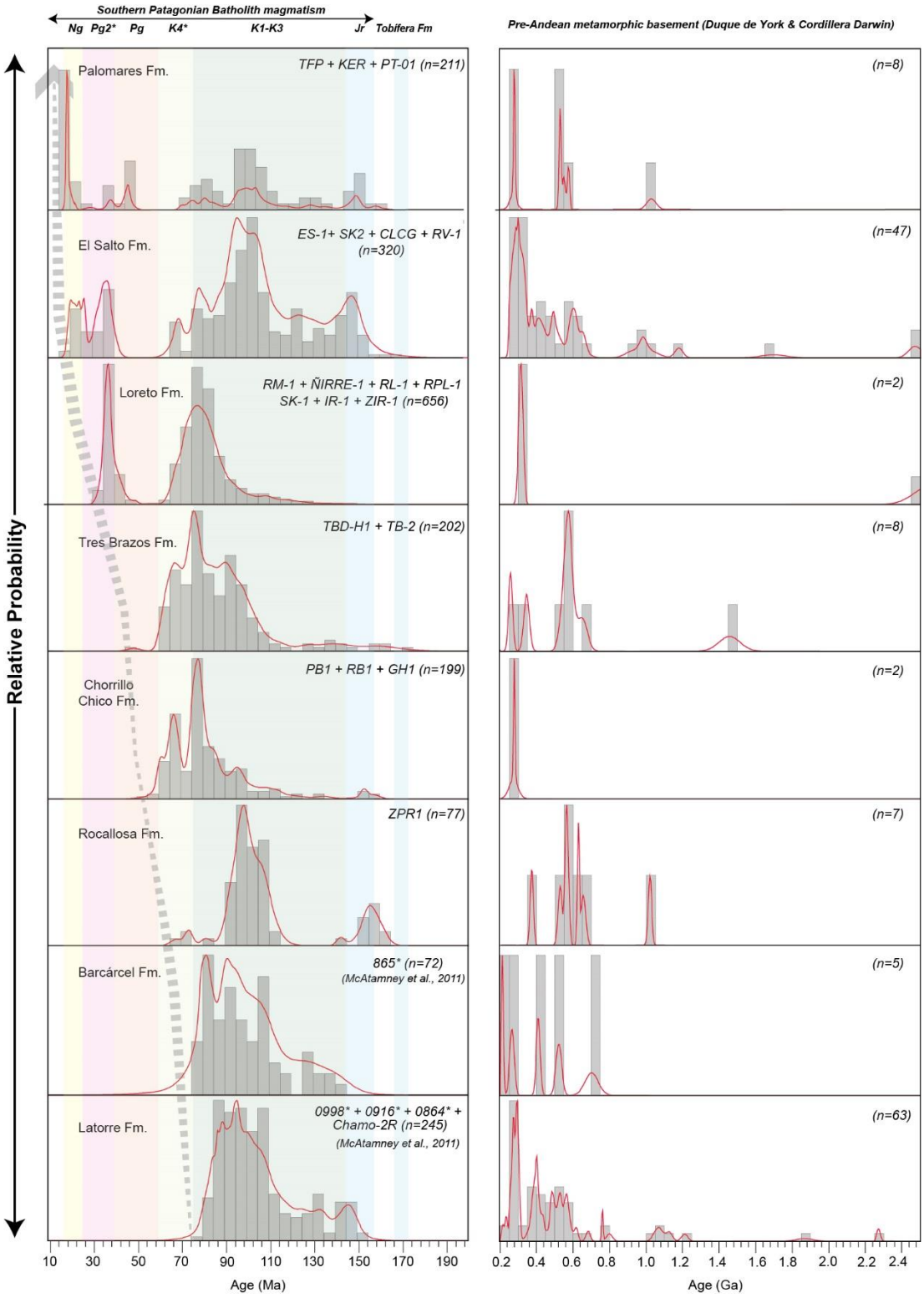

Figure 8. Composite histograms and probability plots from the studied units. The left plot, ages < 200 Ma; the right plot, emphasize age > 200 Ma of pre-Mesozoic metamorphic complexes. Lower case "n" refers to the total number of grains in each plot. Potential source terranes are indicated by coloured rectangles, and Pg2* and K4* are new magmatic arc episodes identified in Rivera et al. (2021). Samples names with asterisks from McAtamney et al. (2011). Note the higher relative proportion of metamorphic-derived

zircons during the Upper Cretaceous (Latorre, Barcárcel and Rocallosa formations), middle Eocene (Tres Brazos Formation) and Oligocene-Miocene (El Salto and Palomares formations).

III-2.6.2 Results and interpretations

The age population distribution from each Cenozoic foreland basin formation analysed here is shown in Fig. 8 and Annex C-4. Previous samples of the Chorrillo Chico Formation (Rivera et al., 2020) and one new sample (GH-01) have a total zircon yield of n = 201 grains, ranging from 54 to 1,057 Ma. A Late Cretaceous to Paleocene population dominates the formation (~91%, distributed in three age peaks at 58-68 Ma, 72-80 Ma, 85-110 Ma), whereas Jurassic (3.5%, peak at 152-168 Ma), and older populations (3.5%, peaks at 380-397 Ma, 534-650 Ma, and 1,003-1,057 Ma) are subordinated. Samples of the Tres Brazos Formation (n = 210 grains) range from 48.6 to 1,456 Ma, showing a dominant Late Cretaceous to Paleocene population (89%, distributed at three prominent age peaks of 64-70 Ma, 73-83 Ma, 88-115 Ma) similar to the previous Chorrillo Chico Formation. Subordinated age groups are represented by Early Cretaceous (3.8%, peak at 127-142 Ma), Jurassic (3.0%, peak at 148-172 Ma), and older populations (3.8%, > 200 Ma). The Loreto Formation samples (n= 658 grains) range from 34 to 2,560 Ma, showing two dominant populations: Late Cretaceous-Danian (68.4%, distributed between 63-100 Ma), and Eocene (~26%, peak at 34-48 Ma). A Late Cretaceous subordinate age group (5.4%, between 110-143 Ma) is also present. The El Salto Formation samples (n = 358 grains) range from 18.8 to 2,479 Ma, showing a dominant Cretaceous population (64.8%; from 66-144 Ma, centred at 90-107 Ma). However, there are comparable middle Eocene to early-Miocene (13.4%; from 20-40 Ma), Jurassic (8.1%, peak at 152 Ma), and older (13.1%; > 200 Ma) subordinate age groups. Samples of the Palomares Formation (n = 216 grains) range from 17.5 to 1,029 Ma, with one dominant early-Miocene population (~61%; peak at 17-21 Ma), followed by a Cretaceous age group (24.1%; from 71-120 Ma but centred at 75-84 Ma, and 97-107 Ma). Additionally, three less defined age groups of Eocene-Oligocene (6.5%; from 30-49 Ma), Jurassic (5.1%; from 146-161 Ma, centred at 152 Ma), and older (3.7%; > 200 Ma) are present.

Detrital zircon U-Pb age populations of the Cenozoic foreland strata exhibit a long-term, continuous, and dominant sediment delivery from the Cretaceous-Neogene Southern Patagonian Batholith (Hervé et al., 2007). However, three magmatic lulls at 144-127 Ma (1.6% of total detrital zircons), at 48-60 Ma (1.1% of total detrital zircons),

and 25-30 Ma (1.4% of total post-Eocene detrital zircons) interrupted the continuous arc-related sourcing (Rivera, 2017; George et al., 2020). Furthermore, two age populations at 74-68 Ma (mean 7.6% of total detrital zircons; max. 12.4%), and 39-26 Ma (mean 11% of total post-Paleocene detrital zircons; max. 25.5%) are difficult to interpret given that intrusive or volcanic rocks belonging to this ages are so far unknown in the Southern Patagonian Batholith (Hervé et al., 2007); the significance of this finding is discussed in the next section. Jurassic volcanic and plutonic rocks (145-190 Ma) of the Tobífera Formation and Southern Patagonian Batholith, and older detrital zircons (> 200 Ma) derived from the Andean metamorphic complexes maintain a relatively constant contribution (mean 7%) during the Paleocene to middle Eocene (Chorrillo Chico and Tres Brazos Formation). However, by the mid-to-upper Eocene (Loreto Formation) abundance of Jurassic and older zircons decrease almost entirely (1.1%), suggesting progressive elimination of these hinterland sources. Contrastingly, zircons derived from the Tobífera Formation, and Andean metamorphic complexes reach their clímax in contribution (~22%) during the mid-Oligocene to early Miocene (El Salto Formation). By the Burdigalian (Palomares Formation), the contribution from the latter hinterlands sources significantly decreases (~9%), obscured by the abundance of syndepositional arc-derived zircons.

III-2.7 Basin subsidence and migration

III-2.7.1 Method

To unravel the history of vertical and lateral movements in the Magallanes-Austral foreland Basin and the evolution of the sedimentary fill, we have constructed subsidence curves (Fig. 9) and isopachs maps (Fig. 10). Basin subsidence curves were performed in different domains of the basin distributed along an E-W transect at the proximal foredeep, distal foredeep, and forebulge (Springhill platform). We apply backstripping to calculate the decompacted thickness of the Cretaceous–Cenozoic strata following Angevine et al. (1990). The sediment load was removed following the method described by Steckler and Watts (1978). Tectonic subsidence is calculated relative to sea level. Due to existing problems with eustatic curves, we have not applied the correction for eustatic changes. Paleobathymetries were assigned based on the lithofacies information, which constitutes the main source of uncertainty along with the thickness and ages of the Springhill platform units. Theoretical subsidence curves for different stretching factors (β) were

calculated based on McKenzie (1978) and assuming an initial 35 km crustal thickness. Input data are reported in Annex C-5. Isopach maps were constructed using 42 well tops, 3 pseudo-well tops based on outcrop data, and some seismic-reflection lines pickings. The thicknesses data were interpolated using a nearest-neighbour interpolation algorithm. Finally, contours were smoothed in ArcGis 10x honouring the point data.

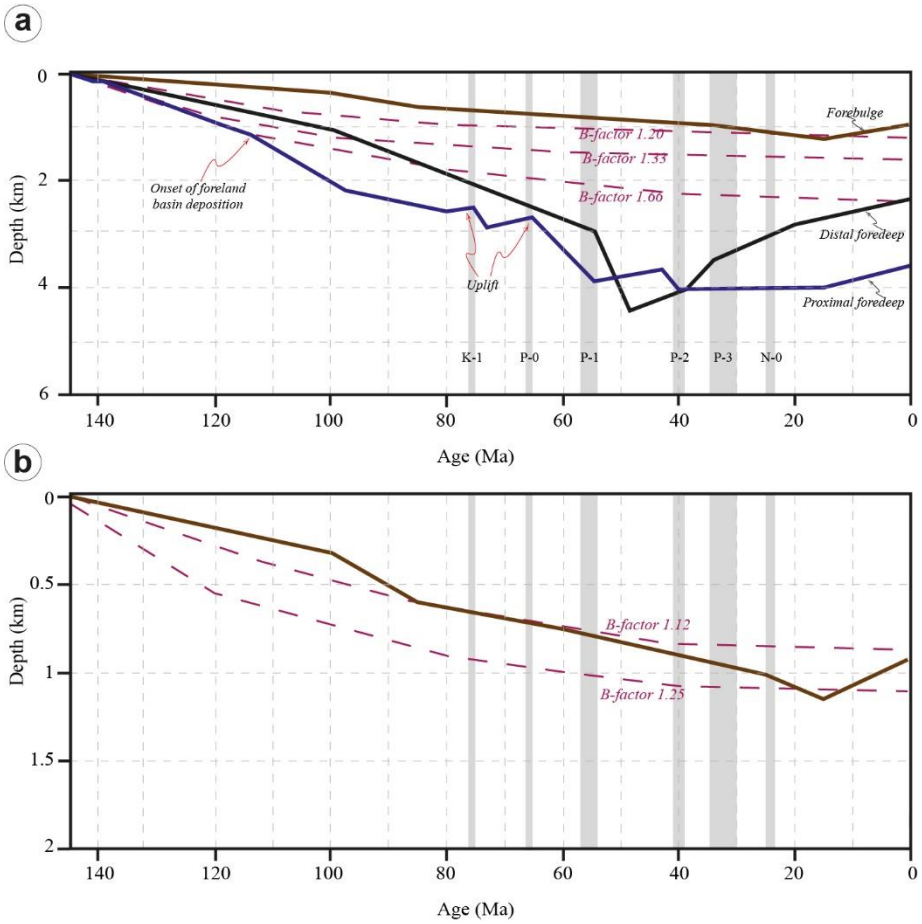

Figure 9. (a) Composite of tectonic subsidence curves obtained from wells in a different position in the basin (see Fig. 1a). (b) Enlarged subsidence curve of the forebulge domain. Grey bars point out unconformities in the study area (see Fig. 11) according to Rivera et al. (2021).

III-2.7.2 Results and interpretations

The reconstruction of tectonic subsidence shows an initial period of basin subsidence that responds to the theoretical model of thermal subsidence according to different stretching factors (Fig. 9a). The stretching degree progressively decreases towards the forebulge, intuitively and predictably in agreement with the tectonic history

of the region. An initial phase of thermal subsidence is recorded in the proximal foredeep between 140-114 Ma (0.035 mm/yr), which extends in time to *ca*. 100 Ma in the distal part of the foredeep (0.02 mm/yr). In the forebulge, there is subtle tectonic subsidence through time, but the thermal subsidence phase probably extends to the Lower Eocene (55 Ma; Fig. 9b). An increase in tectonic subsidence (0.064 mm/yr) is recorded in the proximal foredeep between 114-96 Ma and in the distal foredeep (0.04 mm/yr) from 100 Ma (Fig. 9a). This increase in subsidence marks the beginning of the foreland phase. For the remaining Late Cretaceous (Fig. 9a) the proximal foredeep experiences very subtle subsidence or even periods of possible uplift, whereas the distal foredeep undergoes a protracted subsidence phase. At the same time, the forebulge experiences either an uplift or null subsidence (Fig. 9b).

Between the Cretaceous-Paleogene boundary and the early Eocene (~ 66-55 Ma), occur the highest tectonic subsidence ever recorded in the basin history, with a magnitude of 0.11 mm/yr and 0.25 mm/yr for the proximal and distal foredeep, respectively (Fig. 9a). At the same time, the forebulge experience subtle subsidence (Fig. 9b). This pattern was interpreted by Rivera et al. (2020) as the combined effect of flexural and dynamic subsidence which favoured the Maastrichtian-Danian transgression in the basin. During the middle Eocene (50-40 Ma), a marked decrease in subsidence is recorded in the entire foredeep (about 0.011 mm/yr) (Fig. 9a). However, the forebulge exhibits a relative "acceleration" of subsidence (0.008 mm/yr) (Fig. 9b). We speculate that this pattern may be the result of dynamic topographic changes. For the early Miocene, subsidence is concentrated in the forebulge (0.013 mm/yr) while the foredeep experiences either zero subsidence, uplift and/or unconformity development (Fig. 9a, b). The latter suggests that dynamic subsidence is more important than tectonic loading as the main control in basin accommodation, a mechanism already proposed by Guillaume et al. (2009) and Dávila et al. (2019) that probably begun to operate since Oligocene.

The isopach maps (Fig. 10) provide a first glance regarding the lateral migration of depocentres through time, but due to the reduced areal extension of input data, these results have implications limited to the study area. The ~ 100-80 Ma isopach map (Fig. 10b) shows a broad depocenter deeper northwards (~ 1 km) and a minor thickness towards the east (~ 90-200 m). Regarding the ~ 130-100 Ma isopach map (Fig. 10a), the locus of depocenter (at ~ 100-80 Ma) migrated ~ 20 km eastwards at a rate of 1 mm/yr. At ~ 80-65 Ma (Fig. 10c), the depocenter does not present a significant lateral shift, but it is deeper

(~ 3 km) and much narrower and limited to the SW of the study area. The ~ 65-40 Ma isopach map (Fig. 10d) allows us to fully observe the geometry of the depocenter, which is much narrower and migrated ~ 86 km eastwards at about 3.5 mm/yr. At ~ 40-25 Ma (Fig. 10e) the depocenter appears to migrate towards the SE in Tierra del Fuego (although there is not much data control in this area). Nevertheless, it is possible to affirm that the ~ 40-25 Ma depocenter remains narrow and yielded less accommodation. At ~ 20-15 Ma (Fig. 10f) the location of the depocenter shift ~ 80 km eastwards at a rate of 8 mm/yr, but the accommodation does not exceed 1 km.

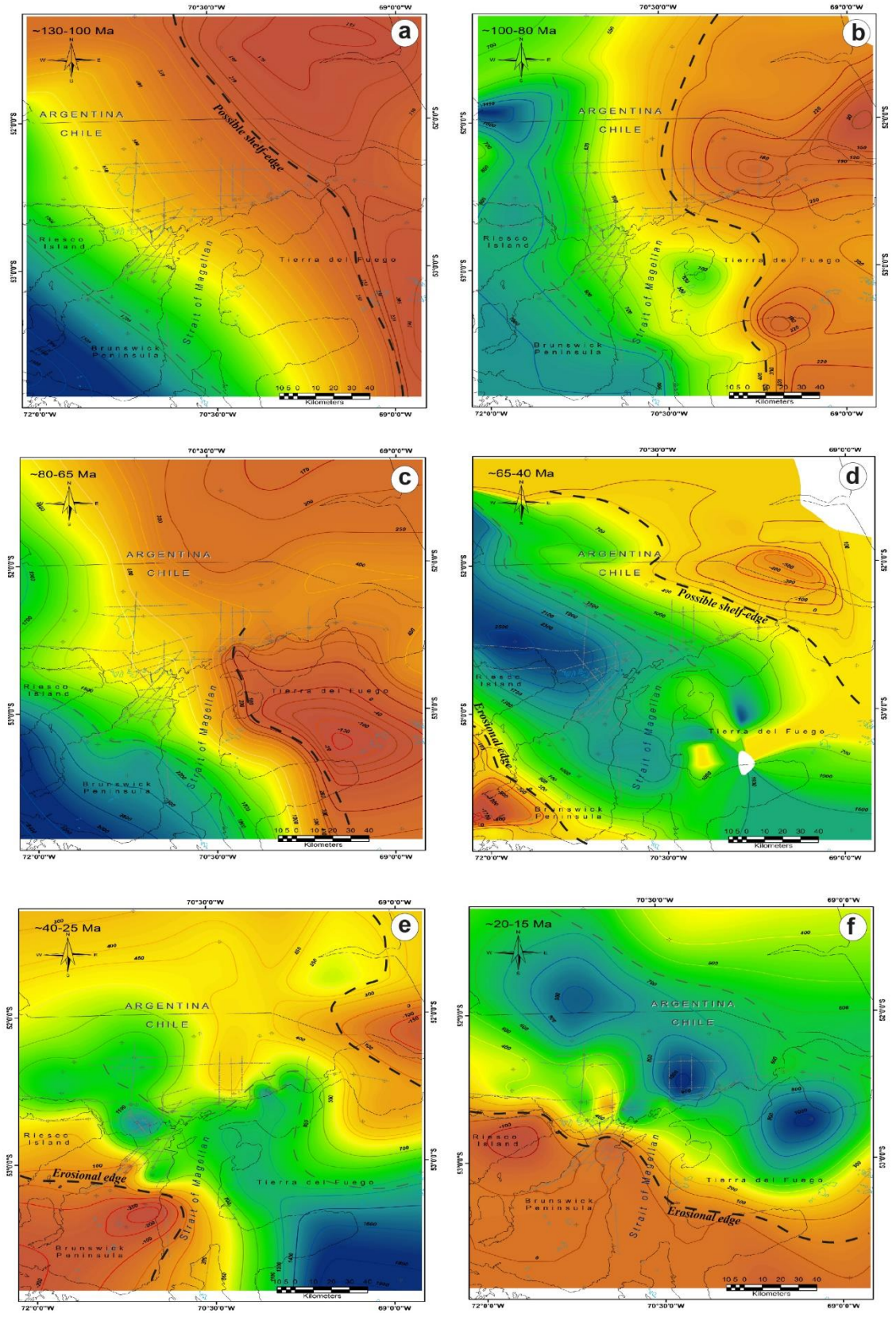

Figure 10. Isopach maps that span ~ 130–15 Ma. Grey dots and dotted lines represent well and 2D seismic-reflection data of control; negative isopach values imply uplift or erosion. Maps spanning (a) ~130–100

Ma, (b) ~100–80 Ma, (c) ~80–65 Ma, and (d) ~65–40 Ma, (e) ~40-25 Ma, (f) ~20-15 Ma. Segmented grey line marks a referential depocenter's front to quantify lateral migration through time.

III-2.8 Discussion and Conclusions

The combination of integrated provenance data, subsidence history, and sedimentation dynamics of Late Cretaceous to Burdigalian strata allows us to reconstruct the evolutionary phases of the Magallanes-Austral foreland basin and the Southern Patagonian Andes, which are summarised following.

III-2.8.1 Evolution of clastic wedges

The first basin clastic wedge (KS1; Fig. 11), which was not fully studied here, spans ~115-75 Ma and comprises the Canal Bertrand, Latorre and Barcárcel formations. McAtmaney et al. (2011) and Mpodozis et al. (2007, 2011) describe these units as deepwater turbidites, an interpretation that agrees with our observations along the east coast of the Magellan strait in Brunswick Peninsula (Fig. 1c). During this early phase of foreland sedimentation, an onset of flexural subsidence (Fig. 9a) and development of a wedge-like foredeep that rapidly migrates eastwards (Figs. 10b, c, and 11) is recorded, conditioning a large accommodation that could not be compensated by the sediment supply in an underfilled basin state. The second Upper Cretaceous clastic wedge (KS2; Fig. 11) spans ~75-66 Ma and comprises the Fuentes and Rocallosa formations, studied in detail by Rivera et al. (2020), during a period of reduced flexural subsidence (Fig 9a) and lateral foredeep migration. This second clastic wedge is characterised by an initial cycle of aggradation portraying the development of a depositional slope (Fuentes Formation; Rivera et al., 2020), which evolve to a shallow-marine depositional system (Rocallosa Formation; Rivera et al., 2020) as the supply of sediment exceeds the available accommodation during a final progradational cycle dominated by an ESE-ward sediment transport pathway.

The PS1 clastic wedge (Fig. 11) spans ~66-57 Ma and marks the onset of Cenozoic basin infilling during a period of accelerated subsidence (Fig. 9a), rapid eastward migration of the foredeep (Fig. 10d), and deeper depositional systems compared to the previous KS2. Sedimentation of PS1 reached bathyal depths in which the prograding turbidite lobes of the Chorrillo Chico Formation were deposited. The gravelly to coarse sandy facies overlying the finer, deeper marine sediments deposited by turbidity currents

in Tierra del Fuego (Sánchez et al., 2010), represent whether a wedge top or proximal foredeep closer to the advancing deformational front. In this way, the facies outcropping in the eastern and western parts of the Brunswick Peninsula represents the most distal and deepest parts of a submarine fan, which showed a clear north-northwesterly progradation (Fig. 2). Thus, the first Cenozoic cycle of sedimentation reveals the existence of ample accommodation compared to sediment supply (underfilled foreland basin). The second Cenozoic clastic wedge (PS2; Fig. 11), which spans ~57-43 Ma, is characterised by a change in the stacking pattern, now dominated by aggradation or vertical accretion (Fig. 11) of pelagic and hemipelagic sediments corresponding to the Agua Fresca Formation (Fig. 2), suggesting an equilibrium between accommodation and sediment input, which was succeeded by the aggrading to prograding river-dominated deltaic system of the Tres Brazos Formation (Fig. 2). Based on the available sedimentological data, we can infer that the Agua Fresca Formation represents the establishment of a slope-shelf depositional system over which the shallow-marine delta of the Tres Brazos Formation developed. During the shallow marine accumulation time, a change in paleocurrent directions towards the north-northeast is observed in the study area (Fig. 2) and elsewhere in the Magallanes-Austral basin (e.g., Gutiérrez et al., 2017; Torres Carbonell and Olivero, 2019).

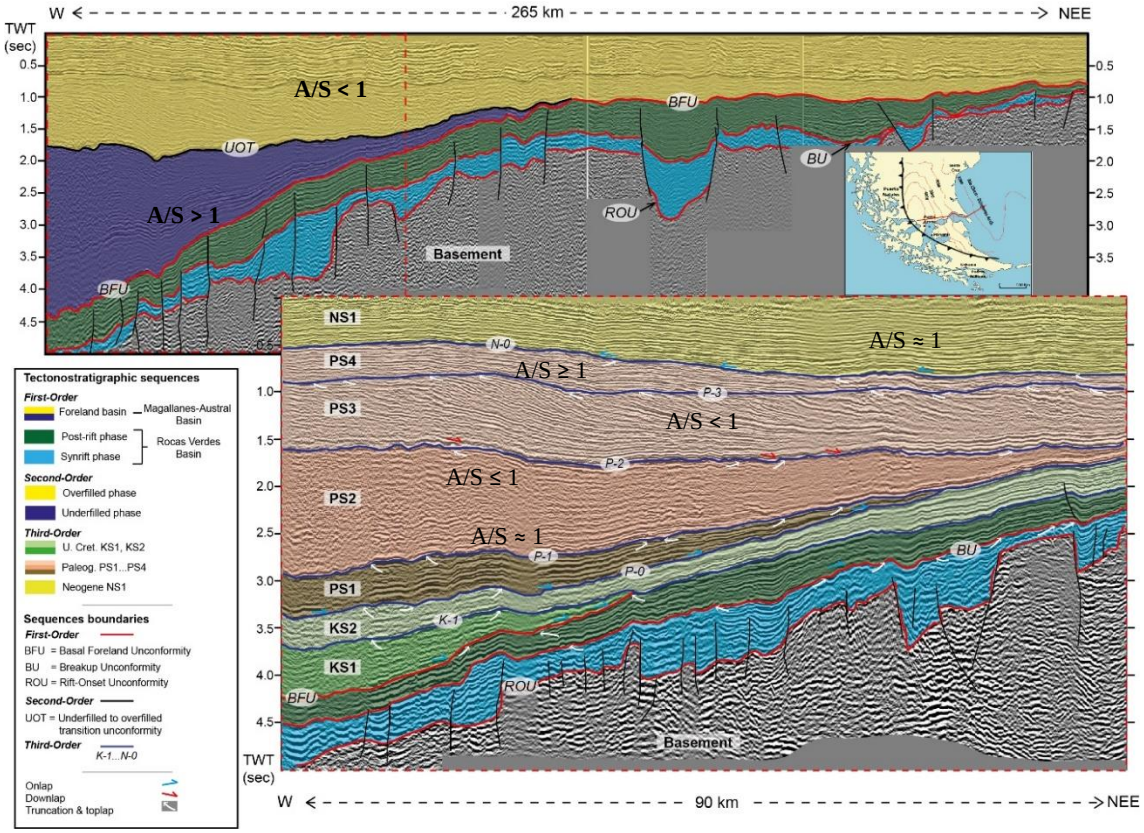

Figure 11. (← *previous page*) Tectonostratigraphic sequences or clastic wedge in the Magallanes-Austral Basin (modified from Rivera et al., 2021). A: accommodation; S: sediment supply. Note the transition from underfilled to overfilled foreland phase (UOT) by ~40 Ma.

The PS3 clastic wedge (Fig. 11) spans ~43-33 Ma, during a period that foredeep rest relatively immobile (Figs. 10e and 11), and the subsidence previously experienced in this depozone is then concentrated toward forebulge (Fig. 9a). A short-lived marine flooding event marks the onset of sedimentation, probably related to a short tectonic load event combined with a eustatic sea-level rise by ~43-40 Ma, which allowed the hemipelagic, outer to inner shelf deposition of the Leña Dura Formation (Fig. 2). Subsequently, an increased sediment supply dominated the study area, leading to the E-NE progradation of the shelf-edge deltaic system of the Loreto Formation (Fig. 2) until reaching (burying) the forebulge (Fig. 11), characterising thus the change from underfilled to overfilled basin stage. The PS4 clastic wedge (Fig. 11) spans ~30-25 Ma, exhibit a subtle wedge-like geometry and is characterized by a high-energy braided fluvial system (lower part of the El Salto Formation; Fig. 2) in the proximal foredeep or wedge top, whereas, towards the distal foredeep and forebulge, a retrogradational to aggrading stacking pattern occurs (Fig. 11) attesting a larger accommodation in distal areas of the foreland basin system (DeCelles and Giles, 1996).

The last Cenozoic clastic wedge (NS1; Fig. 11) spans ~23-15 Ma, comprising the upper part of the El Salto Formation and the Palomares Formation. The NS1 does not show a typical wedge-like geometry and dynamic subsidence seems to control the accommodation in the distal part of the foreland basin system (Fig. 9). Stratigraphically, this transition from a flexural to dynamic subsidence takes place during a regional and widespread progradation of coarse deposits in an overwhelming overfilled basin stage (Fig. 11). In the wedge top or proximal part of the depocenter, occurs a rapid transition of a braided mixed sandy-gravelly fluvial system of the upper El Salto Formation to hyper-concentrated laharic flows and a coarse meandering fluvial system affected by intermittent strong volcanic activity (Palomares Formation; Fig. 2). In general terms, the sediment supply exceeded the available accommodation, but some short cycles of enhanced accommodation can be identified, which may be linked to processes other than tectonic loading, for instance, dynamic topography, climate, or eustatic sea-level rises (e.g., Patagonian Transgression).

The foreland basin phase in the study area begins as early as ~114 Ma, with an eastward shifting of the onset at ~100 Ma due to progressive migration of supracrustal loads, as suggested by the subsidence analysis (Fig. 9). This time-transgressive eastward younging of the contractional influence is shown by independent evidence in the eastern part of the Magallanes-Austral basin (Sachse et al., 2015). Flexure (i.e., tectonic loading) is the main driver of subsidence from Late Cretaceous to late Eocene (?). However, this flexural subsidence was not continuous but rather episodic. The accelerated flexural subsidence phases are coincident with the deepening of depositional systems in our study area (and elsewhere in the basin, e.g., Torres Carbonell and Olivero, 2019) and with an uplift in the forebulge (Springhill platform) as shown also by Sachse et al. (2015). On the other hand, decelerated subsidence phases coincide with shallow-marine depositional systems. A transition to higher rates of subsidence in the eastern or distal part of the basin and less in the west (closer to the tectonic load), dominate from Oligocene to Miocene, and a coarse sediment progradation occurs overpassing the forebulge and ends up reaching depocentres in the Malvinas Basin (Sachse et al., 2015). This pattern is ascribed to dynamic subsidence and post-tectonic progradation, as observed in the Campanian strata of Western Interior Basin, U.S.A. (e.g., Mitrovica et al., 1989; Pang and Nummedal, 1995; DeCelles, 2004). Therefore, the foreland basin phase (*sensu stricto*) ends by the late Oligocene as suggested by Sachse et al. (2015) and Torres Carbonell and Olivero (2019).

III-2.8.2 Kinematic evolution of the Southern Patagonian wedge

The oceanic crust developed during the extension of Rocas Verdes Basin was subducted southward beneath the Southern Patagonian Batholith during the compression that lead to the closure of this basin (Klepeis et al., 2010). As closure progressed (between ~100-80 Ma), a narrow orogenic wedge was formed, which incorporated mainly Andean metamorphic basement thrusts and, to a lesser extent, Late Jurassic volcaniclastic rocks of the Tobífera Formation (Fig. 8; McAtamney et al., 2011). This thrust wedge migrated eastward as did the early foredeep (at 1 mm/yr) which hosted deep-water turbiditic deposits during a pronounced flexural subsidence (Fig. 12a). The following stage during the latest Cretaceous (~73-66 Ma) is characterised by sediments largely derived from a dissected magmatic arc, and terranes of felsic nature found in the hinterland, such as the Andean metamorphic complexes and the Tobífera Formation. This implies that the

creation of relief in the premature and still narrow orogen was subjected to an intense erosion that together with the flexural subsidence in progressive decrease, allowed the development of aggradational to progradational depositional systems (Fuentes and Rocallosa formations). The reduced flexural subsidence in the foredeep and the uplift of the orogenic wedge may be linked to an isostatic rebound process, likely due to the detachment of the underthrust oceanic crust of the Rocas Verdes Basin (Fig. 12b). Therefore, the Late Cretaceous was a stage of thrust wedge thickening and basement imbrication with a minor degree of horizontal wedge broadening (Betka et al., 2015; Rivera et al., 2020).

Figure 12. (→ *following page*) Highly schematic reconstruction of the Southern Patagonian wedge kinematics and the sedimentary response of the Magallanes-Austral basin. (a) Rapidly subsiding underfilled basin and narrow fold-and-thrust belt. (b) Isostatic rebound and reduced tectonic loading due to the detachment of Rocas Verdes Basin oceanic crust. (c) Rapidly subsiding underfilled basin and broadening of the fold-and-thrust belt. (d) Isostatic rebound and tectonic quiescence due to Farallon-Aluk ridge subduction. (e) Last phase of compressional tectonics and progradation and continentalization. (f) Tectonic quiescence and foreland basin abandonment, dynamic subsidence dominate.

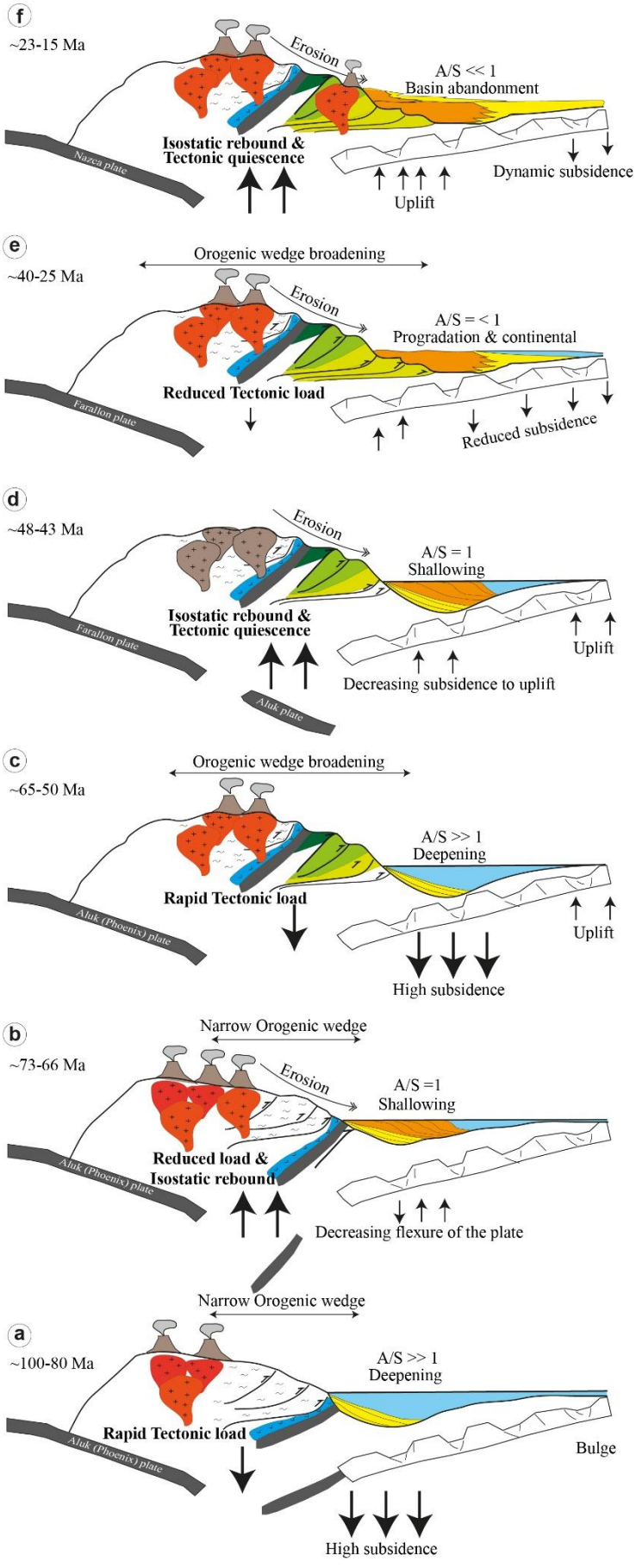
f
~23-15 Ma
Erosion
A/S << 1
Basin abandonment
Isostatic rebound &
Tectonic quiescence
Nazca plate
Dynamic subsidence
Uplift
e
~40-25 Ma
Orogenic wedge broadening
Erosion
A/S = < 1
Progradation & continental
Reduced Tectonic load
Farallon plate
Reduced subsidence
d
~48-43 Ma
Erosion
A/S = 1
Shallowing
Isostatic rebound &
Tectonic quiescence
Farallon plate
Uplift
Decreasing subsidence to uplift
Aluk plate
c
~65-50 Ma
Orogenic wedge broadening
A/S >> 1
Deepening
Rapid Tectonic load
Aluk (Phoenix) plate
Uplift
High subsidence
b
~73-66 Ma
Narrow Orogenic wedge
Erosion
A/S =1
Shallowing
Reduced load &
Isostatic rebound
Aluk (Phoenix) plate
Decreasing flexure of the plate
Narrow Orogenic wedge
a
~100-80 Ma
A/S >> 1
Deepening
Rapid Tectonic load
Aluk (Phoenix) plate
Bulge
High subsidence

The orogenic construction phase of the Lower Paleocene-Eocene (~65-50 Ma) is characterized by both crustal thickening of the inner orogen and by the lateral broadening of the orogenic wedge, where the advance of the deformation front is possibly one of the most accelerated as shown by the foredeep migration at a rate of 2.15 mm/yr (Fig. 12c). The latter interpretation is supported by our provenance data that suggest a mixture between sediments derived from the dissected magmatic arc, hinterland terranes of a mafic and felsic nature, and recycling of upper Cretaceous foreland deposits (Katz, 1961). Furthermore, the highest rates of flexural subsidence recorded and pronounced uplift of the forebulge region (Biddle et al., 1986; Sachse et al., 2015). This accentuated tectonic load promoted the deepening of the depositional system represented by a system of deep-water submarine fans and the development of a depositional slope (Chorrillo Chico and Agua Fresca Formations) with a dominant longitudinal sediment transport routing.

During the middle Eocene (~48-43 Ma; Fig. 12d), the sediments deposited in a shallow marine depositional system derive from hinterland terrains such as the Tobífera Formation, an Andean metamorphic basement, and from the recycling of Cretaceous-Paleocene foreland deposits following a transversal sediment routing system. Although the provenance data are similar to those of the previous stage, the differences lie in the lacking of active magmatic arc-derived detritus, the reduced subsidence or even uplift of the entire foredeep concomitant with an uplift in the forebulge depozone (Sachse et al., 2015), in addition to the evident shallowing of the environments. All the latter suggests a phase of tectonic quiescence, producing a generalised isostatic rebound of the orogenic wedge and the entire foreland basin system (DeCelles and Giles, 1996). This tectonic quiescence that is also interpreted during the middle to late Eocene in Tierra del Fuego (Torres Carbonell and Olivero, 2019), could be the result of the subduction of the active Farallon-Aluk ridge (Cande and Leslie, 1986; Ramos, 2005; Müller et al., 2016). Guillaume et al. (2009) pointed out that subduction of an active ridge shut off the magmatic arc and lead to a mantle-lithosphere interaction that impacts dynamic topography changes producing strong rock uplift in the continents.

The last phase of deformation (Fig. 12e) is recorded during the late Eocene and late Oligocene (~ 40-25 Ma) which does not lead to a significant displacement of the depocenter or an increase in subsidence (neutral to negative). Instead, it is characterized by multiple unconformities development in the wedge top or the proximal foredeep (e.g., Rivera et al., 2021) and a rapid net progradation of the depositional systems evolving

from a shelf (Leña Dura Formation) to shelf-edge deltaic system (Loreto Formation) to high energy fluvial system (El Salto Formation) burying the forebulge. The provenance data suggest contributions from a renewed magmatic arc, hinterland terranes of a mafic and felsic nature (e.g., Andean metamorphic complexes, Rocas Verdes Basin remnants and Tobífera Formation), and recycling of foreland deposits. This deformation scene is also recorded in Tierra del Fuego (Barbeau et al., 2009; Torres Carbonell and Olivero, 2019) but incorporating rocks of a more felsic nature in the hinterland (eg, Cordillera Darwin metamorphic complex), which explains the difference compositional that is recorded between Tierra del Fuego and our study area for this time (see Fig. 7f, g). The rapid progradation could be favoured by a more elevated or prominent orogen subject to enhanced erosion by Oligocene times, as suggested by Gutiérrez et al (2017). It is striking that although during the late Eocene and late Oligocene, deformation, development of unconformities and growth strata are recorded in the wedge top or proximal foredeep, and also is envisaged an orogen high enough to create a rain shadow (Barbeau et al., 2009; Ghiglione et al., 2016; Gutiérrez et al., 2017; Rivera et al., 2021) that generate such little or no subduction and clastic packages with a slight wedge to subtabular geometry (Figs. 9 and 11). This absence of accentuated flexural subsidence could be related to a phase of transpressive deformation associated with a highly oblique convergence, the opening of the Drake Passage, spreading of the Western Scotia Sea and the Farallon plate break-up (Herron and Heirtzler, 1967; Pardo-Casas and Molnar, 1987; Barker, 2001; Eagles et al., 2005, 2006; Barbeau et al., 2009; Eagles and Scott, 2014).

During the Miocene (Fig. 12f), tectonic loading is negligible and dominate uplift, as suggested by our subsidence data (Fig. 9) and the tabular geometry of the NS1 sequence (Fig. 11). Coarse-grained sediments derived from the magmatic arc, hinterland source terranes and local mafic volcanic sources are presented, which reach far distances beyond the forebulge (Sachse et al., 2015), in a context of post-orogenic progradation. Very low subsidence is concentrated in the forebulge, which is interpreted as dynamic subsidence. There is no field evidence of the advance of the deformation front, but a slight eastward tilting of the early Miocene deposits (Katz, 1961; Rivera et al., 2021) and a retro-arc transitional basaltic volcanism (Ramírez de Arellano et al., 2021) were recorded in the base of the Palomares Formation probably linked to the subduction of the Chile Ridge.

ACKNOWLEDGEMENTS

This study was financially and logistically supported by Project Fondecyt 1130006 under the auspices of Project CONICYT/FONDAP 15090013. CONAF-Magallanes kindly gave permission to work in the Magallanes and Laguna Parrillar National Reserves. L.K. Sánchez is thanked for her invaluable assistance during field campaigns. We gratefully acknowledge L. Rojas (Enap-Sipetrol) for permission to review unpublished reports and collaboration in this research, as well as J. Arriagada (Enap-sipetrol) for his assistance in searching through the Enap technical files database. Some detrital zircon dating was carried out by Mathieu Leisen in the Mass Spectometry Laboratory of the Andean Geothermal Centre of Excellence.

FOURTH PART

STRUCTURAL AND LOW-TEMPERATURE THERMOCHRONOLOGICAL ANALYSIS

CHAPTER IV-1:

STRUCTURAL ANALYSIS AND EXHUMATION TIMING OF THE EXTERNAL PATAGONIAN FOLD-AND-THRUST-BELT AND MAGALLANES-AUSTRAL FORELAND BASIN

Chapter IV-1 presents the structural configuration and exhumation history of the external domain of the Southern Patagonian fold and thrust belt and Magallanes-Foreland Basin deposits. This chapter is based on: (1) 2D regional seismic-reflection profiles to interpret the structural architecture, the temporality of the main thrust faults that can contribute to the exhumation processes in each area investigated; (2) detrital apatite fission-track and (U-Th)/He cooling ages analysis and inverse modelling of these source of data. The results exhibit the different stages of compressive deformation, remarking the influence of inherited structural architecture heterogeneities and the quantification of the amount and distribution of exhumation, unravelling genetic links between thrusting events, erosion, and sedimentation in terms of orogenic wedge patterns (steady-state, constructing or decaying).

HIGHLIGHTS:

- From the early to late Oligocene (33-25 Ma), samples were not buried enough to reset the apatite fission-track system.
- The Partial Annealing Zone occurs in shallow depths, suggesting a basin's thermal gradient higher than 30°C/km.
- Samples younger than Burdigalian (19 Ma) were not buried enough to reset the He system.
- The Oligocene exhumation event (24 +- 6 Ma) coincides with the loss of wedge geometry of foreland deposits and a decrease in subsidence.
- The late Miocene exhumation event (9.5 +- 2.5) postdate Chile Ridge collision and predate the onset of Patagonian glaciations.

IV-1.1 Introduction

The study of the formation of fold-thrust belts and the timing of their exhumation is fundamental to the understanding of the mountain-building processes. However, to achieve full and accurate discrimination of the different deformation pulses occurring in orogenic wedges it is required to integrate regional chronostratigraphic (U-Pb and/or biostratigraphic ages) and sedimentological data (depositional systems, provenance, subsidence) of the deposits involved in the fold-thrust belt, the geometry and timing of the structures, and timing of exhumation (e.g., Carrapa et al. 2008; Parra et al., 2009; Pérez et al., 2016).

In the Southern Patagonian Andes (46°S-56°S), most of the structural geological and thermochronological studies are concentrated in the northernmost (47°40'S-51°) and southernmost (Fuegian; ~54°20'S-56°) segments of the Magallanes-Austral fold-thrust belt and Southern Patagonian Batholith (see Fig. 1 and references therein). The central segment (Fig. 1; 51°15'S-53°30'S), however, has been by far less investigated and structural studies are more sparse. The increase in high-precision U-Pb geochronological and sedimentary provenance studies for the Cretaceous strata of the Magallanes-Austral foreland basin (e.g., Fildani et al., 2003; Fildani and Hessler, 2005; Barbeau et al., 2009; Romans et al., 2010) favoured a greater accuracy in the timing of the deformation of the fold-thrust belt in the structural studies post-2003-2010. However, for the Cenozoic deposits, more accurate geochronological information and sedimentary provenance have begun to develop more recently (e.g., Fosdick et al., 2015; Gutiérrez et al., 2017; George et al., 2019; Rivera et al., 2020, 2021 [Chapter III-2]; Leonard et al., 2020; Fosdick et al., 2020), which has lead a poor constraint of the deformation phases during the Paleogene-Miocene in structural studies predating 2015-2020. Despite the timing of deformation limitations, from structural studies, it is evident a southward increase in shortening ranging from 35-90 km at ~47-51°S to up to 300 km at around 55°S and increasing influence of wrenching in Tierra del Fuego (Kraemer, 1998, 2003; Diraison et al., 2000; Ghiglione and Ramos, 2005; Ghiglione et al., 2009, 2014; Fosdick et al., 2011; Betka et al., 2015; Ronda et al., 2019; Torres Carbonell et al., 2020).

On the other hand, thermochronological studies have been focused on the Southern Patagonian Batholith and the Cordillera Darwin metamorphic complex (i.e., in the hinterland part of the fold-thrust belt) (Nelson, 1982; Thomson et al., 2001, 2010; Gombosi et al., 2009; Stevens Goddard and Fosdick, 2019), providing only a restricted vision of the exhumation patterns of the entire orogenic wedge. Exceptionally, Fosdick et al. (2013) present an integrated thermochronological study of the entire Magallanes fold-thrust belt at 50°30'-

51°30'S. In general terms, the exhumation is concentrated in three periods: between the middle to late Eocene, late Oligocene to late Miocene, and the latest Miocene to Pliocene. The formers two periods are ascribed to contractional uplift and migration of the deformation and the latter to the erosive action of glaciers.

In this work, we will focus on the central segment of the Magallanes fold-thrust belt (Fig. 1) to contribute to filling the existing gap in structural and thermochronological studies in this latitudes of the orogenic wedge. This study aims to describe the structural architecture, the timing of the deformation and the exhumation of the fold-thrust belt by integrating new (surface and subsurface) structural interpretations, and new detrital apatite fission tracks and U/Th-He data with previous structural and sedimentological results conducted in the Cerro Castillo-Río Turbio-Natales and Skyring Sound-Brunswick Peninsula areas (Figs. 1, 2, 3).

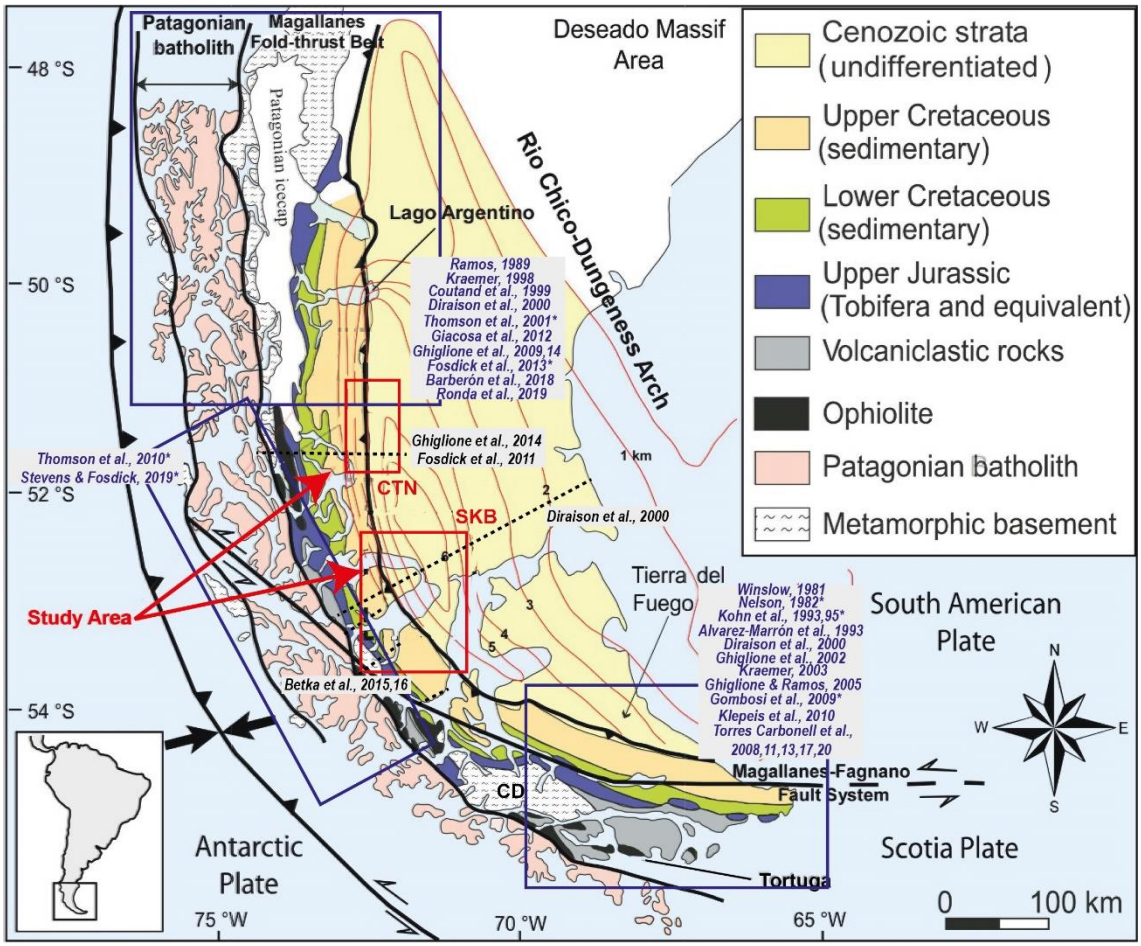

Figure 1. Morphotectonic setting of the Southern Patagonian orogenic wedge and Magallanes-Austral foreland basin. Red isopach lines are the depth to top-Tobífera Formation (Late Jurassic). Blue boxes are areas that concentrate most of previous structural and thermochronological (references with asterisks) studies. Red boxes are study areas, enlarged in Figs. 2 (CTN: Cerro Castillo-Río Turbio-Natales area) and 3 (SKB: Skyring Sound-

Brunswick Peninsula area). Segmented lines are structural transects within the study areas. CD: Cordillera Darwin metamorphic complex.

IV-1.2 Previous works and geological context

Early works have highlighted that the progression of the deformation and, in general, the tectonic evolution of the Southern Patagonian Andes is not homogeneous throughout its full extension (e.g., Suarez, 1976; Ramos, 1989; Ramos and Aguirre-Urreta, 1994; Kraemer, 1998; Suarez et al., 2000a; Diraison et al., 2000). These particularities and differences in its evolution are due to the different morphostructural conformation of the fold-and-thrust belt at different latitudes and the structural configuration and basin geometry inherited from the previous extensional stage (the Rocas Verdes Basin). Nevertheless, three main orogenic and deformational episodes have been documented in the Magallanes fold and thrust belt (Coutand et al., 1999; Suárez et al., 2000a; Ghiglione and Ramos, 2005; Fildani et al., 2008; Ghiglione et al., 2016), namely during the Late Cretaceous, Paleogene-Oligocene, and post-Miocene.

Most of the structural studies agree that the first phase of deformation is related to the closure and inversion of the Rocas Verdes Basin (RVB), which formed during the Late Jurassic to Early Cretaceous due to the extensional regime that prevailed in the Southern Patagonian Andes region by this time. The foreland basin sedimentation (the first medium to coarse-grained sandy turbidite) onset marks the closure of the RVB, thus the time of this contractional event is diachronic from north to south, constrained ~120 Ma at 47-48°S (Ghiglione et al., 2014); ~115-100 at 49-53°S (Fildani et al., 2003; Fosdick et al., 2011; Malkowski et al., 2017a; Rivera et al., 2021 [Chapter III-2]); ~90-85 Ma at 54-56°S (Klepeis et al., 2010; McAtmaney et al., 2011). Thus, the early deep-water coarse-grained turbiditic sedimentation accompanied by flexural subsidence reflects the development of a fold-and-thrust belt and linked foreland basin (Katz, 1963; Biddle et al., 1986; Wilson, 1991; Fildani et al., 2003; Fildani and Hessler, 2005). This first phase of crustal shortening and thickening concentrated the hinterland of the orogen is expressed by the development of imbricated and stacked duplex systems involving the Upper Jurassic synrift metavolcanic rocks of the Tobífera Formation, Upper Jurassic to Early Cretaceous RVB remnants (ophiolites and sedimentary cover), and the Paleozoic metamorphic basement (Farfán, 1994; Klepeis et al., 2010; Fosdick et al., 2011; Betka et al., 2015). In Tierra del Fuego (~56°S), thermochronologic evidence suggests a stage of rapid cooling and associated uplift of the metamorphic rocks from the Cordillera Darwin (Fig. 1) between 90-70 Ma (Nelson et al., 1982; Kohn et al., 1995). Provenance data from the early foreland deposits suggests that

metamorphic-derived detritus begun by ~110-91 Ma in the Cerro Castillo-Río Turbio-Natales area (Fig. 2; e.g., Fildani et al., 2003; Fildani and Hessler, 2005; Malkowski et al., 2017a) and by ~93-80 Ma in the Skyring Sound-Brunswick Peninsula area (Fig. 3; e.g., Mpodozis et al., 2007; McAtmaney et al., 2011; Rivera et al., 2021 [Chapter III-2]).

The second phase of deformation in Paleogene-Oligocene time is by far poorly constrained based only on structural data. Thin-skinned deformation of the Cretaceous depocenter is broadly categorised as sometime between 70-27 Ma (Fosdick et al., 2011) in the Cerro Castillo-Río Turbio-Natales area (~51°S; Fig. 2). Further south, in the Skyring Sound-Brunswick Peninsula area (53°S; Fig. 3), Betka et al. (2015) suggest that continued shortening resulted in a series of out-of-sequence thick-skinned thrusting ranging from Maastrichtian up to Paleocene-Eocene. A similar situation is exposed in Tierra del Fuego (Fig. 1), where basement-involved thrusting concomitant with thin-skinned thrust sheets developed in the internal and external part of the fold-and-thrust belt, respectively, from the Maastrichtian-Danian up to the late Oligocene (see synthesis in Torres Carbonell et al., 2020).

Other lines of evidence that rely on the basin's sedimentary record have supported the idea of a deformation event during the Paleogene. The still origin-unknown hiatus in the Paleocene-Eocene, which comprise >30 Myr in the northernmost part of the basin (49°15'S; Fig. 1) and <5 Myr in the southernmost part (53°-54°S; Fig. 1) (Malumián et al., 2000; Rivera, 2017; Gutiérrez et al., 2017; George et al., 2020; Torres Carbonell and Olivero, 2019; Rivera et al., 2021 [Chapter II-1]), have been ascribed as the result of a major deformation event in the region (Malumián et al., 2000; Fildani et al., 2008; Fosdick et al., 2011; Mpodozis et al., 2011; Ghiglione et al., 2016). Additionally, the fact that over the Paleocene-Eocene unconformity prevail progradational shallow marine and continental deposits during the late Eocene to Oligocene, some units portraying progressive unconformities and growth strata in the Cerro Castillo-Río Turbio-Natales area (Fig. 2; Malumián et al., 2000; Mpodozis et al., 2011; Rivera et al., 2021 [Chapter II-1]), reinforce the idea of a compressive tectonic event between Late Eocene to Oligocene (Kraemer, 1998; Martinioni et al., 1998; Suarez et al., 2000; Marensi et al., 2002; Ghiglione and Ramos, 2005; Fildani et al., 2008; Fosdick et al., 2011; Ghiglione et al., 2016; Leonard et al., 2020; Fosdick et al., 2020). However, in Tierra del Fuego (Fig. 1), the establishing of progradational shallow marine deposits during the middle to late Eocene is interpreted instead as regional uplift due to tectonic quiescence (Torres Carbonell and Olivero, 2019). The foregoing adds to the debate between

compressional vs extensional tectonics dominant in Tierra del Fuego during much of the Paleogene (see synthesis in Ghiglione, 2015). A similar process of tectonic quiescence is interpreted by Rivera et al. (2021; Chapter III-2) for the middle Eocene in the Skyring-Brunswick Peninsula area (Fig. 3).

Thermochronological data from the fold-thrust belt in the Cerro Castillo-Río Turbio-Natales area (51°S; Fig. 2) suggest an episode of cooling between 44-42 Ma likely associated with thrust-related unroofing of the external part of the thrust belt (Fosdick et al., 2013). In the Cordillera Darwin (Fig. 1), there are episodes of rapid cooling between 60-40 Ma (Nelson, 1982; Kohn et al., 1995) and between ~48-34 Ma (Gombosi et al., 2009), but their origin concerning whether to compression, extension or transcurrence is not yet clearly defined. On the other hand, provenance data show a significant change in sediment routing and palaeogeography suggesting hinterland-derived sediment structurally dammed during basinward propagation of the fold-and-thrust belt between 60-40 Ma in the Cerro Castillo-Río Turbio-Natales area (51°S; Gutiérrez et al., 2017; Fosdick et al., 2020), during at least all the Paleocene in the Magallanes Province (52°-53°S; Rivera et al., 2020 [Chapter III-1]). In contrast, in Tierra del Fuego, a major change in provenance occurs from the middle Eocene up to Oligocene, and it is linked to an enhanced contribution of hinterland-derived sediments related to contractional tectonism in the orogen (Barbeau et al., 2009; Torres Carbonell and Olivero, 2019). Finally, it is worth mentioning that independent paleobotanical data indicate the establishment of a rain shadow in the region from the late Eocene-Oligocene, which is interpreted as a reflection of the uplift and growth of the Southern Patagonian Andes (Gutiérrez et al., 2017).

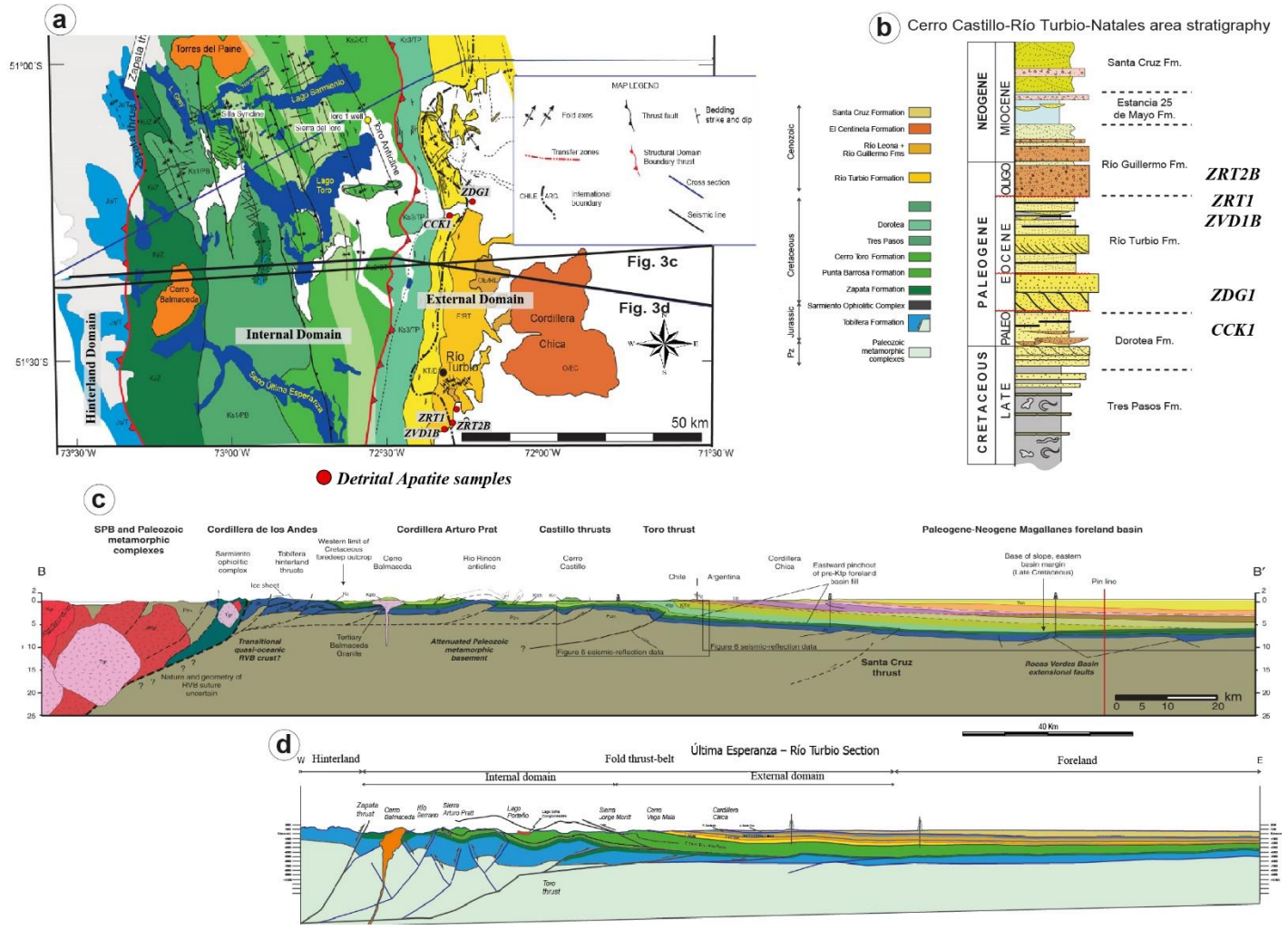

Figure 2. (a) Geological map and distribution of detrital apatite samples in the Cerro Castillo-Río Turbio-Natales study area. (b) Stratigraphic position of detrital apatite samples. (c) Regional structural basin configuration model of Fosdick et al., 2011. (d) Structural configuration model of Ghiglione et al., 2014.

The last deformation phase is thought to begin at the early Miocene (~22 Ma), but while in most of the Southern Patagonian Andes it is manifested as net compression, in Tierra del Fuego, it acquires a more transtensional character (Winslow, 1982; Diraison et al., 2000; Ghiglione, 2015). Structural studies in the north (50°-51°S; Fig. 1) have identified a series of thrust faults associated with the deepening of the decollement and faulting of the Patagonian basement that progressively gave place to a forelandward propagation of deformation and wedge thickening through thin-skinned thrusts during the early Miocene (Kraemer, 1998; Fosdick et al., 2011). The deposition of continental deposits of the Santa Cruz Formation and equivalents (~19-15 Ma) after a short period of transgression is exemplified as a result of this contractional event, and a synorogenic nature is assigned (Ramos, 1982, 1989; Malumián and Ramos, 1984; Kraemer, 1998; Suarez et al., 2000a; Ramos and Ghiglione, 2008; Fosdick et al., 2011; Cuitiño et al., 2012, 2015; Gutiérrez et al., 2017). However, the subsidence occurring in the Skyring Sound-Brunsxick Peninsula area does not reflect tectonic loading during the late Oligocene to early Miocene (Rivera et al., 2021 [Chapter III-2]). Apatite and zircon thermochronometers show increased denudation in the hinterland part of the orogen by 30-23 Ma, which migrated eastward in the external part of the fold-and-thrust belt until 18-12 Ma (Thomson, 2002; Thomson et al., 2001, 2010; Fosdick et al., 2013). This early Miocene period of compression is interpreted as increased plate coupling during the approach of the Chile Ridge (Folguera and Ramos, 2002). A subsequent late Miocene uplift is suggested by the eastward tilt of basalts and Santa Cruz Formation deposits at 51°S (Ramos, 1989; Fosdick et al., 2011) and the emplacement of a series of plutons further east in the foreland (Skarmeta and Castelli, 1997; Coutand et al., 1999; Suarez et al., 2000a; Ramírez de Arellano et al., 2012).

IV-1.3 Methodology and data source

The structural analysis is focused on the Skyring Sound-Brunswick Peninsula area because for the northern Cerro Castillo-Río Turbio-Natales study area there is better structural control. One structural section (Fig. 3c) was constructed based on georeferenced field data (contacts, dip measurements, stratigraphic units) and complemented with surface structural data recorded in unpublished reports provided by ENAP (Empresa Nacional de Petróleos de Chile). The structural section was complemented (merged) with other previous works (Farfán, 1994; Betka et al., 2015) focused on the innermost part of the orogen (see Fig. 3a), where it was not possible to access during the fieldwork campaigns. The projection of the structures in the subsurface and characterisation of the structural geometry of the basin

was supported by multiple 2D seismic lines and exploratory wells data (Fig. 3a). The interpretation of the regional seismic profiles was based on stratigraphic-seismic criteria and their relationship with the structures kinematics. Depth and thickness measurements were derived through velocity-depth conversion models based on check-shot data provided by ENAP. Shortening was measured by retrodeformation of key stratigraphic intervals. The temporality of the deformation is constrained thanks to the U-Pb dating in detrital zircons, sedimentary provenance, growth strata identified in the seismic lines.

Thirty (30) medium-grained sandstones samples were selected and prepared in the Sample Preparation Laboratory of the Geology Department at the University of Chile for thermochronological analyses. The procedures for extraction of apatites is the same as for zircons, described in the previous chapters. Detrital apatite grains were carefully selected from the concentrates for (U-Th)/He age dating (n= 12 samples). The selection of apatites grains was conducted at the Geosciences Environnement Toulouse laboratory and they were hand-picked under an optical microscope (Nikon SMZ1500), favouring those of euhedral morphology and without inclusions of actinide-rich minerals such as zircons or monazite. For each sample, five aliquots were measured (equivalent radius ranging from 30-90 µm, mean 58 µm) and then placed into a platinum capsule for He, U, and Th measurements at Géosciences Montpellier laboratory (France). The aliquots were heated at ~850 °C for 20 min using a 1090 nm diode laser operating at 20 W, allowing total helium (He) degassing. The gas was purified by two SAES AP-10-N getters and trapped on a JANIS cryostat. The released ^{4}He was measured with a Quadrupole PrismaPLus QMG 220 using the peak height method using a ^{3}He spike and are 10–100 times superior to typical blank levels. After helium extraction, aliquots were retrieved for U and Th measurements. Apatite grains were dissolved in 220 ml of doubly spiked (^{230}U, ^{235}Th) HNO_3 13N at 120 °C for two hours, and ^{238}U and ^{232}Th were measured using isotope dilution by a quadrupole ICP-MS (Agilent 7700x). Each calculated apatite age (AHe) was corrected by alpha (α) ejection factor (F_t), determined using the Monte Carlo simulation technique of Ketcham et al. (2011), and equivalent sphere radius (R_s) following Gautheron and Tassan-Got (2010). Durango apatite replicates were analysed for each three analysed aliquots yielding a mean age of 31.2 ± 2.4 Ma (2σ), which agrees with the Durango AHe age of 31.13 ± 1.01 Ma reported by McDowell et al. (2005). The 2σ error on the AHe age calculation is ~8%, reflecting both sample heterogeneity and analytical procedure.

For apatite fission-track (AFT) analysis, 18 samples were prepared at the Geosciences Environnement Toulouse laboratory, but only 14 were finally analysed (fission-track counting). Over 100 detrital apatites (including all possible morphologies, colour, and sizes) compose a single aliquot of a sample mounted in resin epoxy, then polished to reveal internal surface and finally etched with 5 M HNO_3 for 20 s at 20 ± 0.5 ºC to reveal the spontaneous fission-tracks. Low-U muscovite sheets were attached over apatite sample mounts to be used as external detectors (according to the external detector method). The apatite sample mounts intercalated with CN5 glass dosimeters, and Fish Canyon and Durango standard samples were irradiated at the La Reina Nuclear Reactor (Santiago, Chile) with a nominal fluence of 1.10^{16} neutron/cm^2. After irradiation, external detectors of all samples and standards were etched for 40 min in 40% HF at 20 ± 0.5ºC to reveal the induced fission tracks. Fission track densities were measured at the Institut des Sciences de la Terre laboratory (ISTerre, Grenoble-France). Only crystals with polished surfaces parallel to the crystallographic c-axis were counted, using an Olympus BX51 optical microscope with a dry objective at 1250x magnification and a digitising table FTStage 4.04 system (Dumitru, 1993). Fission-track ages were calculated using the zeta-calibration method and the standard fission-track age equation (Hurford and Green, 1983).

The $\chi 2$ test and age dispersion (Galbraith and Green, 1990; Galbraith and Laslett, 1993; Galbraith, 2005) were used to assess the homogeneity of AFT ages. However, due to the high dispersion inherent to sedimentary samples, the central age was chosen as it represents the best measure of the spread in single grain ages. Furthermore, only the youngest peak ages or minimum ages (Brandon et al., 1998) were geologically significant. Due to the low-U content in apatites, horizontal confined track lengths are not abundant, but all those present in each apatite grain were measured to carry out a track length distribution analysis and thermal history reconstruction. Likewise, the D_{par} values (etch pit lengths parallel to the crystallographic c-axis) were measured in all samples and approximated the chemical composition of apatites (crucial parameter for track annealing). The radial plots representation of all AFT ages and computed central ages were conducted with RadialPlotter software (Vermeesch, 2009, 2012). Additionally, to explore plausible t-T trajectories and extract thermal histories consistent with our data, the software HeFTy (Ketcham, 2005) was used to conduct the inverse modelling.

IV-1.4 Structure of the Magallanes fold-thrust belt (53°20'S)

On the east coast of the Brunswick Peninsula (Fig. 3) the Magallanes fold-thrust belt can be subdivided into three morphotectonic domains (hinterland, internal and external) according to their mechanical stratigraphy, structural characteristics, style and age of deformation. In general terms, a hybrid (thick- and thin-skinned) fold-thrust belt is interpreted and a regional SW tilting of structures is also observed.

IV-1.4.1 Hinterland domain

The hinterland domain corresponds to a ~42 km wide segment located in the westernmost part of the fold-thrust belt with an NW-SE orientation and bounded to the east by the east verging San Nicolás thrust (Figs. 3 and 4). This domain comprises the oldest rocks of the region, including the Paleozoic metamorphic basement (northwest extension of the Cordillera Darwin metamorphic complex; Betka et al., 2015), Late Jurassic siliceous volcaniclastic rocks of the Tobífera Formation, the Late Jurassic-Early Cretaceous Rocas Verdes Basin remnants (Capitán Aracena-Carlos III ophiolite complex and post-rift Erezcano Formation) and the early Late Cretaceous foreland strata (Canal Bertrand and Latorre Formations). All these rocks present pervasive foliation and pressure dissolution structures (Farfán, 1994; Betka et al., 2015); particularly, the Canal Bertrand and Latorre formations share the same cleavage characteristics suggesting that deformation of both units corresponds to the same event (Betka et al., 2015). The westernmost part of the hinterland domain presents a thick-skinned style of deformation exhibiting basement thrust sheets with a top-to-the-northeast sense of tectonic transport (Betka et al., 2015) and forming monoclines dipping to the SW. Towards the eastern part of this domain, the basement (metamorphic and Tobífera) thrust over the sedimentary cover forming structural duplexes (Farfán, 1994; Betka et al., 2015). The décollement level is located in the contact between the Tobífera Formation and the metamorphic basement.

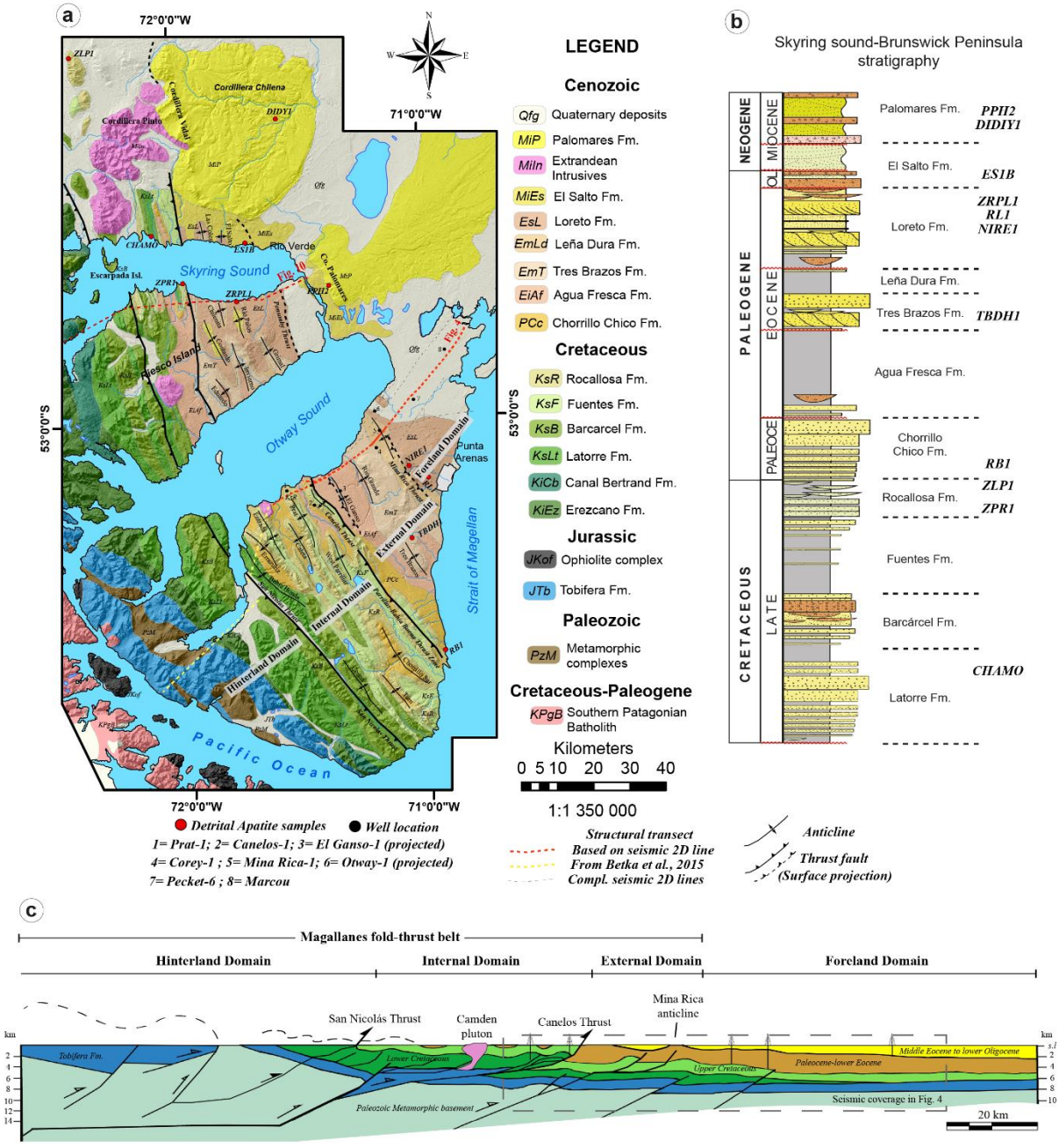

Figure 3. (a) Geological map and distribution of detrital apatite samples in the Skyring Sound-Brunswick Peninsula study area. (b) Stratigraphic position of detrital apatite samples. Note that higher stratigraphic thickness compared to CTN area (Fig. 2b). (c) Regional structural cross-section for the eastern coast of the Brunswick Peninsula.

IV-1.4.2 Internal domain

The internal domain corresponds to an NW-SE-orientated, ~30 km wide segment located in the central part of the fold-thrust belt between the San Nicolás thrust and the east verging Canelos thrust system (Figs. 3 and 4a). This domain comprises Late Cretaceous (Barcárcel, Fuentes and Rocallosa Formations) and Paleocene-early Eocene foreland strata

(Chorrillo Chico and lower Agua Fresca Formations). None of these rocks presents pervasive foliation but they are more intensely deformed westward. At shallow depths, this domain is characterised by a series of fault propagating folds (backlimb angles: 15-28°SW; forelimb angles: 42-61°NE) with a top-to-the-northeast motion and some imbricated thrusts (Fig. 4a). The folds wavelengths increase progressively northeast, passing from 3-4 km near the San Nicolás thrust up to 8-10 km near the Canelos thrust. At deeper depths is possible to interpret duplexes from imbricate thrusts and structural wedges in more ductile layers of the Erezcano-Canal Bertrand and Latorre Formations. The multilayer décollements (at deeper depths) have a roof thrust flat along which the shallower depths structures develop. This type of duplex-roof thrust flat geometry involving ductile rocks has been observed also in the field (Fig. 5). Most of the imbricated thrusts in the internal domain are rooted (shortcuts) in the San Nicolás thrust system (Fig. 3) which present a décollement level likely as depth as the top of the Erezcano Formation (Farfán, 1994). The shortcut structure corresponds to a low-angle ramp that transfers the deformation forward from the San Nicolás fault to the sedimentary cover. The duplex observed in the eastern part of the internal domain (towards the Canelos Fault system; Figs. 3 and 4a) seems to be related to the propagation of the deformation from basement-involved thrusts. This duplex constitutes the décollement level of the thrust sheets that affect the adjacent external domain.

IV-1.4.3 External domain

The external domain corresponds to an NW-SE-orientated, ~23 km wide segment located in the easternmost part of the fold-thrust belt between the Canelos fault system and the Mina Rica thrust (Figs. 3 and 4a). This domain comprises Paleogene strata exclusively, including the Chorrillo Chico, Agua Fresca, Tres Brazos, Leña Dura, Loreto and lower part of the El Salto Formations. It is characterised by a western sector moderately deformed (Fig. 3 and 4a) presenting fault propagation folds (with little surface expression) and imbricated thrust faults with a top-to-the-northeast tectonic transport; the eastern sector does not present significant deformation. The most important characteristic is the conformation of a frontal monocline dipping between 5-9 ° NE. The imbricated fault systems are rooted in the shallower décollement level of the duplex system of the adjacent internal domain (Fig. 4a). Some reactivated normal faults affect the basement in the deeper part of this domain (Fig. 4a).

IV-1.4.4 Timing of deformation and amount of shortening

The deformation in the Magallanes fold-thrust belt developed episodically, beginning with the hinterland domain and culminating in the external domain and proximal part of the foreland. Through the integration of provenance data, high precision U-Pb ages of strata involved in each folding, structural characteristics of each domain and the seismo-stratigraphic interpretation, the following deformation chronology can be interpreted.

The first deformation event concentrates in the hinterland domain, involving the deformation of the metamorphic basement and later developing duplexes in the ductile sedimentary cover and the Tobífera Formation (Betka et al., 2015). This first event is related to the closure of the Rocas Verdes extensional basin and the obduction of part of its components that generate sufficient tectonic load to allow the development of a foreland basin. Therefore, this event may have started around ~ 115 Ma, time of flexural subsidence and foreland sedimentation onset in this sector of the Magallanes-Austral basin (see Rivera et al., 2021 [Chapter III-2]). The deformation advances eastwards until it reaches a rigid block that acts as buttressing and that triggers the deformation of the ductile sedimentary cover of the Lower-mid Cretaceous that is observed in this hinterland domain. During this first event, significant crustal thickening occurs (by stacking duplexes) allowing the growth of the subcritical wedge and leading to exhuming the rocks that make up this domain. The amount of shortening is estimated as a minimum between ~15-32 km (Farfán, 1994; Betka et al., 2015). From the provenance data, it can be interpreted that this hinterland deformation event lasted to the Campanian-Maastrichtian, since foreland deposits of this age are composed of detritus derived from the metamorphic basement, the Tobífera formation, and mafic rocks of the Rocas Verdes Basin (McAtamney et al., 2011; Rivera et al., 2020, 2021 [Chapter III-2]).

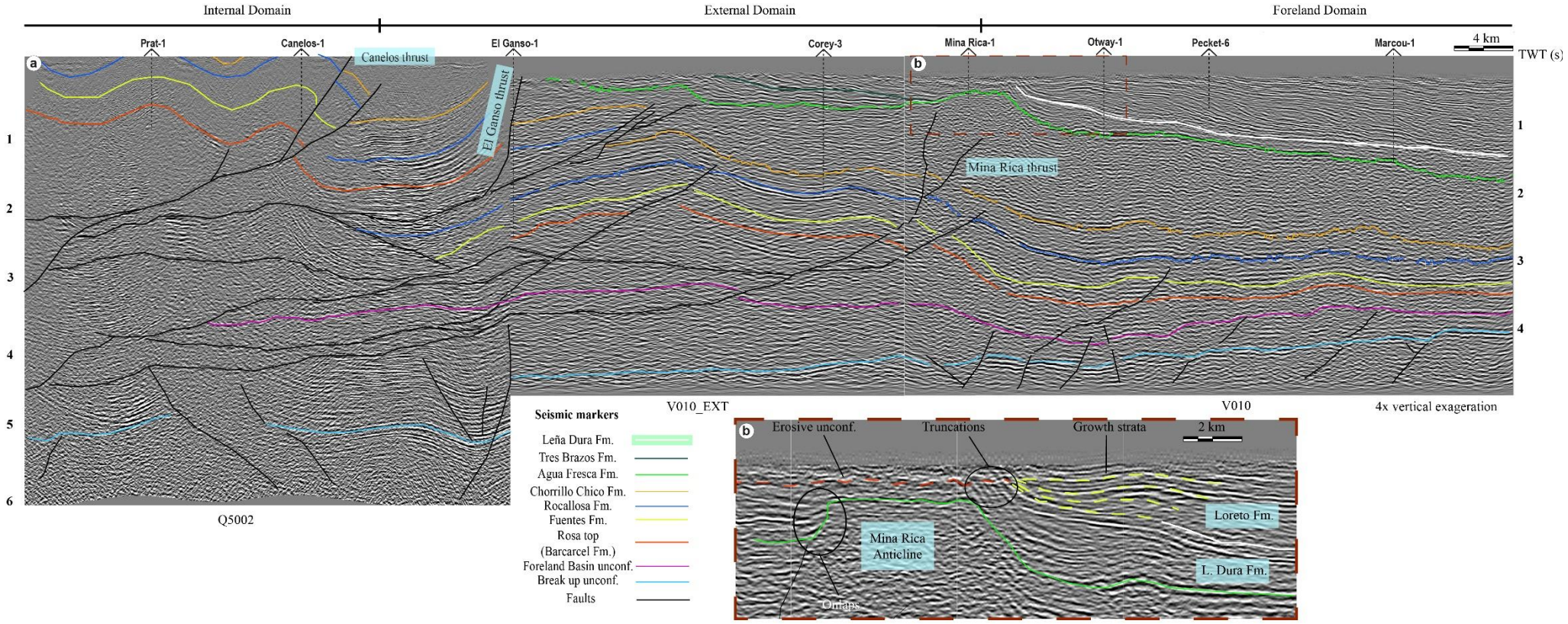

Figure 4. (a) Structural interpretation of the regional seismic profile of Fig. 3. Note structural duplex in the deepest part of the internal domain involving the Erezcano, Canal Bertrand and Latorre formations. (b) Structural and seismostratigraphic interpretation of the Mina Rica anticline, evidencing the syntectonic nature of the late Eocene Loreto Formation. Uninterpreted seismic lines at the end of this chapter.

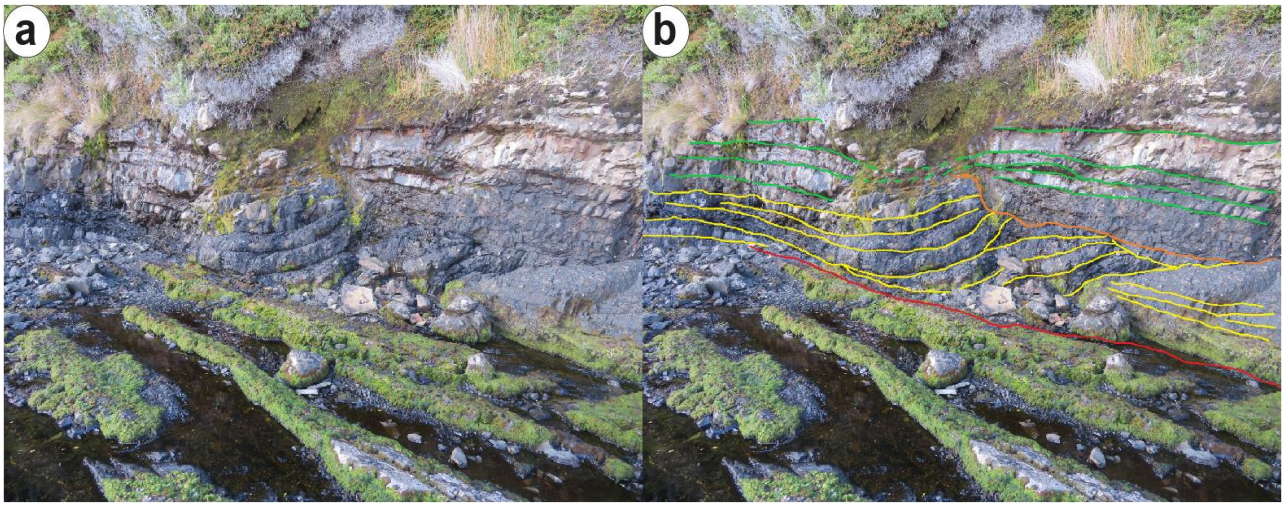

Figure 5. (a) Uninterpreted and (b) interpreted decametric example of an intraformational duplex-roof thrust flat structure in deep-water turbiditic deposits of the Latorre Formation.

The deformation in the internal domain could be started from Maastrichtian and lasted up to the early Eocene. During this second deformation event, accelerated flexural subsidence and eastward advance of the foreland basin occurs (Rivera et al., 2021 [Chapter III-2]). The latter suggests a similar advance of the deformation front from the San Nicolás fault (Fig. 3 and 4a) that gives rise to the development of the imbricated fan thrust system that characterises this internal domain (Fig. 4a). The deformation continues with the development of a basement structure that affects part of the previously developed structures and that allows the structuration of the frontal monocline (characterises the external domain) and duplexes of the lower to mid Cretaceous in the deepest part of the eastern sector of the internal domain. Provenance data suggest the cannibalization of early foreland deposits and mafic rocks of the Rocas Verdes Basin (Rivera et al., 2020, 2021 [Chapter III-2]). The line-length restoration technique used on the top marker of the Barcárcel Formation allowed us estimates 8.2 km of shortening (11.5%) for this internal domain.

The onset of the propagation of the deformation in the external domain is interpreted from the late Eocene. Although the El Ganso structure (Fig. 3 and 4a) dates from the Lower Eocene, the Río Grande and Mina Rica structures are developed after the sedimentation of the middle Eocene Tres Brazos Formation. Flattening the horizon top of the Agua Fresca Formation, deltaic clinoforms of the Tres Brazos Formation can be observed (without the presence of progressive unconformities) (Fig. 6), which are subsequently eroded during the generation of the Río Grande anticline and syntectonic

deposition of the Leña Dura Formation. In contrast, Fig. 4b shows an evident syn-tectonic nature (with progressive unconformities and growth strata) during the deposition of the deltaic clinoforms of the Loreto Formation. A punctual pulse of flexural subsidence is recorded around ~ 40 Ma in this sector of the basin (Rivera et al., 2021 [Chapter III-2]), which confirms this deformation event. This deformation event may have lasted until the middle Oligocene based on provenance data suggesting the erosion of previous foreland strata and the existence of a regional unconformity dating from the Lower Oligocene that separates the Loreto and El Salto Formations. The estimated amount of shortening for the external domain is 0.3 km (0.9%).

We did not observe compelling evidence of post-late Oligocene deformation. Some normal basement faults may have been reactivated during the Miocene, contributing to the eastward tilting of the frontal monocline and part of the foreland. The subsidence during the Miocene loses its flexural character, suggesting the cessation of compressive activity in this part of the Magallanes-Austral basin (Rivera et al., 2021 [Chapter III-2]).

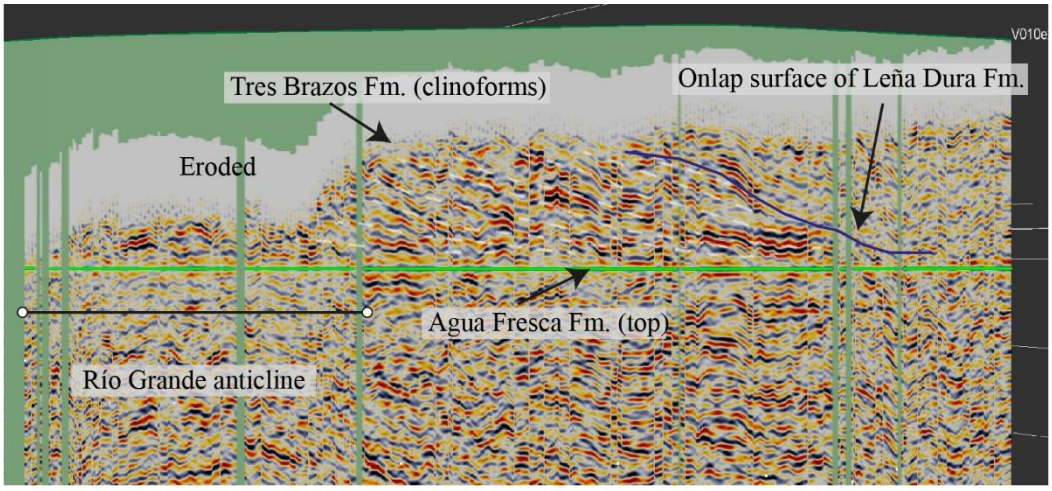

Figure 6. Flatted top of the Agua Fresca Formation on the Río Grande anticline (see Fig. 3a). Note prograding deltaic clinoforms of Tres Brazos Formation unaffected by the formation of the Río Grande structure. Instead, the growth of the Río Grande anticline erode the already deposited Tres Brazos Formation.

IV-1.5 Thermochronological analysis

Most of the detrital apatite samples (80%) are located in the external domain of the Magallanes fold-thrust belt and the remaining samples are in the internal domain

(Figs. 2a and 3a). Apatite fission tracks (AFT) and (U/Th)-He (AHe) cooling ages are presented in Tables 1 and 2, respectively. Further raw AFT data are presented in Annex D-1. A detailed description of the AHe results are found in Annex D-2.

IV-1.5.1 AFT and AHe results and interpretations

By comparing the AFT and AHe ages versus the stratigraphic depth of each sample (Fig. 7), is possible to observe that the Partial Annealing Zone (PAZ) and Partial Retention Zone (PRZ) are in almost the same depth in both study areas. Considering that the temperature windows for the AFT and AHe systems are ~120–60°C and ~80–40°C (e.g., Gallagher et al., 1998; Farley, 2002), respectively, then the geothermal gradient for the studied areas is ~40-43°C/km. A geothermal gradient higher than 30°C/km in the basin has been proposed by Enap geologists, who have presented an actual 35-55°C/km (mean=46°C/km) geothermal gradient for the basin in the framework of the "*First International Seminar of Distrital Energy and Geothermic in Magallanes*". The later geothermal gradient was based on Bottom Hole Temperature (BHT), Amerada RPG, and Drilling Test (DST) data.

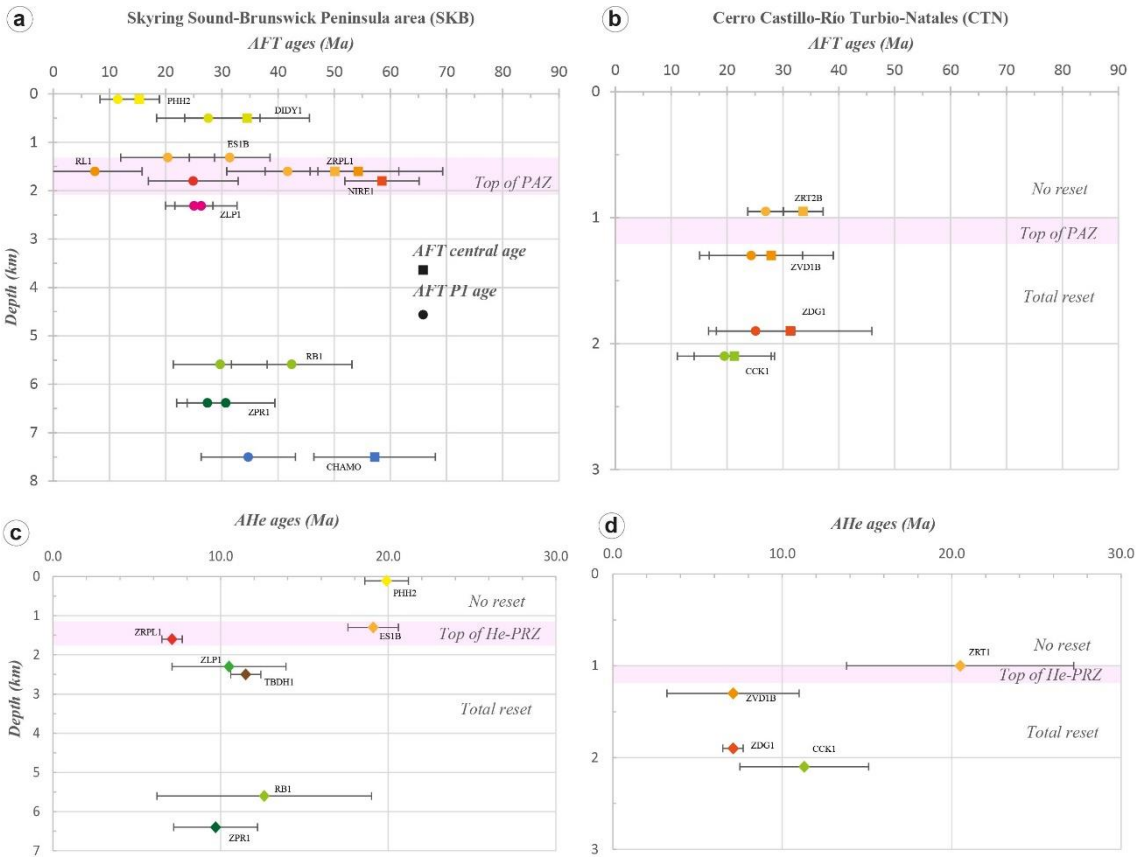

Figure 7. (*previous page* ←) Biplot of AFT and AHe ages versus stratigraphic depth for each study area. PAZ: Partial Annealing Zone; PRZ: Partial Retention Zone.

By comparing the AFT ages versus MDA is evident the complexity of samples (Fig. 8 and 9). Samples younger than the late Oligocene (25 Ma, Chattian) appear to be not experienced reset. In contrast, older samples than Chattian are partially to fully reset (Fig. 8 and 9).

Samples from the Palomares Formation (PPH2 and DIDY1; Fig. 8g), did not experience enough burial and their cooling ages are probably a provenance signal, given the similitude with U-Pb ages peaks (Fig. 8g). However, the central age of 15.3 Ma for the Palomares Formation may be interpreted as a depositional age. To date, this formation has not been dated in the Cerros Palomares sector, and a 15.3 Ma age for the upper levels of this unit is consistent with the interpreted ~15 Ma age for the top of the equivalent Santa Cruz Formation (Cuitiño et al., 2016). Therefore, the younger 11 Ma cooling age (Table 1; Fig. 8g) could reflect a post-depositional signal of exhumation.

The biplot of AFT ages versus maximum depositional ages for each studied sample (Fig. 10) allows us to observe a grouping of the youngest peak cooling ages around the Oligocene-Miocene boundary (26.6 ± 4 Ma). This youngest cooling peak occurs in most of the samples studied regardless of its morphostructural location within the fold-thrust belt or location in the basin. This age is interpreted as a process of regional exhumation of the whole foreland basin system.

Table 1. Synthesis of the AFT central and younger peak (P1) ages calculated from each sample based on RadialPlot and Binomfit software, depositional age (Maximum depositional age) based on detrital zircon U-Pb data.

Sample (#Grains)	Depositional age (Ma)	error (2σ)	Central AFT (Ma)	error (2σ)	P(χ^2)	Dispersion	P1 (Ma)	error (2σ)	U (ppm)	MDpar (µm)	Depth (km)
PHH2 (83)	15-11?	-	15.3	3.6	2	54	11.5	3.2	5	2.52	0.11
DIDY1 (20)	17.87	0.16	34.5	11.1	4	40	27.6	9.2	4	2.8	0.5
ZRT2B (20)	25.46	0.62	33.6	14.6	0	73.7	26.9	7	5	2.83	0.95
ES1B (21)	29.8	1.2	31.4	7.2	0	39.7	20.3	8.4	35	1.91	1.3
RL1 (35)	35.74	0.31	54.3	19.2	0	92.9	7.4	4	14	2.72	1.6
ZRPL1 (41)	36.6	1.8	50.1	6.6	0.3	21.1	41.7	8	11	2.86	1.6
ZVD1B (28)	37.39	0.73	27.9	8.4	0.5	51.3	24.3	6	5	1.98	1.3
NIRE1 (20)	37.9	1.3	58.5	11.2	0	34.3	24.9	18.3	20	2.34	1.8
ZDG1 (20)	42.75	0.77	31.3	6.6	16.3	21.5	25.1	7	12	2.69	1.9
RB1 (20)	64.7	0.67	42.5	10.8	0	42.4	29.7	8.4	9	3.09	5.6
CCK1 (21)	66.45	0.83	21.3	5.2	0	40.1	19.5	2.6	25	2.94	2.1
ZLP1 (20)	67.7	1.2	26.3	6.4	0	40.3	25	3.4	20	2.16	2.3
ZPR1 (20)	73.5	1.3	30.7	8.8	0	54.2	27.4	3.6	19	2.11	6.4
CHAMO (20)	82.1	1.3	57.2	12.6	0	34.5	34.7	9.8	10	2.72	7.5
STATS						**45.71 ± 19.16**			**13.85 ± 9.01**	**2.55 ± 0.38**	

Table 2. Synthesised AHe results for each sample. Aliquots in red and crossed out are excluded from the weighted mean age calculation by alpha implantation problems; depositional age (Maximum depositional age) based on detrital zircon U-Pb data.

Sample	Aliquot	Rs (µm)	weight (µg)	F_T	4He (ncc/g)	U (ppm)	Th (ppm)	eU (ppm)	Th/U (ppm)	Age (Ma)	Age c (Ma)	± 2σ	Weighted mean age (Ma ± 2σ)		Depositional Age (Ma ± 2σ)		Stratigraphic Depth (km)
PHH1-2	C	52	3.2	0.72	15567	4.3	19.9	9.1	4.6	14.3	19.9	1.6	19.9	1.30	16.5	1.50	0.11
	D	59	4.3	0.75	6302	1.9	8.9	4.1	4.6	13.0	17.3	1.4					
	E	54	3.2	0.73	10387	2.6	12.1	5.5	4.7	15.8	21.6	1.7					
	A	63	7.5	0.77	8657	2.4	9.6	4.7	4.1	15.5	20.3	1.6					
	B	62	5.3	0.76	11221	3.3	11.6	6.1	3.5	15.4	20.2	1.6					
	C	68	7.2	0.79	10468	2.8	11.0	5.4	4.0	16.2	20.6	1.7					
	E	37	1.9	0.64	9559	2.9	13.5	6.1	4.7	13.1	20.6	1.6					
ES1B	~~A~~	60	6.2	0.76	4890	1.1	6.0	2.5	5.4	16.1	21.3	1.7	19.1	1.50	29.8	1.20	1.30
	B	57	4.3	0.75	114406	21.8	44.9	32.6	2.1	29.2	38.8	3.1					
	C	50	0.3	0.72	35181	13.4	33.2	21.4	2.5	13.7	19.1	1.5					
	~~D~~	55	3.9	0.75	22051	3.8	7.2	5.6	1.9	32.8	43.9	3.5					
	E	63	5.8	0.77	165380	17.9	54.7	31.0	3.1	44.4	57.7	4.6					
ZRT1	A	30	0.9	0.53	4943	0.9	10.8	3.4	12.6	12.0	22.7	1.8	20.5	6.70	25.5	0.62	1.00
	~~D~~	46	2.4	0.69	5527	1.0	4.7	2.2	4.5	21.3	31.0	2.5					
	E	39	1.7	0.63	4114	0.7	9.4	3.0	13.0	11.5	18.3	1.5					
ZPRL1	A	65	7.5	0.78	81455	15.0	34.2	23.2	2.3	29.2	37.4	3.0	7.1	0.60	36.6	1.80	1.60
	B	65	6.9	0.78	3366	2.5	11.1	5.1	4.5	5.5	7.1	0.6					
	C	57	5.5	0.75	7610	3.0	10.4	5.5	3.4	11.5	15.4	1.2					
ZVD1B	A	46	2.5	0.70	4091	4.8	15.9	8.6	3.3	4.0	5.8	0.5	7.1	3.90	37.4	0.73	1.30
	B	50	2.9	0.75	5428	4.3	22.0	9.6	5.1	4.7	6.3	0.5					
	~~C~~	57	4.9	0.75	3906	1.8	7.2	3.6	3.9	9.2	12.3	1.0					
	~~D~~	58	5.3	0.75	3562	1.2	5.3	2.5	4.5	12.1	16.2	1.3					
	E	57	4.6	0.75	3493	2.0	8.6	4.0	4.3	7.2	9.6	0.8					

ZDG1	~~B~~	47	2.9	0.71	25633	11.4	16.5	15.4	1.4	13.8	19.5	1.6	7.1	0.60	42.8	0.77	1.90
	E	38	1.3	0.65	22091	26.4	55.0	39.6	2.1	4.6	7.1	0.6					
TBD-H1	~~B~~	40	1.9	0.67	5985	2.2	10.3	4.7	4.6	10.6	15.8	1.3	11.5	0.90	43.0	1.00	2.50
	C	39	1.5	0.64	6761	3.4	18.0	7.7	5.3	7.3	11.5	0.9					
RB1	A	68	7.8	0.79	20859	9.5	11.8	12.4	1.2	14.0	17.7	1.4	12.6	6.40	64.7	0.67	5.60
	B	52	3.4	0.72	41130	16.8	58.7	30.9	3.5	11.1	15.3	1.2					
	C	90	4.5	0.84	8629	17.0	20.5	21.9	1.2	3.3	3.9	0.3					
	D	52	3.2	0.73	25253	12.5	36.0	21.2	2.9	9.9	13.7	1.1					
	~~E~~	42	1.7	0.66	11517	4.0	15.8	7.8	4.0	12.4	18.8	1.5					
CCK1	A	64	6.4	0.77	76548	34.3	109.0	60.4	3.2	10.5	13.6	1.1	11.3	3.80	66.5	0.83	2.10
	B	58	5.2	0.76	71332	51.7	48.0	63.2	0.9	9.4	12.3	1.0					
	E	57	4.2	0.76	19385	23.5	10.2	26.0	0.4	6.2	8.1	0.7					
ZLP1	A	71	9.6	0.80	12090	6.7	13.8	10.1	2.0	10.0	12.5	1.0	10.5	3.40	67.7	1.20	2.30
	B	69	8.5	0.79	36708	23.8	46.6	35.0	2.0	8.7	11.0	0.9					
	C	60	5.4	0.79	51438	37.4	19.5	42.0	0.5	10.1	12.7	1.0					
	~~D~~	72	9.0	0.80	5768	1.6	6.9	3.3	4.2	14.6	18.3	1.5					
	E	68	7.2	0.79	5345	4.6	20.8	9.6	4.5	4.6	5.9	0.5					
ZPR1	A	61	5.4	0.76	11468	4.2	20.2	9.0	4.8	10.6	14.0	1.1	9.7	2.50	73.5	1.30	6.40
	B	70	7.6	0.79	8540	5.4	15.8	9.2	2.9	7.7	9.7	0.8					
	C	83	13.1	0.82	6790	4.0	12.4	7.0	3.1	8.1	9.8	0.8					
	D	60	5.1	0.77	17805	26.8	15.5	30.5	0.6	4.8	6.2	0.5					
	E	76	9.3	0.81	14395	11.1	23.0	16.6	2.1	7.2	8.9	0.7					

(U-Th)/He ages were performed by laser heating for He extraction and ICP-MS for U-Th determinations at Géoscience Montpellier, France. The estimated analytical uncertainty for He ages is about 8% (2σ). eU is the effective uranium = U + 0.243Th.

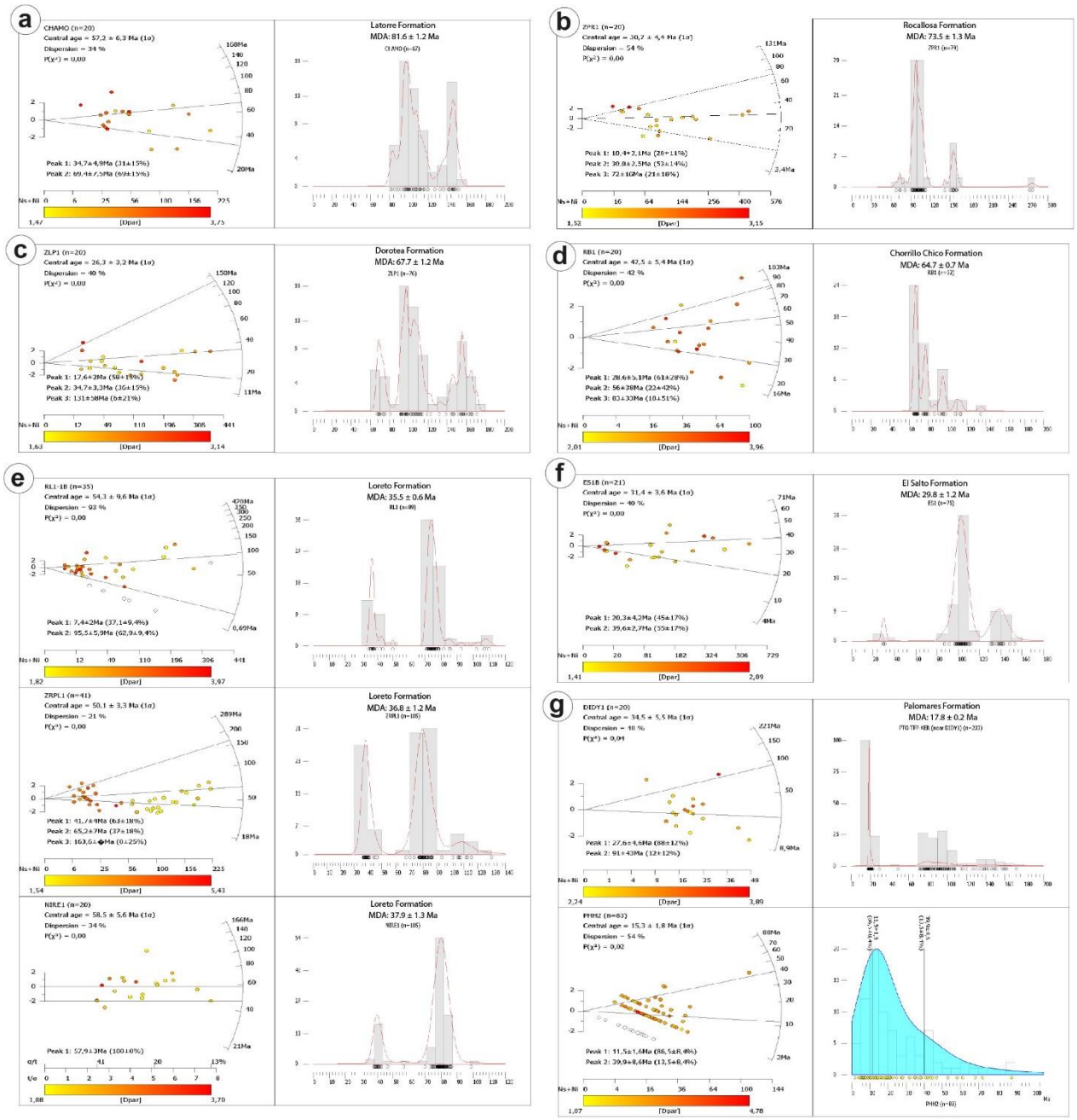

Fig. 8. Composite of AFT ages and detrital zircon U-Pb ages of the studied samples grouped by Formations, outcropping in the Skyring Sound-Brunswick Peninsula area (see Fig. 3a). (a) Latorre Formation. (b) Rocallosa Formation. (c) Dorotea Formation in the northernmost part of the SKB study area. (d) Chorrillo Chico Formation. (e) Loreto Formation; 2σ uncertainty interval for the NIRE1 sample. (f) El Salto Formation. (g) Palomares Formation, including kernel density plot of the cooling ages which are interpreted as provenance signal.

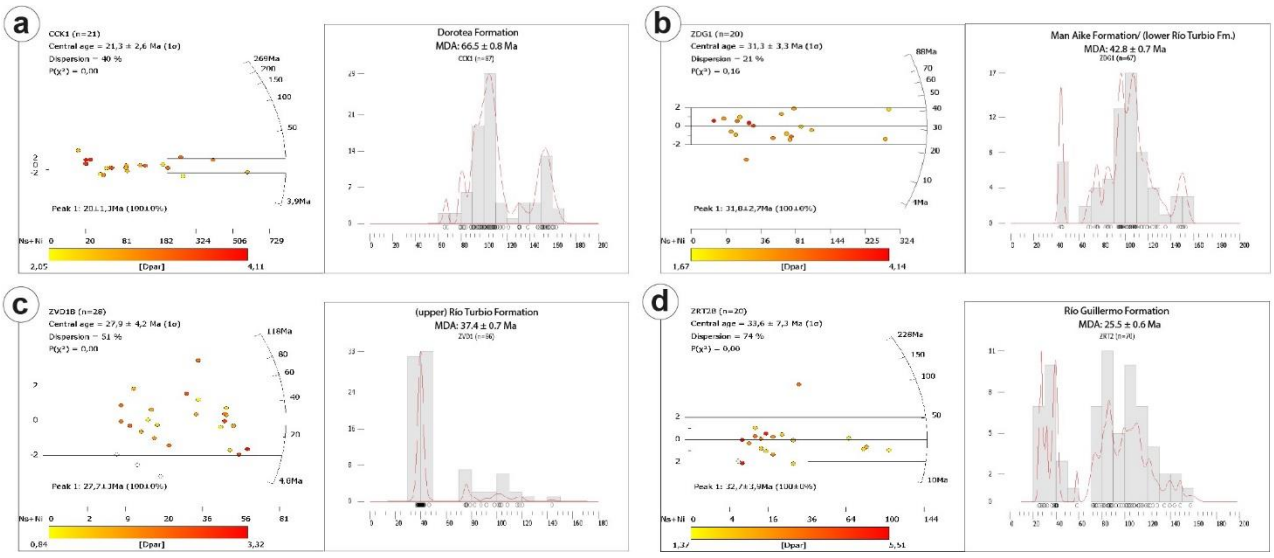

Fig. 9. Composite of AFT ages and detrital zircon U-Pb ages of the studied samples grouped by Formations, outcropping in the Cerro Castillo-Río Turbio-Natales area (see Fig. 2a). (a) Dorotea Formation. (b) Man Aike Formation (equivalent to the lower part of the Río Turbio Formation; see Chapter II-1). (c) Río Turbio Formation. (d) Río GuillermoFormation.

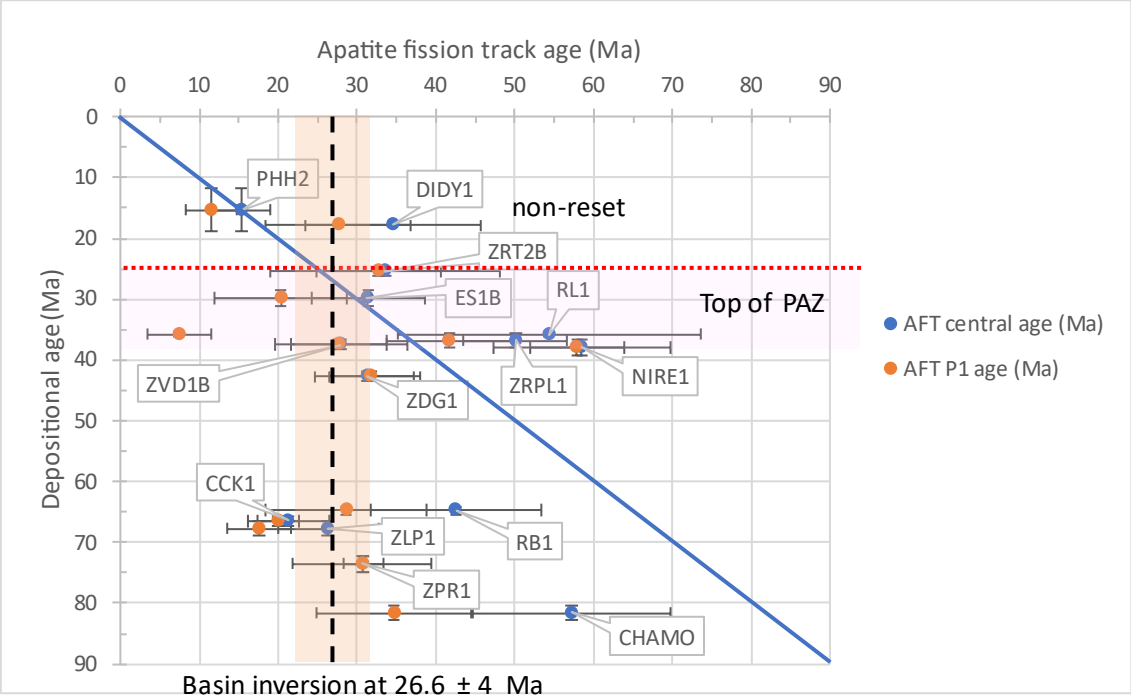

Figure 10. Biplot of AFT ages versus Depositional ages from studied samples. The blue line represents similar AFT and MDA (ratio 1:1).

Regarding the AHe ages (Table 2), again the samples PHH1-2 belonging to the Palomares Formation (~18-15.3 Ma) are the only ones not reset. Additionally, samples ES1, ZRT1, and ZRPL1 (encompassing from ~25-36 Ma) have reached a burial/temperature enough to partially reset and represent the exhumed or fossil He-PRZ in the study areas (Fig. 7). In contrast, all the remaining samples older than ~37 Ma record a total reset, which is

explained by post-depositional burial reaching the PRZ between 40-120°C at 1-3 km depth (according to the slighter elevated geothermal gradient of the basin). In general, there is not a strong correlation between AHe ages and effective uranium (eU; mean R^2 of 0.42) and only 30% of samples present show a mild correlation between Rs (radius of crystal = grain size) and AHe ages (50% is a weak correlation). This fact suggests that variations in He retention, grain composition and size do not significantly influence thermochronologic results and we can confidently interpret the presence or absence of PRZ in the data. However, some apatite crystals present alpha implantation issues, exhibiting older AHe cooling ages than their depositional ages for low eU content (Fig. 11) and a strong positive or negative correlation between AHe ages and eU. The latter suggests some impact of radiation levels probably related to long-residing times of apatites in the partial retention zone (Flowers et al., 2009; Fox and Shuster 2014; Gautheron et al., 2009; Willett et al., 2017) and implying choosing an appropriate model to model their thermal histories. Additional details on AHe analyses are provided in Annex D-2.

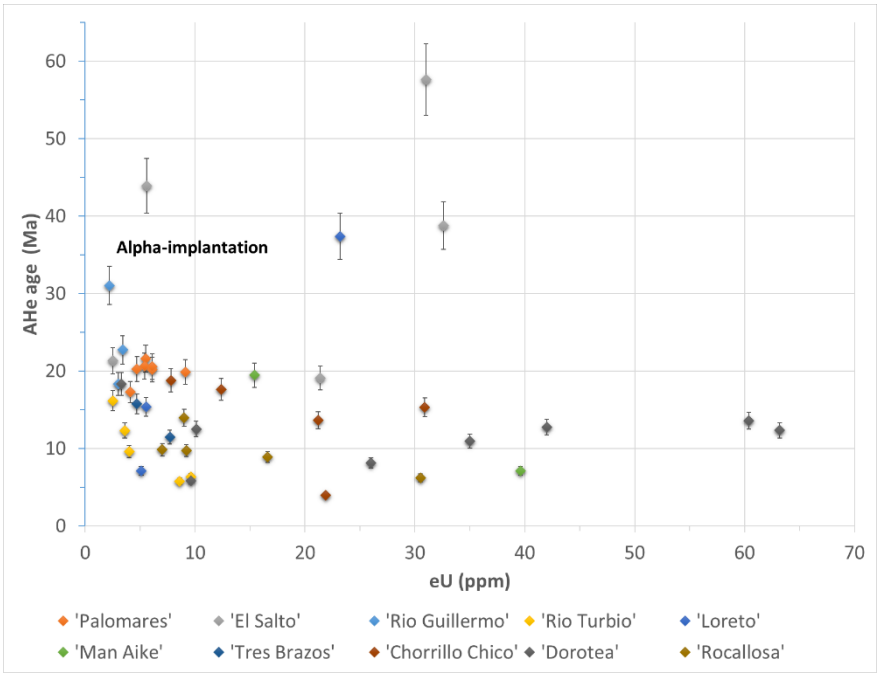

Figure 11. AHe ages versus effective Uranium (eU) content biplot grouping by formations, showing a probable alpha implantation phenomenon for apatite crystals with old ages and low eU content.

Assuming that the AHe weighted mean ages represent the most recent cooling/exhumation signal, it is possible to anticipate two possible exhumation events in the study areas based on AHe data, at 9.5 ± 2.5 Ma and 20 ± 1 Ma (Fig. 12). However, by integrating all the thermochronological data (AFT and AHe), the two basin inversion events are constrained at 8.1 ± 1.3 Ma and 26.4 ± 3.7 Ma (Fig. 13).

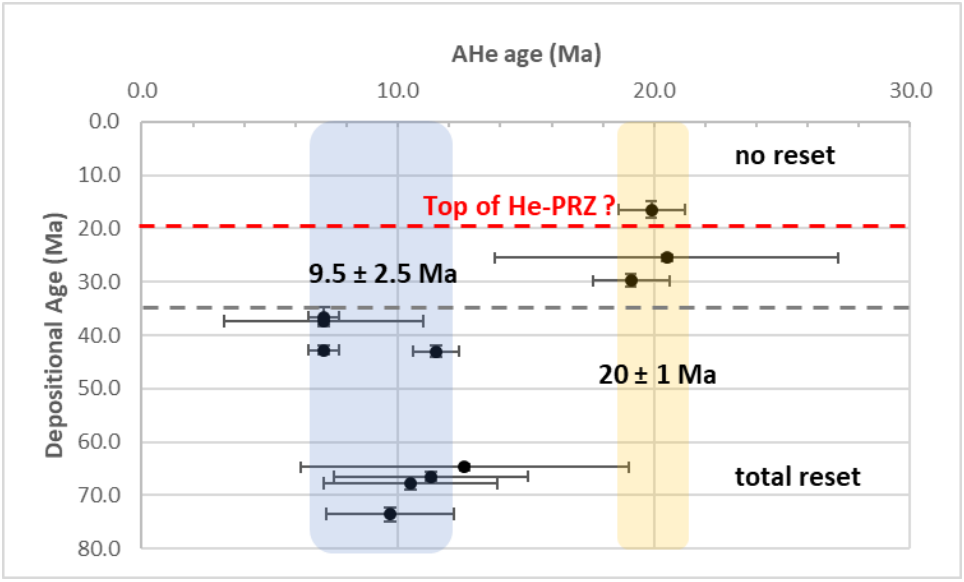

Figure 12. Biplot of AHe ages versus maximum depositional ages from studied samples. Note the two distinct basin exhumation signals.

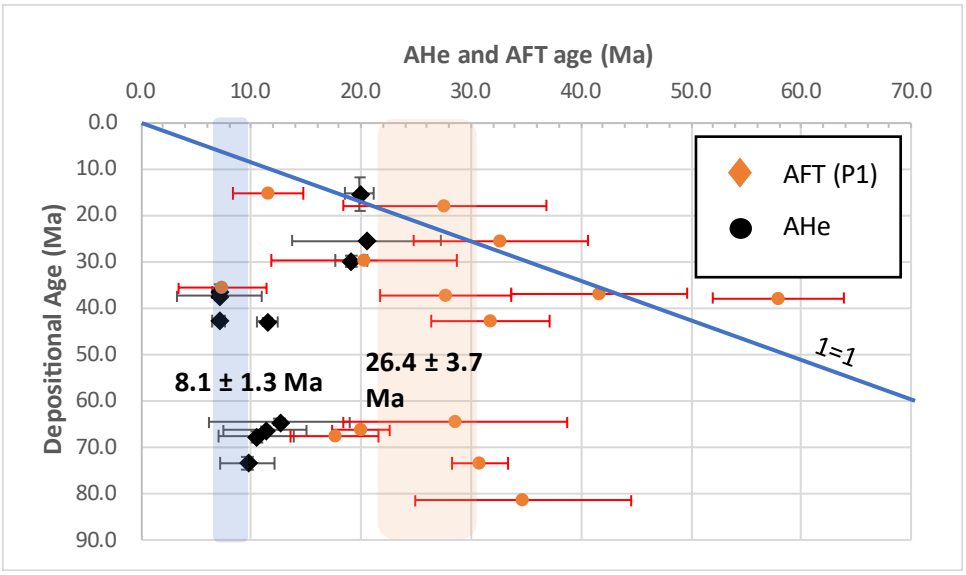

Figure 13. Composite biplot of AFT and AHe ages versus depositional ages from studied samples. The blue line represents similar cooling and depositional ages (ratio 1:1).

IV-1.5.2 Thermal modelling

To gain insights on the thermal history of the Magallanes basin and fold-thrust belt, we conduct a thermal inverse modelling of the AFT and AHe ages, confined lengths, and Dpar data. For the inverse modelling in HeFTy (Ketcham, 2005), incorporating alpha recoil damage and annealing on the He-diffusion kinetics model of Flowers et al. (2009). The inverse modelling results are presented by structural domains (Fig. 14) and they are the best results obtained for all samples based on >100.000 runs per sample (Table 2).

IV-1.5.2a Internal domain

The modelling of the CHAMO sample from the Latorre Formation (early foreland deep-marine turbiditic deposit) located in the central-western part of the internal domain (Fig. 3a) shows a rapid burial (reaching ~ 3 km depth) followed by a short time of residence in the PAZ between 75-64 Ma. Subsequently, rapid cooling started at 65 Ma and lasted 41 Ma. A later protracted exhumation from 40 Ma and up to ~ 22 Ma. From the Burdigalian (~ 20 Ma) the rate of exhumation accelerates and reaches an even higher velocity at 8 Ma (Fig. 14a). The ZPR1 sample, from the shallow water Rocallosa Formation, located to the eastward extreme of the internal domain (Fig. 3a), portrays a similar pattern with a rapid exhumation between 64-48 Ma followed by a more slow cooling rate between 48-12 Ma (Fig. 14b). At ~10 Ma the exhumation rate is abruptly accelerated (Fig. 14b).

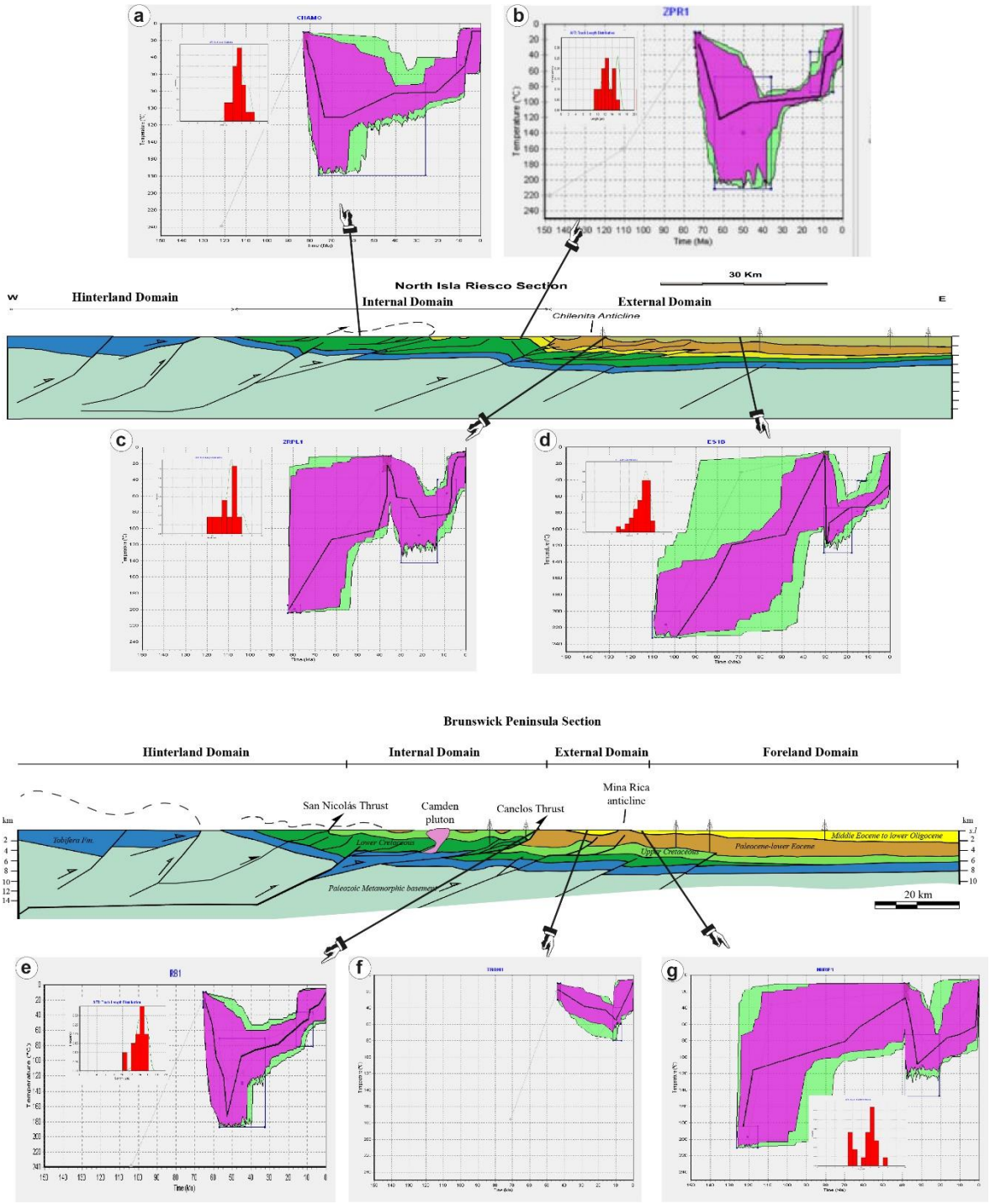

Fig. 14. Results of the inverse thermal modelling in each morphostructural domain of the Magallanes fold-thrust belt. (a) Latorre Formation and (b) Rocallosa Formation in the internal domain. (c, g) Loreto, (e) Chorrillo Chico, (f) Tres Brazos and (d) El Salto formations in the external domain.

IV-1.5.2a External domain

The samples RB1 from the deep-water turbiditic deposits of the Chorrillo Chico Formation is more proximal to the internal domain. The modelling of this sample shows a similar pattern that those samples from the adjacent internal domain. The pattern consists of

a rapid early Paleogene cooling rate (between 55-48 Ma), followed by a more slow exhumation during the middle Eocene to late Oligocene (48-25 Ma) and a renewed rapid cooling rate from the late Oligocene which is intensified around 10 Ma (Fig. 14e). Advancing eastward in the external domain, the burial is shallower reaching depths around 1.5-2 km (samples ZRPL1 and TBDH1) and from 10 Ma an accelerated exhumation is recorded (Figs. 14c, f), after a slow burial of deposits. In the easternmost part, the modelled samples of the El Salto and Loreto Formations, present a rapid and deep burial (~2.5-3 km) after their deposition, followed by a very rapid exhumation period between 30-32 Ma (Fig. 14d, g). A new exhumation period is recorded between 12 Ma (Fig. 14d) and 2.5 Ma (Fig. 14g) in samples ES1B and NIRE1, respectively.

IV-1.5 Discussion and conclusions

From the integration of thermochronological and structural results, together with provenance information presented in previous chapters, a progression towards the east of the deformation and exhumation can be observed. The first period of compression and exhumation of the internal part of the orogen (hinterland and internal domains) occurs from at least the Cenomanian-Albian (~115 Ma). The deep-water sedimentation of the Latorre-Barcárcel Formations records the contribution of sediments from an exhumed metamorphic basement (Cordillera Darwin complex and Tobífera Fm) further west, which leads to a flexural tectonic load allowing all the available accommodation present during this time interval. The deformation continues to advance towards the east (internal domain), through the development of a thin skin deformation (imbricated fan thrust system) concomitant with the development of basement duplexes in the hinterland. In this way, previously deposited deposits are subjected to contractional exhumation by the Campanian (~ 75 Ma).

The deformation and exhumation progressively continue to move towards the external domain of the fold-thrust belt during ~ 65-45 Ma. This exhumation coincides with accelerated subsidence in the foredeep and lateral displacement of the depocenter (Rivera et al. al., 2021 [Chapter III-2]), replicating the lateral advance of the deformation front. The exhumation rate is much more rapid compared to the previous period, based simply on the slope of the T-t curve (Fig. 14). During the middle to late Eocene (~ 45-33 Ma), although it is possible to observe cooling, it manifests itself much more slowly (Fig. 14) and the exhumation is not only concentrated in the external domain since provenance data suggest exhumation of hinterland terranes during deposition of the middle Eocene Tres Brazos

Formation (Rivera et al. al., 2021 [Chapter III-2]). Between 35-30 Ma there is a new accelerated cooling period in the eastern part of the external domain (Fig. 14), which coincides with the easternmost advance of the deformation front (Fig. 4a).

During much of the Miocene (~20-10 Ma), a rapid exhumation is concentrated towards the innermost parts of the fold-thrust belt and a much slowly cooling towards the east at the limit between the external domain and the undeformed foreland. Similar conclusions are suggested by Fosdick et al. (2013) for the northern CTN study area. This pattern of exhumation coincides with the cessation of the advance of the deformation front and ends of the foreland basin stage observed during the Miocene in our study areas (Rivera et al. al., 2021 [Chapter III-2]). Alternatively, we can speculate that the deformation was mostly concentrated in the hinterland, however, we cannot confirm this hypothesis based on our structural data. From the late Miocene (~ 10 Ma), the fastest exhumation recorded in thermal modelling is observed and is manifested simultaneously throughout the entire fold-thrust belt and foreland basin (e.g., Thomson et al., 2001, 2010; Fosdick et al., 2013), which can be linked to fluvioglacial erosive processes.

Our observations and results of the thermal modelling suggest periods of rapid exhumation (~80-70 Ma and ~65-45 Ma), concentred in specific sectors of the fold-thrust belt, interrupted by periods of slower exhumation (~45-33 Ma and ~ 20-10 Ma) more generalised over the entire orogenic wedge (Fig. 14). The former is interpreted as rock-uplift caused by crustal shortening, whereas the latter we interpret as rock-uplift linked to periods of tectonic quiescence. Thermochronological data in the Cordillera Darwin (i.e., hinterland domain), in Tierra del Fuego, show a period of rapid exhumation between 90-70 Ma (Nelson, 1982; Kohn, 1995), coinciding with our observations. This rapid cooling period is interpreted as linked to and lithosphere thickening and crustal shortening leading to the total closure of the extensional Rocas Verdes Basin (Kohn, 1995; Klepeis et al., 2010; Betka et al., 2015). However, cannot be ruled out the possibility that part of this exhumation is due to the isostatic rebound caused by the detachment of the south-southwestward subducted oceanic crust of the Rocas Verdes Basin as originally proposed by Cunningham (1994) and later by Klepeis et al. (2010) and Mpodozis et al. (2011). An isostatic rebound may be an effective mechanism to explain the reduced flexural subsidence observed between the Campanian-Maastrichtian in the foreland basin (Rivera et al., 2021 [Chapter III-2]). On the other hand, the ~50-45 Ma contractional-linked period of rapid exhumation in the Cordillera Darwin (Gombosi et al., 2009), overlap with our shortening-derived and tectonic quiescence-linked

stages of exhumation. We challenge this rock-uplift exhumation linked exclusively to cortical shortening, and rather we suggest that the tectonic quiescence plays an essential role. We are supported on sedimentological, sedimentary provenance, subsidence and structural data, which together suggest a phase of unroofing of the entire orogenic wedge simultaneously with a reduction in flexural subsidence and a shallowing depositional system, reduction of eastward migration of the foredeep and paucity in deformation in our study areas. Similar conclusions have been presented for middle to late Eocene strata in Tierra del Fuego (e.g., Torres Carbonell and Olivero, 2019). Furthermore, between 49-45 Ma there is a marked decrease in the convergence rates between the Aluk and South American plates, at the same time that the subduction of the Farallon-Aluk ridge (Phoenix) migrates southwards (Cande and Leslie et al., 1986; Eagles and Scott, 2014).

For the northernmost part of the Southern Patagonian Andes (44-50°S; Fig. 1), Thomson et al. (2001), based on AFT results, show a concentred denudation of the forearc region of the Patagonian Andes by ~30-23 Ma, followed by an eastward migration of denudation and cooling until 12-8 Ma. They relate this exhumation with coeval retroarc deformation and subduction erosion. In the northern study area (CTN; Fig. 2a), Fosdick et al. (2013) propose a similar retroarc deformation mechanism to explain exhumation observed in the hinterland and internal parts of the fold-thrust belt between 22-18 Ma. However, although our thermochronological data record this exhumation episode from the early Miocene, the cessation of flexural subsidence (replaced by dynamic subsidence concentrated towards the forebulge see Rivera et al., 2021) and little to no deformation observed during this time prevent a link between denudation and shortening. Instead, we propose that this exhumation represents a basin inversion and abandonment phase during the cessation of compression as a consequence of the dynamic uplift of the lithosphere due to the subduction of the Chilean ridge, similar to the model proposed by Guillaume et al. (2009) for the central part of Patagonia (49°S) during the subduction of the Chilean ridge at ~ 7 Ma at that latitude.

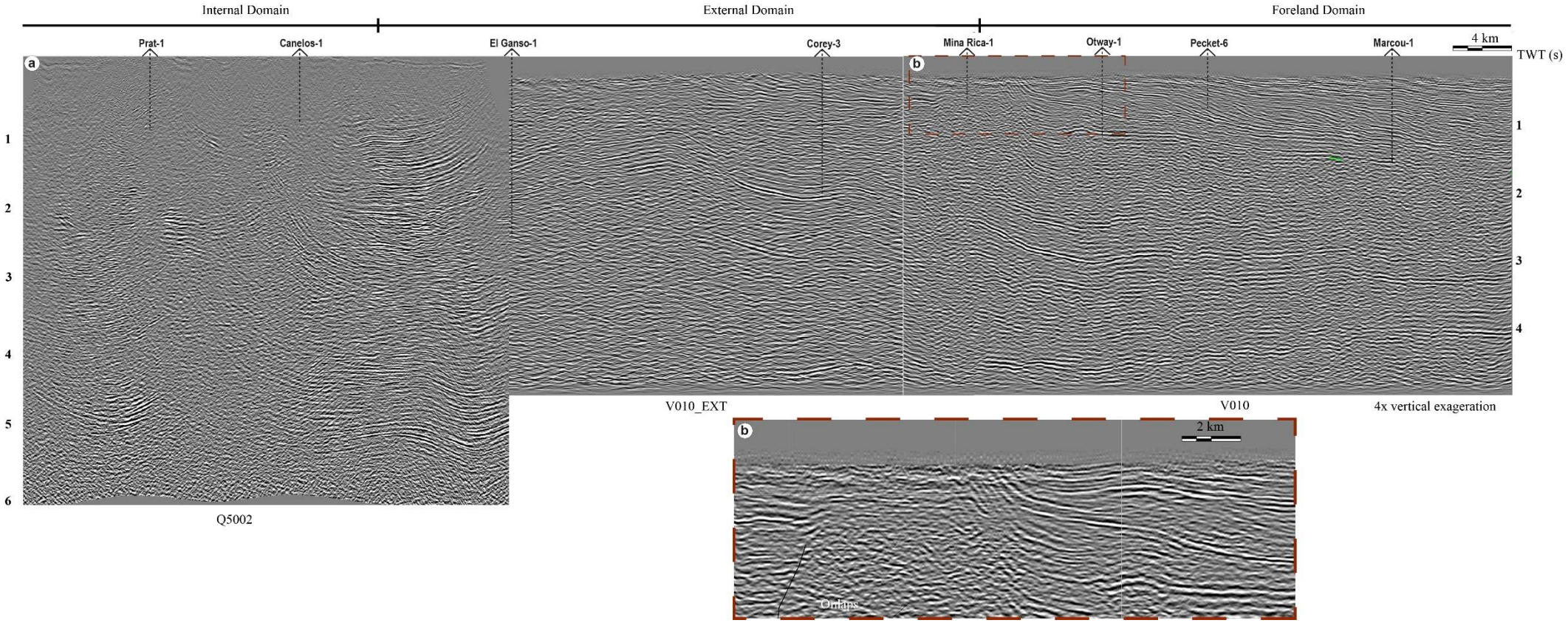
Internal Domain
External Domain
Foreland Domain
Prat-1
Canelos-1
El Ganso-1
Corey-3
Mina Rica-1
Otway-1
Pecket-6
Marcou-1
4 km
TWT (s)
a
b
1
2
3
4
5
6
Q5002
V010_EXT
V010
4x vertical exageration
2 km
Onlaps

FIFTH PART

DISCUSSION AND CONCLUSIONS

CHAPTER V-1:

HYPOTHETICAL MODEL FOR THE SOUTHERN PATAGONIAN ANDES BUILDING AND MAIN FINDINGS

Chapter V-1 is devoted to discussing the multiple hypotheses that attempt to explain the Southern Patagonian Andes building. Subsequently, the conclusion of this thesis and the resposes to the main research questions are exposed.

1) How and to what extent does the inherited crustal architecture of the predecessor Rocas Verdes Basin control the sedimentary system evolution and dispersal of sediments during the Late Cretaceous-early Miocene?

2) How and to what degree does the Cenozoic geodynamic events (subduction of active ridges, opening of Drake Passage) impact the development and evolution of an Andean-type orogen-foreland basin pair?

3) What is the nature of the whole Southern Patagonian Andean growth (including sediment accumulation history) in terms of steady or punctuated episodic behaviour?

V-1.1 Hypothesis for the Southern Patagonian Andes building

Throughout the history of the Southern Patagonian Andes (Fig. 1), three collisions of spreading ridges (two during the Cenozoic and another in the Cretaceous), periods of tectonic erosion, and possible subduction flat-slab events have interacted with the continental margin. Moreover, the opening of the oceanic Drake Passage (i.e., the opening of the Scotia Sea) between the Antarctic Peninsula and South America (Livermore et al., 2000, 2005; Barker, 2001; Lawver and Gahagan, 2003; Eagles et al., 2005, 2006; Lagabrielle et al., 2009) and the overall Cenozoic re-organisation of the tectonic plates setting and kinematic (Cande and Leslie, 1986; Somoza and Ghidella, 2005, 2012; Eagles et al., 2009; Breitsprecher and Thorkelson, 2009; Eagles and Scott, 2014), indeed positions this Andean segment as one of the most complexes of all the Cordilleran system. However, the geodynamic context in which the Patagonian Andes evolved still is a matter of debate, as some authors favour the idea of spreading ridge collisions as the leading cause of uplift. In contrast, other points of view ascribe the orogenic cycle to plate tectonic parameters such as increasing subduction velocity, obliquity of convergence and wrench tectonics, or even to the angle of slab subduction.

V-1.1.1 Spreading ridge collision

By 80 Ma, the first spreading ridge collision against the Patagonian margin (~49°S) is hypothesised. However, evidence is not well established (Ramos et al., 1982; Ramos, 2005). In contrast, several data sources allow constraining the Eocene Farallon-Aluk (Phoenix) and the mid-Miocene Chile ridge collisions (Cande and Leslie, 1986; Somoza and Ghidella, 2005, 2012; Ramos, 2005; Breitsprecher and Thorkelson, 2009; Eagles and Scott, 2014; Müller et al., 2016; Gianni et al., 2018b). Despite complications to accurately determinate the configuration of the Farallon-Aluk (Phoenix) plate boundary, different plate tectonic reconstructions are coincident in showing a northeast orientation for the Farallon-Aluk (Phoenix) ridge and southward migration of the triple junction through time (Fig. 1; Cande and Leslie, 1986; Somoza and Ghidella, 2012; Eagles and Scott, 2014; Eagles and Jokat, 2014; Müller et al., 2016; Gianni et al., 2018b). On the other hand, the Miocene plate reconstructions are better accurate (Cande and Leslie, 1986; Breitsprecher and Thorkelson, 2009) allowing known the kinematics of the Nazca-Antarctic-Aluk (Phoenix) triple junction and later Chile ride-trench interaction, which collides against Tierra del Fuego by ~20-19 Ma and subsequently migrates northwards (Fig. 2).

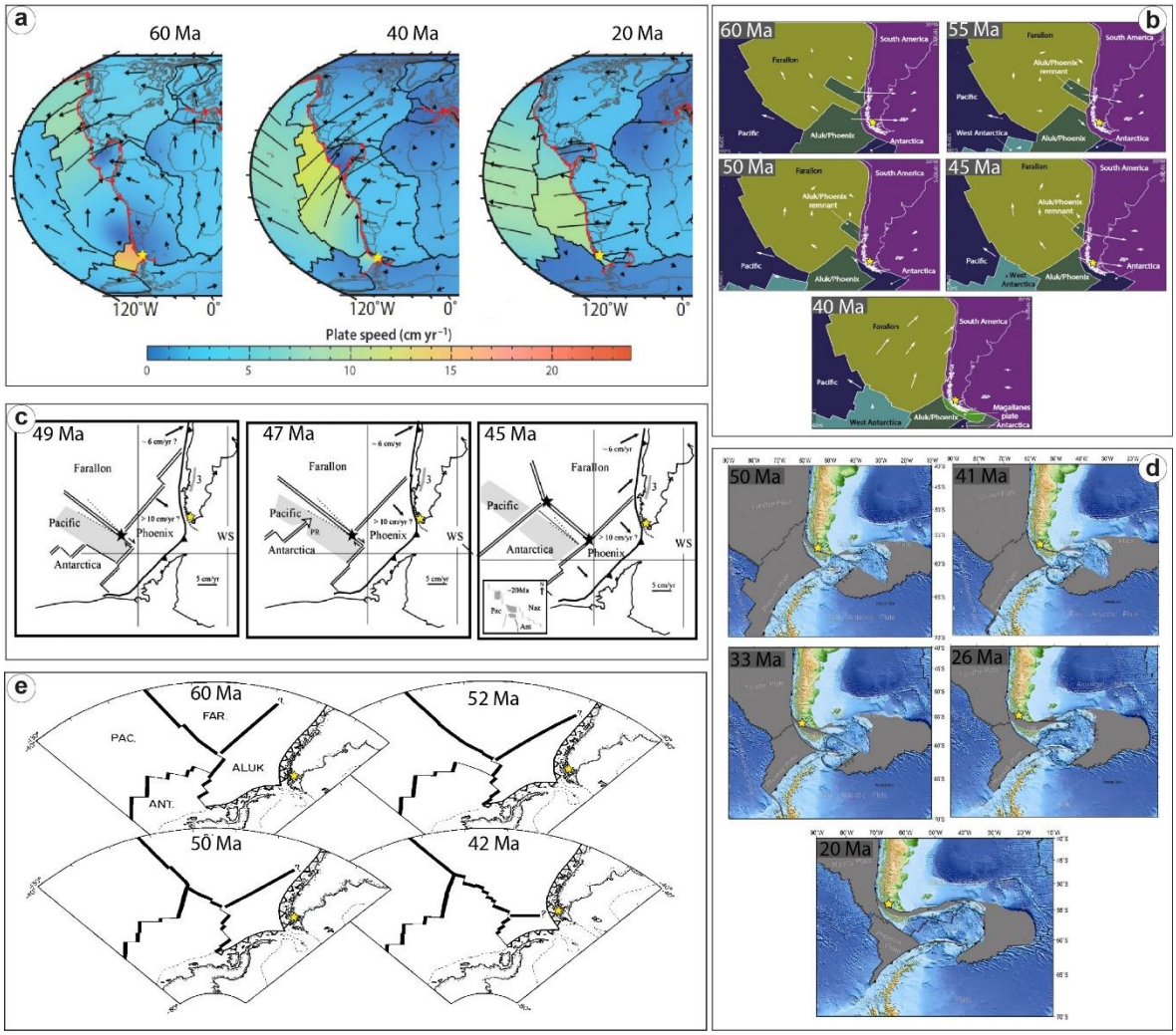

Figure 1. Summary of different Cenozoic plate kinematic reconstructions, showing agreement in the southward migration of the Farallon-Aluk ridge (Phoenix) but disagreement in its migration velocity and exact position through time. (a) Plate reconstruction taken and modified from Müller et al. (2016). (b) Gianni et al. (2018b). (c) Somoza and Ghidella (2012). (d) Eagles and Jokat (2014). (e) Cande and Leslie (1987). Yellow stars signal the approximate position of the thesis study area.

The causal relationship between spreading ridge collisions and pulses of Patagonian Andes uplift and foreland deformation has been proposed by several authors (Ramos, 1989; Forsythe and Prior, 1992; Ramos and Kay, 1992; Flint et al., 1994; Folguera and Ramos, 2002; Lagabrielle et al., 2004; Ramos, 2005; Ghiglione et al., 2016a; Stevens Goddard and Fosdick, 2019). The uplift mechanism rather than thermally driven is thought of as crustal stacking represented by basement shortening and uplift of the inner part of the Patagonian Andes (Ramos, 2005; Ramos and Ghiglione, 2008; Stevens Goddard and Fosdick, 2019). This uplift is mainly concentrated in the fold and thrust belt, absorbed by the sedimentary cover and triggers an eastward shift in the locus of sedimentation (Ramos, 2005; Ghiglione

et al., 2016). The latitudinal ridge migration (northward or southward), is thought to propagate a "crustal welt" that drives a time-transgressive uplift and deformation (Ramos, 2005; Ramos and Ghiglione, 2008; Stevens Goddard and Fosdick, 2019). In cases when a time lag between rapid uplift and collision occurs is interpreted as increased transpression in low partitioning regimes (Folguera and Ramos, 2002). Following will be revised some of the arguments regarding magmatic and deformation thought linked to the spreading-ridge collisions, beginning with the Chile ridge collision and later the Farallon-Aluk (Phoenix).

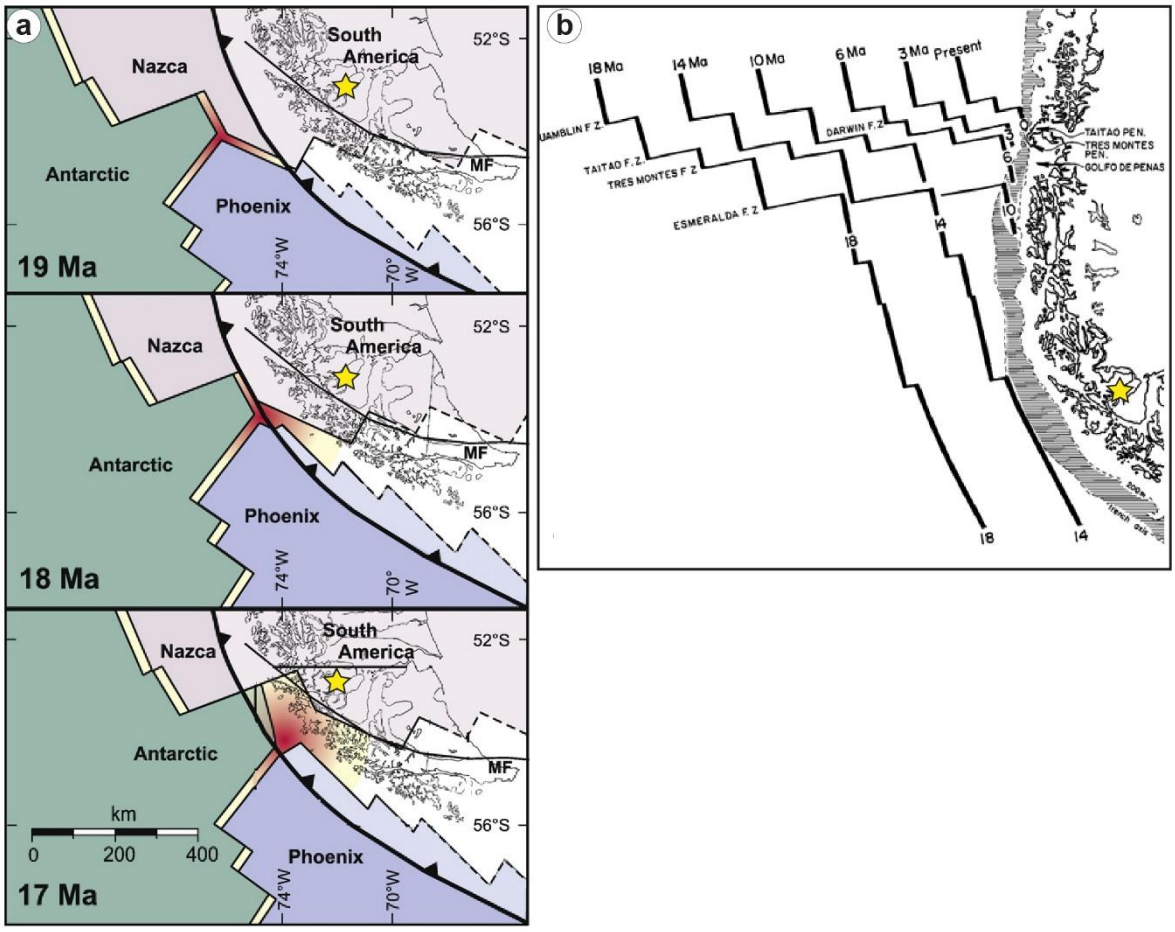

Figure 2. Miocene plate kinematic reconstructions of the Chile ridge. (a) Plate reconstruction taken and modified from Brietsprecher and Thorkelson (2009). (b) Cande and Leslie (1987). Yellow stars signal the approximate position of the thesis study area.

At about 47°S, the uplift of the Cerro San Lorenzo granitoids (6.6-6.2 Ma indicated by Ar/Ar data; Welkner, 2002) and Río de las Nieves pluton (3.2 Ma by K/Ar data; Suárez et al., 2000) (Fig. 3) coincide in time and space with the collision of the Tres Montes-Esmeralda segment of the Chile ridge, which occurred at about 6-8 Ma, and the Taitao-Darwin segment at ~4.95 to present (Cande and Leslie, 1986; Breitsprecher and Thorkelson, 2009; Maksymowicz et al., 2012). Further south in the Torres del Paine Complex (*ca.* 51°S;

Fig. 3), there is also a reasonable constraint on time of deformation, uplift and Chile ridge collision (Ramos, 2005; Ramírez de Arellano et al., 2012). Skarmeta and Castelli (1997), Michael et al. (2008) and Leuthold et al. (2012) constrains the age of magmatism between 13.1-12.2 Ma, which is in agreement with Chile ridge collision at this latitude. The syntectonic nature of these intrusions has been proposed based on structural and subsidence analysis (Skarmeta and Castelli, 1997; Coutand et al., 1999). However, recent mapping campaigns in that region by Ramírez de Arellano et al. (2012), challenge the syntectonic hypothesis for these Miocene intrusions. Furthermore, Suárez et al. (2000, 2001) suggest that compressive deformation predates the Chile ridge collision.

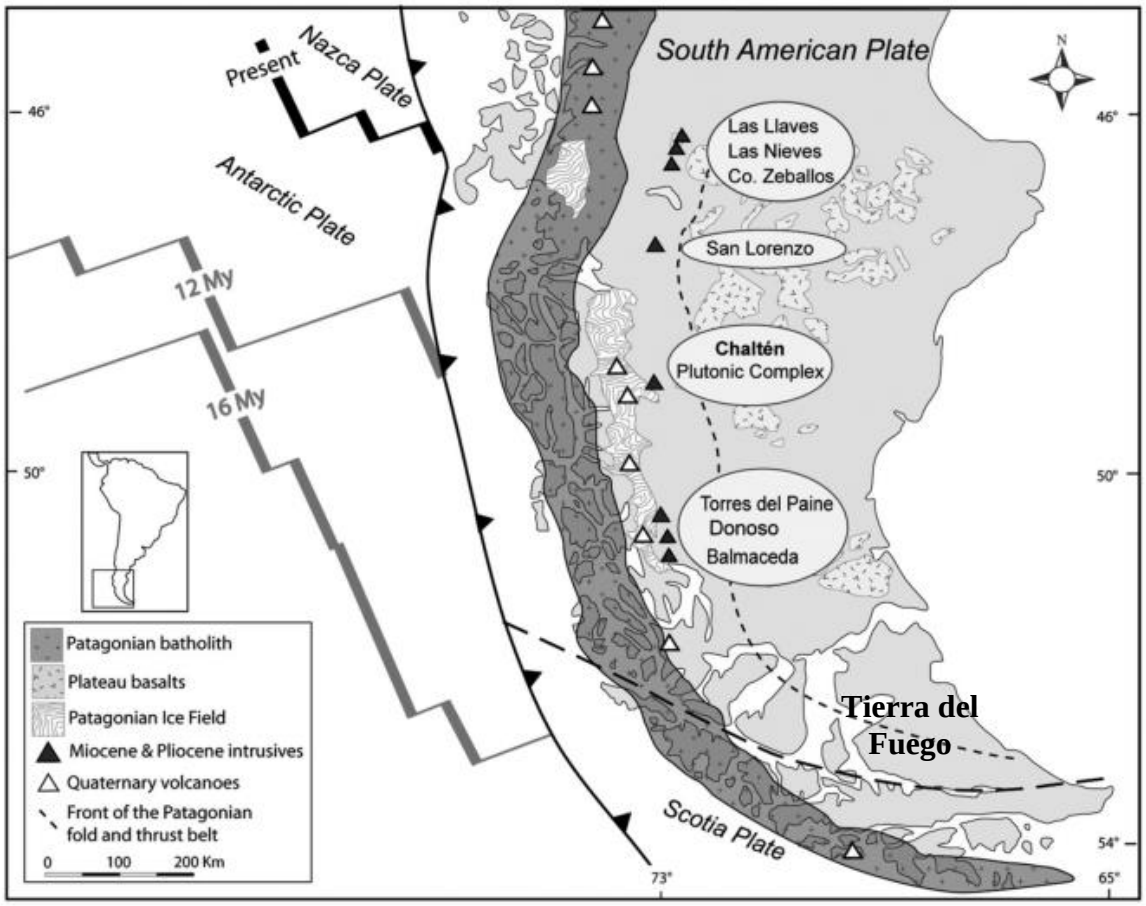

Figure 3. Simplified map of the Miocene to Present plate tectonics setting and localisation of main igneous bodies as the Southern Patagonian magmatic arc, volcanic centres and plutons in the extra-andean region (after Ramírez de Arellano et al., 2012).

Some Paleocene-early Eocene shallow marine, and bearing-coal deposits at 49°S-47°S , have been interpreted as molasses (Kraemer et al., 2002; Suárez et al., 2000b; Troncoso et al., 2002) representing episodes of deformation and important generation of relief linked to the effects of the Farallon-Aluk ridge collision (Ramos, 2005; Ramos and Ghiglione, 2008). At the latitudes of Torres del Paine (51°S) (Fig. 3), Skarmeta and Castelli

(1997) interpreted a late Paleocene-late Eocene basement deformation in the foothills. The latter event coincides with the so-called Paleocene-Eocene unconformity (see Chapter II-1), whose origin is still under discussion (e.g., George et al., 2020; Rivera et al., 2021) but which has been traditionally interpreted as representing a phase of deformation and uplift in the thrust belt and proximal foredeep (Wilson, 1991; Malumián et al., 2000; Fosdick et al., 2015; Gutiérrez et al., 2017).

In Tierra del Fuego (Fig. 3), the maximum deformation recorded in the Fuegian Andes is thought of as a consequence of a more orthogonal orientation regarding the north-northeast trend of the convergence vector (Ramos, 2005). The main Paleogene deformation in the Atlantic coast of Tierra del Fuego (54°S), which is interpreted between 43.6-39.2 Ma (Ghiglione et al., 2002; Ghiglione and Ramos, 2005), is related to the collision of the Farallon-Aluk ridge (Ramos, 2005). In addition, the rapid deformational front and depocenters migration that occurred in the Malvinas basin (Ghiglione et al., 2010) is envisaged due to such a collision. Similarly, further northeast along the Darwin Cordillera (52°S), Nelson (1982) and Gombosi et al. (2009) found a rapid cooling of the Basement Domain from 43 to 30 Ma with uplift rates up to 0.5 mm/yr. This basement compressional exhumation is well recorded in the foreland basin deposits by producing a meaningful shift in provenance from Batholith sources to synrift volcanic and metasedimentary rocks exposed in Darwin Cordillera (Barbeau et al., 2009).

V-1.1.2 Flat-slab subduction

Suárez et al. (2000) and Suárez and De la Cruz (2001) question the causal relationship between Patagonian-Fuegian Andes uplift related to spreading ridge collision. These authors point out that during the two Cenozoic spreading ridge-trench interactions, there were two periods of rapid plate convergences between 50 - 42 Ma and another between 25 - 10 Ma (Pardo-Casas and Molnar, 1987) that may have exerted a significant influence on the geological evolution of the region compared with spreading ridge collision. The following paragraphs, rather than expose arguments against spreading ridge collision as a major mechanism for Patagonian Andes building, are intended to explore the alternative hypothesis for the cause of contractional deformation in the region.

Based on the review of the radiometric data on granitoids of the Patagonian Andes segment ranging between 43°S and 48°S, the notable absence of arc magmatic activity bracketed from 69 to 48 Ma leads to Suárez et al. (2000) and Suárez and De la Cruz (2001)

to propose a flat-slab subduction event. This low-angle subduction could be associated with the Farallon-Aluk ridge subduction as a young crust adjacent to the ridge maintaining its positive buoyancy for some time (*ca.* 10 Ma) would be able to shut off arc magmatism. A combination of flat-slab subduction and other processes related to the subduction regime (e.g., rate and obliquity of subduction; the age, composition, thickness of the subducted plate; the nature of the overriding plate) may explain the episodes of compressional tectonism.

More recently, geochemical analysis of the middle Miocene Zeballos Volcanic Sequence (ZVS) in the Patagonian back-arc region (47°S) (Fig. 3) have laid the basis for proposing another shallowing subduction event (Espinoza et al., 2010). This calc-alkaline magmatism (16-14 Ma) host a geochemical signature typical of subduction processes and magma composition influenced by subducted sediment. Nevertheless, this volcanic sequence presents striking similarities with the volcanism of the present Andean flat-slab region, e.g., high K contents and rare earth elements, and trace elements ratios with similar ranges. The transient middle Miocene shallow subduction would be responsible for the arc migration further east and of the Miocene shortening-uplift, and compressive phase ended at *ca.* 14 Ma at this latitude (Lagabrielle et al., 2004; Blisniuk et al., 2005). Earlier, Gorring et al. (1997) suggested shallow syn-collisional subduction and opening a slab window concerning the subduction at *ca.* 15 Ma of the Chile ridge.

V-1.1.3 Tectonic erosion

Although this hypothesis attempts to explain the eastward migration of magmatic arc activity rather than propose a mechanism for Patagonian fold and thrust belt development, the considerations presented here have important implications in the geodynamic of the Patagonian Andes and the sedimentary system.

The Neogene group of plutons associated with the Southern Patagonian Batholith (SPB, Hervé et al., 2007) located between 48°S and 51°S, shows a trend toward younger ages in the east, i.e., ages from 25-20 Ma in the central part of the SPB and ages as young as 18.4 Ma in the eastern part. This trend is corroborated by the Chaltén Plutonic Complex of 16.9 Ma (Fig. 3) (Ramírez de Arellano et al., 2012) and the external gabbros of Torres del Paine of 16.8 Ma (Fig. 3) located 100 km from the axis of the SPB (Fosdick et al., 2011; Ramírez de Arellano et al., 2012). There is also a time and space coincidence of eastward Miocene exhumation of the Patagonian Andes (Thomson et al., 2001), displacement of the

deformation front in the Patagonian fold and thrust belt (Ramos, 1989; Suárez et al., 2000) between 20 to 17 Ma, besides increasing sedimentation rates in the foreland basin at 18 Ma (Blisniuk et al., 2005). These observations suggest a close relationship between arc migration, tectonics, and sedimentation (Ramírez de Arellano et al., 2012). The latter authors related, at least, the arc migration to subduction erosion with minor variation in slab angle (up to 5°) triggered by high rates of plate convergence after major plate reconfiguration at ca. 26 Ma (Pardo-Casas and Molnar, 1987) and discarded a link with Chile ridge subduction because the absence of similar subduction erosion processes north of the CTJ.

V-1.1.4 Wrench-fault tectonics (terrane slice)

Earlier authors have proposed a wrench tectonics origin for the Southernmost Andes (Dalziel and Brown, 1989; Cunningham, 1993, 1995; Cunningham et al., 1995; Klepeis, 1994, Diraison et al., 1998, 2000; Kraemer, 2003; Menichetti et al., 2008) based on the transcurrent nature of the present northernmost Patagonian (44°S-46°S) and southernmost Fuegian Andes (53°45'S-55°15'S) (Fig. 5). In this context and specifically for the Fuegian Andes, some interpretations suggest that sinistral deformation likely related to the Magallanes-Fagnano Fault System (MFFS) onset in the Late Cretaceous-early Eocene (Cunningham, 1993, 1995; Menichetti et al., 2008), which is coincident with an incipient opening of the Drake Passage before of 50 Ma, developing a wide and relatively shallow epicontinental sea separating South America and Antarctic Peninsula and accompanied extensional phase in the southeast of Tierra del Fuego (Lawver et al., 2014; Livermore et al., 2005; Eagles et al., 2006; Ghiglione et al., 2008). On the other hand, other interpretations suggest that the strike-slip deformation occurred as two separate tectonic events and that since the Oligocene, such a deformation overprinted the fold and thrust belt (Klepeis, 1994; Klepeis and Austin, 1997; Lodolo et al., 2003; Ghiglione and Ramos, 2005). Kinematics analysis carried out by Klepeis (1994) and Klepeis and Austin (1997) demonstrated that sinistral strike-slip deformation in Tierra del Fuego occurred after 60 Ma and dominantly since 30 Ma. This latter phase of deformation was accommodated by the onset of seafloor spreading in the West Scotia Plate (ca. 30 Ma, Barker and Burrell, 1977). In contrast, Lodolo et al. (2003) and Betka et al. (2016) propose a late Miocene (ca. 9-6 Ma) onset of strike-slip deformation coinciding with a widespread pulse of uplift and exhumation in the northern sector of the Patagonian fold and thrust belt (Fosdick et al., 2013) and the emergence of North Scotia Ridge and island of Tierra del Fuego. The latter approach supposes a regional response to changes in the Scotia Arc during the opening of the Drake Passage (development

of West Scotia Sea) able to impact the Patagonian thrust belt. Some models suggest for the MFFS a 20-30 km left-lateral offset since at least the latest Eocene (Olivero and Martinioni, 2001), while others calculated a 48 km offset since 7 Ma (Torres-Carbonell et al., 2008). The results provided by Cunningham (1993,1995) supported by plate reconstruction report up to 1320 km of left-lateral strike-slip displacement between South America and Antarctic Peninsula since ca. 84 Ma, where about 900 km of motion occurred after 50 Ma. This amount of large coastwise displacement is comparable with the transcurrent offset of the Baja British Columbia (Cowan et al., 1997).

V-1.2 The Southern Patagonian Andes under the light of new findings

In this thesis, different multidisciplinary approaches were conducted aimed to contribute as much information and analytical perspectives as possible to the understanding of the evolution of the Patagonian Andes, based on the study of a segment of the basin little studied previously. However, the analytical and spatial-temporal limitations inherent in this study only allow us to shed light on the tectonic evolution of this complex region, which is by no means definitive.

Hypothesis about the relationship of active ridge subduction and contractional deformation phases in the orogenic wedge does not seem to be supported by the spatio-temporal relationships between the ridge subduction and the deformation recorded in the orogen (e.g., Suárez et al., 2000; Folguera et al., 2018). Recent works (e.g., Breitsprecher and Thorkelson, 2009; Scalabrino et al., 2010; Guillaume et al., 2010, 2013; Salze et al., 2018) show that the impact of the subduction of active ridges is translated into a long-wavelength uplift of the orogen (dynamic topography), development of localized extension and lateral migration of the volcanic arc (under certain kinematic conditions, see Salze et al., 2018) and subsequent development of asthenospheric windows producing alkaline volcanism in the extra-Andean region.

Based on recent plate reconstructions of Breitsprecher and Thorkelson (2009; Fig. 2a), it can be assumed that the subduction of the Chilean ridge occurs around 19 Ma in our research area (51°15'S-53°40'S). At this time, a generalised basin inversion and orogenic wedge exhumation are observed, concomitant with a cessation of contractile deformation and change from a flexural to dynamic subsidence regime, in addition to the progradation of continental deposits beyond the forebulge. The latter suggests, the abandonment of the

foreland basin stage and compressional regime by early Miocene at this latitude. Furthermore, this period from ~20 Ma and ongoing, coincides with an important decrease of convergence rates and increase of obliquity of the Antarctic plate (Fig. 5), imposing a change to transpressional to transtensional regime better developed in Tierra del Fuego. However, while in the south (51°15'S-53°40'S) the cessation of compressional regime occurs, in the northernmost part of the Southern Patagonian Andes (46°S-49°S), the compression remains active with a more orthogonal convergence vector (Cande and Leslie et al., 1986; Somoza and Ghidella, 2005, 2012), probably flexural subsidence and foreland basin sedimentation stage. This explains the contrasting nature of the age-equivalents Palomares Formation in the south (post-orogenic unit) and the Santa Cruz Formation (syn-orogenic unit, e.g., Ramos, 1989, 2005; Blisniuk et al., 2005; Folguera et al., 2018; Barberón et al., 2018) in the northernmost part of the Magallanes-Austral Basin.

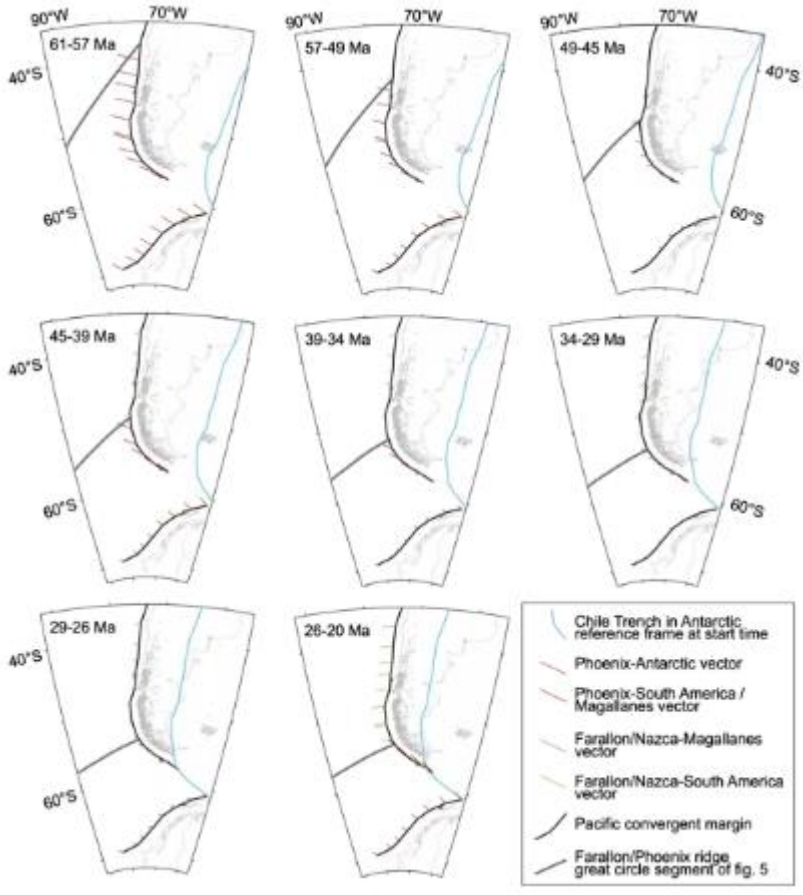

Fig. 4. Reconstruction of the Farallon-Aluk ridge and plate convergence vectors and rates along the Southern Patagonian margin (after Eagles and Scott, 2014). Note how the migration of seismic ridges and bending of the southernmost Fuegian margin conditions differences in plate kinematics.

Exactly the reverse situation occurs during the subduction of the Farallon-Aluk (Phoenix) ridge during much of the Eocene. In the north of the Southern Patagonian Andes,

the magmatic arc shut off, the compressional deformation is replaced by extension and extrusion of alkaline basalts by ~52-42 Ma. Meanwhile, in the south (study area), the continental margin is subjected to a more orthogonal and faster convergence of the Aluk/Phoenix and South American plates (Eagles and Scott, 2014; Fig. 4) promoting a compressional regime and crustal thickening due to shortening. As the Farallon-Aluk ridge migrated southward latitudes (our study area), the magmatic arc, the active compression, the advance of the deformation front and the migration of the foreland depocentres progressively stopped, during a process of quiescence tectonic. Our exhumation data provided by thermochronology and sedimentary provenance allow us to verify this pattern. Likewise, the study of depositional systems reveals shallowing and progradation during the middle Eocene (~48-43 Ma) in response to an isostatic uplift that enhances orogenic denudation/erosion and reduces the flexural loading. In Tierra del Fuego, the change from a deep-sea depositional system to a shallow prograding marine one occurs shortly after that in the Skyring Sound-Brunswick Peninsula area, approximately between ~43-38 Ma (Torres Carbonell and Olivero, 2019), evidencing the southward progression of the effect of the Farallon-Aluk ridge subduction.

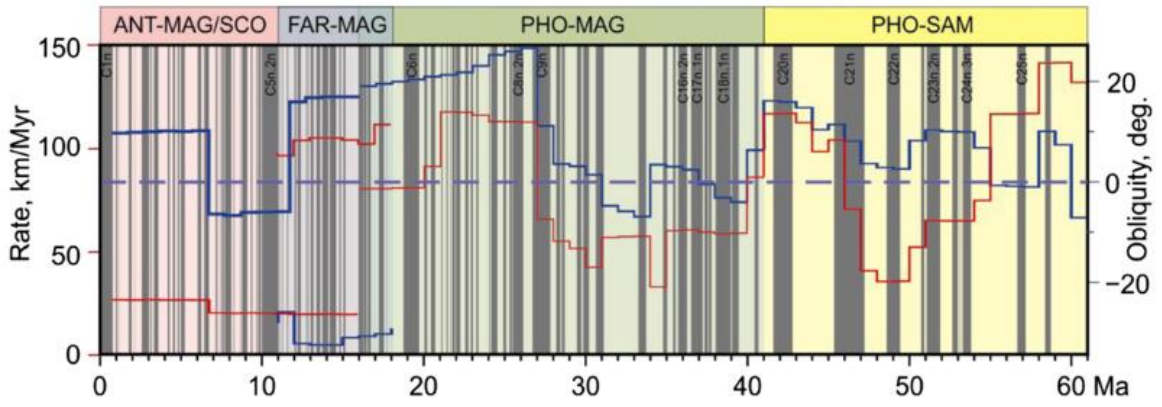

Fig. 5. Convergence rates (red lines) and obliquity (blue lines) of convergence at 56.8°S (after Eagles and Scott, 2014).

The notorious absence or decrease of magmatism recorded in the entire Southern Patagonian Andes during the Eocene, eastward migration of the magmatic arc during the Miocene, has motivated the proposal of hypotheses that link periods of flat subduction with the compressive stages in the Southern Patagonian Andes (see the previous section). Recently, Gianni et al. (2018a) propose the existence of a large flat slab subduction segment (35°30'-48°S; ~1350 km long) between 75-60 Ma, based on the eastward migration of the magmatic arc throughout the entire region where they propose its existence, which links

appealingly the Late Cretaceous to Paleocene mountain building, dynamic subsidence and the Maastrichtian-Danian transgression. The eastward shift of the magmatic arc front remains the most compelling evidence of flat-slab subduction (Ramos et al., 2002; Folguera and Ramos, 2011), but this migration can be explained by multiple factors (see review in Gianni and Luján, 2021). The present-day and Miocene geological record of the Southern Central Andes region provides geological criteria to recognise this geodynamic process. A rapid cratonward propagation of the deformational front and magmatic arc, widespread thrust-belt exhumation coeval with arc magmatism lull, recycling of early Andean foreland basin deposits, and basement-involved uplifts (Jordan and Allmendinger, 1986; Ramos et al., 2002; Folguera and Ramos, 2011). The observed uplift of basement blocks in the internal domain of the Magallanes fold-thrust belt, the rapid eastward migration of deformation front, exhumation, and foredeep during the Campanian-early Eocene simultaneous to and relative eastward shift of the locus of the magmatic arc followed by shut off (Blisniuk et al., 2005; Fosdick et al., 2011, 2013, 2015; Betka et al., 2015; Ghiglione et al., 2016; Chapters II-1, III-1,2, IV-1) could support the transient flat-slab hypothesis. However, there is not any evidence of a basement-involved broken foreland in the Magallanes-Austral basin and all the latter observation can be explained by alternative mechanisms, for instance, tectonic erosion as may be the case for the Miocene (Ramírez de Arellano et al., 2012; Salze et al., 2018).

Regarding the wrenching tectonic hypothesis as the main control in mountain building, we do not have enough data to debate about it. Our structural geological results suggest that the transcurrence occurs after the Cretaceous-Paleocene deformation event. Therefore, the low amount of shortening ascribed to the late Eocene-Oligocene deformation event may be the result of the incorrect orientation along which the shortening was quantified (perpendicular to the main structural grain). Speculatively, much of the shortening may have been transferred laterally.

It is important to emphasise against referring to main orogenic construction phases uniformly for the entire Southern Patagonian Andes. Each segment behaves differently over time, depending on the geodynamic conditions that impact the South American margin in a determined time. It is well known that the pre-Andean extensional regime did not develop uniformly throughout the region, e.g., the onset time and stretching intensity was highly diachronic from south to north. Likewise, the beginning of the inversion of the extensional Rocas Verdes Basin was neither spatially nor temporally homogeneous throughout

Patagonia. Both, in previous chapters as in this brief discussion, is shown that while compression ceases in one segment of the Southern Patagonian Andes, in other segment compression remain active at the same time. The complex geodynamic configuration of the Patagonian margin conditions that each segment of this Cordilleran system and its linked foreland basin evolve independently for determined time intervals.

In this instance, some argumentation can be provided to answer the questions that have motivated this research, trying to contribute to the general knowledge of the evolution of the Andes and Andean-type foreland basins.

1) How and to what extent does the inherited crustal architecture of the predecessor Rocas Verdes Basin control the sedimentary system evolution and dispersal of sediments during the Late Cretaceous-early Miocene?

The more attenuated lithosphere southward triggered enhanced subsidence and establishment of protracted deep-marine sedimentation in southern latitudes, where the predecessor basin underwent greater extension. The timing of the transition from underfilled to overfilled foreland basin phases was controlled by this southward incremental depth gradient. This incremental depth gradient to the south also impacted the development of unconformities and their nature, losing their erosive character (becoming correlatives conformities) and hiatus time. Likewise, the volumetrically important amount of mafic rocks incorporated in the orogenic wedge contributed more tectonic load compared to the north. These mafic rocks printed a very distinctive mafic character that differentiates compositionally the Magallanes-Austral strata from other andean-type foreland sediments.

2) How and to what degree does the Cenozoic geodynamic events (subduction of active ridges, opening of Drake Passage) impact the development and evolution of an Andean-type orogen-foreland basin pair?

The results presented here suggest that the most notorious effect of the subduction of active ridges in the evolution dynamics of Andean-type orogen-foreland basin pair is the cessation of the contractional regime and thus the abandonment of the flexural subsidence that allows the capture of sediments in the mountain foothills, produced by rock-uplift enhanced and denudation. Rapid progradation of deposits in foreland basins does not always suggest compressive tectonic events. Therefore, its use as an indicator of tectonism must entail rigorous discrimination of the controlling mechanisms. Changes in plate kinematics also impact the way how horizontal stress is transferred forward. Although there is

deformation during the time that coincides with the opening of the Drake Passage (more oblique convergence), it does not generate the same crustal shortening (and therefore tectonic load) as during periods of more orthogonal convergence, significantly reducing the amount of flexural subsidence and impacting on sedimentation dynamics.

3) What is the nature of the whole Southern Patagonian Andean growth (including sediment accumulation history) in terms of steady or punctuated episodic behaviour?

The dynamics of sedimentation, timing and magnitude of the exhumation processes show a strong episodic character. Therefore, it can be thought that the orogenic building of the Southern Patagonian Andes responds to punctuated processes.

V-1.3 Conclusions

The main findings and results recorded in each previous chapter of this thesis can be synthesised as follows.

It suggested the abandonment of the use of the Escarpada Formation (in the Magallanes Province, Chile). Unification of the Cerro Cazador, Monte Chico, and Cerro Dorotea formations into a single lithostratigraphic unit called the Dorotea Formation. The lower member of the actual Río Turbio Formation is re-defined as the Man Aike Formation. The actual Río Guillermo Formation becomes a member of the Río Leona Formation.

Several unconformities of minor duration (<5 Myr) were identified in the basin. The most significant Paleocene-Eocene and Eocene-Oligocene unconformities span ~20 and ~12 Myr hiatus around Lago Argentino (Argentina) but southward in Brunswick Peninsula (Chile), both diminishes significantly to represent ~2.5 and ~4 Myr hiatus, respectively. For the Paleocene-Eocene unconformity, a combination of contractional and quiescence tectonic mechanisms are proposed to explain its origin. For the Eocene-Oligocene unconformity, a regional deformational event is ascribed as its causative mechanism.

We constate the episodic behaviour of magmatism of the Southern Patagonian Batholith, with main pulses at Late Jurassic to Early Cretaceous (160-140 Ma), Middle to Late Cretaceous (120-70 Ma), late Eocene (45-35 Ma), late Oligocene to early Miocene (25-15 Ma). Two new phases of magmatism (K4: 75-65 Ma; Pg2; 45-35 Ma) were recognised. Furthermore, we emphasize three first-order magmatic lulls between 25-33 Ma, 45-65 Ma and 120-140 Ma.

The foreland basin phase in the study area begins as early as ~114 Ma, ~15 Myr earlier than previously thought.

Two second-order sequences allow us to interpret changes in the sedimentation dynamics, evolving from an underfilled basin stage (from Late Cretaceous to middle Eocene) to an overfilled basin (from the Middle Eocene to the early Neogene).

Seven third-order sequences allow knowing the basin's responses to tectonic changes, sedimentation rates, and variations in accommodation:

- **KS1** (~115-75 Ma): comprises the Canal Bertrand, Latorre and Barcárcel formations, presents a well-defined wedge-like geometry and is characterised by deep-marine turbiditic sedimentation.

- **KS2** (~75-66 Ma): comprises the Fuentes and Rocallosa formations, presents a wedge to subtabular geometry and is characterised by an initial cycle of aggradation developing a depositional slope evolving to second progradation cycle with a shallow-marine depositional system.

- **PS1** (~66-57 Ma): comprises the Chorrillo Chico Formation, presents a well-defined wedge-like geometry and is characterised by deep-marine turbiditic sedimentation.

- **PS2** (~57-43 Ma): comprises the Agua Fresca and Tres Brazos formations, present a wedge-like geometry and is characterised by an initial aggradation cycle developing a slope-shelf depositional system followed by a second prograding cycle with a shallow-marine river-dominated deltaic system.

- **PS3** (~43-33 Ma): comprises the Leña Dura and Tres Brazos formations, presents a subtabular to wedge geometry and is characterised by hemipelagic sedimentation and progradation of a shelf-edge deltaic system. This sequence marks the transition from underfilled to overfilled basin stage.

- **PS4** (~30-25 Ma): comprises the lower part of the El Salto Formation, presents a subtle wedge-like geometry and is characterized by a high-energy braided fluvial system in the proximal foredeep, and a coastal plain depositional system in distal foredeep and forebulge zones.

- **NS1** (~23-15 Ma): comprises the upper part of the El Salto Formation and the Palomares Formation, presents a tabular geometry and is characterised by progradational high-energy fluvial depositional systems, in the proximal areas, and shallow marine depositional systems far away from the buried forebulge. This sequence marks the overfilled basin stage.

Flexural subsidence is the main driver of accommodation from Late Cretaceous to late Eocene. Dynamic subsidence dominates from the late Oligocene to Miocene.

Orogenic loading of the Southern Patagonian Andes was a primary driver of the Maastrichtian-Danian transgression in the MAB. Additionally, changes in dynamic

topography strongly modulated the extent of the continental flooding event. In contrast, Miocene transgressions could be controlled by eustatic sea-level changes and dynamic topographic changes.

By combining sedimentary provenance, thermochronological and structural analyses, we envisage five phases of Southern Patagonian orogenic growth in the study area. The first phase (~100-80 Ma) is characterised by internal deformation, thickening of the orogenic wedge, and protracted hinterland exhumation. The second phase (~70-50 Ma) is characterised by minor hinterland exhumation and significant forelandward advance of the thrust front and rapid exhumation. The third phase (~48-40 Ma) is characterised by tectonic quiescence leading to isostatic rebound uplift and slow exhumation as the result of the Farallon-Aluk ridge subduction. The fourth phase (~38-25 Ma) is characterised by forelandward advance of the deformational front with a low amount of shortening but a rapid exhumation. The fifth phase (20-10) is characterised by a rapid exhumation concentrated towards the innermost parts of the fold-thrust belt and a much slowly exhumation towards the undeformed foreland. There is no field evidence of the advance of the deformation front, but a slight eastward tilting of the early Miocene deposits is probably linked to the subduction of the Chile Ridge.

The cessation of flexural subsidence and contractional deformation and generalised orogenic wedge and foreland basin exhumation from ~20 Ma is interpreted as basin inversion and abandonment of foreland phase as a consequence of the dynamic uplift of the lithosphere due to the subduction of the Chilean ridge.

Rapid exhumation younger than the late Miocene (~10 Ma) is interpreted as related to erosive fluvioglacial processes.

BIBLIOGRAPHY

Affolter, M. D., and Ingersoll, R. V., 2019. Quantitative analysis of volcanic lithic fragments. Journal of Sedimentary Research, 89(6), 479-486.

Aguirre-Urreta, B., Tunik, M., Naipauer, M., Pazos, P., Ottone, E., Fanning, M., Ramos, V.A., 2011. Malargüe Group (Maastrichtian–Danian) deposits in the Neuquén Andes, Argentina: Implications for the onset of the first Atlantic transgression related to Western Gondwana break-up. Gondwana Research 19, 482-494.

Aitchison, J. (1982). The statistical analysis of compositional data. Journal of the Royal Statistical Society: Series B (Methodological), 44(2), 139-160.

Allen, P. A., & Allen, J. R. (2013). Basin analysis: Principles and application to petroleum play assessment. John Wiley & Sons.

Allen, J. L., & Johnson, C. L. (2010). Facies control on sandstone composition (and influence of statistical methods on interpretations) in the John Henry Member, Straight Cliffs Formation, Southern Utah, USA. Sedimentary Geology, 230(1-2), 60-76.

Alvarez-Marrón, J., McClay, K.R., Harambour, S., Rojas, L., and Skarmeta, J., 1993. Geometry and evolution of the frontal part of the Magallanes foreland thrust and fold belt (Vicuña Area), Tierra del Fuego, southern Chile. American Association of Petroleum Geologists Bulletin, 77, p. 1904–1921.

Álvarez, P., Elgueta, S., Mpodozis, C., Briceño, M., Vieytes, H., Radic, J.P., Mella, P., 2006. Revisión de la estratigrafía y facies de la cuenca de antepaís Cretácica entre Lago Argentino y Península Brunswick. Proyecto Tranquilo-Otway, Informe Final. Empresa Nacional de Petróleo (ENAP), Unpublished technical report, 290 pp.

Angevine, C. L., Heller, P. L., & Paola, C. (1990). Quantitative sedimentary basin modeling. AAPG Special Volumes.

Anguita, N. (2010). Petrogénesis de Diques Lamprofídicos Postectónicos y su Relación con el Magmatismo Shoshonítico Cretácico de la Formación Barros Arana y el Complejo La Pera, Magallanes, XII Región, Chile. Disponible en https://repositorio.uchile.cl/handle/2250/103797

Antoine, P. O., Abello, M. A., Adnet, S., Sierra, A. J. A., Baby, P., Billet, G., ... & Salas-Gismondi, R. (2016). A 60-million-year Cenozoic history of western Amazonian ecosystems in Contamana, eastern Peru. Gondwana Research, 31, 30-59.

Andersen, T., 2002. Correction of common Pb in U–Pb analyses that do not report 204Pb. Chemical Geology 192, 59–79.

Aragón, E., Pinotti, L., Fernando, D., Castro, A., Rabbia, O., Coniglio, J., ... & Aguilera, Y. E. (2013). The Farallon-Aluk ridge collision with South America: Implications for the geochemical changes of slab window magmas from fore-to back-arc. Geoscience Frontiers, 4(4), 377-388.

Aramendía, I., Cuitiño, J. I., Ghiglione, M., & Bouza, P. J. (2019). Tectonostratigraphic significance of the Neogene sedimentary record of northwestern Austral-Magallanes basin, Argentinean Patagonia. Latin American journal of sedimentology and basin analysis, 26(2), 99-126.

Armijo, R., Lacassin, R., Coudurier-Curveur, A., Carrizo, D., 2015. Coupled tectonic evolution of Andean orogeny and global climate. Earth-Science Reviews, 143, p. 1-35, doi: 10.1016/j.earscirev.2015.01.005.

Asiedu, D. K., S. B. Dampare, P. Asamoah Sakyi, B. Banoeng-Yakubo, S. Osae, B. J. B. Nyarko, J. Manu (2004). Geochemistry of Paleoproterozoic metasedimentary rocks from the Birim diamondiferous field, southern Ghana: Implications for provenance and crustal evolution at the Archean-Proterozoic boundary. Geochemical Journal, 38(3), 215-228.

Azcuy, C. L., & Amigo, A. E. (1991). Geología y paleoambiente de la formación Río Turbio (Eoceno), en la Sierra Dorotea, provincia de Santa Cruz. Revista de la Asociación Geológica Argentina, 46(3–1), 201-210.

Bann, K.L., Fielding, C.R., 2004. An integrated ichnological and sedimentological comparison of non-deltaic shoreface and subaqueous delta deposits in Permian reservoir units of Australia. In: McIlroy, D. (Ed.), The Application of Ichnology to Palaeoenvironmental and Stratigraphic Analysis. Geological Society of London, Special Publications 228, pp. 273-310.

Barbeau Jr., D.L., Olivero, E.B., Swanson-Hysell, N.L., Zahid, K.M., Murray, K.E., Gehrels, G.E., 2009. Detrital-zircon geochronology of the eastern Magallanes foreland basin: Implications for Eocene kinematics of the northern Scotia Arc and Drake Passage. Earth and Planetary Letters 284, 489-503.

Barker, P.F., Burell, J., 1977. The opening of the Drake Passage. Marine Geology 25, 15–34.

Barker, P.F., 2001. Scotia regional tectonic evolution: implication for the mantle flow and paleocirculation. Earth-Science Reviews 55, 1-39.

Barreda, V. D., Palazzesi, L., Marenssi, S., 2009. Palynological record of the Paleogene Río Leona Formation (southernmost South America): Stratigraphical and paleoenvironmental implications. Review of Palaeobotany and Palynology 151, 22-33.

Barrera, E., Savin, S.M., 1999. Evolution of late Campanian-Maastrichtian marine climates and oceans. In: Barrera, E., Johnson, C.C. (Eds.), Evolution of the Cretaceous Ocean-Climate System. Geological Society of America, Special Papers 332, pp. 245-282.

Barrio, C.A., 1990. Late Cretaceous-Early Tertiary sedimentation in a semi-arid foreland basin (Neuquén Basin, western Argentina). Sedimentary Geology 66, 255-275.

Barth, A. P., Wooden, J. L., Jacobson, C. E., & Economos, R. C. (2013). Detrital zircon as a proxy for tracking the magmatic arc system: The California arc example. Geology, 41(2), 223-226.

Bascuñán, S., Arriagada, C., Le Roux, J., & Deckart, K. (2016). Unraveling the Peruvian Phase of the Central Andes: stratigraphy, sedimentology and geochronology of the Salar de Atacama Basin (22 30–23 S), northern Chile. Basin Research, 28(3), 365-392.

Basu, A. R., Sharma, M., & DeCelles, P. G. (1990). Nd, Sr-isotopic provenance and trace element geochemistry of Amazonian foreland basin fluvial sands, Bolivia and Peru: implications for ensialic Andean orogeny. Earth and Planetary Science Letters, 100(1-3), 1-17.

Bauer, D. B., Hubbard, S. M., Covault, J. A., & Romans, B. W. (2020). Inherited depositional topography control on shelf-margin oversteepening, readjustment, and coarse-grained sediment delivery to deep water, Magallanes Basin, Chile. Frontiers in Earth Science, 358.

Bayona, G., Cortés, M., Jaramillo, C., Ojeda, G., Aristizábal, J.J., Reyes-Harker, A., 2008. An integrated analysis of an orogen-sedimentary basin pair: Latest Cretaceous-Cenozoic evolution of the linked Eastern Cordillera orogen and the Llanos foreland basin of Colombia. Gological Society Bulletin 120, 1171-1197.

Berggren, W.A., Pearson, P.N., Huber, B.T., Wade, B.S., 2006. Taxonomy, biostratigraphy and phylogeny of Acarinina. Cushman Foundation Special Publication 41, 257-326.

Bernet, M. (2019). Exhumation studies of mountain belts based on detrital fission-track analysis on sand and sandstones. In Fission-track thermochronology and its application to geology (pp. 269-277). Springer, Cham.

Bernet, M., & Spiegel, C. (Eds.). (2004). Detrital thermochronology: Provenance analysis, exhumation, and landscape evolution of mountain belts (Vol. 378). Geological Society of America.

Bernhardt, A., 2011. Paleogeography and sedimentary development of two deep-marine foreland basins: The Cretaceous Magallanes Basin, southern Chile, and the Tertiary Molasse Basin, Austria. Unpublished Ph.D. thesis, Stanford University, pp 218.

Berra, F., & Carminati, E. (2010). Subsidence history from a backstripping analysis of the Permo-Mesozoic succession of the Central Southern Alps (Northern Italy). Basin Research, 22(6), 952-975.

Betka, P., Klepeis, K., Mosher, S., 2015. Along-strike variation in crustal shortening and kinematic evolution of the base of a retroarc fold-and-thrust belt: Magallanes, Chile 53° S–54°. Geological Society of America Bulletin 127, 1108-1134.

Betka, P., Klepeis, K., Mosher, S., 2016. Fault kinematics of the Magallanes-Fagnano fault system, southern Chile; an example of diffuse strain and sinistral transtension along a continental transform margin. Journal of Structural Geology, 85, p. 130-153.

Bhatia, M. R., & Crook, K. A. (1986). Trace element characteristics of graywackes and tectonic setting discrimination of sedimentary basins. Contributions to mineralogy and petrology, 92(2), 181-193.

Bhattacharya, J.P., 2010. Deltas. In: James, N.P., Dalrymple, R.W. (Eds.), Facies Models 4. Geological Association of Canada, St. John's Newfoundland and Labrador, pp. 233-264.

Biddle, K.T., Uliana, M.A., Mitchum Jr, R.M., Fitzgerald, M.G., Wright, R.C., 1986. The stratigraphic and structural evolution of the central and eastern Magallanes Basin, southern South America. In: Allen, P.A., Homewood, P. (Eds.), Foreland basins. International Association of Sedimentologists Special Publication 8, pp. 41-61.

Black, L., Kamo, S., Allen, C., Davis, D., Aleinikoff, J., Valley, J., Foudoulis, C., 2004. Improved 206Pb/238U microprobe geochronology by the monitoring of a trace-element-related matrix effect; SHRIMP, ID–TIMS, ELA–ICP–MS and oxygen isotope documentation for a series of zircon standards. Chemical Geology 205, 115-140.

Blisniuk, P.M., Stern, L.A., Chamberlain, C.P., Idleman, B., Zeitler, P.K., 2005. Andes climatic and ecologic changes during Miocene surface uplift in the southern Patagonian Andes. Earth and Planetary Science Letters 230, 125–142.

Bonarelli, G., 1917. Informe Geológico sobre exploraciones Petrolíferas en Magallanes. Santiago, Chile, Ministerio de Fomento, Dept. Minas y Petróleo.

Borel, C.M., 2007. Algas no silíceas y acritarcos de depósitos costeros holocenos en el arroyo La Ballenera, Buenos Aires, Argentina. Ameghiniana 44, 359-366.

Bostelmann, J.E., Le Roux, J.P., Vásquez, A., Gutiérrez, N.M., Oyarzún, J.L., Carreño, C., Torres, T., Otero, R., Llanos, A., Fanning, M., Hervé, F., 2013. Burdigalian deposits of the Santa Cruz Formation in the Sierra Baguales, Austral (Magallanes) basin: age, depositional environment and vertebrate fossil. Andean Geology 40, 458-489.

Bowman, V.C., Francis, J.E., Askin, R.A., Riding, J.B., Swindles, G.T., 2014. Latest Cretaceous–earliest Paleogene vegetation and climate change at the high southern latitudes: palynological evidence from Seymour Island, Antarctic Peninsula. Palaeogeography, Palaeoclimatology, Palaeoecology 408, 26-47.

Boynton, W. V. (1984). Cosmochemistry of the rare earth elements: meteorite studies. In Developments in geochemistry (Vol. 2, pp. 63-114). Elsevier.

Brandon, M. T., Roden-Tice, M. K., & Garver, J. I. (1998). Late Cenozoic exhumation of the Cascadia accretionary wedge in the Olympic Mountains, northwest Washington State. Geological Society of America Bulletin, 110(8), 985-1009.

Brandmayr, J., 1945. Contribucion al conocimiento geologico del extremo sud sudoeste del Tomtoria de Santa Cruz (Región Cerro Cazador - alto Río Turbo). Boletin de Informes Petroleros de Buenos Aires, 256, 415-437.

Breitsprecher, K., Thorkelson, D.J., 2009. Neogene kinematic history of Nazca–Antarctic–Phoenix slab windows beneath Patagonia and the Antarctic Peninsula. Tectonophysics, 464, p. 10-20.

Bruhn, R.L., Stern, C.R., De Wit, M.J., 1978. Field and geochemical data bearing on the development of a Mesozoic volcano–tectonic rift zone and back–arc basin in southernmost South America. Earth and Planetary Science Letters 41, 32–46.

Bruce, R.M., Nelson, E.P., Weaver, S.G., and Lux, D.R., 1991. Temporal and spatial variations in the southern Patagonian Batholith; constraints on magmatic arc development. In Harmon, R.S., and Rapela, C.W., (Eds.), Andean Magmatism and its Tectonic Setting. Geological Society of America Special Paper, 265, p. 1–12, doi: 10.1130/SPE265-p1.

Buatois, L.A., Mángano, G., 2011. Ichnology: organism-substrate interactions in space and time. Cambridge University Press, pp 358.

Burgess, P.M., Moresi, L.N., 1999. Modelling rates and distribution of subsidence due to dynamic topography over subducting slabs: is it possible to identify dynamic topography from ancient strata? Basin Research 11, 305-314.

Butler, K. L., Horton, B. K., Echaurren, A., Folguera, A., & Fuentes, F. (2020). Cretaceous-Cenozoic growth of the Patagonian broken foreland basin, Argentina: Chronostratigraphic framework and provenance variations during transitions in Andean subduction dynamics. Journal of South American Earth Sciences, 97, 102242.

Calderón, M., 2006. Petrogénesis and tectonic evolution of late Jurassic bimodal magmatic suite (Sarmiento Complex) and migmatites(Puerto Edén igneous metamorphic Complex) in the southern Patagonian Andes, Chile. Tesis (doctor en ciencias, mención geología)--Universidad de Chile.

Calderón, M., Fildani, A., Herve, F., Fanning, C.M., Weislogel, A., Cordani, U., 2007. Late Jurassic bimodal magmatism in the northern sea-floor remnant of the Rocas Verdes basin, southern Patagonian Andes. Journal of the Geological Society 164, 1011-1022.

Calderón, M.M., Fosdick, J.C., Warren, C.C., Massonne, H., Fanning, C.M., Fadel Cury, L.L., and Hervé, F.F., 2012. The low-grade Canal de las Montañas shear zone and its role in the tectonic emplacement of the Sarmiento ophiolitic complex and Late Cretaceous Patagonian Andes orogeny, Chile. Tectonophysics, 524–525, p. 165–185, doi:10.1016/j.tecto.2011.12.034

Calderon, M., Prades, C. F., Herve, F., Avendaño, V., Fanning, C. M., Massonne, H. J., ... & Simonetti, A. (2013). Petrological vestiges of the Late Jurassic-Early Cretaceous transition from rift to back-arc basin in southernmost Chile: New age and geochemical data from the Capitán Aracena, Carlos III, and Tortuga ophiolitic complexes. Geochemical Journal, 47(2), 201-217.

Camacho, H. H., Chiesa, J. O., Parma, S. G., Reichler, V., 2000. Invertebrados marinos de la Formación Man Aike (Eoceno medio), Provincia de Santa Cruz, Argentina. Boletín de la Academia Nacional de Ciencias 64, 187-208.

Cande, S.C., Leslie, R.B., 1986. Late Cenozoic tectonics of the southern Chile trench. Journal of Geophysical Research 91, 471–496.

Cant, D. J. (1992). Subsurface facies analysis. Facies models, 27-45.

Cañón, A., Ernst, M., 1975. Cuadro de correlaciones estratigráfica de la Provincia de Magallanes. Informe Archivo Técnico ENAP, Santiago, (Inédito).

Capaldi, T. N., Horton, B. K., McKenzie, N. R., Mackaman-Lofland, C., Stockli, D. F., Ortiz, G., & Alvarado, P. (2020). Neogene retroarc foreland basin evolution, sediment provenance, and magmatism in response to flat slab subduction, western Argentina. Tectonics, 39(7), e2019TC005958.

Capaldi, T. N., McKenzie, N. R., Horton, B. K., Mackaman-Lofland, C., Colleps, C. L., & Stockli, D. F. (2021). Detrital zircon record of Phanerozoic magmatism in the southern Central Andes. Geosphere, 17(3), 876-897.

Carrapa, B. (2009). Tracing exhumation and orogenic wedge dynamics in the European Alps with detrital thermochronology. Geology, 37(12), 1127-1130.

Carrapa, B. (2010). Resolving tectonic problems by dating detrital minerals. Geology, 38(2), 191-192.

Carrapa, B., & DeCelles, P. G. (2008). Eocene exhumation and basin development in the Puna of northwestern Argentina. Tectonics, 27(1).

Carrillo-Berumen, R., Quattrocchio, M. E., Helenes, J., 2013. Paleogene continental Palynomorphs of the formations Chorrillo Chico and Agua Fresca, Punta Prat, Magallanes, Chile. Andean Geology 40, 539-560.

Casadío, S., Griffin, M., Marenssi, S., Net, L., Parras, A., Rodríguez-Raising, M., Santillana, S., 2009. Paleontology and sedimentology of middle Eocene rocks in Lago Argentino area, Santa Cruz Province, Argentina. Ameghiniana 46, 27-48.

Castelli, J.C., Robertson, R., Harambour, S., 1992. Evaluación Geológica y Petrolera, bloques Última Esperanza Sur e Isla Riesco. Empresa Nacional de Petróleo (ENAP), Unpublished technical report, 160 p.

Castelli, J.C., Robertson, R., Harambour, S., 1993. Evaluación geológica y Petrolera de los bloques Ultima Esperanza sur e Isla Riesco. Informe Archivo Técnico ENAP, Santiago, (Inédito).

Catuneanu, O. 2004. Retroarc foreland systems—evolution through time. Journal of African Earth Sciences 38, 225-242.

Catuneanu, O., 2019a. Scale in sequence stratigraphy. Marine and Petroleum Geology, 106, 128-159.

Catuneanu, O., 2019b. First-order foreland cycles: Interplay of flexural tectonics, dynamic loading, and sedimentation. Journal of Geodynamics, 129, 290-298.

Catuneanu, O., Beaumont, C., Waschbusch, P., 1997. Interplay of static loads and subduction dynamics in foreland basins: Reciprocal stratigraphies and the "missing" peripheral bulge. Geology 25, 1087-1090.

Catuneanu, O., Galloway, W.E., Kendall, C.G.S.C., Miall, A.D., Posamentier, H.W., Strasser, A., Tucker, M E., 2011. Sequence stratigraphy: methodology and nomenclature. Newsletters on Stratigraphy 44, 173-245.

Cawood, P. A. (2005). Terra Australis Orogen: Rodinia breakup and development of the Pacific and Iapetus margins of Gondwana during the Neoproterozoic and Paleozoic. Earth-Science Reviews, 69(3-4), 249-279.

Cecioni, G., 1955. Distribuzione verticale de alcuniKosmmaticeratidae nella Patagonia cilena. Italia Servizio Geol. Boll. 74, 141-149.

Cecioni, G., 1957. Cretaceous flysch and molasse in Departamento Ultima Esperanza, Magallanes Province, Chile. Am. Association of Petroleum Geologist Bulletin 11, 111-120.

Charrier, R., Lahsen, A., 1969. Stratigraphy of Late Cretaceous-Early Eocene, Seno Skyring –Strait of Magellan Area, Magallanes Province, Chile. Am. Association of Petroleum Geologist Bulletin 53, 568-590.

Chapman, J. B., Carrapa, B., DeCelles, P. G., Worthington, J., Mancin, N., Cobianchi, M., ... & Oimahmadov, I. (2019). The Tajik Basin: A composite record of sedimentary basin evolution in response to tectonics in the Pamir. Basin Research, 32(3), 525-545.

Coates, L., & MacEachern, J. A. (2007). The Ichnological Signatures of River- and Wave-Dominated Delta Complexes: Differentiating Deltaic and Non-Deltaic Shallow Marine Successions, Lower Cretaceous Viking Formation and Upper Cretaceous Dunvegan Formation, West-Central Alberta. In J. A. MacEachern, K. L. Bann, M. K. Gingras, & S. G. Pemberton (Eds.), Applied Ichnology (Vol. 52, pp. 227–254). SEPM Society for Sedimentary Geology. https://doi.org/10.2110/pec.07.52.0227.

Coutts, D.S., Matthews, W.A., Hubbard, S.M., 2019. Assessment of widely used methods to derive depositional ages from detrital zircon populations. Geoscience Frontiers 10, 1421-1435.

Condie, K. C. (1991). Another look at rare earth elements in shales. Geochimica et Cosmochimica Acta, 55(9), 2527-2531.

Coutand, I., Diraison, M., Cobbold, P.R., Gapais, D., Rossello, E.A., Millar. M., 1999. Structure and kinematics of a foothills transect, Lago Viedma, southern Andes (49° 30`S). J. S. Am. Earth Science 12, 1–15.

Covault, J.A., Romans, B.W., Graham, S.A., 2009. Outcrop expression of a continental margin-scale shelf-edge delta from the Cretaceous Magallanes Basin, Chile. Journal of Sedimentary Research 79, 523–539, doi:10.2110/jsr.2009.053

Cowan, D.S., Brandon, M.T., Garver, J.I., 1997. Geologic tests of hypotheses for large coastwise displacements a critique illustrated by the baja british-columbia controversy. American Journal of Science, 297, p. 117-173.

Cramer, B.S., Toggweiler, J.R., Wright, J.D., Katz, M.E., Miller, K.G., 2009. Ocean overturning since the Late Cretaceous: Inferences from a new benthic foraminiferal isotope compilation. Paleoceanography 24, PA4216. https://doi.org/10.1029/2008PA001683.

Critelli, S., & Le Pera, E. (1994). Detrital modes and provenance of Miocene sandstones and modern sands to the Southern Apennines thrust-top basins (Italy). Journal of Sedimentary Research, 64(4a), 824-835.

Cross, T.A., Pilger Jr, R.H., 1978. Tectonic controls of Late Cretaceous sedimentation, western interior, USA. Nature 274, 653-657.

Cuitiño, J.I., Scasso, R., 2010. Sedimentología y paleoambientes del Patagoniano y su transición a la Formación Santa Cruz al sur del Lago Argentino, Patagonia Austral. Revista de la Asociación Geológica Argentina 66, 406-417.

Cuitiño, J.I., 2011. Registro sedimentológico e isotópico de paleoambientes marinos y transicionales en el Patagoniano (mioceno) del Lago Argentino. Facultad de Ciencias Exactas y Naturales, Universidad de Buenos Aires, Tesis Doctoral (Inédita).

Cuitiño, J.I., Scasso, R., 2013a. Reworked pyroclastic beds in the early Miocene of Patagonia: reaction in response to high sediment supply during explosive volcanic events. Sedimentary Geology 289, 194-209.

Cuitiño, J.I., Ventura, R., Scasso, R., 2013b. Insights into the distribution of shallow-marine to estuarine early Miocene oysters from Southwestern Patagonia: sedimentological and stable isotope constraints. PALAIOS 28, 583-598.

Cuitiño, J.I., Fernicola, J.C., Kohn, M., Trayler, R., Naipauer, M., Bargo, M.S., Kay, R.F., Vizcaíno, S.F., 2016. U-Pb geochronology of the Santa Cruz Formation (early Miocene) at the Río Bote and Río Santa Cruz (southernmost Patagonia, Argentina): implications for the correlation of fossil vertebrate localities. J. of South American Earth Sciences 70, 198-210.

Cullers, R. L. (2000). The geochemistry of shales, siltstones and sandstones of Pennsylvanian–Permian age, Colorado, USA: implications for provenance and metamorphic studies. Lithos, 51(3), 181-203.

Cunningham, W.D., 1993. Strike-slip faults in the southernmost Andes and the development of the Patagonian Orocline. Tectonics, 12, p. 186-199.

Cunningham, W., 1995. Orogenesis at the southern tip of the Americas; the structural evolution of the Cordillera Darwin metamorphic complex, southernmost Chile. Tectonophysics, 244, p. 197–229, doi: 10 .1016/0040-1951(94)00248-8.

Cunningham, D.W., Dalziel, I.A.W., Tung-Yi, L., Lawver, L.A., 1995. Southernmost South America–Antarctic Peninsula relative plate motions since 84 Ma: Implications for the tectonic evolution of the Scotia Arc region. Journal of Geophysical Research, 100, p. 8257–8266, doi: 10.1029/95JB00033.

Dalrymple, R.W., Zaitlin, B.A., Boyd, R., 1992. Estuarine facies models: conceptual basis and stratigraphic implications. Journal of Sedimentary Petrology 62, 1130-1146.

Dalziel, I.W.D., de Wit, M.F., Palmer, K.F., 1974. Fossil marginal basin in the southern Andes. Nature 250, 291–294.

Dalziel, I.W.D., 1981. Back-arc extension in the southern Andes: A review and critical reappraisal. Philosophical Transactions of the Royal Society London A, 300, 319–335, doi:10.1098/rsta.1981.0067.

Dalziel, I.W.D., Brown, R.L., 1989. Tectonic denudation of the Cordillera Darwin metamorphic core complex in the Andes of Tierra del Fuego, southernmost Chile: Implications for Cordilleran Orogenesis. Geology, 17, p. 699-703.

Daniels, B. G., Auchter, N. C., Hubbard, S. M., Romans, B. W., Matthews, W. A., & Stright, L. (2018). Timing of deep-water slope evolution constrained by large-n detrital and volcanic ash zircon geochronology, Cretaceous Magallanes Basin, Chile. GSA Bulletin, 130(3-4), 438-454.

Daniels, B.G., Hubbard, S.M., Romans, B.W., Malkowski, M.A., Matthews, W.A., Bernhardt, A., Fildani, A., Graham, S.A., 2019. Revised chronostratigraphic framework for the Cretaceous Magallanes-Austral Basin, Última Esperanza Province, Chile. Journal of South American Earth Sciences 94, 102209. https://doi.org/10.1016/j.jsames.2019.05.025.

Dávila, F.M., Ávila, P., Martina, F., 2019. Relative contributions of tectonics and dynamic topography to the Mesozoic-Cenozoic subsidence of southern Patagonia. Journal of South American Earth Sciences 93, 412-423.

Davis, J., C., 2002. Statistics and Data Analysis in Geology, 3rd Edition. Wiley

DeCelles, P.G., Gray, M. B., Ridgway, K.D., Cole, R.B., Pivnik, D.A., Pequera, N., Srivastana, P., 1991. Controls on synorogenic alluvial-fan architecture, Beartooth Conglomerate (Paleocene), Wyoming and Montana. Sedimentology, 38, p. 567-590.

DeCelles, P.G., Giles, K.A., 1996. Foreland basin systems. Basin Research, 8(2), p. 105-123.

DeCelles, P.G., 2004. Late Jurassic to Eocene evolution of the Cordilleran thrust belt and foreland basin system, western USA. American Journal of Sciences, 304, 105-168.

DeCelles, P.G., Ducea, M.H., Kapp, P., Zandt, G., 2009. Cyclicity in Cordilleran orogenic systems. Nature Geosciences, 2, p. 251-257.

DeCelles, P.G., Carrapa, B., Horton, B.K., Gehrels, , G.E., 2011. Cenozoic foreland basin systems in the central Andes of northwestern Argentina: implications for Andean geodynamics and modes of deformation. Tectonic, 30, TC6013.

DeCelles, P.G., 2012. Foreland basin systems revisited: variations in response to tectonic settings. In: Busby, C., Azor, A. (Eds.), Tectonics of sedimentary basins: recent advances. Wiley-Blackwell, Oxford, UK, pp. 405-426.

DeCelles, P.G., Zandt, G., Beck, S.L., Currie, C.A., Ducea, M.N., Kapp, P., Gehrels, G.E., Carrapa, B., Quade, J., Schoenbohm, L.M., 2015. Cyclical orogenic processes in the Cenozoic Central Andes. In: DeCelles, P.G., Ducea, M.N., Carrapa, B., Kapp, P.A. (Eds.), Geodynamics of a Cordilleran Orogenic System: The Central Andes of Argentina and Northern Chile. Geological Society of America Memoir, vol. 212. pp. 459–490 doi:10.1130/2015.1212(22)

Dewey, J.F., and Bird, J., 1970. Mountain belts and the new global tectonics. Journal of Geophysical Research, 75, p. 2625–2647, doi: 10.1029/JB075i014p02625.

Dickinson, W. R. (1970). Interpreting detrital modes of graywacke and arkose. Journal of Sedimentary Research, 40(2), 695-707.

Dickinson, W.R., and Snyder, W.S., 1979. Geometry of subducted slabs related to San Andreas transform. The Journal of Geology 87, p. 609–627, doi: 10.1086/628456.

Dickinson, W.R., Suczek, C.A., 1979. Plate tectonics and sandstone compositions. AAPG Bulletin 63, 2164-2182.

Dickinson, W.R., 1985. Interpreting provenance relations from detrital modes of sandstones. In: Zuffa, G. (Ed.), Provenance of arenites. Springer, Dordrecht, pp. 333-361.

Dickinson, W. R. (1988). Provenance and sediment dispersal in relation to paleotectonics and paleogeography of sedimentary basins. In New perspectives in basin analysis (pp. 3-25). Springer, New York, NY.

Dickinson, W.R., Gehrels, G.E., 2009. Use of U-Pb ages of detrital zircon to infer maximum depositional ages of strata: A test against a Colorado Plateau Mesozoic database. Earth and Planetary Science Letters 288, 115-125.

Diraison, M., Cobbold, P.R., Gapais, D., Rossello, E.A., 1998. Magellan strait: part of a Neogene rift system. Geology, 25, p. 703-706.

Diraison, M., Cobbold, P.R., Gapais, D., Rossello, E.A., Le Corre, C., 2000. Cenozoic crustal thickening, wrenching and rifting in the foothills of the southernmost Andes. Tectonophysics, 316, p. 91–119, doi:10.1016/S0040-1951(99)00255-3.

Dodson, M.H., Compston, W., Williams, I.S., Wilson, J.F., 1988. A search for ancient detrital zircons in Zimbabwean sediments. Journal of the Geological Society of London 145, 977-983.

Dott Jr, R.H., Bourgeois, J., 1982. Hummocky stratification: significance of its variable bedding sequences. Geological Society of America Bulletin 93, 663-680.

Dumas, S., Arnott, R.W., 2006. Origin of hummocky and swaley cross-stratification—The controlling influence of unidirectional current strength and aggradation rate. Geology 34, 1073-1076.

Dumitru, T. A. (1993). A new computer-automated microscope stage system for fission-track analysis. Nuclear Tracks and Radiation Measurements, 21(4), 575-580.

Eagles, G., Livermore, R. A., Fairhead, J. D., & Morris, P. (2005). Tectonic evolution of the west Scotia Sea. Journal of Geophysical Research: Solid Earth, 110(B2).

Eagles, G., Livermore, R., Morris, P., 2006. Small basins in the Scotia Sea: The Eocene Drake Passage gateway. Earth and Planetary Science Letters, 242, p. 343–353, doi: 10.1016/j.epsl.2005.11.060.

Eagles, G., & Scott, B. G. (2014). Plate convergence west of Patagonia and the Antarctic Peninsula since 61 Ma. Global and Planetary Change, 123, 189-198.

Eagles, G., & Jokat, W. (2014). Tectonic reconstructions for paleobathymetry in Drake Passage. Tectonophysics, 611, 28-50.

Espinoza, F., Morata, D., Polvé, M., Lagabrielle, Y., Maury, R.C., Guivel, C., Cotten, J., Bellon, H., Suárez, M., 2010. Middle Miocene calc-alkaline volcanism in central Patagonia (47°S): petrogénesis and implications for slab dynamics. Andean Geology, 37, p. 300-328.

Falk, P.D., Dorsey, R.J., 1998. Rapid development of gravelly high-density turbidity currents in marine Gilbert-type fan deltas, Loreto Basin, Baja California Sur, Mexico. Sedimentology 45, 331-349.

Farfán, L., 1994. Geología Estructural de la Península Brunswick, Región de Magallanes, Chile. Mem. Título, Univ. De Chile, Santiago.

Farley, Kenneth A. (2002). (U-Th)/He Dating: Techniques, Calibrations, and Applications. In: Noble Gases in Geochemistry and Cosmochemistry. Reviews in Mineralogy and Geochemistry. No.47. Mineralogical Society of America, Washington, DC, pp. 819-844. https://resolver.caltech.edu/CaltechAUTHORS:20121116-080830444

Feruglio, E., 1949-50. Descripción Geológica de la Patagonia. Dirección General de Yacimientos Petrolíferos Fiscales. Ministerio de Industria y Comercio de la República de la Argentina. Buenos Aires. v.1, 1-334.

Fildani, A., Cope, T.D., Graham, S.A., Wooden, J.L., 2003. Initiation of the Magallanes foreland basin: Timing of the southernmost Patagonian Andes orogeny revised by detrital zircon provenance analysis. Geology 31, 1081-1084.

Fildani, A., Hessler, A.M., 2005. Stratigraphic record across a retroarc basin inversion: Rocas Verdes-Magallanes Basin, Patagonian Andes, Chile. GSA Bulletin 117, 1596-1614.

Fildani, A., Romans, B.W., Fosdick, J.C., Crane, W.H., Hubbard, S.M., 2008. Orogenesis of the Patagonian Andes as reflected by basin evolution in southernmost South America. In Spencer, J.E., Titley, S.R., /eds), Ores and orogenesis: Circum-Pacific tectonics, geologic evolution, and ore deposits. Arizona Geological Society Digest 22, 259-268.

Fisher, N. I., & Powell, C. M. (1989). Statistical analysis of two-dimensional palaeocurrent data: Methods and examples. Journal of the Geological Society of Australia, 36(1), 91-107.

Flemming, B.W., 2000. A revised textural classification of gravel-free muddy sediments on the basis of ternary diagrams. Continental Shelf Research 20, 1125-1137.

Flint, S.S., Prior, D.J., Agar, S.M., Turner, P., 1994. Stratigraphic and structural evolution of the Tertiary Cosmelli basin and its relationship to the Chile triple junction. Journal of the Geological Society, 151, p. 251-268.

Flowers, R. M., Ketcham, R. A., Shuster, D. L., & Farley, K. A. (2009). Apatite (U–Th)/He thermochronometry using a radiation damage accumulation and annealing model. Geochimica et Cosmochimica acta, 73(8), 2347-2365.

Folguera, A., and Ramos, V.A., 2002. Partición de la deformación durante el Neógeno en los Andes Patagónicos Septentrionales (37°-46°S). Acta Geológica Hispanica, 37, p. 329-353.

Folguera, A., & Ramos, V. A. (2011). Repeated eastward shifts of arc magmatism in the Southern Andes: a revision to the long-term pattern of Andean uplift and magmatism. Journal of South American Earth Sciences, 32(4), 531-546.

Folguera, A., Encinas, A., Echaurren, A., Gianni, G., Orts, D., Valencia, V., & Carrasco, G. (2018). Constraints on the Neogene growth of the central Patagonian Andes at the latitude of the Chile triple junction (45–47 S) using U/Pb geochronology in synorogenic strata. Tectonophysics, 744, 134-154.

Forsythe, R., and Prior, D.J., 1992. Cenozoic continental geology of South America and its relations to the evolution of the Chile triple junction of the Ocean Drilling Program. Initial Report, 141, p. 23-31.

Fossa Mancini, E., Feruglio, E., Yausen de Campana, J.C., 1938. Una reunión de Geólogos de YPF y el problema de la Terminología Estratigráfica. Boletín de Informaciones Petroleras. v.15, 31-95.

Fosdick, J.C., Romans, B.W., Fildani, A., Bernhardt, A., Calderón, M., Graham, S.A., 2011. Kinematic evolution of the Patagonian retro-arc fold-and-thrust belt and Magallanes foreland basin, Chile and Argentina, 51°30'S. Geological Society of America Bulletin 123, 1679-1698.

Fosdick, J.C., Grove, M., Hourigan, J.K., Calderón, M. 2013. Retroarc deformation and exhumation near the end of the Andes, Southern Patagonia. Earth and Planetary Science Letters 361, 504-517.

Fosdick, J.C., Graham, S.A., Hilley, G.E., 2014. Influence of attenuated lithosphere and sediment loading on flexure of the deep-water Magallanes retroarc foreland basin, Southern Andes, Tectonics, 33, 2505–2525, doi: 10.1002/2014TC003684.

Fosdick, J.C., Grove, M., Graham, S.A., Hourigan, J.K., Lovera, O., Romans, B.W., 2015. Detrital thermochronologic record of burial heating and sediment recycling in the Magallanes foreland basin, Patagonian Andes. Basin Research 27, 546-572.

Fosdick, J. C., VanderLeest, R. A., Bostelmann, J. E., Leonard, J. S., Ugalde, R., Oyarzún, J. L., ... & Simms, A. R. (2020). Revised timing of Cenozoic Atlantic incursions and changing hinterland sediment sources during southern Patagonian orogenesis. *Lithosphere, 2020(1).*

Fox, M., & Shuster, D. L. (2014). The influence of burial heating on the (U–Th)/He system in apatite: Grand Canyon case study. Earth and Planetary Science Letters, 397, 174-183.

Gabriel, K. R. (1971). The biplot graphic display of matrices with application to principal component analysis. Biometrika, 58(3), 453-467.

Galaz, G., Hervé, F., & Calderón, M. (2005). Metamorfismo y deformación de la Formación Tobífera en la cordillera Riesco, región de Magallanes, Chile: evidencias para su evolución tectónica. Revista de la Asociación Geológica Argentina, 60(4), 762-774.

Gallagher, K., Brown, R., & Johnson, C. (1998). Fission track analysis and its applications to geological problems. Annual Review of Earth and Planetary Sciences, 26(1), 519-572.

Galbraith, R. F. (2005). Statistics for fission track analysis. Chapman and Hall/CRC.

Galbraith, R. F., & Green, P. F. (1990). Estimating the component ages in a finite mixture. International Journal of Radiation Applications and Instrumentation. Part D. Nuclear Tracks and Radiation Measurements, 17(3), 197-206.

Galbraith, R. F., & Laslett, G. M. (1993). Statistical models for mixed fission track ages. Nuclear tracks and radiation measurements, 21(4), 459-470.

Gallardo, R. E. (2014). Seismic sequence stratigraphy of a foreland unit inthe Magallanes-Austral Basin, Dorado Riquelme Block, Chile: Implications for deep-marine reservoirs. Latin American journal of sedimentology and basin analysis, 21(1), 49-64.

Garver, J. I., Royce, P. R., & Smick, T. A. (1996). Chromium and nickel in shale of the Taconic foreland; a case study for the provenance of fine-grained sediments with an ultramafic source. Journal of Sedimentary Research, 66(1), 100-106.

Garzanti, E., Ando, S., & Scutella, M. (2000). Actualistic ophiolite provenance: the Cyprus case. The Journal of Geology, 108(2), 199-218.

Garzanti, E., Vezzoli, G., & Ando, S. (2002). Modern sand from obducted ophiolite belts (Sultanate of Oman and United Arab Emirates). The Journal of geology, 110(4), 371-391.

Garzanti, E., Padoan, M., Setti, M., López-Galindo, A., & Villa, I. M. (2014). Provenance versus weathering control on the composition of tropical river mud (southern Africa). Chemical Geology, 366, 61-74.

Garzanti, E., & Resentini, A. (2016). Provenance control on chemical indices of weathering (Taiwan river sands). Sedimentary Geology, 336, 81-95.

Garzanti, E., Al-Juboury, A. I., Zoleikhaei, Y., Vermeesch, P., Jotheri, J., Akkoca, D. B., ... & Vezzoli, G. (2016). The Euphrates-Tigris-Karun river system: Provenance, recycling and dispersal of quartz-poor foreland-basin sediments in arid climate. Earth-Science Reviews, 162, 107-128.

Gautheron, C., & Tassan-Got, L. (2010). A Monte Carlo approach to diffusion applied to noble gas/helium thermochronology. Chemical Geology, 273(3-4), 212-224.

Gautheron, C., Tassan-Got, L., Barbarand, J., & Pagel, M. (2009). Effect of alpha-damage annealing on apatite (U–Th)/He thermochronology. Chemical Geology, 266(3-4), 157-170.

Gehrels, G., 2000. Introduction to detrital zircon studies of Paleozoic and Triassic strata in western Nevada and northern California. In: Soreghan, M., Gehrels, G. (Eds.), Paleozoic and Triassic paleogeography and tectonics of western Nevada and northern California. Geological Society of America Special Paper 347, pp. 1-17.

Gehrels, G., 2012. Detrital Zircon U-Pb Geochronology: Current Methods and New Opportunities. In: Busby, C., Azor, A. (Eds.), Tectonics of Sedimentary Basins. Blackwell Publishing Ltd, pp. 47-62.

Gehrels, G. (2014). Detrital zircon U-Pb geochronology applied to tectonics. Annual Review of Earth and Planetary Sciences, 42, 127-149.

George, S.W., Davis, S.N., Fernández, R.A., Manríquez, L.M., Leppe, M.A., Horton, B.K., Clarke, J.A., 2020. Chronology of deposition and unconformity development across the Cretaceous–Paleogene boundary, Magallanes-Austral Basin, Patagonian Andes. Journal of South American Earth Sciences, 102237, https://doi.org/10.1016/j.jsames.2019.102237.

Ghiglione, M.C., Ramos, V.A., Cristallini, E.O., 2002. Estructura y estratos de crecimiento en la faja plegada y corrida de los Andes fueguinos. Andean Geology, 29, p. 17-41.

Ghiglione, M.C., Ramos, V.A., 2005. Chronology of deformation in the Southernmost Andes of Tierra del Fuego. Tectonophysics 405, 25–46.

Ghiglione, M.C., Yagupsky, D., Ghidella, M., Ramos, V.A., 2008. Continental stretching preceding the opening of the Drake Passage: Evidence from Tierra del Fuego. Geology, 36, p. 643–646, doi: 10.1130/G24857A.1.

Ghiglione, M.C., Suárez, F., Ambrosio, A., Da Poian, G., Cristallini, E.O., Pizzio, M.F., Reinoso, R.M., 2009. Structure and evolution of the Austral Basin, Fold-Thrust Belt, Southern Patagonian Andes. Revista de la Asociación Geológica Argentina 65, 215-226.

Ghiglione, M.C., Quinteros, J., Yagupsky, D., Bonillo-Martínez, P., Hlebszevtich, J., Ramos, V.A., Quesada, S., 2010. Structure and tectonic history of the foreland basins of southernmost South America. Journal of South American Earth Sciences, 29, p. 262-277.

Ghiglione, M.C., Likerman, J., Barberón, V., Giambiagi, L.B., Aguirre-Urreta, B., Suárez, F., 2014. Geodynamic context for the deposition of coarse-grained deep-water axial channel systems in the Patagonian Andes. Basin Research, 1–20, doi: 10.1111/bre.12061.

Ghiglione, M.C., Ramos, V.A., Cuitiño, J., Barberón, V., 2016. Growth of the Southern Patagonian Andes (46–53°S) and their relation to subduction processes. In Folguera, A., Naipauer, M., Sagripanti, L., Ghiglione, M., Orts, D. y Giambiagi L. (eds.), Growth of the Southern Andes. Springer Earth System Sciences, Amsterdam, 201-240.

Ghiglione, M. C., Rocha, E., Raggio, M. F., Ramos, M. E., Ronda, G., Moyano-Paz, D., ... & Valencia, V. (2021). Santonian–Campanian continentalization in the Austral-Magallanes basin: regional correlation, provenance and geodynamic setting. Cretaceous Research, 128, 104968.

Giacosa, R., Fracchia, D., Heredia, N., Pereyra, F., 2013. Hoja Geológica 4972-III y 4975-IV, El Chaltén, provincia de Santa Cruz. Instituto de Geología y Recursos Minerales. Servicio Geológico Minero Argentino. Boletín 399, 89p. Buenos Aires.

Gianni, G. M., & Luján, S. P. (2021). Geodynamic controls on magmatic arc migration and quiescence. Earth-Science Reviews, 218, 103676.

Gianni, G.M., Dávila, F., Echaurren, A., Fennell, L., Tobal, J., Navarrete, C.R., Quezada, P., Folguera, A., Giménez, M., 2018a. A geodynamic model linking Cretaceous orogeny, arc migration, foreland basin subsidence and marine ingression in southern South America. Earth-Science Reviews 185, 437-462.

Gianni, G. M., Pesce, A., & Soler, S. R. (2018b). Transient plate contraction between two simultaneous slab windows: Insights from Paleogene tectonics of the Patagonian Andes. Journal of Geodynamics, 121, 64-75.

Gombosi, D. J., Barbeau Jr, D.L., Garver, J.I., 2009. New thermochronometric constraints on the rapid Paleogene exhumation of the Cordillera Darwin complex and related thrust sheets in the Fuegian Andes. Terra Nova, 21, p. 507-515.

Gómez, E., Jordan, T. E., Allmendinger, R. W., & Cardozo, N. (2005). Development of the Colombian foreland-basin system as a consequence of diachronous exhumation of the northern Andes. Geological Society of America Bulletin, 117(9-10), 1272-1292.

González, E., Tapia, G. 1952. Levantamiento geológico estructural en el área de Estancia El Salto y sección Las Coles. Informe Archivo Técnico ENAP, Santiago. (Inédito).

González, E. 1953. Estratigrafía y distribución de los grupos El Salto y Palomares en gran parte de la cuenca de Magallanes. Informe Archivo Técnico ENAP, Santiago. (Inédito).

González Estebenet, G., Guerstein, G. R., & Casadío, S. (2015). Estudio bioestratigráfico y paleoambiental de la Formation Río Turbio (Eoceno medio a tardío) en el sudoeste de Patagonia (Argentina) basado en quistes de dinoflagelados. Revista Brasilera de Paleontología, 18, 429.

Gorring, M.L., Kay, S.M., Zeitler, P.K., Ramos, V.A., Rubiolo, D., Fernandez, M.I., Panza, J.L., 1997. Neogene Patagonian plateau lavas: Continental magmas associated with ridge collision at the Chile Triple Junction. Tectonics 16, 1–17.

Guillaume, B., Martinod, J., Husson, L., Roddaz, M., & Riquelme, R. (2009). Neogene uplift of central eastern Patagonia: Dynamic response to active spreading ridge subduction?. Tectonics, 28(2).

Guillaume, B., Gautheron, C., Simon-Labric, T., Martinod, J., Roddaz, M., & Douville, E. (2013). Dynamic topography control on Patagonian relief evolution as inferred from low temperature thermochronology. Earth and Planetary Science Letters, 364, 157-167.

Guler, M.V., Estebenet, M.S.G., Navarro, E.L., Astini, R.A., Panera, J.P.P., Ottone, E.G., Paolillo, M.A., 2019. Maastrichtian to Danian Atlantic transgression in the north of Patagonia: A dinoflagellate cyst approach. Journal of South American Earth Sciences 92, 552-564.

Gurnis, M. (1992). Rapid continental subsidence following the initiation and evolution of subduction. Science, 255(5051), 1556-1558.

Gutiérrez, N.M., Le Roux, J.P., Vásquez, A., Carreño, C., Pedroza, V., Araos, J., Oyarzún, J.L., Pino, J.P., Rivera, H.A., Hinojosa, L.F., 2017. Tectonic events reflected by palaeocurrents, zircon geochronology, and palaeobotany in the Sierra Baguales of Chilean Patagonia. Tectonophysics 695, 76-99.

Haq, B.U., 2014. Cretaceous eustasy revisited. Global and Planetary Change 113, 44-58.

Haq, B. U., Hardenbol, J. A. N., & Vail, P. R. (1987). Chronology of fluctuating sea levels since the Triassic. Science, 235(4793), 1156-1167.

Haughton, P., Davis, C., McCaffrey, W., Barker, S., 2009. Hybrid sediment gravity flow deposits–classification, origin and significance. Marine and Petroleum Geology 26, 1900-1918.

Hedberg, H.D., 1976. International Stratigraphic Guide: A Guide to Stratigraphic Classification. Terminology and Procedure, by the International Subcommission on Stratigraphic Classification of IUGS Commission of Stratigraphy. Wiley Interscience Publication, New York, pp 200.

Heller, P.L., Angevine, C.L., Winslow, N., Paola, C., 1988. Two-phase stratigraphic model of foreland basin sequences. Geology, 16, 501-504.

Hernández, R.M., Jordan, T.E., Farjat, A.D., Echavarría, L., Idleman, B.D., Reynolds, J.H., 2005. Age, distribution, tectonics, and eustatic controls of the Paranense and Caribbean marine transgressions in southern Bolivia and Argentina. Journal of South American Earth Sciences 19, 495-512.

Herngreen, G.F.W., Kedves, M., Rovnina, L.V., Smirnova, S.B. 1996. Cretaceous palynofloral provinces: a review. In: Jansonius, J., McGregor, D.C. (Eds.), Palynology: Principles and Applications. American Association of Stratigraphic Palynologists Foundation, pp. 1157-1188.

Herron, E., Heirtzler, J., 1967. Sea-floor spreading near the Galápagos. Science 158, 775-780.

Hervé, F., Fanning, C.M., Pankhurst, R.J., 2003. Detrital zircon age patterns and provenance of the metamorphic complexes of southern Chile. Journal of South American Earth Sciences 16, 107-123.

Hervé, F., Godoy, E., Mpodozis, C., Fanning, M., 2004. Monitoring magmatism of the Patagonian Batholith through the U-Pb SHRIMP dating of detrital zircons in sedimentary units of the Magallanes Basin. In:

Carcione, J.; Donda, F.; Lodolo, E. (Eds.), International Symposium on the Geology and Geophysics of the Southernmost Andes, the Scotia Are and the Antarctic Península, GEOSUR. Bolletino di Geofísica Teórica ed Applicata 45, 113-117.

Hervé, F., 2005. Estudio de la cronología y proveniencia de las Formaciones Terciarias de la cuenca de Magallanes mediante la datación U/Pb de sus poblaciones de circones detríticos. Informe Archivo Técnico ENAP, Santiago. (Inédito).

Hervé, F., Pankhurst, R.J., Fanning, C.M., Calderón, M., Yaxley, G.M., 2007. The South Patagonian batholith: 150 my of granite magmatism on a static plate margin. Lithos 97, 373-394.

Hervé, F., Fanning, C.M., Pankhurst, R.J., Mpodozis, C., Klepeis, K., Calderón, M., Thomson, S.N., 2010. Detrital zircon SHRIMP U–Pb age study of the Cordillera Darwin Metamorphic Complex of Tierra del Fuego: sedimentary sources and implications for the evolution of the Pacific margin of Gondwana. Journal of the Geological Society 167, 555-568.

Hiscott, R. N. (1984). Clay mineralogy and clay-mineral provenance of Cretaceous and Paleogene strata, Labrador and Baffin shelves. Bulletin of Canadian Petroleum Geology, 32(3), 272-280.

Hoffstetter, R., Fuenzalida, H., Cecioni, G. 1957. Chile. In: Lexique Stratigraphique International, Vol. 5. Centre National de la Recherche Scientifique V, Paris, pp 444.

Hollister, J.S., 1944. Report petroleum Survey. Informe Archivo Técnico ENAP, Santiago. (Inédito).

Hoorn, C., Guerrero, J., Sarmiento, G. A., & Lorente, M. A. (1995). Andean tectonics as a cause for changing drainage patterns in Miocene northern South America. Geology, 23(3), 237-240.

Hoorn, C., Wesselingh, F. P., Ter Steege, H., Bermudez, M. A., Mora, A., Sevink, J., ... & Antonelli, A. (2010). Amazonia through time: Andean uplift, climate change, landscape evolution, and biodiversity. science, 330(6006), 927-931.

Horton, B. K., & DeCelles, P. G., 2001. Modern and ancient fluvial megafans in the foreland basin system of the central Andes, southern Bolivia: Implications for drainage network evolution in fold-thrust belts. Basin Research, 13 (1), 43-63.

Horton, B. K., Fuentes, F., 2016. Sedimentary record of plate coupling and decoupling during growth of the Andes. Geology, 44, p. 647-650.

Horton, B. K., Fuentes, F., Boll, A., Starck, D., Ramirez, S. G., Stockli, D. F., 2016. Andean stratigraphic record of the transition from backarc extension to orogenic shortening: a case study from the northern Neuquén Basin, Argentina. Journal of South American Earth Sciences, 71, p. 17-40.

Horton, B.K., 2018a. Sedimentary record of Andean mountain building. Earth-Science Reviews, 178, p. 279-309.

Horton, B.K., 2018b. Tectonic regimes of the Central and Southern Andes: responses to variations in plate coupling during subduction. Tectonics, 37, p. 402-429.

Horton, B. K., 2021. Unconformity development in retroarc foreland basins: Implications for the geodynamics of Andean-type margins. Journal of the Geological Society.

Hubbard, S.M., Romans, B.W., Graham, S.A., 2008. Deep-water foreland basin deposits of the Cerro Toro Formation, Magallanes basin, Chile: Architectural elements of a sinuous basin axial channel belt. Sedimentology 55, 1333–1359, doi:10.1111/j.1365-3091.2007.00948.x.

Hubbard, S.M., Fildani, A., Romans, B.W., Covault, J.A., McHargue, T.R., 2010. High-relief slope clinoform development : insights from outcrop, Magallanes Basin, Chile. Journal of Sedimentary Research 80, 357-375.

Hubbard, S. M., Covault, J. A., Fildani, A., & Romans, B. W. (2014). Sediment transfer and deposition in slope channels: Deciphering the record of enigmatic deep-sea processes from outcrop. Bulletin, 126(5-6), 857-871.

Hünicken, M., 1955. Depósitos neocretácicos y terciarios del extremo SSW de Santa Cruz. Cuenca carbonífera de Río Turbio. Revista del Instituto Nacional de Investigaciones de las Ciencias Naturales y Museo Argentino de Ciencias Naturales "Bernardino Rivadavia", Ciencias Geológicas 4, 1-164.

Hurford, A. J. (2019). An historical perspective on fission-track thermochronology. Fission-Track Thermochronology and its application to geology, 3-23.

Hurford, A. J., & Green, P. F. (1983). The zeta age calibration of fission-track dating. Chemical Geology, 41, 285-317.

Hurford, A. J., & Carter, A. (1991). The role of fission track dating in discrimination of provenance. Geological Society, London, Special Publications, 57(1), 67-78.

Ingersoll, R.V., Bullard, T.F., Ford, R.L., Grimm, J.P., Pickle, J.D., Sares, S.W., 1984. The effect of grain size on detrital modes: a test of the Gazzi-Dickinson point-counting method. Journal of Sedimentary Research 54, 103-116.

Ingersoll, R. V., & Cavazza, W. (1991). Reconstruction of Oligo-Miocene volcaniclastic dispersal patterns in north-central New Mexico using sandstone petrofacies.

Ingersoll, R. V., & Eastmond, D. J. (2007). Composition of modern sand from the Sierra Nevada, California, USA: implications for actualistic petrofacies of continental-margin magmatic arcs. Journal of Sedimentary Research, 77(9), 784-796.

Ingersoll, R. V. (2012). Composition of modern sand and Cretaceous sandstone derived from the Sierra Nevada, California, USA, with implications for Cenozoic and Mesozoic uplift and dissection. Sedimentary Geology, 280, 195-207.

Ingle, J. C. (1980). Cenozoic paleobathymetry and depositional history of selected sequences within the southern California continental borderland.

Jackson, S.E., Pearson, N.J., Griffin, W.L. & Belousova, E.A., 2004. The application of laser ablation microprobe-inductively coupled plasma-mass spectrometry (LAM-ICPMS) to in situ U-Pb zircon geochronology. Chemical Geology 211, 47-69.

Jacques, J. M. (2004). The influence of intraplate structural accommodation zones on delineating petroleum provinces of the Sub-Andean foreland basins. Petroleum Geoscience, 10(1), 1-19.

Jaramillo, C., Romero, I., D'Apolito, C., Bayona, G., Duarte, E., Louwye, S., ... & Wesselingh, F. P. (2017). Miocene flooding events of western Amazonia. Science advances, 3(5), e1601693.

Jolivet, M., Brunel, M., Seward, D., Xu, Z., Yang, J., Roger, F., ... & Wu, C. (2001). Mesozoic and Cenozoic tectonics of the northern edge of the Tibetan plateau: fission-track constraints. Tectonophysics, 343(1-2), 111-134.

Jordan, T.E., Isacks, B.L., Allmendinger, R.W., Brewer, J.A., Ramos, V., Ando, C.J., 1983. Andean tectonics related to geometry of subducting Nazca Plate. Geological Society of America Bulletin, 94, 341-361.

Jordan, T.E., and Allmendinger, R.W., 1986. The Sierras Pampeanas of Argentina: A modern analogue of Rocky Mountain foreland deformation. American Journal of Science 286, p. 737–764, doi:10.2475/ajs.286.10.737.

Jordan, T.E., 1995. Retroarc foreland and related basins. In Busby, C.J., and Ingersoll, R.V (Eds.), Tectonics of Sedimentary Basins, Blackwell Science, Oxford. pp. 331-362.

Kamola, D.L., Huntoon, J E., 1995. Repetitive stratal patterns in a foreland basin sandstone and their possible tectonic significance. Geology 23, 177-180.

Katz, H.R., 1961. Descubrimiento de una microflora neocomiana en la Formación Agua Fresca (Eocena) de Magallanes y su significado con respecto a la evolución tectónica de la zona. Universidad de Chile, Facultad de Ciencias Físicas y Matemáticas, Anales 21, 133–141.

Katz, H.R., 1963. Revision of Cretaceous stratigraphy in Patagonian cordillera of Ultima Esperanza, Magallanes Province, Chile. American Association of Petroleum Geologist Bulletin 47, 506-524.

Ketcham, R. A. (2005). Forward and inverse modeling of low-temperature thermochronometry data. Reviews in mineralogy and geochemistry, 58(1), 275-314.

Ketcham, R. A., Gautheron, C., & Tassan-Got, L. (2011). Accounting for long alpha-particle stopping distances in (U–Th–Sm)/He geochronology: Refinement of the baseline case. Geochimica et Cosmochimica Acta, 75(24), 7779-7791.

Klepeis, K.A., 1994. Relationship between uplift of the metamorphic core of the southernmost Andes and shortening in the Magallanes foreland fold and thrust belt, Tierra del Fuego, Chile: Tectonics, v. 13, p. 882–904, doi:10.1029/94TC00628

Klepeis, K.A., Austin, J., 1997. Contrasting styles of superposed deformation in the southernmost Andes. Tectonics, 16, p. 776-755.

Klepeis, K., Betka, P., Clarke, G., Fanning, M., Hervé, F., Rojas, L., Mpodozis, C., Thomson, S., 2010. Continental underthrusting and obduction during the Cretaceous closure of the Rocas Verdes rift basin, Cordillera Darwin, Patagonian Andes, Tectonics, 29, TC3014, doi: 10.1029/2009TC002610.

KOHN, M. J., SPEAR, F. S., & DALZIEL, I. W. (1993). Metamorphic P–T paths from Cordillera Darwin, a core complex in Tierra del Fuego, Chile. Journal of Petrology, 34(3), 519-542.

Kohn, M.J., Spear, F.S., Harrison, T.M., Dalziel, I.W.D., 1995. 40Ar/39Ar geochronology and P-T-t paths from the Cordillera Darwin metamorphic complex, Tierra del Fuego, Chile. Journal of Metamorphic Geology 13, 251-270.

Kraemer, P.E., Ploszkiewicz, J.V., Ramos, V.A., 2002. Estructura de la Cordillera Patagónica Austral entre los 46° y 52°S, provincia de Santa Cruz, Argentina. In Haller, M.J., (Ed.), Geología y Recursos Naturales de Santa Cruz, Relatorio, p. 353-364.

Kraemer, P. E. (1998). Structure of the Patagonian Andes: Regional balanced cross section at 50 S, Argentina. International Geology Review, 40(10), 896-915.

Kraemer, P.E., 2003. Orogenic shortening and the origin of the Patagonian Orocline (56°S.Lat). Journal of South American Earth Sciences, 15, p. 731–748, doi: 10.1016/S0895 -9811 (02)00132-3.

Lagabrielle, Y., Suárez, M., Rosello, E., Hérail, G., Martinod, J., Regnier, M., de la Cruz, R., 2004. Neogene to Quaternary tectonic evolution of the Patagonian Andes at the latitude of the Chile triple junction. Tectonophysics, 385, p. 211-241.

Lawver, L. A., & Gahagan, L. M. (2003). Evolution of Cenozoic seaways in the circum-Antarctic region. Palaeogeography, Palaeoclimatology, Palaeoecology, 198(1-2), 11-37.

Lawver, L.A., Gahagan, L.M., Dalziel, I.W.D., 2014. Reconstructions of the southern ocean and Antarctic regions. In: De Broyer C, Koubbi P, Griffiths HJ, Raymond B, Udekem d'Acoz C d' (Eds), Biogeographic Atlas of the Southern Ocean, Cambridge, pp 36–42.

Leonard, J. S., Fosdick, J. C., & VanderLeest, R. A. (2020). Erosional and tectonic evolution of a retroarc orogenic wedge as revealed by sedimentary provenance: case of the Oligocene–Miocene Patagonian Andes. Frontiers in Earth Science, 7, 353.

Leppe, M., Mihoc, M., Varela, N., Stinnesbeck, W., Mansilla, H., Bierma, H., Cisterna, K., Frey, E., Jujihara, T., 2012. Evolution of the Austral-Antartic flora during the Cretaceous: New insights from a paleobiogeographic perspective. Revista Chilena de Historia Natural 85, 369-392.

Le Roux, J. P. (1991). Paleocurrent analysis using Lotus 1-2-3. Computers & Geosciences, 17(10), 1465-1468.

Le Roux, J.P., Nielsen, S.N., Henríquez, A., 2008. Depositional environment of Stelloglyphus llicoensis isp. nov.: a new radial trace fossil from the Neogene Ranquil Formation, south-central Chile. Andean Geology 35, 307-320.

Le Roux, J.P., Puratich, J., Mourgues, F.A., Oyarzún, J.L., Otero, R.A., Torres, T., Hervé, F., 2010. Estuary deposits in the Río Baguales Formation (Chattian – Aquitanean), Magallanes Province, Chile. Andean Geology 37, 329-344.

Le Roux, J.P., 2012a. A review of Tertiary climate changes in southern South America and the Antarctic Peninsula. Part 1: Ocean conditions. Sedimentary Geology 247-248, 1-20.

Le Roux, J. P., Achurra, L., Henríquez, Á., Carreño, C., Rivera, H., Suárez, M. E., ... & Gutstein, C. S. (2016). Oroclinal bending of the Juan Fernández Ridge suggested by geohistory analysis of the Bahía Inglesa Formation, north-central Chile. Sedimentary Geology, 333, 32-49.

Letelier, J. P. (2019). Petrología y geoquímica del complejo Tortuga en el seno Año Nuevo, isla Hoste (55ºS–55º 20'S) (Undergraduate dissertation, Universidad Andrés Bello).

Leuthold, J., Müntener, O., Baumgartner, J., Putlitz, B., Ovtcharova, M., Schaltegger, U., 2012. Time resolved construction of a bimodal laccolith (Torres del Paine, Patagonia). Earth and Planetary Science Letters, 325-326, p. 85-92, doi:10.1016/j.epsl.2012.01.032.

Livermore, R., Balanyá, J. C., Maldonado, A., Martínez, J. M., Rodríguez-Fernández, J., de Galdeano, C. S., ... & Viseras, C. (2000). Autopsy on a dead spreading center: the Phoenix Ridge, Drake Passage, Antarctica. Geology, 28(7), 607-610.

Livermore, R.A., Nankivell, A.P., Eagles, G., Morris, P., 2005. Paleogene opening of Drake Passage. Earth Planet Sci Lett, 236, P, 459–470.

Lodolo, E., Menichetti, M., Bartole, R., Ben-Avraham, Z., Tassone, A., and Lippai, H., 2003. Magallanes-Fagnano continental transform fault (Tierra de Fuego, southernmost South America). Tectonics, 22, doi:10.1029/2003TC001500.

Lowe, D.R., 1982. Sediment gravity flows; II, Depositional models with special reference to the deposits of high-density turbidity currents. Journal of Sedimentary Research 52, 279-297.

Ludwig, K.R., 2003. Isoplot 3.0. A Geochronological Toolkit for Microsoft Excel. Berkeley Geochron Center, Special Publication 4, 70 pp.

Macellari, C.E., Barrio, C.A., Manassero, M.J., 1989. Upper Cretaceous to Paleocene depositional sequences and sandstone petrography of southwestern Patagonia (Argentina and Chile). Journal of South American Earth Sciences 2, 223-239.

Macellari, C. E. (2021). Recent uplift and the origin of hydrodynamic traps in the Llanos Basin of Colombia. Marine and Petroleum Geology, 132, 105198.

Mahon, K.I., 1996. The New "York" regression: Application of an improved statistical method to geochemistry. International Geology Review 38, 293-303.

Malkowski, M.A., Grove, M., Graham, S.A., 2016. Unzipping the Patagonian Andes-long-lived influence of rifting history on foreland basin evolution. Lithosphere 8, 23-28, doi: 10.1130/L489.1.

Malkowski, M.A., Sharman, G.R., Graham, S.A., Fildani, A., 2017a. Characterisation and diachronous initiation of coarse clastic deposition in the Magallanes–Austral foreland basin, Patagonian Andes. Basin Research 29, 298-326.

Malkowski, M.A., Schwartz, T.M., Sharman, G.R., Sickmann, Z.T., Graham, S.A., 2017b. Stratigraphic and provenance variations in the early evolution of the Magallanes-Austral foreland basin: Implications for the role of longitudinal versus transverse sediment dispersal during arc-continent collision. GSA Bulletin 129, 349-371.

Malkowski, M.A., Jobe, Z.R., Sharman, G.R., Graham, S.A., 2018. Down-slope facies variability within deep-water channel systems: Insights from the Upper Cretaceous Cerro Toro Formation, southern Patagonia. Sedimentology 65, 1918-1946.

Maloney, K. T., Clarke, G. L., Klepeis, K. A., Fanning, C. M., & Wang, W. (2011). Crustal growth during back-arc closure: Cretaceous exhumation history of Cordillera Darwin, southern Patagonia. Journal of Metamorphic Geology, 29(6), 649-672.

Malumián, N., Ramos, V.A., 1984. Magmatic intervals, transgression cycles and oceanic events in the Cretaceous and Tertiary of Southern South America. Earth and Planetary Science Letters 67, 228-237.

Malumián, N., Caramés, A., 1997. Upper Campanian-Paleogene from Río Turbio coal measures in southern Argentina: micropaleontology and the Paleocene/Eocene boundary. Journal of South American Earth Sciences 10, 189-201.

Malumián, N., Panza, J.L., Parisi, C., Náñez, C., Caramés, A., Torres, A., 2000. Hoja Geológica 5172-III, Yacimiento Río Turbio (1:250.000). Servicio Geológico Minero Argentino, Boletín 247, pp 180.

Malumián, N., Nanez, C., 2011. The Late Cretaceous–Cenozoic transgressions in Patagonia and the Fuegian Andes: foraminifera, palaeoecology, and palaeogeography. Biological Journal of the Linnean Society 103, 269-288.

Malumián, N., Hromic, T., Náñez, C., 2013. El paleógeno de la cuenca de Magallanes: bioestratigrafía y discontinuidades. Anales Instituto Patagonia 41, 29-52.

Malumián, N., Náñez, C., & Jannou, G. (2014). The age of the Punta Torcida Formation, Eocene, Magallanes basin, argentina: the genera planorotalites and igorina (planktonic foraminifera). Estratigrafía y Sedimentología T1-30, XIX Congreso Geológico Argentino, Córdoba.

Manríquez, L.M., Lavina, E.L., Fernández, R.A., Trevisan, C., Leppe, M.A., 2019. Campanian-Maastrichtian and Eocene stratigraphic architecture, facies analysis, and paleoenvironmental evolution of the northern Magallanes Basin (Chilean Patagonia). Journal of South American Earth Sciences 93, 102-118.

Marenssi, S.A., Casadío, S., Santillana, S. N., 2002. La Formación Man Aike al sur de El Calafate (Provincia de Santa Cruz) y su relación con la discordancia del Eoceno medio en la cuenca Austral. Revista de la Asociación Geológica Argentina 57, 341-344.

Marenssi, S. A., Casadío, S., & Santillana, S. N. (2003). Estratigrafía y sedimentología de las unidades del Cretácico superior-Paleógeno aflorantes en la margen sureste del lago Viedma, provincia de Santa Cruz, Argentina. Revista de la Asociación Geológica Argentina, 58(3), 403-416.

Marenssi, S., Guler, V., Casadío, S., Guerstein, R., Papú, O., 2004. Sedimentology and palynology of the Calafate Formation (Maastrichtian), Austral Basin, Southern Patagonia, Argentina. Cretaceous Research 25, 907-918.

Marenssi, S. A., Limarino, C. O., Tripaldi, A., & Net, L. I. (2005). Fluvial systems variations in the Rio Leona Formation: Tectonic and eustatic controls on the Oligocene evolution of the Austral (Magallanes) Basin, southernmost Argentina. Journal of South American Earth Sciences, 19(3), 359-372.

Marsaglia, K. M., Johnsson, M. J., & Basu, A. (1993). Basaltic island sand provenance. SPECIAL PAPERS-GEOLOGICAL SOCIETY OF AMERICA, 41-41.

Martinioni, D. R., Olivero, E. B., & Palamarczuk, S. (1998). Conglomerados del Paleógeno en Tierra del Fuego: evidencias de discordancia entre el Cretácico Superior-(Paleoceno) y el Eoceno de Cuenca Austral. Publicación Electrónica de la Asociación Paleontológica Argentina, 5(1).

Martinioni, D.R., Olivero, E.B., Medina, F.A., Palamarczuk, S.C., 2013. Cretaceous stratigraphy of Sierra de Beauvoir, Fuegian Andes, Argentina. Revista de la Asociación Geológica Argentina 70, 70-95.

Martinod, J., Gérault, M., Husson, L., Regard, V., 2020. Widening of the Andes: an interplay between subduction dynamics and crustal wedge tectonics. Earth-Science Reviews. https://doi.org/10.1016/j.earscirev.2020.103170.

McAtamney, J., Klepeis, K., Mehrtens, C., Thomson, S., Betka, P., Rojas, L., Snyder, S., 2011. Along-strike variability of back-arc basin collapse and the initiation of sedimentation in the Magallanes foreland basin, southernmost Andes (53-54.5°S). Tectonics 30, TC5001, doi:10.1029/2010TC002826.

McDowell, F. W., McIntosh, W. C., & Farley, K. A. (2005). A precise 40Ar–39Ar reference age for the Durango apatite (U–Th)/He and fission-track dating standard. Chemical Geology, 214(3-4), 249-263.

McKenzie, D. (1978). Some remarks on the development of sedimentary basins. Earth and Planetary science letters, 40(1), 25-32.

McLennan, S. M., & Taylor, S. R. (1984). Archaean sedimentary rocks and their relation to the composition of the Archaean continental crust. In Archaean geochemistry (pp. 47-72). Springer, Berlin, Heidelberg.

McLennan, S. M., Hemming, S., McDaniel, D. K., & Hanson, G. N. (1993). Geochemical approaches to sedimentation, provenance, and tectonics. Special Papers-Geological Society of America, 21-21.

McQuarrie, N., Horton, B. K., Zandt, G., Beck, S., & DeCelles, P. G. (2005). Lithospheric evolution of the Andean fold–thrust belt, Bolivia, and the origin of the central Andean plateau. Tectonophysics, 399(1-4), 15-37.

Mella, P., Sánchez, J., 2000. Modelación cuantitativa de la subsidencia tectónicaen el extremo sur de la Cuenca Austral, XII Región-Chile. IX Congreso Geológico Chileno. Puerto Varas, Chile, pp. 221-225.

Mella, P. 2001. Control tectónico de la Cuenca de antepaís de Magallanes, XII Región, Chile. Departamento de Ciencias de la Tierra, Universidad de Concepción, Memoria de pregrado (Inédito).

Menichetti, M., Lodolo, E., Tassone, A., 2008. Structural geology of the Fuegian Andes and Magallanes fold-and-thrust belt, Tierra del Fuego Island. Geol. Acta 6, p. 19-42.

Miall, A. D. (1992). Exxon global cycle chart: An event for every occasion?. Geology, 20(9), 787-790.

Miall, A.D. 2014. Fluvial depositional systems. Springer, Berlin.

Miall, A. D. (2016). Stratigraphy: the modern synthesis. In Stratigraphy: A modern synthesis (pp. 311-370). Springer, Cham.

Michael, J., Baumgartner, J., Putlitz, B., Schaltegger, U., Ovtcharova, M., 2008. Incremental growth of the Patagonian Torres del Paine laccolith over 90 k.y. Geology, 36, p. 459-462, doi:10.1130/G24546A.1.

Miller, K.G., Wright, J.D., Fairbanks, R.G., 1991. Unlocking the ice house: Oligocene–Miocene oxygen isotopes, eustasy, and margin erosion. Journal of Geophysical Research 96, 6829–6848.

Mitchum Jr, R. M., & Vail, P. R. (1977). Seismic stratigraphy and global changes of sea level: Part 7. Seismic stratigraphic interpretation procedure: Section 2. Application of seismic reflection configuration to stratigraphic interpretation.

Mitchum Jr, R. M., Vail, P. R., & Thompson III, S. (1977a). Seismic stratigraphy and global changes of sea level: Part 2. The depositional sequence as a basic unit for stratigraphic analysis: Section 2. Application of seismic reflection configuration to stratigraphic interpretation.

Mitchum Jr, R. M., Vail, P. R., & Sangree, J. B. (1977b). Seismic stratigraphy and global changes of sea level: Part 6. Stratigraphic interpretation of seismic reflection patterns in depositional sequences: Section 2. Application of seismic reflection configuration to stratigraphic interpretation.

Mitrovica, J. X., Beaumont, C., & Jarvis, G. T. (1989). Tilting of continental interiors by the dynamical effects of subduction. Tectonics, 8(5), 1079-1094.

Morello, F., San Román, M, Prieto, A., Stern, C., 2001. Nuevos antecedentes para una discusión arqueológica en torno a la obsidiana verde en Patagonia meridional. Anales del Instituto de la Patagonia, SerieCs. Hs. 29: 129-148. Punta Arenas.

Montero-Serrano, J. C., Palarea-Albaladejo, J., Martín-Fernández, J. A., Martínez-Santana, M., & Gutiérrez-Martín, J. V. (2010). Sedimentary chemofacies characterization by means of multivariate analysis. Sedimentary Geology, 228(3-4), 218-228.

Mpodozis, C., Ramos, V.A., 1989. The Andes of Chile and Argentina. In Ericksen, G.E., Cañas Pinochet, M.T., and Reinemud, J.A., (Eds.), Geology of the Andes and Its Relation to Hydrocarbon and Mineral Resources: Circumpacific Council for Energy and Mineral Resources, Earth Sciences Series, 11, p. 59–90.

Mpodozis, C. 2007, Tectonics of the southernmost Patagonian Andes: A critical review: Geosur 2007 International Congress on the Geology and Geophysics of the Southern Hemisphere, Santiago, Chile.

Mpodozis, C., Mella, P., Padva, D. 2011. Estratigrafía y megasecuencias sedimentarias en la cuenca Austral-Magallanes, Argentina y Chile. VIII Congreso de Exploración y desarrollo de Hidrocarburos.

Müller, R. D., Seton, M., Zahirovic, S., Williams, S. E., Matthews, K. J., Wright, N. M., ... & Cannon, J. (2016). Ocean basin evolution and global-scale plate reorganization events since Pangea breakup. Annual Review of Earth and Planetary Sciences, 44, 107-138.

Muller, V. A., Calderón, M., Fosdick, J. C., Ghiglione, M. C., Cury, L. F., Massonne, H. J., ... & Sternai, P. (2021). The closure of the Rocas Verdes Basin and early tectono-metamorphic evolution of the Magallanes Fold-and-Thrust Belt, southern Patagonian Andes (52–54° S). Tectonophysics, 798, 228686.

Myrow, P.M., Fischer, W., Goodge, J.W. 2002. Wave-modified turbidites: combined-flow shoreline and shelf deposits, Cambrian, Antarctica. Journal of Sedimentary Research 72, 641-656.

Náñez, C., Malumián, N., 2008. Paleobiogeografía y paleogeografía del Maastrichtiense marino de la Patagonia, Tierra del Fuego y la Plataforma Continental Argentina, según sus foraminíferos bentónicos. Revista Española de Paleontología 23, 273-300.

Natland, M., Gonzalez, E., Cañón, A., Ernst, M., 1974. A System of stages for correlation of Magallanes basin sediments. The Geological Society of America Memoir 139, 1-57.

Nelson, E.P., 1982. Post-tectonic uplift of the Cordillera Darwin orogenic core complex: evidence from fission track geochronology and closing temperature–time relationships. Journal of the Geological Society 139, 755-761.

Nesbitt, H., & Young, G. M. (1982). Early Proterozoic climates and plate motions inferred from major element chemistry of lutites. Nature, 299(5885), 715-717.

Nie, J., Horton, B. K., Saylor, J. E., Mora, A., Mange, M., Garzione, C. N., ... & Parra, M. (2012). Integrated provenance analysis of a convergent retroarc foreland system: U–Pb ages, heavy minerals, Nd isotopes, and sandstone compositions of the Middle Magdalena Valley basin, northern Andes, Colombia. Earth-Science Reviews, 110(1-4), 111-126.

Nullo, F., Blasco, G., Risso, C., Combina, A., Otamendi, J., 2006. Hoja geológica 5172-I y 5175-II, El Calafate, provincia de Santa Cruz. Instituto de Geología y Recursos Minerales, Servicio Geológico Minero Argentino. Boletín 396, 86p. Buenos Aires

Odino Barreto, A.L., Cereceda, A., Gómez Peral, L., Coronel, M.D., Tettamanti, C., Poire, D.G., 2018. Sedimentology of the shallow marine deposits of the Calafate Formation during the Maastrichtian transgression at Lago Argentino, Austral-Magallanes Basin, Argentina. Latin American Journal of Sedimentology and Basin Analysis 25,169-191.

Olariu, C., Bhattacharya, J.P., 2006. Terminal distributary channels and delta front architecture of river-dominated delta systems. Journal of Sedimentary Research 76, 212-233.

Olivero, E.B., Martinioni, D.R., 2001. A review of the geology of the Argentinian Fuegian Andes. Journal of South American Earth Sciences 14, 175-788.

Olivero, E.B., Malumian, N., Palamarczuk, S., 2003. Estratigrafía del Cretácico Superior-Paleoceno del área de Bahía Thetis, Andes fueguinos, Argentina: acontecimientos tectónicos y paleobiológicos. Andean Geology 30, 245-263.

Otero, R.A, Torres, T., Le Roux, J.P., Hervé, F., Fanning, M., Yury-Yáñez, R., Rubilar-Rogers, D., 2012. A Late Eocene age proposal for the Loreto Formation (Brunswick Peninsula, southernmost Chile), based on fossil cartilaginous fishes, paleobotany and radiometric evidence. Andean Geology 39, 180-200.

Otero, R.A., Soto-Acuña, S., Salazar, C., Oyarzún, J.-L., 2015. New elasmosaurids (Sauropterygia, Plesiosauria) from the Late Cretaceous of the Magallanes Basin, Chilean Patagonia: Evidence of a faunal turnover during the Maastrichtian along the Weddellian Biogeographic Province. Andean Geology 42, 237-267.

Otero, A., Carballido, J. L., Salgado, L., Canudo, J. I., & Garrido, A. C. (2021). Report of a giant titanosaur sauropod from the Upper Cretaceous of Neuquén Province, Argentina. Cretaceous Research, 122, 104754.

Painter, C.S., Carrapa, B., DeCelles, P.G., Gehrels, G. E., Thomson, S.N., 2014. Exhumation of the North American Cordillera revealed by multi-dating of Upper Jurassic–Upper Cretaceous foreland basin deposits. Geological Society of America Bulletin, B30999-1.

Palma-Heldt, S., 1983. Estudio palinológico del Terciario sedimentario de Lonquimay, provincia de Malleco, Chile. Andean Geology 18, 55-75.

Pang, M., & Nummedal, D. (1995). Flexural subsidence and basement tectonics of the Cretaceous Western Interior basin, United States. Geology, 23(2), 173-176.

Pankhurst, R. J., Leat, P. T., Sruoga, P., Rapela, C. W., Márquez, M., Storey, B. C., & Riley, T. R. (1998). The Chon Aike province of Patagonia and related rocks in West Antarctica: a silicic large igneous province. Journal of volcanology and geothermal research, 81(1-2), 113-136.

Pankhurst, R.J., Riley, T.R., Fanning, C.M., Kelley, S.P., 2000. Episodic silicic volcanism in Patagonia and the Antarctic Peninsula: chronology of magmatism associated with the break–up of Gondwana. Journal of Petrology 41, 605–625.

Pardo-Casas, F., Molnar, P., 1987. Relative motion of the Nazca (Farellon) and South American Plates since Late Cretaceous times. Tectonics 6, 233-248.

Parker, A. (1970). An index of weathering for silicate rocks. Geological Magazine, 107(6), 501-504.

Parra, M., Mora, A., Sobel, E. R., Strecker, M. R., & González, R. (2009). Episodic orogenic front migration in the northern Andes: Constraints from low-temperature thermochronology in the Eastern Cordillera, Colombia. Tectonics, 28(4).

Paton, C., Hellstrom, J., Paul, B., Woodhead, J., Hergt, J., 2011. Iolite: Freeware for the visualisation and processing of mass spectrometric data. Journal of Analytical Atomic Spectrometry 26, 2508-2518.

Paterson, S. R., & Ducea, M. N. (2015). Arc magmatic tempos: Gathering the evidence. Elements, 11(2), 91-98.

Pearson, N.J., Mángano, G., Buatois, L., Casadío, S., Rodríguez Raising, M., 2012. Ichnology, sedimentology and sequence Stratigraphy of outer-estuarine and coastal plain deposits: implications for the distinction between allogenic and autogenic expressions of the Glossinfungites ichnofacies. PALAEO 333: 192-217.

Pearson, N.J., Mángano, G., Buatois, L.A., Casadío, S., Raising, M.R., 2013. Environmental variability of Macaronichnus ichnofabrics in Eocene tidal-embayment deposits of Southern Patagonia, Argentina. Lethaia 46, 341-354.

Perez, N. D., Horton, B. K., & Carlotto, V. (2016). Structural inheritance and selective reactivation in the central Andes: Cenozoic deformation guided by pre-Andean structures in southern Peru. Tectonophysics, 671, 264-280.

Petrus, J.A., Kamber B.S., 2012. VizualAge: a novel approach to laser ablation ICP-MS U–Pb geochronology data reduction. Geostandars and Geoanalytical Research 36, 247–27.

Peyton, S.L., Carrapa, B., 2013. An Introduction to Low-temperature Thermochronologic Techniques, Methodology, and Applications. In C. Knight and J. Cuzella, (Eds.), Application of structural methods to Rocky Mountain hydrocarbon exploration and development. AAPG Studies in Geology 65, p. 37–70.

Pierson, T. C. (2005). Hyperconcentrated flow—transitional process between water flow and debris flow. In Debris-flow hazards and related phenomena (pp. 159-202). Springer, Berlin, Heidelberg.

Plink-Björklund, P., Hampson, G.J., Steel, R.J., Burgess, P.M., Dalrymple, R.W., 2008. Wave-to-tide facies change in a Campanian shoreline complex, Chimney Rock Tongue, Wyoming-Utah, USA. In: Hampson, G.J., Steel, R.J., Burgess, P.M.; Dalrymple, R.W. (Eds.), Recent advances in models of shallow-marine stratigraphy. SEPM Special Publication 90, pp. 265-291.

Ponce, J.J., Olivero, E.B., Martinioni, D.R., 2008. Upper Oligocene-Miocene clinoforms of the foreland Austral Basin of Tierra del Fuego, Argentina: Stratigraphy, depositional sequences and architecture of the foredeep deposits. Journal of South American Earth Sciences 26, 36-54.

Povilauskas, L., 2017. Palynostratigraphy of the Cretaceous–Paleogene in the Austral basin, SW Santa Cruz Province, Argentina. Revista Brasileira de Paleontología 20, 299-320.

Prades, C. F. (2008). Petrología y metamorfismo de las rocas basálticas en la isla Capitán Aracena, isla Carlos III y Estero La Pera, Region de Magallanes, Chile. Undergraduate Thesis, Univ. Chile.

Quattrocchio, M.E., Martínez, M.A., Pavisich, A.C., Volkheimer, W., 2006. Early Cretaceous palynostratigraphy, palynofacies and palaeoenvironments of well sections in northeastern Tierra del Fuego, Argentina. Cretaceous Research 27, 584-602.

Quattrocchio, M.E., 2009. Paleogene dinoflagellate cysts from Punta Pratt, southern Chile. Palynology 33, 141-156.

Ramírez de Arellano, C., Putlitz, B., Müntener, O., Ovtcharova, M., 2012. High precision U/Pb zircon dating of the Chaltén Plutonic Complex (Cerro Fitz Roy, Patagonia) and its relationship to arc migration in the southern Andes. Tectonics, 31, doi: 10.1029/2011TC003048.

Ramírez de Arellano, C., Calderón, M., Rivera, H., Valenzuela, M., Fanning, C. M., & Paredes, E. (2021). Neogene Patagonian magmatism between the rupture of the Farallon plate and the Chile Ridge subduction. Journal of South American Earth Sciences, 110, 103238.

Ramos, V.A., 1982. Geología de la región del Lago Cardiel, provincia de Santa Cruz. Revista Asociación Geológica Argentina 37, 23-49.

Ramos, V.A., Niemeyer, H., Skarmeta, J., Muñoz, J., 1982. Magmatic evolution of the Austral Patagonian Andes. In Cordani, H., Linares, E., (Eds.), Symposium on magmatic evolution of the Andes, Earth-Science Reviews, 18, p. 411-443.

Ramos, V.A., 1989. Foothills structure in Northern Magallanes Basin, Argentina. AAPG Bulletin, 73, p. 887-903.

Ramos, V.A., Aguirre–Urreta, M.B., 1994. Cretaceous evolution of the Magallanes Basin. In Salfity, J.A. (Ed.), Cretaceous Tectonics of the Andes. Earth Evolution Series, Fried. Vieweg & Sohn, Braunschweig/Wiesbaden, 315-345, doi: 10.1007/978-3-322-85472-8_7.

Ramos, V.A., 2002. Evolución tectónica. In: Haller, M.J. (ed.), Geología y Recursos Naturales de Santa Cruz. Abstracts XV Congreso Geológico Argentino, Buenos Aires, Vol. I-23, 365–387.

Ramos, V.A., Kay, S.M., 1992. The Southern Patagonian plateau basalts: retroarc testimony of a ridge collision, Argentina. In Oliver, R.A., Vatin-Perignon, N., Laubacher, G., (Eds.), Andean Geodynamics Sysmposium (Grenoble, France). Tectonophysics, 205, p. 261-282.

Ramos, V.A., Cristallini, E., Pérez, D.J., 2002. The Pampean flat-slab of the Central Andes: Journal of South American Earth Sciences, 15, p. 59–78, doi: 10.1016/S0895-9811(02)00006-8.

Ramos, V.A., 2005. Seismic ridge subduction and topography: foreland deformation in the Patagonian Andes. Tectonophysics, 399, p. 73-86, doi: 10.1016/j.tecto.2004.12.016

Ramos, V.A., 2009. Anatomy and global context of the Andes: main geologic features and the Andean orogenic cycle. In Kay, S.M., Ramos, V.A., and Dickinson, W.R., (Eds.). Backbone of the Americas: Shallow Subduction, plateau Uplift, and Ridge and Terrane Collision. Geological Society of America Memoir, 204, p. 31–65, doi: 10.1130/2009.1204(02).

Ramos, V. A., & Ghiglione, M. C. (2008). Tectonic evolution of the Patagonian Andes. Developments in quaternary sciences, 11, 57-71.

Ramos, V.A., and Folguera, A., 2009. Andean flat slab subduction through time. In: Murphy, B. (ed.) Ancient Orogens and Modern Analogues. The Geological Society, Special Publication, 327, p. 31–54, doi:10.1144/SP327.3.

Rapalini, A E., Calderón, M., Singer, S., Hervé, F., Cordani, U., 2008. Tectonic implications of a paleomagnetic study of the Sarmiento Ophiolitic Complex, southern Chile. Tectonophysics 452, 29-41.

Reiners, P.W., Campbell, I.H., Nicolescu, S., Allen, C.A., Hourigan, J.K., Garver, J.I., Mattinson, J.M., Cowan, D.S., 2005. (U-Th)/(He-Pb) “double-dating” of detrital zircons. Am. J. Sci., 305, 259–311.

Reiners, P.W., Brandon, M.T., 2006. Using thermochronology to understand orogenic erosion. Annu. Rev. Earth Planet. Sci., 34, p. 419–466.

Reinson, G.E., 1992. Transgressive barrier island and estuarine systems. In: Walker, R.G., James, N.P. (Eds.), Facies Models: Response to Sea Level Changes. Geological Association of Canada, St. Johns, Newfoundland and Labrador, pp. 179-194.

del Río, C.J., Martínez, S.A., 2015. Paleobiogeography of the Danian molluscan assemblages of Patagonia (Argentina). Palaeogeography, Palaeoclimatology, Palaeoecology 417, 274-292.

Rivera, H.A., 2017. Insights into the tectonostratigraphic evolution of the Southern Magallanes Basin, Southern Chile, during the Cenozoic. (Master's thesis) Universidad de Chile, Santiago, Chile, 149 pp.

Rivera, H.A., Le Roux, J.P., Sánchez, L.K., Mariño-Martínez, J.E., Salazar, C., Barragán, J.C., 2018. Palaeoredox conditions and sequence stratigraphy of the Cretaceous storm-dominated, mixed siliciclastic-carbonate ramp in the Eastern Cordillera Basin (Colombia): Evidence from sedimentary geochemical proxies and facies analysis. Sedimentary Geology 372, 1-24.

Rivera, H. A., Le Roux, J. P., Farías, M., Gutiérrez, N. M., Sánchez, A., & Palma-Heldt, S. (2020). Tectonic controls on the Maastrichtian-Danian transgression in the Magallanes-Austral foreland basin (Chile): Implications for the growth of the Southern Patagonian Andes. Sedimentary Geology, 403, 105645.

Roddaz, M., Viers, J., Brusset, S., Baby, P., & Hérail, G. (2005). Sediment provenances and drainage evolution of the Neogene Amazonian foreland basin. Earth and Planetary Science Letters, 239(1-2), 57-78.Rodríguez-Raising, M., Casadío, S., Pearson, N., Mángano, G., Buatois, L., Griffin, M., 2014. Paleoenvironmental setting and description of an estuarine oyster reef in the Eocene of Patagonia, southern Argentina. Journal of South American Earth Sciences 56, 242-250.

Rojas, E., Le Roux, J.P., 2005. Sedimentary processes on a Gilbert-type delta in Lake Llanquihue, southern Chile. Andean Geology 32, 19-31.

Romans, B.W., Hubbard, S.M., Graham, S.A., 2009. Stratigraphic evolution of an outcropping continental slope system, Tres Pasos Formation at Cerro Divisadero, Chile. Sedimentology 56, 737-764.

Romans, B.W., Fildani, A., Graham, S.A., Hubbard, S.M., Covault, J.A., 2010. Importance of predecessor basin history on sedimentary fill of a retroarc foreland basin: Provenance analysis of the Cretaceous Magallanes basin, Chile (50–52°S), Basin Res., 22, 640–658, doi:10.1111/j.13652117.2009.00443.x.

Romans, B.W., Fildani, A., Hubbard, S.M., Covault, J.A., Fosdick, J.C., Graham, S.A., 2011. Evolution of deep-water stratigraphic architecture, Magallanes Basin, Chile, Mar. Pet. Geol., 28,612–628, doi:10.1016/j.marpetgeo.2010.05.002.

Rosello, E. A., Haring, C. E., Suárez, F., Laffitte, G. A., & Nevistic, A. V. (2008). Hydrocarbons and petroleum of Tierra del Fuego, Argentina. Geologica Acta: an international earth science journal, 6(1), 69-83.

Roser, B. P., Cooper, R. A., Nathan, S., & Tulloch, A. J. (1996). Reconnaissance sandstone geochemistry, provenance, and tectonic setting of the lower Paleozoic terranes of the West Coast and Nelson, New Zealand. New Zealand Journal of Geology and Geophysics, 39(1), 1-16.

Rossignol, C., Hallot, E., Bourquin, S., Poujol, M., Jolivet, M., Pellenard, P., Dabard, M.P., 2019. Using volcaniclastic rocks to constrain sedimentation ages: To what extent are volcanism and sedimentation synchronous? Sedimentary Geology 381, 46-64.

Rossi, V.M., Steel, R.J., 2016. The role of tidal, wave and river currents in the evolution of mixed-energy deltas: Example from the Lajas Formation (Argentina). Sedimentology 63, 824-864.

Sachse, V.F., Strozyk, F., Anka, Z., Rodriguez, J.F., Di Primio, R., 2015. The tectono-stratigraphic evolution of the Austral Basin and adjacent areas against the background of Andean tectonics, southern Argentina, South America. Basin Research 28, 462-482.

Salvador, A., and Murphy, M. A., (1999). International stratigraphic guide—an abridged version. Episodes Journal of International Geoscience, 22(4), 255-271.

Salze, M., Martinod, J., Guillaume, B., Kermarrec, J. J., Ghiglione, M. C., & Sue, C. (2018). Trench-parallel spreading ridge subduction and its consequences for the geological evolution of the overriding plate: Insights from analogue models and comparison with the Neogene subduction beneath Patagonia. Tectonophysics, 737, 27-39.

Sánchez, A., 2006. Proveniencia sedimentaria de estratos de Cabo Naríz y Formación Cerro Toro, Cretácico Tardío-Paleoceno, Magallanes, Chile. (Master's thesis), Universidad de Chile, Santiago, Chile, 153 pp.

Sánchez, A., Pavlishina, P., Godoy, E., Hervé, F., Fanning, M., 2010. On the presence of Upper Paleocene rocks in the foreland succession at Cabo Nariz, Tierra del Fuego, Chile: geology and new palynological and U-Pb data. Andean Geology 37, 413-432.

Santos-García, J. S. (1988). Caracterización sedimentológica del área de Río Turbio, Cuenca Austral, Provincia de Santa Cruz, República Argentina. Estudios Geológicos, 44(3-4), 199-210.

Scalabrino, B., Lagabrielle, Y., Rupelle, A. D. L., Malavieille, J., Polvé, M., Espinoza, F., ... & Suarez, M. (2009). Subduction of an active spreading ridge beneath southern South America: A review of the Cenozoic geological records from the Andean foreland, central Patagonia (46–47 S). Subduction zone geodynamics, 227-246.

Scalabrino, B., Lagabrielle, Y., Malavieille, J., Dominguez, S., Melnick, D., Espinoza, F., ... & Rossello, E. (2010). A morphotectonic analysis of central Patagonian Cordillera: Negative inversion of the Andean belt over a buried spreading center?. Tectonics, 29(2).

Scasso, R.A., Aberhan, M., Ruiz, L., Weidemeyer, S., Medina, F.A., Kiessling, W., 2012. Integrated bio-and lithofacies analysis of coarse-grained, tide-dominated deltaic environments across the Cretaceous/Paleogene boundary in Patagonia, Argentina. Cretaceous Research 36, 37-57.

Schenk, C.J., Charpentier, R.R., Pitman, J.K., Tennyson, M.E., Brownfield, M.E., Gaswirth, S.B., Le, P.A., Leathers-Miller, H.M., and Marra, K.R., 2016. Assessment of unconventional tight-gas resources of the

Magallanes Basin Province, Chile, 2015. U.S. Geological Survey Fact Sheet 2015–3085, http://dx.doi.org/10.3133/fs20153085.

Schwartz, T.M., Graham, S.A., 2015. Stratigraphic architecture of a tide-influenced shelf-edge delta, Upper Cretaceous Dorotea Formation, Magallanes-Austral Basin, Patagonia. Sedimentology 62, 1039-1077.

Schwartz, T.M., Fosdick, J., Graham, S.A., 2017. Using detrital zircon U-Pb ages to calculate Late Cretaceous sedimentation rates in the Magallanes-Austral Basin, Patagonia, Basin Research. doi:10.1111/bre.12198

Sclater, J. G., & Christie, P. A. (1980). Continental stretching: An explanation of the post-mid-Cretaceous subsidence of the central North Sea basin. Journal of Geophysical Research: Solid Earth, 85(B7), 3711-3739.

Selley, R.C., 1976. An Introduction to Sedimentology. Academic Press, London, 408 p.

Sernageomin., 2003. Mapa Geológico de Chile: versión digital, escala 1:1, 000,000. Servicio Nacional de Geología y Minería, Santiago, Chile.

Shultz, M.R., Fildani, A., Cope, T.D., Graham, S.A., 2005. Deposition and stratigraphic architecture of an outcropping ancient slope system: Tres Pasos Formation, Magallanes Basin, southern Chile. In: Hodgson, D.M., Flint, S.S. (Eds.), Submarine Slope Systems: Processes and Products. Geological Society of London, Special Publications 244, pp. 27-50.

Sial, A.N., Ferreira, V.P., Toselli, A.J., Parada, M.A., Acenolaza, F.G., Pimentel, M.M., Alonso, R.N., 2001. Carbon and oxygen isotope compositions of some Upper Cretaceous–Paleocene sequences in Argentina and Chile. International Geology Review 43, 892-909.

Sickmann, Z. T., Schwartz, T. M., & Graham, S. A. (2018). Refining stratigraphy and tectonic history using detrital zircon maximum depositional age: an example from the Cerro Fortaleza Formation, Austral Basin, southern Patagonia. Basin Research, 30(4), 708-729.

Skarmeta, J., and Castelli, J.C., 1997. Intrusión sintectónica del Granito de las Torres del Paine, Andes Patagónicos de Chile. Andean Geology, 24, p. 55-74.Suárez, M., de la Cruz, R., Bell, C.M., 2000a. Timing and origin of deformation along the Patagonian fold and thrust belt. Geological Magazine, 137, p. 345-353.

Slama, J., Kosler, J., Condon, D.J., Crowley, J.L., Gerdes, A., Hanchar, J.M., Whitehouse, M.J., 2008. Plesovice zircon - A new natural reference material for U-Pb and Hf isotopic microanalysis. Chemical Geology 249, 1-35.

Smith, G. A., & Lowe, D. R. (1991). Lahars: volcano-hydrologic events and deposition in the debris flow—hyperconcentrated flow continuum. Sedimentation in volcanic settings, SEPM Special Publication No. 45.

Solari, L.A., Gómez-Tuena, A., Bernal, J.P., Pérez-Arvizu, O., Tanner, M., 2010. U-Pb zircon geochronology by an integrated LA-ICPMS microanalytical workstation: achievements in precision and accuracy: Geostandards and Geoanalytical Research 34, 5-18.

Solari, L.A., Tanner, M., 2011. UPb.age, a fast data reduction script for LA-ICP-MS U-Pb geochronology. Revista Mexicana de Ciencias Geológicas 28, 83-91.

Somoza, R., 1998. Updated Nazca (Farallon)–South America relative motions during the last 40 Ma: implications for mountain building in the central Andean region. Journal of South American Earth Sciences 11, 211-215.

Somoza, R., Ghidella, M.E., 2005. Convergencia en el margen occidental de América del Sur durante el Cenozoico: subducción de las placas de Nazca, Farallón y Aluk. Revista de la Asociación Geológica Argentina, 60, p. 797-809.

Somoza, R., Ghidella, M.E., 2012. Late Cretaceous to recent plate motions in western South America revisited. Earth and Planetary Science Letters, 331, p. 152-163.

Stacey, J.S., Kramers, J.D., 1975. Approximation of terrestrial lead isotope evolution by a two-stage model. Earth and Planetary Science Letters 26, 207-221.

Steckler, M. S., & Watts, A. B. (1978). Subsidence of the Atlantic-type continental margin off New York. Earth and planetary science letters, 41(1), 1-13.

Stevens Goddard, A. L., & Fosdick, J. C. (2019). Multichronometer thermochronologic modeling of migrating spreading ridge subduction in southern Patagonia. Geology, 47(6), 555-558.

Stern, C. R. (1991). Isotopic composition of Late Jurassic and Early Cretaceous mafic igneous rocks from the southernmost Andes: implications for Sub-Andean mantle. Andean Geology, 18(1), 15-23.

Stern, C.R., Mohseni, P.P., Fuenzalida, P.R., 1991. Petrochemistry and tectonic significance of lower Cretaceous Barros Arana Formation basalts, southernmost Chilean Andes. Journal of South American Earth Sciences 4, 331-342.

Stern, C.R., Mukasa, S.B., Fuenzalida, R., 1992. Age and petrogenesis of the Sarmiento ophiolite complex of southern Chile. Journal of South American Earth Sciences 6, 97–104.

Suárez, M., De la Cruz, R., Bell, C.M., 2000a. Timing and origin of deformation along the Patagonian fold and thrust belt. Geological Magazine 137, 345–353.

Suárez M., de la Cruz, R., Troncoso, A., 2000b. Tropical/subtropical upper Paleocene-lower Eocene fluvial deposits in Eastern central Patagonia, Chile (46°45'S). Journal of South America Earth Sciences, 13, p. 527-536.

Suárez M., de la Cruz, R., 2001. Jurassic to Miocene K-Ar dates from Eastern central Patagonian Cordillera plutons (45°-48°S). Geological Magazine, 138, p. 53-66.

Taylor, S. R., & McLennan, S. M. (1981). The composition and evolution of the continental crust: rare earth element evidence from sedimentary rocks. Philosophical Transactions of the Royal Society of London. Series A, Mathematical and Physical Sciences, 301(1461), 381-399.

Taylor, S. R., & McLennan, S. M. (1985). The continental crust: its composition and evolution.

Thomas, W. A. (2011). Detrital-zircon geochronology and sedimentary provenance. Lithosphere, 3(4), 304-308.

Thomas, C.R., 1949. Geology and petroleum exploration in Magallanes province, Chile. Am. Association of Petroleum Geologist Bull. 33, 1553-1578.

Thomas, R.G., Smith, D.G., Wood, J.M., Visser, J., Calverley-Range, E.A., Koster, E.H., 1987. Inclined heterolithic stratification—terminology, description, interpretation and significance. Sedimentary Geology 53, 123-179.

Thomson, S. N. (2002). Late Cenozoic geomorphic and tectonic evolution of the Patagonian Andes between latitudes 42 S and 46 S: An appraisal based on fission-track results from the transpressional intra-arc Liquiñe-Ofqui fault zone. Geological Society of America Bulletin, 114(9), 1159-1173.

Thomson, S., Hervé, F., Stöckhert, B., 2001. Mesozoic-Cenozoic denudation history of the Patagonian Andes (southern Chile) and its correlation to different subduction processes. Tectonics, 20, p. 693-711, doi:10.1029/2001TC900013.

Thomson, S. N., Brandon, M. T., Tomkin, J. H., Reiners, P. W., Vásquez, C., & Wilson, N. J. (2010). Glaciation as a destructive and constructive control on mountain building. nature, 467(7313), 313-317.

Todd, R., Kniker, H., 1952. An Eocene foraminiferal fauna from the Agua Fresca Shale of Magallanes Province, Southernmost, Chile. Cushman Foundation Foraminiferal Research Special Publication 1, pp 28.

Tolosana-Delgado, R. (2012). Uses and misuses of compositional data in sedimentology. Sedimentary geology, 280, 60-79.

Torres Carbonell, P.J., Olivero, E.B., Dimieri, L.V., 2008a. Structure and evolution of the Fuegian Andes foreland thrust-fold belt, Tierra del Fuego, Argentina: paleo-geographic implications. Journal of South American Earth Sciences 25, 417-439.

Torres Carbonell, P. J., Dimieri, L. V., & Martinioni, D. R. (2013). Early foreland deformation of the Fuegian Andes (Argentina): Constraints from the strain analysis of Upper Cretaceous-Danian sedimentary rocks. Journal of Structural Geology, 48, 14-32.

Torres Carbonell, P.J., Olivero, E.B., 2019. Tectonic control on the evolution of depositional systems in a fossil, marine foreland basin: Example from the SE Austral Basin, Tierra del Fuego, Argentina. Marine and Petroleum Geology 104, 40-60.

Torres Carbonell, P. J., Cao, S. J., Guillot, M. G., González, V. M., Dimieri, L. V., Duval, F., & Scaillet, S. (2020). The Fuegian thrust-fold belt: From arc-continent collision to thrust-related deformation in the southernmost Andes. Journal of South American Earth Sciences, 102, 102678.

Troncoso, A., Suárez, M., de la Cruz, R., Palma-Heldt, S., 2002. Paleoflora de la formación Ligorio Márquez (XI Región, Chile) en su localidad tipo: sistematica, edad e implicancias paleoclimáticas. Andean Geology, 29, p. 113-135.

Uliana, M.A., Biddle, K.T., 1988. Mesozoic-Cenozoic paleogeographic and geodynamic evolution of southern South America. Revista Brasileira de Geociencias 18, 172-190.

Varela, A. N., Poiré, D. G., Martin, T., Gerdes, A., Goin, F. J., Gelfo, J. N., & Hoffmann, S. (2012). Edades U-Pb en circones de la Formación Mata Amarilla (Cretácico), Patagonia Austral, Argentina: su relación con la evolución de la Cuenca Austral. Andean geology, 39(3), 359-379.

Varela, A. N., Raigemborn, M. S., Richiano, S., White, T., Poiré, D. G., & Lizzoli, S. (2018). Late cretaceous paleosols as paleoclimate proxies of high-latitude southern hemisphere: Mata Amarilla Formation, Patagonia, Argentina. Sedimentary Geology, 363, 83-95.

Velázquez, A., 2016. Condiciones depositacionales de la Formación Palomares, XII Región de Magallanes. Undergraduate thesis (Unpublished), Department of Geology, University of Chile.

Vermeesch, P., 2004. How many grains are needed for a provenance study? Earth and Planetary Science Letters 224, 351-441.

Vermeesch, P. (2006). Tectonic discrimination diagrams revisited. Geochemistry, Geophysics, Geosystems, 7(6).

Vermeesch, P. (2009). RadialPlotter: A Java application for fission track, luminescence and other radial plots. Radiation Measurements, 44(4), 409-410.

Vermeesch, P. (2012). On the visualisation of detrital age distributions. Chemical Geology, 312, 190-194.

Vollmer, F. W. (1995). C program for automatic contouring of spherical orientation data using a modified Kamb method. Computers & Geosciences, 21(1), 31-49.

Vollmer, F. W. (2015). Orient 3: a new integrated software program for orientation data analysis, kinematic analysis, spherical projections, and Schmidt plots. In Geological Society of America Abstracts with Programs (Vol. 47, No. 7, p. 49).

Von Goetsche, G., 1953. Informe Geológico del área Tres Morros-Agua Fresca- San Isidro. Informe Archivo Técnico ENAP, Santiago. (Inédito).

Welkner, D.R., 2002. Geocronología de los plutones del área del Cerro San Lorenzo, XI Región de Aysén. IX Congreso Geológico Chileno, Puerto Varas, Actas vol. 2, p. 269-273.

Weltje, G. J. (2002). Quantitative analysis of detrital modes: statistically rigorous confidence regions in ternary diagrams and their use in sedimentary petrology. Earth-Science Reviews, 57(3-4), 211-253.

Weltje, G. J. (2006). Ternary sandstone composition and provenance: an evaluation of the 'Dickinson model'. Geological Society, London, Special Publications, 264(1), 79-99.

Weltje, G. J. (2012). Quantitative models of sediment generation and provenance: state of the art and future developments. Sedimentary Geology, 280, 4-20.

Willett, C. D., Fox, M., & Shuster, D. L. (2017). A helium-based model for the effects of radiation damage annealing on helium diffusion kinetics in apatite. Earth and Planetary Science Letters, 477, 195-204.

Williams, I.S., 1998 U-Th-Pb Geochronology by Ion Microprobe. In: McKibben, M.A., Shanks III, W.C., Ridley, W.I. (Eds.), Applications of Microanalytical Techniques to Understanding Mineralizing Processes. Reviews in Economic Geology SEG 7, pp. 1-35.

Willis, B. J. (2005). Deposits of tide-influenced river deltas. River Deltas, 87-129.

Wilson, T.J., 1991. Transition from back-arc to foreland basin development in southernmost Andes: stratigraphic record from the Ultima Esperanza District, Chile. Geological Society of America Bulletin 103 98-111.

Winslow, M. A. (1982). The structural evolution of the Magallanes Basin and neotectonics in the southernmost Andes. Antarctic Geoscience, 4, 143-154.

de Wit, M. J., & Stern, C. R. (1981). Variations in the degree of crustal extension during formation of a back-arc basin. Tectonophysics, 72(3-4), 229-260.

Yang, Y., Miall, A.D., 2008. Marine transgressions in the mid-Cretaceous of the Cordilleran foreland basin re-interpreted as orogenic unloading deposits. Bulletin of Canadian Petroleum Geology 56, 179-198.

Zahid, K. M., & Barbeau Jr, D. L., 2010. Provenance of eastern Magallanes foreland basin sediments: Heavy mineral analysis reveals Paleogene tectonic unroofing of the Fuegian Andes hinterland. Sedimentary Geology, 229(1-2), 64-74.

Zahid, K. M., & Barbeau Jr, D. L., 2013. Geochemical signatures from the Atlantic coast of Tierra del Fuego and their provenance implications for Magallanes basin sediments. Chemical Geology, 347, 69-81.

Zaitlin, B.A., Dalrymple, R.W., Boyd, R.O., 1994. The stratigraphic organization of incised-valley systems associated with relative sea-level change. In: Dalrymple, R.W., Boyd, R.J., Zaitlin, B.A. (Eds.), Incised valley systems: Origin and Sedimentary Sequences. SEPM Special Publications 51, pp. 45-60.

Zachos, J., Quinn, T.M., Salamy, K.A., 1996. High-resolution (104 yr) deep-sea foraminifer stable isotope records of the Eocene–Oligocene climate transition. Paleoceanography 11, 251-266.

Zecchin, M., & Catuneanu, O. (2013). High-resolution sequence stratigraphy of clastic shelves I: units and bounding surfaces. Marine and Petroleum Geology, 39(1), 1-25.

Zecchin, M., Catuneanu, O., & Caffau, M. (2017). High-resolution sequence stratigraphy of clastic shelves V: criteria to discriminate between stratigraphic sequences and sedimentological cycles. Marine and Petroleum Geology, 85, 259-271.

Zurita, E., Carpinelli, A., Trejo, S., Saa, A., 2013. Gas Resource Potential from Maastrichtian–Eocene Reservoir in Magallanes Basin, Chile. AAPG International Conference and Exhibition, Cartagena, Colombia. Search and Discovery Article # 90166.

ANNEXES

ANNEX A-1

Evolución tectono-estratigráfica de la cuenca de antepaís Magallanes-Austral y su relación a la orogénesis de los Andes Patagónicos

Rivera, H.[1,2], Gutiérrez, N.[1,3], Le Roux, J.P.[1,4], Barbosa, C.[1], Farías, M.[1]

Resumen

La cuenca Magallanes-Austral, es una cuenca antepaís de retroarco que ofrece una posibilidad única para evaluar la interacción entre el tectonismo y la sedimentación y su registro sedimentológico permite conocer la evolución tectónica de los Andes Patagónicos. En el presente trabajo se detallan unidades tectono-estratigráficas definidas a partir de información sedimentológica, geocronológica, paleobotánica e información sísmica 2D y pozos, estos últimos datos constituyen la base para la caracterización de las unidades en términos sismoestratigráficos. Entre los principales resultados están: 1) el reconocimiento de 3 dominios tectónicos: el basamento; la faja plegada y corrida interna; la faja plegada y corrida externa. 2) La identificación de 9 discordancias regionales cada una de las cuales delimita 8 unidades tectono-estratigráficas que registran la evolución de la cuenca de antepaís relacionados a 6 pulsos orogénicos principales. El crecimiento más prominente de los Andes Patagónicos durante el Oligoceno generó una sombra de lluvia que causó un marcado descenso en los niveles de precipitación, temperaturas y de la diversidad de morfo-especies. Lo anterior puede ser atribuido a la fase final de la apertura del pasaje Drake durante la separación de la Antártida con la parte más Sur de Sudamérica.

1 Departamento de Geología, Facultad de Ciencias Físicas y Matemáticas, Universidad de Chile

2 Centro de Excelencia en Geotermia de los Andes, Universidad de Chile

3 IDIEM, Universidad de Chile

ANNEX A-2

XV CONGRESO GEOLÓGICO CHILENO
"GEOCIENCIAS HACIA LA COMUNIDAD"
18 AL 23 DE NOVIEMBRE DE 2018, UNIVERSIDAD DE CONCEPCIÓN,
CONCEPCIÓN, CHILE

ESEG-4: Evolución tectónica del arco de Scotia en Sudamérica y la Península Antártica

Underfilled-to-overfilled cycles in the Magallanes Foreland Basin, Chilean Patagonia: Unraveling the growth of the Southern Patagonian Andes

Huber A. Rivera[1,2], Marcelo Farias[1,2], Jacobus P. Le Roux[1], Alejandro Sanchez[3], Nestor M. Gutierrez[4].
(1) Departamento de Geología, Facultad de Ciencias Físicas y Matemáticas, Universidad de Chile, Santiago, Chile
(2) Laboratorio de Tectónica y Paleomagnetismo, Facultad de Ciencias Físicas y Matemáticas, Universidad de Chile, Santiago, Chile
(3) Departamento de Ingeniería de Minas, Facultad de Ingeniería, Universidad de Santiago de Chile, Santiago, Chile
(4) Centro de Investigación, Desarrollo e Innovación de Estructuras y Materiales IDIEM, Universidad de Chile, Santiago, Chile

The stratigraphic record of the Magallanes/Austral foreland basin has proved to be very sensitive to changes in the tectonic regimes, as well as climatic variability. However, the long-term evolution of the accommodation space and location of major sediment accumulation zones, the sedimentary evolution of the basin and the dynamic response of the stratigraphic cycles to steady or unsteady pulses of deformation remains uncertain. In this work, we present a multidisciplinary approach including sedimentological analysis, backstripping results and detrital zircon U-Pb geochronology of the Late Cretaceous-early Miocene strata in the Magallanes and Tierra del Fuego Provinces of the Magallanes foreland basin. The sedimentary evolution is interpreted in terms of underfilled-to-overfilled cycles and reciprocal stratigraphy throughout the proximal foredeep to distal forebulge to illustrate the different evolving stages of the stratigraphic architecture, basin dynamics, and long-term sedimentary evolution. Three second-order shallowing cycles are recognized, which can be roughly compared to overfilled cycles. However, only one true overfilled cycle is recognized during the Miocene. Almost all these cycles are represented by the progressive shift of bathyal-pelagic facies dominated by longitudinal sediment transport to shallow marine facies with sediment transport direction preferentially transversal to the basin axis, as shown, for instance, in the assemblage of the Chorrillo Chico-Agua Fresca-Tres Brazos Formations. During the underfilled phases, the detrital zircon age spectra are very narrow, compared to the final phases of each cycle, where the detrital zircon age spectra are much more variated and spread i.e. increasing proportion of Jurassic and older zircon grains. The geohistory analysis shows an accelerated subsidence from latest Cretaceous to Paleocene in the proximal foredeep but scarce to null subsidence in the forebulge zone and a progressive deceleration in the foredeep while in the distal forebulge increase the subsidence from the Eocene to early Miocene. The latter results allow us, at least partially, to questioning the link between the progradational deposits and pulses of deformation in the Southern Patagonian Andes, and considering the evolution of an orogenic wedge, we propose that decreasing contractional deformation will induce the migration of deformation front to the foreland, thus decreasing the pro-side slope to sustain the wedge stability.

ANNEX A-3

17ème Congrès Français de Sédimentologie, Beauvais – Livre des résumés, 2019, Publ. ASF n°81, Paris, 169 p.

SOUTHERN PATAGONIAN WEDGE DYNAMICS INFERRED BY TECTONO-STRATIGRAPHIC SEQUENCES AND EVOLUTION OF THE MAGALLANES-AUSTRAL FORELAND BASIN (CHILE)

Huber Rivera *[1,2], Joseph Martinod [2], Marcelo Farías [1], Jacobus Le Roux [1]

[1] Department of Geology, FCFM, University of Chile – Chili

[2] Institut des Sciences de la Terre (ISTerre) – Université Grenoble Alpes, Université Savoie Mont Blanc, CNRS, IRD, IFSTTAR, ISTerre, 38000 Grenoble, France – France

*intervenant - riverarh@univ-grenoble-alpes.fr

Active mountain chains in zones of convergence are the result of the tectonic activity generating relief. This relief under the influence of climate and surface processes develops different erosion patterns, drainage network, and sediment dispersal routing that finally contributes to the sedimentary basins growth. Therefore, the close relationship between tectonic processes occurring in the orogen and the sedimentary sequences hosted in foreland basins gives insights into the dynamics of orogenic wedges. In the southernmost Andes, the difficulty of access to study the thrust sheets, style, and stages of deformation in the Southern Patagonian orogen, have obscured the well understanding of this part of the chain. Then, the comprehension of the evolution of the Magallanes-Austral Basin, in terms of its sedimentary fill evolution, basin architecture and subsidence, routing systems, and the evolution of the source rock terranes helps in knowing the development of the Southern Patagonian Andes. In this work, we present the combination of subsurface and outcrop data, including seismostratigraphic analysis, sedimentology, backstripping, and integrated provenance (sandstone/conglomerate petrography, geochemistry, and detrital zircon U-Pb geochronology) results of the Late Cretaceous through Miocene strata of the Magallanes-Austral Foreland Basin. We evaluate the long-term evolution of the accommodation space and the location of major sediment accumulation zones, the sedimentary evolution of the basin and the dynamic response of the stratigraphic sequences to pulses of deformation in the orogen. With this approach, it is possible to obtain better constraints on the temporality, duration, and velocity of the sedimentary and tectonic processes and ultimately to infer changes in the wedge dynamics of the orogen in terms of the critical-taper theory. Three second-order shallowing cycles are recognized that last from the Late Cretaceous to early Miocene. They can roughly be compared to underfilled-overfilled cycles. However, only one true overfilled cycle represented by the onset of the continentalization of the environments is recognized during the Oligocene-early Miocene. This cycle occurs when the Southern Patagonian orogen reaches a greater topographic expression that leads to the establishment of a rain shadow in the foreland basin. The first two underfilled-to-overfilled are represented by the progressive shift from bathyal-pelagic facies dominated by longitudinal sediment transport to shallow marine facies with sediment transport direction preferentially transversal to the basin axis. The backstripping results show accelerated subsidence from latest Cretaceous to Paleocene in the proximal foredeep but scarce to null subsidence in the forebulge zone. Afterward, we observe a progressive deceleration in the foredeep subsidence, while subsidence increases in the distal forebulge from the early Eocene to early Miocene. Additionally, we recognize eight tectono-stratigraphic sequences (2 for the Late Cretaceous and 6 for the Cenozoic) bounded by regional unconformities visible both in surface and subsurface data. They are mainly linked to tectonic loading and unloading phases, but some of them are enhanced by base-level changes. Considering the evolution of the Southern Patagonian Andes as a critical-taper wedge, we can infer that a supercritical state occurred twice during its evolution. The first occurrence, from *ca.* 85-67 Ma, is characterized by the incorporation of the basement, and mafic rock terranes in the hinterland. The second one, from *ca.* 30-20 Ma, represents another phase of internal rejuvenation and uplift of early foreland strata, metamorphic, and volcanoclastic terranes in the rear of the wedge (hinterland), by means of whether back-thrusting, out-of-sequence thrusting, or basal accretion in the orogenic wedge. Accentuated erosion and frontal accretion of new thrust sheets are the two possible mechanisms to make critical the taper. However, given the difficulty in eroding certain types of rocks in the hinterland, the latter mechanism seems to be the most effective, leading to the widening of the thrust-belt and migration of the foredeep. This occurred ca. 66-47 Ma, and ca.19-15 Ma ago. In this way, the migration of deformation front to the foreland decreases internal contractional deformation, abating the pro-side slope to sustain the wedge stability.

Mots-Clés: Southern Patagonian Andes, Magallanes/Austral foreland basin, basin evolution, provenance, seismostratigraphy

ANNEX B-1

Neogene Patagonian magmatism between the rupture of the Farallon plate and the Chile Ridge subduction by Ramírez de Arellano, Calderón, **Rivera** et al., 2021
https://doi.org/10.1016/j.jsames.2021.103238

ANNEX C-1

FURTHER DETAILS ABOUT DETRITAL ZIRCON U-Pb MAXIMUM DEPOSITIONAL AGES

Maximum depositional age calculation

Sample PB1 (53° 9'18.80"S; 71°31'2.00"W). Sixty-three (63) detrital grains were analysed (~70% concordant ages), which ranges from 53.6-131.2 Ma (Figure 1). The dominant age cluster is 65.1-102.7 Ma representing about 87% of all measured U-Pb ages. A minor subpopulation range from 53.6-60.2 Ma (Paleogene), and 110.7-131.2 Ma (Early Cretaceous), constituting about 5% and 8% of the analyses, respectively. For this sample's detrital zircon age distribution, the *Unmix* routine (Ludwig, 2003) gets more worthwhile to elucidate the youngest age peak and conduct the maximum depositional age calculation. The maximum depositional age of the three (3) concordant younger grains (except for the youngest single grain suspect of Pb loss) that constitute the YP-WMA is 60.7 ± 2.2 Ma with an MSWD=2.1 (acceptable values range from 0.025-3.690; after Mahon, 1996) and POF=0.12, which imply a Selandian age. We considered this age as a statistically robust one because it is (1) consistent with fossil ages (Charrier and Lahsen, 1969; Quattrocchio, 2009; Carrillo-Berumen et al., 2013), (2) the analysis has a good precision (max. standard error= 2%), and (3) the scatter of ages is statistically consistent (Mahon, 1996).

Sample RB1 (53°34'26.80"S; 70°56'15.10"W). Fifty-four (54) detrital grains were analysed (100% concordant), which ranges from 64.4-655.3 Ma (Figure 2). Three dominant age clusters are observed at 67 Ma, 77 Ma, 95 Ma, and a small peak at 108-113 Ma. Additionally, a few Early Cretaceous (134 Ma; 1 grain), and Paleozoic-Neoproterozoic (528-655 Ma; 2 grains) grains are present. Overall, about 72% of measured U-Pb ages fall in the Late Cretaceous (66-100.5 Ma), a minor proportion of about 15% corresponds to the Danian (64.4-65.8 Ma), and 9% corresponds to the Early Cretaceous (108-134.73 Ma). In contrast, only a ca. 4% corresponds to Paleozoic-Neoproterozoic (528.3-655.3 Ma). Based on the four (4) youngest detrital zircons components, the maximum depositional age is 64.7 ± 0.67 Ma with an MSWD=0.13 (acceptable values from 0.072-3.117) and POF=0.94. A slightly older but similar robust ages of 65.2 ± 0.46 Ma with an MSWD=0.61 value (acceptable values range from 0.273-2.188) and POF=0.77 can be obtained considering the nine (9) youngest detrital zircons component. We also consider this age as a robust one according to the same arguments presented for sample PB1.

Sample ZPR1 (52°39'14.86"S; 71°58'9.06"W). Seventy-nine (79) detrital zircons grains were analysed (~96.2% concordant ages), ranging from 67.7-276.5 Ma (Figure 3). This sample shows three significant age peaks at 68-81 Ma, 93-107 Ma, and between 142-160 Ma and a small peak at 277 Ma. The 44.3% of measured U-Pb ages fall in the Late Cretaceous (67.7-100.3 Ma), the 38% in the Early Cretaceous (100.8-113.1 Ma), and the 15.2% fall in the Upper Jurassic (150.5-160.8 Ma). The Permian zircons (272.6-276.5 Ma; 2 grains) represent only 2.5% of all measured U-Pb ages. The maximum depositional age of the two (2) younger grains (excepting the youngest single grain) that yield concordant ages is 73.5 ± 1.3 Ma with an MSWD=0.21 value (acceptable values range from 0.001-5.020) and POF=0.65. When the youngest zircon (67.7±2.4 Ma) is incorporated into the maximum depositional age calculation, the MSWD overcomes the acceptable range for a statistically robust age. The final maximum depositional age calculated (73.5 ± 1.3 Ma) is statistically robust and consistent with the palaeontological age (late Campanian-Maastrichtian; Charrier and Lahsen, 1969; Castelli et al., 1992). However, the presence of the youngest zircon of 67.7±2.4 Ma suggests that this sample might be younger.

Sample ZLP1 (52° 3'54.90"S; 72°23'51.52"W). Eighty-three (83) detrital zircons grains were analysed (~90% concordant ages), which ranges from 67.1-2204 Ma, showing three significant peaks at 69-73 Ma, 92-108 Ma, and 146-171 Ma, also minor but significant peaks at 272-315 Ma, 615-640 Ma, and 1930-2200 Ma are well represented (Figure 4). The 36.1% of measured U-Pb ages fall in the Late Cretaceous (67.1-98.9 Ma), the 31.3% in the Early Cretaceous (101.8-143.9 Ma), and the 22.9% fall in the Upper and Middle Jurassic (145.5-170.9 Ma). The Paleozoic zircons (271.7-315 Ma; 3 grains) represent only 3.6% of all measured U-Pb ages, whereas the Proterozoic grains (614-2204 Ma; 4 grains) represents 4.8%. The maximum depositional age is 67.7 ± 1.2 Ma considering the three (3) youngest zircons with an MSWD=0.71 (acceptable values ranges from 0.025-3.690) and POF=0.5. This result is considered statistically robust and consistent with the palaeontological age.

FIGURES ANNEX C-1

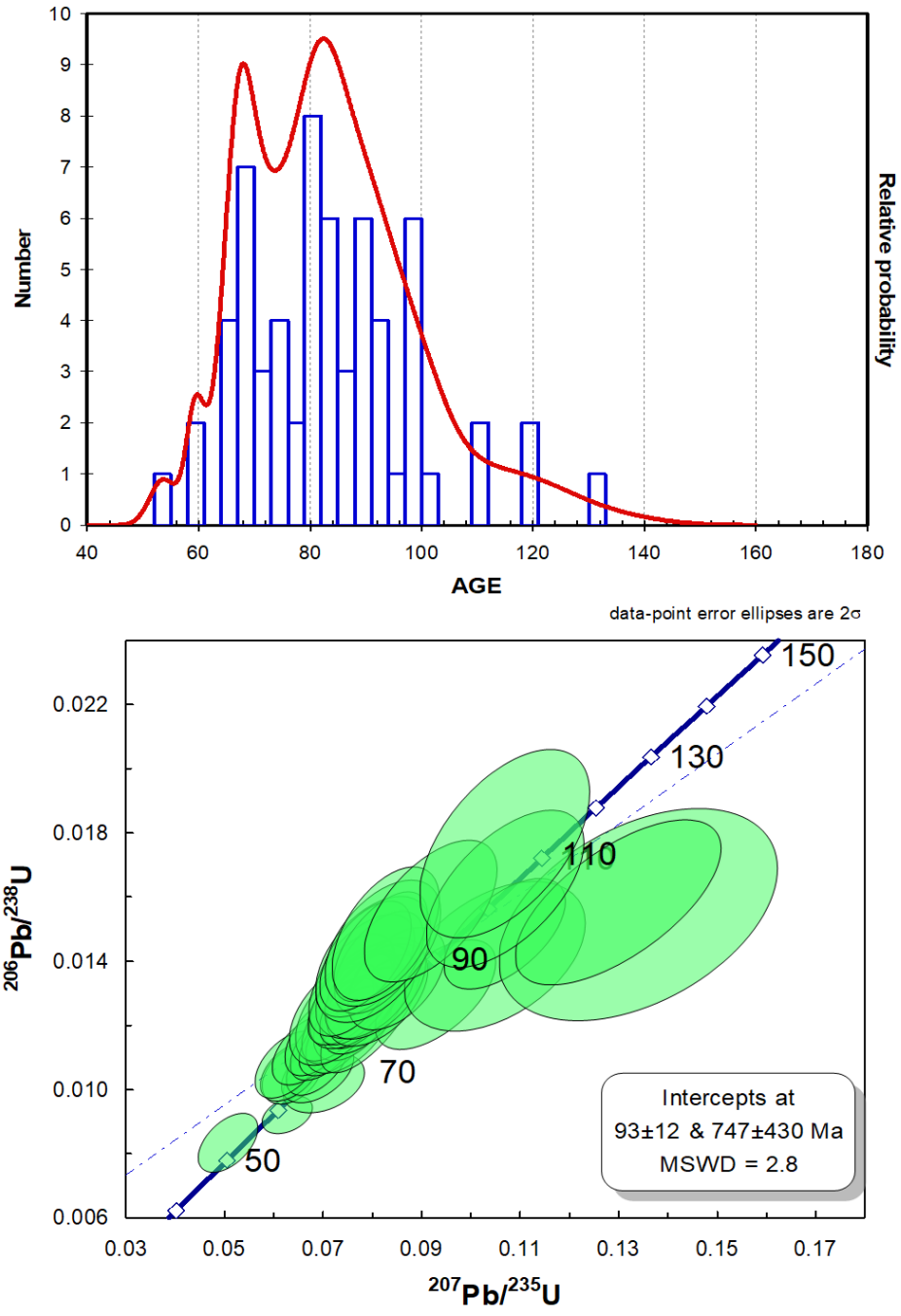

Figure 1. Probability density plot and Wetherill Concordia diagram for sample PB1.

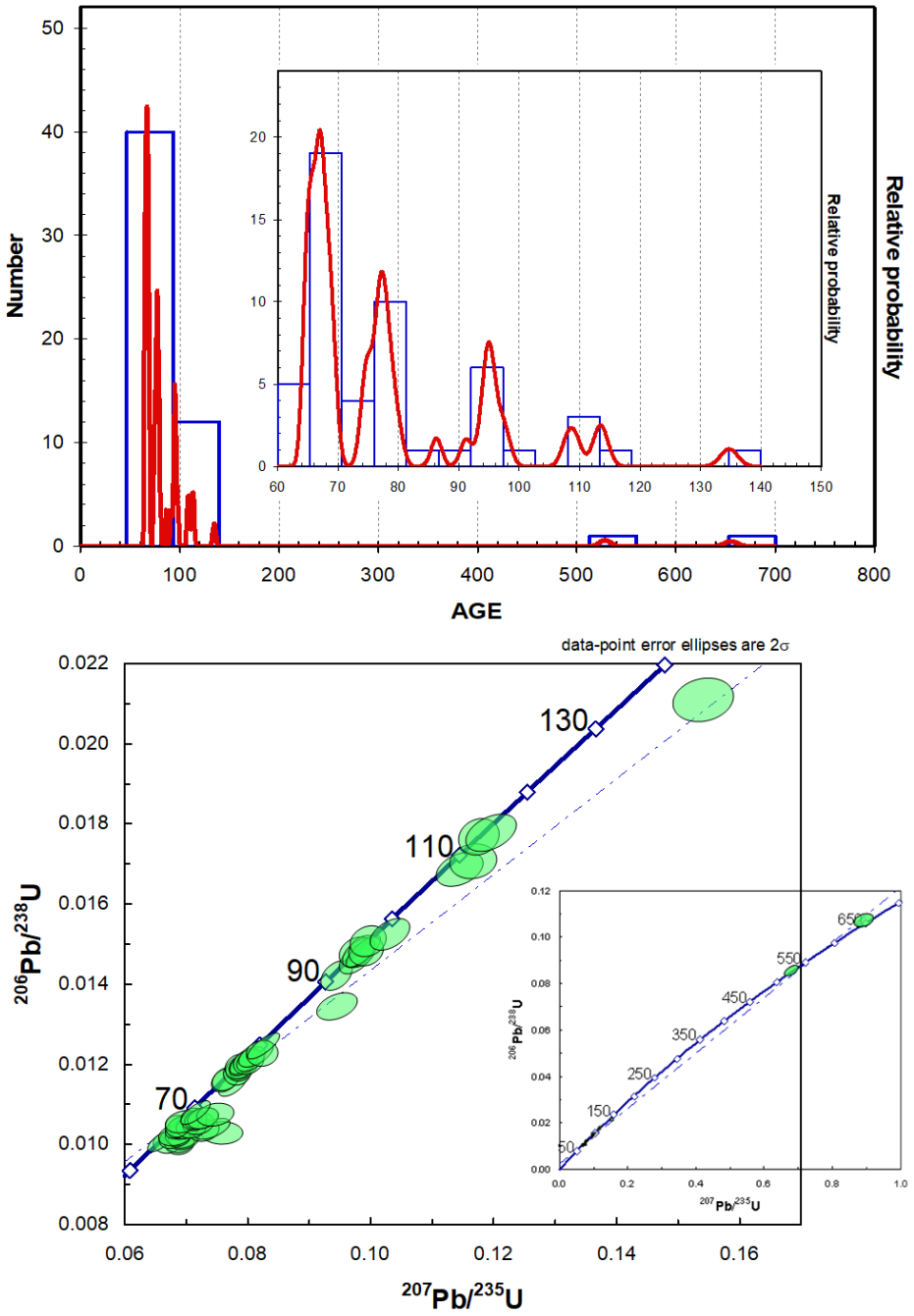

Figure 2. Probability density plot and Wetherill Concordia diagram for sample RB1.

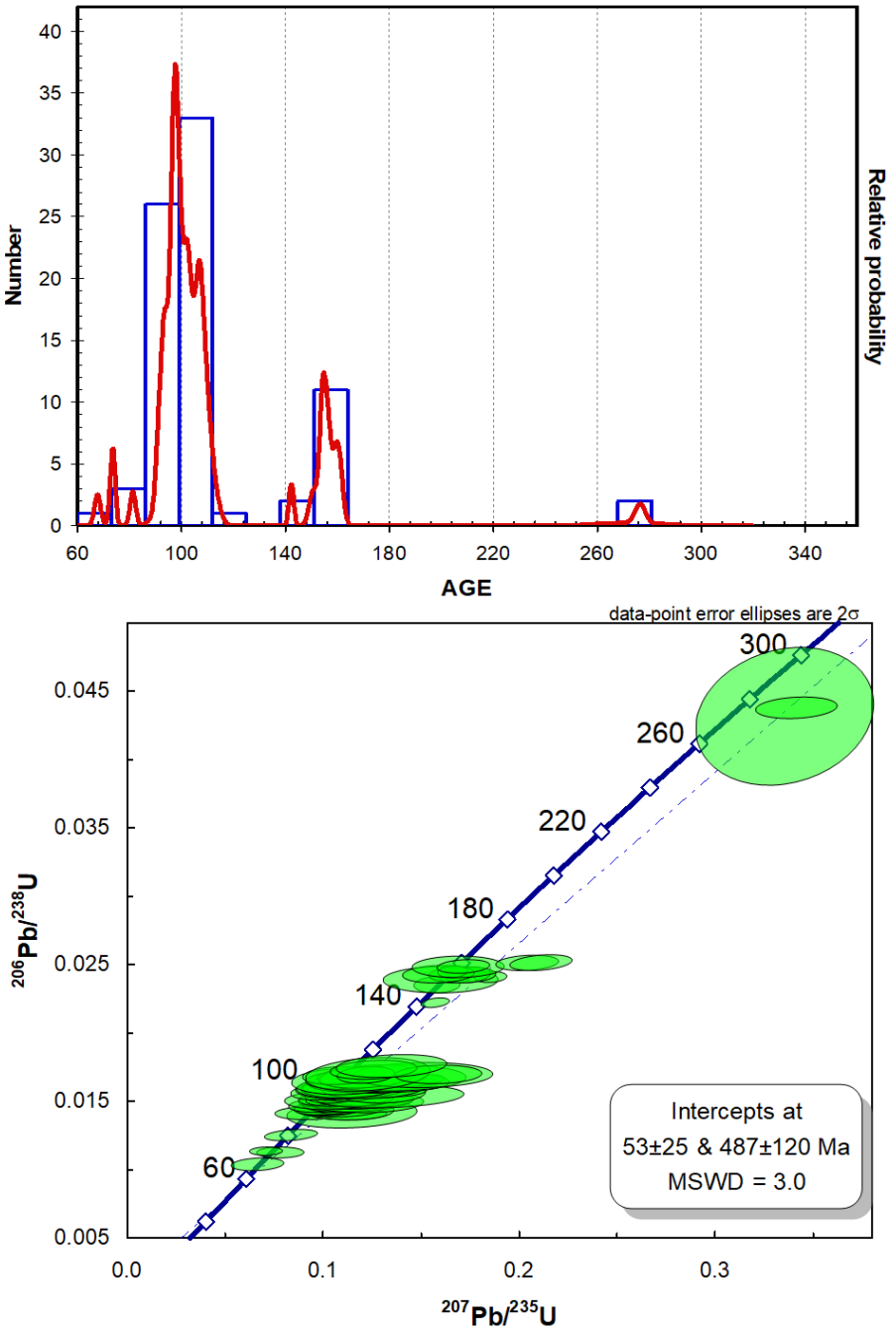

Figure 3. Probability density plot and Wetherill Concordia diagram for sample ZPR1.

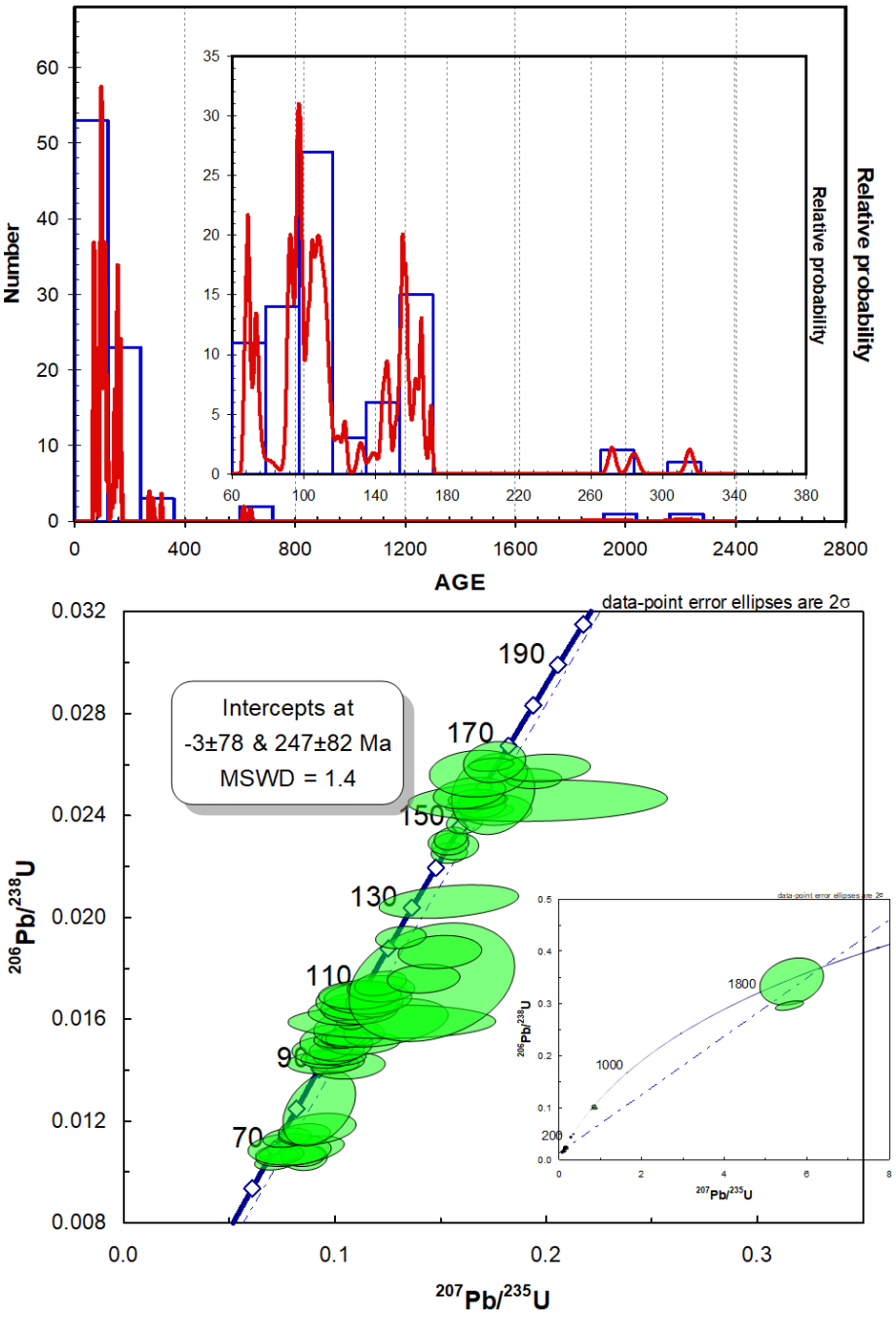

Figure 4. Probability density plot and Wetherill Concordia diagram for sample ZLP1.

ANNEX C-2

DETRITAL ZIRCON U-PB GEOCHRONOLOGIC ANALYSES BY USING LA-ICP-MS & LA-MC-ICP-MS ANALYSIS

Table D. Detrital zircon U-Pb geochronologic analyses by using LA-ICP-MS and LA-MC-ICP-MS analysis

Analysis	U (ppm)	U/Th	Apparent ages (Ma) $^{206}Pb^*/^{238}U$	± 2σ (Ma)	$^{207}Pb^*/^{235}U$	± 2σ (Ma)	$^{207}Pb^*/^{206}Pb^*$	± 2σ (Ma)	Preferred age ± 2σ (Ma)		conc (%)
Sample PB1-Chorrillo Chico Formation (SERNAGEOMIN Lab.)											
PB1_38	116	0.97	53.7	4.8	49.5	4.6	170.0	120.0	53.6	4.8	108.5
PB1_42	88	0.99	59.4	3.0	61.5	4.0	210.0	110.0	59.2	3.1	96.6
PB1_16	108	0.80	61.4	4.4	76.9	5.7	610.0	120.0	60.2	4.4	79.8
PB1_12	57	1.14	65.7	4.8	68.6	6.3	300.0	150.0	65.1	4.8	95.8
PB1_62	56	0.81	73.8	6.3	182.0	15.0	1920.0	150.0	65.5	5.7	40.5
PB1_51	91	0.73	67.4	5.3	91.1	6.9	820.0	120.0	65.6	5.2	74.0
PB1_2	85	0.92	69.0	4.6	101.1	6.7	890.0	110.0	66.7	4.4	68.2
PB1_9	79	0.80	67.3	4.7	62.6	4.8	90.0	120.0	67.3	4.8	107.5
PB1_37	92	0.82	70.8	5.1	114.1	8.2	1150.0	120.0	67.6	4.9	62.1
PB1_50	75	0.96	67.8	5.0	67.3	5.7	150.0	120.0	67.7	5.0	100.7
PB1_39	92	0.79	67.8	4.8	61.7	4.7	150.0	110.0	67.8	4.8	109.9
PB1_36	77	1.20	79.5	7.2	200.0	18.0	2170.0	140.0	69.0	6.2	39.8
PB1_34	130	0.78	69.7	5.4	67.2	4.9	230.0	100.0	69.5	5.3	103.7
PB1_43	87	1.07	69.2	5.4	60.9	5.1	-10.0	110.0	69.6	5.5	113.6
PB1_1	72	0.71	73.7	6.3	99.9	8.1	820.0	130.0	71.2	6.2	73.8
PB1_63	97	0.96	77.2	6.4	139.0	10.0	1430.0	120.0	71.8	6.0	55.5
PB1_47	87	1.28	72.0	5.6	65.0	5.3	140.0	110.0	72.1	5.6	110.8
PB1_40	138	0.95	73.4	5.9	68.4	5.5	150.0	100.0	73.4	6.0	107.3
PB1_48	192	0.83	75.3	6.5	67.0	5.3	120.0	100.0	74.8	6.4	112.4
PB1_60	107	0.90	74.6	6.6	70.0	5.8	110.0	110.0	74.9	6.4	106.6
PB1_49	89	1.07	76.0	6.7	71.9	6.6	180.0	130.0	75.9	7.0	105.7
PB1_28	109	1.28	77.9	6.7	72.5	6.1	210.0	120.0	77.7	7.0	107.4
PB1_25	116	0.89	78.3	6.9	73.1	6.1	210.0	120.0	78.2	7.0	107.1
PB1_54	111	1.00	79.0	7.3	69.5	6.0	170.0	120.0	79.1	7.6	113.7
PB1_22	370	0.43	79.4	9.6	76.6	7.6	120.0	120.0	79.1	9.5	103.7
PB1_61	81	1.14	78.9	8.4	69.4	7.1	150.0	150.0	79.2	8.3	113.7
PB1_52	132	0.80	79.5	7.1	75.1	6.3	210.0	110.0	79.6	7.0	105.9
PB1_44	225	0.61	81.7	7.4	75.9	6.3	160.0	100.0	81.5	7.6	107.6
PB1_56	88	0.92	81.7	7.4	73.3	6.9	140.0	130.0	81.6	7.6	111.5
PB1_46	84	1.14	82.8	8.8	88.5	9.1	470.0	150.0	81.7	8.8	93.6

Table D . Detrital zircon U-Pb geochronologic analyses by using LA-ICP-MS and LA-MC-ICP-MS analysis (continued)

Analysis	U (ppm)	U/Th	Apparent ages (Ma) $^{206}Pb^*/^{238}U$	± 2σ (Ma)	$^{207}Pb^*/^{235}U$	± 2σ (Ma)	$^{207}Pb^*/^{206}Pb^*$	± 2σ (Ma)	Preferred age ± 2σ (Ma)		conc (%)
PB1_18	107	0.80	82.3	7.7	72.3	6.5	230.0	130.0	81.8	7.6	113.8
PB1_19	118	0.81	82.5	7.8	74.4	6.2	210.0	120.0	82.2	7.6	110.9
PB1_6	63	1.43	82.8	8.2	76.7	7.7	180.0	160.0	82.8	8.3	108.0
PB1_41	61	1.61	83.6	7.9	73.9	7.3	90.0	150.0	83.4	7.6	113.1
PB1_45	40	1.29	83.8	8.6	68.6	9.5	190.0	190.0	83.8	8.9	122.2
PB1_8	68	1.21	84.1	8.0	76.8	7.7	230.0	150.0	83.9	8.2	109.5
PB1_35	99	1.11	84.7	8.1	72.9	6.6	210.0	120.0	84.6	8.2	116.2
PB1_4	72	1.20	86.1	8.0	81.9	7.5	370.0	140.0	85.3	8.2	105.1
PB1_27	112	0.80	86.0	11.0	70.0	8.9	30.0	180.0	86.0	11.5	122.9
PB1_24	121	0.90	86.9	8.2	69.3	6.3	50.0	120.0	87.1	8.3	125.4
PB1_55	51	1.21	90.0	12.0	99.0	14.0	530.0	220.0	88.0	11.8	90.9
PB1_3	78	1.22	89.0	8.6	76.0	7.7	50.0	140.0	88.9	8.3	117.1
PB1_29	123	0.80	89.8	8.5	77.6	6.7	200.0	130.0	89.0	8.2	115.7
PB1_10	117	0.68	93.6	9.6	127.0	11.0	1020.0	130.0	89.4	9.1	73.7
PB1_58	73	0.96	89.0	10.0	77.3	8.7	190.0	170.0	89.8	10.2	115.1
PB1_31	108	1.16	91.0	8.6	75.3	6.9	110.0	130.0	90.7	8.9	120.8
PB1_32	127	1.02	92.3	9.1	78.6	7.2	130.0	130.0	92.1	8.9	117.4
PB1_20	93	0.96	94.5	9.1	100.6	9.0	600.0	140.0	92.9	8.7	93.9
PB1_30	76	1.06	93.0	10.0	77.5	8.8	130.0	160.0	93.1	10.2	120.0
PB1_5	106	1.10	99.0	17.0	121.0	19.0	1010.0	280.0	93.9	16.4	81.8
PB1_57	117	0.91	95.0	10.0	78.0	8.0	140.0	140.0	94.4	10.7	121.8
PB1_17	58	0.98	98.0	12.0	77.6	9.6	320.0	190.0	97.3	12.0	126.3
PB1_13	130	0.93	98.0	10.0	78.9	7.8	110.0	130.0	97.7	10.7	124.2
PB1_59	78	1.00	101.0	13.0	121.0	15.0	720.0	180.0	98.7	13.0	83.5
PB1_11	109	1.09	99.1	9.9	81.8	7.8	140.0	130.0	99.1	10.1	121.1
PB1_26	80	1.21	100.0	12.0	88.0	10.0	210.0	170.0	99.3	11.4	113.6
PB1_7	99	0.98	99.0	10.0	78.4	7.9	140.0	140.0	99.7	10.1	126.3
PB1_53	81	0.95	103.0	13.0	102.0	12.0	330.0	160.0	102.7	12.6	101.0
PB1_33	80	1.38	110.0	12.0	87.7	9.2	190.0	160.0	110.7	12.0	125.4
PB1_23	119	0.93	112.0	15.0	100.0	12.0	310.0	180.0	111.3	15.0	112.0
PB1_21	92	0.95	120.0	15.0	88.0	10.0	90.0	160.0	119.8	14.5	136.4

Table D . Detrital zircon U-Pb geochronologic analyses by using LA-ICP-MS and LA-MC-ICP-MS analysis (continued)

Analysis	U (ppm)	U/Th	Apparent ages (Ma) $^{206}Pb^*/^{238}U$	± 2σ (Ma)	$^{207}Pb^*/^{235}U$	± 2σ (Ma)	$^{207}Pb^*/^{206}Pb^*$	± 2σ (Ma)	Preferred age ± 2σ (Ma)		conc (%)
PB1_14	88	0.96	121.0	15.0	95.0	11.0	110.0	170.0	120.8	15.1	127.4
PB1_15	71	1.27	131.0	18.0	99.0	15.0	260.0	210.0	131.2	18.2	132.3
Sample RB1-Chorrillo Chico Formation (CEGA Lab.)											
B531_53	113	0.43	64.4	1.3	67.9	1.8	161.0	41.0	64.4	1.3	94.9
B531_44	197	0.40	64.7	1.4	66.1	1.7	141.0	33.0	64.7	1.4	97.8
B531_43	115	0.45	64.9	1.4	67.9	1.9	198.0	47.0	64.9	1.4	95.6
B531_36	438	0.96	65.0	1.4	65.1	1.6	82.0	22.0	65.0	1.4	99.8
B531_35	140	0.40	65.2	1.4	68.7	1.9	183.0	44.0	65.2	1.4	94.9
B531_49	105	0.48	65.5	1.5	67.2	1.9	128.0	46.0	65.5	1.5	97.5
B531_27	139	0.36	65.6	1.4	68.5	1.9	139.0	36.0	65.6	1.4	95.8
B531_48	397	0.67	65.8	1.4	67.7	1.6	141.0	23.0	65.8	1.4	97.2
B531_41	93	0.41	66.0	1.4	67.4	2.2	132.0	48.0	66.0	1.4	97.9
B531_47	58	0.39	66.3	1.4	74.5	2.5	359.0	59.0	66.3	1.4	89.0
B531_33	96	0.41	66.6	1.4	71.8	1.9	233.0	36.0	66.6	1.4	92.8
B531_31	108	0.53	66.9	1.4	73.0	2.2	273.0	52.0	66.9	1.4	91.7
B531_16	259	0.47	67.0	1.4	68.1	1.7	103.0	31.0	67.0	1.4	98.3
B531_22	166	0.44	67.1	1.4	68.6	1.9	122.0	47.0	67.1	1.4	97.9
B531_42	261	0.60	67.2	1.5	67.8	1.8	96.0	31.0	67.2	1.5	99.1
B531_30	124	0.43	67.2	1.4	69.7	1.9	167.0	45.0	67.2	1.4	96.4
B531_28	636	1.12	67.3	1.4	67.6	1.5	78.0	17.0	67.3	1.4	99.6
B531_39	101	0.45	67.8	1.4	70.8	2.0	186.0	45.0	67.8	1.4	95.7
B531_24	91	0.49	68.1	1.5	68.5	2.2	97.0	53.0	68.1	1.5	99.3
B531_23	189	0.68	68.5	1.5	70.2	1.6	123.0	29.0	68.5	1.5	97.6
B531_20	117	0.46	68.6	1.4	71.3	2.1	175.0	50.0	68.6	1.4	96.2
B531_34	106	0.46	68.6	1.4	71.6	2.0	167.0	35.0	68.6	1.4	95.9
B531_26	71	0.45	69.2	1.5	73.5	2.4	222.0	56.0	69.2	1.5	94.1
B531_21	436	1.07	69.5	1.5	70.4	1.8	121.0	21.0	69.5	1.5	98.8
B531_51	597	0.60	74.1	1.6	76.1	1.8	133.0	25.0	74.1	1.6	97.3
B531_15	669	0.71	74.7	1.6	75.0	1.7	94.0	17.0	74.7	1.6	99.7
B531_32	802	0.59	74.9	1.5	75.0	1.7	68.0	23.0	74.9	1.5	99.8
B531_9	723	0.61	75.7	1.6	76.7	1.7	107.0	17.0	75.7	1.6	98.7

Table D. Detrital zircon U-Pb geochronologic analyses by using LA-ICP-MS and LA-MC-ICP-MS analysis (continued)

Analysis	U (ppm)	U/Th	Apparent ages (Ma) $^{206}Pb^*/^{238}U$	± 2σ (Ma)	$^{207}Pb^*/^{235}U$	± 2σ (Ma)	$^{207}Pb^*/^{206}Pb^*$	± 2σ (Ma)	Preferred age ± 2σ (Ma)		conc (%)
B531_4	1061	0.47	76.4	1.6	77.1	1.7	106.0	17.0	76.4	1.6	99.1
B531_1	342	0.55	76.7	1.6	77.9	1.8	134.0	22.0	76.7	1.6	98.5
B531_45	745	0.51	76.9	1.6	77.0	1.7	84.0	18.0	76.9	1.6	99.8
B531_6	825	0.72	77.4	1.6	77.8	1.8	101.0	17.0	77.4	1.6	99.5
B531_0	1043	0.51	77.6	1.6	77.9	1.8	95.5	11.0	77.6	1.6	99.5
B531_3	359	0.67	77.6	1.7	78.5	1.8	142.0	18.0	77.6	1.7	98.8
B531_29	426	0.53	78.0	1.6	78.9	1.8	113.0	21.0	78.0	1.6	98.9
B531_17	156	0.45	78.8	1.7	79.7	2.2	114.0	35.0	78.8	1.7	98.9
B531_38	405	0.48	78.9	1.6	80.6	1.9	145.0	27.0	78.9	1.6	97.9
B531_7	427	0.56	80.1	1.7	80.8	2.0	105.0	20.0	80.1	1.7	99.2
B531_46	234	0.36	86.3	1.8	92.0	2.5	240.0	40.0	86.3	1.8	93.8
B531_5	1432	1.65	91.2	1.9	91.8	2.0	113.8	12.0	91.2	1.9	99.3
B531_37	1571	0.68	93.9	2.0	94.7	2.0	104.0	13.0	93.9	2.0	99.2
B531_19	284	0.70	94.9	1.9	94.9	2.3	106.0	28.0	94.9	1.9	100.0
B531_14	624	0.49	94.9	1.9	95.2	2.1	105.0	14.0	94.9	1.9	99.7
B531_11	1484	1.11	95.1	2.0	95.8	2.1	121.0	12.0	95.1	2.0	99.3
B531_50	541	0.61	95.2	1.9	96.2	2.1	113.0	18.0	95.2	1.9	99.0
B531_18	285	0.66	96.7	2.0	96.6	2.3	115.0	25.0	96.7	2.0	100.1
B531_8	376	0.28	97.8	2.0	99.8	2.4	144.0	23.0	97.8	2.0	98.0
B531_13	147	0.47	108.0	2.2	110.2	2.8	166.0	30.0	108.0	2.2	98.0
B531_12	213	0.34	109.3	2.2	112.1	2.8	172.0	30.0	109.3	2.2	97.5
B531_40	563	0.27	113.1	2.3	113.1	2.4	116.0	15.0	113.1	2.3	100.1
B531_25	152	0.58	113.8	2.4	114.8	3.0	124.0	31.0	113.8	2.4	99.1
B531_52	124	0.73	134.7	2.9	145.5	3.5	319.0	34.0	134.7	2.9	92.6
B531_10	139	0.59	528.3	11.0	526.3	9.8	533.0	13.0	528.3	11.0	100.4
B531_2	25	0.02	655.3	13.0	647.2	12.0	643.0	17.0	655.3	13.0	101.3
Sample ZPR1-Rocallosa Formation (UNAM Lab.)											
Zircon-07	156	2.48	67.7	2.4	66.6	9.8	0.0	270.0	67.7	2.4	101.7
Zircon-78	144	1.03	73.2	2.0	76.3	9.3	220.0	250.0	73.2	2.0	95.9
Zircon-24	263	0.92	73.8	1.7	70.8	6.3	-30.0	190.0	73.8	1.7	104.2
Zircon-05	175	1.98	81.3	2.2	82.0	11.0	20.0	250.0	81.3	2.2	99.1

Table D. Detrital zircon U-Pb geochronologic analyses by using LA-ICP-MS and LA-MC-ICP-MS analysis (continued)

Analysis	U (ppm)	U/Th	Apparent ages (Ma) $^{206}Pb^*/^{238}U$	± 2σ (Ma)	$^{207}Pb^*/^{235}U$	± 2σ (Ma)	$^{207}Pb^*/^{206}Pb^*$	± 2σ (Ma)	Preferred age ± 2σ (Ma)		conc (%)
Zircon-93	37	1.37	91.2	5.5	107.0	24.0	270.0	460.0	91.2	5.5	85.2
Zircon-77	149	1.40	91.3	2.3	107.0	15.0	320.0	290.0	91.3	2.3	85.3
Zircon-94	102	1.77	91.5	2.5	89.0	13.0	-10.0	290.0	91.5	2.5	102.8
Zircon-44	43	2.23	92.8	3.9	113.0	18.0	380.0	330.0	92.8	3.9	82.1
Zircon-61	86	1.67	93.1	2.9	104.0	16.0	230.0	330.0	93.1	2.9	89.5
Zircon-85	248	1.76	93.1	1.9	101.1	7.7	250.0	180.0	93.1	1.9	92.1
Zircon-06	102	1.09	93.7	2.8	99.0	13.0	240.0	270.0	93.7	2.8	94.6
Zircon-46	164	1.55	93.8	2.6	97.0	12.0	200.0	250.0	93.8	2.6	96.7
Zircon-39	121	2.11	94.4	2.9	104.0	11.0	380.0	240.0	94.4	2.9	90.8
Zircon-26	118	1.08	95.3	2.8	96.0	13.0	90.0	270.0	95.3	2.8	99.3
Zircon-75	76	1.22	95.9	3.1	108.0	16.0	360.0	310.0	95.9	3.1	88.8
Zircon-28	449	3.31	96.4	1.7	97.0	5.0	118.0	120.0	96.4	1.7	99.4
Zircon-83	54	2.22	96.5	3.6	110.0	21.0	230.0	390.0	96.5	3.6	87.7
Zircon-66	64	1.02	96.6	4.0	114.0	21.0	350.0	350.0	96.6	4.0	84.7
Zircon-57	100	2.53	96.9	2.9	110.0	14.0	330.0	280.0	96.9	2.9	88.1
Zircon-92	58	1.78	97.0	3.0	108.0	17.0	270.0	320.0	97.0	3.0	89.8
Zircon-60	321	3.14	97.1	2.1	94.6	7.1	80.0	180.0	97.1	2.1	102.6
Zircon-34	73	1.31	97.3	3.1	115.0	18.0	460.0	320.0	97.3	3.1	84.6
Zircon-64	80	1.31	97.3	3.5	102.0	18.0	140.0	340.0	97.3	3.5	95.4
Zircon-89	440	3.55	97.6	2.1	93.5	6.6	-10.0	160.0	97.6	2.1	104.4
Zircon-16	163	4.49	97.7	2.5	100.8	9.7	190.0	210.0	97.7	2.5	96.9
Zircon-67	152	1.37	97.8	2.2	117.0	11.0	520.0	210.0	97.8	2.2	83.6
Zircon-95	437	2.80	97.8	1.8	101.2	6.1	150.0	150.0	97.8	1.8	96.6
Zircon-47	167	1.42	98.2	2.7	116.0	11.0	480.0	220.0	98.2	2.7	84.7
Zircon-73	428	3.25	98.2	1.8	102.5	7.5	190.0	160.0	98.2	1.8	95.8
Zircon-49	73	1.20	98.5	3.3	110.0	14.0	270.0	290.0	98.5	3.3	89.5
Zircon-51	46	1.48	99.2	4.3	123.0	28.0	610.0	400.0	99.2	4.3	80.7
Zircon-87	167	2.71	99.4	2.5	99.3	9.5	90.0	210.0	99.4	2.5	100.1
Zircon-43	628	2.30	99.5	1.5	103.5	5.4	190.0	130.0	99.5	1.5	96.1
Zircon-53	134	1.28	100.1	2.4	108.0	11.0	220.0	230.0	100.1	2.4	92.7
Zircon-30	614	1.83	100.3	2.6	100.6	5.5	130.0	140.0	100.3	2.6	99.7
Zircon-98	65	2.32	100.8	3.8	126.0	17.0	520.0	310.0	100.8	3.8	80.0
Zircon-96	356	2.34	101.5	2.3	101.3	6.0	60.0	130.0	101.5	2.3	100.2
Zircon-09	75	1.46	101.8	3.4	98.0	13.0	70.0	280.0	101.8	3.4	103.9
Zircon-79	91	2.48	102.1	2.8	124.0	16.0	540.0	290.0	102.1	2.8	82.3
Zircon-71	164	2.78	102.2	7.6	127.0	83.0	490.0	420.0	102.2	7.6	80.5
Zircon-14	78	2.19	102.4	3.6	101.0	15.0	10.0	300.0	102.4	3.6	101.4
Zircon-56	454	2.39	102.5	2.3	105.6	6.0	190.0	140.0	102.5	2.3	97.1
Zircon-02	65	1.14	102.9	3.5	113.0	19.0	230.0	350.0	102.9	3.5	91.1
Zircon-25	94	1.63	102.9	3.1	108.0	13.0	140.0	260.0	102.9	3.1	95.3
Zircon-72	79	2.29	103.1	4.1	107.0	17.0	160.0	320.0	103.1	4.1	96.4
Zircon-97	53	1.63	103.7	4.5	121.0	19.0	420.0	370.0	103.7	4.5	85.7
Zircon-11	57	2.25	104.0	4.5	107.0	21.0	110.0	330.0	104.0	4.5	97.2
Zircon-36	86	2.98	105.5	2.8	126.0	18.0	450.0	310.0	105.5	2.8	83.7
Zircon-15	57	2.51	105.6	4.0	116.0	21.0	330.0	380.0	105.6	4.0	91.0
Zircon-22	67	2.77	105.6	3.7	125.0	22.0	460.0	340.0	105.6	3.7	84.5
Zircon-59	64	1.24	106.0	3.9	111.0	17.0	30.0	310.0	106.0	3.9	95.5
Zircon-32	40	2.24	106.1	5.0	112.0	21.0	120.0	370.0	106.1	5.0	94.7
Zircon-37	890	6.01	106.7	2.2	140.2	9.3	670.0	150.0	106.7	2.2	76.1
Zircon-65	71	1.37	106.8	3.4	107.0	16.0	100.0	300.0	106.8	3.4	99.8
Zircon-63	309	1.97	107.5	2.2	110.0	6.0	150.0	140.0	107.5	2.2	97.7
Zircon-40	45	1.69	107.8	5.0	124.0	28.0	220.0	450.0	107.8	5.0	86.9
Zircon-52	62	1.21	108.4	4.3	119.0	17.0	240.0	320.0	108.4	4.3	91.1
Zircon-03	122	2.75	108.8	3.4	104.0	15.0	-20.0	280.0	108.8	3.4	104.6
Zircon-23	52	1.79	109.0	4.6	139.0	25.0	420.0	350.0	109.0	4.6	78.4
Zircon-76	35	1.94	109.0	6.3	115.0	24.0	540.0	310.0	109.0	6.3	94.8
Zircon-10	103	2.18	109.2	3.1	118.0	11.0	270.0	230.0	109.2	3.1	92.5
Zircon-80	106	2.14	109.3	3.5	156.0	15.0	850.0	240.0	109.3	3.5	70.1
Zircon-84	75	1.18	111.4	3.6	119.0	16.0	170.0	280.0	111.4	3.6	93.6
Zircon-45	50	2.01	113.1	4.3	131.0	21.0	400.0	360.0	113.1	4.3	86.3
Zircon-68	1462	1.87	142.3	1.8	148.4	5.2	241.0	96.0	142.3	1.8	95.9
Zircon-74	232	1.72	150.5	3.0	148.8	8.5	160.0	150.0	150.5	3.0	101.1

TableD . Detrital zircon U-Pb geochronologic analyses by using LA-ICP-MS and LA-MC-ICP-MS analysis (continued)

Analysis	U (ppm)	U/Th	Apparent ages (Ma) $^{206}Pb^*/^{238}U$	± 2σ (Ma)	$^{207}Pb^*/^{235}U$	± 2σ (Ma)	$^{207}Pb^*/^{206}Pb^*$	± 2σ (Ma)	Preferred age ± 2σ (Ma)		conc (%)
Zircon-29	55	2.01	152.9	4.9	149.0	21.0	40.0	280.0	152.9	4.9	102.6
Zircon-18	1270	2.00	154.3	2.4	157.2	6.0	189.0	110.0	154.3	2.4	98.2
Zircon-70	1025	1.23	154.3	2.1	172.7	5.8	433.0	99.0	154.3	2.1	89.3
Zircon-31	492	3.13	155.1	3.0	162.6	8.1	286.0	120.0	155.1	3.0	95.4
Zircon-91	156	1.64	155.2	3.0	159.0	13.0	220.0	180.0	155.2	3.0	97.6
Zircon-86	126	2.56	155.5	3.3	151.0	12.0	50.0	180.0	155.5	3.3	103.0
Zircon-62	1054	1.07	156.6	2.2	156.1	5.4	141.0	110.0	156.6	2.2	100.3
Zircon-81	88	1.68	158.9	4.1	159.0	17.0	210.0	240.0	158.9	4.1	99.9
Zircon-54	245	2.41	159.0	2.7	160.4	9.4	180.0	140.0	159.0	2.7	99.1
Zircon-99	383	2.92	160.6	2.9	188.0	11.0	460.0	150.0	160.6	2.9	85.4
Zircon-88	356	3.46	160.8	2.9	193.9	11.0	620.0	130.0	160.8	2.9	82.9
Zircon-100_ZPR-1	1190	15.08	272.6	25.0	293.0	26.0	430.0	110.0	272.6	25.0	93.0
Zircon-20	281	1.00	276.5	3.9	297.0	13.0	454.0	120.0	276.5	3.9	93.1
Sample ZLP1-Dorotea Formation (UNAM Lab.)											
Zircon-57	282	0.98	67.1	1.6	70.7	7.6	210.0	210.0	67.1	1.6	94.9
Zircon-95	116	1.50	68.3	2.8	83.3	8.6	440.0	200.0	68.3	2.8	82.0
Zircon-88	149	1.77	68.6	2.2	82.9	7.8	510.0	210.0	68.6	2.2	82.8
Zircon-25	260	1.45	69.0	1.5	72.3	7.3	190.0	220.0	69.0	1.5	95.4
Zircon-31	140	1.55	69.0	2.0	72.2	8.8	200.0	250.0	69.0	2.0	95.6
Zircon-44	75	1.76	69.8	3.2	81.0	16.0	270.0	380.0	69.8	3.2	86.2
Zircon-14	69	1.32	70.3	3.2	78.0	15.0	180.0	400.0	70.3	3.2	90.1
Zircon-93	126	1.42	73.1	2.5	101.0	10.0	900.0	210.0	73.1	2.5	72.4
Zircon-73	203	1.08	73.2	2.0	75.5	9.1	120.0	220.0	73.2	2.0	97.0
Zircon-77	154	1.19	74.0	2.2	83.0	9.3	280.0	230.0	74.0	2.2	89.2
Zircon-64	121	1.61	75.3	3.2	89.0	14.0	370.0	320.0	75.3	3.2	84.6
Zircon-68	3260	1.26	80.5	7.7	90.3	12.0	353.0	120.0	80.5	7.7	89.1
Zircon-58	118	1.09	91.1	2.7	104.0	12.0	410.0	250.0	91.1	2.7	87.6
Zircon-24	274	1.30	91.6	1.8	97.5	9.0	240.0	200.0	91.6	1.8	93.9
Zircon-37	119	1.12	91.9	2.4	94.0	14.0	120.0	280.0	91.9	2.4	97.8
Zircon-96	75	1.76	92.3	3.8	128.0	17.0	800.0	230.0	92.3	3.8	72.1
Zircon-10	160	1.02	92.8	1.9	93.2	9.5	90.0	220.0	92.8	1.9	99.6
Zircon-41	531	2.08	93.2	1.7	99.1	9.1	330.0	160.0	93.2	1.7	94.0
Zircon-33	92	1.28	94.8	2.9	93.0	13.0	70.0	280.0	94.8	2.9	101.9
Zircon-22	355	2.27	95.1	2.1	95.0	7.8	100.0	180.0	95.1	2.1	100.1
Zircon-23	706	1.92	96.6	1.2	96.4	6.0	54.0	130.0	96.6	1.2	100.2
Zircon-50	91	1.15	96.6	2.1	108.0	12.0	340.0	250.0	96.6	2.1	89.4
Zircon-61	87	1.39	96.7	3.6	119.0	17.0	460.0	340.0	96.7	3.6	81.3
Zircon-60	79	1.71	96.8	3.8	103.0	13.0	280.0	270.0	96.8	3.8	94.0
Zircon-71	124	1.19	97.2	2.9	120.0	13.0	600.0	210.0	97.2	2.9	81.0
Zircon-49	220	2.76	97.6	1.8	102.0	10.0	200.0	220.0	97.6	1.8	95.7
Zircon-12	406	2.69	98.1	1.7	99.6	7.0	160.0	160.0	98.1	1.7	98.5
Zircon-99	715	2.09	98.2	2.2	101.7	7.2	190.0	150.0	98.2	2.2	96.6
Zircon-59	240	2.21	98.5	2.0	118.9	7.9	530.0	150.0	98.5	2.0	82.8
Zircon-92	235	2.47	98.9	2.5	110.8	7.2	320.0	140.0	98.9	2.5	89.3
Zircon-76	47	1.46	101.8	4.9	114.0	23.0	340.0	370.0	101.8	4.9	89.3
Zircon-82	82	1.18	101.8	3.3	123.0	17.0	480.0	290.0	101.8	3.3	82.8
Zircon-86	92	1.85	102.0	3.4	120.0	32.0	350.0	320.0	102.0	3.4	85.0
Zircon-54	708	2.30	102.5	2.0	104.3	5.4	148.0	110.0	102.5	2.0	98.3
Zircon-06	102	2.72	104.4	2.7	102.0	13.0	20.0	280.0	104.4	2.7	102.4
Zircon-39	359	1.80	104.6	1.6	101.3	7.4	30.0	150.0	104.6	1.6	103.3
Zircon-52	62	1.15	105.4	3.2	109.0	14.0	180.0	270.0	105.4	3.2	96.7
Zircon-29	61	1.59	105.8	2.7	133.0	19.0	520.0	280.0	105.8	2.7	79.5
Zircon-16	59	1.41	107.2	3.7	106.0	14.0	70.0	270.0	107.2	3.7	101.1
Zircon-55	172	4.34	107.2	3.2	114.0	10.0	210.0	190.0	107.2	3.2	94.0
Zircon-46	65	1.30	107.6	3.5	148.0	16.0	790.0	250.0	107.6	3.5	72.7
Zircon-07	82	1.99	107.9	3.3	110.0	15.0	210.0	290.0	107.9	3.3	98.1
Zircon-20	113	1.27	108.7	2.9	109.0	14.0	150.0	240.0	108.7	2.9	99.7
Zircon-45	173	1.31	109.0	3.0	152.0	16.0	840.0	180.0	109.0	3.0	71.7
Zircon-30	67	1.65	109.8	3.9	150.0	26.0	860.0	310.0	109.8	3.9	73.2
Zircon-65	168	2.18	110.3	2.7	117.8	11.0	310.0	190.0	110.3	2.7	93.6
Zircon-85	238	1.45	111.6	2.4	117.0	9.3	300.0	160.0	111.6	2.4	95.4
Zircon-62	47	1.33	112.0	12.0	136.0	27.0	540.0	300.0	112.0	12.0	82.4

Table D. Detrital zircon U-Pb geochronologic analyses by using LA-ICP-MS and LA-MC-ICP-MS analysis (continued)

Analysis	U (ppm)	U/Th	Apparent ages (Ma) $^{206}Pb^*/^{238}U$	± 2σ (Ma)	$^{207}Pb^*/^{235}U$	± 2σ (Ma)	$^{207}Pb^*/^{206}Pb^*$	± 2σ (Ma)	Preferred age ± 2σ (Ma)		conc (%)
Zircon-66	50	1.68	112.6	5.2	150.0	23.0	640.0	340.0	112.6	5.2	75.1
Zircon-56	165	1.24	112.7	2.9	137.0	12.0	510.0	200.0	112.7	2.9	82.3
Zircon-34	91	1.98	112.8	3.6	156.0	18.0	870.0	230.0	112.8	3.6	72.3
Zircon-89	97	2.69	114.3	3.6	142.0	14.0	560.0	230.0	114.3	3.6	80.5
Zircon-53	115	1.70	119.3	3.3	141.0	14.0	430.0	200.0	119.3	3.3	84.6
Zircon-42	267	2.29	122.9	2.2	126.2	8.3	170.0	150.0	122.9	2.2	97.4
Zircon-13	71	0.99	131.7	3.4	143.0	23.0	230.0	310.0	131.7	3.4	92.1
Zircon-18	105	1.64	138.8	5.0	193.0	29.0	840.0	260.0	138.8	5.0	71.9
Zircon-87	1358	1.39	143.9	2.1	145.7	6.2	194.0	81.0	143.9	2.1	98.8
Zircon-90	466	1.29	145.5	2.7	149.0	7.8	204.0	120.0	145.5	2.7	97.7
Zircon-67	790	2.06	146.3	2.4	145.1	6.9	125.0	100.0	146.3	2.4	100.8
Zircon-84	1689	3.15	147.3	2.2	146.2	5.8	131.0	81.0	147.3	2.2	100.8
Zircon-91	1552	1.56	151.3	2.4	152.0	6.2	146.0	87.0	151.3	2.4	99.5
Zircon-03	571	1.49	153.9	1.7	160.6	10.0	290.0	150.0	153.9	1.7	95.8
Zircon-01_ZLP-1	125	1.19	154.4	3.1	164.0	13.0	300.0	200.0	154.4	3.1	94.1
Zircon-19	1716	2.62	155.2	1.1	152.9	7.3	92.0	120.0	155.2	1.1	101.5
Zircon-100_ZLP-1	579	1.63	155.3	2.4	159.8	7.9	186.0	110.0	155.3	2.4	97.2
Zircon-94	391	1.74	156.6	4.1	184.0	37.0	460.0	260.0	156.6	4.1	85.1
Zircon-32	890	1.24	156.8	1.5	160.4	8.5	202.0	130.0	156.8	1.5	97.8
Zircon-48	283	1.57	157.0	2.0	156.7	9.4	160.0	150.0	157.0	2.0	100.2
Zircon-09	454	3.17	158.4	8.0	163.8	13.0	200.0	150.0	158.4	8.0	96.7
Zircon-21	221	2.09	158.6	3.1	154.0	12.0	100.0	190.0	158.6	3.1	103.0
Zircon-47	467	1.49	162.2	2.0	181.0	9.5	469.0	130.0	162.2	2.0	89.6
Zircon-75	110	1.34	163.3	4.6	161.0	17.0	100.0	210.0	163.3	4.6	101.4
Zircon-28	171	2.91	164.9	2.8	183.0	15.0	340.0	190.0	164.9	2.8	90.1
Zircon-02	3140	2.31	165.6	1.3	163.0	7.5	104.0	120.0	165.6	1.3	101.6
Zircon-79	300	1.39	166.2	4.1	163.8	11.0	90.0	130.0	166.2	4.1	101.5
Zircon-51	977	2.88	170.9	1.6	199.8	10.0	582.0	110.0	170.9	1.6	85.5
Zircon-26	157	0.97	271.7	4.0	279.0	15.0	290.0	140.0	271.7	4.0	97.4
Zircon-40	144	1.82	283.9	5.2	281.0	17.0	310.0	150.0	283.9	5.2	101.0
Zircon-80	1275	0.72	315.0	4.3	329.2	12.0	448.0	82.0	315.0	4.3	95.7
Zircon-38	101	1.61	614.0	8.4	646.0	29.0	750.0	130.0	614.0	8.4	95.0
Zircon-69	374	1.51	637.3	9.8	638.0	22.0	639.0	86.0	637.3	9.8	99.9
Zircon-70	167	1.16	1898.0	200.0	1921.0	200.0	1932.0	100.0	1932.0	100.0	98.8
Zircon-81	143	2.10	1671.0	36.0	1913.0	41.0	2204.0	59.0	2204.0	59.0	87.3

* indicates radiogenic Pb (corrected for common Pb).
All errors are reported at the 2σ level of uncertainty
Discordance filter of 20%

ANNEX C-3

BULK-ROCK GEOCHEMICAL RAW DATA (ACTLABS)

Analyte Symbol	SiO2	Al2O3	Fe2O3(T)	MnO	MgO	CaO	Na2O	K2O	TiO2	P2O5	LOI	Total	Sc
Unit Symbol	%	%	%	%	%	%	%	%	%	%	%	%	ppm
Detection Limit	0.01	0.01	0.01	0.001	0.01	0.01	0.01	0.01	0.001	0.01		0.01	1
Analysis Method	FUS-ICP	FUS-ICP	FUS-ICP	FUS-ICP	FUS-ICP	FUS-ICP	FUS-ICP	FUS-ICP	FUS-ICP	FUS-ICP	FUS-ICP	FUS-ICP	FUS-ICP
ROC-3G	75.96	11.41	3.22	0.029	1	1.15	2.03	1.95	0.483	0.04	3.45	100.7	11
ROC-4G	58.33	15.81	8.44	0.094	3.34	2.3	3.74	1.73	0.762	0.31	4.63	99.49	20
AGF-1G	65.78	15.06	6.14	0.055	1.85	1.02	1.7	2.12	0.68	0.1	5.65	100.2	17
AGF-2G	65.04	15.68	5.99	0.046	1.93	0.91	1.58	2.18	0.717	0.1	6.25	100.4	18
AGF-3G	64.47	14.74	6.27	0.037	1.92	1.07	1.4	2.19	0.665	0.1	5.93	98.79	17
CHC-1G	72.51	11.19	3.47	0.036	1.19	2.31	2.3	1.69	0.552	0.08	4.91	100.3	12
CHC-2G	67.12	14.14	5.51	0.076	2.05	2.57	2.61	1.59	0.589	0.13	3.74	100.1	14
LOR-1G	62.22	19.1	3.96	0.06	2.1	1.19	0.91	1.44	0.682	0.09	8.78	100.5	17
LOR-2G	63.58	18.09	3.9	0.059	2.16	1.49	0.9	1.38	0.692	0.08	8.35	100.7	18
ROC-2G	60.91	14.89	7.83	0.072	3.09	3.36	3.37	1.25	0.671	0.17	4.76	100.4	17
CHC-4G	70.28	11.87	5.59	0.05	1.68	1.28	2.17	1.63	0.563	0.07	5.14	100.3	14
PAL-2G	54.57	20.08	6.87	0.101	2.62	8.61	2.51	0.62	0.703	0.16	3.14	99.99	20
PAL-3G	59.85	16.06	5.93	0.103	2.51	4.99	2.08	1.23	0.89	0.08	6.59	100.3	21
CHC-3G	74.54	9.92	4.28	0.032	1.53	1.35	1.85	1.51	0.463	0.06	5.2	100.7	11
TRB-1G	64.86	13.93	6.07	0.075	1.92	1.68	1.77	1.82	0.742	0.09	7.01	99.96	18
ROC-1G	63.69	11.94	5.01	0.071	1.68	5.34	2.15	1.82	0.496	0.12	7.65	99.97	13
LOR-3G	49	16.6	15.35	0.319	1.49	3.04	1.95	1.63	0.805	0.21	9.69	100.1	17
ELS-1G	56.85	17.84	10.13	0.082	1.73	3.78	2.18	1.2	0.994	0.11	5.77	100.7	23
ELS-2G	54.93	18.04	7.41	0.137	3.23	6.11	2.73	1.09	0.99	0.09	4.78	99.54	25
PAL-1G	50.29	16.48	8.33	0.142	3.65	7.52	3.25	2.14	0.827	0.32	7.68	100.6	24

Analyte Symbol	Be	V	Ba	Sr	Y	Zr	Cr	Co	Ni	Cu	Zn	Ga	Ge
Unit Symbol	ppm	ppm	ppm	ppm	ppm	ppm	ppm	ppm	ppm	ppm	ppm	ppm	ppm
Detection Limit	1	5	2	2	1	2	20	1	20	10	30	1	1
Analysis Method	FUS-ICP	FUS-ICP	FUS-ICP	FUS-ICP	FUS-ICP	FUS-ICP	FUS-MS	FUS-MS	FUS-MS	FUS-MS	FUS-MS	FUS-MS	FUS-MS
ROC-3G	< 1	97	479	150	8	77	40	9	< 20	20	50	12	1
ROC-4G	2	163	478	311	21	138	60	14	< 20	10	100	26	< 1
AGF-1G	2	138	424	197	18	131	60	16	< 20	50	110	17	< 1
AGF-2G	2	143	401	125	18	129	60	14	30	30	110	17	1
AGF-3G	2	148	358	180	16	96	50	13	30	30	110	17	< 1
CHC-1G	1	101	438	174	13	111	40	11	< 20	30	80	12	< 1
CHC-2G	1	123	506	322	18	140	40	29	< 20	20	80	16	< 1
LOR-1G	1	135	360	131	20	137	50	18	30	60	120	19	< 1
LOR-2G	1	143	361	142	21	140	50	13	< 20	50	100	20	< 1
ROC-2G	1	138	312	324	15	111	50	47	< 20	10	80	16	2
CHC-4G	1	135	447	131	13	86	40	10	< 20	50	80	14	< 1
PAL-2G	1	137	243	612	17	149	< 20	26	< 20	30	80	19	1
PAL-3G	1	135	260	242	27	189	< 20	15	< 20	30	60	17	< 1
CHC-3G	1	109	367	138	11	75	40	15	< 20	30	80	11	< 1
TRB-1G	1	131	411	219	20	144	60	17	20	20	90	15	< 1
ROC-1G	1	108	448	628	17	93	40	9	< 20	20	90	13	< 1
LOR-3G	1	139	453	314	19	167	40	25	< 20	30	80	17	< 1
ELS-1G	2	188	492	417	19	215	70	32	60	40	100	19	1
ELS-2G	< 1	207	357	560	18	99	40	27	< 20	80	110	17	1
PAL-1G	1	229	556	725	16	120	50	26	< 20	110	110	16	< 1

Analyte Symbol	As	Rb	Nb	Mo	Ag	In	Sn	Sb	Cs	La	Ce	Pr	Nd
Unit Symbol	ppm	ppm	ppm	ppm	ppm	ppm	ppm	ppm	ppm	ppm	ppm	ppm	ppm
Detection Limit	5	2	1	2	0.5	0.2	1	0.5	0.5	0.1	0.1	0.05	0.1
Analysis Method	FUS-MS	FUS-MS	FUS-MS	FUS-MS	FUS-MS	FUS-MS	FUS-MS	FUS-MS	FUS-MS	FUS-MS	FUS-MS	FUS-MS	FUS-MS
ROC-3G	< 5	60	3	< 2	< 0.5	< 0.2	< 1	< 0.5	2.1	5.8	13.9	1.78	7.1
ROC-4G	5	55	5	< 2	< 0.5	< 0.2	< 1	< 0.5	1.7	32.9	64.7	6.99	27.8
AGF-1G	< 5	84	5	< 2	< 0.5	< 0.2	1	< 0.5	5.5	21.5	49.7	5.03	20.2
AGF-2G	< 5	88	5	< 2	< 0.5	< 0.2	2	< 0.5	5.3	20.3	51.8	5.21	20.4
AGF-3G	< 5	86	4	< 2	< 0.5	< 0.2	1	< 0.5	5.2	18.2	45.5	4.47	17.1
CHC-1G	< 5	59	4	< 2	< 0.5	< 0.2	< 1	< 0.5	3.6	15.7	34.5	4.09	16
CHC-2G	< 5	48	3	< 2	< 0.5	< 0.2	< 1	< 0.5	1.6	18.2	39.8	4.53	17.3
LOR-1G	< 5	49	5	< 2	< 0.5	< 0.2	2	< 0.5	2.8	24.1	52.5	6.08	24.8
LOR-2G	< 5	48	5	< 2	< 0.5	< 0.2	1	< 0.5	2	23	48.9	5.6	22.2
ROC-2G	< 5	43	5	< 2	< 0.5	< 0.2	1	< 0.5	1.3	15.7	35.6	4.25	17.5
CHC-4G	7	51	2	< 2	< 0.5	< 0.2	3	< 0.5	3	10.4	24.2	2.59	10.6
PAL-2G	< 5	18	5	< 2	< 0.5	< 0.2	< 1	< 0.5	0.6	18	40.7	5.28	22.7
PAL-3G	< 5	55	6	< 2	0.5	< 0.2	2	< 0.5	3.1	20.8	44.4	5.59	23.6
CHC-3G	< 5	48	3	< 2	< 0.5	< 0.2	< 1	< 0.5	2.4	9.9	22.5	2.59	10.2
TRB-1G	< 5	64	5	< 2	< 0.5	< 0.2	1	< 0.5	3.1	18.8	42	4.96	20
ROC-1G	< 5	54	3	< 2	< 0.5	< 0.2	< 1	< 0.5	2.9	16.3	35.2	4.16	16.9
LOR-3G	< 5	39	8	< 2	< 0.5	< 0.2	1	< 0.5	1.3	18.5	41.8	4.89	19.7
ELS-1G	< 5	43	8	< 2	0.6	< 0.2	2	< 0.5	2.5	25	57	6.87	28.5
ELS-2G	< 5	23	3	< 2	< 0.5	< 0.2	< 1	< 0.5	0.6	9.4	24.3	3.37	15.3
PAL-1G	< 5	71	3	< 2	< 0.5	< 0.2	1	< 0.5	6.2	22.9	50.8	6.42	27.4

Analyte Symbol	Sm	Eu	Gd	Tb	Dy	Ho	Er	Tm	Yb	Lu	Hf	Ta
Unit Symbol	ppm	ppm	ppm	ppm	ppm	ppm	ppm	ppm	ppm	ppm	ppm	ppm
Detection Limit	0.1	0.05	0.1	0.1	0.1	0.1	0.1	0.05	0.1	0.01	0.2	0.1
Analysis Method	FUS-MS	FUS-MS	FUS-MS	FUS-MS	FUS-MS	FUS-MS	FUS-MS	FUS-MS	FUS-MS	FUS-MS	FUS-MS	FUS-MS
ROC-3G	1.8	0.5	1.5	0.3	1.7	0.3	1	0.18	1.2	0.17	1.7	0.3
ROC-4G	5.7	1.37	4.7	0.6	3.9	0.7	2.3	0.34	2	0.32	3.3	0.4
AGF-1G	4.3	1	3.7	0.6	3.9	0.7	2.1	0.32	2.1	0.33	3.4	0.5
AGF-2G	4.4	1.01	4.1	0.6	3.9	0.8	2.5	0.35	2.4	0.37	2.8	0.6
AGF-3G	3.6	0.85	3.3	0.5	3.1	0.7	2	0.31	2.1	0.32	2.2	0.5
CHC-1G	3.5	0.81	3.2	0.5	3	0.6	1.8	0.27	1.7	0.28	2.6	0.4
CHC-2G	4	0.99	3.3	0.5	3.2	0.6	2	0.28	1.8	0.29	3.2	0.3
LOR-1G	5.3	1.28	4.9	0.7	4.3	0.9	2.4	0.35	2.3	0.35	3.3	0.5
LOR-2G	4.7	1.2	4.2	0.7	4	0.8	2.2	0.31	2	0.35	3.6	0.3
ROC-2G	3.9	1.15	3.5	0.5	3.2	0.6	1.8	0.26	1.7	0.26	2.5	0.4
CHC-4G	2.6	0.63	2.4	0.4	2.5	0.5	1.5	0.24	1.6	0.26	2	0.2
PAL-2G	4.8	1.51	4.1	0.6	3.5	0.7	2	0.28	1.8	0.27	3.2	0.3
PAL-3G	5.3	1.39	5	0.8	4.9	1	3	0.44	2.9	0.44	4.2	0.5
CHC-3G	2.3	0.61	2.1	0.3	2.1	0.4	1.2	0.19	1.3	0.19	1.7	0.3
TRB-1G	4.5	1.06	4.1	0.7	4	0.8	2.4	0.37	2.4	0.36	3.3	0.5
ROC-1G	3.6	0.84	3.1	0.5	3	0.6	1.9	0.27	1.9	0.29	2	0.3
LOR-3G	4.4	1.25	3.9	0.7	3.9	0.8	2.3	0.33	2.2	0.33	4	0.6
ELS-1G	5.8	1.6	4.8	0.7	4.1	0.8	2.2	0.35	2.3	0.35	4.6	0.6
ELS-2G	3.8	1.31	3.9	0.6	3.8	0.8	2.2	0.33	2.2	0.33	2.3	0.2
PAL-1G	5.6	1.57	4.4	0.6	3.2	0.6	1.7	0.25	1.5	0.22	2.8	0.2

Analyte Symbol	W	Tl	Pb	Bi	Th	U
Unit Symbol	ppm	ppm	ppm	ppm	ppm	ppm
Detection Limit	1	0.1	5	0.4	0.1	0.1
Analysis Method	FUS-MS	FUS-MS	FUS-MS	FUS-MS	FUS-MS	FUS-MS
ROC-3G	28	0.2	9	< 0.4	5	1.8
ROC-4G	31	< 0.1	11	< 0.4	7.8	2.1
AGF-1G	23	3.7	18	< 0.4	8	2.3
AGF-2G	9	0.4	11	< 0.4	8.4	2.3
AGF-3G	7	0.4	11	< 0.4	7.8	2.1
CHC-1G	10	0.2	8	< 0.4	5.7	1.7
CHC-2G	192	1.4	12	< 0.4	5.9	1.9
LOR-1G	12	0.2	15	< 0.4	6.7	2.1
LOR-2G	42	0.4	19	< 0.4	6.3	1.8
ROC-2G	215	< 0.1	8	< 0.4	4.1	1.3
CHC-4G	10	0.2	14	< 0.4	5.4	2
PAL-2G	77	< 0.1	8	< 0.4	4.3	0.9
PAL-3G	37	0.2	11	< 0.4	6.8	1.8
CHC-3G	23	0.2	7	< 0.4	4.2	1.7
TRB-1G	23	0.3	5	< 0.4	6.4	1.8
ROC-1G	6	0.2	7	< 0.4	4.9	2.1
LOR-3G	72	< 0.1	10	< 0.4	6.1	1.6
ELS-1G	12	0.2	14	< 0.4	7.7	2.1
ELS-2G	10	< 0.1	6	< 0.4	2.2	0.7
PAL-1G	4	0.1	9	< 0.4	6.1	1.8

ANNEX C-4

DETRITAL ZIRCON U-PB GEOCHRONOLOGIC ANALYSES BY USING LA-ICP-MS & LA-MC-ICP-MS ANALYSIS

https://drive.google.com/file/d/1bXbaXLITtjRSo70QLzoLKiFUhu-o25xR/view?usp=sharing

ANNEX C-5

INPUT DATA FOR BACKSTRIPPING CALCULATION

Outcrop Data (proximal foredeep)

Units	Age Base (Ma)	Age Top (Ma)	Duration (Ma)	Thickness (m)	Water depth avg (m)	Surface porosity (%)	Compaction rate (m^{-1})	Sedim density (kg/m^{-3})	rock_type	Reference	Subsid rate (mm/yr)
Rodados	15	0	15	225	-500	0.428	0.000614	2670	ss_c		
Palomares	19.3	15	4.3	370	-100	0.428	0.000614	2670	ss_c		0.002
El Salto	29.8	19.3	10.5	715	-50	0.428	0.000614	2670	ss_c	Gallagher and Lambeck, 1989	0.001
Loreto	40	34.1	5.9	1025	40	0.49	0.00027	2650	ss		0.002
Leña Dura	43	40	3	667	250	0.63	0.00051	2720	sh	Sclater and Christie, 1980	0.030
Tres Brazos	48.6	43	5.6	830	105	0.49	0.00027	2650	ss		0.011
Agua Fresca	54.5	48.6	5.9	2100	380	0.63	0.00051	2720	sh		-0.008
Chorrillo Chico	65.4	54.5	10.9	1140	1000	0.56	0.00039	2680	sh_ss		0.11
Rocallosa	73	65.4	7.6	376	120	0.56	0.00039	2680	sh_ss		-0.013
Fuentes	76	73	3	2010	380	0.63	0.00051	2720	sh	Sclater and Christie, 1980	0.117
Barcárcel	80	76	4	545	750	0.49	0.00027	2650	ss		-0.025
Latorre	96	80	16	725	1000	0.56	0.00039	2680	sh_ss		0.022
Canal Bertrand	114	96	18	900	1000	0.56	0.00039	2680	sh_ss		0.064
Erezcano	145	114	31	867	380	0.63	0.00051	2720	sh	Sclater and Christie, 1980	0.035

Manzano 7 Data (distal foredeep)

Units	Age Base (Ma)	Age Top (Ma)	Duration (Ma)	Thickness (m)	Water depth avg (m)	Surface porosity (%)	Compaction rate (m^{-1})	Sedim density (kg/m^{-3})	rock_type	Reference	Subsid rate (mm/yr)
Rodados	15	0	15	225	-500	0.428	0.000614	2670	ss_c		-0.021
Palomares	19.3	15	4.3	200	-100	0.49	0.00027	2650	ss		
El Salto	34.1	19.3	14.8	371	10	0.49	0.00027	2650	ss	Gallagher and Lambeck, 1989	-0.047
Loreto	40	34.1	5.9	1115	750	0.56	0.00039	2680	sh_ss		-0.102
Leña Dura + Tres	48.6	40	8.6	640	1500	0.63	0.00051	2720	sh	Sclater and Christie, 1980	-0.047
Agua Fresca	54.5	48.6	5.9	1960	2000	0.63	0.00051	2720	sh		0.254
Chorrillo Chico	65.4	54.5	10.9	485	1200	0.56	0.00039	2680	sh_ss		0.037
K Sup	100	65.4	34.6	1700	800	0.63	0.00051	2720	sh		0.043
Kinf	129	100	29	600	200	0.63	0.00051	2720	sh	Sclater and Christie, 1980	0.021
Jr-Kinf	150	129	21	250	50	0.63	0.00051	2720	sh		0.019

PINGUINO-ALMEJA Data (forebulge)

Units	Age Base (Ma)	Age Top (Ma)	Duration (Ma)	Thickness (m)	Water depth avg (m)	Surface porosity (%)	Compaction rate (m^{-1})	Sedim density (kg/m^{-3})	rock_type	Reference	Subsid rate (mm/yr)
Rodados	15	0	15	225	-250	0.428	0.000614	2670	ss_c		-0.016
Palomares + Fila	25	15	10	619	30	0.49	0.00027	2650	ss		0.013
Bahia Inutil Gro	65.4	25	40.4	567	90	0.56	0.00039	2680	sh_ss	Gallagher and Lambeck, 1989	0.008
Lutitas Arenosas	85	65.4	19.6	284	75	0.56	0.00039	2680	sh_ss		0.006
Lutitas gris verd	100	85	15	200	125	0.63	0.00051	2720	sh	Sclater and Christie, 1980	0.017
Margas + Lutitas	129	100	29	242	75	0.4	0.0006	2710	lm		0.006
Springhill + Estra	145	129	16	104	20	0.49	0.00027	2650	ss	Sclater and Christie, 1980	0.008

Coarse sandstone (ss_c); Sandstone (ss); Shaly Sandstone (sh_ss); Shale (sh); Limestone (lm)

ANNEX D-1

APATITE FISSION TRACKS COUNTING RAW DATA

https://drive.google.com/file/d/1X1DAA9SFQ4j6N5tsJLLyDIwDtvlsiNG7/view?usp=sharing

ANNEX D-2

DETAILED AHE ANALYSIS BY BY SAMPLE

The ES1 sample (n=5 grains) yielded a broad span of AHe dates younger (n=2) and older (n=3) than the maximum depositional age or biostratigraphic age for the studied unit (Fig. 1a). The variation in dates is far greater than can be accounted for by analytical uncertainty (8%, 2σ). The aliquots ES1-A and ES1-D yield the lower values of effective uranium content (eU) of 2.5 ppm and 5.6 ppm, respectively; but AHe dates as older as those with a higher eU. ***This pattern can reflect some alpha implantation by neighbouring minerals***. Without considering the two aliquots with possible He implantation problems, there is a positive correlation (R^2=0.64) between AHe dates and eU, ***which implies an episode of partial He loss*** caused by either radiation damage increasing He retentivity or because the sample has not achieved a temperature enough (burial) to diffuse out He. The latter is the most likely explanation, as the ES-1 sample was buried to depths ~1.3 km (~40 °C, under an average geothermal gradient). On the other hand, AHe dates correlate positively with Rs (Fig. 1b; R2=0.91) when excluding aliquot ES1-A. It is striking that aliquot ES1-A despite having one of the most greater crystal sizes (Rs=60) yield a very young age. This fact confirms the need to exclude this aliquot of further modelling/analysis. Thus, the older population can be momentarily disregarded, and the younger AHe dates can be interpreted to represent the most recent signal of exhumation at 19.1 ± 1.5 Ma. Although this assumption can be equivocal (considering the partial reset of the sample), the fact that this age overlaps well within an AFT cooling age of 20.3 ± 8.4 Ma from the same sample supports an interpretation of a possible exhumation event by this time.

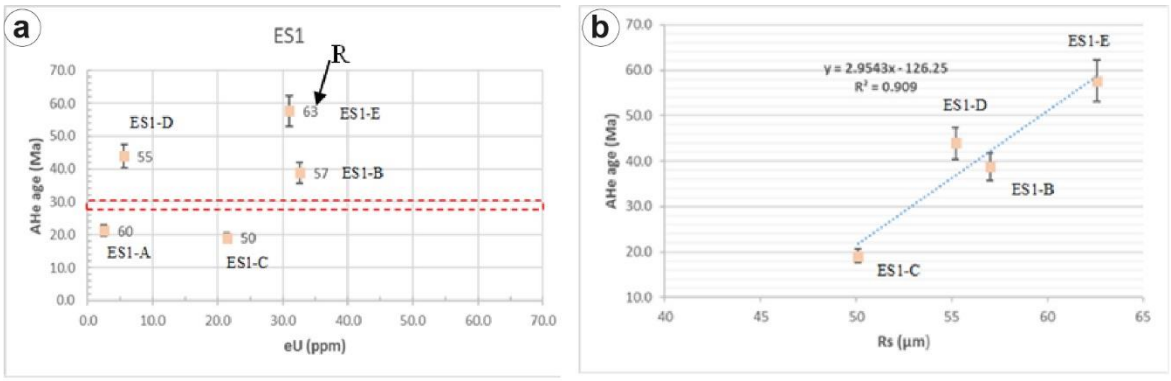

Fig. 1. (a) eU vs Age plot. (b) Rs vs Age plot. Red dotted boxes signal sample maximum depositional or biostratigraphic age.

The **PHH1** and **PHH2** samples are combined because they are spaced away by <60 m (stratigraphic) and belong to the same Palomares Formation. Six of the seven apatites analysed are older than the maximum depositional age for the unit (Fig. 2). A systematic correlation among grain size (Rs), effective Uranium content (eU), and AHe dates are nonexistent in this dataset. The set of older AHe dates is interpreted as a provenance signal since the studied unit has not reached a burial enough (~100 m) to reset. The weighted mean AHe date is 19.9 ± 1.3 Ma, coincident with a magmatic and volcanic event by 19-20 Ma, which originated this volcaniclastic unit.

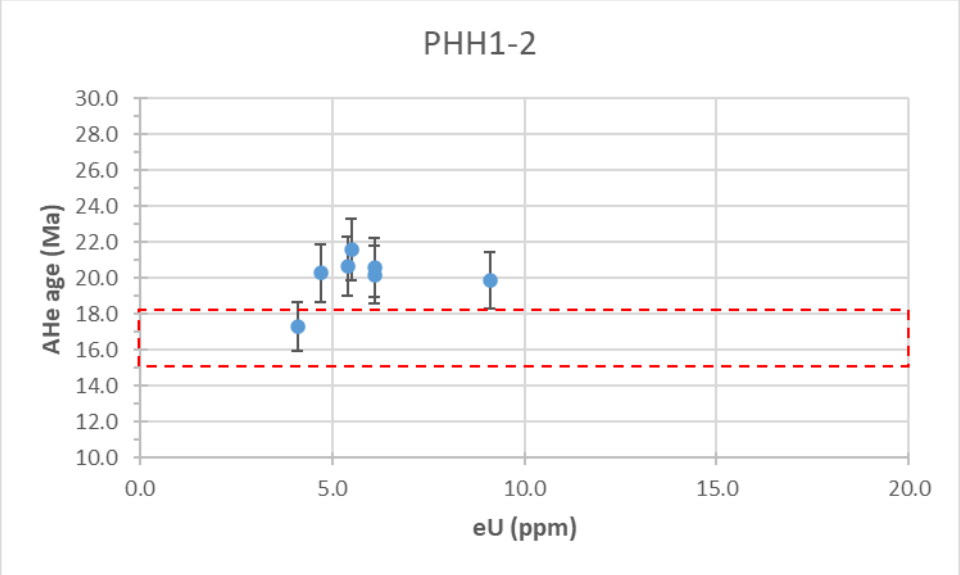

Fig. 2. eU vs Age plot. Red dotted boxes signal sample maximum depositional or biostratigraphic age.

The ZRT1 sample (n=3 grains) yielded both AHe dates younger (n=2) and older (n=1) than the maximum depositional age or biostratigraphic age for the studied unit (Fig. 3). The overall apatites show very low values of Uranium (< 4 ppm). However, aliquot ZRT1-D exhibits the lowest eU value (2.2 ppm) and the oldest AHge date (31 Ma) of the sample, ***which suggest an alpha implantation problem.*** The sample does not display any correlation between crystal size (Rs) and AHe dates. However, there is a strong correlation between AHe dates and eU (R^2=1; if discarding the aliquot ZRT1-D), suggesting ***a thermal history involving long periods in the He-PRZ*** (~40-80°C). The young clustered population of AHe dates yield a weighted mean age of 20.5 ± 6.7 Ma, overlapping consistently with an AFT cooling age (26.9 ± 7) of another nearby sample from the same stratigraphic unit. This age can be interpreted as a signal of exhumation.

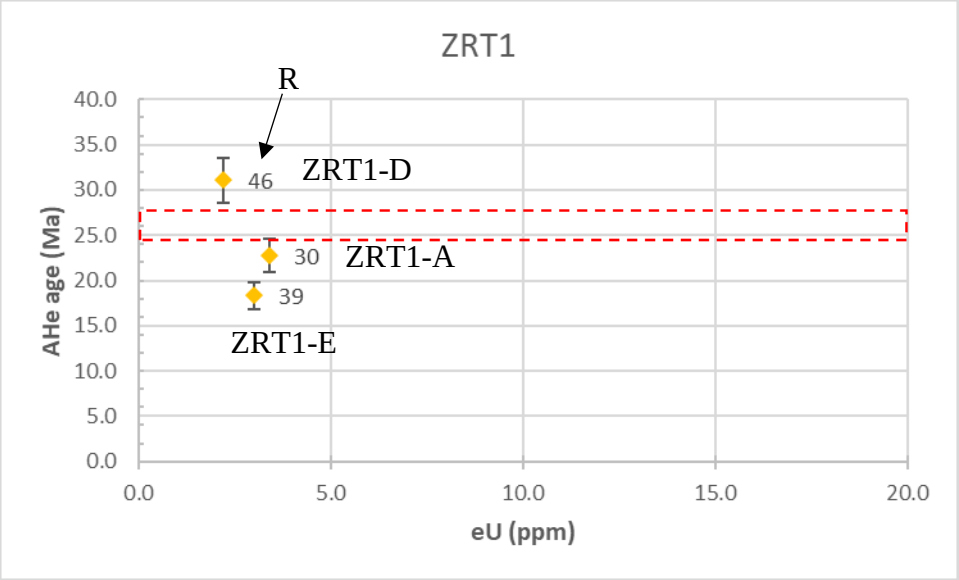

Fig. 3. eU vs Age plot. Red dotted boxes signal sample maximum depositional or biostratigraphic age

The ZRPL1 sample (n=3 grains) yielded a broad span of AHe dates both younger (n=2) and within/older (n=1) than the maximum depositional age (Fig. 4). A correlation between crystal size (Rs) and AHe dates is nonexistent, but it is noteworthy that while the crystal size is identical for aliquots ZRPL1-B and ZRPL1-A, the uranium content varies greatly. This observation may warn of a likely He retentivity due to radiation damage (triggering a higher closure temperature) in the aliquot ZRPL1-A. It is observed a strong positive correlation between eU and AHe dates (R^2=0.94), suggesting a very slow cooling or prolonged residence in the He-PRZ for this sample. The latter can be supported by the fact that the same sample for AFT shows evidence of not resetting, which can assume that this sample has actually resided at depths with temperatures between 40-65°C probably for a long time.

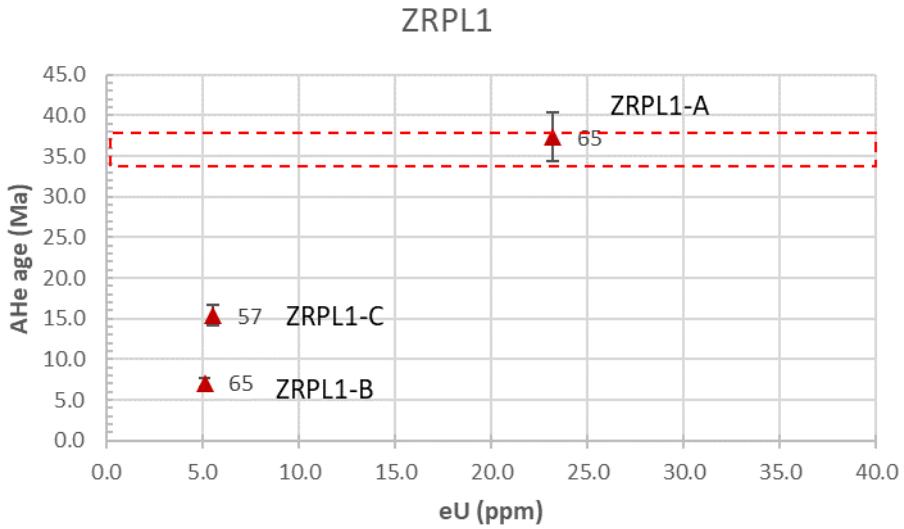

Fig. 4. eU vs Age plot. Red dotted boxes signal sample maximum depositional or biostratigraphic age.

All the AHe dates for the five apatite grains from **Sample ZVD1** are significantly younger than the maximum depositional age (37.4 ± 0.73; Fig. 5). The fact that AHe dates are significantly younger than MDA suggests that this sample was entirely thermally reset and all these dates represent a signal of recent cooling. However, two clusters of AHe dates are observed: one, characterised by higher eU and younger AHe dates; another, characterised by lower eU and older AHe dates. Some alpha implantation problems can be envisaged for the latter cluster, but the aliquot ZDV1-D appears to be most problematic. A strong correlation between AHe and eU (R^2=0.86) and crystal size (R^2=0.81) further suggest a long-term, low-T thermal history for this sample. The youngest four aliquots' weighted mean age (excluding ZVD1-D) is used to approximate the exhumation timing at 7.1 ± 3.9 Ma.

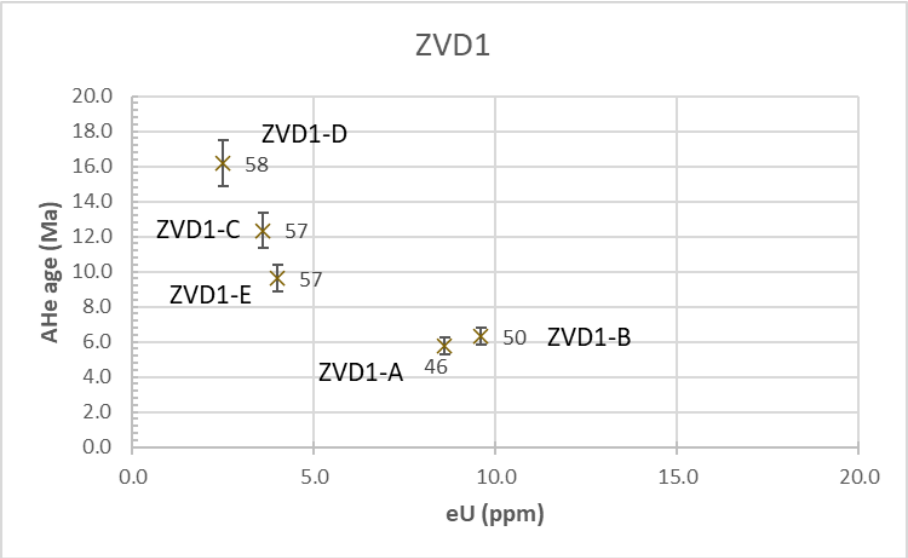

Fig. 5. eU vs Age plot.

The sample ZDG1 (n=2 grains) presents AHe dates significantly younger than the maximum depositional age (42.8 ± 0.8 Ma) spanning from 19.5 ± 1.6 Ma to 7.1 ± 0.6 Ma (Fig. 6). However, the older AHe date (aliquot ZDG1-B) present the lowest eU value, and the crystal size does not justify such an old date. Therefore, this grain is suspected of having an alpha implantation problem. In this case, the remaining AHe dates are interpreted as a signal of recent cooling at 7.1 ± 0.6 Ma, which is consistent with the exhumation timing of sample ZVD1 belonging to the upper part of the same unit.

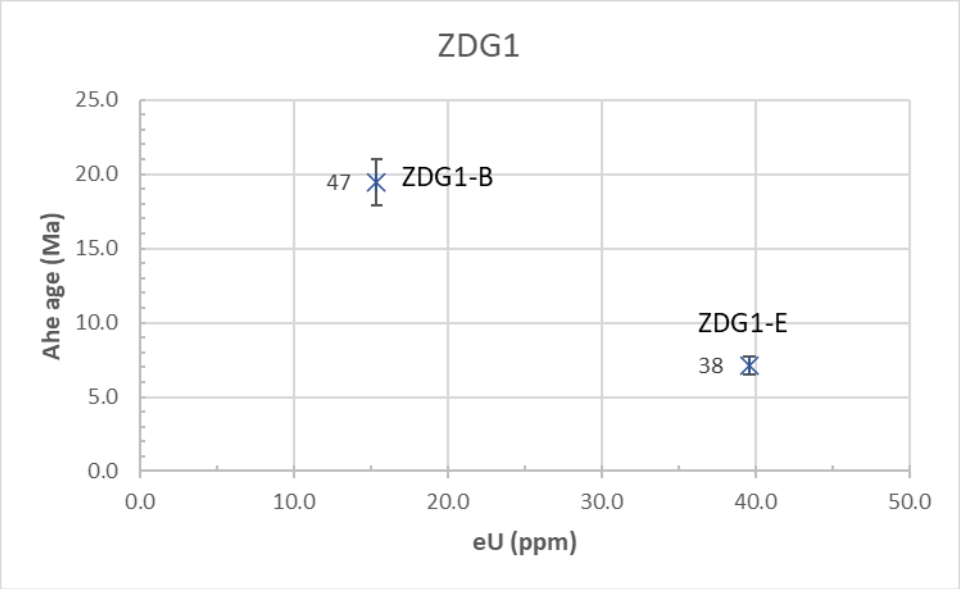

Fig. 6. eU vs Age plot.

The TBDH1 sample (n=2 grains) presents AHe significantly younger than the maximum depositional age (44-42 Ma) yield narrow spectra of dates of 15.8 ± 1.3 Ma to 11.5 ± 0.9 Ma (Fig. 7). There exists a correlation positive between AHe and crystal size, but it is not significant. On the other hand, there is a correlation negative between AHe and eU. The aliquot TBDH1-B presents the lower eU value and the older AHe date, suspecting having alpha implantation problems. Additionally, the variation in dates between the two aliquots is far greater than can be accounted for by analytical uncertainty (8%, 2σ). Although it may be equivocal, the signal of recent cooling is interpreted at 11.5 ± 0.9 Ma. This date's choice is also supported by consistency with the cooling age interpreted for the following RB1 sample placed at the same area and supposed to have experienced a similar thermal history.

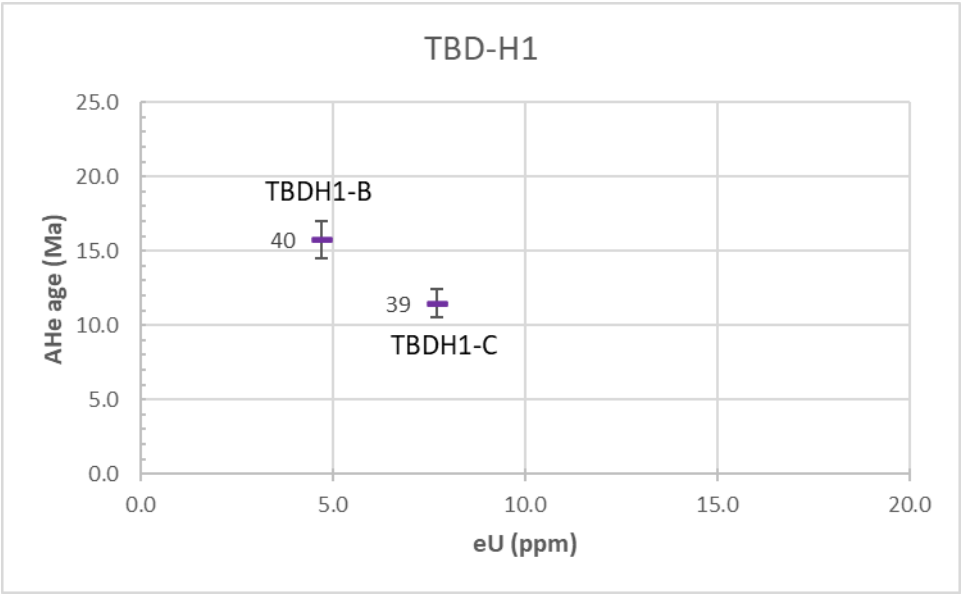

Fig. 7. eU vs Age plot.

The RB1 sample (n=5 grains) presents AHe significantly younger than the maximum depositional age (64.7 ± 0.7 Ma) grouped into two clusters. The first cluster yielded higher eU (>20 ppm) and younger dates (Fig. 8), presenting neither correlation among AHe, eU, or Rs. The second cluster yield lower eU (<15 ppm) and older dates, presenting a robust negative correlation among AHe, eU and Rs. In this second cluster, the aliquot RB1-E appears to be the most affected by alpha implantation as has the lowermost Rs and eU but the oldest AHe date. The remaining aliquots' weighted mean age (excluding RB1-E) is used to approximate the exhumation timing at 12.6 ± 6.4 Ma.

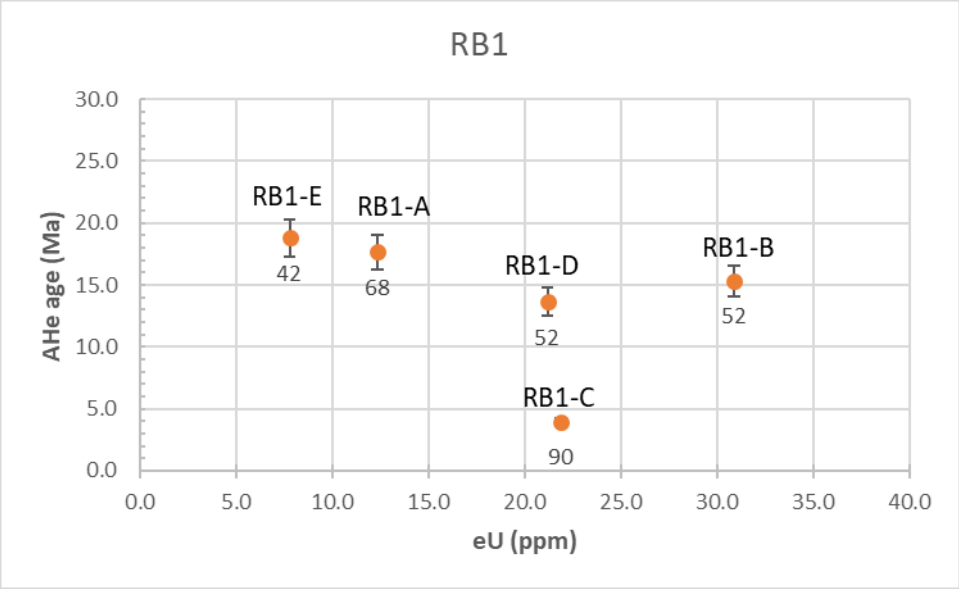

Fig. 8. eU vs Age plot.

All the AHe dates for the three apatite grains from **Sample CCK1** are significantly younger than the maximum depositional age (66.5 ± 0.83; Fig. 9) suggesting that this sample was entirely thermally reset and all these dates represent a signal of recent cooling. There is a strong correlation positive between AHe and eU (R^2=0.92) and an acceptable one between AHe and Rs (R^2=0.66). The latter observations suggest a very slow cooling or prolonged residence in the He-PRZ for this sample. The calculated weighted mean age of 11.3 ± 3.8 is interpreted as the most recent exhumation event.

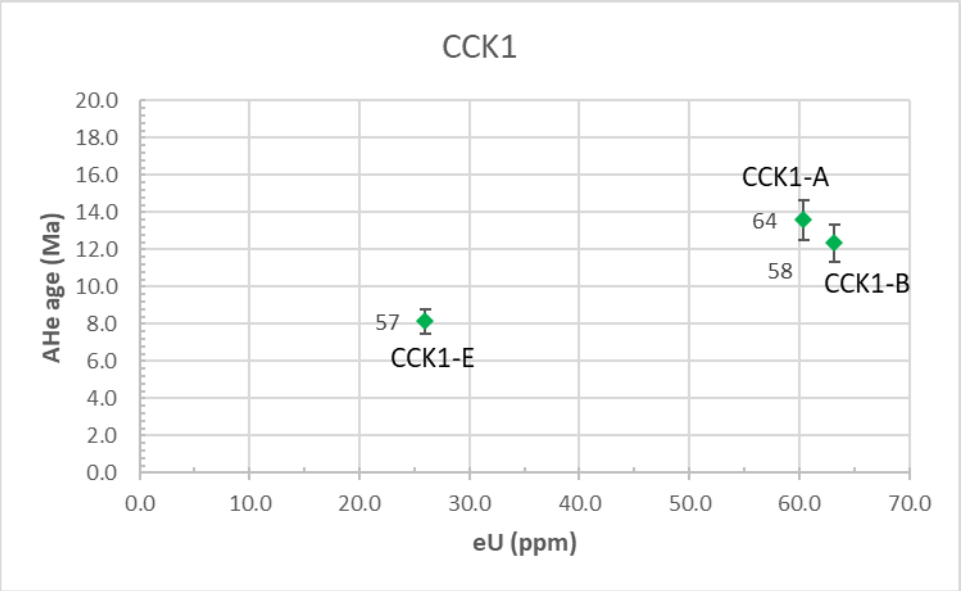

Fig. 9. eU vs Age plot.

The ZLP1 sample (n=5 grains) presents AHe significantly younger than the maximum depositional age (67.7 ± 1.2 Ma) grouped into two clusters according to the effective uranium content (Fig. 10). From the cluster with lower uranium content (<15 ppm), the aliquot ZLP1-D appears to be the most affected by alpha implantation as has the lowermost eU and the oldest AHe date for the higher Rs in the sample. There is a weak to nonexistent correlation between AHe and eU in the remaining aliquots. The weighted mean age (excluding ZLP1-D) is used to approximate the exhumation timing at 10.5 ± 3.4 Ma.

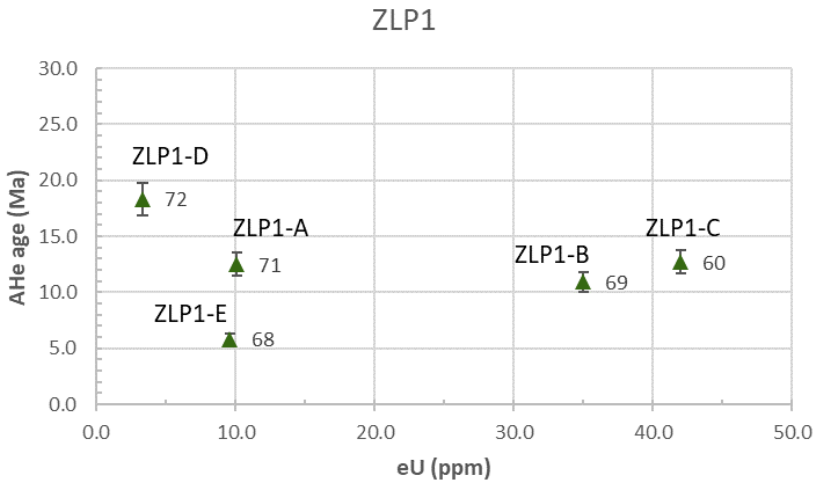

Fig. 10. eU vs Age plot.

The ZPR1 sample (n=5 grains) presents AHe significantly younger than the maximum depositional age (73.5 ± 1.3 Ma) spanning from 6.2 ± 0.5 Ma to 14 ± 1.1 Ma (Fig. 11) which in most cases is explained by analytical uncertainty (8%, 2σ). There is no evidence to suspect any alpha implantation or radiation damage in these grains, as a correlation among AHe, eU or Rs is nonexistent. However, it is noteworthy that aliquot ZPR1-D being the grain with the highest eU is at the same time the youngest. The weighted mean age considering all the aliquots is 9.7 ± 2.5 Ma, which does not differ much (within the analytical uncertainty) from that age calculated when discarding the aliquot ZPR1-D.

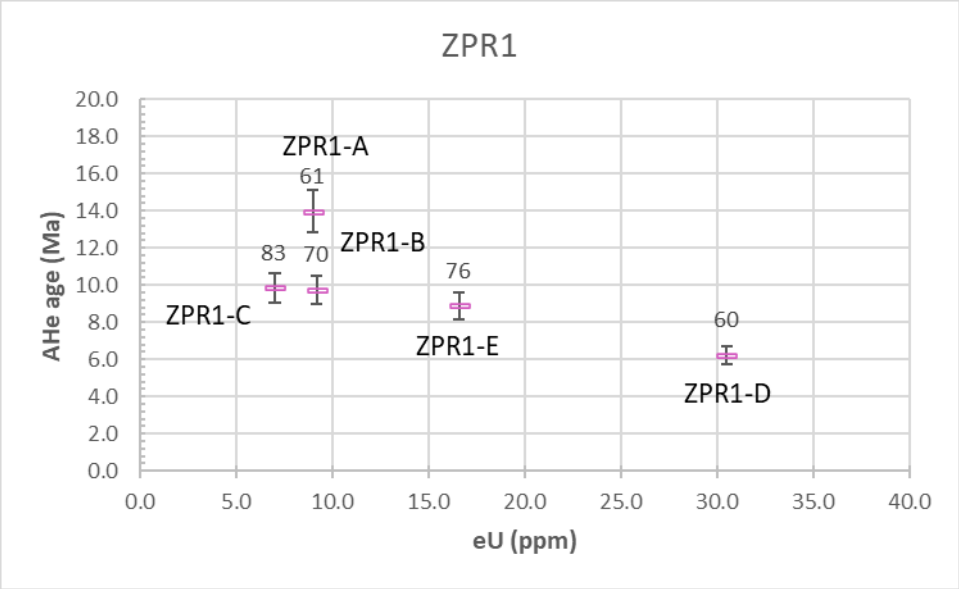

Fig. 11. eU vs Age plot.